Evolution of mafic rock-types of the Kolvitsa Complex, Kola Peninsula (Russia): Implications for the metamorphic evolution of the Kolvitsa Belt and characterisation of related fluid-rock interactions

Dissertation

zur

Erlangung des Doktorgrades (Dr. rer. nat.)

der

Mathematischen-Naturwissenschaftlichen Fakultät

der

Rheinischen Friedrich-Wilhelms-Universität Bonn

vorgelegt von

Nicol Susann Ecke

Bonn 2004

TABLE OF CONTENTS

DANKSAGUNG

GENERAL INTRODUCTION 1

1. Reaction textures in mafic rock-types: Implication for the metamorphic evolution of the Kolvitsa Belt, Kola Peninsula (Russia)

1.1. Introduction 3

1.2. Lapland-Kola Orogen 4

1.3. Geological setting of the Kolvitsa Belt 5

1.4. Petrography, microstructures and mineral reactions 8

1.4.1. Granulite-facies assemblages from the south-eastern boundary of the Kolvitsa Massif 8

1.4.2. Corona reactions involving garnet 10

1.4.2.1. Garnet-consuming reaction textures from the south-eastern boundary of the Kolvitsa Massif 10

1.4.2.2. Garnet-producing corona textures from the central part of the Kolvitsa Massif 12

1.4.3. Amphibolite-facies assemblages 14

1.5. Mineral chemistry 17

1.5.1. Garnet 17

1.5.2. Clinopyroxene 20

1.5.3. Orthopyroxene 24

1.5.4. Plagioclase 27

1.5.5. Amphibole 31

1.5.6. Fe-Ti-oxides & minerals 33

1.6. Temperature and pressure estimates 35

1.6.1. Granulite-facies stage for the mylonitic rock types from the south-eastern boundary of the Kolvitsa Massif 35

1.6.2. Decompressional stage in mafic rock types from the south-eastern boundary of the Kolvitsa Massif 45

1.6.3. Garnet-producing corona textures in rock types from the central Kolvitsa Massif 51

1.6.4. Amphibolite-facies stage 54

1.7. Discussion 59

1.7.1. Interpretation of results – P-T path 59

1.7.2. Age constraints 60

1.8. Conclusion 61

TABLE OF CONTENTS

2. Characterisation of fluid-rock interactions during exhumation of mafic granulites of the Kolvitsa-Umba suture zone, Kola Peninsula (Russia)

2.1. Introduction 63

2.2. Geological setting 64

2.3. Examples of fluid infiltration zones
2.3.1. Description of the examined case studies 67

2.4. Major and trace element geochemistry 72
2.4.1. Analytical techniques 72
2.4.2. Geochemical characterisation of the magmatic protoliths
2.4.3. Geochemical characterisation of the hydration zones 80
2.4.4. Mass balance 85
2.4.5. Volume of fluids and estimates of fluid influx 94

2.5. Stable isotope geochemistry 98
2.5.1. Analytical technique 98
2.5.2. Results 98
2.5.3. Interpretation

2.6. Age determination and isotopic data 107
2.6.1. U-Pb dating of titanite
2.6.1.1. Analytical technique 108
2.6.1.2. Results 108
2.6.1.3. Interpretation 111
2.6.2. $^{40}Ar/^{39}Ar$ mineral ages 112
2.6.2.1. Analytical technique 112
2.6.2.2. Age spectra of hornblende 112
2.6.2.3. Interpretation 120
2.6.3. Cooling history and P-T-t evolution 121
2.6.4. Sm-Nd systematics 124
2.6.4.1. Analytical technique 124
2.6.4.2. Results 124

2.7. Conclusions 127

2.8. References 129

****
Verstand wird Russland nie verstehn,
Normales Maß will auch nichts taugen:
Es hat ein sonderbares Wesen –
An Russland kann man einzig glauben.

28. November 1866, Fjodor Tjutčev

****
Умом Россию не понять,
Аршином общим не измерить:
У ней особенная стать –
В Россию можно только верить.

ноябрь 28тю 1866, Фйодор Тйутцев

Danke!

Zum Gelingen dieser Arbeit haben viele Leute beigetragen und allen von ihnen gilt mein persönlicher Dank!
Zu Anfang möchte ich den Initiatoren dieses Deutsch-Russischen Projekts, Prof. Dr. M. Raith, Prof. Dr. S. Hoernes, Prof. Dr. V. Glebovitsky und Dr. D. Krylov danken, ohne die diese Arbeit nicht möglich gewesen wäre. Besonders herzlich möchte ich meinem Doktorvater Prof. Dr. M. Raith für die Unterstützung während dieser Arbeit, die kritischen Denkanstöße und die "Ausflüge" in Kunst, Kultur und Literatur danken. Bei den Geländekampagnen auf der Kola Halbinsel stand er mir aufmunternd und tatkräftig zur Seite. In diesem Zusammenhang möchte ich mich auch bei Prof. Dr. S. Hoernes, Ralf Simmat und Kay Scheffler für ihre Hilfe während der Geländearbeiten bedanken.
Für die herzliche Gastfreundschaft und für die Einblicke in ihre langjährige geologische Erfahrung auf der Kolahalbinsel möchte ich Dr. Mischa Yefimov und Dr. Mascha Bogdanova danken. Bei Dr. Dima Krylov möchte ich mich für seine Gastfreundschaft in St. Petersburg und seine Hilfe bei der Sauerstoffisotopenanalytik bedanken. Mischa Yefimov, dem Kapitän der Dora, Walodja und Sergej gilt ein besonderes Dankeschön, da sie uns durch das stürmische Weiße Meer immer sicher ans Land gebracht haben. Für die Verpflegung, weit ab jeglicher menschlicher Zivilisation, sei Mascha und Sergej gedankt, die mit gesammelten Blaubeeren und Pilzen, Blinis, Bortsch und Kascha hervorragend für unser leibliches Wohl gesorgt haben.
Bei meinen russischen Kollegen am Institut für Präkambrische Geologie und Geochronologie in St. Petersburg möchte ich mich für die Sm-Nd and U-Pb Analytik bedanken. Ein besonderer Dank gilt dabei Dr. Viktor Kovach und Dr. Katja Salnikova.
Prof. Dr. W. Frank möchte ich für die Ar-Ar Analytik am Geologischen Institut in Wien danken und dafür, dass er mir ganz unkompliziert ein Quartier in Wien gegeben hat.
Meinem Co-Korrektor, Dr. Ingo Braun, danke ich für die zügige Durchsicht dieser Arbeit. Bei Andrea Beer möchte ich mich für die Präparation der allseits gelobten Dünnschliffe, bei Dorothée Dohle für die Umsätze an der Fluoranlage und Messungen am Massenspektrometer bedanken.
Für die zugesandte, umfangreiche Literatur möchte ich Dr. M. Timmerman danken.
Meiner Familie möchte ich für die Unterstützung und das Interesse an meiner Arbeit danken, gerade weil die Geowissenschaften für sie fremd waren, und ich trotzt aller Hoffnungen kein Gold und keine Diamanten gefunden habe...
Für die vielen Aufmunterungen und die moralische Unterstützung, aber auch für die schöne Zeit während dieser Arbeit, gilt Kay Scheffler ein besonders herzliches Dankeschön.

GENERAL INTRODUCTION

This study forms part of the German-Russian DFG-RFBR project "The collision suture zone between the Archaean terranes of Karelia and the Kola peninsula" of the Mineralogical-Petrological Institute, University Bonn and the Institute of Precambrian Geology and Geochronology Russian of the Academy of Science, St. Petersburg. Joint field work was undertaken during two campaigns in August 1999 and 2000.

Ancient orogenic belts give insights into the metamorphic and tectonic processes operating during orogeny. Granulites exposed in high-grade regional metamorphic belts provide a window into the lower crust and thus are an important clue to the understanding of crust-building processes and continental growth. Shear and thrust zones help to reconstruct the dynamics and mechanisms of mass and fluid transport at middle to deep crustal levels.

Within the Lapland-Kola Orogen, situated in the north-eastern Baltic Shield, the Kolvitsa-Umba Belt forms part of a major suture zone. Remnants of this important Svecofennian collision zone separating the Late Archaean Belomorian terrane from crustal plates of the Central Kola terrane are exposed along the north-eastern coast of the White Sea. Whereas the litho-tectonic structures of individual nappe units were studied in detail by Yefimov and Bogdanova (1993), modern petrological and isotope geochemical work is missing or at it beginnings.

The mafic rock associations of the Kolvitsa Complex comprise layered gabbro and anorthosite bodies as well as several generations of mafic dykes, all formed in an extensional setting *c.* 2.45 Ga ago (Frisch *et al.*, 1995, Mitrofanov *et al.*, 1995b). Results from geochronology indicate a polymetamorphic history, comprising an early episode of high-grade metamorphism and ductile shearing *c.* 2.42 – 2.43 Ga ago and a younger period of metamorphic reworking *c.* 1.91 Ga ago (Frisch *et al.*, 1995, Kaulina, 1996). In high-strain zones, multiple injection of dykes occurred coeval with pervasive deformation and shearing. In low-strain zones, which escaped ductile deformation, magmatic textures, such as cumulate texture and magmatic layering are well preserved. In unique exposures along the coast, multistage magmatism, primary magmatic textures as well as the imprints of high-grade shearing which occurred during or immediately after solidification can be observed. Prominent strain-gradients across small-scale shear zones with continuous transitions from static magmatic textures to domains of intense ductile deformation with dynamic recrystallisation are exposed.

Svecofennian compressional tectonics *c* 1.91 Ga ago led to the up-thrusting of nappe units and crustal thickening. At the south-eastern boundary of the Kolvitsa Massif, strongly mylonitic granulites form part of a prominent thrust zone, which separates the Kolvitsa Massif from the overthrust nappe units of the Por'ya Guba and Umba Complex. Contrary to the evolution of typical high-grade granulites, mafic rock types in the central part of the Kolvitsa Massif commonly preserve relict igneous minerals and garnet occurs exclusively as a coronitic phase.

During tectonic exhumation of the nappe units hydrous fluids infiltrated the high-grade rocks along shear zones and fractures. Zones of amphibolitisation show conspicuous strain and fluid gradients between the centre of hydration and the outer hydration front. The hydration processes were pervasive and resulted in a complete mineralogical and textural re-equilibration at grain-scale.

The layered intrusions and the related dyke swarms of the Kolvitsa Complex are an impressive example of the complex and polymetamorphic evolution of the Kolvitsa Belt. In excellent coastal outcrops, the tectonometamorphic imprints on primary magmatic textures and mineralogy can be studied from large to very small scales. Retrograde zones of amphibolitisation are direct evidence of fluid infiltration and provide important clues to the understanding of processes in deep-crustal metamorphic flow systems, such as textural re-equilibration, re-crystallisation, element and mass transfer and help to identify the driving forces of fluid flux.

The first part of this study details the mineral chemistry, petrology and textural relationships of mafic granulites and zones of amphibolitisation from the Kolvitsa Complex in order to provide an insight into their metamorphic evolution. Highly sheared metagabbros from the south-eastern boundary of

the Kolvitsa Complex were investigated to constrain the *P-T* conditions of high-grade granulite-facies shear deformation in the thrust zones.
In comparison to the metamorphic evolution of gabbroic and anorthositic rocks in a high-grade shear zone, examples from the tectonically lower, south-western and central part of the Kolvitsa Complex were studied. The mafic rock types differ significantly in texture and mineral assemblages from the strongly mylonitic mafic granulites of the south-eastern thrust boundary of the Kolvitsa Complex. Primary magmatic textures and even relict igneous minerals can be preserved and coronal textures document static conditions during recrystallisation. The garnet corona textures are object of a controversial discussion. Their formation has been attributed either to isobaric cooling after the emplacement of the intrusions and dykes at deep crustal levels (Bridgwater *et al.*, 1994, 1995; Glebovitsky *et al.*, 1997) or to increasing pressures during up-thrusting of the hanging-wall nappe units *c.* 1.91 Ga ago (Timmerman, 1996; Balagansky *et al.*, 2001).
The retrograde *P-T* trajectory was deduced from decompressional reaction textures in sheared metagabbros and from mineral assemblages in zones of amphibolitisation. The latter characterise the *P-T* conditions that prevailed during fluid infiltration and retrogression. The results from thermobarometry were linked to geochronological data from the literature (for a compilation see Balagansky *et al.*, 2001) and this study.

The second part of the thesis focuses on the systematics of fluid-rock interaction and the mechanisms of fluid flow systems at middle to deep crustal levels. Shear and fault zones may act as pathways for large volumes of ascending fluids. Fluid migration through shear zones causes mineralogical changes and is commonly accompanied by changes in bulk chemistry and stable isotope signatures (e.g. O'Hara, 1988; Selverstone *et al.*, 1991; McCaig *et al.,* 1990; Dipple & Ferry, 1992; Marquer *et al.*, 1994; Streit & Cox, 1998; Cartwright & Barnicoat, 2003; Yonkee *et al.*, 2003).
The effects of fluid infiltration were examined across decimetric to metric hydration zones in gabbroic and dioritic rock systems of the Kolvitsa nappe unit. In the zones of amphibolitisation increasing degree of hydration caused changes in the rheological properties of the rocks. As a result of the decreasing viscosity in hydration zones with marked fluid and strain gradients, strain became strongly focused into zones of amphibolitisation. Regardless if hydration occurred under dynamic or static conditions, end-members in the centre of hydration zones are characterised by a complete textural and mineralogical re-equilibration.
The aim of this study is to analyse the textural, mineralogical and chemical changes caused by fluid-rock interactions. Petrological data and observations, whole rock geochemical data (major and trace elements, Sm-Nd systematics) and oxygen isotope systematics are then combined to quantify the chemical and mineralogical changes, the compositional characteristics and volumes of involved fluids and to determine the driving forces of fluid flow. For the understanding of metamorphic fluid flow systems, also the knowledge of the geological context plays a decisive role. To determine the timing of hydration, U-Pb and Ar-Ar dating of titanite and amphibole was carried out. Together with geochronological data from the literature (for a compilation see Balagansky *et al.*, 2001) and constraints on the metamorphic evolution presented in the thesis, these data make a contribution to the cooling and exhumation history of the Kolvitsa Belt.

1. Reaction textures in mafic rock-types: Implication for the metamorphic evolution of the Kolvitsa Belt, Kola Peninsula (Russia)

1.1 Introduction

The evaluation of the *P-T* history of high-grade granulite-facies rocks is afflicted with the problem that prograde textures and mineral compositions are commonly lost or modified (equilibrated) during the thermal peak of metamorphism. Therefore, this study focuses on the reconstruction of the retrograde *P-T* evolution of mafic rock types from the layered Kolvitsa Complex in the north-eastern Baltic Shield, aimed to make a contribution to the exhumation history of the south-eastern part of the Lapland-Kola Orogen, the Kolvitsa Belt.

The Kolvitsa Belt was formed during compressional tectonics *c.* 1.91 Ga ago. Its deeply eroded nappe units and the core zone of the Lapland-Kola Orogen are well exposed along the northern coast of the White Sea. The evolution of the Kolvitsa Massif started *c.* 2.44 – 2.46 Ga ago (Mitrofanov *et al.*, 1995; Frisch *et al.*, 1995; Kaulina, 1996; Balagansky *et al.*, 1998) with the emplacement of the gabbro-anorthosite magmas of the host rocks. The following multiple injection of dykes occurred coeval with pervasive deformation and shearing (Balagansky *et al.*, 2001). Results from geochronology indicate a polymetamorphic history, beginning with early amphibolite-facies metamorphism and shearing *c.* 2.42 – 2.43 Ga ago (Balagansky *et al.,* 1998b & 2001) and younger metamorphic reworking *c.* 1.91 Ga ago (Frisch *et al.*, 1995, Kaulina, 1996).

At the south-eastern boundary of the Kolvitsa Complex, strongly mylonitic granulites form part of a prominent thrust zone which separates the structurally underlying rocks of the Kolvitsa Massif from overthrust nappe units of the Por'ya Guba and Umba complex. The highly sheared metagabbros were investigated to constrain the *P-T* conditions of high-grade granulite-facies shear deformation in the thrust zones. Since peak-metamorphic equilibrium mineral assemblages and phase compositions are partially destroyed or modified along the retrograde *P-T* path through a variety of micro-scale reactions (e.g. coronitic reactions, exsolution, melt-back reactions, hydration, carbonation etc.) and continued diffusional resetting (inter-crystalline cation exchange), assessment of peak-metamorphic conditions is difficult. As temperature estimates for mafic granulites are commonly based on the Fe-Mg fractionation between garnet and pyroxenes, and the closure temperature inferred for the Fe-Mg exchange lies below peak granulite-facies temperatures, Fe-Mg exchange thermometry does not provide meaningful estimates for the thermal peak of metamorphism as emphasised in several studies (e.g. Lasaga, 1983, Frost & Chacko, 1989; Spear & Florence, 1992; Fitzsimons & Harley, 1994; Pattison & Bégin, 1994; Bégin & Pattison, 1994; Harley, 1998; Pattison *et al.*, 2003). To acquire high-grade metamorphic conditions the obtained *P-T* results were, if necessary, corrected for retrograde Fe-Mg exchange (Fitzsimons & Harley, 1993, Pattison & Bégin, 1994, Pattison *et al.*, 2003).

Contrary to the evolution of the high-grade granulites, mafic rock types from the central part of the Kolvitsa Massif may even contain relictic igneous minerals and garnet occurs exclusively as a coronal phase. These corona textures are object of a controversy discussion. On the one hand corona formation may be attributed to isobaric cooling after the emplacement of the intrusions and dykes at deep crustal levels (Bridgwater *et al.*, 1994, 1995; Glebovitsky *et al.*, 1997). Otherwise, garnet coronas may be developed much later in response of increasing pressures during up-thrusting of nappe units *c.* 1.91 Ga ago (Timmerman, 1996; Balagansky *et al.*, 2001).

Both, the highly sheared granulites and the coronitic rock types were affected by fluid infiltration and retrogression under amphibolite-facies conditions during exhumation of the nappe pile. The amphibolite-facies mineral assemblages are characterised by Hbl-Pl ±Grt, Ttn, Qtz.

The retrograde *P-T* trajectory was deduced from decompressional symplectitic reaction textures in sheared metagabbros and from mineral assemblages in zones of amphibolitisation.
Since textural equilibrium does not necessarily reflect chemical equilibrium (e.g. Fitzsimons & Harley, 1994; Pattison & Bégin, 1994) and on the contrary, disequilibrium textures like symplectite and corona textures need not necessarily imply chemical disequilibrium (e.g. Mengel & Rivers, 1991) as quoted by St. Onge and Ijewliw (1996), information on intra-grain compositions are required. Therefore, detailed analysis of compositional variations in minerals (compositional profiles and X-ray maps) is a powerful tool to assess chemical equilibria or disequilibria. The pattern of chemical zonation also provides an insight into the nature of zoning, e.g. growth zoning or diffusional zoning. Additionally, multi-equilibrium techniques (Berman, 1988 & 1991; Powell & Holland, 1988; Holland & Powell, 1990) using internally consistent databases (e.g. Berman & Aranovich, 1996) may be used to prove whether chemical equilibrium between coexisting mineral phases was preserved or not.
This study details the mineral chemistry, the petrology and textural relationships of mafic granulites and zones of amphibolitisation from the Kolvitsa Complex to provide an insight into the metamorphic evolution of this important rift-related mafic rock association. Detailed data for the granulite-facies shear deformation, coronitic garnet textures, retrograde symplectitic reaction textures and amphibolite-facies hydration are presented and infer a *P-T* path for the rocks from the south-eastern and central part of the Kolvitsa Complex for their passage through different crustal levels.

1.2 Lapland-Kola Orogen

The Lapland-Kola Orogen (LKO) is situated in the north-eastern part of the Fennoscandian Shield and has been correlated to the west with the Torngart Orogen in Labrador, the Nagssugtoqidian Orogen in Greenland and the Laxfordian in Scotland (Bridgwater *et al.*, 2001; Bridgwater *et al.*, 1992).. These Palaeoproterozoic orogenes are believed to be fragments of a once continuos orogenic system (Bridgwater *et al.*, 2001). The LKO is predominantly build up by Neo-Archaean crust and comprises several terranes such as the Murmansk, Central Kola, Belomorian and Inari terranes (Fig. 1.1). The Archaean terranes are bound by Palaeoproterozoic high-strain zones and rift-belts.
The LKO is believed to be a collisional orogen. The evolution may be described in terms of plate tectonic processes, comparable to those operating today, and started with intracratonic rifting of the Archaean crust *c.* 2.5 - 2.4 Ga ago (Barbey & Raith, 1990; Balashov *et al.*, 1993; Park, 1994; Bridgwater *et al.*, 1995, Amelin *et al.*, 1996). Ongoing rifting led to crustal separation and the formation of the 'Lapland-Kola' ocean, which is documented by rift-related layered gabbro-anorthosite intrusions/complexes (Kolvitsa Belt, Tanaelv Belt, Imandra-Varzuga Belt, Main Ridge) (Fig. 1.1). Rifting occurred under a regional WSW-ENE extensional stress field and was connected with dextral transtensional shearing (Balagansky *et al.*, 1998a; Balagansky *et al.*, 2001; Daly *et al.*, 2001).
The tectonic regime changed to convergence, and NNE-SSW compression led to the closure of the ocean basin *c.* 2.0 - 1.9 Ga ago (Balagansky *et al.*, 1998a). The Lapland Granulite, Umba Granulite and Tersc terranes are composed of Palaeoproterozoic juvenile crustal material and developed in a subduction-related island-arc setting (Daly *et al.*, 2001; Balagansky *et al.*, 1998b; Daly *et al.*, 1997). The juvenile character of most of the metasedimentary and metaigneous rocks is confirmed by young Sm-Nd model ages ranging from 1.95 – 2.5 Ga (Bridgwater *et al.*, 2001; Daly *et al.*, 2001; Timmerman, 1996). Also detrital zircon populations from metasedimentary rocks of the Lapland Granulite and Umba Granulite terranes yield conformable ages between 1.91 – 2.3 Ga (Tugarinov & Bibikova, 1980; Sorjonen-Ward *et al.*, 1994; Bridgwater *et al.*, 1999; Bridgwater *et al.*, 2001). This indicates that surrounding Archaean regions supplied only subordinate amounts of sedimentary detritus and that deposition may have occurred on the margin of an Archaean cratonic foreland with an exposed Palaeoproterozoic magmatic arc source (Bridgwater *et al.*, 2001).
Progressing subduction resulted in continental collision of the southern Belomorian foreland with the Central Kola terrane (northern hinterland) and accretion of the juvenile Lapland Granulite, Umba Granulite and Tersc terranes *c.* 1.9 Ga ago. Connected with continental collision, southward thrusting, crustal thickening and burial of the island arcs occurred. The core zone and footwall of the LKO

experienced a high-pressure and high-temperature metamorphic overprint *c.* 1.91 – 1.90 Ga ago, as dated by metamorphic zircons from high-grade leucosomes (Kislitsyn *et al*, 1999) and metagabbro-anorthosite associations (Frisch *et al*, 1995; Kaulina, 1998, Bernard-Griffiths *et al*., 1984), metamorphic overgrowths on detrital zircons from metasediments (Sorjonen-Ward *et al*, 1994) as well as zircons from late-tectonic pegmatites (Tersc terrane, Daly *et al*., 2001). The age constraints indicate that granulite-facies metamorphism occurred immediately after deposition of the metasedimentary protoliths and that the deposition may have taken place during orogenesis (Bridgwater *et al*., 2001).

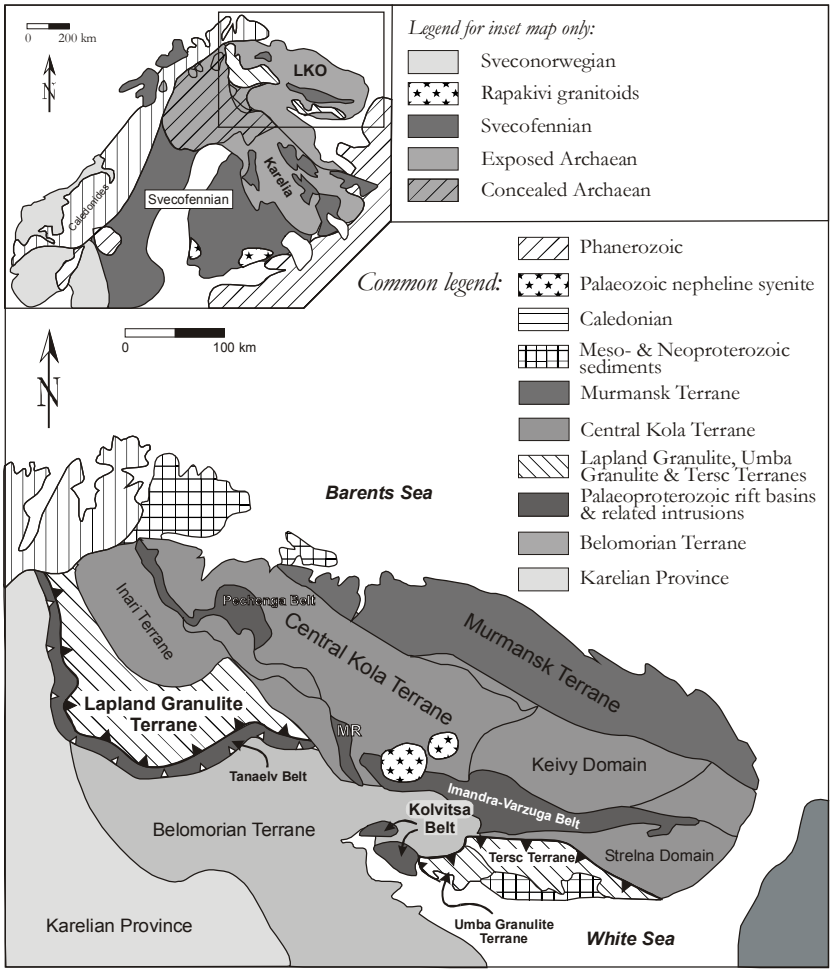

Fig. 1.1. Major tectonic divisions of the Kola region (after Balagansky *et al*., 1998a; Daly *et al*., 2001). Balagansky (1998a) subdivided the terranes of the Kola peninsula into dispersed terranes dominated by Neoarchaean rocks, such as the Belomorian, Central Kola, Inari and Murmansk terranes, and accreted terranes. The latter are composed of Palaeoproterozoic rocks and represent remainders of island-arc formations, such as the Lapland Granulite and the Umba Granulite terranes. Palaeoproterozoic rift basins and related intrusions comprise the Kolvitsa, Imandra-Varzuga, Tanaelv and Pechenga Belt. The Main Ridge gabbro-anorthosite intrusion (MR) was emplaced during dextral transtension and possibly marks the original offset of the evolving Lapland-Kola Ocean (Daly *et al*., 2001).
Inset map at the top left shows major divisions of the Fennoscandian Shield after Hjelt *et al*., 1996). LKO= Lapland-Kola Orogen.

Due to continental collision also the southern foreland, the Belomorian Belt, has experienced metamorphic reworking in the Palaeoproterozoic and was affected by strong deformation and anatectic melting. Widespread pegmatites yield U-Pb zircon ages in the range of 1.80 – 1.75 Ga (Tugarinov & Bibikova, 1980; Bibikova *et al*., 2001). Also titanite U-Pb ages of 1.94 – 1.88 Ga obtained from amphibolites and subordinate diorites and tonalites confirm that metamorphic heating occurred and that temperatures exceeded 650 °C (closure temperature) (Bibikova *et al*., 2001). Part of the metamorphic heat budget may have been contributed by the overthrust hot granulite nappes. In the Tanaelv Belt and presumably also in the Kolvitsa Belt, heat influx from the overthrust granulite nappes is documented by an inverted metamorphic zonation across the suture zone of the LKO (Barbey & Raith, 1990; Krill, 1985; Timmerman, 1996; Daly *et al*., 2001).

1.3 Geological setting of the Kolvitsa Belt

The mafic rock associations of the Kolvitsa Belt are exposed at the north-eastern coast of the White Sea (Fig. 1.2). To the NW the Kolvitsa Belt can be correlated with the Tanaelv Belt in Finland and Norway and is believed to be its analogue (Fig. 1.1). The different lithotectonic units and nappes of the Kolvitsa Belt strike NW and dip gently to the NE (Fig. 1.2). From the West to the East six lithotectonic units have been distinguished (Glebovitsky *et al.,* 2001, Balagansky *et al.,* 2001).
The lowermost unit is built up by Neoarchaean tonalitic to dioritic orthogneisses of the Belomorian Supergroup. Magmatic protoliths of the gneisses were formed at *c.* 2.7 Ga (Bogdanova & Bibikova, 1993; Bibikova *et al.*, 1995, 1996; Balagansky *et al.*, 1998b).
To the NE the gneisses are overlain by the **Kandalaksha sequence** comprising strongly deformed amphibolites. The sequence is dominated by basic/mafic metavolcanic rocks but also contains metasedimentary rocks, such as graywackes and conglomerates. A Palaeoproterozoic age of the volcano-sedimentary sequence (*c.* 2.47 Ga) is indicated by U-Pb zircon data from a meta-andesite and is confirmed by Rb-Sr whole rock ages from mafic to intermediate metavolcanics (Balagansky *et al.*, 1998b).

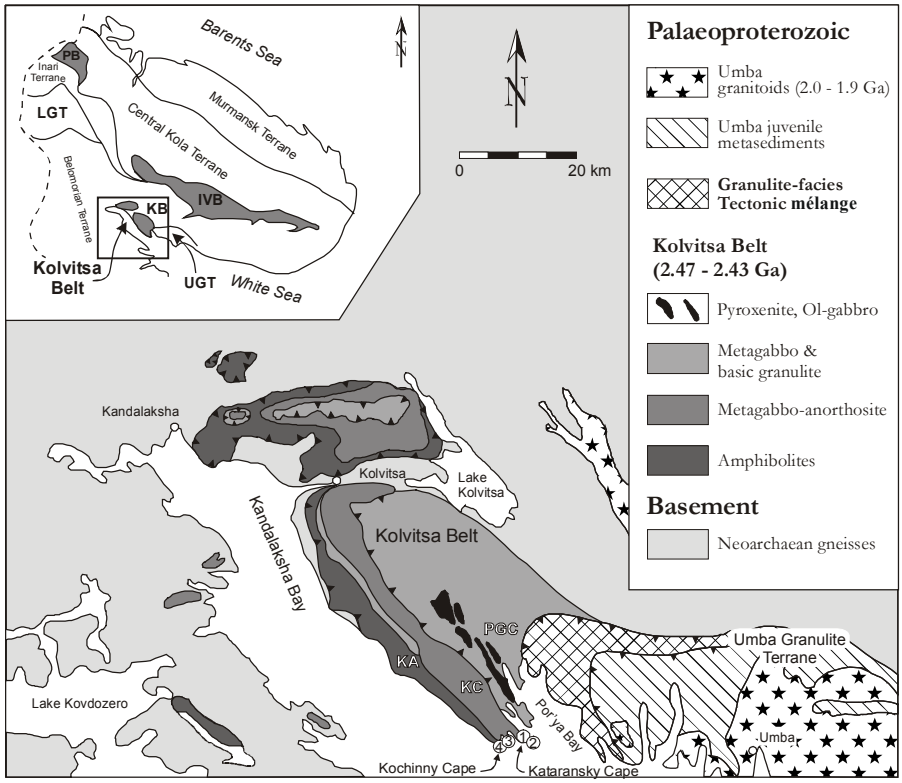

Fig. 1.2. Simplified geological map of the Palaeoproterozoic Kolvitsa Belt (after Mitrofanov, 1996; Balagansky *et al.*, 2001). PGC: Por'ya Guba complex, KC: Kolvitsa complex, KA: Kandalaksha amphibolites. 1: Kataransky Cape, 2: Bolschoi Khed *Island, 3: Nikolkina Island, 4: Leonard Cape.*

The **Kolvitsa Complex** represents an extended, 2 km thick, layered gabbro-anorthosite complex which despite of the strong ductile deformation and granulite facies metamorphic overprint shows well preserved magmatic textures (cumulate texture, magmatic layering). The complex was emplaced at 2.45 – 2.46 Ga (U-Pb ages of magmatic zircon: Frisch *et al.*, 1995; Mitrofanov *et al.*, 1995b) and is cut by several mafic to intermediate dyke swarms. Multiple injection of the dykes has taken place between 2.44 and 2.43 Ga (U-Pb zircon ages: Kaulina, 1996; Balagansky *et al.*, 1998b). In high-strain zones, pervasive deformation and shearing occurred during or immediately after solidification (Balagansky *et al.*, 2001). Structural observations in gabbro-anorthosites and dykes indicate an extensional setting during multistage magmatism (Balagansky *et al.*, 2001) with injection of mafic melts into a large scale

NW-trending shear zone. Prevailing dextral shear movements are indicated by asymmetric morphology and σ-structures of boudinaged dykes. The transtensional setting is attributed to WSW-ENE extension and concomitant dextral movements along NW-trending shear zones (Balagansky *et al.*, 2001), a tectonic regime which operated at a regional scale in the Kola region (Balagansky *et al.*, 1998). U-Pb zircon ages for an undeformed hornblendite and cross-cutting pegmatitic dykes from Kochinny Cape area are 2.43 and 2.39 Ga, respectively (Bogdanova *et al.*, 1993; see also Balagansky *et al.*, 2001), which suggests that deformation and shearing had ceased 2.43 Ga ago. Metamorphic zircons from gabbro-anorthosites yielded younger U-Pb ages of 1.92-1.90 Ga (Frisch *et al*, 1995; Kaulina, 1996) and are attributed to nappe thrusting during continental collision.

The **Por'ya Guba complex** is bound by shear zones and made up of mafic to intermediate granulites. Garnet-clinopyroxene-plagioclase assemblages in mafic lithologies indicate that metamorphism occurred under high pressure granulite facies conditions. Large domains were affected by retrograde *(amphibolite facies)* hydration leading to widespread development of garnet amphibolites. Subordinate ultrabasic lenses, enderbitic gneisses and carbonate layers are intercalated. On the north-eastern coast of the Por'ya Bay a major shear zone separates the Kolvitsa Belt from the accreted Umba Granulite Terrane (Balagansky *et al.*, 1994). This granulite-facies shear zone represents a tectonic mélange zone in which mafic to intermediate granulites of the Por'ya Guba Complex are interleaved with tectonic lenses of juvenile metasediments from the Umba Granulite Terrane. The sheared granulite-facies paragranulites containing orthopyroxene-sillimanite-quartz assemblages represent high strain zones between tectonic lenses (Balagansky *et al.*,1986a; Kozlova *et al.*, 1991; Gastreich, 2000; Balagansky *et al.*, 2001). The orthopyroxene-sillimanite-quartz assemblage defines a gently SE-plunging stretching lineation, which is also developed in the overthrust rocks of the Kolvitsa Belt and the Neoarchaean Basement (Timmerman *et al.*, 1997; Daly *et al.*, 2001, Glebovitsky *et al.*, 2001). Zircons from garnet-sillimanite gneisses and crosscutting high-grade leucosome within the shear zone yielded U-Pb ages of *c.* 1.9 Ga and date high-grade metamorphism and shearing (Bibikova *et al.*, 1973; Kislitsyn *et al.*, 1999a).

To the east of the Por'ya Guba Complex, migmatitic paragneisses of the accreted **Umba Granulite Terrane** are exposed and are regarded to be the south-eastern extension of the Lapland Granulite Belt in northern Finland and Norway. The juvenile character of the metasediments is confirmed by Sm-Nd model ages in the range of 2.5 – 2.1 Ga (Huhma & Meriläinen, 1991; Timmerman, 1996; Daly *et al.*, 1997; Bridgwater *et al.*, 2001; Daly *et al.*, 2001). Since granulitic metamorphism occurred *c.* 1.9 Ga ago, deposition of the sedimentary protolith presumably has taken place at *c.* 2.0 Ga (Timmerman, 1996; Daly *et al.*, 2001; Balagansky *et al.*, 2001).

The eastern part of the Umba Granulite Terrane is intruded by a magmatic suite of enderbites, charnockites and porphyritic granites (Glebovitsky *et al.*, 2001). Crystallisation ages of the **Umba Igneous Complex** were obtained from magmatic zircons and yielded *c.* 1.91 Ga (Glebovitsky *et al.*, 2001) and comply with Sm-Nd model ages that range from 2.1 to 1.9 Ga (Timmerman & Balagansky, 1994). The rocks of the Umba Igneous Complex were presumably formed in a subduction-related island arc setting (Glebovitsky *et al.*, 2001).

1.4 Petrography, microstructures and mineral reactions

1.4.1 Granulite-facies assemblages from the south-eastern boundary of the Kolvitsa Massif

The metagabbros are strongly foliated mylonitic rocks. Mafic layers are composed of garnet, clino- and orthopyroxene in variable modal amounts. Felsic layers consist of aggregates of recrystallised plagioclase and minor quartz. Their equigranular-polygonal granoblastic fabric with grain sizes ranging from 0.1 to 0.3 mm indicates attainment of textural equilibrium. In the metagabbro at Bolschoi Khed Island a subhorizontal stretching lineation is defined by torn-out aggregates of ortho-and clinopyroxene and garnet, indicating dynamic recrystallisation and mineral growth during granulite-facies shear deformation (Fig. 1.3c-d). Individual garnet and orthopyroxene clasts range from 0.5 to 1 mm in size. Individual clinopyroxene clasts (0.4 - 0.8 mm) often show finer-grained recrystallisation.
The metagabbro at Kataransky Cape exhibits a foliated fabric of near-equigranular (0.2 - 0.5 mm) garnet, clinopyroxene and plagioclase (Fig. 1.3a-b). Individual larger garnet grains (0.7 - 0.9 mm) are crossed by numerous cracks. Recrystallised clinopyroxene grains form small cluster. In contrast to the metagabbro at Bolschoi Khed Island, orthopyroxene is rare and was built through the breakdown of garnet and clinopyroxene after the peak of metamorphism as a result of decompression during the exhumation of the rocks.
In the meta-anorthosite thin mafic layers are composed of garnet, clinopyroxene and plagioclase with minor amphibole, magnetite and quartz (Fig. 1.3e). The large garnet grains vary from 0.5 to 4mm in size, whereas clinopyroxene grains may attain grain sizes up to 1 mm and often underwent recrystallisation to fine-grained aggregates. Inclusions of clinopyroxene (0.1-0.6 mm), amphibole (0.1 mm) and plagioclase (0.1 - 0.4 mm) in garnet porphyroblasts preserve armoured relics of the high-grade assemblage and thus allow the estimation of near-peak *P-T* conditions. Felsic layers are made up of recrystallised plagioclase (0.1 to 0.2 mm) with few larger clasts (up to 1-2.5 mm) presumably representing igneous relics.
The presence of garnet and the absence of orthopyroxene in the granulite-facies assemblages depend on the *P-T* conditions and the whole rock chemistry, in particular the *Mg*-number. In Mg-rich rocks such as the metagabbro at Bolschoi Khed Island (Mg# 0.75), orthopyroxene has not been completely consumed by the pressure-sensitive reaction

$$\mathrm{Opx + Pl \rightarrow Grt + Cpx + Qtz\ .} \qquad (1)$$

In contrast, in the more ferroan metagabbro at Kataransky Cape (Mg# 0.65), orthopyroxene ceased to exist. Garnet-clinopyroxene assemblages in Mg-rich systems such as the banded anorthosite indicate high-pressure conditions of metamorphism.
Metagabbros as well as the banded anorthosites provide textural evidence for local re-equilibration of the granulite-facies assemblage (i.e. sympelctitic corona textures) after peak metamorphism and deformation.

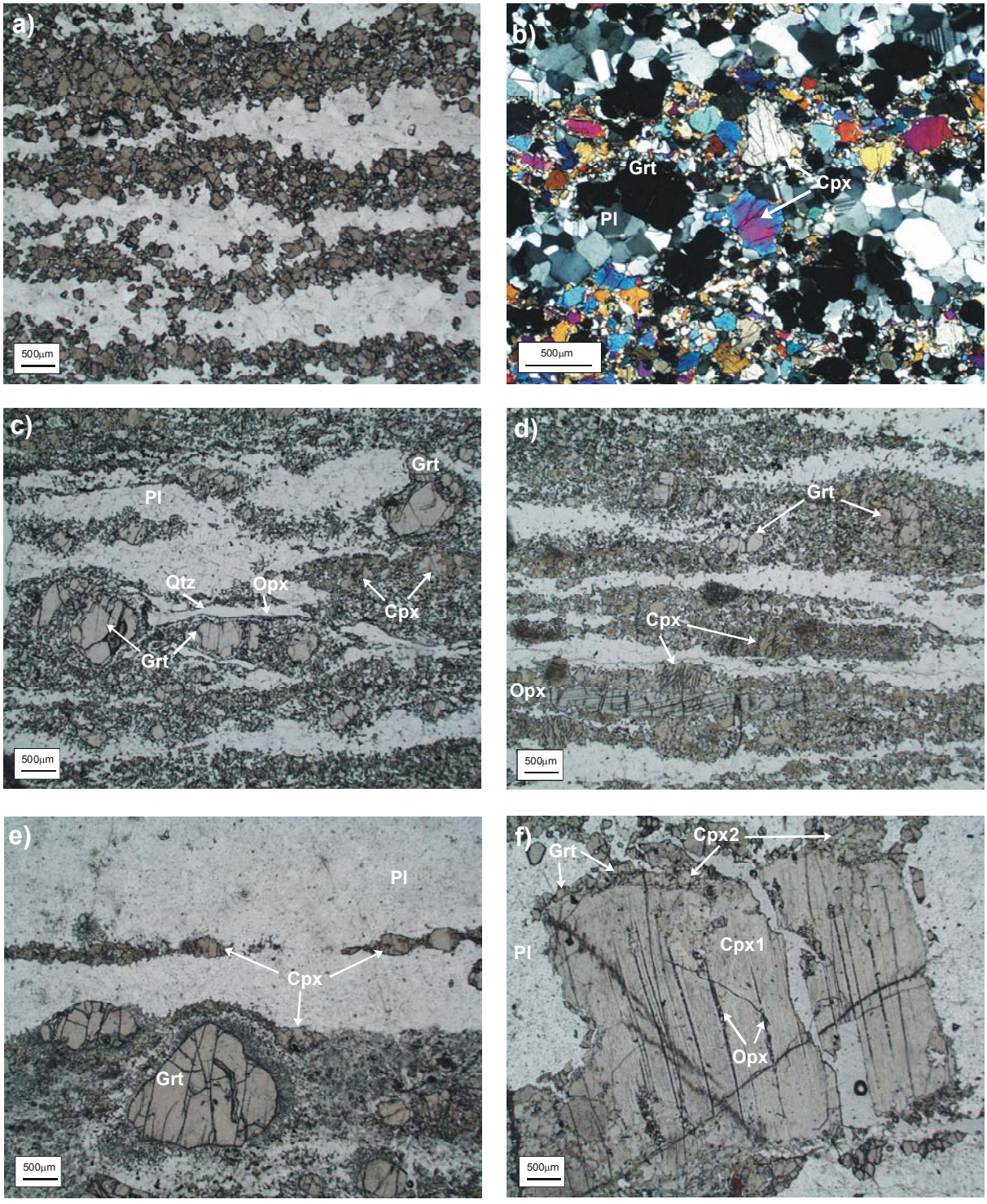

Fig. 1.3a-e. Granulite-facies mineral assemblages and microstructures of mafic granulites. Foliated metagabbro with paragenesis Grt-Cpx-Pl ±Opx, Qtz, Rt; Kataransky Cape (**a & b:** crossed polarisers). Foliation is defined by garnet, clino- and orthopyroxene and quartz, Bolschoi Khed Island (**c-d**). Anorthosite with mafic layers contains large garnet porphyroblasts, clinopyroxene and plagioclase ±Mag, Qtz, Hbl, Beloozerskaya Guba (**e**). (**f**) Noritic dyke containing large clinopyroxene crystals with orthopyroxene exsolution lamellae, Water Sign.

1.4.2 Corona reactions involving garnet

In the lithological association of the Kolvitsa layered complex garnet was involved in two kinds of coronitic reactions: garnet-consuming and garnet-producing reactions. The appearance of garnet strongly depends on bulk rock chemistry. In Fe-rich systems garnet is produced at lower pressures compared to Mg-rich bulk compositions (Fig. 1.4 & reaction (1)). Therefore, depending on the bulk composition of the protolith, garnet may either act as a reactant (breakdown of porphyroblastic garnet in Mg-rich rocks) or as product (growth of coronitic garnet in Fe-rich rocks) in approximately the same *P-T* regime.

Since porphyroblastic garnet is bound to mylonitic granulites at the south-eastern boundary of the Kolvitsa Massif, forming part of a prominent thrust, and coronitic garnet is characteristic for mafic rock types in the central part of the Kolvitsa Massif, mineral assemblages and microtextures presumably reflect differences in the metamorphic evolution. The reaction textures in different rock types are described with regard to their host rock and their position in the Kolvitsa Complex (south-eastern boundary and central part of the Kolvitsa Complex).

1.4.2.1 Garnet-consuming reaction textures from the south-eastern boundary of the Kolvitsa Massif

Metagabbros and banded anorthosites exhibit garnet breakdown textures which document a partial re-equilibration of the HT-assemblages after peak metamorphism and ductile deformation accompanying the exhumation of the nappe complex. These reactions are indicative for decompression. At fluid-deficient conditions orthopyroxene+plagioclase symplectites were formed at garnet-clinopyroxene interfaces (metagabbros, Fig. 1.5a-b) through the reaction

$$Grt + Cpx + Qtz \rightarrow Opx + Pl. \quad (1)$$

In the banded anorthosite, hornblende+plagioclase symplectites formed at the expense of garnet and clinopyroxene at fluid-present conditions via the model reaction (Fig. 1.5c-d)

$$Grt + Cpx + H_2O \rightarrow Hbl + Pl + Qtz. \quad (2)$$

In both cases, the symplectite plagioclase is Ca-rich (80 - 90 mol% An) and the resorbed garnet grains show a rimward decrease of X_{Mg}.

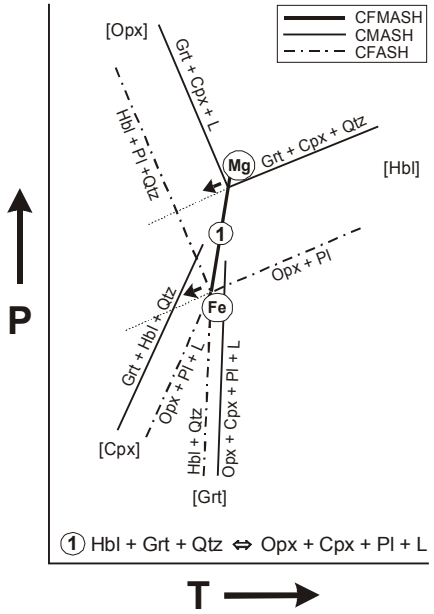

Fig. 1.4. Schematic P-T diagram in the CFMASH system assuming the presence of quartz and liquid or vapor in excess (after Pattison, 2003). At fluid absent conditions or fluids with low a_{H2O}, the stability field of Grt-Cpx-Qtz and Opx-Pl expands to lower temperatures (arrows).

Depending on a_{H2O}, a_{SiO2} and bulk rock chemistry, both reactions could have occurred at the same *P-T* conditions. Figure 1.4 shows a schematic *P-T* diagram with the idealised model reactions in the CFMASH system (Pattison, 2003). The model reaction (1) strongly depends on bulk composition and occurs at lower pressures in the CFASH system compared to the CMASH system. In the CFMASH system the univariant CMASH or CFASH-reactions become divariant bands linked by the univariant reaction (Fig. 1.4):

$$\text{Hbl} + \text{Grt} + \text{Qtz} \leftrightarrow \text{Opx} + \text{Cpx} + \text{Pl} + \text{V or L.} \quad (3)$$

Under fluid-absent conditions or decreased a_{H2O} the stability fields of grt + cpx and opx + pl extend to lower temperatures. In the presence of quartz, decompression would result in grt-breakdown following reaction (1) (metagabbros). The presence of a hydrous fluid (increased a_{H2O}), on the other hand, would favour reaction (2) (anorthosite). In contrast to reaction (1), where quartz is a reactant phase, reaction (2) can also set in at lower a_{SiO2} since quartz is a product phase.
Symplectites of plagioclase intergrown with orthopyroxene or hornblende resorbing garnet grains that are not in contact to clinopyroxene, suggest the following reactions:

$$\text{Grt1} + \text{Pl1} + \text{Qtz} \rightarrow \text{Opx} + \text{Grt2} + \text{Pl2} \quad (4)$$

$$\text{Grt1} + \text{Pl1} + \text{Qtz} + \text{H}_2\text{O} \rightarrow \text{Hbl} + \text{Grt2} + \text{Pl2} \quad (5)$$

In contrast to the reacting plagioclase (Pl1), the symplectite plagioclase 2 is extremely calcic (80-90 mol% An). The garnet grains are zoned, with Prp contents decreasing from core (grt1) towards the rim (grt2).

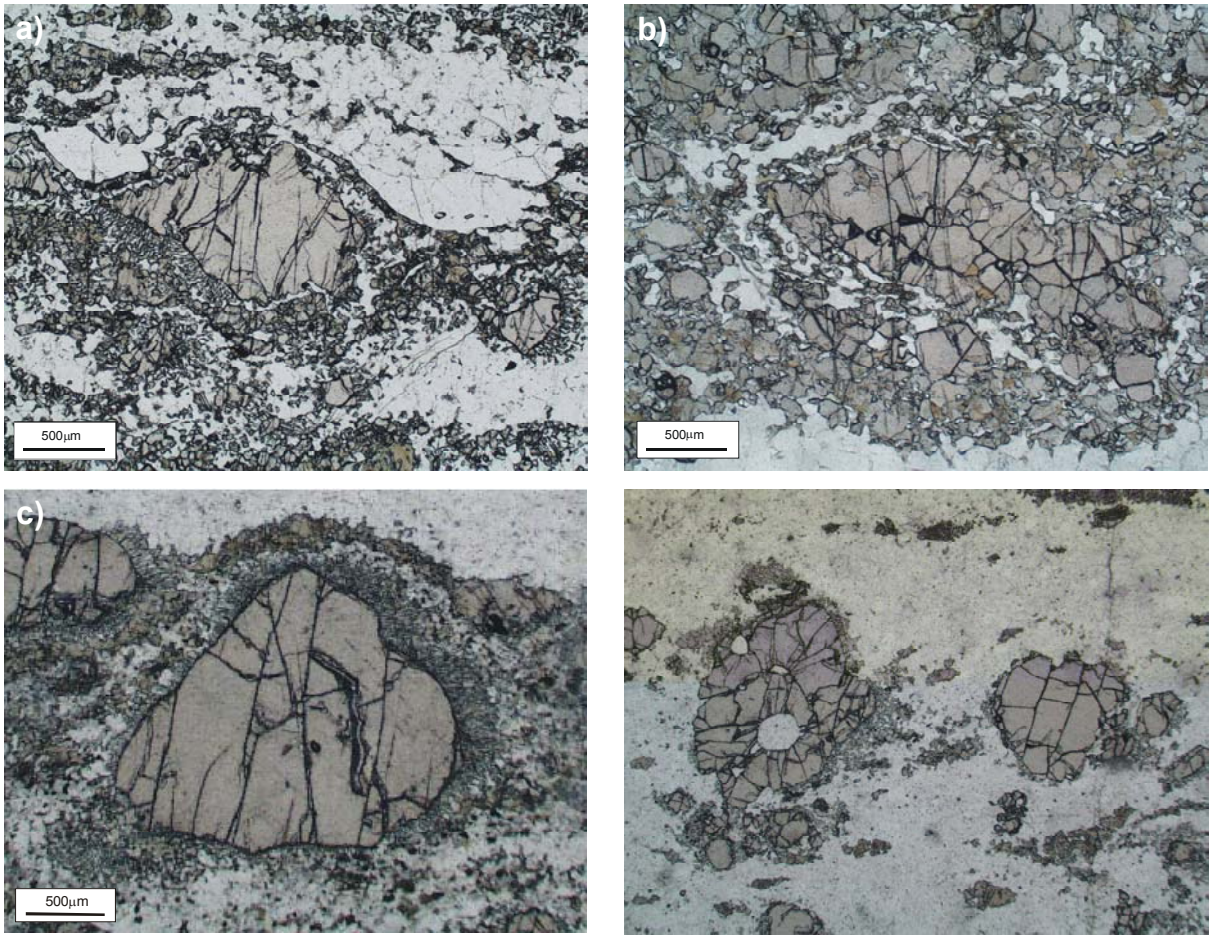

Fig. 1.5a-d. Garnet breakdown in the presence of clinopyroxene and quartz giving way to orthopyroxene and plagioclase, (a) Bolschoi Khed Island & (b)Kataransky Cape. **(c & d)** Garnet breakdown under fluid-present conditions. Hornblede symplectites with Ca-rich plagioclase are developed at the expense of garnet and clinopyroxene .

1.4.2.2 Garnet-producing corona textures from the central part of the Kolvitsa Massif

In the central part of the Kolvitsa Massif igneous textures can be observed in different kinds of basic dykes and anorthosites. In a low-strain dyke at Kataransky Cape large plagioclase crystals (5-10 mm) and recrystallised amphibole aggregates (4-6 mm) are outlined by coronitic garnet defining a subophitic texture (i.e. Fig. 1.6f). In low-strain domains of anorthosites or noritic dykes, large plagioclase and/or clinopyroxene crystals are preserved, that are believed to have a magmatic origin (i.e. Fig. 1.3f). In these rock types garnet occurs exclusively as a coronal phase developed between plagioclase and adjacent clino- and orthopyroxene, hornblende, ilmenite or olivine grains (Fig. 1.6a-f). Commonly, coronitic garnet (0.1-0.3mm) is anhedral and free of inclusions. Continuos, thin garnet rims may completely mantle individual grains as well as recrystallised aggregates. In low-strain basic dykes at Kataransky Cape a subophitic texture is preserved with large plagioclase laths and outlined by coronitic garnet rimming the interstitial amphibole matrix (Fig. 1.6f). Another type of coronal garnet is developed in the basic dyke at Nikolkina Island. Beside continuous garnet coronas, subhedral to euhedral garnet crystals occur that only partially rim the grains, as well as clusters of garnet grains that contain numerous minute inclusions of plagioclase, quartz and amphibole. The garnet coronas mantling plagioclase in contact with clinopyroxene and amphibole most likely formed via the simplified reactions (Fig. 1.6c & d):

$$\mathrm{Cpx + Pl \rightarrow Grt + Qtz} \quad (6)$$

$$\mathrm{Hbl + Pl \rightarrow Grt + Qtz + H_2O} \quad (7)$$

The textural relations between amphibole and coronal garnet suggest that corona growth and hydration of clinopyroxene occurred coevally and would support the following reaction:

$$\mathrm{Cpx + Pl + H_2O \rightarrow Grt + Hbl + Qtz.} \quad (8)$$

Noritic dykes contain composite coronas developed between ortho- or clinopyroxene grains and adjacent plagioclase. The orthopyroxene grains are separated from the matrix plagioclase by an inner corona of clinopyroxene containing minor amounts of quartz rimmed by plagioclase and an outer corona of garnet (Fig. 1.6a). Development of the double-layer corona can be explained by the general reaction:

$$\mathrm{Opx + Pl1 \rightarrow Grt + Cpx + Pl2 + Qtz} \quad (9)$$

Compared to the rather calcic matrix plagioclase (1) (57 - 58 mol% An), the corona plagioclase (2) has a more sodic composition (40 – 42 mol% An). In the studied sample from the Water Sign outcrop, the double-layer corona between orthopyroxene and adjacent plagioclase can be related to the following reaction in the CNMASH system:

$$\mathrm{2Mg_2Si_2O_6 + 3.5Na_{0.43}Ca_{0.57}Al_{0.157}Si_{2.43}O_8 \rightarrow}$$
$$\mathrm{Mg_3Al_2Si_3O_{12} + CaMgSi_2O_6 + 2.5Na_{0.6}Ca_{0.4}Al_{1.4}Si_{2.6}O_8 + SiO_2} \quad (10)$$

The presence of double-layer corona between clinopyroxene grains and matrix plagioclase suggests that reaction textures evolved according the schematic reaction (Fig. 1.3f & 1.6a-b) :

$$\mathrm{Cpx1 + Pl1 \rightarrow Grt + Cpx2 + Pl2 + Qtz} \quad (11)$$

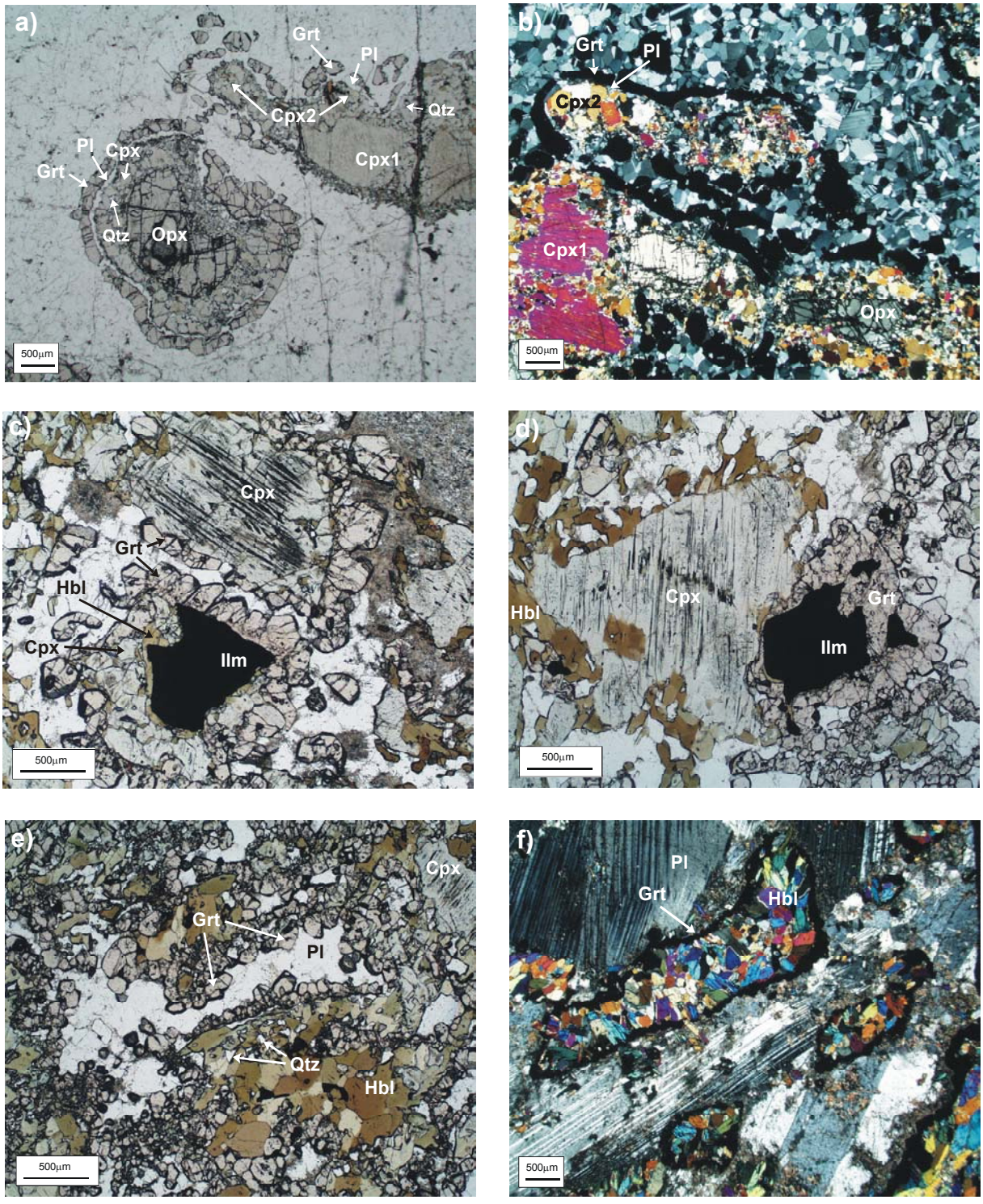

Fig. 1.6a-f. Photomicrographs of coronal garnet formed between ferro-magnesian mineral phases and adjacent plagioclase grains. Multiple garnet-plagioclase-clinopyroxene-quartz-corona developed between orthopyroxene and matrix plagioclase. Noritic dyke, Water Sign (**a**). Garnet-plagioclase-clinopyroxene-quartz-corona developed between clinopyroxene and plagioclase, noritic dyke, Water Sign (**a & b** (crossed polarisers)). Coronal garnet and clinopyroxene formed between ilmenite and clinopyroxene, respectively and plagioclase, basic dyke, Nikolkina Island (**c**). Hornblende growth at the expense of clinopyroxene and garnet corona on ilmenite, basic dyke, Nikolkina Island (**d**). Coronal garnet rimming plagioclase patches in contact to hornblende and clinopyroxene, basic dyke, Nikolkina Island (**e**). Thin anhedral garnet bands mantle hornblende aggregates. In the low-strain dyke ophitic texture is preserved by large plagioclase laths and outlined by garnet coronas, Kataransky Cape (**f:** crossed polarisers).

The composition of recrystallised matrix clinopyroxene is similar to the rim composition of clinopyroxene clasts. Therefore, in the given example matrix clinopyroxene should be regarded as reactant rather than a product phase. The resulting reaction in the CNMASH system can be written as follows:

$$3CaMgSi_2O_6 + 12Na_{0.48}Ca_{0.57}Al_{1.58}Si_{2.42}O_8 \rightarrow$$
$$Mg_3Al_2Si_3O_{12} + 2Ca_3Al_2Si_3O_{12} + 9Na_{0.56}Ca_{0.44}Al_{1.44}Si_{2.56}O_8 + 3SiO_2 \qquad 12)$$

Garnet-producing reactions involving anhydrous phases such as reactions (6), (9) and (11) have moderate to shallow positive slopes in the *P-T* space, suggesting re-equilibration occurred at lower temperature, increasing pressure or both. Model reactions including amphibole and hydrous fluid posses steeper *dP/dT* slopes implying that re-equilibration took place at lower temperatures.

1.4.3 Amphibolite-facies assemblage

Amphibolite-facies retrogression in the Kolvitsa nappe is generally connected to fluid infiltration along shear zones or network-like fractures/channels. In contrast to the metagabbro-anorthosite association of the Kolvitsa nappe, the mafic granulites of the Por'ya Guba nappe were affected by large-scale pervasive retrogression. Therefore, the predominant part of the former mafic granulites have been retrogressed to garnet-amphibolites. In the Kolvitsa nappe hydration at outcrop scale was channelled (i.e. shear zones, fractures), but has a pervasive character on decimetre- to metre-scale, resulting in a complete mineralogical and textural re-equilibration at grain scale. Hydration due to fluid infiltration was accompanied by significant mineralogically controlled element-transfer.

The common amphibolite-facies assemblage is hornblende+plagioclase with quartz, garnet, biotite and titanite as minor to accessory constituents (Fig. 1.7a-d). The occurrence of epidote, prehnite and chlorite can be attributed to low-temperature retrogression coeval with sericitisation of plagioclase. There is a systematic increase in the grain size of hornblende from the transition zone (0.1-0.5 mm) towards the completely hydrated central zone of most intense fluid influx (0.4-2 mm) (Fig. 1.7a-d). In both zones hornblende is fresh and unaltered. Microstructural types of amphibole in transition zones such as hornblende containing sieve-like inclusions of plagioclase and symplectitic aggregates of hornblende and Ca-rich plagioclase are believed to have replaced clinopyroxene and probably also garnet (Fig. 1.7a). In well equilibrated domains hornblende is unzoned and free of inclusions. Nearly monomineralic amphibole felses represent extreme end members of hydration and element-transfer (Fig. 1.7d).

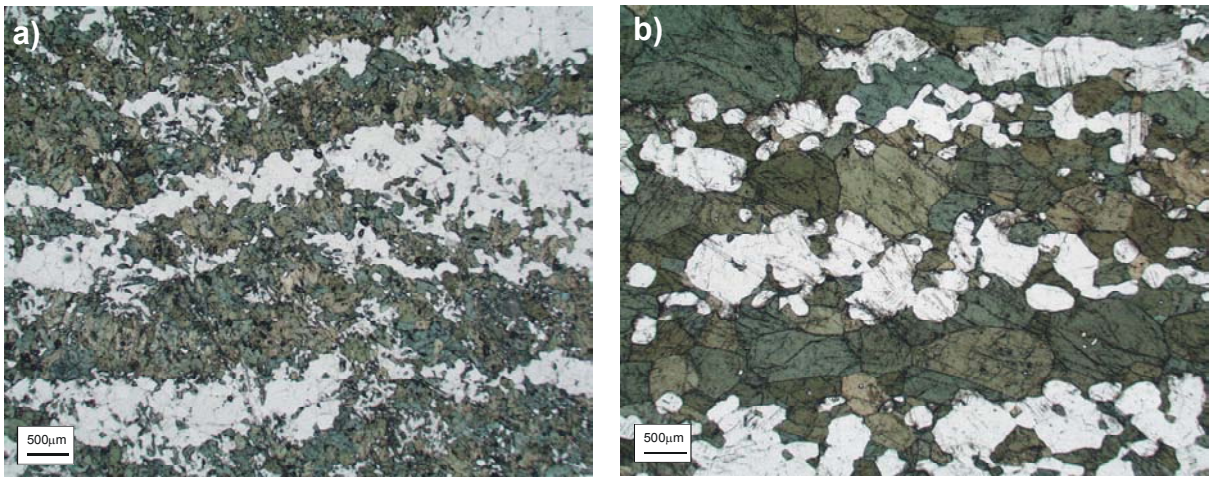

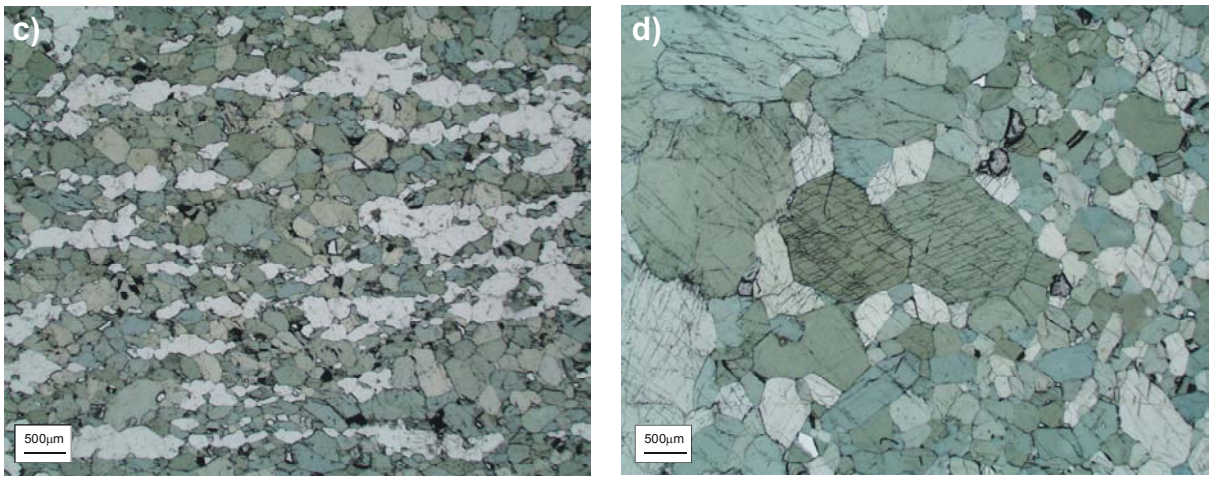

Fig. 1.7a-d. Photomicrographs of hydrated metagabbros under amphibolite-facies conditions. (**a**) Intergrowth of hornblende and plagioclase in the transition zone (metagabbro, Kataransky Cape). (**b**) Well-equilibrated metagabbro near to centre of hydration (metagabbro, Kataransky Cape). (**c**) Transition zone of amphibolite-facies metagabbro at Bolschoi Khed Island. (**d**) Extreme case of hydration under static conditions resulting in a monomineralic amphibolite fels (Bolschoi Khed Island).

In contrast to amphibole, larger plagioclase grains are commonly compositionally zoned which indicates cessation of intracrystalline cation-exchange (Fig. 1.8a-b). The observed discontinuous zoning is interpreted to represent rims formed on granulite grade relic grains by infiltrating fluids.

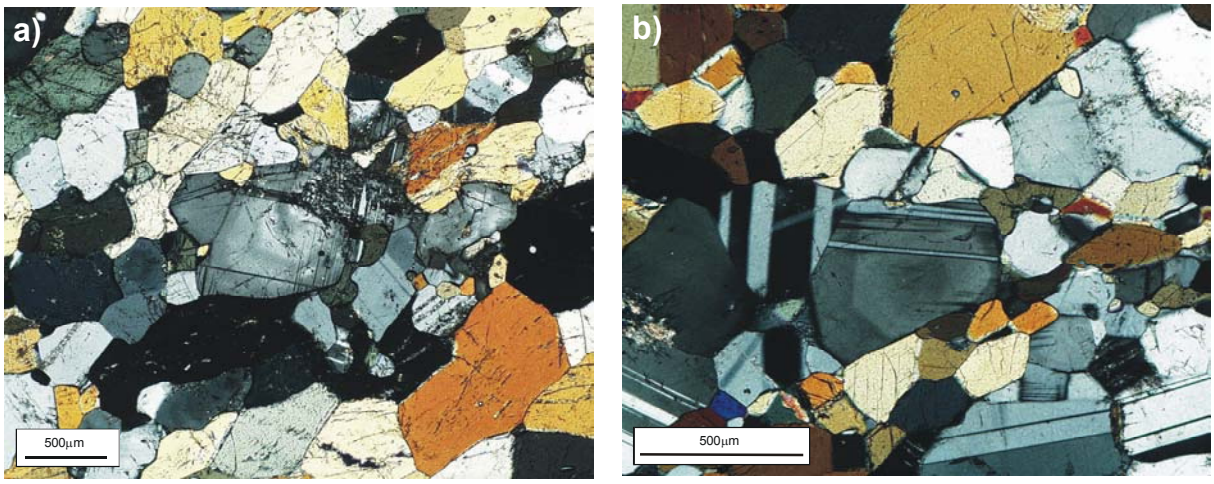

Fig. 1.8a & b. Example of optically and chemically zoned plagioclase crystals (crossed-polarisers). In contrast to the plagioclase crystals, hornblende grains are homogeneous in composition. Metagabbro near to centre of fluid infiltration (Kataransky Cape) (**a**). Transition zone Bolschoi Khed Island (**b**).

Skeletal intergrowth of ilmenite and titanite is evidence of partial to complete replacement of ilmenite and an indicator of the intensity of retrogression of the earlier granulite-facies assemblages (Fig. 1.9a). In dynamically recrystallised amphibolites titanite crystals with rhombic to sphenoidal cross-sections are well-orientated in the new foliation, and evidently titanite grew synchronous with deformation and fabric reorganisation (Fig. 1.9b). Hydration under static conditions completely erased the mylonitic foliation of the precursor granulite and giving way to a granoblastic isotropic fabric.

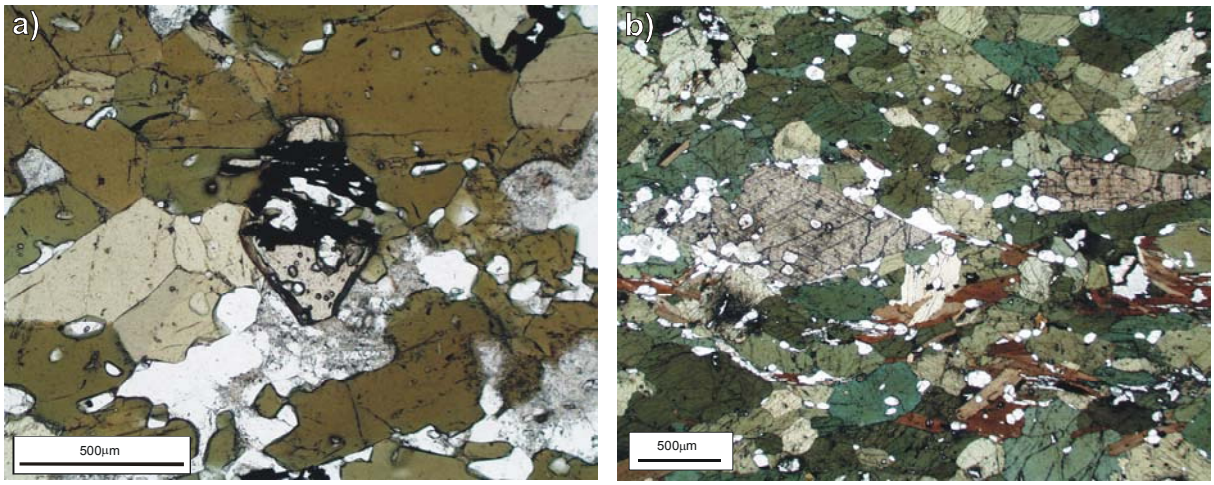

Fig. 1.9a & b. Titanite crystals with rhombic cross-sections. Skeletal ilmenite intergrown with titanite (a). Well-orientated titanite crystals (b).

1.5 Mineral chemistry

1.5.1 Garnet

Isolated anhedral garnet is a characteristic constituent of the granulite-facies assemblage in metagabbros and banded anorthosites. Coronal garnet also formed in reaction rims separating plagioclase from orthopyroxene, clinopyroxene, hornblende or ilmenite in noritic, basic and ophitic dykes. Representative electron microprobe analyses and structural formulae of porphyroblastic and coronal garnet are given in Table 1.1.

The triangular plot (Alm+Sps)-(Grs+Adr)-Prp reveals two distinct compositional trends (Fig. 1.10): $Alm_{22-50}Prp_{30-59}Grs_{8.5-20}Adr_{3-10}Sps_{0.6-2.1}$ in the metagabbros, banded anorthosite and noritic dyke and $Alm_{45-60}Prp_{9-28}Grs_{14-32}Adr_{0-9}Sps_{1.2-9}$ in the different basic dykes. Garnet in the basic dykes is characterised by the lowest Prp contents and is only weakly zoned with Ca decreasing from core to rim, whereas Fe shows a slight rimward increase. Compositional trends of coronitic garnet in the noritic dyke and garnet porphyroblasts in the metagabbros show a positive correlation between Alm+Sps and Prp, while the Ca content seems to be buffered (*c.* Grs_{18}). X_{Mg} of coronitic garnet in the noritic dyke depends on the X_{Mg} of the reactant phases opx (X_{Mg}0.7) and cpx (X_{Mg}0.82), respectively.

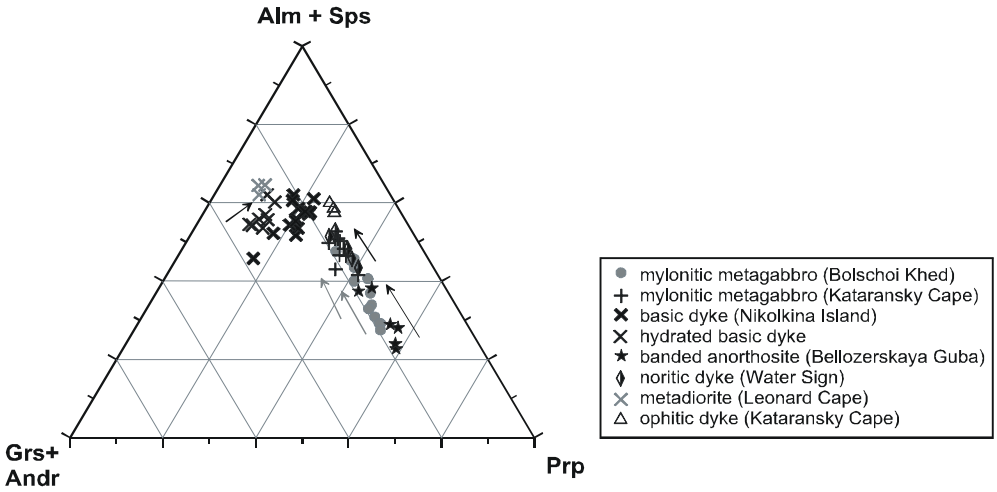

Fig. 1.10. (Alm+Sps)-(Grs+Adr)-Prp triangular plot showing compositional trends of garnet from different rock types. Arrows indicate zonation trends from core to crystal rim.

The compositional trend of porphyroblastic garnets reflects the pronounced zoning. Fe and Mn increase towards the rims while Mg shows a concomitant decrease (Fig. 1.10 & 1.11). X-Ray maps of grains that are largely resorbed by Opx+Pl or Hbl+Pl symplectite rims reveal diffusional zonation patterns for Mg and Fe which follow the resorbed grain boundaries and obviously were induced by the symplectite reaction (Fig. 1.11 & 1.12). As the symplectite phases orthopyroxene and hornblende have $X_{Mg} > X_{Mg}^{Grt}$, intragranular diffusion towards the reaction front caused the observed rimward depletion in Mg. Ca, on the other hand, shows only a slight increase towards the rim. The observed zonation patterns are in agreement with the slower diffusivity of this element in garnet (Chakraborty & Ganguly, 1991) and thus provide clear evidence for continued late Fe-Mg exchange after cessation of intracrystalline Ca diffusion (Pattison & Bégin, 1994). Even in garnet grains with flat compositional profiles (Fig. 1.11), Fe and Mg may have been completely reset by late cation-exchange, if cooling rates were slow relative to diffusion rates (Lasaga, 1983). Therefore, in contrast to Fe-Mg exchange equilibria, temperature- and pressure-sensitive net transfer equilibria involving the much slower Al or Ca exchange, for example Al solubility in orthopyroxene in equilibrium with garnet, should provide better information about peak near temperatures and pressures (Fitzsimons & Harley, 1994; Bégin & Pattison, 1994; Pattison & Bégin, 1994).

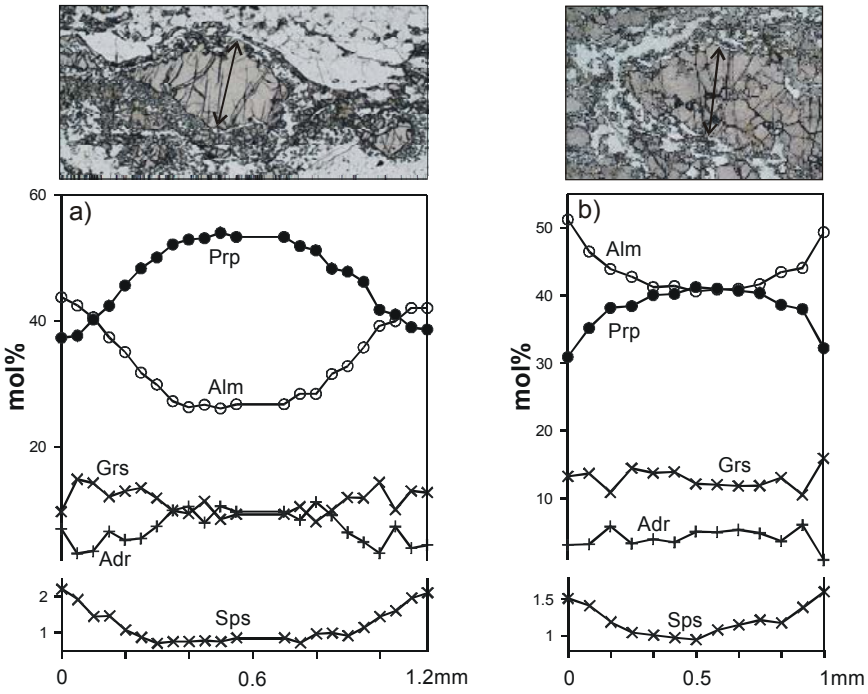

Fig. 1.11. Profiles of Prp, Alm, Grs, Adr and Sps (mol%) across garnet grains affected by symplectitic breakdown from metagabbros, a) Bolschoi Khed & b) Kataransky Cape.

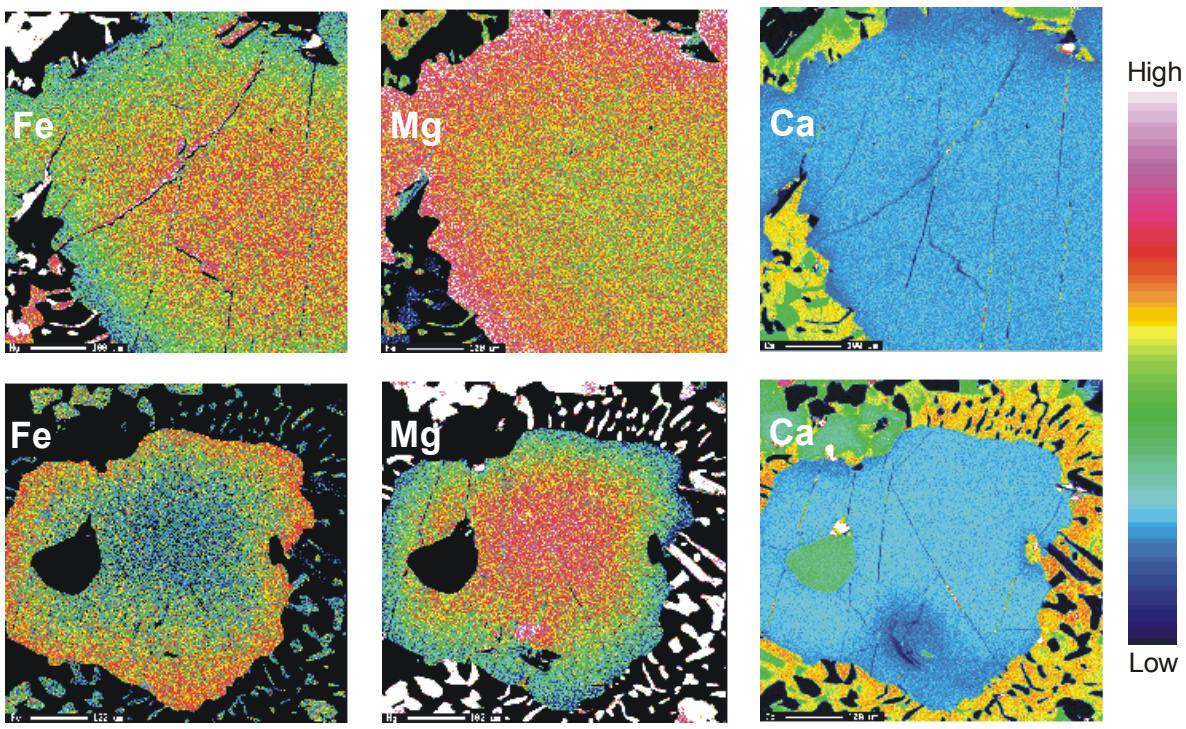

Fig. 1.12. X-Ray maps showing the distribution of Mg, Fe and Ca intensity of garnet grains (metagabbro, Bolschoi Khed).

If temperature estimates based on Al solubility in orthopyroxene in equilibrium with garnet are higher than those derived from Fe-Mg cation exchange thermometry, the latter are likely to reflect closure temperatures below peak conditions (Bégin & Pattison, 1994). It follows that in order to derive meaningful P-T estimates, the retrograde cation-exchange history of individual samples has to be studied in detail through element mapping and compositional profile analysis of the major reactants, such as garnet, orthopyroxene, clinopyroxene, amphibole and plagioclase.

Table 1.1. Representative analyses of garnet cores, rims and coronal garnet from different rock types. Analyses were recalculated on the basis of 12 oxygens.

	metagabbro		metagabbro		anorthosite			basic dyke					hydrated basic dyke					noritic dyke		ophitic dyke		diorite
	Bolschoi Khed		Kataransky Cape		Beloozerskaya Guba			Nikolkina Island					Nikolkina Island					Water Sign		Kataransky		Leonard
wt.-%	11 c	1 r	18 c	7 c	22 r	105 c	31 c	83 r	21 c	28 c	78 cor.	7 cor.	1 c	32 c	9 r	19 r	33 r	87 cor.	54 cor.	5 cor.	38 cor.	22 c
SiO_2	39.74	39.13	39.88	39.45	39.38	40.76	41.10	40.14	38.51	37.68	38.17	37.06	37.61	37.89	38.05	37.88	37.66	39.10	38.57	38.75	38.31	37.61
TiO_2	0.13	0.05	0.01	0.08	0.04	0.08	0.06	0.09	0.06	0.07	0.05	0.06	0.35	0.30	0.10	0.07	0.09	0.03	0.02	0.04	0.03	0.05
Al_2O_3	22.96	22.73	21.66	22.46	21.75	23.57	23.15	22.66	21.73	22.12	21.51	21.57	20.28	20.88	21.15	21.25	21.04	22.30	21.93	21.85	22.04	21.58
Cr_2O_3	0.13	0.00	0.04	0.02	0.04	0.00	0.01	0.02	0.06	0.02	0.01	0.02	0.02	0.00	0.00	0.01	0.00	0.11	0.05	0.00	0.01	0.03
Fe_2O_3	3.00	1.42	0.32	1.84	0.20	2.85	1.54	0.95	1.87	2.21	1.12	2.48	1.28	0.67	1.17	0.95	0.35	2.22	1.98	0.00	0.99	0.81
FeO	12.73	18.03	20.02	19.19	23.18	10.76	13.54	17.56	20.29	22.82	25.75	25.34	23.84	23.43	25.10	26.13	26.50	19.86	23.62	26.82	25.70	25.24
MnO	0.37	0.69	0.53	0.43	0.71	0.31	0.27	0.44	0.83	0.52	0.59	0.67	0.83	0.97	0.87	1.16	1.47	0.45	0.80	0.89	0.86	3.75
MgO	14.19	10.82	9.54	10.93	8.54	16.14	15.62	11.72	4.29	5.77	5.85	4.96	2.89	3.76	3.48	3.56	2.90	10.60	7.91	6.61	7.19	2.46
CaO	7.22	6.88	7.92	6.34	6.25	7.01	5.89	7.18	13.52	8.96	6.96	7.43	12.05	11.28	10.46	9.15	9.34	5.90	5.93	4.97	5.04	9.05
Σ	100.46	99.77	99.92	100.73	100.09	101.49	101.18	100.76	101.16	100.17	100.01	99.58	99.16	99.19	100.40	100.16	99.35	100.57	100.82	99.94	100.16	100.57
Si	2.91	2.95	3.02	2.95	3.01	2.92	2.97	2.98	2.96	2.92	2.98	2.92	2.99	2.99	2.98	2.98	3.00	2.94	2.95	3.01	2.96	2.97
Al^{IV}	0.09	0.05	0.00	0.05	0.00	0.08	0.03	0.02	0.04	0.08	0.02	0.08	0.01	0.01	0.02	0.02	0.00	0.06	0.05	0.00	0.04	0.03
Al^{VI}	1.90	1.97	1.94	1.93	1.96	1.91	1.94	1.96	1.92	1.94	1.95	1.92	1.89	1.93	1.94	1.95	1.97	1.92	1.93	2.00	1.97	1.98
Cr	0.01	0.00	0.00	0.00	0.00	0.00	0.00	0.00	0.00	0.00	0.00	0.00	0.00	0.00	0.00	0.00	0.00	0.01	0.00	0.00	0.00	0.00
Fe^{3+}	0.17	0.08	0.02	0.10	0.01	0.15	0.08	0.05	0.11	0.13	0.07	0.15	0.08	0.04	0.07	0.06	0.02	0.13	0.11	0.00	0.06	0.05
Ti	0.01	0.00	0.00	0.00	0.00	0.01	0.00	0.01	0.00	0.00	0.00	0.00	0.02	0.02	0.01	0.00	0.01	0.00	0.00	0.00	0.00	0.00
Mg	1.55	1.22	1.08	1.22	0.97	1.72	1.68	1.30	0.49	0.67	0.68	0.58	0.34	0.44	0.41	0.42	0.34	1.19	0.90	0.77	0.83	0.29
Fe^{2+}	0.78	1.14	1.27	1.20	1.48	0.65	0.82	1.09	1.30	1.48	1.68	1.67	1.59	1.55	1.65	1.72	1.76	1.25	1.51	1.74	1.66	1.67
Mn^{2+}	0.02	0.04	0.03	0.03	0.05	0.02	0.02	0.03	0.05	0.03	0.04	0.05	0.06	0.07	0.06	0.08	0.10	0.03	0.05	0.06	0.06	0.25
Ca	0.57	0.56	0.64	0.51	0.51	0.54	0.46	0.57	1.11	0.75	0.58	0.63	1.03	0.95	0.88	0.77	0.80	0.48	0.49	0.41	0.42	0.77
Prp	53.10	41.19	35.63	41.24	32.29	58.92	56.59	43.45	16.58	22.78	22.83	19.90	11.39	14.72	13.59	14.00	11.46	40.39	30.58	25.69	27.95	9.73
Alm	26.70	38.51	41.98	40.60	49.19	22.04	27.52	36.51	44.01	50.58	56.33	57.09	52.64	51.41	55.05	57.60	58.74	42.46	51.20	58.50	56.07	56.08
Sps	0.79	1.49	1.12	0.95	1.53	0.65	0.54	0.94	1.82	1.16	1.31	1.54	1.86	2.16	1.94	2.58	3.30	0.99	1.76	1.95	1.89	8.45
Adr	8.01	3.96	0.92	5.05	0.61	7.45	4.15	2.63	5.30	6.23	3.27	7.09	3.91	2.03	3.44	2.79	1.05	6.13	5.57	0.00	2.81	2.37
Grs	11.40	14.86	20.35	12.15	16.39	10.94	11.20	16.47	32.28	19.25	16.27	14.38	30.20	29.68	25.98	23.03	25.45	10.03	10.89	13.87	11.29	23.38
X_{Mg}	0.67	0.52	0.46	0.50	0.40	0.73	0.67	0.54	0.27	0.31	0.29	0.26	0.18	0.22	0.20	0.20	0.16	0.49	0.37	0.31	0.33	0.15

1.5.2 Clinopyroxene

Clinopyroxene occurs in mylonitic metagabbros, banded anorthosites as well as in different types of basic dykes. Representative electron microprobe analyses are given in Table 1.2. Structural formulae were calculated on the basis of 6 oxygens and Fe^{3+} contents were estimated after Robinson (1982). End-member compositions were calculated following the scheme of Morimoto et al. (1988). The clinopyroxenes can be described in terms of quadrilateral pyroxene components, with most of the analyses falling in the diopside field (Fig. 1.13).

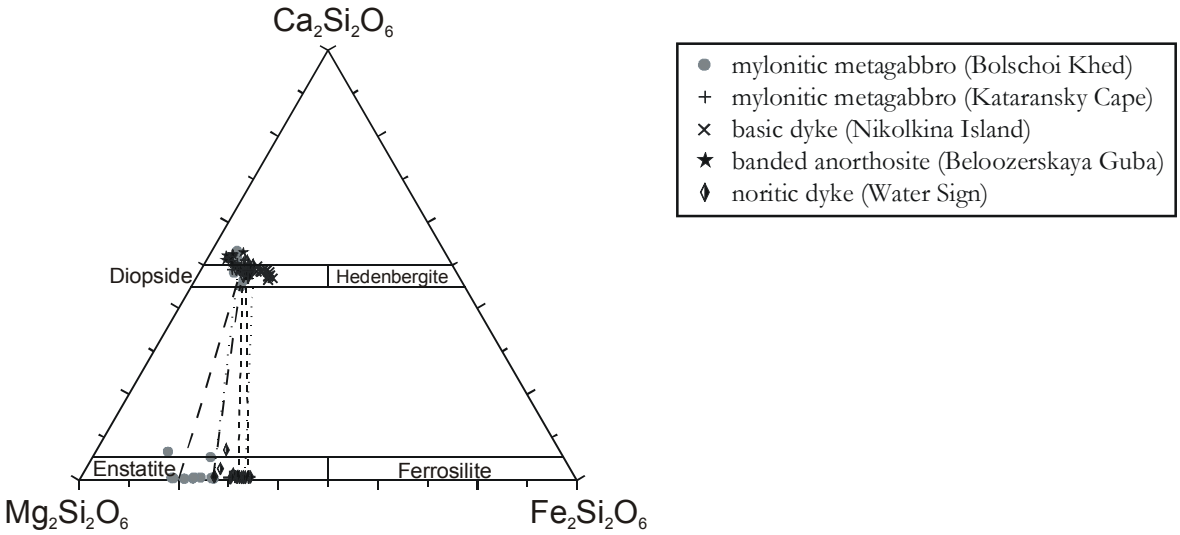

Fig. 1.13. Composition and nomenclature of pyroxenes in the Wo-En-Fs triangular plot (after Morimoto *et al.* 1988). Illustrated are tie lines between coexisting ortho- and clinopyroxene cores. Dashed lines, small dashed lines and dotted lines correspond to metagabbro (Bolschoi Khed), metagabbro (Kataransky Cape) and noritic dyke (Water Sign), respectively.

A few analyses are characterised by higher Ca-content and can be qualified as calcic diopsides. The compositional variation of clinopyroxenes in terms of En and Di components is illustrated in the diagram En-Fs-Di-Hd (Fig. 1.14).

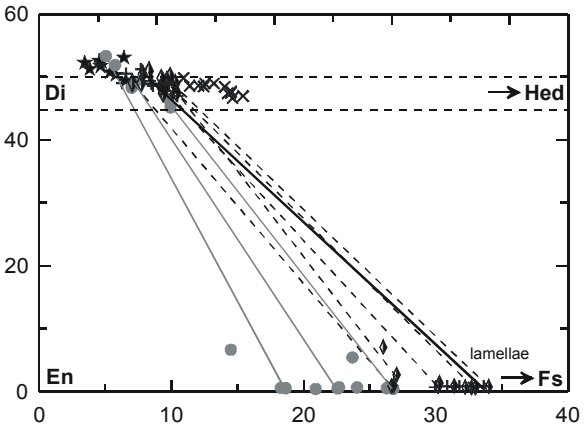

Fig. 1.14. Di-En-Hed-Fs plot of quadrilateral pyroxenes. Superimposed are tie lines between coexisting ortho- and clinopyroxene cores and rims, respectively. Dashed, grey and black lines correspond to noritic dyke (Water Sign), metagabbro (Bolschoi Khed) and metagabbro (Kataransky Cape), respectively.

A correlation with the bulk rock composition is obvious and especially well seen in the Al_{tot} versus *mg*# diagram (Fig. 1.15) . The most magnesian clinopyroxenes occur in the banded anorthosite and metagabbro samples (Bolschoi Khed Island; whole rock *mg*# *c.* 075) whereas the least magnesian clinopyroxene was found in the basic dyke of Nikolkina Island (whole rock *mg*# (0.45).

The clinopyroxenes show a systematic decrease of the Al content and a concomitant increase in the *mg*# from core to rim. The tie lines connecting coexisting clino-and orthoyroxenes in the Di-En-Hed-Fs plot, however, show no differences for core and rim compositions.

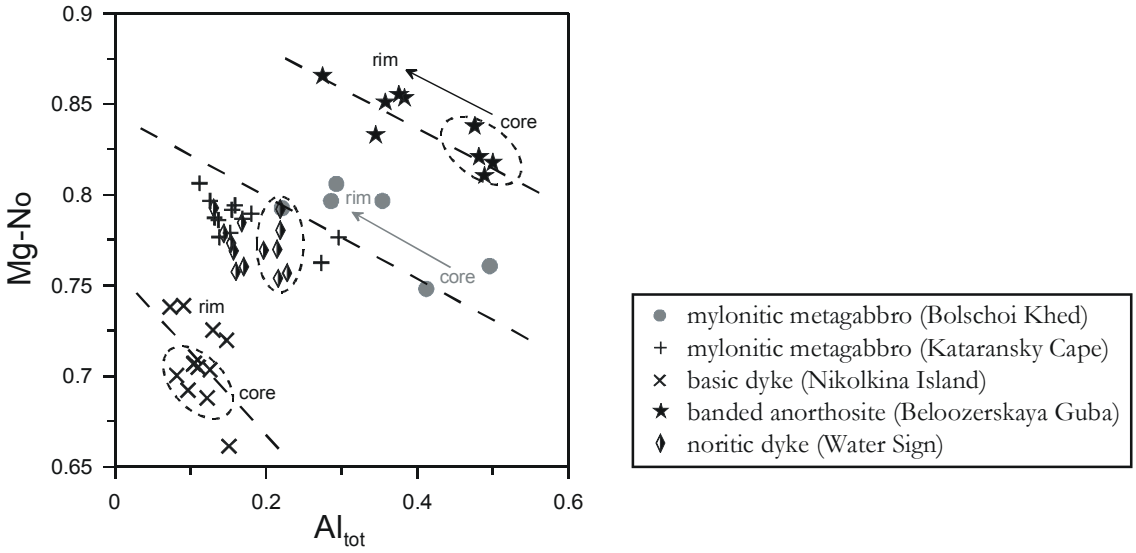

Fig. 1.15. Mineral composition of clinopyroxene from different rock types. Core-rim relations are indicated by arrows and show a concomitant Al decrease with increasing mg-number from core to rim.

Figs. 1.16 and 1.17a & b illustrate the role of different non-quadrilateral substitutions in the studied clinopyroxenes (Robinson, 1982). Al^{3+}, Fe^{3+} and $2Ti^{4+}$ substitutions in the M1-site are illustrated in Fig. 1.16. Clinopyroxenes in metagabbros and the noritic dyke show a decrease in Al^{VI}+Cr with a concomitant increase in Fe^{3+} from core to rim.

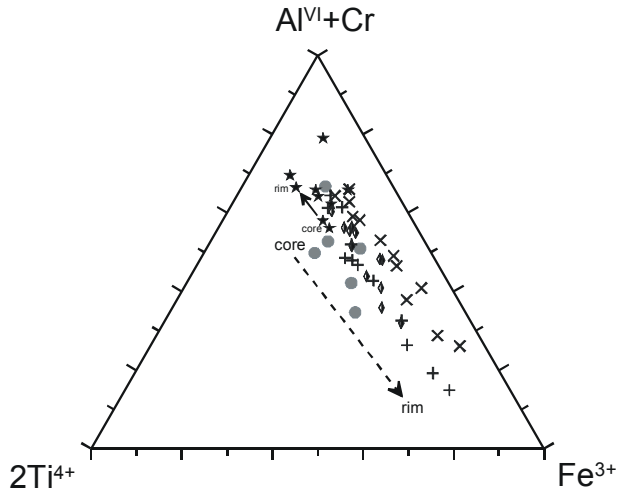

Fig. 1.16. Non-quadrilateral substitutions in clinopyroxenes after Robinson (1982). Dashed arrow illustrates core-rim relations of clinopyroxene from metagabbros and the noritic dyke. The black arrow shows core to rim development of clinopyroxene from the banded anorthosite.

The substitution of trivalent cations must be coupled with a tschermak-type substitution or jadeite and acmite substitutions, respectively. This is illustrated in Fig. 1.17a & b. Rimward zoning in isolated clinopyroxene grains is indicated by arrows. In general $Al^{VI}Al^{IV}$ (CATS) and $Na^{VIII}Al^{VI}$ (Jd) substitutions decrease from core to rim.

In clinopyroxene of the metagabbro (Kataransky Cape) and in newly formed coronitic clinopyroxenes of the noritic dyke (Water Sign) tschermaks ($Al^{VI}Al^{IV}$) and ferritschermaks ($Fe^{3+}Al^{IV}$) substitutions predominate. Clinopyroxene inclusions in garnet (noritic dyke & banded anorthosite) are characterised by elevated jadeite content (5.9-7.6 and 9.8-12 Jd%) indicating higher pressure conditions of metamorphism.

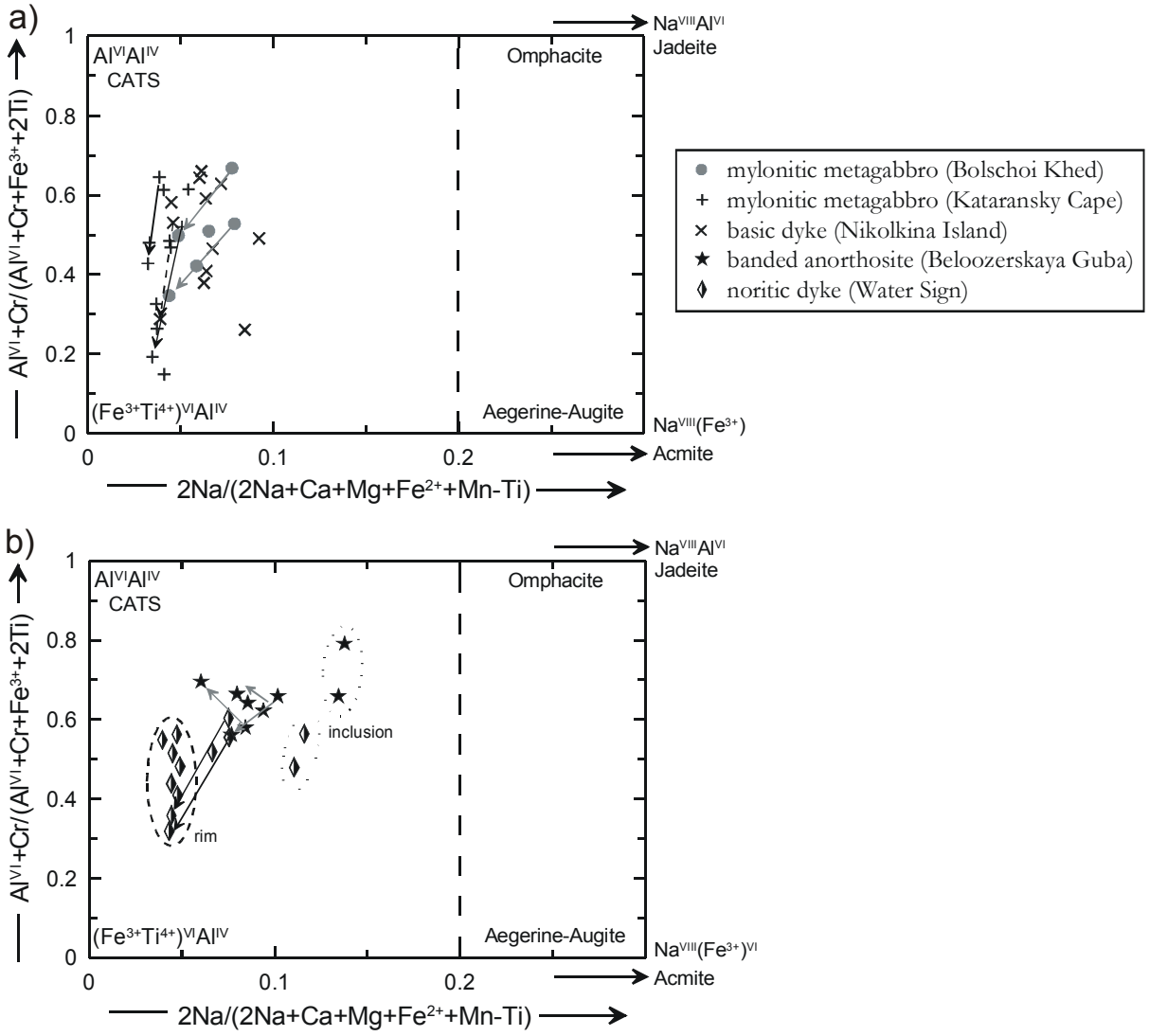

Fig. 17a & b. $Al^{VI}+Cr/(Al^{VI}+Cr+Fe^{3+}+2Ti)$ vs. $2Na/(2Na+Ca+Mg+Fe^{2+}+Mn-Ti)$ plot illustrates non-quadrilateral substitutions in clinopyroxene (Robinson, 1982). On the left side substitutions of 3 valent cations are compensated by Al^{IV} exchange, on the right side by Na exchange. Arrows indicate zonation from core to crystal rims. The dashed domain illustrates the range in composition of clinopyroxene rims and coronal clinopyroxene from the noritic dyke.

Table 1.2. Representative analyses of clinopyroxene cores, rims, inclusions and coronal clinopyroxene from different rock types. Analyses were recalculated on the basis of 6 oxygens.

	metagabbro			metagabbro			anorthosite				basic dyke			noritic dyke					
	Bolschoi Khed			Kataransky Cape			Beloozerskaya Guba				Nikolkina Island			Water Sign					
wt.-%	80 core	79 core	77 rim	1 core	9 core	5 rim	15 sympl.	49 core	50 rim	70 incl.	46 core	106 core	47 rim	8 corona	38 core	67 incl.	100 core	47 rim	80 corona
SiO_2	48.64	48.36	49.07	49.26	52.26	51.52	50.72	49.23	51.40	51.30	52.39	52.06	52.65	51.78	51.00	51.77	50.52	51.32	52.24
TiO_2	0.76	1.09	1.09	0.68	0.34	0.53	0.37	1.06	0.76	0.48	0.24	0.22	0.17	0.24	0.52	0.54	0.56	0.40	0.29
Al_2O_3	8.19	8.78	6.71	6.78	3.68	4.49	3.01	8.98	6.43	8.86	2.87	2.78	2.08	3.43	4.98	5.08	5.21	3.29	3.01
Fe_2O_3	3.41	1.94	2.04	2.60	0.92	0.65	0.04	2.37	0.68	1.23	1.12	2.03	0.93	2.43	1.95	2.24	2.19	2.64	1.25
Cr_2O_3	0.14	0.15	0.25	0.10	0.09	0.04	3.79	0.11	0.06	0.02	0.00	0.01	0.01	0.00	0.00	0.05	0.03	0.00	0.17
FeO	2.76	4.61	4.08	4.33	5.83	6.10	3.65	2.08	3.37	2.86	8.52	8.28	7.48	8.68	5.83	4.24	5.48	4.61	5.56
MnO	0.06	0.08	0.10	0.10	0.09	0.07	0.09	0.07	0.14	0.05	0.08	0.07	0.06	0.08	0.12	0.12	0.08	0.08	0.07
MgO	12.82	12.58	13.78	12.97	14.41	13.74	14.66	13.79	14.33	13.11	12.66	12.51	13.20	11.90	12.99	13.37	13.02	13.82	14.32
CaO	22.83	21.84	21.63	22.49	22.45	22.63	22.34	21.88	22.90	21.08	21.21	21.49	22.76	20.65	21.65	21.08	21.90	23.21	22.72
Na_2O	0.82	0.77	0.61	0.64	0.51	0.52	0.54	1.07	0.79	1.83	0.97	0.91	0.61	1.23	0.99	1.55	0.87	0.57	0.53
K_2O	0.04	0.04	0.13	0.06	0.02	0.00	0.00	0.03	0.02	0.01	0.00	0.02	0.01	0.00	0.00	0.00	0.02	0.02	0.01
Σ	100.48	100.24	99.49	100.01	100.59	100.31	99.23	100.69	100.88	100.84	100.08	100.37	99.98	100.43	100.03	100.05	99.89	99.97	100.16
Si	1.78	1.78	1.82	1.82	1.92	1.90	1.89	1.78	1.86	1.85	1.95	1.94	1.96	1.93	1.89	1.90	1.87	1.90	1.93
Al^{IV}	0.22	0.22	0.18	0.18	0.08	0.10	0.11	0.22	0.14	0.15	0.05	0.06	0.04	0.07	0.11	0.10	0.13	0.10	0.07
Al^{VI}	0.14	0.16	0.11	0.12	0.08	0.09	0.02	0.17	0.14	0.22	0.08	0.06	0.05	0.08	0.10	0.12	0.10	0.05	0.06
Fe^{3+}	0.09	0.05	0.06	0.07	0.03	0.02	0.11	0.07	0.02	0.03	0.03	0.06	0.03	0.07	0.05	0.06	0.06	0.07	0.04
Ti	0.02	0.03	0.03	0.02	0.01	0.02	0.01	0.03	0.02	0.01	0.01	0.01	0.01	0.01	0.01	0.02	0.02	0.01	0.01
Cr	0.00	0.00	0.01	0.00	0.00	0.00	0.00	0.00	0.00	0.00	0.00	0.00	0.00	0.00	0.00	0.00	0.00	0.00	0.01
Mg	0.70	0.69	0.76	0.72	0.79	0.75	0.81	0.75	0.77	0.70	0.70	0.69	0.73	0.66	0.72	0.73	0.72	0.76	0.79
Fe^{2+}	0.09	0.14	0.13	0.13	0.18	0.19	0.11	0.06	0.10	0.09	0.27	0.26	0.23	0.27	0.18	0.13	0.17	0.14	0.17
Mn^{2+}	0.00	0.00	0.00	0.00	0.00	0.00	0.00	0.00	0.00	0.00	0.00	0.00	0.00	0.00	0.00	0.00	0.00	0.00	0.00
Ca	0.90	0.86	0.86	0.89	0.88	0.89	0.89	0.85	0.89	0.81	0.85	0.86	0.91	0.82	0.86	0.83	0.87	0.92	0.90
Na	0.06	0.06	0.04	0.05	0.04	0.04	0.04	0.08	0.06	0.13	0.07	0.07	0.04	0.09	0.07	0.11	0.06	0.04	0.04
K	0.00	0.00	0.01	0.00	0.00	0.00	0.00	0.00	0.00	0.00	0.00	0.00	0.00	0.00	0.00	0.00	0.00	0.00	0.00
	4.00	4.00																	
Wo(Ca)	53.32	50.86	49.18	51.21	47.72	48.65	49.02	51.25	50.38	50.73	46.64	47.38	48.47	46.96	48.89	49.04	49.45	50.42	48.37
En(Mg)	41.65	40.76	43.58	41.10	42.61	41.11	44.73	44.94	43.84	43.90	38.74	38.37	39.11	37.63	40.82	43.26	40.90	41.77	42.40
Fs(Fe^{2+})	5.03	8.38	7.24	7.69	9.67	10.24	6.26	3.81	5.78	5.37	14.62	14.26	12.43	15.40	10.28	7.70	9.65	7.81	9.23
X_{Mg}	0.89	0.83	0.86	0.84	0.82	0.80	0.88	0.92	0.88	0.89	0.73	0.73	0.76	0.71	0.80	0.85	0.81	0.84	0.82

1.5.3 Orthopyroxene

Isolated orthopyroxene grains occur exclusively in the metagabbro of Bolschoi Khed Island and in the noritic dyke of the Water Sign locality. Otherwise orthopyroxene was formed in symplectitic intergrowths with plagioclase replacing porphyroblastic garnet during a decompressional stage related to the exhumation of the nappe stack. Structural formulae were calculated on the basis of 6 oxygens and Fe^{3+} contents were estimated after Robinson (1982). Table 1.3 includes some representative electron microprobe analyses. Orthopyroxene compositions plot in the enstatite field of Ca-Mg-Fe quadrilateral pyroxenes after Morimoto et al. (1988, Fig. 1.13). As mentioned before, no marked differences between coexisting pyroxene cores and rims can be observed (Fig. 1.14). Similar to the clinopyroxenes, the compositional variation of orthopyroxenes in terms of *mg#* depends on the whole rock chemistry. Compared to the clinopyroxenes no negative correlation between Al content and *mg*-number is observed (Fig. 1.18).

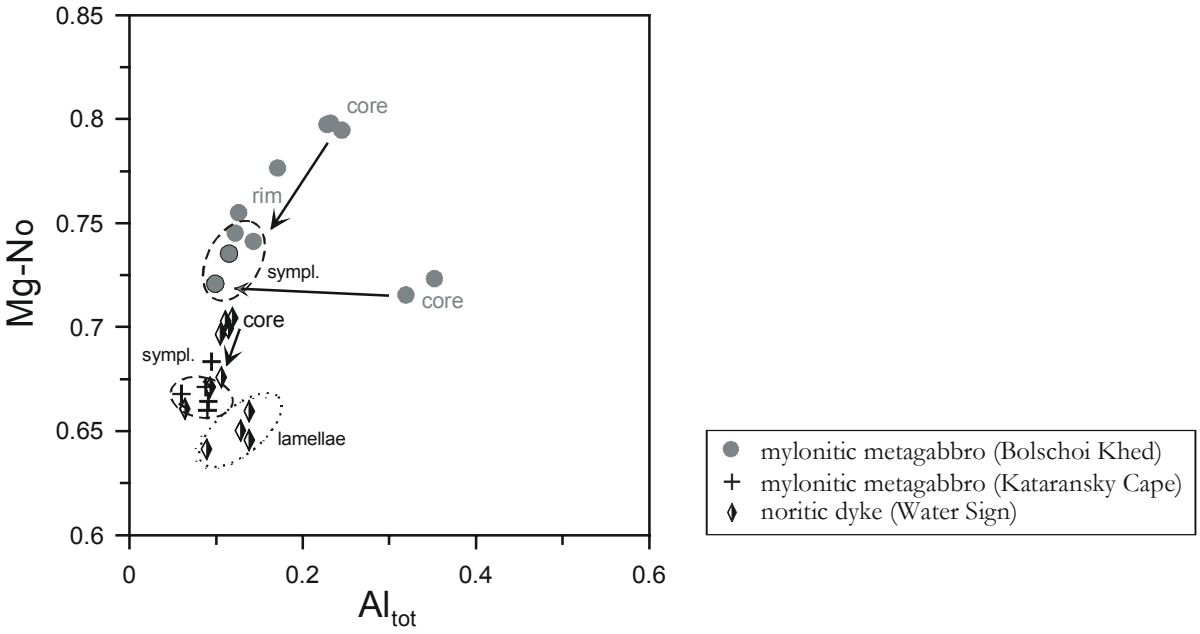

Fig. 1.18. Mineral composition of orthopyroxene from different rock types. Core-rim relations are indicated by arrows. Dashed envelopes indicate composition range of symplectitic orthopyroxene.

X-Ray maps of an anhedral orthopyroxene grain (Bolschoi Khed) illustrate the Al, Ca and Mg distribution (Fig. 1.19). Except for a zonation in Al content decreasing from core to rim, the orthopyroxene grains of the metagabbro are unzoned (Fig. 1.18 & 1.19). The central part of the grain shows Ca-enriched exsolution lamellae, probably pigeonite. The width of the lamellae is small, which indicates low diffusion rates and/or fast cooling. These domains are interpreted as older, perhaps magmatic cores (lower *mg#*) with development of exsolution lamellae possibly during metamorphic processes. The rims of large grains and the symplectite vermicules are very similar in composition (Fig. 1.18). In the noritic dyke (Water Sign) exsolution lamellae of orthopyroxene occur in large clinopyroxene grains believed to be of igneous origin. In contrast to the cores of larger orthopyroxene grains, these lamellae are characterised by higher Fs component.

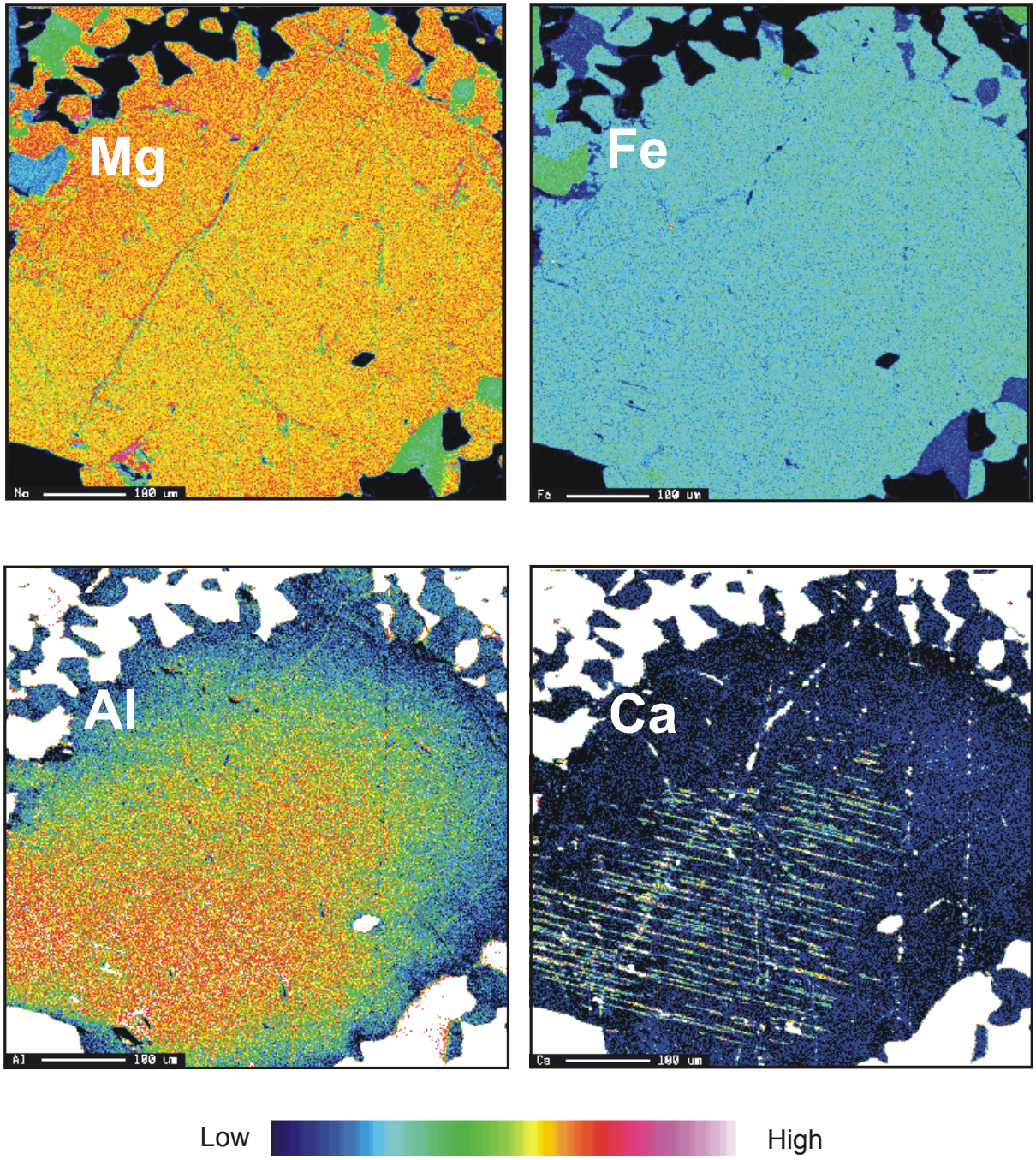

Fig. 1.19.. X-Ray maps showing the distribution of Mg, Fe, Al and Ca intensities of a orthopyroxene grain (metagabbro, Bolschoi Khed).

Table 1.3. Representative analyses of orthopyroxene cores, rims, symplectites and coronas from different rock types. Analyses were recalculated on the basis of 6 oxygens.

	metagabbro Bolschoi Khed						metagabbro Kataransky Cape		noritic dyke Water Sign			
wt.-%	101 core	71 core	104 rim	37 core	42 rim	26 sympl.	18 sympl.	11	15 corona	69 core	78 rim	99 l
SiO_2	52.23	52.45	52.71	50.32	53.61	52.64	52.02	52.79	52.81	52.03	52.36	51.83
TiO_2	0.11	0.09	0.11	0.12	0.04	0.05	0.08	0.08	0.05	0.07	0.07	0.12
Al_2O_3	5.86	5.45	4.03	7.49	2.34	2.88	2.08	2.31	1.48	2.77	2.44	3.17
Cr_2O_3	0.04	0.08	0.15	0.10	0.09	0.26	2.50	0.00	0.02	0.11	0.08	0.04
Fe_2O_3	1.54	1.61	1.22	1.57	1.00	2.45	0.01	0.00	1.53	2.58	2.04	1.16
FeO	11.64	11.44	13.15	15.93	17.07	14.19	19.46	21.06	20.29	16.52	18.83	20.20
MnO	0.08	0.10	0.17	0.30	0.38	0.21	0.19	0.23	0.20	0.25	0.24	0.33
MgO	28.31	28.52	27.78	24.50	26.02	26.94	23.63	23.05	23.70	25.21	24.16	23.08
CaO	0.25	0.29	0.19	0.25	0.21	0.32	0.36	0.41	0.34	0.42	0.39	0.31
Na_2O	0.01	0.01	0.00	0.01	0.00	0.02	0.00	0.00	0.00	0.01	0.00	0.00
K_2O	0.01	0.00	0.01	0.01	0.01	0.02	0.01	0.00	0.00	0.00	0.01	0.00
Σ	100.08	100.04	99.54	100.60	100.77	99.98	100.34	99.93	100.41	99.98	100.64	100.25
Si	1.85	1.86	1.89	1.82	1.94	1.90	1.92	1.95	1.95	1.90	1.92	1.91
Al^{IV}	0.15	0.14	0.11	0.19	0.07	0.10	0.08	0.05	0.06	0.10	0.08	0.09
Al^{VI}	0.10	0.09	0.06	0.13	0.03	0.02	0.01	0.05	0.01	0.02	0.02	0.05
Cr	0.00	0.00	0.00	0.00	0.00	0.01	0.00	0.00	0.00	0.00	0.00	0.00
Fe^{3+}	0.04	0.04	0.03	0.04	0.03	0.07	0.07	0.00	0.04	0.07	0.06	0.03
Ti	0.00	0.00	0.00	0.00	0.00	0.00	0.00	0.00	0.00	0.00	0.00	0.00
Mg	1.50	1.51	1.49	1.32	1.40	1.45	1.30	1.27	1.30	1.37	1.32	1.27
Fe^{2+}	0.35	0.34	0.40	0.48	0.52	0.43	0.60	0.65	0.63	0.51	0.58	0.62
Mn^{2+}	0.00	0.00	0.01	0.01	0.01	0.01	0.01	0.01	0.01	0.01	0.01	0.01
Ca	0.01	0.01	0.01	0.01	0.01	0.01	0.01	0.02	0.01	0.02	0.02	0.01
Na	0.00	0.00	0.00	0.00	0.00	0.00	0.00	0.00	0.00	0.00	0.00	0.00
K	0.00	0.00	0.00	0.00	0.00	0.00	0.00	0.00	0.00	0.00	0.00	0.00
Wo(Ca)	0.52	0.59	0.39	0.53	0.42	0.66	0.75	0.84	0.69	0.86	0.80	0.65
En(Mg)	80.83	81.14	78.70	72.88	72.79	76.68	67.88	65.56	67.08	72.49	69.02	66.64
Fs(Fe^{2+})	18.65	18.27	20.91	26.59	26.79	22.66	31.36	33.60	32.23	26.65	30.18	32.72
X_{Mg}	0.81	0.82	0.79	0.73	0.73	0.77	0.68	0.66	0.68	0.73	0.70	0.67

1.5.4 Plagioclase

In the granulite-facies rocks plagioclase typically occurs in equigranular polygonal aggregates which developed through (dynamic) recrystallisation and static annealing of former igneous crystals. The grains are generally unzoned. Representative electron microprobe analyses of plagioclase from granulite-facies and amphibolite-facies rocks are given in Tables 1.4 and 1.5. In the metagabbros and the noritic dyke plagioclase with anorthite contents ranging from An_{45} to An_{52} (andesine to labradorite) forms the felsic ground mass. Matrix plagioclase in the anorthosites is characterised by the highest anorthite contents varying from An_{70} to An_{76} (bytownite). Plagioclase within the mafic bands of the banded anorthosite and inclusions in garnet show lower An contents in the range of An_{40}-An_{72}.
Plagioclase occurs also in symplectitic intergrowths with orthopyroxene (metagabbros) or hornblende (anorthosite) resorbing porphyroblastic garnet and is characterised by high anorthite contents up to An_{84-88}. In the clinopyroxene-plagioclase-garnet coronas rimming ortho- and clinopyroxene grains (noritic dyke), the anorthite content of plagioclase is similar to that of matrix plagioclase, but is generally higher in coronas around clinopyroxene (An_{42-45}) than around orthopyroxene (An_{37-42}). Plagioclase in the basic dyke (Nikolkina Island) and in the metadiorite shows the lowest An contents ranging from An_{20-27} to An_{28-31}, respectively, which reflects the bulk chemistry of the rocks. In these rocks plagioclase is affected by sericitisation.
Plagioclase in amphibolite-facies hydration zones developed in metagabbros is often chemically zoned. Its compositional features as observed at the studied sites of Kataransky Cape and Bolschoi Khed provide insight into the cooling/retrograde history of the complex.
At Kataransky Cape, in the narrow transition zones separating the metagabbro host and completely amphibolitised central parts of the fluid infiltration zones, garnet and pyroxene are completely replaced by symplectitic aggregates of hornblende and calcic plagioclase (An_{65-80}). Larger plagioclase grains preserve granulite-facies cores (An_{47-49}) and show margins increased in anorthite content (An_{51-58}) (Fig. 1.20).

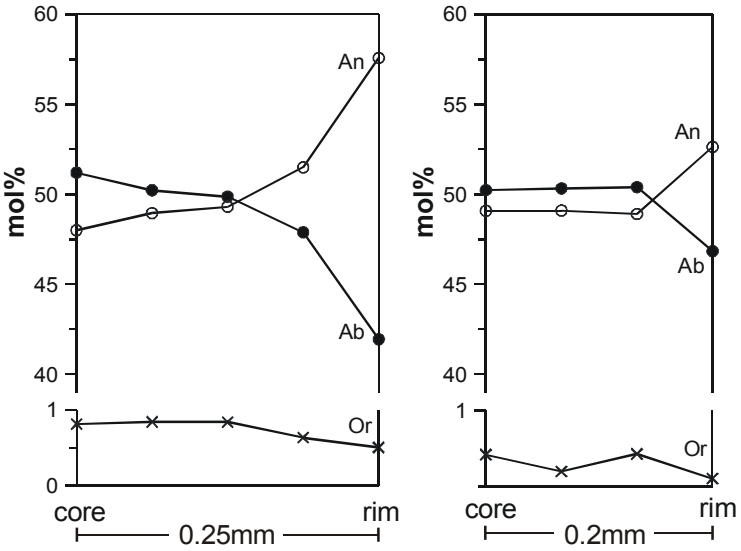

Fig. 1.20. Profiles of An, Ab and Or (mol%) from core to crystal rim of plagioclase grains from a weakly hydrated metagabbro at Kataransky Cape.

Core-rim inhomogeneities reflect incomplete re-equilibration of granulite-facies plagioclase during the amphibolite-facies overprint. In the centre of fluid infiltration zones, completion of metagabbro hydration led to the development of coarse-grained aggregates of hornblende and plagioclase. The cores of plagioclase grains are partially re-equilibrated with anorthite contents (An_{50-53}) ranging between the granulite-facies cores and the later rims of the transition zone. The rims show an abrupt increase in albite content (An_{40-45}) and are not re-equilibrated with the cores (Fig. 1.21a & 1.22a).
An example of complex zonation is provided by plagioclase grains in the hydrated metagabbro (Bolschoi Khed Island). The cores have compositions (An_{47-49}) that resemble those of plagioclase in the host metagabbro and are interpreted as relics of the granulite-facies grains. Discontinuous zonation patterns reflect disequilibrium (Fig. 1.21b & 1.22b).

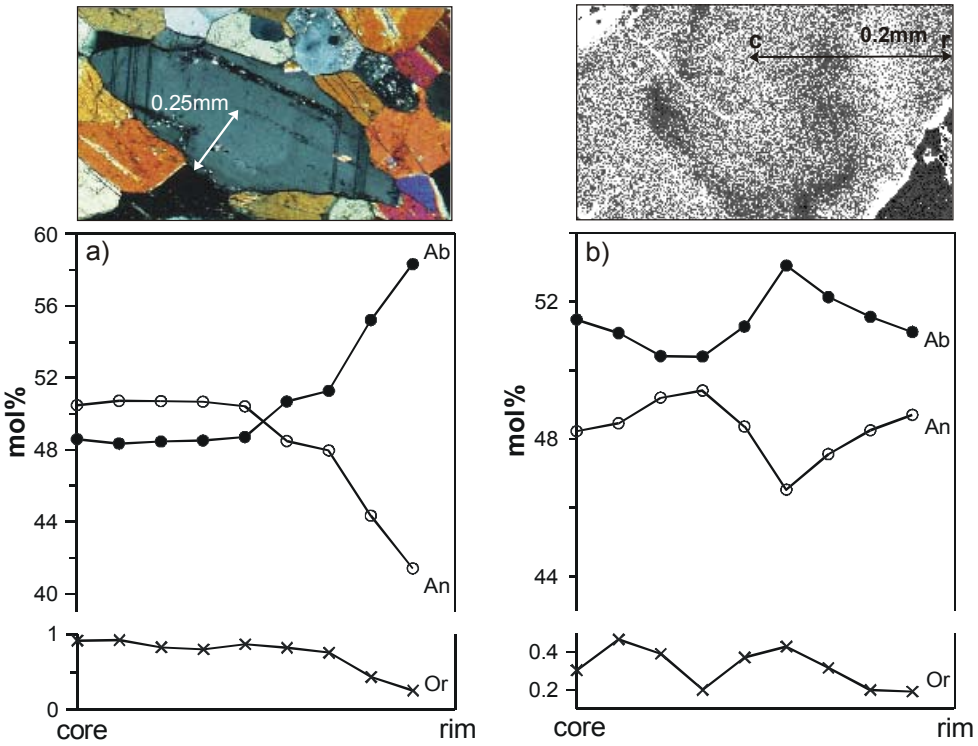

Fig. 1.21a & b. Profiles of An, Ab and Or (mol%) from core to crystal rim of plagioclase grains from hydrated metagabbros a) Kataransky Cape and b) Bolschoi Khed. Above pictures are a photomicrograph with crossed polarisers (a) and a element map of the Ca intensity (b) of the measured plagioclase grain.

In contrast to the zoned plagioclase grains, amphibole grains are compositionally homogeneous. In the rigid framework of the plagioclase lattice the coupled substitution CaAl ↔ NaSi ceases at high temperatures, whereas amphibole composition seems to be re-equilibrated.

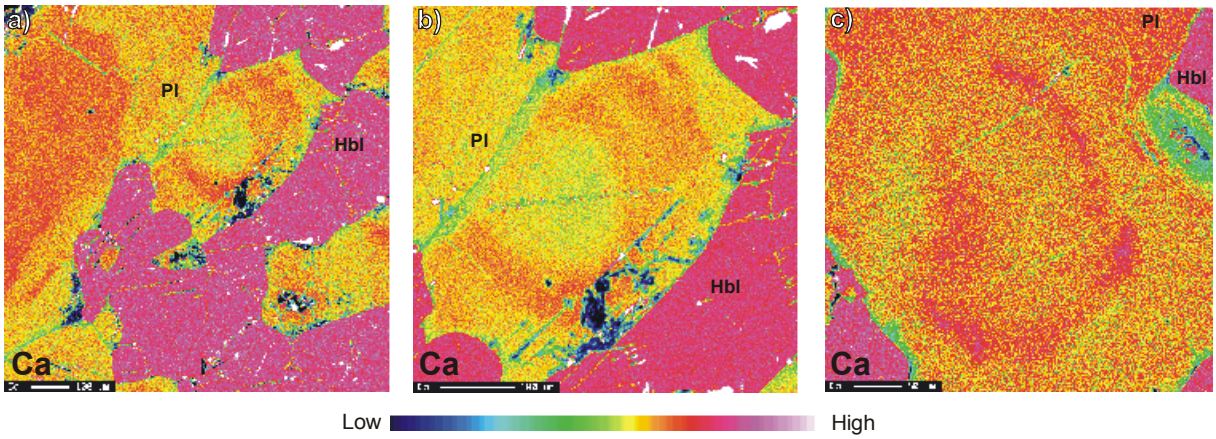

Fig. 1.22a-c. X-Ray maps illustrating the Ca intensity across plagioclase grains from hydrated metagabbros **a) & b)** Kataransky Cape and **c)** Bolschoi Khed.

Plagioclase compositions in the hydrated basic dyke (Nikolkina Island) and in the metadiorite (Leonard Cape) are similar to their protoliths (An_{27-31}) and are strongly affected by the hydration alteration. Secondary plagioclase (An_{7}) closely associated with prehnite, epidote, chlorite and titanite formed during a stage of low-grade hydration (c. 350°C). Thereby, Ca release due to sericitisation of plagioclase is involved in the reaction An + Bt + H_2O ↔ Prh + Chl + Ttn + Ms (Tulloch, 1979). Hydration proceeding from felsic veins is direct evidence for fluid infiltration. Plagioclase of a felsic vein at Kataransky Cape (metagabbro) is andesine (An_{38-44}), whereas vein plagioclase at Nikolkina Island (basic dyke) has a more sodic composition (An_{18-29}). Again plagioclase is affected by sericitisation (An_{7-12}).

Table 1.4. Representative analyses of plagioclase cores, rims, symplectites, inclusions and coronas from different rock types. Analyses were recalculated on the basis of 8 oxygens.

	metagabbro				metagabbro			anorthosite				basic dyke	noritic dyke				oph. dyke	diorite
	Bolschoi Khed				Kataransky Cape			Beloozerskaya Guba				Nikolkina Island	Water Sign				Kataransky	Leonard
wt.-%	56 core	25 incl.	16 rim	23 sympl.	24 core	17 rim	19 sympl.	61 core	71 incl.	92 incl.	81 sympl.	81 core	38 core	118 core	51 cor. cpx	92 cor. opx	45 core	20 core
SiO_2	55.31	52.95	56.51	46.33	55.94	55.40	54.11	49.90	50.56	55.02	46.36	63.56	61.73	53.64	57.43	57.80	53.39	59.48
Al_2O_3	28.57	29.60	27.83	34.03	28.09	28.67	29.02	32.06	30.94	28.50	33.94	23.17	24.17	29.13	26.39	26.74	29.93	25.14
Fe_2O_3	0.03	0.21	0.05	0.27	0.08	0.16	0.15	0.06	0.01	0.26	0.48	0.09	0.08	0.10	0.20	0.21	0.03	0.10
MgO	0.01	0.01	0.00	0.00	0.01	0.00	0.00	0.00	0.02	0.00	0.18	0.00	0.00	0.01	0.00	0.00	0.00	0.00
CaO	9.97	12.40	10.10	17.68	10.34	11.01	11.01	14.68	13.88	10.85	17.39	3.87	5.07	11.41	8.84	8.63	11.97	6.17
Na_2O	6.17	4.98	6.10	1.83	5.61	5.35	5.53	3.10	3.75	5.70	1.64	9.74	8.67	5.16	6.56	6.89	4.93	8.43
K_2O	0.25	0.18	0.20	0.05	0.28	0.20	0.24	0.08	0.14	0.18	0.02	0.36	0.30	0.27	0.26	0.10	0.07	0.15
Σ	100.33	100.34	100.81	100.20	100.34	100.79	100.06	99.88	99.32	100.53	100.02	100.82	100.04	99.73	99.70	100.36	100.34	99.50
Si	2.49	2.40	2.52	2.13	2.51	2.48	2.45	2.28	2.32	2.47	2.13	2.79	2.74	2.43	2.59	2.58	2.41	2.67
Al	1.51	1.58	1.46	1.85	1.49	1.51	1.55	1.72	1.67	1.51	1.84	1.20	1.26	1.56	1.40	1.41	1.59	1.33
Fe^{3+}	0.00	0.01	0.00	0.01	0.00	0.01	0.01	0.00	0.00	0.01	0.02	0.00	0.00	0.00	0.01	0.01	0.00	0.00
Mg	0.00	0.00	0.00	0.00	0.00	0.00	0.00	0.00	0.00	0.00	0.01	0.00	0.00	0.00	0.00	0.00	0.00	0.00
Na	0.54	0.44	0.53	0.16	0.49	0.46	0.48	0.27	0.33	0.50	0.15	0.83	0.75	0.45	0.57	0.60	0.43	0.73
Ca	0.48	0.60	0.48	0.87	0.50	0.53	0.53	0.72	0.68	0.52	0.86	0.18	0.24	0.56	0.43	0.41	0.58	0.30
K	0.02	0.01	0.01	0.00	0.02	0.01	0.01	0.00	0.01	0.01	0.00	0.02	0.02	0.02	0.02	0.01	0.00	0.01
Ab	52.06	41.66	51.62	15.73	48.76	46.24	46.97	27.52	32.57	48.23	14.56	80.39	74.29	44.32	56.46	58.78	42.51	70.60
An	46.52	57.37	47.24	84.00	49.65	52.61	51.70	72.04	66.62	50.76	85.31	17.68	24.00	54.13	42.07	40.68	57.09	28.55
Or	1.42	0.97	1.14	0.27	1.59	1.14	1.33	0.44	0.81	1.01	0.14	1.94	1.71	1.55	1.47	0.53	0.41	0.85

Table1.5. Representative analyses of plagioclase cores, rims, symplectites, inclusions and coronas from different hydrated rock types. Analyses were recalculated on the basis of 8 oxygens.

	hydrated metagabbro Bolschoi Khed			hydrated metagabbro Kataransky Cape						hydrated basic dyke Nikolkina Island			hydrated diorite Leonard Cape			
wt.-%	1 core	6 rim1	9 rim2	30 core	34 rim	3 sympl.	4 core	14 rim	26 incl.	63 vein	29 core	35 vein	30 vein alt.	8 core	10 rim	22 kfsp	18 alt.
SiO_2	55.50	54.78	54.17	55.90	52.58	48.11	54.75	57.55	57.09	56.65	61.73	60.59	64.11	58.76	58.23	63.56	63.91
Al_2O_3	28.44	28.27	28.79	27.92	30.01	32.72	28.99	27.13	27.64	27.50	24.73	24.91	21.89	25.82	25.94	19.35	22.63
Fe_2O_3	0.04	0.12	0.09	0.07	0.08	0.17	0.06	0.18	0.12	0.07	0.08	0.02	0.03	0.08	0.13	0.28	0.11
MgO	0.00	0.01	0.01	0.00	0.01	0.01	0.00	0.02	0.00	0.00	0.00	0.00	0.00	0.00	0.00	0.01	0.02
CaO	10.00	9.91	10.16	10.33	12.13	16.20	10.66	8.81	9.23	9.51	5.73	6.50	3.33	6.55	6.72	0.00	1.87
Na_2O	5.90	6.24	5.89	6.09	4.89	2.58	5.67	6.86	6.64	6.57	8.63	8.50	10.13	8.37	8.24	0.15	11.06
K_2O	0.05	0.08	0.03	0.15	0.09	0.05	0.16	0.05	0.14	0.08	0.08	0.07	0.07	0.10	0.09	16.46	0.20
Σ	99.94	99.40	99.14	100.45	99.80	99.86	100.34	100.59	100.86	100.39	100.98	100.60	99.57	99.68	99.35	99.82	99.81
Si	2.50	2.48	2.46	2.51	2.39	2.21	2.46	2.57	2.54	2.54	2.72	2.69	2.84	2.63	2.62	2.95	2.83
Al	1.51	1.51	1.54	1.48	1.61	1.77	1.54	1.43	1.45	1.45	1.28	1.30	1.14	1.36	1.38	1.06	1.18
Fe^{3+}	0.00	0.00	0.00	0.00	0.00	0.01	0.00	0.01	0.00	0.00	0.00	0.00	0.00	0.00	0.00	0.01	0.00
Mg	0.00	0.00	0.00	0.00	0.00	0.00	0.00	0.00	0.00	0.00	0.00	0.00	0.00	0.00	0.00	0.00	0.00
Na	0.52	0.55	0.52	0.53	0.43	0.23	0.49	0.59	0.57	0.57	0.74	0.73	0.87	0.73	0.72	0.01	0.95
Ca	0.48	0.48	0.50	0.50	0.59	0.80	0.51	0.42	0.44	0.46	0.27	0.31	0.16	0.32	0.32	0.00	0.09
K	0.00	0.00	0.00	0.01	0.01	0.00	0.01	0.00	0.01	0.00	0.01	0.00	0.00	0.01	0.01	0.98	0.01
Ab	51.48	53.05	51.11	51.19	41.94	22.32	48.60	58.33	56.12	55.33	72.83	70.02	84.29	69.43	68.59	1.39	90.49
An	48.22	46.52	48.70	48.00	57.56	77.41	50.49	41.42	43.07	44.24	26.70	29.60	15.31	30.04	30.92	0.02	8.46
Or	0.30	0.43	0.19	0.81	0.50	0.27	0.91	0.25	0.80	0.44	0.47	0.38	0.40	0.53	0.50	98.59	1.05

1.5.5 Amphibole

Amphibole is the dominant phase in the amphibolite-facies hydration zones, while in the mafic host granulites its occurrence is restricted to retrograde reaction domains such as symplectitic garnet breakdown or replacement of clinopyroxene. Representative electron microprobe analyses are given in Table 1.6. The structural formulae were calculated with the program Minpet and represent averages of formulae based on 15 cations excluding Na and K and 13 cations excluding Na, K and Ca. All amphiboles are calcic with Ti contents less than 0.5 atoms p.f.u. and, according to the classification scheme of Leake et al. (1998) range in composition from magnesio-hornblende to tschermakite and edenite to pargasite and ferro-pargasite, respectively (Fig. 1.23a & b).

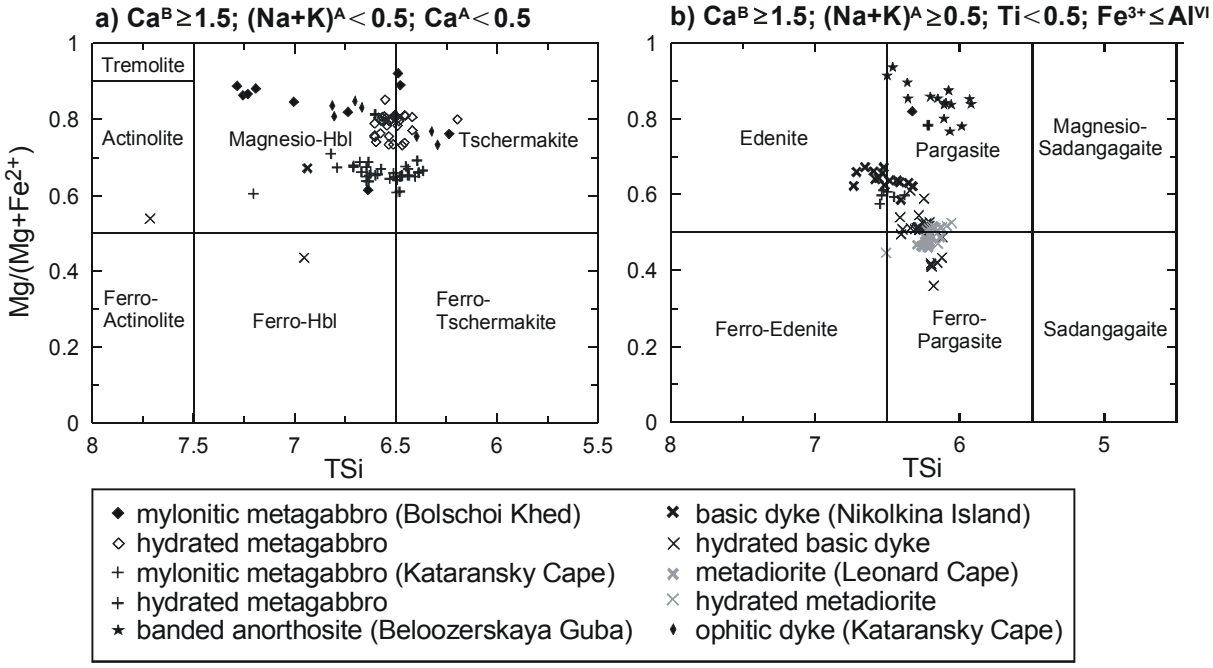

Fig. 1.23a & b. Composition and nomenclature of calcic amphiboles from different rock types (Leake et al., 1998).

Figures 1.24, 1.25 and 1.26 illustrate the most important substitutions. Plots of Al^{VI} versus Al^{IV} (Fig. 1.24a) and Al^{IV}-$(Na+K)^A/2$ versus $(Na+K)^A$ (Fig. 1.24) indicate the involvement of at least 3 substitutions. The tschermakite substitution is coupled with the edenite substitution resulting in the pargasite substitution $\square^A+(Mg, Fe^{2+})+2Si \leftrightarrow (Na, K)^A+Al^{VI}+2Al^{IV}$.

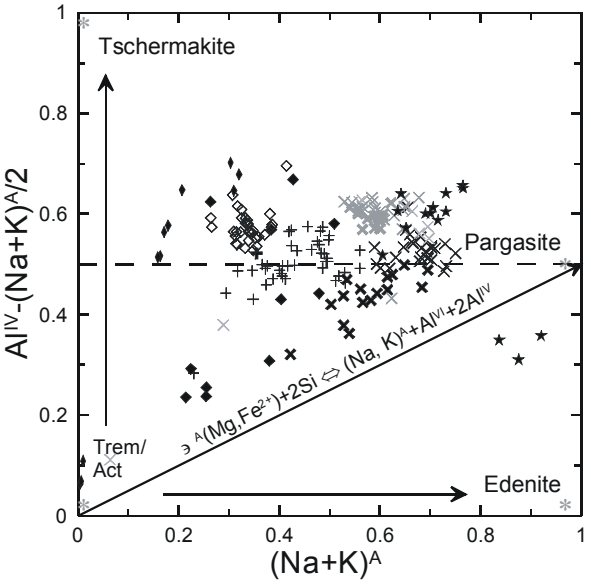

Fig. 1.24. Plot of Al^{IV} -(Na+K)/2 vs. /(Na+K) A-site occupancy for amphiboles from different rock types. Illustrated are amphibole endmembers resulting from different substitution types.

Ti and Al^{IV} show a positive correlation in the ratio 1:2 which is mainly due to the Ti-tschermakite substitution (Fig. 1.25b).

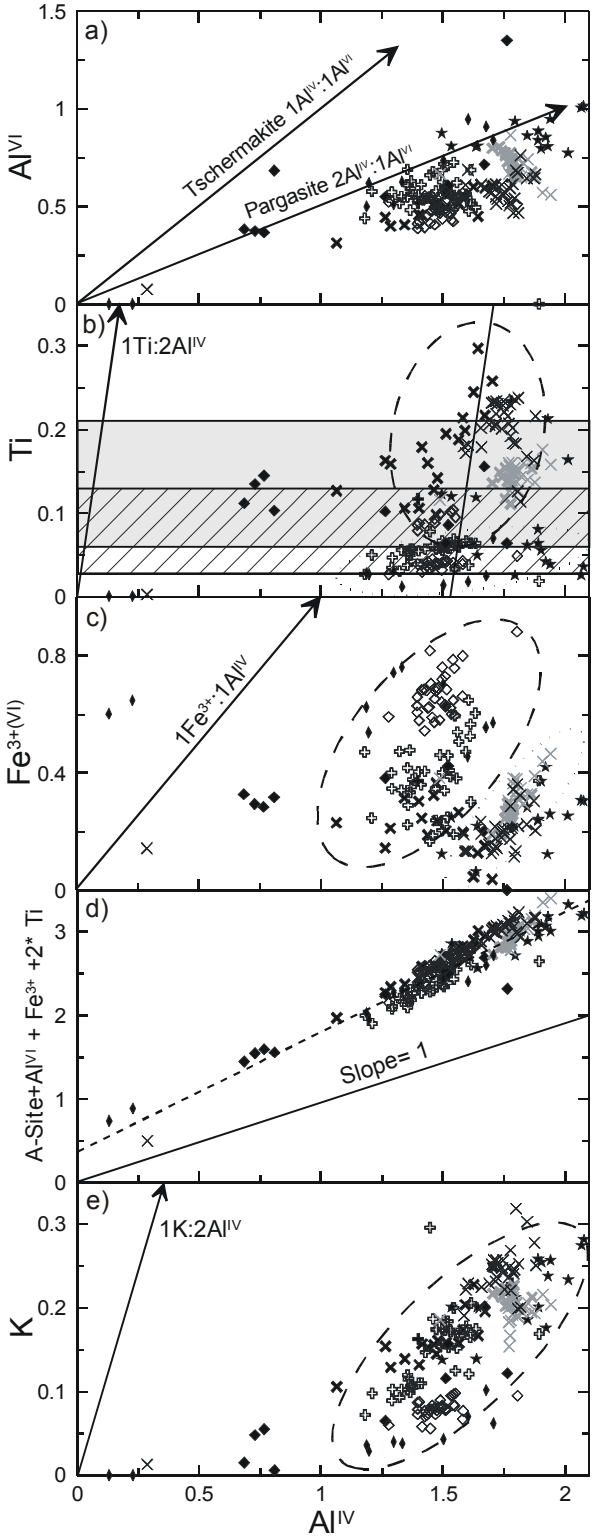

Fig. 1.25. Binary diagrams on the basis of the Al^{IV} content illustrating a couple of substitution mechanisms. In plot **1.25b**) the correlation between Ti content and metamorphic grade is indicated, grey field correspond to the higher grade amphibolite facies, dashed field to lower-grade amphibolite facies (Raase, 1974).

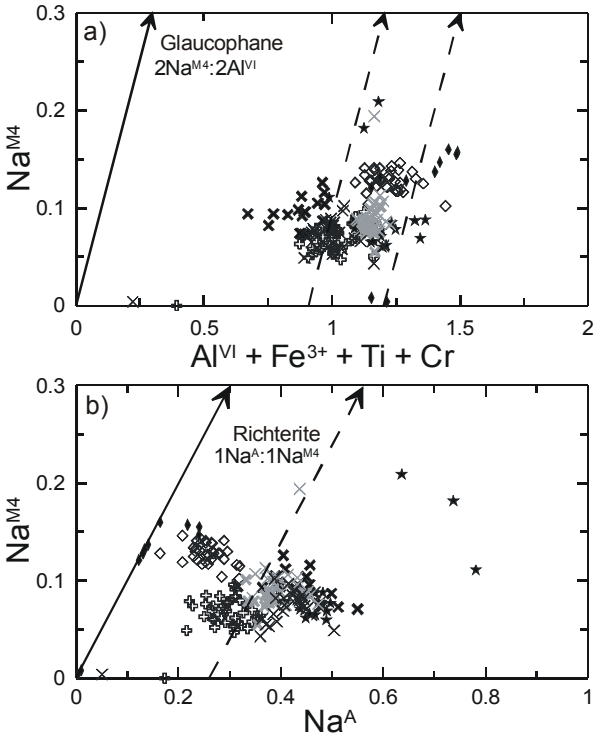

Fig. 1.26a & b. Plot of Na^{M4} vs. Al^{VI} illustrating glaucophane-type substitution (**a**). Plot of Na^{M4} vs. $Al^{VI}+Fe^{3+}+Ti+Cr$ with arrows indicating richterite-type substitution (**b**).

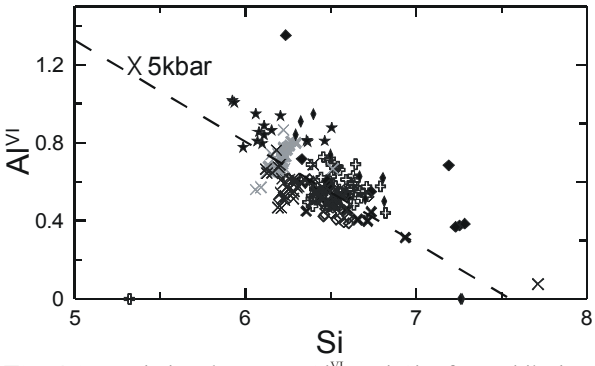

Fig. 1.27. Relation between Al^{VI} and Si of amphiboles from different rock types. Dashed line corresponds to a pressure of 5kbar (Raase, 1974).

- mylonitic metagabbro (Bolschoi Khed)
- hydrated metagabbro
- mylonitic metagabbro (Kataransky Cape)
- hydrated metagabbro
- basic dyke (Nikolkina Island)
- hydrated basic dyke
- metadiorite (Leonard Cape)
- hydrated metadiorite
- banded anorthosite (Beloozerskaya Guba)
- ophitic dyke (Kataransky Cape)

Variations in Fe^{3+} result primarily from the ferritschermakite substitution (Fig. 1.25c). In Fig. 1.25d substitutions involving Al^{IV} show a positive correlation with a slope close to 1. The intercept on the abscissa indicates the presence of A-site cations, Ti, Al^{VI} or Fe^{3+} that are related to other substitutions, for example the glaucophane, richterite or $2Na^{M4}+Ti^{VI} \leftrightarrow 2Ca^{M4}+Mg^{VI}$ substitutions (Fig. 1.26a & b). In summary, the compositional variations in the amphiboles can be described in terms of tschermakite, pargasite as well as Ti- and ferritschermakite substitutions and Fe^{2+}-Mg^{2+} exchange. In few cases also glaucophane and richterite substitutions (ophitic dyke, metadiorite, banded anorthosite) occurred.

The compositional attributes of amphibole are controlled by the whole rock composition, the *P-T* regime and the character of the infiltrating fluids. Many authors emphasise the dependence on metamorphic grade and fO_2 (Engel & Engel, 1962b; Leake, 1965; Raase, 1974; Laird & Albee, 1981; Spear, 1981). Na, K, Ti and Al contents increase with rising temperature (Spear, 1981). The substitution of Al^{VI} and Al_{total} seems to be more pressure sensitive (Fig. 1.27). In both cases, Si is depleted.

The plot of total Na/(Ca+Na) versus total Al/(Al+Si) is independent of the scheme of data normalisation (Fig. 1.28). Also indicated in this diagram are the fields of amphiboles from high-pressure, medium-pressure and low-pressure rocks as well as the 'oligoclase isograd' after Laird & Albee (1981), which separates the fields of low-grade albite-bearing assemblages from higher-grade assemblages with calcic plagioclase.

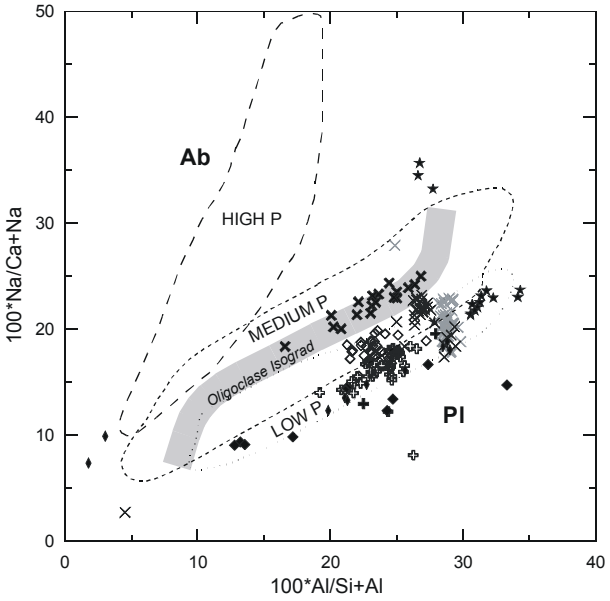

Fig. 1.28. Compositional variations of amphibole from different rock types after Laird & Albee (1981). The plot is independent of data normalisation. Indicated are the fields of high pressure amphiboles (long-dashed line), medium pressure (dashed line) and low pressure (dotted line). The superimposed 'oligoclase isograd' separates the stability fields of coexisting feldspar.

Most of the studied samples are characterised by medium to low pressure amphiboles and plot in the plagioclase field. Only amphiboles coexisting with coronitic garnet (basic dyke) plot along the oligoclase isograd. Amphibole inclusions in porphyroblastic garnet (banded anorthosite) are relics related to a higher pressure regime (Fig. 1.28).

1.5.6 Fe-Ti-oxides & minerals

Ilmenite occurs as anhedral and locally skeletal grains in the basic dyke (Nikolkina Island, Water Sign) and the metadiorite (Leonard Cape). Ilmenite ($FeTiO_3$) is the major constituent with contents ranging from 89 to 98 mol%. Hematite, geikielite and pyrophanite components account for 0.4-2.6, 0.3-3.4 and 0.4-5.1 mol%, respectively. **Rutile** occurs besides ilmenite in the higher-grade assemblages of metagabbros and basic dykes. In the amphibolite-facies hydration zones, ilmenite is replaced by **titanite**. In completely recrystallised amphibolite domains, titanite forms euhedral grains which are well orientated in foliated rocks. Al_2O_3 contents of 1.3 to 2 wt% indicate a retrograde origin (Franz & Spear, 1985).

Table 1.6. Representatitve analyses of amphibole cores, rims, symplectites and inclusions from different rock types. Analyses were recalculated on an unhydrous basis of 23 oxygens. General amphibole formulae were recalculated with minpet.

	hydrated metagabbro				hydrated metagabbro				hydrated basic dyke				hydrated diorite				anorthosite		ophitic dyke	
	Bolschoi Khed				Kataransky Cape				Nikolkina Island				Leonard Cape				Beloozerskaya G.		Kataransky	
wt.-%	1 core	13 rim	12 core	8 rim	40 core	18 sympl.	24 core	15 rim	7 core	90 core	25 core	39 incl.	33 core	26 core	28 rim	37 core	38 rim	2 incl.	20 sympl.	7 core	30 core
SiO_2	45.02	45.77	44.30	45.57	45.44	45.49	43.70	44.70	44.87	43.39	41.73	42.09	40.52	41.36	41.34	41.37	40.21	44.41	42.97	44.49	48.10
TiO_2	0.38	0.30	0.87	0.86	0.52	0.50	0.58	0.51	0.90	1.92	2.08	1.82	1.10	1.41	1.12	1.42	1.39	1.10	0.58	0.23	0.26
Al_2O_3	12.00	12.33	11.96	11.65	11.40	11.43	12.42	12.40	11.40	12.29	13.10	13.25	13.78	14.10	14.21	14.01	14.10	14.47	16.07	15.45	10.12
FeO	12.53	11.47	13.40	13.50	14.82	14.03	15.62	14.71	14.21	13.83	17.52	16.42	20.60	18.06	18.40	17.31	18.14	4.12	7.05	11.78	10.75
Cr_2O_3	0.00	0.04	0.00	0.00	0.00	0.00	0.04	0.04	0.00	0.00	0.00	0.04	0.00	0.00	0.00	0.00	0.00	0.00	0.00	0.00	0.00
MnO	0.21	0.25	0.24	0.20	0.20	0.25	0.22	0.20	0.00	0.05	0.11	0.10	0.24	0.33	0.35	0.21	0.33	0.04	0.07	0.00	0.02
MgO	14.34	14.66	13.18	13.50	11.88	12.14	11.88	11.81	12.84	11.80	9.27	9.87	6.90	8.36	8.21	9.02	9.00	17.20	15.34	13.24	15.71
CaO	11.33	11.67	11.25	11.32	11.85	12.10	11.80	12.00	11.57	11.39	11.47	11.36	11.72	11.25	11.39	11.39	11.51	11.67	12.28	11.19	11.48
Na_2O	1.36	1.35	1.51	1.45	1.33	1.23	1.40	1.19	1.75	1.93	1.75	1.77	1.36	1.69	1.66	1.86	1.88	3.21	1.84	1.36	0.89
K_2O	0.46	0.44	0.53	0.44	0.57	0.62	0.94	0.85	0.78	0.92	1.27	1.22	1.02	1.04	0.87	1.00	1.06	0.76	1.02	0.56	0.20
Σ	97.63	98.31	97.24	98.49	98.01	97.79	98.79	98.48	98.32	97.52	98.38	97.95	97.24	97.60	97.55	97.59	97.62	96.98	97.22	98.30	97.53
TSi	6.46	6.51	6.45	6.53	6.63	6.64	6.37	6.50	6.53	6.42	6.25	6.29	6.19	6.23	6.23	6.22	6.06	6.36	6.15	6.32	6.81
TAl	1.54	1.50	1.55	1.47	1.37	1.36	1.63	1.50	1.47	1.58	1.75	1.72	1.81	1.77	1.78	1.78	1.94	1.64	1.85	1.68	1.19
TFe^{3+}	0.00	0.00	0.00	0.00	0.00	0.00	0.00	0.00	0.00	0.00	0.00	0.00	0.00	0.00	0.00	0.00	0.00	0.00	0.00	0.00	0.00
TTi	0.00	0.00	0.00	0.00	0.00	0.00	0.00	0.00	0.00	0.00	0.00	0.00	0.00	0.00	0.00	0.00	0.00	0.00	0.00	0.00	0.00
CAl	0.49	0.57	0.50	0.50	0.59	0.61	0.50	0.63	0.48	0.56	0.56	0.62	0.67	0.73	0.74	0.70	0.56	0.81	0.86	0.91	0.50
CCr	0.00	0.00	0.00	0.00	0.00	0.00	0.01	0.01	0.00	0.00	0.00	0.01	0.00	0.00	0.00	0.00	0.00	0.00	0.00	0.00	0.00
CFe^{3+}	0.79	0.64	0.60	0.57	0.33	0.29	0.61	0.40	0.37	0.20	0.20	0.22	0.36	0.26	0.30	0.24	0.47	0.06	0.28	0.56	0.63
CTi	0.04	0.03	0.10	0.09	0.06	0.06	0.06	0.06	0.10	0.21	0.23	0.20	0.13	0.16	0.13	0.16	0.16	0.12	0.06	0.03	0.03
CMg	3.07	3.11	2.86	2.89	2.59	2.64	2.58	2.56	2.79	2.60	2.07	2.20	1.57	1.88	1.84	2.02	2.02	3.67	3.28	2.81	3.32
CFe^{2+}	0.61	0.63	0.93	0.94	1.42	1.39	1.24	1.34	1.27	1.42	1.93	1.76	2.25	1.95	1.97	1.87	1.78	0.34	0.51	0.71	0.53
CMn	0.01	0.02	0.02	0.01	0.01	0.02	0.01	0.01	0.00	0.00	0.01	0.01	0.02	0.02	0.02	0.01	0.02	0.00	0.00	0.00	0.00
BFe^{2+}	0.11	0.09	0.10	0.11	0.06	0.03	0.06	0.05	0.09	0.09	0.07	0.08	0.02	0.07	0.05	0.06	0.05	0.10	0.05	0.14	0.12
BMn	0.01	0.02	0.02	0.01	0.01	0.02	0.01	0.01	0.00	0.00	0.01	0.01	0.02	0.02	0.02	0.01	0.02	0.00	0.00	0.00	0.00
BCa	1.74	1.78	1.76	1.74	1.85	1.89	1.84	1.87	1.80	1.81	1.84	1.82	1.92	1.82	1.84	1.83	1.86	1.79	1.88	1.70	1.74
BNa	0.14	0.12	0.13	0.14	0.08	0.06	0.08	0.07	0.11	0.10	0.09	0.10	0.04	0.10	0.09	0.09	0.08	0.11	0.06	0.16	0.12
ACa	0.00	0.00	0.00	0.00	0.00	0.00	0.00	0.00	0.00	0.00	0.00	0.00	0.00	0.00	0.00	0.00	0.00	0.00	0.00	0.00	0.00
ANa	0.24	0.25	0.30	0.27	0.30	0.29	0.31	0.27	0.39	0.45	0.42	0.42	0.36	0.40	0.40	0.45	0.47	0.78	0.45	0.22	0.12
AK	0.08	0.08	0.10	0.08	0.11	0.12	0.18	0.16	0.15	0.17	0.24	0.23	0.20	0.20	0.17	0.19	0.20	0.14	0.19	0.10	0.04

1.6 Temperature and pressure estimates

To quantify the *P-T* conditions of different evolutionary stages of the granulitic precursors as well as the zones of amphibolite facies hydration, conventional geothermobarometry and multi-equilibrium thermobarometry (TWEEQU *2.02b* & *1.02*, Berman, 1991) have been applied to the observed microstructures and reaction textures in different basic rock types. At the south-eastern boundary of the Kolvitsa Massif, strongly mylonitic granulites form part of a prominent thrust. Peak metamorphic conditions for granulite-facies assemblages were recovered accounting for late Fe-Mg exchange (Pattison *et al.* 2003). In mafic rock types from the central part of the Kolvitsa Massif garnet occurs exclusively as a coronal phase and rocks may even preserve relictic igneous minerals. In amphibolitised zones multi-equilibrium techniques (TWEEQU *1.02*, Berman, 1991) could only be applied to garnet-bearing domains. These domains allowed the estimation of pressure and assessment of the composition of the hydrous fluid phase (aH_2O).
Temperature and pressure-depending equilibria were calculated assuming all Fe to be Fe^{2+}. In the case of clinopyroxene, however, this assumption seems not to be justified, and Fe^{2+}/Fe^{3+} corrections based on stoichiometry were taken into account. TWEEQU *2.02b* calculation routines were performed with the internally consistent thermodynamic data-base of Berman (1988), Berman *et al.* (1995) and Berman & Aranovich (1996), and the activity-composition formulations for garnet, clino- and orthopyroxene by Berman & Aranovich (1995) and for plagioclase by Fuhrman & Lindsley (1988). Equilibria involving amphibole were calculated with the TWEEQU *1.02* version. The activity models used in this version are Berman (1990) for garnet, the ideal-mixing model of Newton (1983) for pyroxene, the Fuhrman & Lindsley (1988) model for plagioclase and the amphibole model of Mäder *et al.* (1994). The results of conventional and multi-equilibrium thermobarometry are summarised in Tables 1.8 & 1.9-1.12.

1.6.1 Granulite-facies stage for mylonitic mafic rock types from the south-eastern boundary of the Kolvitsa Massif

Chemical equilibrium of an assemblage should be ideally characterised by compositionally homogeneous mineral grains and each mineral phase should have the same composition throughout the sample (Fitzsimons & Harley, 1994). Detailed electron microprobe studies, such as X-Ray element mapping and profile analysis along core-rim traverses, however, reveal zonation patterns in garnet and orthopyroxene grains. In the metagabbro from Bolschoi Khed the rimward increase in Fe and decrease in Mg in porphyroblastic garnet and the negligible or slight decrease of Mg/(Mg+Fe) in adjacent orthopyroxene point to retrograde diffusion zonation acquired during cooling (Tracy, 1982). Thereby intracrystalline diffusion driven by retrograde Fe-Mg exchange with adjacent Fe-Mg-phases across 'passive' grain boundaries and/or by retrograde net-transfer reactions, such as the symplectitic breakdown of garnet, across a retreating 'reactive' grain boundary (Fitzsimons & Harley, 1994). The observed zonation pattern indicates that the peak composition of garnet has been re-equilibrated along the grain margins and eventually also the cores. In consequence of diffusional mobility and the low blocking temperatures (<800 °C) for Fe-Mg exchange between garnet and ferromagnesian minerals, calculated temperature estimates are generally significantly lower than expected for the thermal peak of granulite-facies metamorphism (e.g. Lasaga, 1983; Harley, 1989; Frost & Chacko, 1989; Fitzsimons & Harley; 1994; Pattison & Bégin, 1994).
Contrary to octahedrally coordinated Fe and Mg, tetrahedrally coordinated Al in orthopyroxene is characterised by slow diffusion and its concentration hence is expected to preserve the equilibrium composition attained during peak granulite conditions (Anovitz, 1991; Pattison *et al.* 2003). Core-rim Al gradients in orthopyroxene grains with uniform Mg/(Mg+Fe) and with highest Al-contents in the core, indicate that Al diffusion ceased at temperatures at which intracrystalline Fe-Mg exchange still continued (metagabbro, Bolschoi Khed). Orthopyroxene zonation patterns may record cooling from UHT with Al contents decreasing from core to rim at constant pressure and X_{Mg} (Harley & Green,

1982). Similar to Al in orthopyroxene, the absence of Ca-zonation in garnet grains indicate that this element was frozen-in at temperatures well above the symplectite-reaction driven retrograde Fe-Mg exchange. For this reason pressure estimates from net-transfer reactions and temperature estimates from Fe-Mg exchange equilibria reflect decoupled physical conditions (Harley, 1989; Frost & Chacko, 1989; Fitzsimons & Harley, 1994). Late Fe-Mg exchange also affects the equilibrium constant in pressure-sensitive net-transfer reactions (feedback effect) (Harley, 1989; Fitzsimons & Harley, 1994; Pattison *et al.* 2003) and thus their position in *P-T* space. Yet, compared to Fe-Mg exchange thermometry, net-transfer equilibria depending on Al-solubility in orthopyroxene should provide more reliable peak temperature estimates, provided the effects of late Fe-Mg exchange are corrected for (Fitzsimons & Harley, 1994; Pattison & Bégin 1994; Bégin & Pattison, 1994).
For the Grt-Opx-Cpx-Pl-Qtz assemblage of the metagabbro from Bolschoi Khed Fe-Mg exchange temperatures were calculated for Opx-Grt and Cpx-Grt pairs based on the equilibria

$$\underset{\text{almandine}}{1/3\ Fe_3Al_2Si_3O_{12}} + \underset{\text{enstatite}}{1/2\ Mg_2Si_2O_6} \Leftrightarrow \underset{\text{pyrope}}{1/3\ Mg_3Al_2Si_3O_{12}} + \underset{\text{ferrosilite}}{1/2\ Fe_2Si_2O_6} \qquad (13)$$

and

$$\underset{\text{almandine}}{1/3\ Fe_3Al_2Si_3O_{12}} + \underset{\text{diopside}}{CaMgSi_2O_6} \Leftrightarrow \underset{\text{pyrope}}{1/3\ Mg_3Al_2Si_3O_{12}} + \underset{\text{hedenbergite}}{CaFeSi_2O_6} \qquad (14).$$

Application of the calibrations of Harley (1984a) and Bhattacharya *et al.* (1991) of equilibrium (13) to the core compositions give temperatures of 885-895 °C and 950-960 °C respectively, at a reference pressure of 13 kbar. As expected, significantly lower temperature estimates are obtained for rim compositions, i.e. *c.* 690 °C and *c.* 750 °C respectively, at a reference pressure of 12 kbar. Grt-Cpx thermometry results in higher temperatures, 990-1030 °C (core) and 745 °C (rim) for the Ravna Krogh (2000) calibration and unreasonable high temperatures of 1120 - 1150 °C (core) and 820 °C (rim) for the calibrations of Powell (1985) and Krogh (1988). These overestimated temperatures may be a result of not negligible amounts of Fe^{3+} in the clinopyroxene (see also mineral chemistry).
The net-transfer reaction 15 which controls the Al-solubility in orthopyroxene co-existing with garnet was calibrated by Harley & Green (1982) and Harley (1984b; with corrections by Fitzsimons & Harley, 1994).

$$\underset{\text{enstatite}}{Mg_2Si_2O_6} + \underset{\text{Mg-Ts component}}{MgAl_2SiO_6} \Leftrightarrow \underset{\text{pyrope}}{Mg_3Al_2Si_3O_{12}} \qquad (15)$$

Because of its relatively steep slope in *P-T* space, equilibrium 15 is used as pressure-sensitive geothermometer in this study. The calculated temperature values are 1030 °C (core) and 990 °C (rim) for the Harley & Green (1982) calibration and 1250 °C (core) and 1400 °C (rim) for the Harley calibration (1984b; with corrections of Fitzsimons & Harley, 1994). The unreasonable high temperature estimates obtained with the latter calibration are due to the strong dependency of the K_D on the Fe-Mg partitioning data and hence are attributed to late Fe-Mg exchange. On the contrary, the calibration of the thermometer by Harley & Green (1982) is considered as relatively insensitive to Fe-Mg exchange and thus should give reasonable temperature estimates for granulites (Harley, 1984b; Pattison & Bégin 1994). As expected, the Al-solubility temperatures are higher than the Fe-Mg exchange temperatures. The following hierarchy of closure temperatures is observed:

$$T_{Al}(\text{core}) > T_{Al}(\text{rim}) > T_{Fe\text{-}Mg}(\text{core}) > T_{Fe\text{-}Mg}(\text{rim}),$$

indicating that Al diffusion ceased prior to inter- and intragranular Fe-Mg exchange. In consequence of the non-simultaneous closure of Fe-Mg and Al in orthopyroxene and Ca in garnet, also multi-equilibrium techniques (TWEEQU *2.02b*, Berman, 1991) do not lead to convergence of equilibria. To test the state of equilibrium and to retrieve peak *P-T* conditions for the Grt-Opx bearing metagabbro (Bolschoi Khed), the amount of Fe-Mg resetting that occurred at down-temperature re-equilibration was attempted to estimate. This has been achieved by two similar approaches, the convergence method of Harley & Fitzsimons (1994) and Pattison & Bégin (1994) and calculations performed with

the computer programs RCLC and RCLC-P (Pattison *et al.* 2003). Both methods are based on the assumption that diffusion of Al is extremely slow (Anovitz, 1991) and that therefore Al concentrations in orthopyroxene preserve peak granulite-facies conditions. With the knowledge of pressure, the effects of down-temperature Fe-Mg exchange between garnet and orthopyroxene can be corrected bringing the Fe-Mg exchange and Al-solubility equilibria into convergence (Harley & Fitzsimons, 1994; Pattison & Bégin, 1994; Chacko *et al.*, 1996; Pattison *et al.*, 2003). In case of the convergence method a graphical approach was used (Figs. 1.29 & 1.30). Calibrations of the equilibria (13) and (15) by Harley (1984a), Harley & Green (1982) and Harley (1984b) were applied, because they are based on the same experimental data and assure internal consistency. Theoretically, if Fe, Mg and Al diffusion would close simultaneously, the Fe-Mg and Al-solubility temperatures should be the same. However, because of the different diffusivities, garnet becomes Fe-richer and orthopyroxene Mg-richer during cooling, while the Al-content in orthopyroxene remains frozen-in. As consequence, the two equilibria diverge and the Fe-Mg temperatures are lowered, whereas the Al-solubility temperatures raise (Figs. 1.29 & 1.30). Because the two equilibria behave in a opposite sense, the degree of divergence indicates the amount of Fe-Mg resetting. In Figures 1.29 & 1.30 the results for core compositions of grt (#11), opx (#71) and rim compositions of grt (#1), opx (#104) from the metagabbro (Bolschoi Khed) are illustrated, assuming that all change in Mg/(Mg+Fe) was taken up by garnet. The intersection of the two equilibria defines a line that lies close to the empirical Harley & Green (1982) calibration of equilibrium 3. For a given pressure the resulting temperature and the appropriate Mg/(Mg+Fe) changes can be determined. In most cases, all Fe-Mg phases, in our example garnet, orthopyroxene and clinopyroxene will change in Mg/(Mg+Fe) in response to cooling. The knowledge of the modal proportions of garnet and orthopyroxene for a fixed bulk rock composition, enables to recalculate incremental changes in Mg/(Mg+Fe) ratios for garnet and orthopyroxene, because the X_{Mg} values of orthopyroxene and garnet are allowed to vary antithetically (Harley & Fitzsimons, 1994; Harley 1998a). In the strongly foliated rocks discussed here, the distribution of garnet and orthopyroxene is not homogenous and estimation of mineral modes is difficult. Because steep zonation patterns in the garnet grains are mainly due to the symplectitic breakdown of this phase, the assumption that all changes in X_{Mg} were taken up by garnet seems to be reasonable, especially regarding mineral rims. However, the simplifying assumption that X_{Mg} changes are taken up by either garnet or orthopyroxene seems to cause only little error on *P-T* calculations (Pattison & Bégin, 1994).
Peak-pressure estimates necessary to be known for the retrieval technique were obtained by Grt-Opx-Pl-Qtz (16), Cpx-Pl-Qtz (17) and Grt-Opx-Cpx-Pl-Qtz (18) barometers, which seem to be robust or independent in regard to Fe-Mg exchange and may therefore act as independent reference barometers. To take the 'feedback' effect into account results from Grt-Opx-Pl-Qtz barometry were recalculated for late Fe-Mg exchange.

$$\underset{\text{grossular}}{Ca_3Al_2Si_3O_{12}} + \underset{\text{pyrope}}{2Mg_3Al_2Si_3O_{12}} + \underset{\text{quartz}}{2SiO_2} \Leftrightarrow \underset{\text{enstatite}}{3Mg_2Si_2O_6} + \underset{\text{anorthite}}{3CaAl_2Si_2O_8} \qquad (16)$$

$$\underset{\text{Ca-tschermak}}{CaAl_2Si_2O_6} + \underset{\text{quartz}}{SiO_2} \Leftrightarrow \underset{\text{anorthite}}{CaAl_2Si_2O_8} \qquad (17)$$

$$\underset{\text{pyrope}}{Mg_3Al_2Si_3O_{12}} + \underset{\text{diopside}}{CaMgSi_2O_6} + \underset{\text{quartz}}{SiO_2} \Leftrightarrow \underset{\text{enstatite}}{2Mg_2Si_2O_6} + \underset{\text{anorthite}}{CaAl_2Si_2O_8} \qquad (18)$$

Grt-Opx-Pl-Qtz (Bhattacharya *et al.*, 1991) and Grt-Opx-Cpx-Pl-Qtz (Paria *et al.*, 1988) barometry for mineral cores gives pressure estimates of about 13 kbar at a reference temperature of 1050 °C. Cpx-Pl-Qtz barometry (McCarthy & Patiño Douce, 1998) for clinopyroxene cores and plagioclase inclusions and matrix plagioclase, respectively, yields pressure estimates between 12.9 - 13.3 kbar and 13.3 - 13.5 kbar, respectively. Taking a pressure value of 13 kbar as best estimate, the graphical convergence method gives an intersection temperature of 1060 °C.

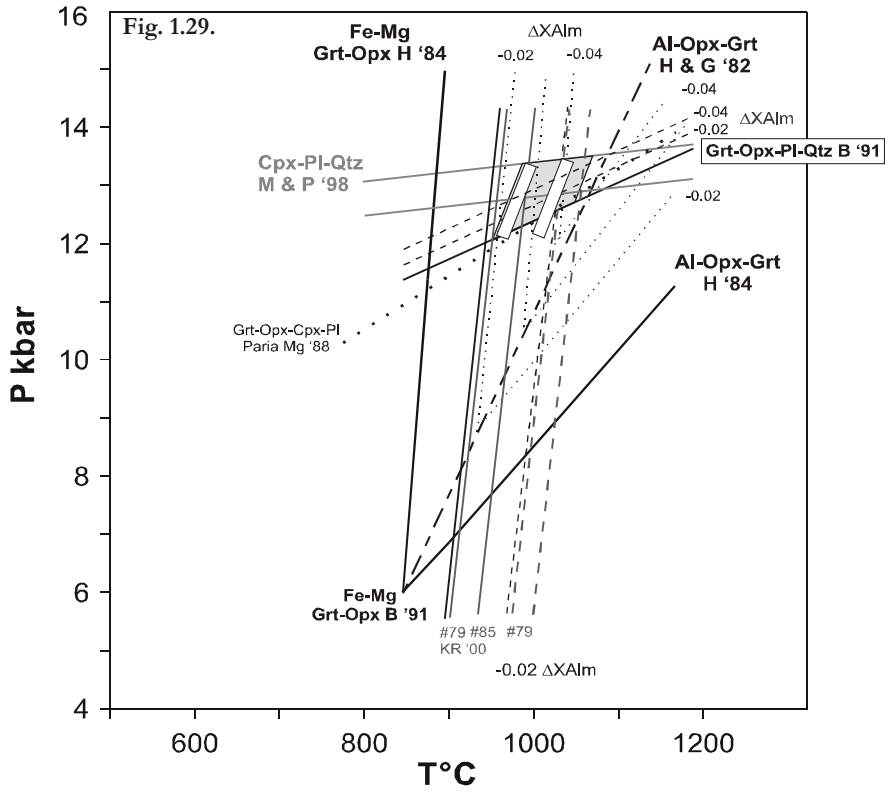

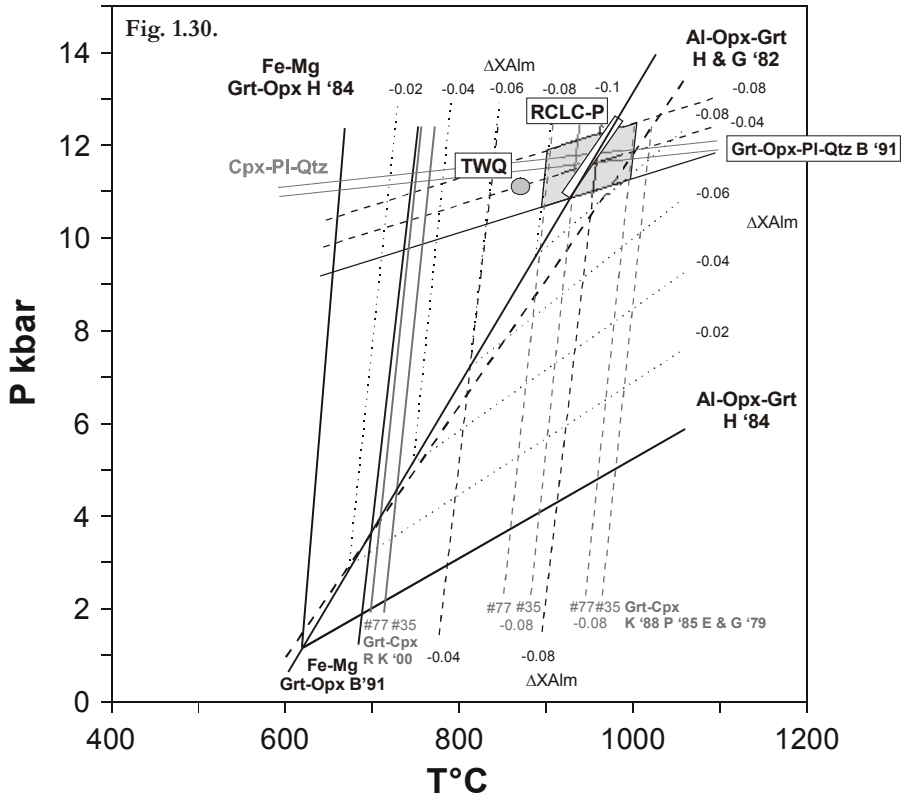

Fig. 1.29 & 1.30. P-T diagrams showing the results of the convergence method of Fitzsimons & Harley (1994) for the recovery of *P-T* conditions of the granulite-facies stage. Illustrated are the position of Fe-Mg exchange (Harley 1984a) and Al-solubility equilibria of Harley (1984b) and Harley & Green (1982) using core compositions of garnet (#11) & orthopyroxene (#71) (Fig. 1.29) and rim compositions of garnet (#1) & orthopyroxene (#104) (Fig. 1.30) from metagabbro (Bolschoi Khed Island). Dotted lines show the effect of decreasing X_{Alm} on the position of Fe-Mg and Al-solubility equilibria . The intersections of the two equilibria define a line close to the Harley & Green (1982)reaction. The position of the Grt-Opx-Pl-Qtz barometer (Bhattacharya et al. 1991) and Fe-Mg exchange thermometers for Grt-Opx (Bhattacharya *et al.* 1991) and Grt-Cpx (Krogh Ravna, 2000) with changing X_{Alm} are also illustrated. For comparison the Cpx-Pl-Qtz and Grt-Opx-Cpx-Pl-Qtz barometer (Paria *et al.* 1988) are plotted.

Corrected Fe-Mg temperature estimates for the Grt-Opx exchange thermometer (Bhattacharya *et al.*, 1991) are in the range of 1020 °C and for the Cpx-Grt exchange thermometer (Ravna Krogh, 2000) between 1030 – 1050 °C (corrected for Fe^{3+}).

Beside thermal resetting during cooling, geothermometer based on the exchange of Fe^{2+} between mineral phases are problematic since electron microprobe data only provide information on the total iron content (Spear, 1993; Ravna Krogh, 2000). Calculations of Fe^{3+} and Fe^{2+} contents based on stoichiometry criteria, however, are very sensitive to analytical imprecision, especially in the case of magnesian clinopyroxenes. Fe^{3+} correction in clinopyroxene may lower the Fe^{2+}/Mg ratios significantly and result in higher K_D values and thus lower temperatures. If no independent measure of the ferric iron content was made, Fe^{3+} correction based on stoichiometry should be handled with care.

In our case, Cpx-Grt thermometry that is not adjusted for Fe^{3+} gives unrealistic high estimates. However, when corrected for the presence of Fe^{3+} in clinopyroxene, the data closely match the restored Grt-Opx and Al-solubility temperatures and are therefore regarded as plausible. This assumption is supported by results from TWEEQU (*2.02b*), where no convergence was achieved of the equilibria involving the end-members phases almandine, pyrope, enstatite, ferrosilite, 'aluminium-orthopyroxene', diopside, hedenbergite, anorthite and quartz (Fig. 1.31a). Fe^{3+} correction for clinopyroxene, on the other hand, resulted in an improved convergence of equilibria (Fig. 1.31b) and the *P-T* estimate of 13 kbar & 1000 °C coincides with results from classical thermobarometry (Fig. 1.29; Table 1.8). Grossular was omitted from the calculations because equilibria involving grossular plot outside the convergence field defined by the other equilibria, presumably due to the less reliable thermodynamic data for this phase (Berman, 1991; Zhao *et al.* 2000).

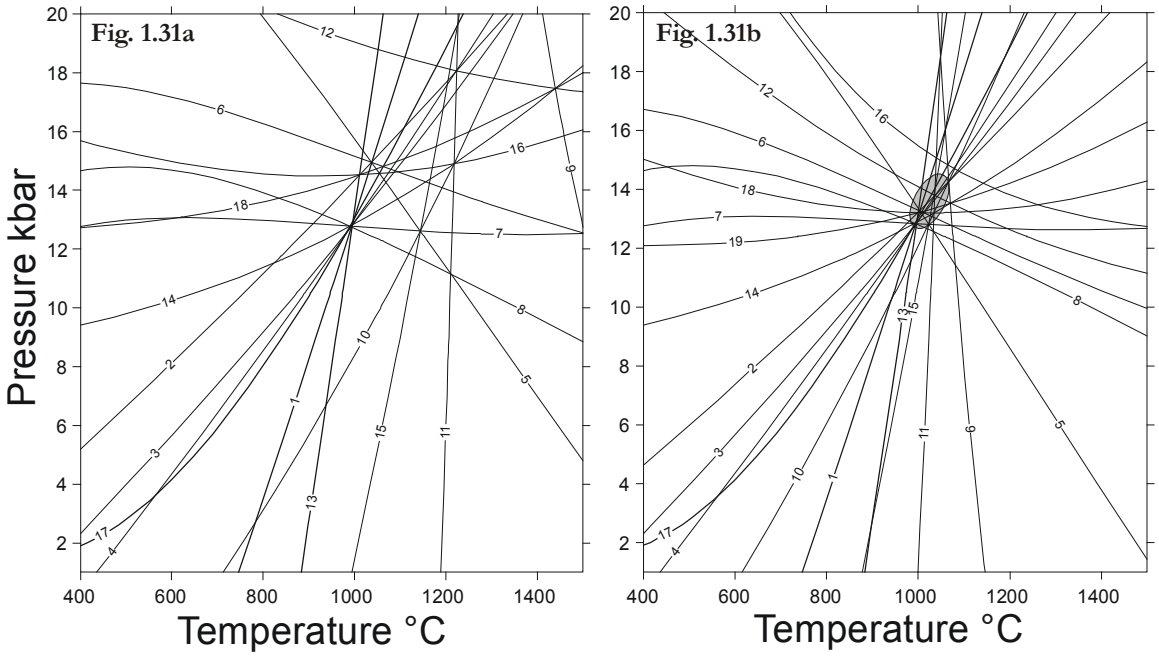

Fig. 1.31a & b. P-T estimations with TWEEQU 202b for core compositions of garnet (#11), orthopyroxene (#71), clinopyroxene (#79), plagioclase (#56) and quartz from metagabbro (Bolschoi Khed Island). The garnet composition is corrected (ΔX_{Alm}= -0.02) to account for retrograde Fe-Mg exchange due to symplectitic breakdown. 1.31a**.** All Fe is assumed to be Fe^{2+}. **1.31b.** Fe^{2+}-correction for Cpx.

1): Alm = Al-Opx + 3 Fs
2): βQtz + Hd + Alm = An + 4 Fs
3): βQtz + Di + Alm = An + 3 Fs + En
4): 3 βQtz + 3 Di + 4 Alm = 3 An + 12 Fs + Py
5): 3 βQtz+ 3 Hd + 4 Al-Opx = Alm + 3 An
6): bβQtz + Hd + Al-Opx = An + Fs
7): Al-Opx + Di + βQtz = En + An
8): 4 Al-Opx + 3 Di + 3 βQtz = Prp + 3 An
9): En + Hd = Di + Fs
10): Alm + 4 Di + βQtz = 4 En + 3 Hd + An
11): Alm + 3 Di = Prp + 3 Hd
12): βQtz + Prp + 4 Hd = An + 3 Di + 4 Fs
13): Alm + 3 En = Prp + 3 Fs
14): βQtz + Prp + Di = An + 4 En
15): Alm + 3 Di = 3 En + 3 Hd + Al-Opx
16): Prp + 3 Hd = Al-Opx + 3 Di + 3 Fs
17): Prp = 3 En + Al-Opx
18): βQtz + 4 Prp + 3 Hd = Alm + 3 An + 12 En
19): βQtz + Prp + Hd = An + Fs + 3 En

Tab. 1.7. Mineral equilibria considered in TWEEQU calculations:
Calculations for granulite-facies stage 1(metagabbro, Bolschoi Khed) were performedfor the CFMAS subsystem using the following end-members: Alm, Prp, Al-OpxEn, Fs, Di, Hd, An, β-Qtz.

The method of Pattison *et al.* (2003) is similar to the convergence method described above and is largely the same as is reported in Chacko *et al.* (1996). The thermobarometry scheme used by the computer program RCLC and RCLC-P is the thermodynamic database of TWEEQU *2.02b* and provides internal consistency. Recalculated temperatures from metagabbro for mineral cores are 980 - 1000 °C at a reference pressure of 13 kbar and 950 – 960 °C at a reference pressure of 12 kbar for rim compositions.
Results obtained with the convergence method for rim compositions are illustrated in Figure 1.30. The Fe-Mg exchange equilibrium (Harley, 1984a) diverges significantly from the equilibrium based on Al-solubility (Harley, 1984b) and give temperatures of 670 °C and 1400 °C, respectively. The large degree of divergence indicates significant Fe-Mg resetting during cooling. Corrected temperature estimates of 970 °C at a reference pressure of 12 kbar are in accordance with RCLC-P calculations (960 °C). Pressure estimates of the Cpx-Pl-Qtz barometer (McCarthy & Patiño Douce, 1998) and the Grt-Opx-Pl-Qtz barometer (Bhattacharya *et al.*, 1991) were used as reference pressures and give 11.5 - 12 kbar and 12 - 12.2 kbar (corrected for late Fe-Mg exchange), respectively. Opx-Grt temperatures corrected for Fe-Mg exchange are in the range of 960 - 970 °C and 905 - 950°C for the Bhattacharya *et al.* (1991) and Harley (1984) calibrations, respectively. Temperatures for the uncorrected Al-Opx thermometer (Harley & Green, 1982) are close to 1000 °C. Temperatures corrected for late Fe-Mg exchange assuming all iron to be in the ferrous state give temperatures of 905 - 910 °C for the Ravna Krogh (2000) calibration and 960 – 990 °C for the Powell (1985) and Krogh (1988) calibrations and are in agreement with other temperature estimates. Temperatures corrected for Fe^{3+} are *c.* 100 °C lower and approximate 900 °C for the Powell (1985) and Krogh (1988) calibrations. The lower temperature estimates of about 800°C for the Ravna Krogh (2000) calibration seem to be unreasonably low. However, Fe^{3+} contents in garnet and clinopyroxene are lower and have a minor effect on temperature estimations.
P-T results for core-rim relations of the metagabbro (Bolschoi Khed) document only minor cooling and decompression (ΔT= 100 °C and ΔP = 1 kbar) from peak-metamorphic conditions. The temperature decrease is also indicated by the zonation patterns in orthopyroxene. As a first approximation the Harley & Green (1982) Al-solubility expression gives reasonable temperatures, even if Fe-Mg exchange was decoupled from Al during cooling. Therefore the difference between the temperature estimates derived from the Al-solubility (Harley & Green, 1982) and Fe-Mg partition data (Harley, 1984a) gives an idea of the temperature difference between the closure of Al-Si and Mg-Fe exchange (Pattison & Bégin, 1994). For cores of garnet #11 and orthopyroxene #71, Al-solubility temperature is 1060 °C and Fe-Mg exchange temperature 890 °C, indicating that Fe-Mg exchange ceased 170 °C below the closure of Al-Si exchange. Assuming that no significant diffusive Al transfer has taken place, temperature estimates corrected for late Mg-Fe exchange (1050 °C) are believed to

represent near-peak temperatures. Lower estimates retrieved for mineral rims represent the temperature at which Al-Si diffusion closed.

Where orthopyroxene is absent in the granulite-facies assemblages, such as in the metagabbro at Kataransky Cape and the banded anorthosite from Beloozerskaya Guba, interpretation of pressure and temperature estimates are difficult in regard to Fe-Mg resetting. Fe-Mg exchange thermometry for Cpx-Grt core pairs from metagabbro (Kataransky Cape) yield temperatures in the range of 850 - 900 °C for the Powell (1985), Krogh (1988) and Ellis & Green (1979) calibrations at a given pressure of 12 kbar (Fig. 1.32, Table 1.8). Temperatures for the Ravna Krogh (2000) calibration are 100 °C lower and vary from 780 - 830 °C.

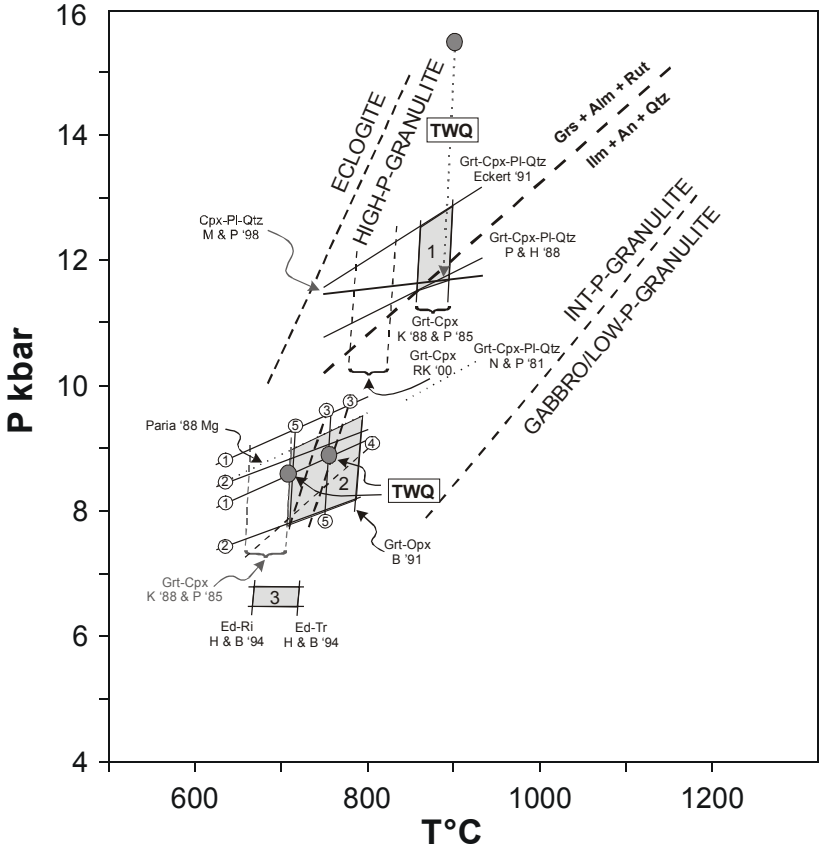

Fig. 1.32. P-T diagram illustrating different evolutionary stages for the metagabbro from Kataransky Cape. Stability fields of eclogite, high-, medium- and low-pressure granulite are from Green & Ringwood (1967). Model reaction An + Ilm + Qtz = Grs + Alm + Rt is from Bohlen & Liotta (1986).

Pressure estimates:

Grt-Cpx-Pl-Qtz: (1) Eckert '91, (2) Powell & Holland '88, Perkins & Newton '81;
CaTs: (M & P) McCarthy '98; Grt-Opx-Cpx-Pl-Qtz: Paria *et al.* '88

Temperature estimates:

Grt-Cpx: (RK) Ravna Krogh '00, (K) Krogh '88, (P) Powell '85; Al-Opx-Grt: (3) Harley & Green '82, (4) Harley '84b; Grt-Opx: (5) Harley '84a, (B) Bhattacharya *et al.* '91, Hbl-Pl: (H & B) Holland & Blundy '94

Granulite-facies temperature estimates for garnet cores and clinopyroxene inclusions of the anorthosite are higher and reveal that near peak temperatures were close to 1000 °C (calibrations: Powell, 1985; Krogh, 1988; Ellis & Green, 1979) at an inferred pressure of 15 kbar (Fig. 1.33). Again the Ravna Krogh (2000) calibration yields lower temperatures about 880 - 915 °C. Because Fe^{3+} assessments on the basis of stoichiometry indicates low Fe^{3+} contents in garnet and clinopyroxene, temperatures were calculated assuming all iron to be in the ferrous state. Even if temperatures were lowered by retrograde Fe-Mg exchange and Cpx-Grt thermometry strongly depends on Fe^{3+} normalisation, the calculated temperatures seem to be reasonable. The temperature interval of 900 - 1000 °C is in agreement with temperature estimates of the orthopyroxene-bearing assemblages (Fig. 1.33).

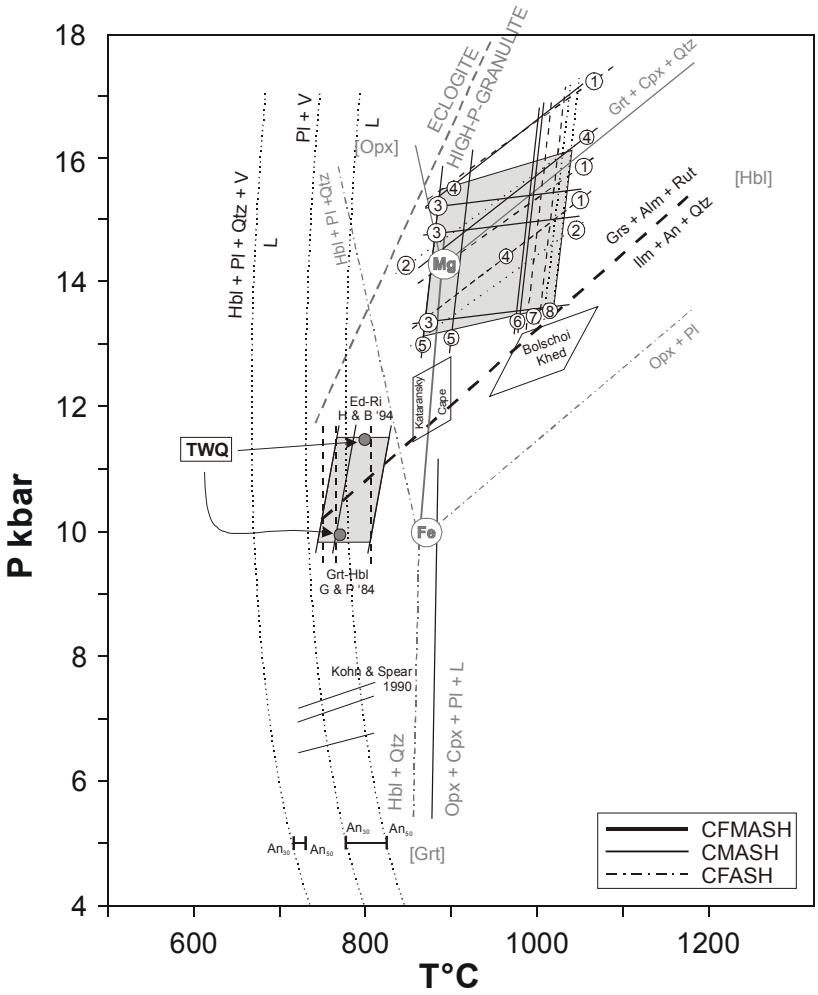

Fig. 1.33. P-T diagram illustrating different evolutionary stages for the banded anorthosite from Beloozerskaya Guba. Indicated are the position of the tonalite wet solidus: Pl + Qtz ⇆ Hbl + H_2O = L from Piwinskii (1968), Wolf & Wyllie (1993) and the positions of the anorthosite wet solidus: Pl + H_2O from Johannes (1978). Brackets at 5 kbar show displacement of the solidi due to varying An contents (An_{30-50}) (Johannes, 1978). Model reactions in the CFMASH system are from Pattison (2003) and are based on experimental and thermodynamic data. Reaction Grs + Alm + Rut = Ilm + An + Qtz is from Bohlen & Liotta (1986). Transparent boxes indicate *P-T* estimates for metagabbros from Bolschoi Khed and Kataransky Cape.

Pressure estimates:

Grt-Cpx-Pl-Qtz: (1) Eckert '91, (2) Powell & Holland '88; CaTs: (3) McCarthy '98; Jd-contet: (4) Holland '83; Grt-Hbl-Pl-Qtz: Kohn & Spear '90

Temperature estimates:

Grt-Cpx: (5) Ravna Krogh '00, (6) Krogh '88, (7) Powell '85, (8) Ellis & Green '79; Hbl-Pl (edenite-richterite): (H & B) Holland & Blundy '94; Grt-Hbl: (G & P) Graham & Powell '84

Pressure estimates from Grt-Cpx-Pl-Qtz barometry based on equilibria (19) & (20) (calibrations of Newton & Perkins, 1981; Powell & Holland, 1985; Eckert *et al.*, 1991) were applied.

$$\underset{\text{anorthite}}{3CaAl_2Si_2O_8} + \underset{\text{diopside}}{3CaMgSi_2O_6} \Leftrightarrow \underset{\text{grossular}}{2Ca_3Al_2Si_3O_{12}} + \underset{\text{pyrope}}{Mg_3Al_2Si_3O_{12}} + \underset{\text{quartz}}{SiO_2} \qquad (19)$$

$$\underset{\text{anorthite}}{3CaAl_2Si_2O_8} + \underset{\text{hedenbergite}}{3CaFeSi_2O_6} \Leftrightarrow \underset{\text{grossular}}{2Ca_3Al_2Si_3O_{12}} + \underset{\text{almandine}}{Fe_3Al_2Si_3O_{12}} + \underset{\text{quartz}}{SiO_2} \qquad (20)$$

Cpx-Pl-Qtz barometry (McCarthy & Patiño Douce, 1998) for core compositions (metagabbro, Kataransky Cape) yield pressures between 11.5 and 11.7 kbar closely matching the estimates of Grt-Cpx-Pl-Qtz barometry (11 - 12 kbar) for the Powell & Holland (1985) and Eckert *et al.* (1991) calibrations at a reference temperature of 900 °C. The peak-assemblage from the banded anorthosite is characterised by higher pressures (14 - 15.5 kbar) at a reference temperature of 1000 °C (Tab. 1.8). High pressures are indicated by elevated Na_2O contents in clinopyroxene cores and inclusions in garnet (*c.* 1.9 wt%) and are consistent with pressures of 14.7 - 15.5 kbar obtained from barometry based on Jd-content in clinopyroxene (21) (Holland, 1983).

$$\underset{\text{albite}}{NaAlSi_3O_8} \Leftrightarrow \underset{\text{jadeite}}{NaAlSi_2O_6} + \underset{\text{quartz}}{SiO_2} \qquad (21)$$

Equilibrium (17) which controls the content of Ca-tschermaks component in clinopyroxene gives pressure in the range of 13.5 to 15.3 kbar. Equilibria based on equation (17) and (21) have an opposite effect on the plagioclase composition. Whereas in equilibrium (17) the increase of the Ca-tschermak content in clinopyroxene causes a decrease in the anorthite content of coexisting plagioclase, an increase in jadeite content in clinopyroxene (21) leads to an increase in anorthite content in plagioclase. Compared to matrix plagioclase (An_{75}), plagioclase in mafic bands is characterised by distinctly lower anorthite content (An_{45}), leading to the assumption that the anorthite content was lowered by the increased take-up of Ca-tschermak component in clinopyroxene. Due to the strong influence that equilibrium (17) has on the plagioclase composition, the effect caused by elevated jadeite content is compensated.

Because of the uncertainty of late Fe-Mg exchange, *P-T* estimates for mineral rims have not been undertaken. The absence of orthopyroxene in the granulite-facies Grt-Cpx-Pl ±Qtz assemblages indicate high pressure granulite facies (Green & Ringwood, 1967; Harley, 1992; Carswell & O'Brian, 1993). Beside pressure also bulk rock composition and temperature have influence on orthopyroxene stability. In Fe-rich bulk rock compositions orthopyroxene is consumed at lower pressures to give Opx-free Grt-Cpx-Pl ±Qtz assemblage than in Mg-rich compositions. In Figure 1.32 & 1.33 the dashed lines indicate stability fields of eclogite, high-, medium- and low-pressure granulite from Green & Ringwood, 1967. To display the dependency on bulk rock composition, schematic phase equilibria for the CFMASH system at amphibolite and granulite from Pattison (2003) were pictured in Figure 1.33. *P-T* slopes of the reactions are consistent with the present experimental and thermodynamic knowledge (Pattison, 2003). For comparison, *P-T* estimates for the banded anorthosite and the metagabbro samples from Kataransky Cape and Bolschoi Khed are illustrated. Whereas in the more magnesian metagabbro (Bolschoi Khed; *mg*-number 0.75) orthopyroxene is still present, the less magnesian metagabbro (Kataransky Cape; *mg*-number 0.65) is characterised by the Opx-free assemblage Grt-Cpx-Pl±Qtz. At similar pressures (13 kbar & 12 kbar, respectively) lower temperatures can also favour the stability of the Grt-Cpx-Pl±Qtz assemblage. However, the lower temperature estimates for the metagabbro from Kataransky Cape may be underestimated because temperatures are not corrected for late Fe-Mg exchange and because of the uncertainty connected with Cpx-Grt thermometry. The anorthosite has a Mg-rich bulk composition (see mineral chemistry), but is characterised by high pressures of equilibration up to 15 kbar. As a consequence, orthopyroxene was consumed giving way to the assemblage Grt-Cpx-Pl±Qtz. High pressures in the range of 13 - 15 kbar are linked to crustal thickening and thrusting of the nappe piles during the formation of the Lapland-Kola collisional orogen.

Tab. 1.8. Results of geothermobarometry for granulite-facies stage 1a (core). *P-T* estimates labelled with an asterisk are corrected for retrograde Fe-Mg exchange.

Pressure estimates stage 1a						
sample	combination	assemblage	barometer	calibration	P kbar	(T°C)
metagabbro	core-core	Grt-Opx-Pl-Qtz-Cpx	Grt-Opx-Pl-Qtz	Bhattacharya *et al.* '91	12.7 (Mg)*	1000
Bolschoi K.	core-core	Grt-Opx-Pl-Qtz-Cpx	Grt-Opx-Pl-Qtz	Bhattacharya *et al*. '91	14.5 (Fe)*	1000
	core-core	Grt-Opx-Pl-Qtz-Cpx	Opx(Al)-Grt	Harley '84	10.5	1000
	core-core	Grt-Opx-Pl-Qtz-Cpx	Opx(Al)-Grt	Harley & Green '82	11	1000
	core-core	Grt-Opx-Pl-Qtz-Cpx	CaTs	McCarthy '98	13-13.6	1000
	core-core	Grt-Opx-Pl-Qtz-Cpx	Grt-Opx-Cpx-Pl-Qtz	Paria '88	12.3	1000
	core-core	Grt-Opx-Pl-Qtz-Cpx	**TWEEQU 202**		**13**	**1000**
metagabbro	core-core	Grt-Cpx-Pl +/-Qtz	Grt-Cpx-Pl-Qtz	Eckert '91	11.1-12.0	900
Kataransky C.	core-core	Grt-Cpx-Pl +/-Qtz	Grt-Cpx-Pl-Qtz	Powell & Holland '85	10.8-11.0	900
	core-core	Grt-Cpx-Pl +/-Qtz	Grt-Cpx-Pl-Qtz	Perkins & Newton '81	9.2-9.4	900
	core-core	Grt-Cpx-Pl +/-Qtz	CaTs	McCarthy '98	11.5-11.7	900
	core-core	Grt-Cpx-Pl +/-Qtz	**TWEEQU 202**		**15.5**	**900**
banded	core-core	Grt-Cpx-Pl +/-Qtz	Grt-Cpx-Pl-Qtz	Eckert '91	14.5-15.5	900
anorthosite	core-inclusion	Grt-Cpx-Pl +/-Qtz	Grt-Cpx-Pl-Qtz	Eckert '91	14.3	900
Beloozers. G.	core-core	Grt-Cpx-Pl +/-Qtz	Grt-Cpx-Pl-Qtz	Powell & Holland '88	13.8	900
	core-inclusion	Grt-Cpx-Pl +/-Qtz	Grt-Cpx-Pl-Qtz	Powell & Holland '88	13.5	900
	core	Grt-Cpx-Pl +/-Qtz	Jd-content	Holland '83	13.7-15.7	900
	inclusion	Grt-Cpx-Pl +/-Qtz	Jd-content	Holland '83	14.7-15.6	900
	core-core	Grt-Cpx-Pl +/-Qtz	CaTs	McCarthy '98	14.8-15.3	900
	core-inclusion	Grt-Cpx-Pl +/-Qtz	CaTs	McCarthy '98	13.5	900

Temperature estimates stage 1a						
sample	combination	assemblage	thermometer	calibration	T°C	(P kbar)
metagabbro	core-core	Grt-Opx-Pl-Qtz-Cpx	Opx-Grt	Bhattacharya '91	1025*	13
Bolschoi K.	core-core	Grt-Opx-Pl-Qtz-Cpx	Opx-Grt	Harley '84	980*	13
	core-core	Grt-Opx-Pl-Qtz-Cpx	Opx(Al)-Grt	Harley & Green '82	1000 - 1050	13
	core-core	Grt-Opx-Pl-Qtz-Cpx	Cpx-Grt	Krogh Ravna '00	1100 (1030)*	13
	core-core	Grt-Opx-Pl-Qtz-Cpx	Cpx-Grt	Krogh '88	1200 (1030)*	13
	core-core	Grt-Opx-Pl-Qtz-Cpx	Cpx-Grt	Powell '85	1200 (1050)*	13
	core-core	Grt-Opx-Pl-Qtz-Cpx	**RCLC-P**		**985-1000**	**13**
	core-core	Grt-Opx-Pl-Qtz-Cpx	**TWEEQU 202**		**1000**	**13**
metagabbro	core-core	Grt-Cpx-Pl +/-Qtz	Cpx-Grt	Krogh Ravna '00	780-830	12
Kataransky C.	core-core	Grt-Cpx-Pl +/-Qtz	Cpx-Grt	Krogh '88	850-900	12
	core-core	Grt-Cpx-Pl +/-Qtz	Cpx-Grt	Powell '85	860-890	12
	core-core	Grt-Cpx-Pl +/-Qtz	Cpx-Grt	Dahl '80	900-950	12
	core-core	Grt-Cpx-Pl +/-Qtz	Cpx-Grt	Ellis & Green '79	870	12
	core-core	Grt-Cpx-Pl +/-Qtz	Cpx-Grt	Ganguly '79	950	12
	core-core	Grt-Cpx-Pl +/-Qtz	**TWEEQU 202**		**900**	15.5
banded	core-core	Grt-Cpx-Pl +/-Qtz	Cpx-Grt	Krogh Ravna '00	880-915	15
anorthosite	core-core	Grt-Cpx-Pl +/-Qtz	Cpx-Grt	Krogh '88	980-990	15
Beloozers. G.	core-core	Grt-Cpx-Pl +/-Qtz	Cpx-Grt	Powell '85	1000-1010	15
	core-core	Grt-Cpx-Pl +/-Qtz	Cpx-Grt	Ellis & Green '79	1010-1025	15

Tab. 1.9. Results of geothermobarometry for granulite-facies stage 1b (rim). *P-T* estimates labelled with an asterisk are corrected for retrograde Fe-Mg exchange.

Pressure estimates stage 1b						
sample	combination	assemblage	barometer	calibration	P kbar	(T°C)
metagabbro	rim-rim	Grt-Opx-Pl-Qtz-Cpx	Grt-Opx-Pl-Qtz	Bhattacharya *et al.* '91	12.2(Mg)	950
Bolschoi K.	rim-rim	Grt-Opx-Pl-Qtz-Cpx	Grt-Opx-Pl-Qtz	Bhattacharya *et al.* '91	13.2 (Fe)	950
	rim-rim	Grt-Opx-Pl-Qtz-Cpx	Opx(Al)-Grt	Harley '84	11.5	950
	rim-rim	Grt-Opx-Pl-Qtz-Cpx	Opx(Al)-Grt	Harley & Green '82	10.5	950
	rim-rim	Grt-Opx-Pl-Qtz-Cpx	CaTs	McCarthy '98	11.5 - 12.0	950
	rim-rim	Grt-Opx-Pl-Qtz-Cpx	Grt-Opx-Cpx-Pl-Qtz	Paria '88		
	rim-rim	Grt-Opx-Pl-Qtz-Cpx	**TWEEQU 202**		**11.5**	**875**

Temperature estimates stage 1b						
sample	combination	assemblage	thermometer	calibration	T°C	(P kbar)
metagabbro	rim-rim	Grt-Opx-Pl-Qtz-Cpx	Opx-Grt	Bhattacharya *et al.* '91	960-970	12
Bolschoi K.	rim-rim	Grt-Opx-Pl-Qtz-Cpx	Opx-Grt	Harley '84	905-930	12
	rim-rim	Grt-Opx-Pl-Qtz-Cpx	Opx(Al)-Grt	Harley & Green '82	1000	12
	rim-rim	Grt-Opx-Pl-Qtz-Cpx	Cpx-Grt	Krogh Ravna '00	910 (720 - 800)	12
	rim-rim	Grt-Opx-Pl-Qtz-Cpx	Cpx-Grt	Krogh '88	960-980 (870 - 905)	12
	rim-rim	Grt-Opx-Pl-Qtz-Cpx	Cpx-Grt	Powell '85	980-990 (870 - 910)	12
	rim-rim	Grt-Opx-Pl-Qtz-Cpx	**RCLC-P**		**960**	**12**
	rim-rim	Grt-Opx-Pl-Qtz-Cpx	**TWEEQU 202**		**875**	**11.5**

1.6.2 Decompressional stage in mafic rock types from the south-eastern boundary of the Kolvitsa Massif

In metagabbros and anorthosites, porphyroblastic garnet is resorbed by orthopyroxene + plagioclase and/or amphibole + plagioclase symplectitic intergrowths. These reaction textures give evidence for a stage of decompression

$$Grt + Cpx + Qtz \Leftrightarrow Opx + Pl \quad (1)$$
$$Grt + Pl_1 + Qtz + H_2O \Leftrightarrow Hbl + Pl_2 + Grt_2 \quad (5)$$
$$Grt + Cpx + H_2O \Leftrightarrow Hbl + Pl + Qtz \quad (2).$$

Garnet grains in the metagabbro sample from Bolschoi Khed show concentric resorption by symplectitic orthopyroxene + plagioclase intergrowths. The causative reaction has a shallow positive slope in *P-T*-space and is commonly related to decompression (Harley, 1988).
Temperature estimates obtained from Mg-Fe exchange thermometry on vermicular orthopyroxene and proximal garnet rim are 815 - 825 °C for the Bhattacharya (1991) calibration and 760 – 770 °C for the Harley (1984a) calibration at a pressure of 10 kbar (Fig. 1.34, Tab. 1.10). Al-solubility thermometry (Harley & Green, 1982) yields 810 °C. The close agreement with Fe-Mg exchange temperatures suggests that no significant retrograde Fe-Mg exchange has occurred. Pressure estimates are 7 - 11 kbar for Grt-Opx-Pl-Qtz barometry (calibrations of Bhattacharya *et al.*, 1991; Perkins & Chipera, 1985; Perkins & Newton, 1981), 9.4 - 9.5 kbar for the Cpx-Pl-Qtz barometer (McCarthy & Patiño Douce, 1998) and 9.5 - 10.5 kbar for the Grt-Opx-Cpx-Pl-Qtz barometer (Paria *et al.* 1988).

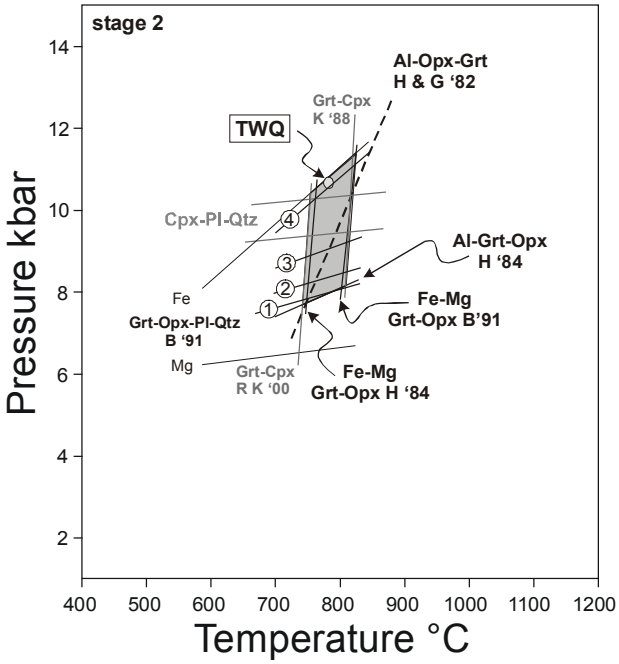

Fig. 1.34. P-T conditions for the formation of Opx-Pl symplectites (metagabbro, Bolschoi Khed).
Pressure estimates:
Grt-Opx-Pl-Qtz: (1) Eckert '91, (2) Perkins & Newton '82, (3) Mg & (4) Fe Perkins & Chipera '85, (B) Bhattacharya *et al.* '91; Cpx-Pl-Qtz: McCarthy '98
Temperature estimates:
Opx-Grt: (B) Bhattacharya *et al.* '91, (H) Harley, '84; Al-Opx-Grt: (H & G) Harley & Green '82, (H) Harley '84; Grt-Cpx: (RK) Ravna Krogh '00, Krogh '88

Multi-equilibrium thermobarometry (TWEEQU *2.02b*, Berman, 1991) for the CFMAS system was performed including eight end-members (Alm, Prp, Grs, Fs, En, Al-Opx, An, Qtz) and hence yields three independent equilibria. Convergence of the equilibria occurs at c. 780 °C & 10.7 kbar (Fig. 1.35). Thermobarometric results for the decompressional stage are summarised in Figure 1.34 and Table 1.10.

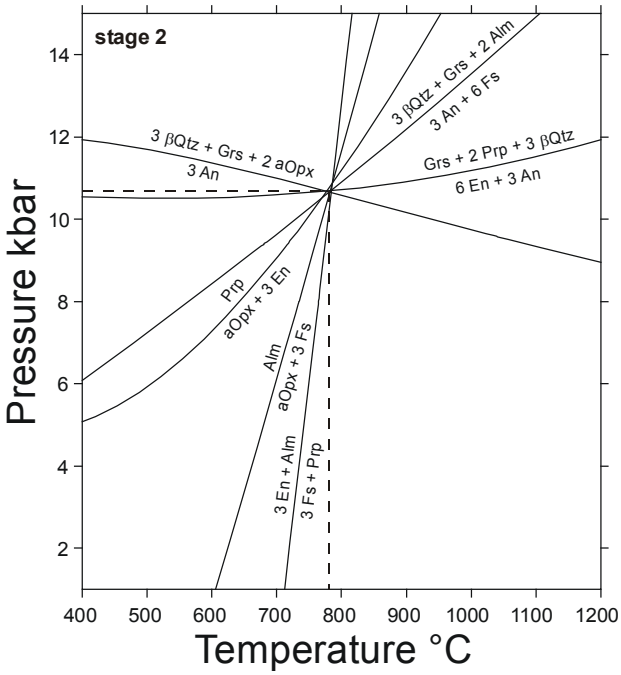

Fig. 1.35. *P-T* Results of TWEEQU calculations for Opx-Pl symplectite formation (metagabbro, Bolschoi Khed). Calculations were performed on the CMASH-subsystem involving the end-member pahses Alm, Prp, Grs, En, Fs, Al-Opx.

P-T estimates for Opx-Pl coronas (metagabbro, Kataransky Cape) developed at the interface of garnet and clinopyroxene are somewhat lower. Opx-Grt and Cpx-Grt Mg-Fe exchange thermometry yields 710 - 785 °C (calibrations of Harley, 1984a; Bhattacharya *et al.*, 1991) and 660 - 725 °C (calibrations of Krogh, 1988; Powell, 1985; Ellis & Green, 1979) at a pressure of 8.5 kbar. Al-solubility temperatures of 750 - 760 °C (calibration of Harley & Green, 1982; Harley, 1984b) agree with Opx-Grt Fe-Mg exchange temperatures, suggesting that no significant down-temperature Fe-Mg diffusion has taken place. Pressure estimates range from 8.2 to 9.4 kbar at a reference temperature of 730 °C (Fig. 1.32,

Tab. 1.10). *P-T* estimates obtained from TWEEQU (*2.02b*) calculations for 9 end-members (Alm, Prp, Fs, En, Al-Opx, Hd, Di, An, Qtz) in the CFMAS system yield 700 °C & 8.7 kbar and 760 °C & 9 kbar (Fig. 1.36 & Tab. 1.10).

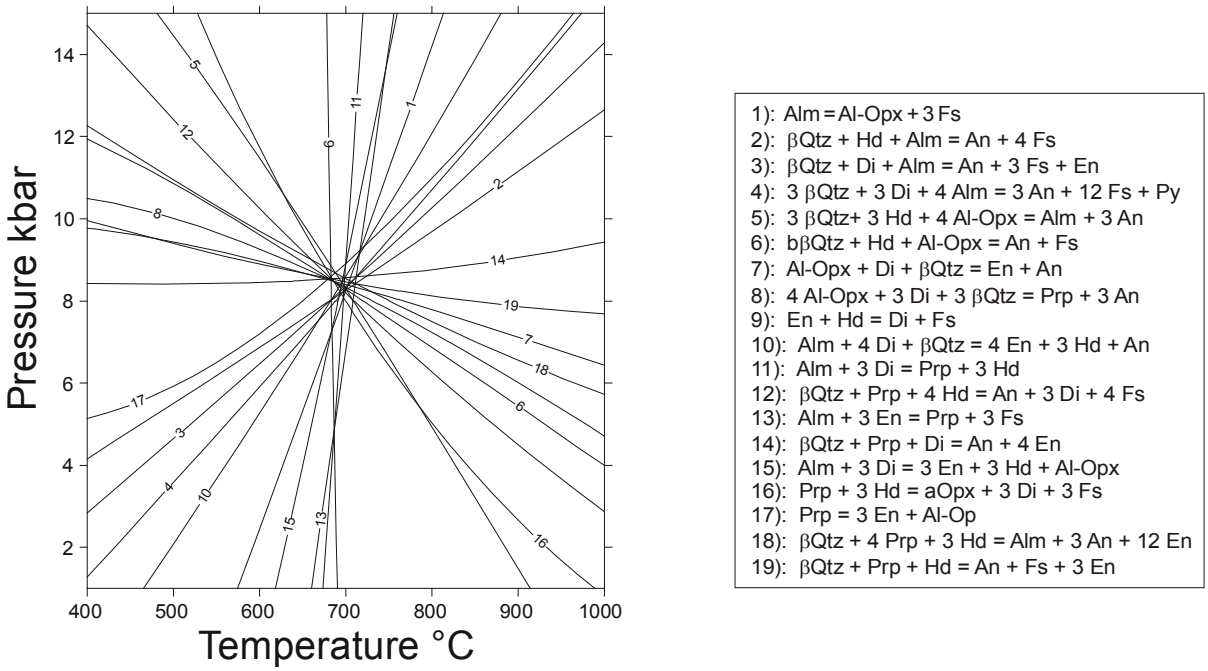

Fig. 1.36. P-T Results of TWEEQU calculations for Opx-Pl symplectite formation (metagabbro, Kataransky Cape).The calculations were performed on the CFMAS subsystem including end-members phases Alm, Prp, En, Fs, Al-Opx, Di, Hd, An, Qtz. The mineral equilibria considered in the TWEEQU calculations are listed above.

Porphyroblastic garnet grains in anorthosite from Beloozerskaya Guba are resorbed by symplectitic amphibole + plagioclase intergrowths. Contrary to the example described above, the presence of a fluid phase is required. Temperature estimates based on Fe-Mg exchange between garnet and amphibole are 750 - 810 °C for the Graham & Powell (1984) and Perchuk (1985) calibrations at a pressure of 10 kbar. Amphibole-plagioclase thermometry based on the coupled substitution NaSi ⇔ CaAl (Holland & Blundy, 1994) was also performed.

$$\underset{\text{edenite}}{NaCa_2Mg_5(AlSi_3)Si_4O_{22}(OH)_2} + \underset{\text{albite}}{NaAlSi_3O_8} \Leftrightarrow \underset{\text{richterite}}{Na(CaNa)Mg_5Si_8O_{22}(OH)_2} + \underset{\text{anorthite}}{CaAl_2Si_2O_8} \quad (22)$$

$$\underset{\text{edenite}}{NaCa_2Mg_5(AlSi_3)Si_4O_{22}(OH)_2} + 4\underset{\text{quartz}}{SiO_2} \Leftrightarrow \underset{\text{tremolite}}{Ca_2Mg_5Si_8O_{22}(OH)_2} + \underset{\text{albite}}{NaAlSi_3O_8} \quad (23)$$

Equilibrium (22) does not involve quartz and therefore can also be applied to silica deficient assemblages. The temperature estimates obtained for both equilibria are in the range of 750 - 810 °C at a given pressure of 10 kbar.

Results from Grt-Hbl-Pl-Qtz barometry (Kohn & Spear, 1990) are unreasonably low (6.5 – 7.5 kbar) and are regarded as suspect, because the compositional criteria for plagioclase (An < 70) and amphibole (X_{Fe} between 0.4 and 0.6) are not fulfilled. Pressure values in the range of 8 – 8.9 kbar are obtained from Grt-Cpx-Pl-Qtz barometry (calibrations of Eckert, 1991; Powell, 1985) at a reference temperature of 750 °C (Fig. 1.33; Tab. 1.10). Multi-equilibria calculations were performed with TWEEQU *1.02*, because this version contains thermodynamic properties for amphibole. Results are illustrated in Figures 1.37 a-c.

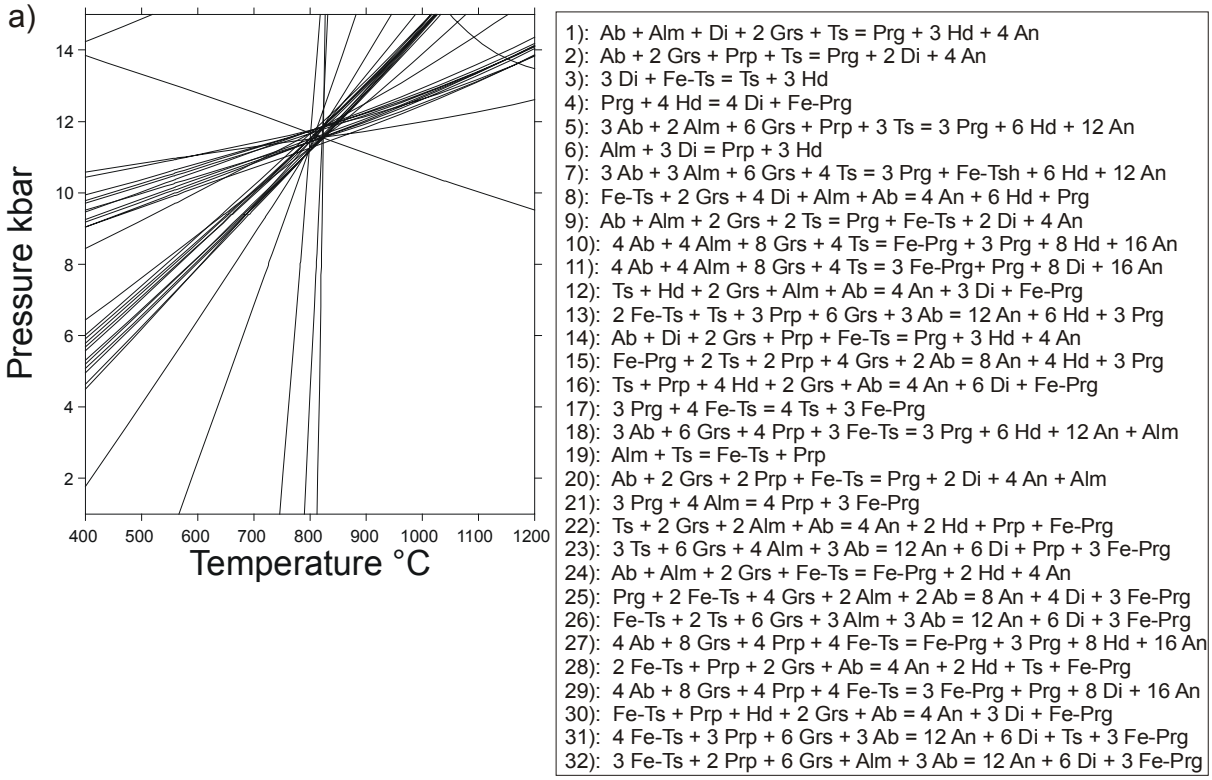

Fig. 1.37a-c. Results of TWEEQU (*1.02*) calculations for Hbl-Pl symplectite formation (banded anorthosite, Beloozerskaya Guba). End-member phasesconsidered are Alm, Prp, Di, Hd, Prg, Fe-Prg, Ts, Fe-Ts, An, Ab, Qtz, H_2O. **(a)** Possible anhydrous mineral equilibria in the CMFASH system that have been applied in TWEEQU calculations are listed above. **(b)** T-aH_2O diagram at a reference pressure of 11.6 kbar. **(c)** P-T estimates for symplectite formation including H_2O dependent equilibria at a fixed aH_2O of 0.4.

To constrain the *P-T* conditions of equilibration initial calculations excluded H_2O-present equilibria (NCFMASH system: Alm, Prp, Di, Hed, Prg, Fe-Prg, Ts, Fe-Ts, An, Ab, Qtz) (Fig. 1.37a). Then calculations were extended on the H_2O-present NCFMASH system choosing the phases Alm, Prp, Grs, Hd, Di, Prg, Fe-Prg, Ts, Fe-Ts, Ab, An, Qtz, H_2O. *P* estimates retrieved from anhydrous equilibria were used to generate isobaric *T*-aH_2O phase diagrams. In Figure 1.37b a pressure of 11.6 kbar is taken as fixed reference. The hydrous equilibria converge at a water activity of *c.* 0.4. Because quartz is absent in the mafic bands, calculated pressures represent maximum estimates. Low water activities in the range of 0.3 are characteristic for many mafic granulites (Mäder *et al.*, 1994; Pattison, 2003).
The rather high *P-T* estimates (*c.* 750 – 800°C; *c.* 8 – 11.5 kbar) at low water activities (*c.* 0.4) are problematic, because no migmatitic textures have been observed. The presence of quartz is regarded as an important factor controlling amphibole-melting reactions (Pattison, 1991; Hartel & Pattison, 1996), for example

$$\text{Hbl} + \text{Pl} + \text{Qtz} + \text{V} \Leftrightarrow \text{L} \quad (24)$$
$$\text{Hbl} + \text{Pl} + \text{Qtz} \Leftrightarrow \text{Cpx} + \text{Grt} + \text{L} \quad (25)$$
$$\text{Grt} + \text{Hbl} + \text{Qtz} \Leftrightarrow \text{Opx} + \text{Cpx} + \text{Pl} + \text{L}. \quad (26)$$

The presence of quartz also lowers the melting temperatures in the CNASH system. At an assumed pressure of 5 kbar, the wet tonalite solidus is *c.* 100 °C lower than the wet solidus for anorthosites (Johannes, 1978; Pattison, 1991).

$$\text{Pl} + \text{Qtz} + \text{H}_2\text{O} \Leftrightarrow \text{L} \quad \text{(tonalite wet solidus)} \quad (27)$$
$$\text{Pl} + \text{H}_2\text{O} \Leftrightarrow \text{L} \quad \text{(anorthosite wet solidus)} \quad (28)$$

Also elevated Na and K contents lower the solidus temperatures (Johannes, 1978 & 1980). In Figure 1.33 the wet tonalite solidi from Piwinskii (1968), Johannes (1978) and Wolf & Wyllie (1993) and the anorthosite solidus from Johannes (1978) are shown. Brackets at 5 kbar illustrate the effect that the An content has on the position of the solidi. *P-T* estimates for corona forming textures are indicated and lie close to the wet anorthosite solidus. Considering that the anorthosite from Beloozerskaya Guba is quartz-absent and that plagioclase composition varies from An_{50} to An_{70}, infiltration of fluids with moderate aH_2O would cause rehydration rather than melting. However, *P-T* estimates based on equilibria involving amphibole are problematic, because of the poorly constrained activity-composition relations of this compositionally and structurally complex phase (Pattison, 1991). Additionally, most of the available experimental data on hornblende breakdown reactions are unreversed (Pattison, 1991).. Also the lack of a melt model causes problems in thermodynamic modelling.
At Beloozerskaya Guba, Kataransky Cape and Bolschoi Khed symplectitic reaction textures developed due to a *P-T* decrease in the order of 3 - 5 kbar and 100 – 200 °C. Hence, the occurrence of either Pl-Opx or Pl-Amph symplectites in the studied rocks indicates dry respective fluid-present conditions during decompression.

Tab. 1.10. Results of geothermobarometry for the decompressional stage 2.

Pressure estimates stage 2						
sample	combination	assemblage	barometer	calibration	P kbar	(T°C)
metagabbro	rim-symplectite	Grt-Opx-Pl-Qtz	Grt-Opx-Pl-Qtz	Bhattacharya *et al.* '91	7 (Mg)	800
Bolschoi K.	rim-symplectite	Grt-Opx-Pl-Qtz	Grt-Opx-Pl-Qtz	Bhattacharya *et al.* '91	11 (Fe)	800
	rim-rim	Grt-Opx-Pl-Qtz-Cpx	Grt-Opx-Cpx-Pl-Qtz	Eckert et al. '91	8.05	800
	rim-rim	Grt-Opx-Pl-Qtz-Cpx	Grt-Opx-Cpx-Pl-Qtz	Perkins & Newton '82	8.45	800
	rim-rim	Grt-Opx-Pl-Qtz-Cpx	Grt-Opx-Cpx-Pl-Qtz	Perkins & Chipera '85 Mg	9.25	800
	rim-rim	Grt-Opx-Pl-Qtz-Cpx	Grt-Opx-Cpx-Pl-Qtz	Perkins & Chipera '85 Fe	10.9	800
	rim-symplectite	Grt-Opx-Pl-Qtz	Opx(Al)-Grt	Harley '84	8.1 -12.1	800
	rim-symplectite	Grt-Opx-Pl-Qtz	Opx(Al)-Grt	Harley & Green '82	9.75	800
	rim-symplectite	Grt-Opx-Pl-Qtz-Cpx	CaTs	McCarthy '98	9.45	800
	rim-rim	Grt-Opx-Pl-Qtz-Cpx	Grt-Opx-Cpx-Pl-Qtz	Paria '88 Fe	10.45	800
	rim-rim	Grt-Opx-Pl-Qtz-Cpx	Grt-Opx-Pl-Qtz	Paria '88 Mg	19.6	800
	rim-symplectite	Grt-Opx-Pl-Qtz	**TWEEQU 202**		**10.7**	**780**
metagabbro	rim-symplectite	Grt-Cpx-Opx-Pl +/-Qtz	Grt-Cpx-Opx-Pl-Qtz	Paria et al. '89	8.9 (Mg)	700
Kataransky C.	rim-rim	Grt-Cpx-Opx-Pl +/-Qtz	Grt-Cpx-Pl-Qtz	Eckert '91	8.6	700
	rim-rim	Grt-Cpx-Opx-Pl +/-Qtz	Grt-Cpx-Pl-Qtz	Powell & Holland '88	7.7	700
	rim-rim	Grt-Cpx-Opx-Pl +/-Qtz	Grt-Opx-Pl-Qtz	Eckert '91	9.4	700
	rim-rim	Grt-Cpx-Opx-Pl +/-Qtz	Grt-Opx-Pl-Qtz	Perkins & Chipera '85	8.4 (Mg)	700
	rim-rim	Grt-Cpx-Opx-Pl +/-Qtz	Grt-Opx-Pl-Qtz	Perkins & Chipera '85	8.8 (Fe)	700
	rim-rim	Grt-Cpx-Opx-Pl +/-Qtz	Grt-Opx-Pl-Qtz	Perkins & Newton '81	9.2	700
	rim-symplectite	Grt-Cpx-Opx-Pl +/-Qtz	Opx(Al)-Grt	Harley & Green '82	8.6	730
	rim-symplectite	Grt-Cpx-Opx-Pl +/-Qtz	Opx(Al)-Grt	Harley '84	8.2	730
	rim-symplectite	Grt-Cpx-Opx-Pl +/-Qtz	**TWEEQU 202**		**8.7**	**700**
banded	rim-symplectite	Grt-Cpx-Hbl-Pl-Mag	Grt-Hbl-Pl-Qtz	Kohn & Spear '90 (Mg)	7.3-7.4	750
anorthosite	rim-symplectite	Grt-Cpx-Hbl-Pl-Mag	Grt-Hbl-Pl-Qtz	Kohn & Spear '90 (Fe)	6.5-6.9	750
Beloozers. G.	rim-rim	Grt-Cpx-Hbl-Pl-Mag	Grt-Cpx-Pl-Qtz	Eckert '91	8.25 - 8.85	800
	rim-rim	Grt-Cpx-Hbl-Pl-Mag	Grt-Cpx-Pl-Qtz	Powell & Holland '88	7.8 - 8.7	800
	rim-symplectite	Grt-Cpx-Hbl-Pl-Mag	**TWEEQU 102**	*a* **H_2O= 0.4**	**10**	**780**
	rim-symplectite	Grt-Cpx-Hbl-Pl-Mag	**TWEEQU 102**	*a* **H_2O= 0.4**	**11.5**	**800**

Temperature estimates stage 2						
sample	combination	assemblage	thermometer	calibration	T°C	(P kbar)
metagabbro	rim-symplectite	Grt-Opx-Pl-Qtz	Opx-Grt	Bhattacharya *et al.* '91	815-825	10
Bolschoi K.	rim-symplectite	Grt-Opx-Pl-Qtz	Opx-Grt	Harley '84	760-770	10
	rim-symplectite	Grt-Opx-Pl-Qtz	Opx-Grt	Ganguly '79	765-780	10
	rim-symplectite	Grt-Opx-Pl-Qtz	Opx(Al)-Grt	Harley & Green '82	810	10
	rim-rim	Grt-Opx-Pl-Qtz-Cpx	Cpx-Grt	Krogh Ravna '00	755	10
	rim-rim	Grt-Opx-Pl-Qtz-Cpx	Cpx-Grt	Krogh '88	815	10
	rim-rim	Grt-Opx-Pl-Qtz-Cpx	Cpx-Grt	Powell '85	845	10
	rim-symplectite	Grt-Opx-Pl-Qtz	**TWEEQU 202**		**780**	**10.7**
metagabbro	rim-symplectite	Grt-Cpx-Opx-Pl +/-Qtz	Opx-Grt	Bhattacharya *et al.* '91	785	8.5
Kataransky C.	rim-symplectite	Grt-Cpx-Opx-Pl +/-Qtz	Opx-Grt	Harley '84	710 - 750	8.5
	rim-symplectite	Grt-Cpx-Opx-Pl +/-Qtz	Opx(Al)-Grt	Harley & Green '82	750	8.5
	rim-rim	Grt-Cpx-Opx-Pl +/-Qtz	Cpx-Grt	Krogh Ravna '00		8.5
	rim-rim	Grt-Cpx-Opx-Pl +/-Qtz	Cpx-Grt	Krogh '88	660	8.5
	rim-rim	Grt-Cpx-Opx-Pl +/-Qtz	Cpx-Grt	Powell '85	710	8.5
	rim-rim	Grt-Cpx-Opx-Pl +/-Qtz	Cpx-Grt	Ellis & Green '79	725	8.5
	rim-rim	Grt-Cpx-Opx-Pl +/-Qtz	Cpx-Grt	Ganguly '79	830	8.5
	rim-rim	Grt-Cpx-Opx-Pl +/-Qtz	Cpx-Opx (Ca)	Brey & Köhler '90	705	8.5
	rim-rim	Grt-Cpx-Opx-Pl +/-Qtz	Opx (Cr-Al)	Witt-Eickschen '91	680	8.5
	rim-symplectite	Grt-Cpx-Opx-Pl +/-Qtz	**TWEEQU 202**		**700**	**8.7**
banded	rim-symplectite	Grt-Cpx-Hbl-Pl-Mag	Grt-Hbl	Graham & Powell '84	750-810	10
anorthosite	rim-symplectite	Grt-Cpx-Hbl-Pl-Mag	Grt-Hbl	Perchuck '85	750-810	10
Beloozers. G.	symplectites	Grt-Cpx-Hbl-Pl-Mag	Hbl (Ed-Ri)-Pl	Holland & Blundy '94	750 - 810	10
	rim-symplectite	Grt-Cpx-Hbl-Pl-Mag	**TWEEQU 102**	*a* **H_2O= 0.4**	**780**	**10**
	rim-symplectite	Grt-Cpx-Hbl-Pl-Mag	**TWEEQU 102**	*a* **H_2O= 0.4**	**800**	**11.5**

1.6.3 Garnet-producing corona textures in rock types from the central Kolvitsa Massif

Coronal garnet rimming clinopyroxene, orthopyroxene and ilmenite porphyroclasts in a well-recrystallized granoblastic matrix of plagioclase are developed in basic lithologies of the Kolvitsa nappe. In the basic dyke from Nikolkina Island, temperature estimates for composite Cpx-Grt coronas overgrowing ilmenite grains yield 760 °C (Grt-Ilm thermometry; Pownceby, 1991) and 770 – 790 °C (Grt-Cpx thermometry; calibrations of Krogh, 1988; Powell, 1985; Ellis & Green, 1979) and 710 – 720 °C (Grt-Cpx thermometry; Ravna Krogh, 2000) at a pressure of 12.5 kbar (Fig. 1.38, Tab. 1.11). Grt-Cpx-Pl-Qtz barometry gives pressures in the range of 11.5 – 13 kbar (Eckert *et al.* 1991; Powell & Holland, 1985) and Cpx-Pl-Qtz barometry *c.* 9 kbar (McCarthy & Patiño Douce, 1998). Estimates of the emplacement level of the dyke can not be deduced from the mineral assemblage. Corona forming textures as well as elevated sodium content in clinopyroxene (1.3 wt% Na_2O) and the occurrence of rutile indicate equilibration at higher pressure, presumably due to crustal thickening during the formation of the collisional LKO.

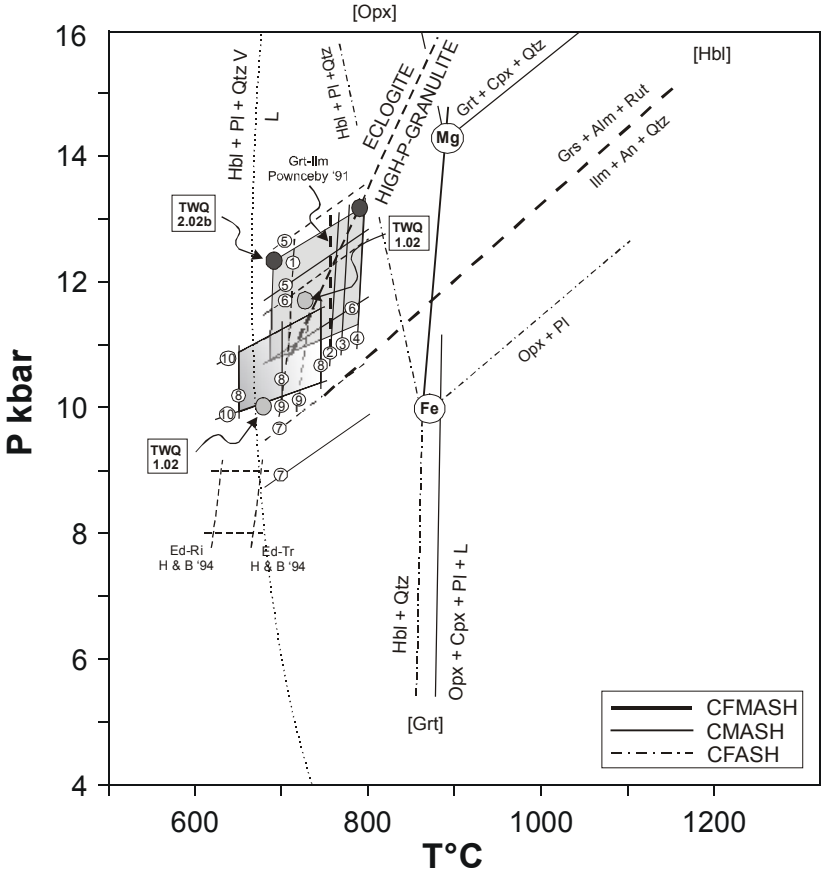

Fig. 1.38. *P-T* diagram illustrating different evolutionary stages for the basic dyke from Nikolkina Island. Indicated are the positions of the tonalite wet solidus: Pl + Qtz ⇔ Hbl + H_2O = L from Piwinskii (1968), Wolf & Wyllie (1993). Model reactions in the CFMASH system are from Pattison (2003) and are based on experimental and thermodynamic data. Reaction Grs + Alm + Rut = Ilm + An + Qtz is from Bohlen & Liotta (1986). Dark grey-shaded circles illustrate the results from TWEEQ (*2.20b*) calculations for the Grt-Cpx-Pl corona assemblage. Light grey-shaded circles show results from TWEEQU (*1.02*) calculations for the garnet bearing hydration zone.
Pressure estimates:
Grt-Cpx-Pl-Qtz: (5) Eckert '91, (6) Powell & Holland '88, (7) Perkins & Newton '81;
Grt-Hbl-Pl-Qtz: (10) Kohn & Spear '90
Temperature estimates:
Grt-Cpx: (1) Ravna Krogh '00, (2) Krogh '88, (3) Powell '85, (4) Ellis & Green '79; Grt-Ilm: Pownceby '91; Grt-Hbl: (8)

In the noritic dyke from the Water Sign outcrop large clino- and orthopyroxene porphyroblasts are believed to have a magmatic origin. Again the estimation of pressure is difficult, because garnet is lacking in the assemblage. Large clinopyroxene crystals contain exsolution lamellae of orthopyroxene. The development of lamellae may be related to cooling following magmatic solidification or may be due to the metamorphic thermal overprint. Two-pyroxene thermometry was performed using the QUILF software (Andersen *et al.*, 1983 & 1998) and yields temperatures between 740 – 760 °C for exsolution lamellae and 810 – 840 °C for pyroxene cores and inclusions, respectively. The reference pressure was constrained with Cpx-Pl-Qtz barometry (McCarthy & Patiño Douce, 1998) giving a value of 9.2 - 9.4 kbar. These pressure estimates are maximum pressures because quartz is lacking from the assemblage.

Temperature estimates for composite corona textures (Grt-Pl-Qtz-Cpx) developed between plagioclase (granoblastic matrix) and orthopyroxene crystals are 680 – 770 °C for Fe-Mg exchange between Grt-Cpx, and for Opx-Grt pairs 750 °C (Al-solubility, Harley & Green, 1982) and 770 °C (Fe-Mg exchange, Bhattacharya *et al.*, 1991) at 10.5 kbar (Fig. 1.39, Tab. 1.11). Grt-Cpx-Pl-Qtz (Eckert, 1991; Powell & Holland, 1985), Grt-Opx-Cpx-Pl-Qtz (Paria *et al.*, 1988) and Cpx-Pl-Qtz barometry (McCarthy & Patiño Douce, 1998) gives pressures in the range of 9.8 – 11 kbar, 10.7 – 12 kbar and 8.9 – 9.7 kbar, respectively.

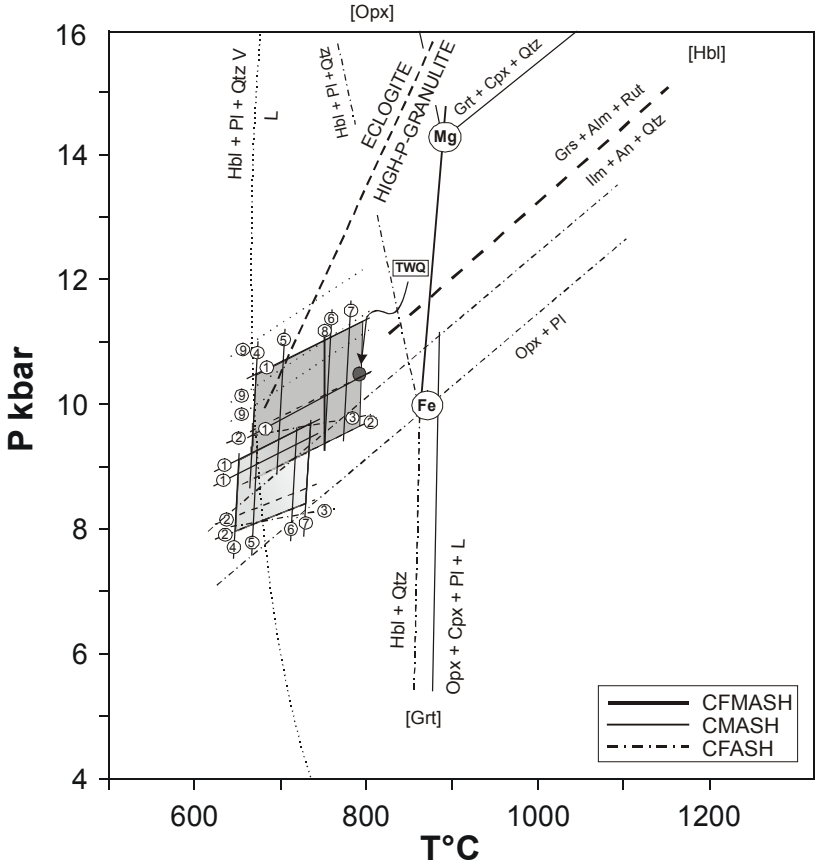

Fig. 1.39. *P-T* diagram for coronal garnet formation in the noritic dyke (Water Sign). *P-T* results for the composite corona rimming orthopyroxene have been plotted as dark grey-shaded box. *P-T* estimates for coronas rimming clinopyroxene are illustrated as light grey-shaded box. Indicated is the position of the tonalite wet solidus: Pl + Qtz ⇔ Hbl + H_2O = L from Piwinskii (1968), Wolf & Wyllie (1993). Model reactions in the CFMASH system are from Pattison (2003) and are based on experimental and thermodynamic data. Theposition of the Grs + Alm + Rut = Ilm + An + Qtz equilibrium is from Bohlen & Liotta (1986).

Pressure estimates:

Grt-Cpx-Pl-Qtz: (1) Eckert '91, (2) Powell & Holland '88; Cpx-Pl-Qtz: (3) McCarthy '98; Grt-Opx-Cpx-Pl-Qtz: (9) Paria *et al.* '88

Temperature estimates:

Grt-Cpx: (4) Ravna Krogh '00, (5) Krogh '88, (6) Powell '85, (7) Ellis & Green '79; Opx-Cpx: (8) Brey & Köhler '90

TWEEQU (*2.02b*) calculations in the CFMAS-subsystem involving the end-members Alm, Prp, Fs, En, Hd, Di, An, Qtz constrain the *P-T* conditions of coronal garnet formation at 790 °C & 10.5 kbar (Fig. 1.40). Grossular was omitted from calculations, because equilibria plot outside the field of convergence (see above).

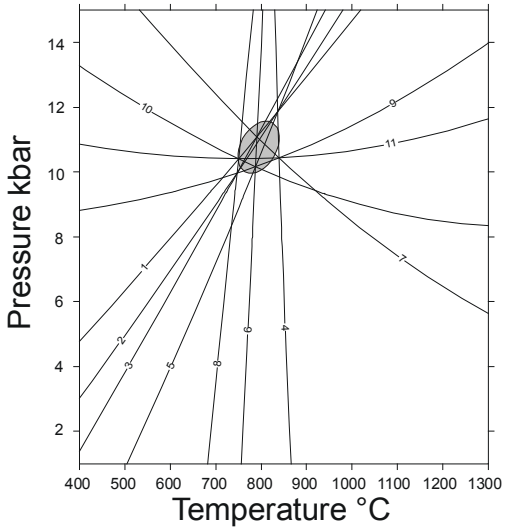

The mineral equilibria that have been applied in TWEEQU calculations (CFMAS system):

1): bQtz + Hd + Alm = An + 4 Fs
2): bQtz + Di + Alm = An + 3 Fs + En
3): 3 bQtz + 3 Di + 4 Alm = 3 An + 12 Fs + Pr
4): En + Hd = Di + Fs
5): Alm + 4 Di + bQtz = 4 En + 3 Hd + An
6): Alm + 3 Di = Prp + 3 Hd
7): bQtz + Prp + 4 Hd = An + 3 Di + 4 Fs
8): Alm + 3 En = Prp + 3 Fs
9): bQtz + Prp + Di = An + 4 En
10): 3 bQtz + 4 Prp + 3 Hd = Alm + 3 An + 12 En
11): bQtz + Py + Hd = An + Fs + 3 En

Fig. 1.40. Results of TWEEQU 2.02b calculations for corona formation (Water Sign). End-member phases used in calculations are: Alm, Prp, En, Fs, Di, Hd, An, Qtz. The mineral reactions in the CFMAS system are listed above.

Composite coronas developed between clinopyroxene and adjacent plagioclase give somewhat lower *P-T* estimates of 650 – 740 °C (Cpx-Grt, Ravna Krogh, 2000; Krogh, 1988; Powell 1985; Ellis & Green, 1979) and 8.2 – 9.5 kbar for Grt-Cpx-Pl-Qtz barometry (Eckert, 1991; Powell & Holland, 1985) and 8.2 kbar for the Cpx-Pl-Qtz barometer (McCarthy & Patiño Douce, 1998) (Tab. 1.11).
Garnet-bearing coronas in basic dykes developed at lower temperatures (700 - 800 °C) than the granulite-facies peak assemblages of sheared metagabbros and anorthosites (900 – 1050 °C), but also indicate a high pressure overprint (9 - 12.5 kbar). High pressures may be correlated with tectonic thickening during the Paleoproterozoic collisional event (see discussion).

Tab.1.11. Results of geothermobarometry for garnet-bearing corona textures.

Pressure estimates grt corona						
sample	combination	assemblage	barometer	calibration	P kbar	(T°C)
basic dyke	corona	Grt-Cpx-Pl-Qtz-Ilm	Grt-Cpx-Pl-Qtz	Eckert '91	12.5-13.2	780
Nikolkina I.	corona	Grt-Cpx-Pl-Qtz-Ilm	Grt-Cpx-Pl-Qtz	Powell & Holland '85	11.5-12.5	780
	corona	Grt-Cpx-Pl-Qtz-Ilm	Grt-Cpx-Pl-Qtz	Perkins & Newton '81	9.7-10.3	780
	corona	Grt-Cpx-Pl-Qtz-Ilm	CaTs	McCarthy '98	9.1	780
	corona Cpx	Grt-Cpx-Pl-Qtz-Ilm	**TWEEQU 202**		**13.2**	**780**
	corona Ilm	Grt-Cpx-Pl-Qtz-Ilm	**TWEEQU 202**		**12.3**	**690**
noritic dyke	corona	Grt-Cpx-Opx-Pl +/-Qtz	Grt-Cpx-Pl-Qtz	Eckert '91	10.2-11.0	750
Water Sign	corona	Grt-Cpx-Opx-Pl +/-Qtz	Grt-Cpx-Pl-Qtz	Powell & Holland '88	9.8-10.2	750
	corona	Grt-Cpx-Opx-Pl +/-Qtz	Grt-Opx-Cpx-Pl-Qtz	Paria '88 Mg	10.8-12.2	750
	corona	Grt-Cpx-Opx-Pl +/-Qtz	CaTs	McCarthy '98	8.85-9.7	750
	corona	Grt-Cpx-Pl +/-Qtz	Grt-Cpx-Pl-Qtz	Eckert '91	9.3-9.5	700
	corona	Grt-Cpx-Pl +/-Qtz	Grt-Cpx-Pl-Qtz	Powell & Holland '88	8.2-8.5	700
	corona	Grt-Cpx-Pl +/-Qtz	CaTs	McCarthy '98	8.2	700
	corona	Grt-Cpx-Opx-Pl +/-Qtz	**TWEEQU 202**		**10.5**	**790**

Temperature grt corona						
sample	combination	assemblage	thermometer	calibration	T°C	(P kbar)
basic dyke	corona	Grt-Cpx-Pl-Qtz-Ilm	Cpx-Grt	Krogh Ravna '00	710-720	12.5
Nikolkina I.	corona	Grt-Cpx-Pl-Qtz-Ilm	Cpx-Grt	Krogh '88	770	12.5
	corona	Grt-Cpx-Pl-Qtz-Ilm	Cpx-Grt	Powell '85	780	12.5
	corona	Grt-Cpx-Pl-Qtz-Ilm	Cpx-Grt	Ellis & Green '79	790	12.5
	corona	Grt-Cpx-Pl-Qtz-Ilm	Ilm-Grt	Pownceby '91	760	12.5
	corona Cpx	Grt-Cpx-Pl-Qtz-Ilm	**TWEEQU 202**		**780**	**13.2**
	corona Ilm	Grt-Cpx-Pl-Qtz-Ilm	**TWEEQU 202**		**690**	**12.3**
noritic dyke	corona	Grt-Cpx-Opx-Pl +/-Qtz	Cpx-Grt	Krogh Ravna '00	675	10.5
Water Sign	corona	Grt-Cpx-Opx-Pl +/-Qtz	Cpx-Grt	Krogh '88	700	10.5
	corona	Grt-Cpx-Opx-Pl +/-Qtz	Cpx-Grt	Powell '85	750	10.5
	corona	Grt-Cpx-Opx-Pl +/-Qtz	Cpx-Grt	Ellis & Green '79	770	10.5
	corona	Grt-Cpx-Opx-Pl +/-Qtz	Ca-in-Opx	Brey & Köhler '90	755	10.5
	corona	Grt-Cpx-Opx-Pl +/-Qtz	Opx-Grt	Harley '84a	770	10.5
	corona	Grt-Cpx-Opx-Pl +/-Qtz	Al-Opx-Grt	Harley & Green '82	750	10.5
	corona	Grt-Cpx-Pl +/-Qtz	Cpx-Grt	Krogh Ravna '00	650	9
	corona	Grt-Cpx-Pl +/-Qtz	Cpx-Grt	Krogh '88	670	9
	corona	Grt-Cpx-Pl +/-Qtz	Cpx-Grt	Powell '85	710	9
	corona	Grt-Cpx-Pl +/-Qtz	Cpx-Grt	Ellis & Green '79	735	9
	corona	Grt-Cpx-Opx-Pl +/-Qtz	**TWEEQU 202**		**790**	**10.5**

1.6.4 Amphibolite-facies stage

The common amphibolite-facies assemblage in zones of complete hydration contains hornblende-plagioclase ± titanite ± quartz. Only in amphibolite domains transitional to the granulite hosts at Nikolkina Island (basic dyke) and Leonard Cape (metadiorite) garnet occurs in the amphibolite-facies paragenesis. The general absence of garnet causes problems, because quantitative pressure estimations are not possible and the high-variance assemblage is unsuitable for multi-equilibrium thermobarometry. Relations between Al^{VI} and Si contents in amphiboles suggest that the prevailing pressure was greater than 5 kbar (Raase, 1974; see mineral chemistry). Hornblende barometry is based on the total Al content of hornblende in igneous assemblages (Anderson & Smith, 1995; Schmidt, 1992; Johnson & Rutherford, 1989). In this study, hornblende barometry provides only approximate pressure estimates and is used in comparison to results obtained from Grt-Hbl-Pl-Qtz barometry (29) & (30) (Kohn & Spear, 1990).

$$\underset{\text{anorthite}}{6CaAl_2Si_2O_8} + \underset{\text{tremolite}}{3Ca_2Mg_5Si_8O_{22}(OH)_2} \quad \Leftrightarrow$$

$$\underset{\text{grossular}}{2Ca_3Al_2Si_3O_{12}} + \underset{\text{pyrope}}{Mg_3Al_2Si_3O_{12}} + \underset{\text{tschermakite}}{3Ca_2Mg_4Al_2Si_7O_{22}(OH)_2} + \underset{\text{quartz}}{6SiO_2} \qquad (29)$$

$$\underset{\text{anorthite}}{6CaAl_2Si_2O_8} + \underset{\text{Fe-tremolite}}{3Ca_2Fe_5Si_8O_{22}(OH)_2} \quad \Leftrightarrow$$

$$\underset{\text{grossular}}{2Ca_3Al_2Si_3O_{12}} + \underset{\text{almandine}}{Fe_3Al_2Si_3O_{12}} + \underset{\text{Fe-tschermakite}}{3Ca_2Fe_4Al_2Si_7O_{22}(OH)_2} + \underset{\text{quartz}}{6SiO_2} \qquad (30)$$

Temperature estimates were obtained from the net-transfer equilibria (22) and (23) (Holland & Blundy, 1994). The coupled substitution NaSi ⇔ CaAl in the edenite-richterite equilibrium (22) is independent of the presence of quartz in the assemblage and can also be used to silica-undersaturated assemblages. Calculations based on the edenite-richterite (22) and edenite-tremolite (23) equilibria give similar temperatures for mineral rims in the range of 650 – 720 °C (Kataransky Cape) and 700 – 740 °C (Bolschoi Khed) at an assumed pressure of 6 kbar. Temperature estimates for mineral cores are only slightly higher (10 - 20 °C). Thermometry based on Fe-Mg exchange between garnet and amphibole for the hydrated basic dyke (Nikolkina Island) yields 740 – 770 °C for mineral cores and inclusions and slightly lower temperatures (640 – 730 °C) for mineral rims (Fig. 1.38). Temperatures from Hbl-Pl thermometry for mineral rims are 705 – 730 °C at a pressure of 10 – 11 kbar and match the temperature data from Grt-Hbl thermometry.

Pressure estimates show differences between the localities Bolschoi Khed/Kataransky Cape and Nikolkina Island/Leonard Cape located farther to the west. Thereby, pressures recorded in hydrated metagabbros (6 – 7 kbar) from the south-eastern boundary of the Kolvitsa Complex are lower than in hydrated basic dyke/metadiorite (8 – 11.5 kbar) from the central part. Grt-Hbl-Pl-Qtz barometry on the garnet-bearing transitional hydration domains from Nikolkina Island/Leonard Cape yields pressure estimates of 10 - 12 kbar. Results from hornblende barometry indicate somewhat lower, but still comparable pressure estimates of 9 – 10 kbar. Therefore pressure data from hornblende barometry may be regarded as reasonable minimum estimates.

P-T estimates for the transitional hydration domain (Nikolkina Island) obtained from multi-equilibrium thermobarometry (TWEEQU *1.02*) on the CFMASH-subsystem involving the phases Alm, Prp, Grs, Ts, Fe-Ts, Trem, Fe-Trem, An, Qtz and H_2O range between 680 – 730 °C and 10 – 11.8 kbar (Fig. 1.41 & 1.42a-b).

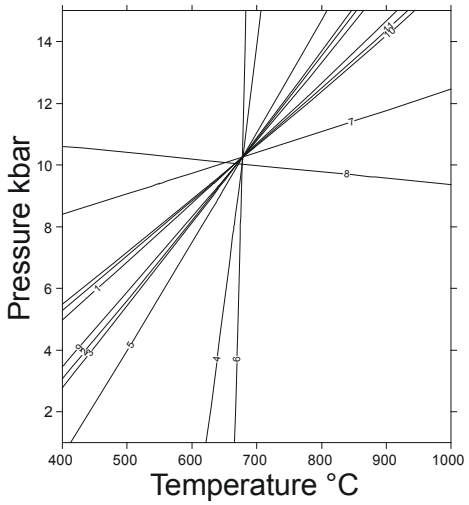

Mineral equilibria used in the TWEEQU calculations:

1): 4 Grs + 2 Prp + 12 βQtz + 3 Ts = 3 Trem + 12 An
2): 10 Alm + 20 Grs + 60 βQtz + 15 Ts = 6 Fe-Trem + 9 Trem + 60 An
3): 5 Ts + 12 βQtz + 4 Grs + 2 Alm = 12 An + 3 Trem + 2 Fe-Ts
4): 3 Trem + 5 Alm = 5 Prp + 3 Fe-Trem
5): 5 Alm + 4 Grs + 12 βQtz + 3 Ts = 3 Fe-Trem + 3 Prp + 12 An
6): Ts + Alm = Prp + Fe-Ts
7): 4 Grs + 5 Prp + 12 βQtz + 3 Fe-Ts = 3 Trem + 12 An + 3 Alm
8): 3 Trem + 5 Fe-Ts = 5 Ts + 3 Fe-Trem
9): 3 Fe-Ts + 12 βQtz + 4 Grs + 2 Alm = 12 An + 3 Fe-Trem
10): 4 Grs + 2 Prp + 12 βQtz+ 5 Fe-Ts = 2 Ts + 3 Fe-Trem + 12 An
11): 20 Grs + 10 Prp + 60 βQtz + 15 Fe-Ts = 9 Fe-Trem + 6 Trem + 60 An

Fig. 1.41. TWEQU (*1.02*) results using rim analyses for Grt (#33), Hbl (#34), Pl (#36) (transition zone, Nikolkina Island). End-member phases that were used for calculations are: Alm, Prp, Grs, Ts, Fe-Ts, Trem, Fe-Trem, An, Qtz. Anhydrous mineral equilibria are listed above.

Although amphibole has a pargasitic/ferro-pargasitic composition (see mineral chemistry) and plagioclase is sodium-rich (An_{30}), Na_2O was excluded in the calculations, because equilibria curves involving sodic end-members plot outside the *P-T* field of convergence. This may be due to the less reliable thermodynamic data for Na-bearing amphibole end-members (Mäder *et al.*, 1994; St-Onge & Ijewliw, 1996). Constraints on the H_2O-activity of the fluid phase were obtained from *T-a*H_2O phase diagrams calculated at pressure values as determined from anhydrous equilibria (Fig.1.42a).

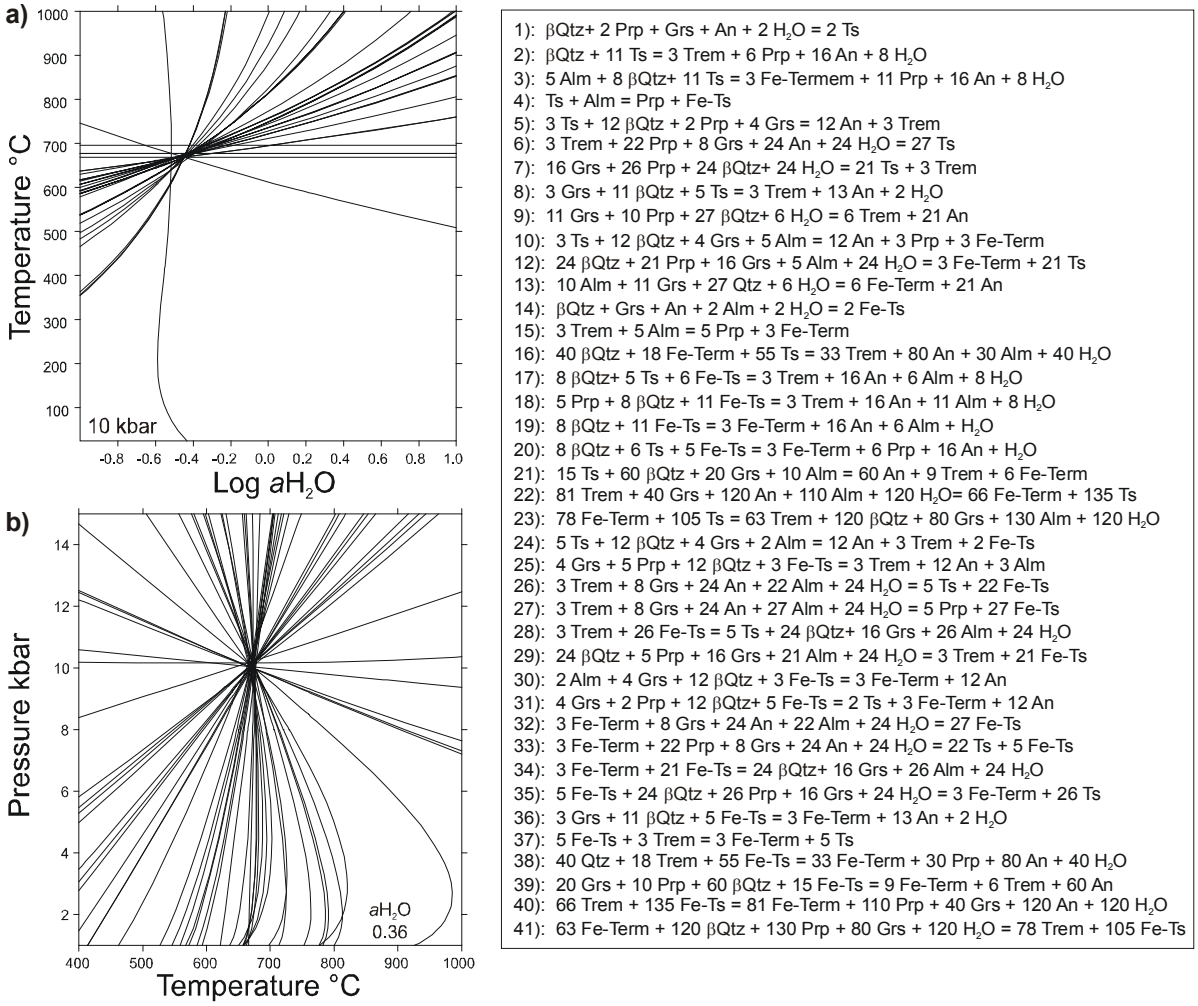

Fig. 1.42 a & b. TWEQU (*1.02*) results using rim analyses for Grt (#33), Hbl (#34), Pl (#36) (transition zone, Nikolkina Island). End-member phases that were used for calculations are: Alm, Prp, Grs, Ts, Fe-Ts, Trem, Fe-Trem, An, Qtz, H_2O. **(a)** *T-a*H_2O plots at a fixed reference pressure of 10 kbar **(b)** *P-T* results of TWEEQU calculations including hydrous mineral equilibria at fixed *a*H_2O (0.36). Mineral equilibria in the CFMASH system are listed above.

Water activities are reduced and range from 0.4 to 0.6. The results from *P-T* estimations for hydration zones in the metabasic dyke are summarised in Figure 1.38. *P-T* estimates for the transitional hydration domain plot close to the wet tonalite solidus, whereas results for the completely hydrated central part of fluid infiltration zones, plot below the solidus. In both zones no migmatitic features are observed indicating subsolidus conditions.

Tab. 1.12a. Pressure estimates for amphibolite-facies stage 3.

Pressure estimates stage 3						
sample	combination	assemblage	barometer	calibration	P kbar	(T°C)
transition zone	core	Hbl-Pl +/-Qtz	Al-Hbl	Anderson & Smith '95	5.0-5.6	720
metagabbro	core	Hbl-Pl +/-Qtz	Al-Hbl	Schmidt '92	6.0-6.4	720
Bolschoi K.	core	Hbl-Pl +/-Qtz	Al-Hbl	Johnson & Rutherford '89	5.0-5.4	720
	core	Hbl-Pl +/-Qtz	Al-Hbl	Hollister et al. '87	5.9 - 6.4	720
	rim	Hbl-Pl +/-Qtz	Al-Hbl	Anderson & Smith '95	5.4-5.8	720
	rim	Hbl-Pl +/-Qtz	Al-Hbl	Schmidt '92	5.8-6.8	720
	rim	Hbl-Pl +/-Qtz	Al-Hbl	Johnson & Rutherford '89	5.2-5.8	720
	rim	Hbl-Pl +/-Qtz	Al-Hbl	Hollister et al. '87	06/02/2003	720
hydrated	core	Hbl +/-Qtz, Pl	Al-Hbl	Anderson & Smith '95	6.8	700
metagabbro	core	Hbl +/-Qtz, Pl	Al-Hbl	Schmidt '92	6.7	700
Bolschoi K.	core	Hbl +/-Qtz, Pl	Al-Hbl	Johnson & Rutherford '89	5.7	700
	core	Hbl +/-Qtz, Pl	Al-Hbl	Hollister et al. '87	6.8	700
	rim	Hbl +/-Qtz, Pl	Al-Hbl	Anderson & Smith '95	6.0-6.5	700
	rim	Hbl +/-Qtz, Pl	Al-Hbl	Schmidt '92	6	700
	rim	Hbl +/-Qtz, Pl	Al-Hbl	Johnson & Rutherford '89	5	700
	rim	Hbl +/-Qtz, Pl	Al-Hbl	Hollister et al. '87	5.4 - 6.4	700
transition zone	core	Hbl-Pl +/-Qtz	Al-Hbl	Anderson & Smith '95	6	720
metagabbro	core	Hbl-Pl +/-Qtz	Al-Hbl	Schmidt '92	6.0-6.3	720
Kataransky C.	core	Hbl-Pl +/-Qtz	Al-Hbl	Johnson & Rutherford '89	5.3	720
	core	Hbl-Pl +/-Qtz	Al-Hbl	Hollister et al. '87	7.3 - 7.5	720
	symplectite	Hbl-Pl +/-Qtz	Al-Hbl	Anderson & Smith '95	5.6-6.0	720
	symplectite	Hbl-Pl +/-Qtz	Al-Hbl	Schmidt '92	6.0-6.3	720
	symplectite	Hbl-Pl +/-Qtz	Al-Hbl	Johnson & Rutherford '89	5.0-5.4	720
	symplectite	Hbl-Pl +/-Qtz	Al-Hbl	Hollister et al. '87	7.0 - 7.2	720
hydrated	core	Hbl +/-Qtz, Pl	Al-Hbl	Anderson & Smith '95	6.7-6.8	700
metagabbro	core	Hbl +/-Qtz, Pl	Al-Hbl	Schmidt '92	7.1-7.4	700
Kataransky C.	core	Hbl +/-Qtz, Pl	Al-Hbl	Johnson & Rutherford '89	6.1-6.5	700
	rim	Hbl +/-Qtz, Pl	Al-Hbl	Anderson & Smith '95	6.6-6.8	700
	rim	Hbl +/-Qtz, Pl	Al-Hbl	Schmidt '92	7.0-7.1	700
	rim	Hbl +/-Qtz, Pl	Al-Hbl	Johnson & Rutherford '89	6	700
	rim	Hbl +/-Qtz, Pl	Al-Hbl	Hollister et al. '87	7.0 - 7.2	700
transition zone	rim-rim	Grt-Hbl-Pl-Qtz	Grt-Hbl-Pl-Qtz	Kohn & Spear '90	10.1-10.4 (Mg)	700
Nikolkina I.	rim-rim	Grt-Hbl-Pl-Qtz	Grt-Hbl-Pl-Qtz	Kohn & Spear '90	10.3-10.6 (Fe)	700
	rim-rim	Grt-Hbl-Pl-Qtz	Grt-Hbl-Pl-Qtz	Kohn & Spear '90	11.3 (Mg)	700
	rim-rim	Grt-Hbl-Pl-Qtz	Grt-Hbl-Pl-Qtz	Kohn & Spear '90	11.2 (Fe)	700
	rim	Grt-Hbl-Pl-Qtz	Al-Hbl	Anderson & Smith '95	8.5 - 8.10	700
	rim	Grt-Hbl-Pl-Qtz	Al-Hbl	Schmidt '92	8.0 - 8.2	700
	rim	Grt-Hbl-Pl-Qtz	Al-Hbl	Hollister et al. '87	8.0 - 8.5	700
	rim-rim	Grt-Hbl-Pl-Qtz	**TWEEQU 102**	*a* **H_2O= 0.4**	**10**	**680**
	rim-rim	Grt-Hbl-Pl-Qtz	**TWEEQU 102**	*a* **H_2O= 0.6**	**11.8**	**730**
hydrated	rim	Hbl-Ttn +/- Pl, Qtz	Al-Hbl	Anderson & Smith '95	8.8-9.4	630
basic dyke	rim	Hbl-Ttn +/- Pl, Qtz	Al-Hbl	Schmidt '92	8.8-9.0	630
Nikolkina I.	rim	Hbl-Ttn +/- Pl, Qtz	Al-Hbl	Johnson & Rutherford '89	7.8-8.0	630

Tab.1.12b. Temperature estimates for amphibolite-facies stage 3.

Temperature estimates stage 3						
sample	combination	assemblage	thermometer	calibration	T°C	(P kbar)
transition zone	core-core	Hbl-Pl +/-Qtz	Hbl (Ed-Tr)-Pl	Holland & Blundy '94	730-760	6
metagabbro	core-core	Hbl-Pl +/-Qtz	Hbl (Ed-Ri)-Pl	Holland & Blundy '94	710-750	6
Bolscoi K.	rim-rim	Hbl-Pl +/-Qtz	Hbl (Ed-Tr)-Pl	Holland & Blundy '94	700-740	6
	rim-rim	Hbl-Pl +/-Qtz	Hbl (Ed-Ri)-Pl	Holland & Blundy '94	710-735	6
transition zone	core-core	Hbl-Pl +/-Qtz	Hbl (Ed-Tr)-Pl	Holland & Blundy '94	710	6
metagabbro	core-core	Hbl-Pl +/-Qtz	Hbl (Ed-Ri)-Pl	Holland & Blundy '94	680	6
Kataransky C.	rim-rim	Hbl-Pl +/-Qtz	Hbl (Ed-Tr)-Pl	Holland & Blundy '94	710	6
	rim-rim	Hbl-Pl +/-Qtz	Hbl (Ed-Ri)-Pl	Holland & Blundy '94	710	6
hydrated	core-core	Hbl-Pl +/-Qtz	Hbl (Ed-Tr)-Pl	Holland & Blundy '94	720-750	6.5
metagabbro	core-core	Hbl-Pl +/-Qtz	Hbl (Ed-Ri)-Pl	Holland & Blundy '94	680-720	6.5
Kataransky C.	rim-rim	Hbl-Pl +/-Qtz	Hbl (Ed-Tr)-Pl	Holland & Blundy '94	690-720	6.5
	rim-rim	Hbl-Pl +/-Qtz	Hbl (Ed-Ri)-Pl	Holland & Blundy '94	650-690	6.5
transition zone	core-inclusion	Grt-Hbl-Pl-Qtz-Ttn	Grt-Hbl	Graham & Powell '84	770	11
Nikolkina I.	core-core	Grt-Hbl-Pl-Qtz-Ttn	Grt-Hbl	Graham & Powell '84	740	11
	rim-rim	Grt-Hbl-Pl-Qtz-Ttn	Grt-Hbl	Graham & Powell '84	640-670	11
	rim-rim	Grt-Hbl-Pl-Qtz-Ttn	Grt-Hbl	Graham & Powell '84	730	11
	rim-rim	Grt-Hbl-Pl-Qtz-Ttn	Hbl (Ed-Tr)-Pl	Holland & Blundy '94	720-730	11
	rim-rim	Grt-Hbl-Pl-Qtz-Ttn	Hbl (Ed-Ri)-Pl	Holland & Blundy '94	705-715	11
	rim-rim	Grt-Hbl-Pl-Qtz-Ttn	**TWEEQU 102**	***a*** **H_2O= 0.4**	**680**	**10**
	rim-rim	Grt-Hbl-Pl-Qtz-Ttn	**TWEEQU 102**	***a*** **H_2O= 0.6**	**730**	**11.8**
hydrated	rim-rim	Hbl-Ttn +/- Pl, Qtz	Hbl (Ed-Tr)-Pl	Holland & Blundy '94	680	8.5
basic dyke	rim-rim	Hbl-Ttn +/- Pl, Qtz	Hbl (Ed-Ri)-Pl	Holland & Blundy '94	630	8.5

The presence of secondary Ca-Al silicates in hydrations zones from Nikolkina Island and Leonard Cape are evidence of low-grade alteration. Prehnite, epidote, chlorite and titanite are alteration products and have been found in hornblende-plagioclase-biotite assemblages with chloritised biotite and sericitised plagioclase. Lens-shaped prehnite is intergrown with biotite along the biotite basal cleavage. Additional phases like, sericite, titanite, chlorite and sometimes K-feldspar can be observed, suggesting that a reaction, such as

$$\text{anorthite} + \text{biotite} + H_2O \Leftrightarrow \text{prehnite} + \text{chlorite} + \text{titanite} + \text{sericite} \qquad (31)$$

has taken place (Tulloch, 1979). Potassium released by the breakdown of biotite is incorporated in muscovite (sericite) and sometimes K-feldspar. Fe-Mg and Ti is taken up by chlorite and titanite, respectively. Sericitisation of plagioclase is also common in biotite-absent amphibolites. Potassium was derived from plagioclase itself or was supplied by the infiltrating fluids.

Low-grade alteration affecting biotite and plagioclase is linked to fluid infiltration. Whether fluid infiltration continued down to *P-T* conditions of prehnite-facies, was related to a later episode of fluid flux or reflect the attendance of a residual pore fluid, cannot be definitely resolved. Considering the large difference between *P-T* conditions of the amphibolite-facies and prehnite-facies overprints, a polyphase fluid activity seams more likely. The temperatures did not exceed 400 °C, the upper thermal stability limit of prehnite (Liou, 1971; Liou *et al.* 1983). Iron-rich epidote points to temperatures below 350 °C, but P_{fluid} and fO_2 also control the stability relations and compositions of prehnite and epidote (Liou *et al.*, 1983; Leake, 1989). Minor amounts of calcite in amphibolites from Nikolkina Island indicate the presence of CO_2 in the hydrous fluids ($P_{fluid} > P_{H2O}$). Prevailing pressures must have been greater than 3 kbar and probably were below 4 kbar and comply with the intermediate pressure type described by Liou (1971).

1.7 Discussion

1.7.1 Interpretation of results - P-T path

Only the retrograde parts of the *P-T* trajectory/path are documented in highly sheared metagabbros and anorthosites from the south-eastern boundary of the Kolvitsa Massif. Due to the ultra-high temperature of metamorphism (900 – 1050 °C) linked with high diffusion rates, no prograde zonation patterns and reaction textures are preserved. Mafic lithologies show the peak-assemblages Grt-Cpx-Opx-Pl-Qtz and Grt-Cpx-Pl ±Qtz, depending on bulk rock chemistry and *P-T* conditions Orthopyroxene and clinopyroxene are both Al-rich, indicating ultra-high temperatures and high pressures respectively. The occurrence of an earlier static granulite-facies stage is suggested by cores of large orthopyroxene porphyroblasts with compositions not in equilibrium with garnet and clinopyroxene.

High pressures are also documented by the Opx-absent Grt-Cpx-Pl ±Qtz±Rt assemblages and elevated Na-contents in clinopyroxene ($Jd_{5\text{-}12}$). Yet, no eclogites have been found in the Kolvitsa and Por'ya Guba area. Pressure and temperature estimates range from 12 -15 kbar and 900 - 1050 °C and are related to crustal thickening und burial during formation of the Lapland-Kola collisional orogen. Due to southwest-directed compressional tectonics *c.* 1.9 Ga ago, crustal plates of the Kola terrane were accreted to the Late Archaean Belomorian terrane. Up-thrusting of nappe units caused crustal thickening. Thereby, part of metamorphic heat was released from overthrusted hot granulite nappes of the Umba Granulite Terrane. In the sheared metagabbros a subhorizontal stretching lineation is defined by torn-out aggregates of ortho- and clinopyroxene and garnet, documenting dynamic recrystallisation and mineral growth during granulite-facies shear deformation.

The second stage is documented by garnet resorbed by symplectitic intergrowths of Ca-rich plagioclase + orthopyroxene or Ca-rich plagioclase + hornblende at similar *P-T* conditions (8 – 11 kbar and 680 – 800 °C). What kind of symplectitic assemblage formed, depends on whether a hydrous fluid was present or not and if so also on the prevailing aH_2O and $aSiO_2$. The deduced *P-T* path is characterised by decompression (2 – 5 kbar) and moderate cooling (100 – 200 °C), reflecting rapid uplift following crustal thickening and shearing.

Compared to mylonitic granulites from the south-eastern boundary of the Kolvitsa Complex, metamorphic textures in basic rocks types from the central part document metamorphism under relatively static conditions. Composite garnet-bearing coronas developed between magmatic minerals, such as olivine and clino- and orthopyroxene and adjacent plagioclase, and commonly preserve the primary ophitic texture. Ilmenite is rimmed by Cpx-Grt coronas. *P-T* estimates for corona formation are 9 – 12.5 kbar and 700 – 800 °C. Temperatures are lower than in the granulite-facies assemblages from the south-eastern boundary of the Kolvitsa Complex, but pressures are rather high. The development and chronology of corona formation is not entirely resolved. A possible interpretation favoured by Bridgwater *et al.* (1994, 1995) and Glebovitsky *et al.* (1997) assumes that the garnet-bearing coronas formed in response to isobaric cooling immediately after emplacement and crystallisation of the igneous protoliths at deep crustal levels *c.* 2.45 Ga ago. On the other hand, corona textures may have formed due to pressure increase during crustal thickening and tectonic loading (Timmerman, 1996, Balagansky *et al.*, 2001). These processes occurred *c.* 1.9 Ga ago during SW-directed accretion of the Umba Granulite Terrane with the Kolvitsa Belt.

U-Pb zircon ages from anorthosites of the Kolvitsa Complex document metamorphism *c.* 1.91 Ga, ago (Frisch *et al.*, 1995; Kaulina, 1996). The metamorphic age, the occurrence of rutile in the metamorphic mineral assemblage and rather high pressures during amphibolite-facies hydration (8 - 10.5 kbar) favour a burial and tectonic loading scenario. Additionally, up-thrusting of nappe units and crustal thickening in the course of the Lapland-Kola orogeny should have affect also the structurally deeper parts.

During the following stage(s) of uplift and exhumation, the nappe pile was affected by localised shear deformation and fluid infiltration. At regional scale, fluid influx was strongly channelled (shear zones,

fractures), but had a pervasive character at grain-size scale. Fluid infiltration led to a complete hydration of the granulite-facies rocks with development of amphibolite-facies assemblages. This stage is characterised by uniform temperatures between 630 – 750 °C throughout the Kolvitsa Belt, while pressures seem to increase towards the west, i.e. towards structurally deeper units (Nikolkina Island & Leonard Cape: 8 – 10.5 kbar vs. Kataransky Cape: 5.5 –7 kbar). Notwithstanding the problems associated with barometry on the high-variance amphibolite-facies assemblages, consistent results of Grt-Hbl-Pl-Qtz barometry and hornblende barometry argue for applicability of both methods. The pressure gradient may than indicate that basic rocks of the central part of the Kolvitsa Complex were located at greater depth belonging to a tectonically lower thrust sheet. Alternatively, fluid infiltration into the basic lithologies may not have been coeval.
Low-grade hydrous alteration processes, such as prehnitisation of biotite and sericitisation of plagioclase document a later episode of limited fluid influx. at 350 – 400 °C and 3 – 4 kbar. The subsequent final stage of exhumation to the present exposure level has left no trace in the rock.
The part of the retrograde *P-T* path that is documented in the basic lithologies indicates substantial decompression. Near-isothermal decompression paths (ITD) may be linked to metamorphic belts evolved through thrust tectonics during continental collision (England & Richardson, 1977; England & Thompson, 1984; Thompson & England, 1984; Harley, 1989). Thereby ITD is associated with a clockwise *P-T* evolution. Whether the documented ITD-segment for the Kolvitsa Belt is part of a clockwise or anticlockwise *P-T* loop, can not entirely resolved. Assuming that the *P-T* trajectory belongs to an anticlockwise *P-T* evolution, the documented *P-T* segment should have developed from higher temperatures. This seems to be unlikely, because the calculated near-peak temperatures are extreme. A clockwise *P-T* evolution argues for plate-tectonic processes operating in collisional orogens in conformity with evolutionary models for the Lapland-Kola Orogen.

1.7.2 Age constraints

A compilation of geochronological constrains on the geological events for the Kochinny Cape area of the Kolvitsa Complex is given in Balagansky *et al.* (2001). The time of anorthosite emplacement is constrained by U-Pb zircon ages at 2.45 – 2.46 Ga (Frisch *et al.*, 1995; Mitrofanov *et al.,* 1995). Multiple injections of mafic dykes occurred presumably between 2.45 and 2.44 Ga as indicated by magmatic zircon ages of 2.44 Ga for a dioritic dyke (Kaulina, 1996; Balagansky *et al.*, 2001). The emplacement of the gabbro-anorthosite and dykes occurred in an extensional setting and the injection of basaltic melts into a large-scale shear zone was accompanied by shearing (Balagansky *et al.*, 2001). Zircons from sheared dykes and gabbro-anorthosites are believed to document metamorphic reworking during shearing and yielded U-Pb ages between 2.42 and 244 Ga (Balagansky *et al.*, 1998b). The U-Pb age of euhedral zircons with magmatic zoning from a crosscutting undeformed pegmatite strongly suggests that shearing was terminated 2.39 Ga ago (unpublished result from Kislitsyn in Balagansky *et al.*, 2001).
After a time gap of *c.* 500 Ma, the Svecofennian metamorphic reworking of the complex is documented by metamorphic zircons from an anorthosite lens near to Kataransky Cape and from dioritic dykes at the Kochinny Cape, yielding near-concordant U-Pb ages of 1905 ±26 Ma (Frisch *et al.*, 1995) and 1919 ±18 Ma. (Kaulina, 1996; Kaulina & Apanasevich, 1998). Zircons from high-grade leucosomes, post-dating shearing in the granulitic mélange yielded 1906 ±1 Ma (Kislitsyn *et al.*, 1998) and 1912 ±2 Ma (Kislitsyn *et al.*, 1999) and are consistent with U-Pb ages of *c.* 1910 ±60 Ma from the paragranulites of the Umba Granulite terrane (Tugiranov & Bibikova, 1980). This strongly suggests that the metamorphic overprint occurred between 1905 and 1910 Ma ago.
Although pristine magmatic textures are often well preserved in low-strain igneous rock types from the Kolvitsa Massif, the *P-T* evolution following the magmatic emplacement and subsequent

deformation and the Svecofennian metamorphic reworking at *c.* 1.91 Ga, is not entirely understood. If a tectonic burial scenario is assumed for the formation of the coronitic garnet in rock types of the Kolvitsa Massif, ages for the metamorphic reworking at *c.* 1.91 Ga, may be directly linked to results from thermobarometry. The prograde metamorphic history has been completely erased in the sheared metagabbros and anorthosites from the south-eastern boundary of the Kolvitsa Complex as well as in the weakly deformed coronal rock types of the central part.
The cooling history is constrained by U-Pb titanite ages of 1896 – 1898 Ma (this study/part II) and an Ar-Ar amphibole cooling age of *c.* 1880 Ma (this study/part II) from the hydration zones. These results agree with cooling ages of 1885 – 1890 Ma obtained from Sm-Nd garnet-whole rock data (Alexejev *et al.*, 1999). Whereas U-Pb titanite ages are believed to document crystallisation during amphibolite facies hydration at 650 – 750 °C, ^{40}Ar-^{39}Ar amphibole ages and Sm-Nd garnet-whole rock ages are interpreted as cooling ages through the respective closure temperature (450 °C and 550 °C, respectively).
Integrated cooling and exhumation rates range from 10 to 20 °C/Ma and from 0.7 to 2 mm/a (this study/part II). The data points to fast exhumation following tectonic crustal thickening in the course of plate-collision during the formation of the Lapland-Kola Orogen. Elevated cooling and uplift rates indicate that plate tectonic processes in the Proterozoic was presumably rather similar to those operating today.

1.8 Conclusion

The evolutionary history of the Kolvitsa Complex started with the emplacement of layered gabbro-anorthosite bodies and multiple dyke injections between 2.46 – 2.44 Ga (Frisch *et al.*, 1995; Mitrofanov *et al.,* 1995, Kaulina, 1996; Balagansky *et al.*, 2001). An early metamorphic overprint at *c.* 2.43 Ga is documented by U-Pb zircon data for highly sheared dykes and metagabbros at the Kochinny Cape (Balagansky *et al.*, 1998b) The metamorphic evolution of the Kolvitsa Complex in the extended period between the magmatic emplacement and metamorphism and the Svecofennian reworking *c.* 1.91 Ga ago, is not resolved. Important features of the early to middle Palaeoproterozoic tectonometamorphic evolution, recorded from highly sheared metagabbros of the south-eastern boundary and from coronal rock types of the central part of the Kolvitsa Complex are summarised as follows.

- No prograde reaction textures and paragenesis are preserved in mafic granulites from the south-eastern thrust boundary. Only the cores of large orthopyroxene porphyroclasts, out of chemical equilibrium with garnet and clinopyroxene, suggest a previous static granulite-facies stage.
- Rims and to a lesser extent also cores of garnet porphyroclasts of the granulite-facies assemblages in sheared mafic granulites were affected by retrograde diffusional Fe-Mg exchange. Temperature estimates for the high-grade shear deformation, if necessary corrected for late Fe-Mg exchange, range from 900 to 1050 °C, at pressures of 12 to 15 kbar. High pressures are also indicated by Opx-absent Grt-Cpx-Pl assemblages and elevated jadeite contents in clinopyroxene. This points to crustal thickening and burial of the Kolvitsa complex down to crustal levels of 40 to 50 km during collision of the crustal plates of the Central Kola Terrane with the Late Archaean Belomorian foreland *c.* 1.91 Ga ago.
- Partial re-equilibration of the granulite-facies mineral assemblages during exhumation led to symplectitic garnet breakdown and diffusional zonation patterns in garnet grains. *P-T* estimates deduced from decompressional reaction textures yielded 680 – 800 °C and 8 – 11 kbar which document moderate cooling and decompression to lower and mid crustal levels (28 – 35 km).
- Reaction textures and mineral assemblages in coronal rock types from the south-western and central part of the Kolvitsa Complex differ significantly from those of the mylonitic granulites from the high-grade shear zone. Temperatures estimates inferred from garnet-bearing corona textures did not exceed 800 °C, while prevailing pressures were rather high (10 to 12.5 kbar). If corona formation resulted from as a consequence of increasing pressure, crustal thickening and

burial can be attributed to accretion and up-thrusting of the Umba Granulite terrane *c.* 1.9 Ga ago., in which case part of the metamorphic heat budget was released from the overthrust hot granulite nappes of the Por'ya Guba and Umba complexes. The inverted metamorphic gradient in the suture zone of the LKO has been established by several authors (Barbey & Raith, 1990; Krill, 1985; Timmerman, 1996; Daly *et al.*, 2001) is in support with interpretation.

- The ongoing south-west directed up-thrusting and stacking of nappe units and crustal thickening caused metamorphism and corona formation in the central part of the Kolvitsa Complex and finally to the juxtaposition of highly sheared granulites and amphibolite-facies coronal rock types.
- The amphibolite-facies hydration occurred *c.* 1896 to 1898 Ma ago. Temperature estimates range from 650 to 750 °C, whereas pressure estimates decrease from the south-eastern boundary to central and south-western part of the Kolvitsa Complex. The pressure gradient may then indicate that basic rocks of the south-western and central part of the Kolvitsa Complex were located at greater depth and belonged to a tectonically lower thrust sheet.
- Deduced integrated cooling and exhumation rates vary from 10 to 20 °C/Ma and from 0.7 to 2 mm/a, respectively and are consistent with what is known from modern orogenic belts.

The tectonometamorphic evolution of mafic rock types in the south-eastern thrust zone and the central part of the Kolvitsa Complex differs significantly and could have been even more complex in detail. The inferred integrated exhumation and cooling rates are therefore a approximation to the differential tectonic exhumation history.

2. Characterisation of fluid-rock interactions during exhumation of mafic granulites from the Kolvitsa-Umba suture zone, Kola Peninsula (Russia)

2.1 Introduction

Shear and fault zones play a decisive role in controlling the metamorphic flow system in mid to deep crustal levels (e.g. Etheridge *et al.*, 1983; Kerrich, 1986; Selverstone *et al.*, 1991; Dipple & Ferry, 1992; Oliver, 1996; Cartwright & Barnicoat, 2003). Whereas diffusion prevails at small-scale fluid flow and is driven by concentration gradients, large-scale fluid flow for length scales at which diffusion is negligible, is controlled by deformation and gradients in temperature and pressure (Dipple & Ferry, 1992). Dynamic recrystallisation and deformation in shear zones increase the permeability and fluid flow thus becomes strongly focussed (Cartwright & Barnicoat, 2003 & including references). As a consequence, shear and fault zones commonly act as pathways for large volumes of ascending fluids. Beside mineralogical changes, fluid migration through shear zones commonly causes marked changes in bulk chemistry and stable isotope systematics (e.g. O'Hara, 1988; Selverstone *et al.*, 1991; McCaig *et al.,* 1990; Dipple & Ferry, 1992; Marquer *et al.*, 1994; Streit & Cox, 1998; Cartwright & Barnicoat, 2003; Yonkee *et al.*, 2003).

In the Lapland-Kola collisional orogen, during west-directed tectonic exhumation, significant fluid flow occurred in the basal parts of the nappe pile. Hydration phenomena are particularly widespread in the rocks of the Kolvitsa-Umba Belt and include decimetre to metre-scale amphibolitisation along shear zones and fractures, felsic veins and lithological boundaries. Retrograde zones of amphibolitisation are thus direct evidence for fluid influx and are an important clue to the understanding of processes in metamorphic flow system in the crust, such as textural re-equilibration, re-crystallisation, element and mass transfer as well as the driving forces of fluid flux. Hydration zones in the mafic rock associations of the Kolvitsa Complex are well exposed along the coast line of the Kandalaksha Bay, being an excellent place to study fluid-rock interactions.

For the understanding of metamorphic fluid flow systems, the geological context, the fluid source (locally generated versus externally derived fluids), the direction of fluid flow (up-temperature or down-temperature fluid flow) and the volume of fluids are of interest. Estimates of fluid volume and flow direction are based on key assumptions, e.g. the attainment of chemical equilibrium between fluid and solids (wall rock) along the flow path through a rock with uniform permeability and a steady state temperature gradient. Unfortunately, geological flow systems are far more complex to be described through simple modelling of one-dimensional fluid flow along temperature gradients (Cartwright & Buick, 1996). Obviously, small scale variations in lithology and localised zones of increased permeability, like shear and fault zones, cause spatially heterogeneous fluid flow conditions. However, temperature gradients are ubiquitous in the crust (Dipple & Ferry, 1992) and even if fluid flow was channelled obliquely to the geothermal gradient, the flow directions may be deduced (Cartwright & Buick, 1996).

So far, the systematics of fluid flow and involved fluid-rock interactions have not been studied in the Kolvitsa Complex. The source and volumes of the fluids are unknown and the alteration patterns between protoliths and their retrogressed equivalents not constrained. Whether fluid flow in the different sites of hydration occurred contemporaneously and was part of a single large-scale flow system or rather reflects multiple episodes of small-scale fluid migration, is not clear. It is obvious that small-scale fluid-rock interaction phenomena may well be the expression of a large metamorphic fluid

flow system. The chemical and mineralogical changes, the volumes of involved fluids and the driving forces of fluid flow can be assessed by combining petrological and geochemical whole-rock data, oxygen and Sm-Nd isotope systematics and age constraints. Towards this goal, the geochemical characteristics (major and trace elements, Sm-Nd systematics, oxygen isotopes) of hydration zones and unaltered mafic protoliths have been analysed and compared. U-Pb and ^{40}Ar-^{39}Ar dating of titanite and amphibole from hydration zones was carried out to constrain the timing of hydration and to provide information on the cooling and unroofing history. Mass balance calculations (Potdevin & Marquer, 1987) were undertaken to characterise element mobility, mass transfer and volume changes associated with the development of the hydration zones. Alteration patterns of depleted or enriched elements in combination with oxygen isotope data are used to constrain the nature and amount of the infiltrating fluids.

2.2 Geological setting

Within the Lapland-Kola Orogen (north-eastern Baltic Shield), the Umba-Kolvitsa Belt forms part of a major suture zone (Fig. 2.1). Crustal plates of the Central Kola Terrane were accreted to the Late Archaean Belomorian Terrane during southwest-directed compressional tectonics *c.* 1.9 Ga ago (Barbey et al., 1984; Glebovitsky, 1993).

Mafic rock associations of the Kolvitsa Belt are exposed at the north-eastern coast of the White Sea (Fig. 2.1) and comprise gabbroic rocks and anorthosite bodies formed in an extensional rift-related setting *c.* 2.45 Ga ago (Frisch *et al.*, 1995; Mitrofanov *et al.*, 1995b, Amelin *et al.*, 1996). Rifting occurred in a transtentional setting, attributed to WSW-ENE directed extension and concomitant dextral movements along NW-trending shear zones (Balagansky *et al.*, 2001). To the NW the Kolvitsa Belt can be correlated to the Tanaelv Belt in Finland and Norway and is believed to be its analogue. When the tectonic regime changed to convergence, compressional tectonics resulted in the collision of the southern Belomorian foreland with the Central Kola terrane and the accretion of the juvenile Umba Granulite Terrane. In consequence of continental collision, up-thrusting of nappe units and crustal thickening occurred *c.* 1.9 Ga ago. Part of the metamorphic heat was released from the overthrust hot granulite nappes of the Umba Granulite Terrane. Metamorphic overprint in the core zone and in the footwall of the Lapland-Kola Orogen resulted in the formation of high-pressure and high-temperature granulites. In the Tanaelv Belt and presumably also in the Kolvitsa Belt overthrust granulite nappes caused an inverted metamorphic gradient in the suture zone of the Lapland-Kola Orogen (Barbey & Raith, 1990; Timmerman, 1996; Daly *et al.*, 2001).

The different lithotectonic units and nappes of the Kolvitsa Belt strike NW and dip gently to the NE (Fig. 2.1). The lowermost unit is built up by *c.* 2.7 Ga old Neo-Archaean tonalitic to dioritic orthogneisses of the Belomorian Supergroup (Bogdanova & Bibikova, 1993; Bibikova *et al.*, 1995, 1996).

To the NE the Belomorian gneisses are overlain by the Palaeoproterozoic Kandalaksha sequence, comprising metavolcanic rocks and subordinate metasedimentary rocks, such as graywackes and conglomerates. The magmatic crystallisation age of volcanic protoliths is assumed to be *c.* 2.47 Ga (U-Pb age of zircon and Rb-Sr whole rock ages, Balagansky *et al.*, 1998b).

The Kolvitsa gabbro-anorthosite association is characterised by crystallisation ages of 2.45 – 2.46 Ga (U-Pb zircon ages: Frisch *et al.*, 1995; Mitrofanov *et al.*, 1995b) and is cut by several mafic to intermediate dyke swarms. In low-strain zones magmatic bodies partially preserved their magmatic textures (cumulate texture, magmatic layering). In high-strain zones pervasive deformation and shearing occurred during or immediately after solidification (Balagansky *et al.*, 2001).

The Por'ya Guba complex is bounded by shear zones and contains mafic to intermediate granulites and subordinate ultrabasic lenses, enderbitic gneisses and rare intercalated carbonate layers. In mafic lithologies, garnet-clinopyroxene-plagioclase assemblages indicate high pressures.

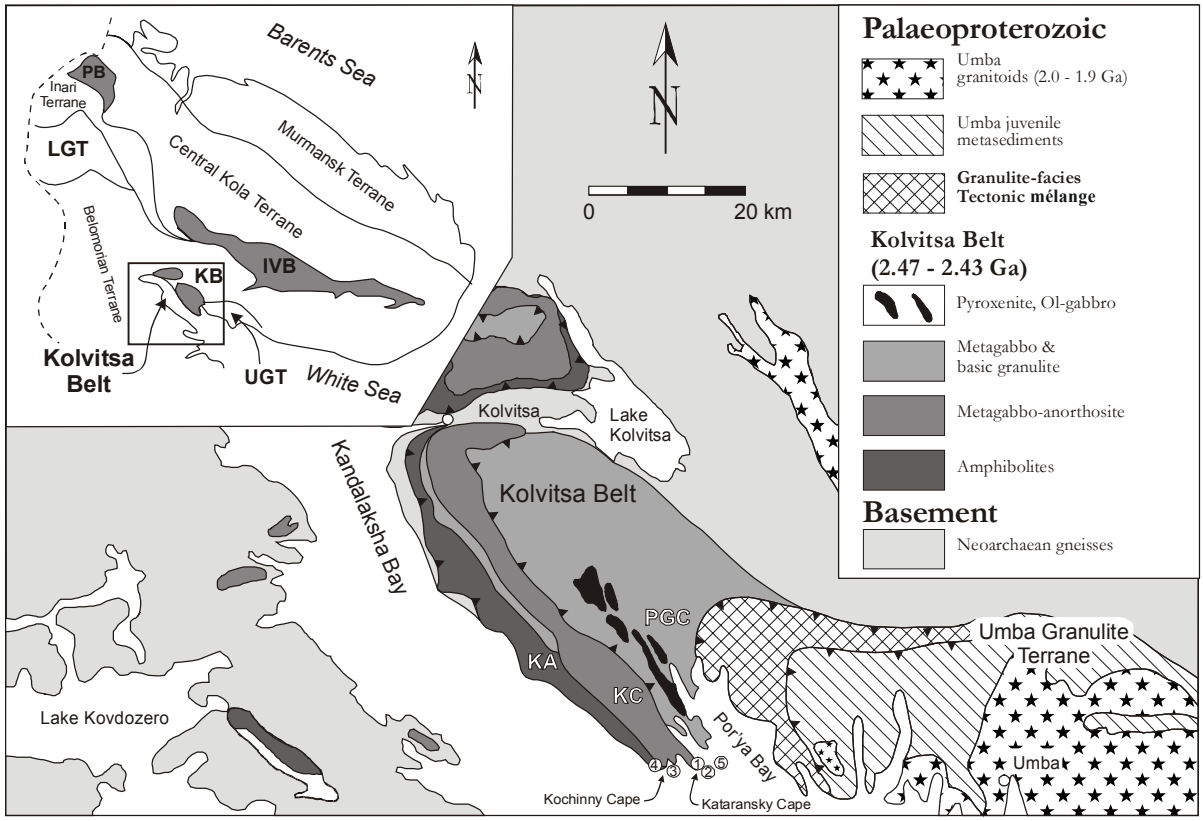

Fig. 2.1. Simplified geological map of the Palaeoproterozoic Kolvitsa Belt (after Mitrofanov, 1996; Balagansky *et al.*, 2001). PGC: Por'ya Guba complex, KC: Kolvitsa complex, KA: Kandalaksha amphibolites. Sample localities are indicated by numbers, 1: Kataransky Cape, 2: Bolschoi Khed Island, 3: Nikolkina Island, 4: Leonard Cape, 5: Medvezhy Island.

On the north-eastern coast of the Por'ya Bay a major granulite-facies shear zone is exposed between the Kolvitsa Belt and the accreted Umba Granulite Terrane (Balagansky *et al.*, 1994). This zone is interpreted as a tectonic mélange zone, where mafic to intermediate granulites of the Por'ya Guba Complex are interleaved with tectonic lenses of juvenile metasediments from the Umba Granulite Terrane. U-Pb ages for zircons from high-grade garnet-sillimanite gneisses and crosscutting leucosome yielded *c.* 1.9 Ga and date high-grade metamorphism and shearing (Bibikova *et al.*, 1973; Kislitsyn *et al.*, 1999a)

To the east migmatitic paragneisses of the accreted Umba Granulite Terrane are exposed. The juvenile character of the metasediments is confirmed by young Sm-Nd model ages (2.5 – 2.1 Ga, Huhma & Meriläinen, 1991; Timmerman, 1996; Daly *et al.*, 1997; Bridgwater *et al.*, 2001; Daly *et al.*, 2001). The Umba Granulite Terrane is believed to be the south-eastern extension of the Lapland Granulite Belt in northern Finland and Norway. To the east the Umba Granulite Terrane is intruded by a magmatic suite of enderbites, charnockites and porphyritic granites with crystallisation ages of *c.* 1.91 Ga (U-Pb zircon ages, Glebovitsky *et al.*, 2001).

Exhumation of the nappe units was accompanied by infiltration of hydrous fluids along shear zones and fractures. The mafic rock association of the Kolvitsa Complex and of the Por'ya Guba Complex were affected by hydration at amphibolite-facies conditions. Whereas in the Kolvitsa Complex hydration proceeded from small-scale shear zones and fractures (dm–m scale), in the Por'ya Guba Complex larger domains were affected by hydration and are now transformed to garnet amphibolites.

2.3 Examples of fluid infiltration zones

The effects of fluid infiltration were examined across decimetre to metre wide hydration zones in gabbroic and dioritic rocks of the Kolvitsa nappe unit. Sampled localities are indicated in Fig. 2.1.
Fluid flow was strongly channelled at outcrop scale with hydration proceeding from shear zones, fractures and felsic veins (Fig. 2.2 & 2.3). On decimetre- to metre-scale, hydration has a pervasive character, resulting in a complete textural and mineralogical re-equilibration at grain scale. Fluid influx caused a dramatic change in mineralogy from the granulite-facies assemblage Grt-Cpx-Pl ±Opx, Qtz of the pristine basic lithologies to the assemblage Hbl-Pl ±Ttn, Qtz in the amphibolite centre of fluid infiltration zones. Monomineralic amphibole felses represent end-members of fluid infiltration. There is a textural change across the hydration zones depending on the strain gradient. In the marginal, partially hydrated zones, the amphibolite-facies assemblage mimics the fabric of the precursor, e.g. the granulite-facies foliation, and clearly indicates hydration under static conditions. Progressing hydration resulted in a change of the rheological properties, with viscosity decreasing. As a result marked strain gradients developed towards the centre of hydration zones of amphibolitisation (Fig. 2.2a-b).

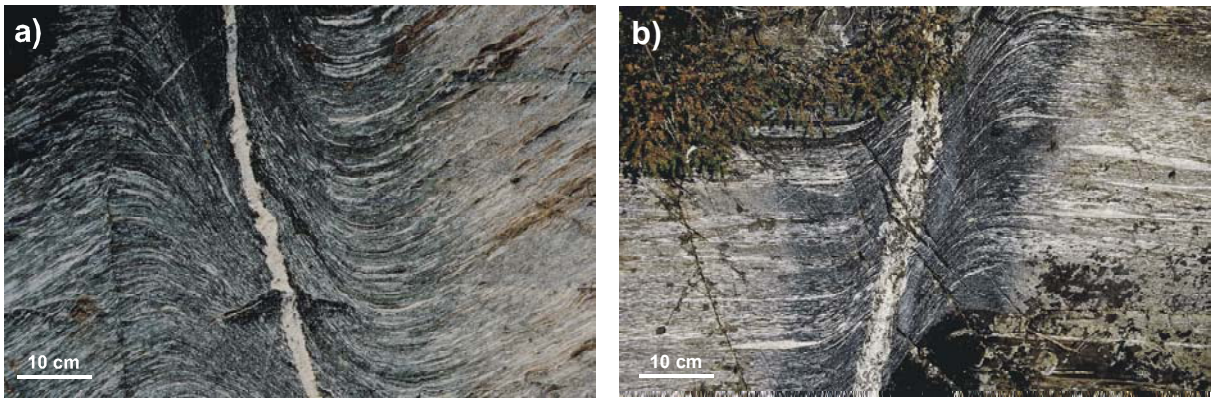

Fig. 2.2. Zones of amphibolitisation bound to shear zones. Changes in the rheological properties of the pristine granulite caused the decrease of viscosity and strain became strongly focused into the zones of amphibolitisation.

In the centre of the shear zones, the amphibolite-facies assemblage was subjected to dynamic re-crystallisation followed by a stage of static annealing. Fluid-enhanced deformation in the Kolvitsa Complex may be bound to shear zones with dextral or sinistral displacement. The lateral offset of these shear zones ranges from 10 to 50 cm. Hydration under static conditions is characterised by a complete textural reorganisation. In the centre of the fluid infiltration zone, the pristine fabric of the sheared metagabbro disappeared (Fig. 2.3a).

Fig. 2.3. Examples of hydration under static conditions. Fluid infiltration was related to fractures and partially progressing hydration resulted in the formation of networklike structures.

The amphibolite domains exhibit an irregular, felsic fabric and show an increase in grain-size. During static hydration, the infiltrating fluids were channelled along fractures or zones of weakness. Progressing hydration resulted in the formation of network-like structures (Fig. 2.3b).
The static and dynamic hydration zones represent cross-cutting structures with regard to the prevailing NW-trending foliation and banding. At Kataransky Cape, shear zones are discordant and cut perpendicular to the foliation of the granulite-facies host rock (Fig. 2.2a).
Although hydration processes in the Kolvitsa nappe are confined to small-scale shear and hydration zones, fluid infiltration presumably can be attributed to larger scale dehydration processes in the footwall of the nappe. Coeval with the tectonic exhumation of the nappe pile, larger thrusts and lithological boundaries formed pathways for the ascending fluids.

2.3.1 Description of the studied localities

Kataransky Cape

The studied example documents hydration of a mylonitic gabbroic granulite across a small-scale shear zone (Fig. 2.1 & 2.4). Fluid-enhanced deformation occurred under amphibolite-facies conditions. Hbl-Pl thermometry (Holland & Blundy, 1994) yielded 650 – 720 °C at an assumed pressure of 6 – 6.5 kbar. Decreasing viscosity towards the centre of hydration caused ductile deformation and strain became focused in the central zone of amphibolitisation. A dextral sense of shearing is indicated by the lateral offset of the foliation. Zone I shows the pristine mylonitic granulite-facies metagabbro. Mafic layers are composed of garnet (X_{Mg}0.45) and Al-rich diopside (X_{Mg}0.8). Felsic layers mainly consists of recrystallised plagioclase (An_{50}). The granulite-facies foliation is mimicked by the amphibolite facies assemblage Hbl-Pl. Near the centre of the fluid infiltration, zone IIIa is characterised by increasing grain sizes of hornblende and plagioclase. Hornblende is homogeneous in composition (X_{Mg}0.65), whereas plagioclase is characterised by pronounced zonation patterns (An_{40-50}), indicating incomplete chemical re-equilibration. Zone IIIb represent the centre of the fluid infiltration zone. The felsic vein is composed of plagioclase (An_{38-44}). Plagioclase was affected by sericitisation. In the contact to the felsic vein, the retrogressed metagabbro is dominated by hornblende. Changes in the composition of hornblende, classified after Leake (1997), range from magnesio-hornblende in zone II to tschermakite in zone III and is accompanied by an increasing influence of pargasite substitution. A detailed description of the petrography and mineral chemistry is given in part I. Zone II presents the marginal part of the hydration zone.

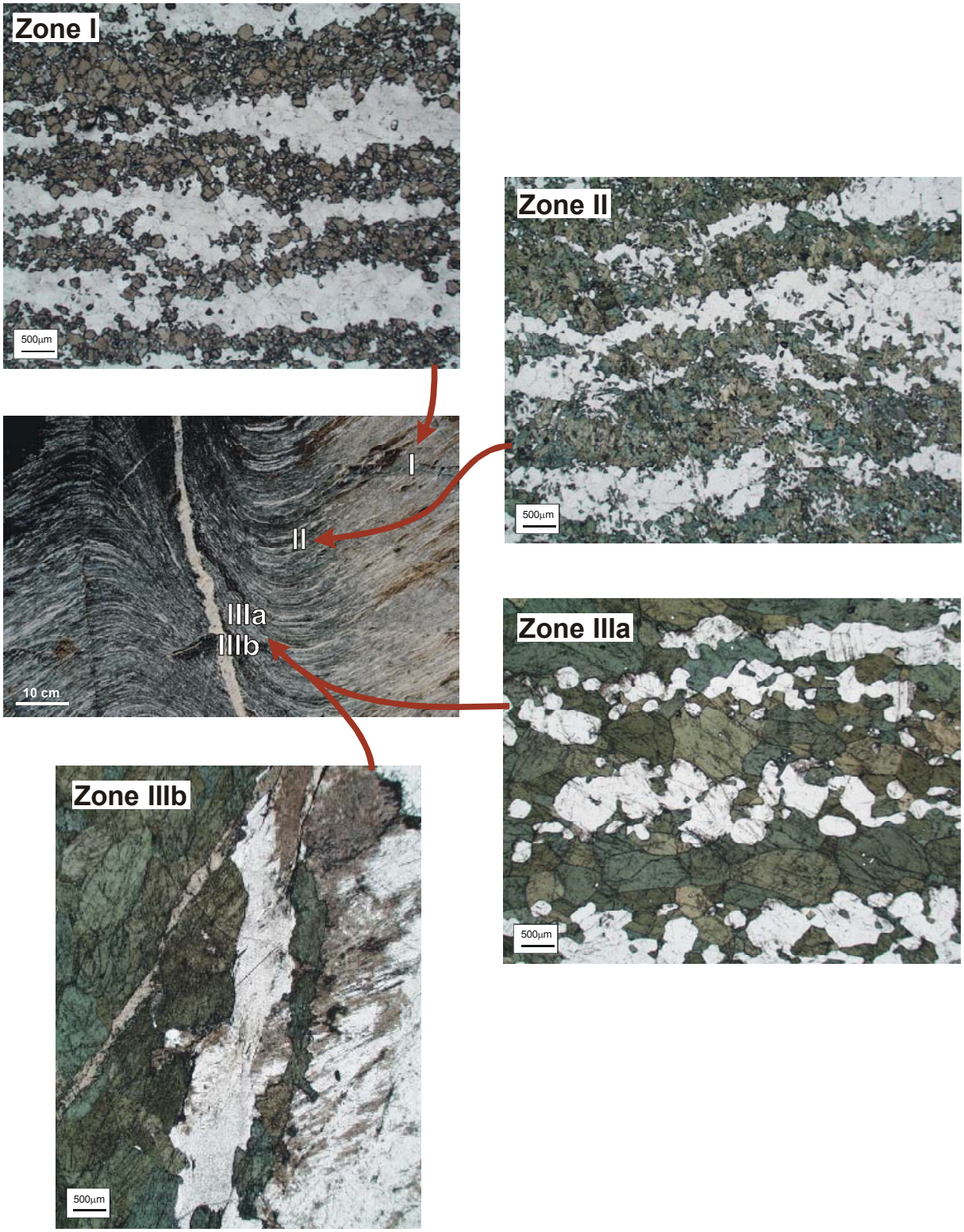

Fig. 2.4. At Kataransky Cape (Kolvitsa Complex) fluid infiltration was confined to small-scale shear zones. Decreasing viscosity in the hydration zone led to a marked strain gradient. Zone I shows the pristine metagabbro formed during granulite-facies shear deformation. The mineral assemblage is Grt-Cpx-Pl +/-Qtz. The transition zone II is characterised by the amphibolite-facies assemblage Hbl-Pl +/-Qtz. Symplectitic Hbl + Pl aggregates mimic the former granulite-facies minerals (Grt, Cpx). In zone IIIa fluid infiltration caused an increase in the grain size of Hbl and Pl. Zone IIIb presents the centre of the fluid infiltration zone. Hornblende is prevailing and plagioclase occurs only in the felsic vein.

Bolschoi Khed

The studied hydration zone from Bolschoi Khed Island documents hydration under static conditions (Fig. 2.1 & 2.5). The protolith is a mylonitic metagabbro (zone I). Mafic layers are composed of Grt ($X_{Mg\ core}$0.65) and aluminium-rich Cpx (X_{Mg}0.85) and Opx (X_{Mg}0.8). Felsic layers contain recrystallised plagioclase (An_{45}) and subordinate quartz. Hydration occurred under amphibolite facies conditions with temperatures (Hbl-Pl thermometry; Holland & Blundy, 1994) ranging from 700 to 750 °C at an assumed pressure of 6 kbar. In the outer zone II, hydration has caused the complete replacement of the granulite-facies assemblage. The well equilibrated mineral assemblage Hbl-Pl mimics the granulite-facies foliation of the precursor. At the centre of the hydration zone (zone III), a monomineralic amphibolite fels represents the end-member of hydration. Grain size coarsening and re-crystallisation under static conditions have erased the foliation. Textural and chemical re-equilibration is indicated by the polygonal fabric and the homogeneous hornblende composition (X_{Mg}0.75). X_{Mg} of hornblende shows a minor decrease from zone II (X_{Mg}0.8) to zone III (X_{Mg}0.75).

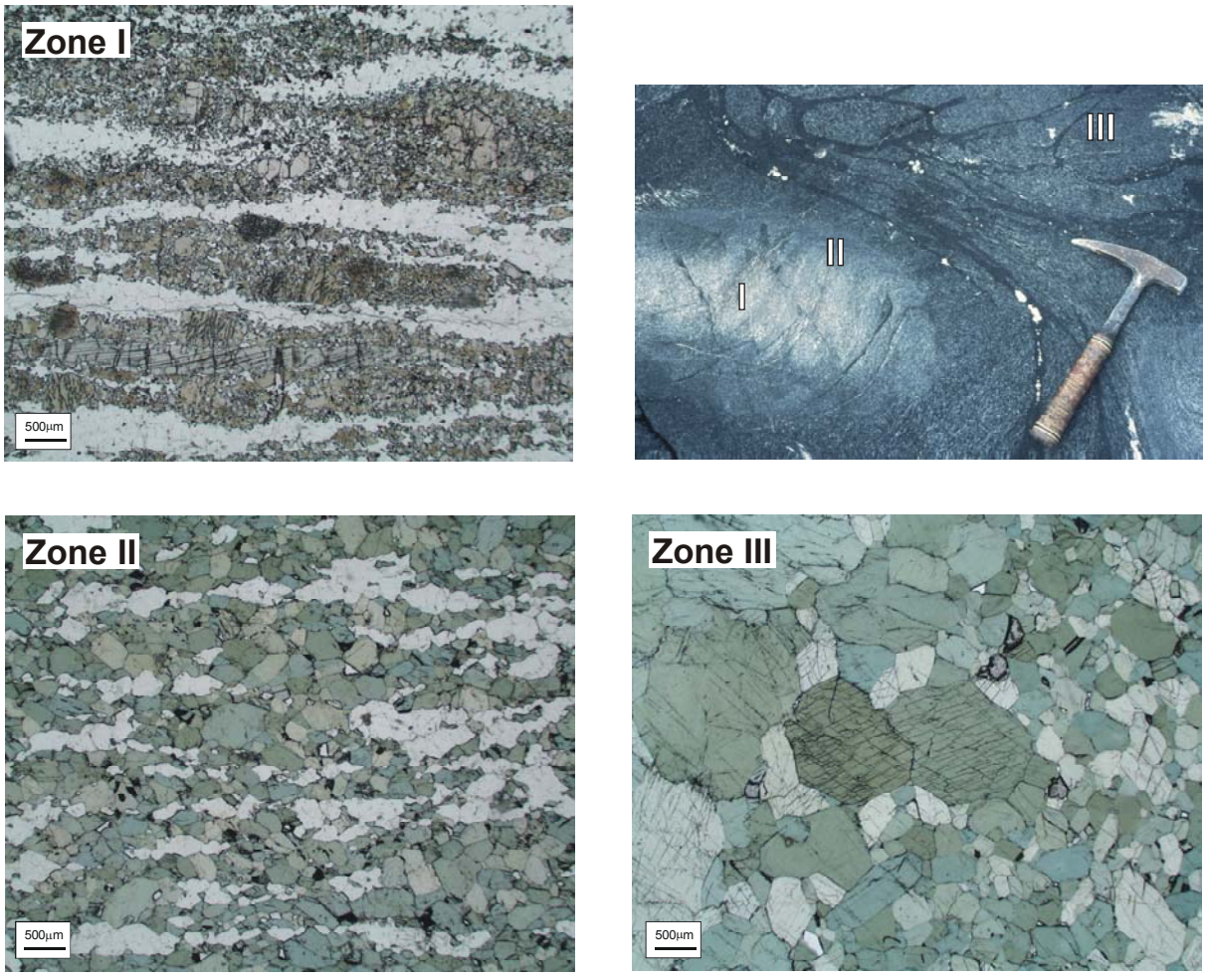

Fig. 2.5. Profile across a hydration zone from Bolschoi Khed Island (Kolvitsa Complex). Hydration occurred under static conditions along network-like veins. Zone I shows the pristine metagabbro. Granulite-facies shear deformation produced a pronounced foliation and subhorizontal stretching lineation defined by torn-out aggregates of Cpx, Opx and Grt. In the transition zone II, the mineral assemblage Hbl-Pl +/- Qtz has replaced the granulite assemblage but still mimics the foliation. Zone III was most strongly affected by fluid infiltration and is characterised by a monomineralic amphibole fels. Textural re-equilibration is indicated by increasing grain size of hornblende and the loss of the foliation.

Nikolkina Island

At Nikolkina Island hydration affected a basic dyke. A felsic vein in the centre of the hydration zone documents fluid influx. In the basic protolith (Zone I), clinopyroxene (X_{Mg}0.75) is supposed to have a magmatic origin. Garnet (X_{Mg}0.3) occurs exclusively as a coronal phase developed between plagioclase and adjacent clinopyroxene and ilmenite. Clinopyroxene is partially replaced by hornblende (X_{Mg}0.65).

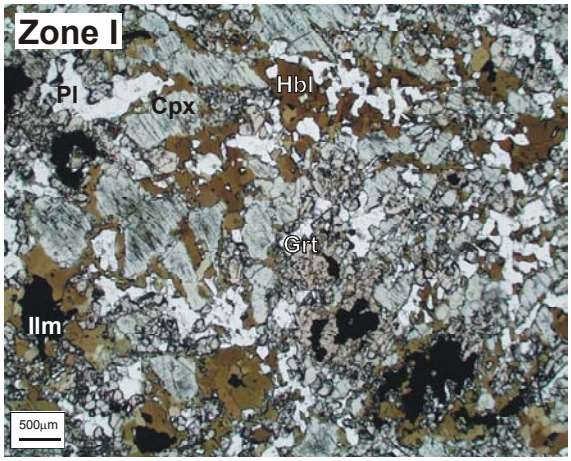

Fig. 2.6. Pristine basic dyke with corona texture from Nikolkina Island (Kolvitsa Complex). Magmatic fabric and minerals (e.g. Cpx) are preserved. Garnet occurs exclusively as a coronal phase. Clinopyroxene is partially altered to hornblende.

The outer zone (II) of the hydration front is characterised by the mineral assemblage Grt-Hbl-Pl-Qtz-Ttn. Compared to coronal garnet in the protolith, garnet from zone II is characterised by decreasing X_{Mg} (0.2). Temperatures obtained from Hbl-Grt (Graham & Powell, 1984) and Hbl-Pl (Holland & Blundy, 1994) thermometry yielded 650 – 750 °C at 10 – 11 kbar. Pressure estimates based on Grt-Hbl-Pl-Qtz barometry (Kohn & Spear, 1990) range between 10 and 11 kbar. Results from classical thermobarometry agree with *P-T* estimates obtained from multi-equilibrium thermobarometry (TWEEQU 1.02, Berman, 1991). Constraints on the H_2O-activity of the fluid phase were obtained from *T-a*H_2O phase diagrams and range from 0.4 to 0.6. In Zone III, progressing hydration caused the complete breakdown of garnet. Biotite aggregates document the Pseudomorphic replacement of garnet. Zones IVa and IVb represent the centre of the hydration zone. Nearly monomineralic amphibolite fels represents the end-member of fluid infiltration. Titanite and calcite form accessory constituents. Prehnite formation together with sericitisation may be attributed to low-grade alteration, affecting biotite and plagioclase. The felsic vein in the centre of the fluid infiltration zone (IVB) is composed of plagioclase (An_{20-30}). By comparing hornblende compositions, a decrease in X_{Mg} from zone I (X_{Mg}0.65) to zone IV (X_{Mg}0.4) becomes obvious and is accompanied by pargasite substitution. As a consequence of, hornblende compositions classified after Leake (1997) change from edenitic to ferro-pargasitic.

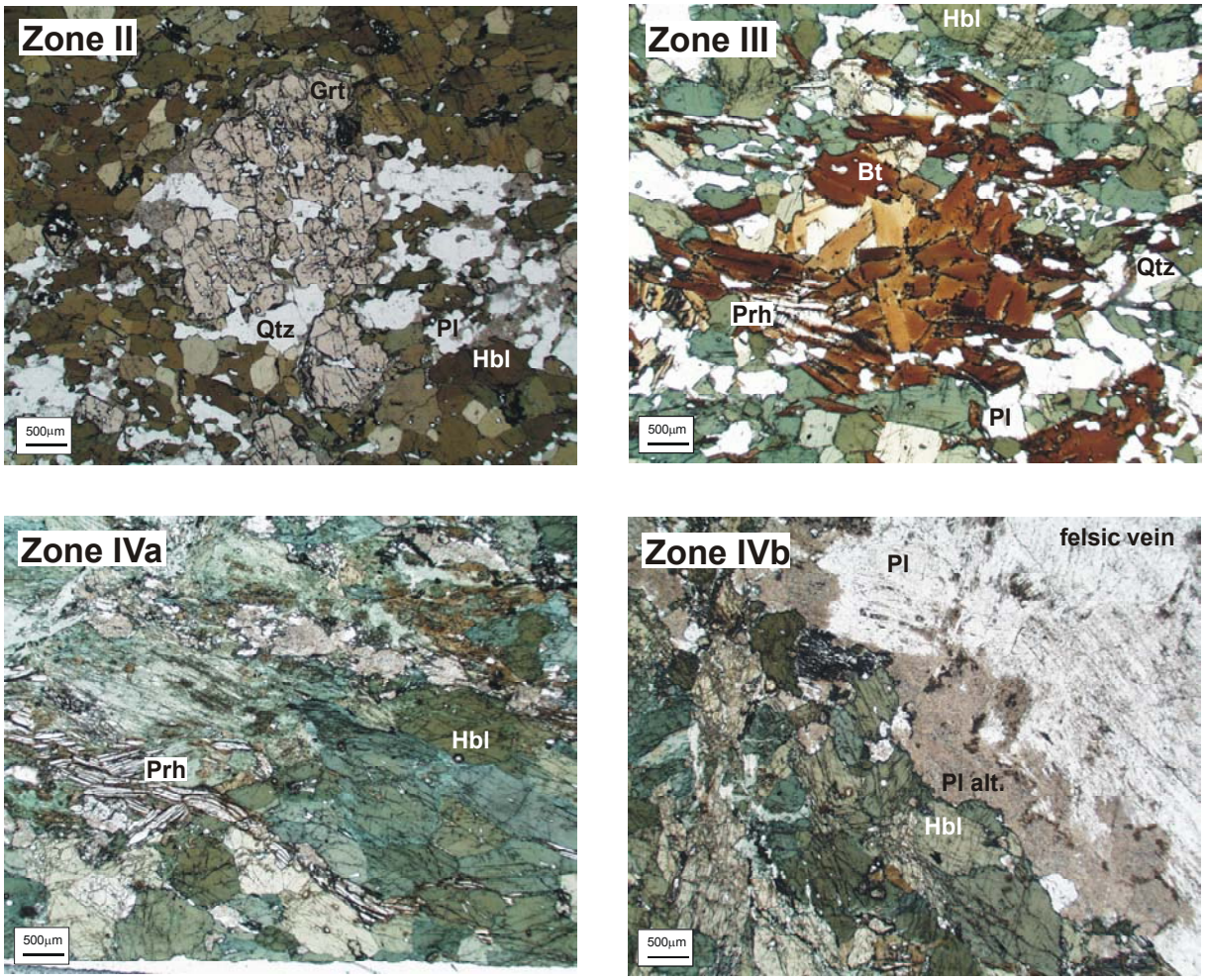

Fig. 2.7. Profile across a hydration zone in a basic dyke at Nikolkina Island, from the weakly hydrated marginal zone II to the centre of fluid infiltration (zone IV). Zone II is characterised by the well equilibrated assemblage Grt-Hbl-Qtz-Pl +/-Ttn. In zone III progressing fluid infiltration caused the breakdown of garnet. Biotite aggregates form pseudomorphs after garnet. In the centre of the fluid infiltration zone, the mineral assemblage is dominated by hornblende +/- Pl, Ttn. Biotite became unstable and later alteration to prehnite resulted in a complete replacement of biotite. The felsic vein in the centre of fluid infiltration is dominated by plagioclase.

Leonard Cape

At Leonard Cape, metadiorites with the relict mineral assemblage Amph-Pl-Bt ±Grt were affected by large-scale alteration, caused by infiltrating fluids. Fluid infiltration occurred at amphibolite-facies conditions of 680 – 720 °C (Hbl-Pl thermometry: Holland & Blundy, 1994; Hbl-Grt thermometry: Graham & Powell, 1984) and 8 – 9 kbar (Grt-Hbl-Pl-Qtz barometry: Kohn & Spear, 1990) and proceeded along network like structures. Relict metadiorite 'fragments' are surrounded by domains of amphibolite felses. Highly altered zones (III) have lost plagioclase and are characterised by an enrichment of zircon and titanite. Nearly monomineralic amphibole felses consist of pargasitic to ferropargasitic hornblende with X_{Mg} of 0.5. Prehnite and sericitisation are low-grade alteration products (see also Nikolkina Island).

2.4 Major and trace element geochemistry

2.4.1 Analytical technique

Geochemical whole rock analysis were performed at the Mineralogisch-Petrologisches Institut of the University Bonn using a Philips PW 1480 X-ray fluorescence spectrometer. The crashed and powdered samples were mixed 1:10 with Lithium-tetra-borate. Glass discs were automatically measured in the XRF machine.

2.4.2 Geochemical characterisation of the magmatic protoliths

The pristine magmatic mineral assemblages are best preserved in various mafic dykes and coronitic mafic rock types of the Kolvitsa Complex. The study of coronitic assemblages indicates that their formation represents an isochemical process. This finding is supported by other studies of coronitic gabbros (e.g. Rivers & Mengel, 1988; Johnson & Carlson, 1990; Alirezaei & Cameron, 2002). Especially in low-strain zones at Kataransky- and Kochinny Capes and Nikolkina Island (Fig. 2.1), mafic dyke swarms widely preserved their igneous textures and mineral assemblages (see also Balagansky *et al.,* 2001).

Despite the well-known problem regarding the mobility of Na_2O and K_2O during hydrous metamorphism, the TAS and the AFM diagrams were used for graphical representation of the geochemical data. The majority of the studied basic rock types from the Kolvitsa gabbro-anorthosite complex fall into the gabbro field of the TAS diagram and belong to the sub-alkalic series (Fig. 2.8). Two samples from Leonard Cape are diorites.

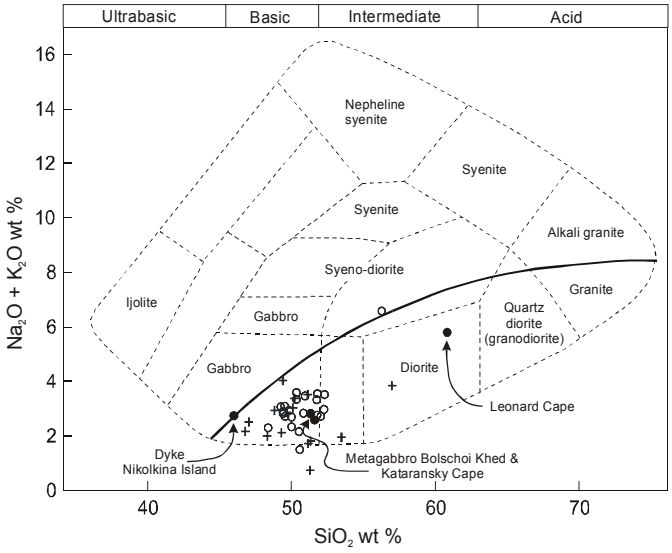

Fig. 2.8. TAS diagram (Cox *et al.* 1979, Wilson 1989) for mafic rock types of the Kolvitsa complex (circles). For comparison also mafic rocks from the Por'ya Guba complex are shown (crosses). The line dividing alkalic and sub-alkalic magma series is from Miyashiro (1978).

In the AFM diagram the mafic dykes define a tholeiitic fractionation trend with iron enrichment in the early stages of differentiation (Fig. 2.9). Dykes containing large plagioclase phenocrysts (Kochinny Cape) fall into the field of calc-alkaline series. This might rather reflect the irregular distribution of plagioclase than a calc-alkaline differentiation trend. This interpretation is supported by studies of porphyritic dyke swarms of the Kochinny Cape area (Balagansky *et al.*, 2001). For comparison, also metagabbros are shown. Because of their cumulate nature, these rocks obviously do not document a tholeiitic differentiation trend. The metadiorites from Leonard Cape plot in the calc-alkaline field. The presence of amphibole and altered plagioclase (sericitisation) points to reaction with metamorphic fluids. In the course of hydrous alteration, elements may have been mobilised. Furthermore, low FeO_{tot} and MgO contents (9 – 10 wt%) may cause artificial trends (Butler, 1979; Rollinson, 1993).

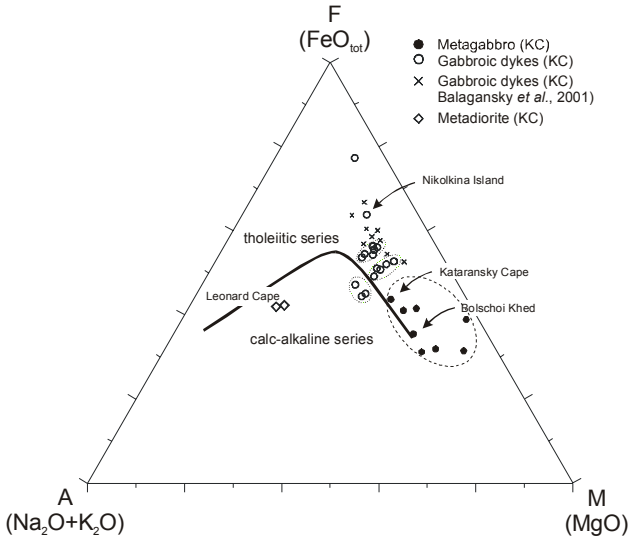

Fig. 2.9. AFM diagram for gabbroic rocks from the Kolvitsa complex and two metadiorites from Leonard Cape. Additionally gabbroic dykes from the Kochinny area (Kolvitsa complex) (Balagansky *et al.*, 2001) are shown.

Mg#-values of basic to ultrabasic rock types [(Mg/(Fe^{2+}+Mg))*100 mol%] are highly sensitive to fractional crystallisation and accumulation of Fe-Mg mineral phases. Mafic melts with Mg#-values between 68 – 75 are considered as 'primitive'. Their parental magmas were presumably in equilibrium with a lherzolitic mantle source (Wilson, 1995). The majority of MORB magmas, however, are characterised by lower Mg#-values (55 – 65), pointing to fractionation after segregation from the mantle source (Wilson, 1995). In figures 2.10a-g, magmatic fractionation and accumulation trends for the dykes and the cumulate-type metagabbros are illustrated. The latter are characterised by higher Mg#-values ranging from 65 to 80 and a positive correlation between Mg# and Ni and Cr which mirrors the modal variation of the cumulate phases ortho- and clinopyroxene in the studied rocks (Fig. 2.10b & d). Contrary to this, the gabbroic and mafic dykes show Mg#-values decreasing from 61 to 45, which reflects the evolution from Mg-rich to Fe-rich rock types, characteristic for a tholeiitic fractionation trend in the early stages of differentiation. Ti, P, K and Zr behaved incompatible during crystallisation and became enriched with decreasing Mg#. The spread in K_2O contents may not only be caused by increased differentiation of the melt but may also indicate mobilisation of potassium during the hydrous metamorphic overprint. The occurrence of abundant ilmenite in the basic dyke from Nikolkina Island complies with the high TiO_2 content (*c.* 2 wt%). Negative correlation between TiO_2 and Mg#, while SiO_2 contents remain constant, is also characteristic of a tholeiitic differentiation.
Ni and Cr behave compatible during crystallisation (Fig. 2.10b & d & h). The Ni content was presumably controlled by fractionation (dykes) or accumulation (metagabbros) of clinopyroxene and orthopyroxene. In the dykes, magmatic differentiation is caused by Cpx and Opx fractionation and documented by decreasing Ni contents and Mg#-values. In the gabbros, accumulation of ortho- and clinopyroxene caused a conspicuous increase of Cr (150 to 900 ppm) and Ni contents (100 to 400 ppm).
A similar trend is documented by the change of the CaO content with Mg-value (Fig. 2.10e). Cumulate-type metagabbros evolved by orthopyroxene and clinopyroxene accumulation. Dominant orthopyroxene accumulation is reflected by decreasing CaO contents with decreasing Mg#, whereas accumulation of clinopyroxene resulted in increased CaO contents and Mg#. In the dykes, clinopyroxene and plagioclase fractionation was important as documented in a positive correlation between CaO content and Mg#.
Since the Al_2O_3 contents show no marked variation with Mg#, plagioclase is an important phase in both, the dykes and the cumulate-type gabbros (Fig. 2.10g).

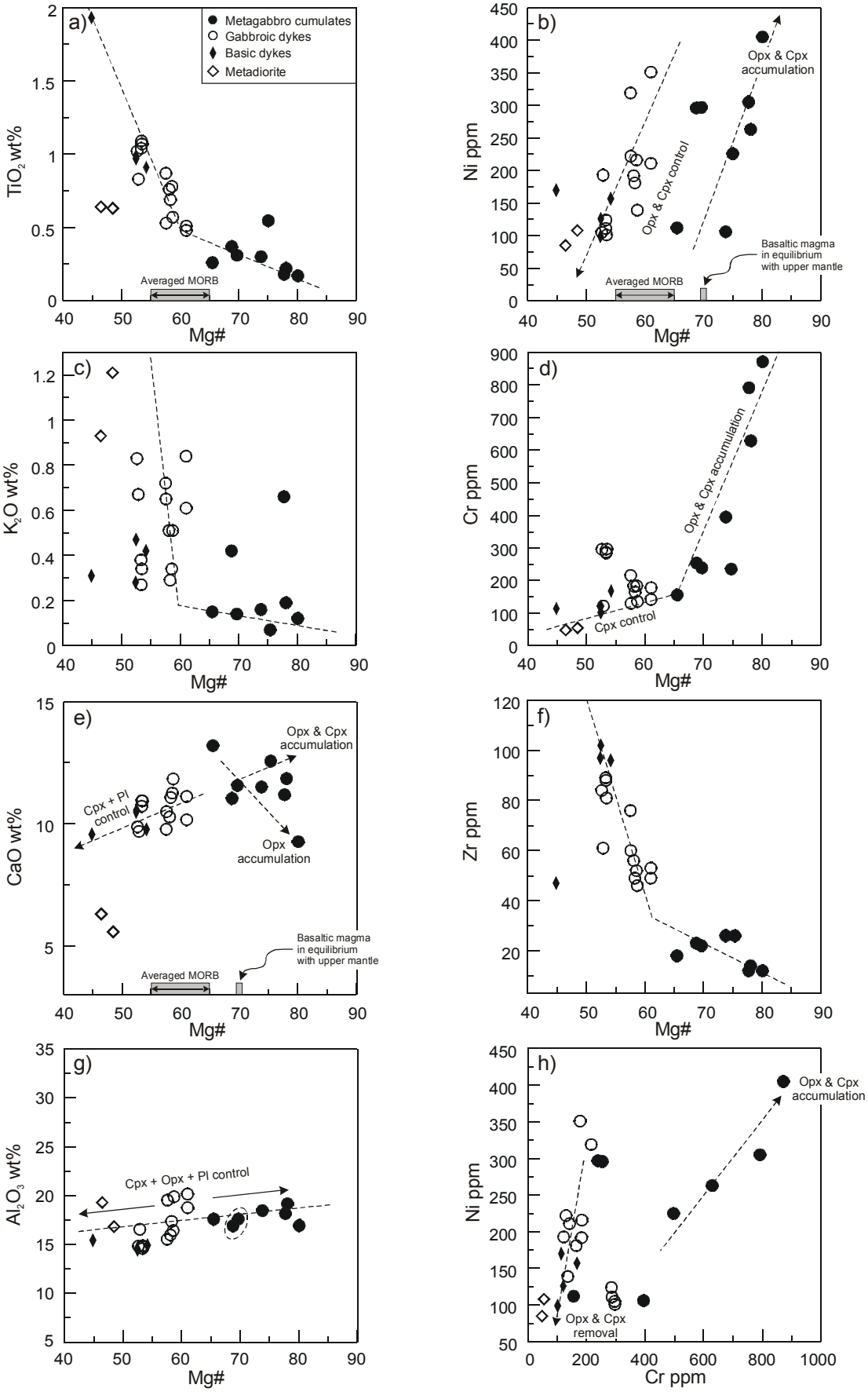

Fig. 2.10a-h. a-g) Variation diagrams of major oxides and trace elements versus Mg# for gabbroic and basic rock types of the Kolvitsa Complex. **h)** Variation of Ni (ppm) versus Cr (ppm) for gabbroic and basic rock types of the Kolvitsa Complex. Mg-values for average MORB magmas and primary basaltic magmas in equilibrium with the upper mantle are from Wilson (1995) and Wilkinson (1982).

Table 2.1. Representative XRF analyses of mafic rock types of the Kolvitsa complex. Oxides in wt%; elements in ppm. Fe_2O_3 content was estimated, assuming a Fe_2O_3/FeO ratio of 0.15. Density in g/cm^3.

Locality	Bolschoi Khed		Kataransky Cape		Chernobayekha/Kochinny Cape												
Rock type	gabbro				gabbroic dykes												
Sample	0708-2	0708-3	1008-B3	0308-2	P-16	P-17	P-18	P-15	P3a	P3b	P4a	0808-B1	0808-B2	0808-B3	0808-B4	0808-B5	0808-B6
density	n.d.	3.05	2.98	n.d.	n.d.	n.d.	n.d.	n.d.	n.d.	n.d.	n.d.	n.d.	n.d.	n.d.	n.d.	n.d.	n.d.
SiO_2	46.92	51.00	50.66	49.99	49.91	50.11	48.03	48.12	51.79	49.44	51.14	48.55	48.46	47.42	48.18	49.36	49.68
TiO_2	0.54	0.30	0.26	0.17	0.22	0.31	0.37	0.18	0.51	0.48	0.53	0.57	0.69	0.78	0.76	1.09	1.04
Al_2O_3	9.28	18.46	17.59	16.92	19.17	17.59	16.90	18.15	18.76	20.15	19.53	19.87	17.36	16.42	15.96	14.85	14.58
Fe_2O_3	1.41	0.82	0.93	0.91	0.73	1.11	1.13	0.79	1.03	0.98	1.03	1.11	1.34	1.51	1.48	1.62	1.55
FeO	9.42	5.49	6.22	6.07	4.85	7.41	7.52	5.24	6.87	6.50	6.89	7.38	8.94	10.05	9.87	10.79	10.35
MnO	0.15	0.11	0.14	0.12	0.10	0.14	0.14	0.11	0.13	0.12	0.13	0.14	0.17	0.18	0.18	0.20	0.19
MgO	16.17	8.68	6.62	13.69	9.69	9.55	9.30	10.26	6.04	5.71	5.25	5.89	7.01	7.97	7.68	6.93	6.64
CaO	12.56	11.50	13.19	9.26	11.84	11.56	11.03	11.18	10.16	11.11	10.49	11.83	11.07	11.25	10.27	10.94	10.71
Na_2O	0.57	2.61	2.40	1.36	1.94	2.20	2.57	2.34	2.88	2.69	2.86	2.27	2.55	1.91	2.14	2.39	2.39
K_2O	0.07	0.16	0.15	0.12	0.19	0.14	0.42	0.66	0.61	0.84	0.65	0.51	0.29	0.34	0.51	0.27	0.38
P_2O_5	0.01	0.01	0.01	0.01	0.01	0.01	0.01	0.01	0.03	0.04	0.05	0.04	0.05	0.06	0.06	0.12	0.11
SO_3	0.37	0.05	0.01	0.05	0.02	0.01	0.01	0.01	0.06	0.06	0.06	0.01	0.01	0.01	0.01	0.01	0.01
Mg#	75.4	73.8	65.5	80.1	78.1	69.7	68.8	77.7	61.0	61.0	57.6	58.7	58.3	58.6	58.1	53.4	53.3
Cr	521	383	154	872	629	239	254	792	178	142	130	217	132	226	161	285	287
Ni	225	98	109	405	263	297	296	305	351	211	222	127	149	204	177	124	111
Sc	45	35	41	17	25	30	30	6	21	15	20	27	20	32	24	44	43
V	348	249	305	104	108	146	164	89	137	130	131	212	265	300	337	247	240
Zn	89	48	52	48	35	57	62	38	70	66	65	63	71	97	99	102	101
Cu	136	45	53	77	30	97	82	26	111	94	97	88	110	108	97	208	161
Rb	3	1	1	6	8	4	12	32	21	33	21	17	6	9	16	4	9
Ba	63	136	97	63	96	76	29	98	128	186	161	192	99	98	140	108	160
Sr	119	324	249	177	223	238	213	190	209	227	225	206	195	152	179	180	195
Zr	26	26	18	12	14	22	23	12	53	49	60	46	49	52	56	88	89
Y	10	11	9	2	2	11	12	7	15	12	15	13	15	19	18	23	21
La	6	5	2	6	29	12	7	11	5	5	15	4	5	6	6	26	5
Ce	20	11	4	47	23	6	11	6	36	6	6	10	11	15	14	24	26
Σ	*97.66*	*99.38*	*98.27*	*98.89*	*98.84*	*100.27*	*97.57*	*97.20*	*99.08*	*98.26*	*98.80*	*98.30*	*98.11*	*98.06*	*97.26*	*98.77*	*97.80*

Table 2.1 continued Representative XRF analyses of mafic rock types of the Kolvitsa complex. Oxides in wt%; elements in ppm. Fe_2O_3 content was estimated, assuming a Fe_2O_3/FeO ratio of 0.15. Density in g/cm^3.

Locality	Chernobayekha/Kochinny Cape				Nikolkina Island					Leonard Cape	
Rock type	gabbroic dyke				mafic dyke					diorite	
Sample	0808-B7	0808-B8	0808-10	0808-11b	0308-K1	0308-12	0308-13	P5	0308-15	0808-1	0808-4
density	n.d.	n.d.	n.d.	n.d.	3.10	n.d.	n.d.	n.d.	n.d.	2.87	2.87
SiO_2	49.93	49.09	50.82	49.86	45.66	51.66	51.39	41.00	51.33	55.58	59.44
TiO_2	1.02	1.07	0.83	0.87	1.93	0.91	0.97	3.24	0.99	0.64	0.63
Al_2O_3	14.82	14.77	16.55	15.53	15.42	14.92	14.44	13.36	14.57	19.29	16.81
Fe_2O_3	1.57	1.61	1.40	1.51	2.18	1.51	1.55	2.96	1.57	0.92	0.83
FeO	10.47	10.73	9.34	10.06	14.50	10.05	10.31	19.74	10.45	6.12	5.51
MnO	0.15	0.21	0.18	0.21	0.22	0.18	0.20	0.41	0.20	0.17	0.11
MgO	6.53	6.92	5.88	7.65	6.62	6.67	6.39	4.76	6.46	2.98	2.91
CaO	9.87	10.93	9.68	9.77	9.56	9.77	10.55	9.97	10.47	6.30	5.57
Na_2O	2.57	2.55	2.60	2.59	2.39	2.52	2.22	1.14	2.46	5.72	4.48
K_2O	0.83	0.34	0.67	0.72	0.31	0.42	0.47	0.65	0.28	0.93	1.21
P_2O_5	0.11	0.11	0.11	0.08	0.33	0.09	0.12	0.46	0.11	0.16	0.14
SO_3	0.01	0.01	0.02	0.04	0.05	0.05	0.06	0.20	0.06	0.05	0.01
Mg#	52.6	53.5	52.9	57.5	44.9	54.2	52.5	30.1	52.4	46.5	48.5
Cr	296	297	122	216	138	168	121	67	102	48	55
Ni	105	101	193	319	231	157	126	161	99	85	108
Sc	29	33	35	31	48	32	42	34	37	15	24
V	231	251	172	227	449	224	248	383	260	69	67
Zn	137	97	99	93	233	100	91	210	101	63	79
Cu	243	264	133	127	277	67	126	368	137	28	49
Rb	15	6	24	23	9	12	6	17	6	27	50
Ba	175	94	240	132	333	148	103	112	150	163	209
Sr	144	153	194	143	343	183	178	65	176	313	259
Zr	84	81	61	76	47	96	102	365	97	279	129
Y	27	26	16	21	35	22	21	77	24	37	26
La	38	28	36	23	14	5	5	32	16	21	8
Ce	6	46	6	55	34	18	65	119	24	71	18
Σ	*98.06*	*98.57*	*98.26*	*99.10*	*99.35*	*98.91*	*98.82*	*98.16*	*99.19*	*99.04*	*97.79*

REE concentrations of the metagabbros and gabbroic dykes are low (5 – 20 × chondrite). Only the basic dyke from Nikolkina Island shows conspicuous elevated REE concentrations up to 40 × chondrite which point to a derivation from a more differentiated magma. REE behave incompatible during fractional crystallisation of mafic melts and are enriched with decreasing Mg#. The vertical spread of the REE patterns in the dykes reflects the degree of magmatic differentiation (Fig. 2.11), whereas elevated REE concentrations in metagabbros should rather reflect relative enrichment of the accumulated mineral phases e.g. plagioclase, pyroxene. Positive Eu anomalies were caused by accumulation of plagioclase, consistent with the cumulate character of the intrusions of the Kolvitsa complex.

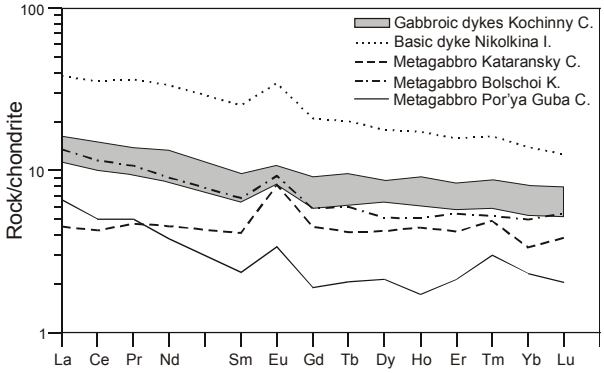

Fig. 2.11. Chondrite-normalised REE patterns of gabbroic and basic rock types of the Kolvitsa Complex. Shown for comparison is a metagabbro from the Por'ya Guba Complex. The normalizing values are those of Taylor & McLennan (1985).

If the degree of partial melting in the mantle was high enough (>10%), the REE of the gabbroic intrusions and dykes should reflect characteristics of their mantle source. Otherwise it should be taken into account that accumulation or removal of mineral phases may also affect the REE patterns of cumulate systems. The REE patterns of gabbros and dykes are flat and show a slight decrease from LREE to HREE. Typical N-type MORB derived from a depleted mantle source, on the other hand, are characterised by unfractionated HREE patterns, but are depleted in LREE. Elevated LREE concentrations point to a derivation of the magma from mantle sources enriched in LREE (plume or an enriched mantle source) or to crustal contamination. Element ratios, such as $(La/Sm)_N$, La/Ce and La/Nb provide information on possible crustal contamination or mantle sources. The $(La/Sm)_N$ ratios range from 1.2 to 2 and correspond to ratios for primordial mantle or P-type MORB ($(La/Sm)_N$ >1). La/Ce ratios are in the range of 0.4 – 0.5. High La/Nb ratios between 2.4 – 9 may point to crustal contamination (Thompson *et al.*, 1984; Wilson, 1995).

Mantle-normalised and MORB-normalised spider diagrams give further information on the petrogenesis of the gabbros (Fig. 2.12 & 2.13). The patterns are characterised by marked Th, U, Nb, P and Hf troughs, which are most conspicuous in the high Mg# (65 – 75) gabbros from Kataransky Cape and Bolschoi Khed. These rocks show also a minor trough for Ti in the primordial mantle-normalised trace element patterns (Fig. 2.12). Enrichment of LIL elements caused positive Ba , K, Pb and Sr spikes. Because of the mobility of these element during hydrous metamorphism, conclusions about the source or possible contaminations are questionable.

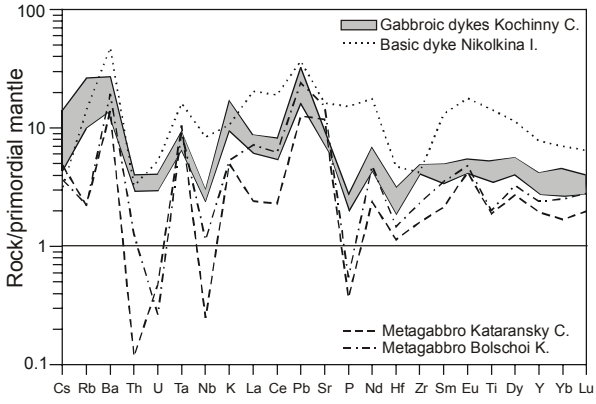

Fig. 2.12. Mantle-normalised trace element diagram for gabbroic and basic rock types of the Kolvitsa Complex. Normalisation values are those of Sun & McDonough (1989).

Assuming a mantle plume or an enriched mantle source for the basaltic magmas, trace element abundances of gabbros and dykes were compared to P- and N-type MORB. Compared to N-type MORB, the gabbros and dykes are enriched in LIL elements. With regard to P-type MORB only positive Ba spikes are conspicuous. Th, Nb, P and minor Hf troughs are distinctive in both MORB-normalised trace element patterns (Fig. 2.13a & b). Depletion of Nb, Th and P may be attributed to contamination by lower crustal material, characterised by low contents of these elements. Alternatively, residual Nb-, Th- and P-bearing phases in the mantle source would also account for the observed negative anomalies. Likely mineral phases are phlogopite (Nb, Ta), amphibole (Ta, Nb), Apatite (Th, P) or Fe-Ti-oxides. Old lithospheric mantle, once modified through subduction processes, is also enriched in LIL and depleted in HFS elements (Wilson, 1995). Magmas derived from such a mantle may therefore also be characterised by negative HFSE anomalies and may occur also in subcontinental intra-plate settings.

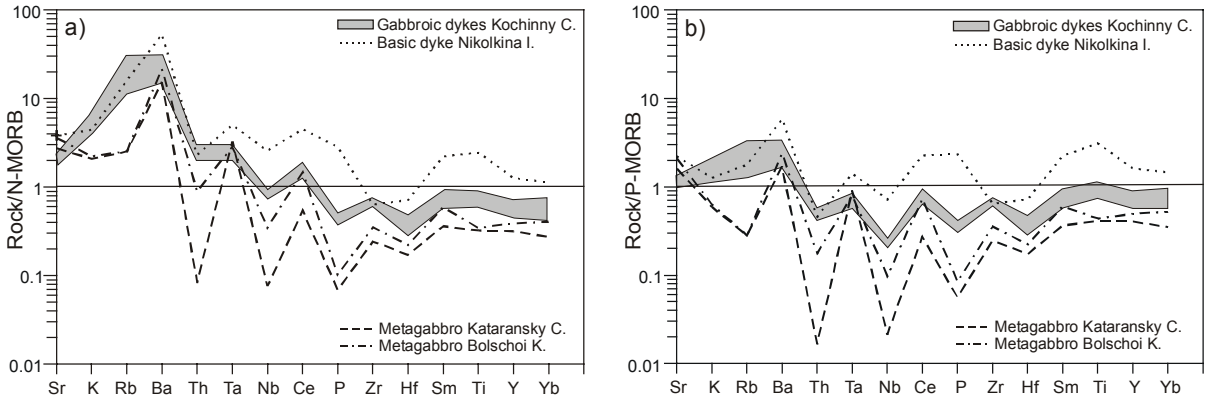

Fig. 2.13a-b. N-MORB- and P-MORB-normalised trace element patterns for gabbroic and basic rock types of the Kolvitsa Complex. Normalising values are those of Sun & McDonough (1989).

Derivation of the magma from a mantle plume or an enriched mantle source alone does not account for the observed negative anomalies, especially of Nb. Mixing of these sources with crustal contamination or an old subcontinental lithospheric mantle may cause the observed trace element patterns. In the geological context, the evolution of the Lapland-Kola Orogen complex is initiated by intracratonic rifting of the Archaean crust *c.* 2.5 – 2.4 Ga ago (Barbey & Raith, 1990; Bridgwater *et al.,* 1995; Amelin *et al.,* 1996). Progression of rifting led to the formation of the layered mafic intrusions and several dyke generations of the Kolvitsa complex. Field observations and structural data (Balagansky *et al.*, 2001) together with the prevailing regional stress field *c.* 2.45 Ga ago, indicate an extensional setting during multiple injection of the dykes. Interpreting the observed geochemical signatures in the geodynamic context, magmas of the gabbro-anorthosite complex presumably reflect an initial stage of rifting and magmas were derived from a plume-type source which either was modified by mixing with lithospheric mantle or contaminated by continental crust.

Table 2.2. Trace element analyses (ICP-MS) for mafic protoliths of the Kolvitsa complex (in ppm). Sample 0208-11 from Maly Khed belongs to the Por'ya Guba complex.

Locality	Kataransky	Bolschoi	Chernobayekha				Nikolkina	Maly Khed
Rock type	gabbro		gabbroic dyke				mafic dyke	gabbro
Samples	1008-B3	0708-3	0808-B1	0808-B2	0808-B3	0808-B4	0308-K-1	0208-11
Li	7.35	4.74	8.19	6.79	9.59	17.79	11.77	10.46
Be	0.21	0.31	0.24	0.42	0.68	0.41	1.00	0.20
Sc	40.69	34.85	25.62	30.15	39.28	37.55	47.96	29.87
V	305	249	212	265	300	337	449	163
Cr	154	383	217	132	226	161	138	345
Ni	109	97	127	149	204	177	231	171
Ga	20.58	17.54	17.49	17.28	20.95	20.53	36.39	13.36
Rb	1.41	1.42	16.71	6.29	8.75	16.16	8.96	7.58
Sr	249.20	323.78	205.64	195.12	152.40	178.79	343.02	326.55
Y	8.86	10.91	12.52	15.13	19.49	18.31	35.33	4.36
Zr	18.00	26.00	46.00	49.00	52.00	56.00	47.00	17.00
Nb	0.18	0.81	1.68	1.91	1.97	2.10	5.98	0.12
Cs	0.16	0.12	0.44	0.14	0.23	0.32	0.10	0.51
Ba	96.77	135.85	191.69	98.88	98.41	139.65	333.17	131.10
La	1.65	4.95	4.13	4.87	5.95	5.80	14.05	2.43
Ce	4.08	11.04	9.57	11.43	14.50	14.14	33.85	4.81
Pr	0.64	1.46	1.28	1.60	2.00	1.89	4.99	0.69
Nd	3.22	6.44	5.98	7.42	8.86	9.51	23.83	2.70
Sm	0.95	1.56	1.49	2.00	2.50	2.22	5.81	0.54
Eu	0.71	0.81	0.72	0.76	0.89	0.93	3.00	0.29
Gd	1.37	1.78	1.79	2.23	3.08	2.78	6.39	0.58
Tb	0.24	0.34	0.36	0.42	0.59	0.56	1.17	0.12
Dy	1.61	1.95	2.43	2.66	3.40	3.28	6.77	0.81
Ho	0.38	0.43	0.52	0.60	0.81	0.78	1.48	0.15
Er	1.05	1.35	1.42	1.82	2.56	2.05	3.92	0.53
Tm	0.17	0.19	0.21	0.27	0.34	0.31	0.58	0.11
Yb	0.83	1.24	1.32	1.74	2.26	2.02	3.46	0.58
Lu	0.15	0.21	0.20	0.26	0.29	0.30	0.48	0.08
Hf	0.35	0.45	0.57	0.63	0.96	0.79	1.47	0.18
Ta	0.43	0.38	0.27	0.39	0.31	0.32	0.66	0.09
Pb	2.34	4.44	3.81	5.30	2.96	6.09	6.82	2.85
Th	0.01	0.11	0.28	0.34	0.34	0.25	0.28	0.04
U	0.01	0.01	0.06	0.09	0.09	0.07	0.11	0.01

2.4.3 Geochemical characterisation of the hydration zones

Fluid infiltration is often accompanied by element transfer, causing conspicuous changes in whole rock chemistry. A comparison of major and trace element data from the protoliths and their hydration zones reveals element mobility. Except for hydration zones from Bolschoi Khed Island, the protoliths and their hydrated equivalents show similar Al_2O_3 contents indicating an immobile behaviour of this element. Element mobility, therefore may be qualitatively assessed using Al_2O_3 as reference, as shown in Figure 2.14a-k. The inset shows that immobile elements plot along a line connecting the origin of the binary diagram with the protolith composition. Residual enrichment or depletion of immobile elements in the altered sample, are then caused by net volume loss and net volume gain, respectively. Mobile elements plot above or below the line, indicating mass gain or mass loss, respectively.

Hydration zones in metadiorites from Leonard Cape are characterised by an enrichment of MgO, FeO_{tot}, TiO_2, CaO and Zr and a minor volume gain, consistent with the increased modal abundance of titanite and zircon in the hydration zones. SiO_2, Na_2O and Sr concentrations, on the other hand, indicate mass loss of these elements and minor volume gain. Hydration zones in metagabbroic rocks from Kataransky Cape and Nikolkina Island are characterised by complementary enrichment and depletion patterns for SiO_2, MgO, FeO_{tot} and TiO_2 concentrations between the outer and central parts of the hydration zones. Variations of Cr, Ni, Sr and CaO (Kataransky Cape) concentrations show a mass loss of these elements for the entire hydration zones. At both localities, hydration zones document addition of K_2O. A significant gain of Zr in the hydration zones from Nikolkina Island is reflected by the modal enrichment of zircon.

At Bolschoi Khed, the metagabbro and related hydration zones show a positive correlation between SiO_2 and Al_2O_3 concentrations. Assuming immobility of Al, this correlation points to a mass gain of SiO_2 associated with a volume gain. Compared with other hydration zones, a significant volume gain coupled with increasing SiO_2 concentrations seems improbable. In this case, both Al and Si, are regarded as slightly mobile. However, element patterns indicate mass gains for FeO_{tot}, MgO, TiO_2, K_2O, Cr and Ni in the hydration zones.

Elements considered to behave relatively immobile during hydrous alteration and deformation are Al, Ti, Zr, Nb, Y, Cr and Ni (e.g. Grant, 1986; Dipple *et al.*, 1990; Selverstone *et al.*, 1991; Dipple & Ferry, 1992; Marquer & Burkhard, 1992; Streit & Cox, 1998; Cartwright & Barnicoat, 2003). In the studied hydration zones, however, element correlations (Figure 2.13 c, i, j & k), indicate mobility of Ti, Cr, Ni and Zr. The enrichment of Ti and Zr concentrations is mirrored by the higher modal abundances of titanite and zircon, respectively. Titanite may also incorporate HFS elements (especially Ta, Nb, U, Th, Y) and REE, which are regarded as relative immobile. REE, Th, U, Y and Hf may reside also in zircon. Especially Hf is considered as a good proxy for zircon (Condie & Sinah, 1996) and shows an increase with advanced hydration (Nikolkina Island, Leonard Cape). Nb and Y concentrations increase in the hydration zones. Changes in element ratios of Y/Nb, Zr/Nb and Zr/Y across the hydration zone point to the mobility of these elements.

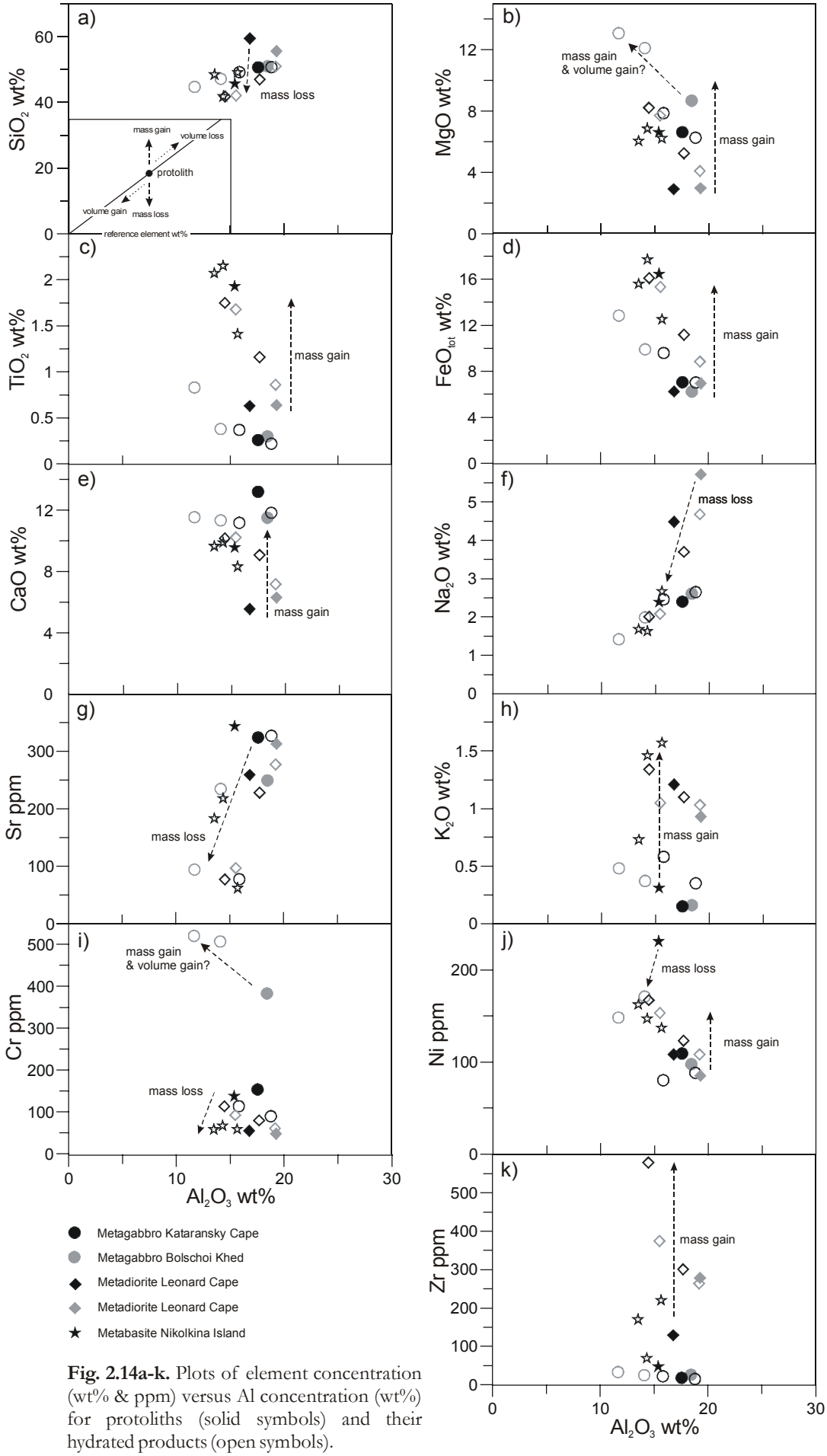

Fig. 2.14a-k. Plots of element concentration (wt% & ppm) versus Al concentration (wt%) for protoliths (solid symbols) and their hydrated products (open symbols).

Table 2.3. Represantative major and trace element analyses from hydration zones of the Kolvitsa complex. Fe_2O_3 content was estimated, assuming a Fe_2O_3/FeO ratio of 0.15. Density in g/cm^3.

Locality	Kataransky Cape		Bolschoi Khed		Nikolkina Island			Leonard Cape			
Hydr. z.	zone II	zone III	zone II	zone III	zone II	zone III	zone IV	zone II	zone III	zone II	zone III
Samples	1008-B2	1008-B1	0708-4	0708-5	0308-K2	0308-K4	0308-K3	0808-2	0808-3	0808-5	0808-6
density	3.02	3.08	3.02	3.2	3.17	3.3	3.1	2.9	3.2	2.9	3.2
SiO_2	50.74	49.20	47.17	44.72	48.48	49.09	41.80	50.96	42.12	46.99	41.78
TiO_2	0.22	0.37	0.38	0.83	2.07	1.41	2.15	0.86	1.68	1.16	1.75
Al_2O_3	18.82	15.85	14.12	11.69	13.54	15.69	14.35	19.21	15.53	17.74	14.50
Fe_2O_3	0.93	1.27	1.31	1.70	2.06	1.65	2.34	1.17	2.03	1.48	2.13
FeO	6.19	8.46	8.74	11.31	13.75	11.03	15.61	7.80	13.51	9.85	14.19
MnO	0.13	0.15	0.17	0.19	0.24	0.16	0.20	0.20	0.27	0.19	0.25
MgO	6.26	7.87	12.10	13.07	6.04	6.22	6.85	4.09	7.70	5.25	8.22
CaO	11.82	11.17	11.33	11.53	9.64	8.31	9.89	7.17	10.21	9.07	10.16
Na_2O	2.65	2.46	1.99	1.42	1.68	2.67	1.63	4.68	2.08	3.70	2.01
K_2O	0.35	0.58	0.37	0.48	0.73	1.57	1.46	1.03	1.05	1.10	1.34
P_2O_5	0.01	0.01	0.01	0.05	0.32	0.16	0.30	0.21	0.33	0.25	0.36
SO_3	0.01	0.01	0.03	0.04	0.07	0.03	0.01	0.02	0.06	0.06	0.01
Cr	90	114	508	521	58	67	59	61	93	80	114
Ni	88	80	171	148	162	147	137	108	153	123	167
Sc	26	27	48	47	46	21	48	20	35	21	25
V	195	221	305	458	444	208	435	99	209	122	204
Zn	50	74	84	107	148	126	189	91	173	119	192
Cu	152	50	44	39	249	275	98	76	45	41	40
Rb	5	1	2	2	14	60	44	31	23	30	40
Ba	110	54	101	96	201	467	533	145	152	236	266
Sr	235	94	327	77	183	218	62	277	97	228	77
Zr	15	22	25	33	170	69	220	264	375	301	579
Y	5.64	0.64	16	25	45.23	17.94	54.71	37	74	49	65
La	1.4	0.7	6.5	8.6	25.9	8.2	30.2	28.0	83.0	74.0	86.0
Ce	2.9	2.0	20.0	30.5	61.4	18.8	61.2	64.0	151.0	56.0	167.0
Σ	*98.21*	*97.51*	*97.87*	*97.21*	*98.82*	*98.18*	*96.81*	*97.58*	*96.77*	*97.02*	*96.91*

Chondrite-normalised REE patterns for gabbroic protoliths and related hydration zones show similar element distribution, but differ in the degree of overall depletion and enrichment indicating mobility of the REE (Fig. 2.15a-c). Positive Eu anomalies are characteristic for the protoliths and disappear with increasing degree of hydration. Hydration zones from Bolschoi Khed are enriched in REE, especially in MREE, resulting in a concave pattern (Fig. 2.15a). REE patterns of hydration zones from Kataransky Cape share the flat pattern of their gabbroic protolith, but are depleted in REE (Fig. 2.15b). The basic protolith from Nikolkina Island shows a moderately fractionated pattern (Fig. 2.15c) which is preserved in the hydration zones. Compared to hydration zones II and IV, zone III shows a significant overall depletion. Within this zone garnet is replaced by biotite. The garnet breakdown releases REE. Biotite may incorporate parts of Ti, Fe and Mg but no REE. Titanite or zircon which could act as containers for the released REE are absent in hydration zone III . As a consequence, lateral element transfer via the fluid phase most likely caused the depletion of the REE. Enrichment of titanite and zircon in zones II and IV is consistent with increasing REE and HFS element contents and supports the view that element transfer was mineralogically controlled. In addition, leaching of weakly bounded REE from grain boundaries by infiltrating fluids may also account for the observed element loss.

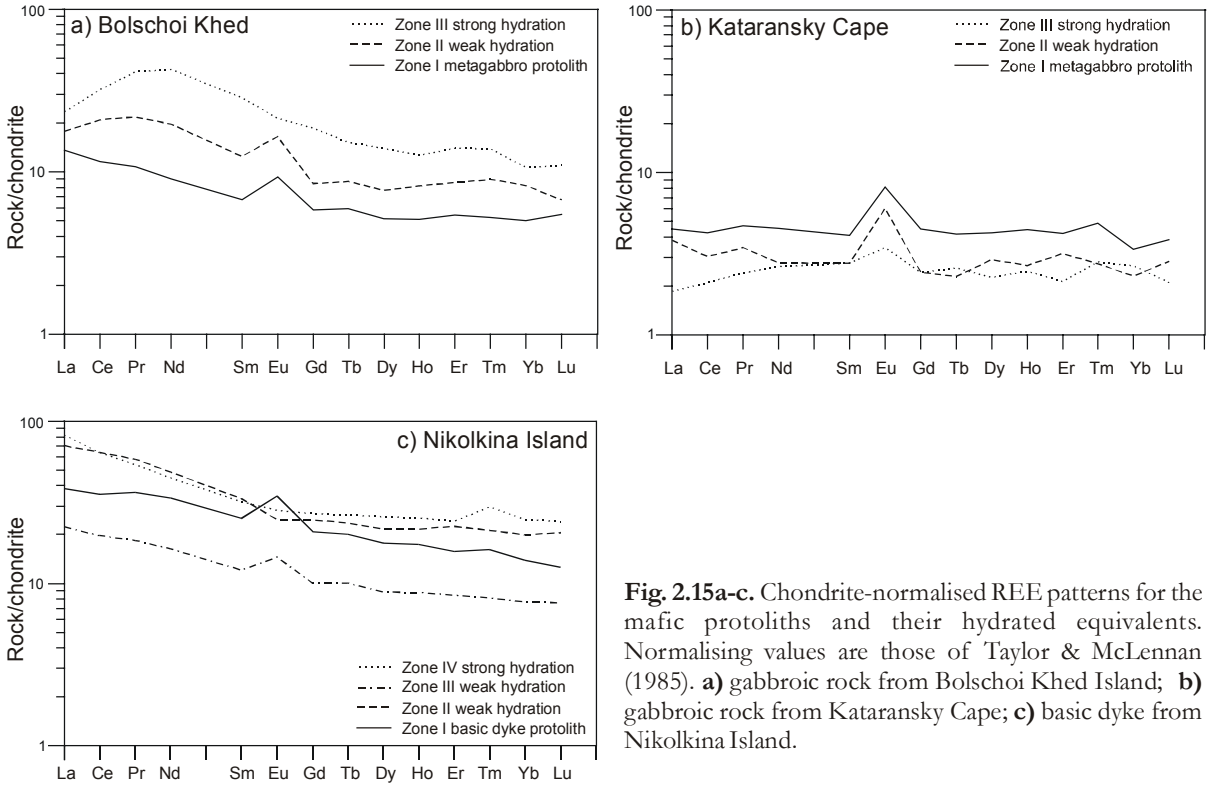

Fig. 2.15a-c. Chondrite-normalised REE patterns for the mafic protoliths and their hydrated equivalents. Normalising values are those of Taylor & McLennan (1985). **a)** gabbroic rock from Bolschoi Khed Island; **b)** gabbroic rock from Kataransky Cape; **c)** basic dyke from Nikolkina Island.

In almost monomineralic amphibole felses (Bolschoi Khed, Kataransky Cape), REE patterns correspond to the REE distribution in amphibole, with enrichment of the MREE and LREE. At Nikolkina Island, the REE are mainly incorporated in titanite (zone II) and close to the centre of fluid infiltration in titanite and zircon (zone IV). The centre of hydration zone shows stronger enrichment in LREE and HREE than in MREE. A pattern which nicely reflects the preferential partitioning of LREE into titanite and of HREE into zircon.

Although Ti, Nb, Y, Zr and REE are commonly regarded as relative immobile, mobilisation of these elements during alteration/metasomatism has been documented by several authors (e.g. Selverstone *et al.*,1991; O'Hara, 1988 & 1990, MacLean, 1988; Kerrich, 1986; van Baalen 1993; Stähle *et al.*, 1987). This study provides further evidence for the mobility of HFS elements and REE during amphibolite facies hydration processes. Mobility is reflected by the modal increase of accessory phases, such as titanite and zircon. *P-T* conditions, fluid composition, fluid flux and fluid pathways appear to be important factors, controlling the distribution of elements (Condie & Sinah, 1996). These factors control the stability of accessory phases, which play an important role as sinks for trace elements.

Table 2.4. Trace element analyses (ICP-MS) for hydration zones of the Kolvitsa complex (in ppm). Sample 0208-12 & 0208-13 from Maly Khed belongs to the Por'ya Guba complex.

Locality	Bolschoi Khed		Kataransky Cape		Nikolkina Island			Maly Khed	
Hydration zone	zoneII	zone III	zoneII	zone III	zoneII	zone III	zone IV	zoneII	zone III
Samples	0708-4	0708-5	1008-B2	1008-B1	0308-K-2	0308-K-4	0308-K-3	0208-12	0208-13
Li	13.69	8.73	4.27	3.62	7.54	22.30	39.37	8.40	14.17
Be	0.51	0.57	0.14	0.27	1.48	0.91	1.56	0.35	0.76
Sc	47.62	46.63	26.50	27.00	46.43	20.86	47.54	28.80	34.07
V	305	458	195	221	444	208	435	148	155
Cr	508	521	90	114	58	67	59	183	238
Ni	171	148	88	80	162	147	137	129	115
Ga	20.52	21.12	18.71	10.56	24.77	20.71	30.49	16.13	20.50
Rb	2.48	1.94	5.08	0.55	14.07	60.02	43.85	6.69	4.33
Sr	326.79	77.49	234.53	94.22	183.39	217.98	61.74	478.09	258.74
Y	16.51	25.92	5.64	5.24	45.23	17.94	54.71	5.39	8.12
Zr	25.00	33.00	15.00	22.00	170.00	69.00	220.00	32.00	21.00
Nb	1.28	2.19	0.15	0.75	8.76	4.99	19.92	0.59	2.10
Cs	0.11	0.02	0.35	0.06	0.09	0.89	0.75	0.58	0.16
Ba	101.35	96.09	109.65	54.19	201.47	466.66	533.26	165.81	158.86
La	6.49	8.58	1.40	0.68	25.86	8.22	30.16	6.72	1.95
Ce	19.99	30.54	2.90	2.01	61.37	18.82	61.18	14.64	5.91
Pr	2.98	5.62	0.47	0.33	7.98	2.52	7.40	1.82	0.95
Nd	13.93	30.20	1.97	0.01	34.53	11.61	31.77	7.58	4.31
Sm	2.86	6.56	0.64	5.83	7.68	2.79	7.36	1.37	1.20
Eu	1.43	1.85	0.52	0.30	1.26	2.45	2.15	0.68	0.57
Gd	2.58	5.67	0.74	0.74	7.53	3.08	8.23	1.14	1.25
Tb	0.50	0.88	0.13	0.15	1.37	0.58	1.53	0.16	0.25
Dy	2.92	5.29	1.11	0.86	3.37	9.77	8.21	1.21	1.56
Ho	0.70	1.07	0.23		1.84	0.75	2.16	0.26	0.32
Er	2.14	3.47	0.79	0.74	5.60	2.11	6.01	0.73	1.04
Tm	0.32	0.49	0.10	0.15	0.76	0.29	1.06	0.08	0.15
Yb	2.04	2.63	0.57	0.66	1.91	6.13	4.92	0.70	0.83
Lu	0.26	0.42	0.11	0.08	0.29	0.92	0.78	0.07	0.12
Hf	0.59	1.52	0.13	0.21	3.07	1.41	3.99	0.20	0.55
Ta	0.23	0.17	0.13	0.15	0.83	0.41	1.45	0.17	0.26
Pb	4.88	2.47	5.29	3.01	5.75	10.59	8.96	4.04	6.69
Th	0.01	0.05	0.05	0.01	2.09	0.57	9.90	0.02	0.11
U	0.01	0.03	0.01	0.01	1.66	0.52	1.68	0.01	0.05

2.4.4 Mass balance

A comparison of chemical compositions of protoliths and hydrated equivalents, reflects only relative compositional changes. For example, dilution effects caused by a volume gain, may falsely suggest element losses. Quantitative estimates of chemical variation requires the knowledge of density and volume changes and the knowledge of elements which behaved immobile during the alteration process (Marquer *et al.*, 1994).
Rock densities were estimated from modal mineralogy and range from 2.9 – 3.1 gcm^{-3} for the protoliths and 3.1 – 3.2 gcm^{-3} for the altered samples (Table 2.1 & 2.3). Mass balance calculations accounting for volume and density changes were developed by Gresens (1967). The absolute gain or loss Xn of a given element n in the altered rock compared to its protolith is given by the linear equation:

$$Xn = fv * (d_a/d_o) * Cn_a - Cn_o, \quad (1)$$

where Cn_o and Cn_a are the concentrations of a given element n in the original protolith (o) and the altered rock (a). d_a/d_o and fv (volume factor v_a/v_o) reflect the density and volume changes between the altered rock and the protolith.
Potdevin & Marquer (1987) modified the equation of Gresens (1967) to express the relative changes in concentration (%):

$$\Delta Xn = [fv * (d_a/d_o) * (Cn_a/Cn_o) - 1] * 100. \quad (2)$$

This method is especially useful to compare the behaviour of major and trace elements in widely differing abundances (Marquer, 1989; Marquer et al., 1994). In composition-volume diagrams (ΔXn vs. fv) elements with the same behaviour define lines through the origin of the diagram which have the same slope. This facilitates the identification of several immobile elements (Potdevin & Marquer, 1987). With the knowledge of immobile elements, the prevailing volume change (fv) and absolute element changes can then be calculated (Fig. 2.16-2.19 & Tab. 2.5).
For the studied hydration zones, an almost immobile behaviour of Al was indicated by the correlations with major and trace elements (Fig. 2.14a-k). In the composition- volume diagrams presented below, Al_2O_3 is therefore considered as a perfectly immobile component. With this assumption, it follows that hydration was nearly isovolumetric (Fig. 2.15-2.17). Hydration processes at Bolschoi Khed Island are an exception, because mass transfer patterns indicate a slightly mobile behaviour of Al_2O_3 (see below).

Kataransky Cape

Hydration of the gabbroic protolith was accompanied by negligible volume changes, i.e. a loss of 8% in the weakly altered front (zone II) and a gain of 5% in the centre (zone III) of the fluid infiltration zone. REE and HFS elements show a mobile behaviour. REE are depleted in the entire hydration zone. SiO_2, FeO_{tot}, MgO and LIL elements together with particular HFS elements (Ti, Nb, Zr) show complementary element distributions in zones II and III, indicating a bilateral mass transfer between the centre and the front of the infiltration zone (Fig. 2.16 & 2.17a). LIL elements are enriched in zone II but depleted near the centre of hydration (zone III). Contrary to the LIL elements, SiO_2, FeO_{tot}, MgO and HFS elements (Ti, Nb, Zr) are depleted in zone II and enriched in the innermost zone III . The central part of the hydration zone is injected by a feldspar dominated felsic vein which explains the increase of alkaline elements in this direction. Absolute changes in concentrations of major and trace elements are given in Figure 2.16a and Table 2.5. The following mass balance equations give the gains and losses for major elements (in grams) with reference to 100g of the gabbroic protolith

$$100g\ protolith - 3.3g SiO_2 - 0.06g TiO_2 - 0.5g FeO - 0.8g MgO - 2.2g CaO - 0.02g MnO + 0.1g Na_2O + 0.2g K_2O = 93.4g\ amphibolite\ zone\ II$$

$$100g\ protolith - 0.8g CaO + 4g SiO_2 + 0.2g TiO_2 + 3.7g FeO + 2.2g MgO + 0.03g MnO + 0.3g Na_2O + 0.5g K_2O = 110.1g\ amphibolite\ zone\ III.$$

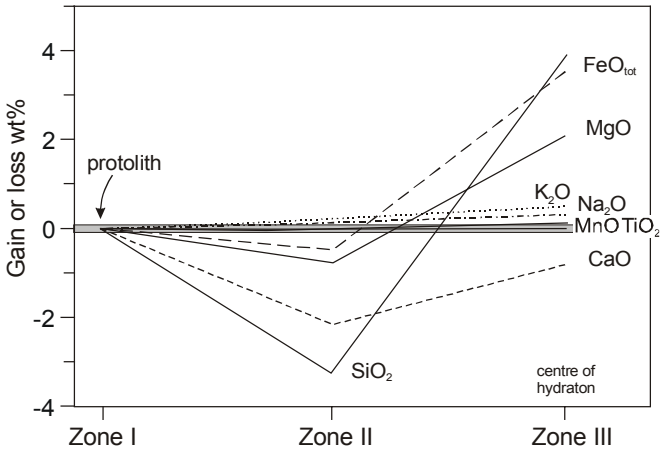

Fig. 2.16. Absolute changes of major elements across the shear zone from Kataransky Cape. Mass balance calculation were performed with the assumption that Al_2O_3 behaved immobile during hydration.

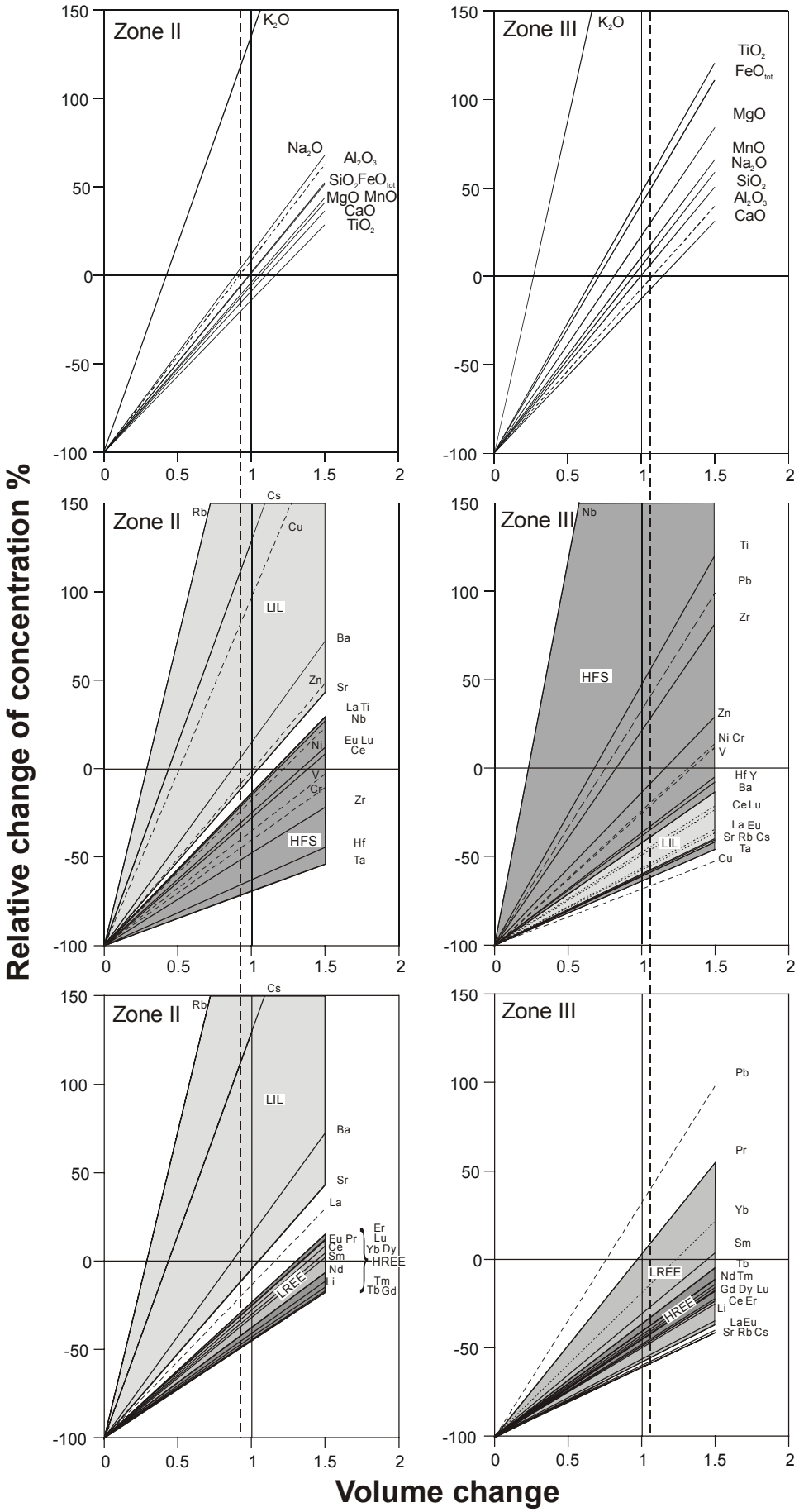

Fig. 2.17. Composition-volume diagrams for different stages of hydration across a shear zone at Kataransky Cape: Zone II weakly hydrated metagabbro; zone III near to the centre of hydration.

Nikolkina Island

The front of the fluid infiltration zone (zone II) is characterised by a slight volume gain (10%), whereas in its inner parts (zones III & IV) no volume changes are obvious . As a first approximation, hydration can be regarded as an isovolumetric process. Due to mobilisation of feldspar material in the centre of the infiltration zone, K_2O and Cs show a consistent increase towards the hydration centre. Hydration zones II– IV document complementary enrichment and depletion patterns (Fig. 2.18 & 2.19b). Beside major elements, complementary distribution patterns are also shown by REE, HFS and LIL elements (Fig. 2.19). The decrease of REE, HFS and femic elements in the hydration zone III is attributed to the breakdown of garnet. The loss of the released elements from zone III is due to the general absence of titanite and zircon which could have acted as sinks. In the innermost hydration zone IV, the nearly monomineralic amphibole fels is characterised by a substantial increase in Zr (190 ppm) consistent with the augmented occurrence of zircon. The following mass balance equations give the gains and losses for major elements (in grams) with reference to 100g of the gabbroic protolith:

$$100g\ protolith - 0.48gNa_2O + 9.7gSiO_2 + 0.4gTiO_2 + 1.3gFeO + 0.3gMgO + 0.1gMnO + 1.4gCaO + 0.5gK_2O = 113.2g\ amphibolite\ zone\ II.$$

$$100g\ protolith - 0.6gTiO_2 - 4.2gFeO - 0.5gMgO - 0.06gMnO - 1.4gCaO + 2.6gSiO_2 + 0.2gNa_2O + 1.3gK_2O = 97.3g\ amphibolite\ zone\ III$$

$$100g\ protolith - 1gSiO_2 - 0.01gMnO - 0.7gNa_2O + 0.4gTiO_2 + 2.5gFeO + 0.7gMgO + 1\ gCaO + 1.3gK_2O = 104.2g\ amphibolite\ zone\ IV.$$

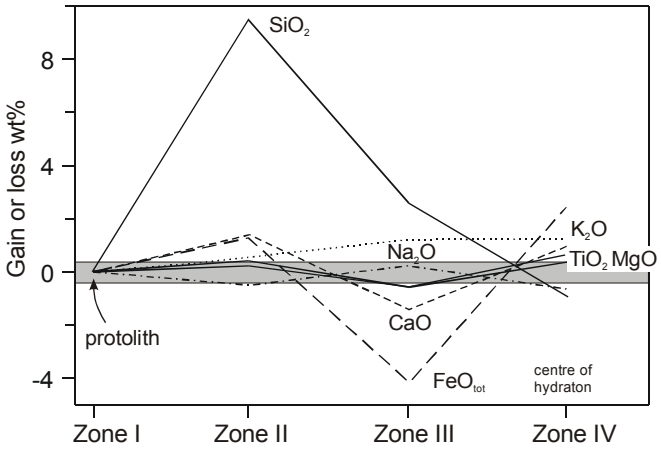

Fig. 2.18. Absolute changes of major elements across the shear zone from Nikolkina Island. Mass balance calculations were performed with the assumption that Al_2O_3 behaved immobile during hydration.

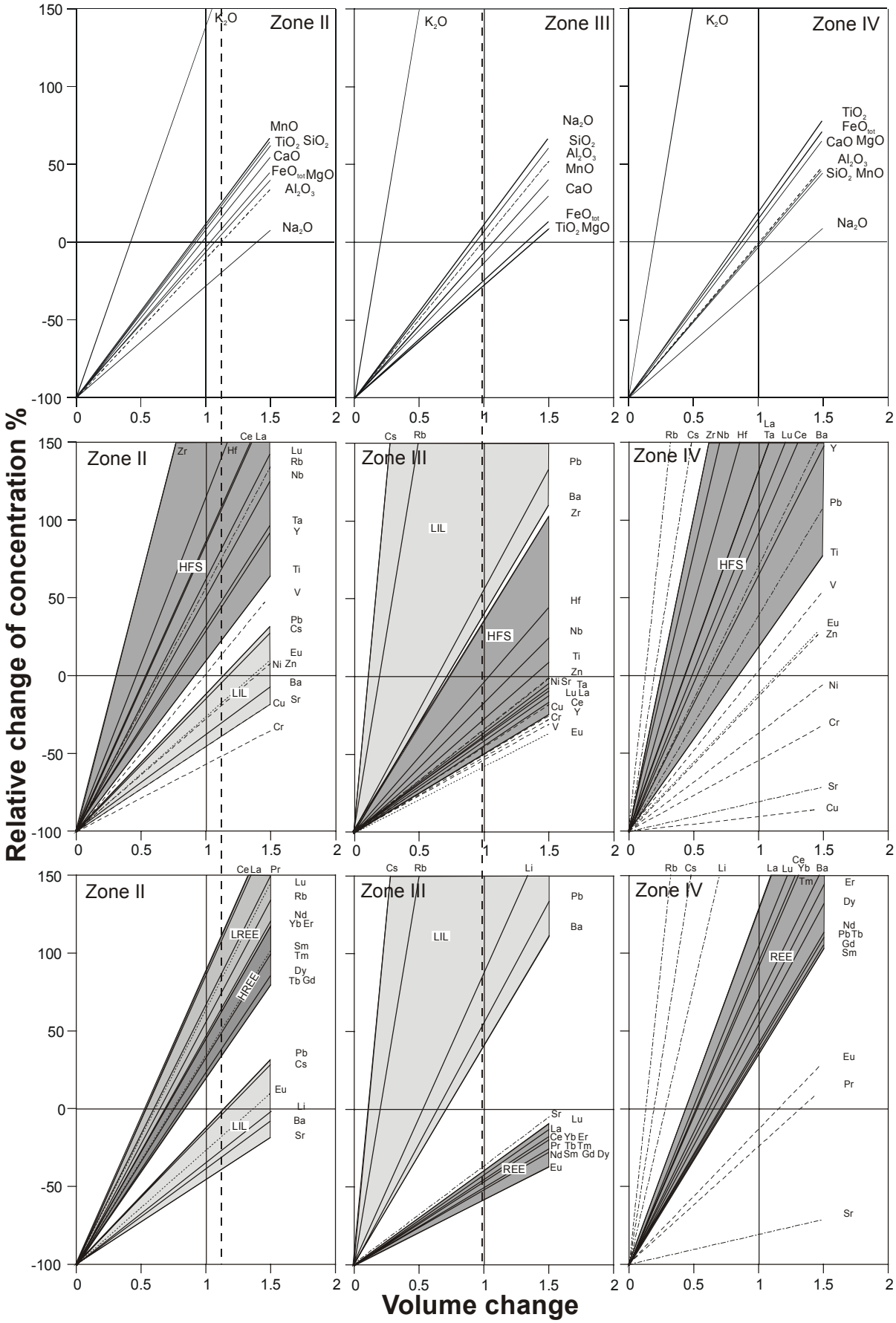

Fig. 2.19. Composition-volume diagrams for different stages of hydration in a basic dyke from Nikolkina Island: Zone II weakly hydrated basic dyke; zone III stronger hydrated basic dyke; zone IV near to the centre of hydration.

Leonard Cape

Assuming immobility of Al, hydration processes in both examples studied did not involve/cause changes in volume (Fig. 2.20 & Tab. 2.5).

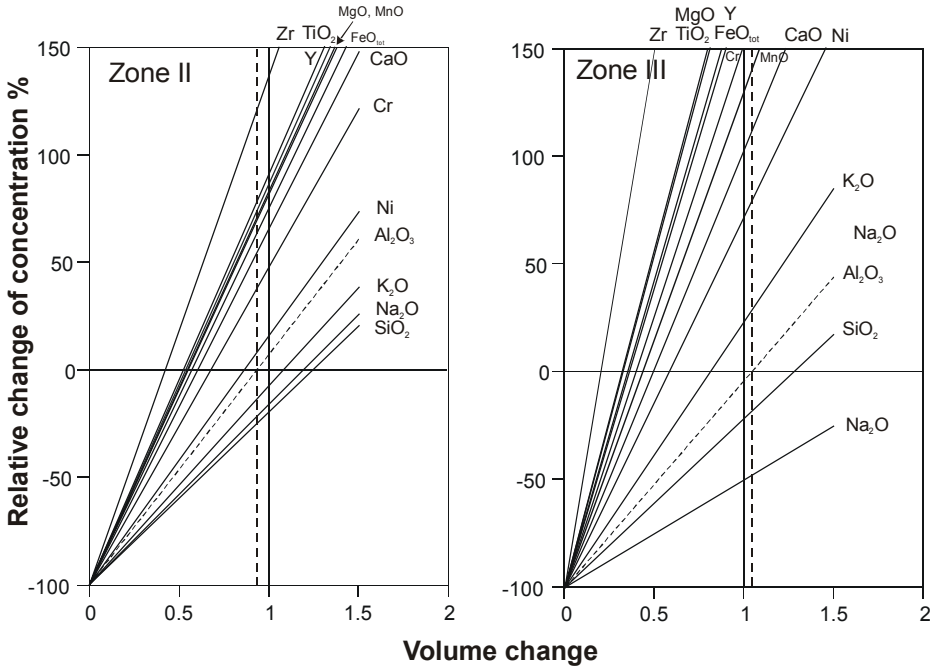

Fig. 2.20. Composition-volume diagrams for different stages of hydration from Leonard Cape (0808-4 - 0808-6): Zone II weakly hydrated metagabbro; zone III near to the centre of hydration.

Towards the centre of the hydration zones, CaO, MgO, FeO, MnO, Ni and Cr and HFS (Ti, Zr, Y, Nb) elements show a continuous increase. Near to the centre, gains of Zr and TiO_2 up to 540 ppm and 1.4 wt%, respectively, are reflected by increased modal amounts of zircon and titanite. The hydration zones are depleted in SiO_2 and Na_2O (Fig. 2.21a & b). The following mass balance equations give the gains and losses for major elements (in grams) with reference to 100g of the gabbroic protolith:

Example 1 (0808-4 to 0808-6)

100g protolith - 15.3 gSiO_2 – 1gNa_2O - 0.2gK_2O + 0.5gTiO_2 + 4.5gFeO + 2.1gMgO + 0.1gMnO + 3.1gCaO = 93.9g amphibolite zone II

100g protolith – 11.3 gSiO_2 – 2.2gNa_2O + 1.4gTiO_2 + 12.7gFeO + 6.8gMgO + 0.2gMnO + 6.4gCaO + 0.4gK_2O = 85.3g amphibolite zone III

&

Example 2 (0808-1 to 0808-3)

100g protolith – 4.5gSiO_2 – 1gNa_2O - 0.1gK_2O + 0.2gTiO_2 + 2gFeO + 1.1gMgO + 0.03gMnO + 0.9gCaO = 98.9g amphibolite zone II

100g protolith – 3.3 gSiO_2 – 3.2gNa_2O + 1.5gTiO_2 + 12.2gFeO + 6.7gMgO + 0.2gMnO + 6.5gCaO + 0.4gK_2O = 121.2g amphibolite zone III.

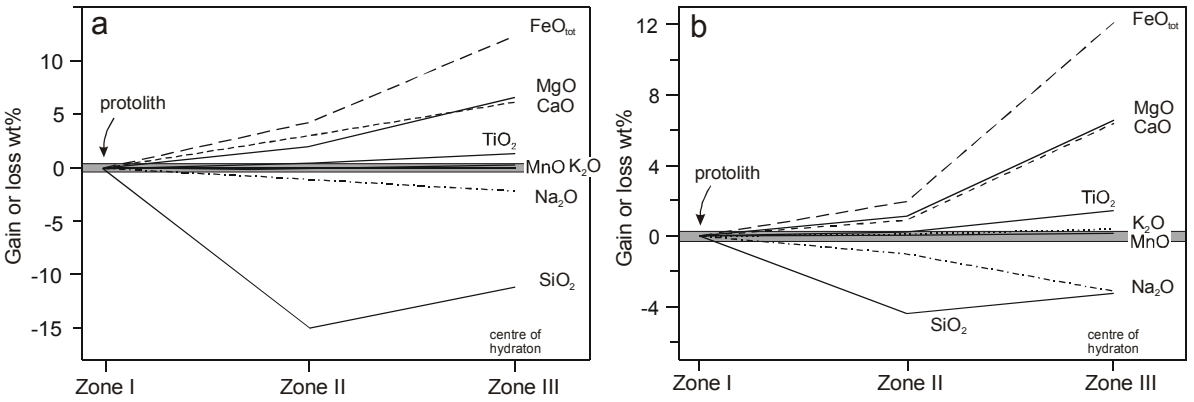

Fig. 2.21. Absolute changes of major elements across hydration zones from Leonard Cape. a) example 1: sample sequence 0808-4 to 0808-6. b) example 2: sample sequence 0808-1 - 0808-3.

Bolschoi Khed

Assuming an immobile behaviour of Al as in the previously discussed cases, the development of hydration zones at this locality would have been accompanied by a dramatic volume increase (up to 50%)(Fig. 2.23 & Tab. 2.5). In this case, beside femic elements also SiO_2 would have been significantly supplied by the infiltrating fluid (up to 20 wt%) (Fig. 2.22a). Since a significant volume increase is not supported by the field observations, it appears more reasonable to consider the hydration process as isovolumetric in accordance with the findings from the other localities. This means that Al_2O_3 behaved slightly mobile during hydration at Bolschoi Khed (Fig. 2.22b), leading to the following mass balance equations for the major elements:

$$100g\ protolith - 4.3\ gSiO_2 - 4.5gAl_2O_3 - 0.3gCaO - 0.6gNa_2O + 0.1gTiO_2 + 3.6gFeO + 3.3gMgO + 0.1gMnO + 0.2gK_2O = 97.5g\ amphibolite\ zone\ II$$

$$100g\ protolith - 3.7\ gSiO_2 - 6.1gAl_2O_3 - 1.1gNa_2O + 0.6gTiO_2 + 7.4gFeO + 5.2gMgO + 0.1gMnO + 0.7gCaO + 0.4gK_2O = 103.5g\ amphibolite\ zone\ III.$$

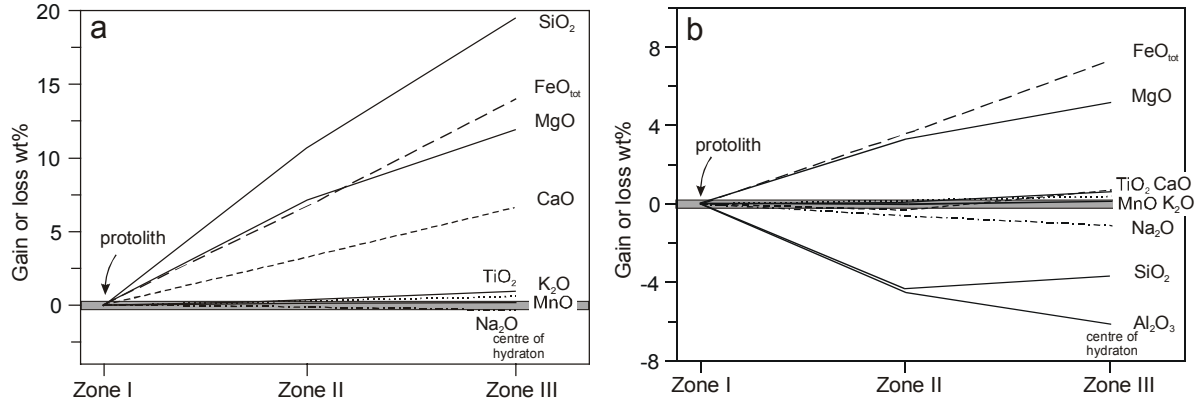

Fig. 2.22. Absolute changes of major elements across hydration zones from Bolschoi Khed Island. a) provided that Al_2O_3 behaved immobile during hydration. b) provided that hydration occurred under isovolumetric conditions.

Close to the centre of hydration, monomineralic amphibole felses (zone III) represent the extreme stage of hydrous alteration. Large amphibole blast with diameters up to 5 mm are chemically unzoned. This indicates high fluid/rock ratios and a complete re-equilibration during hydration. The decrease in Na_2O and Al_2O_3 may be explained by partitioning of these elements into the fluid phase during the breakdown of plagioclase.

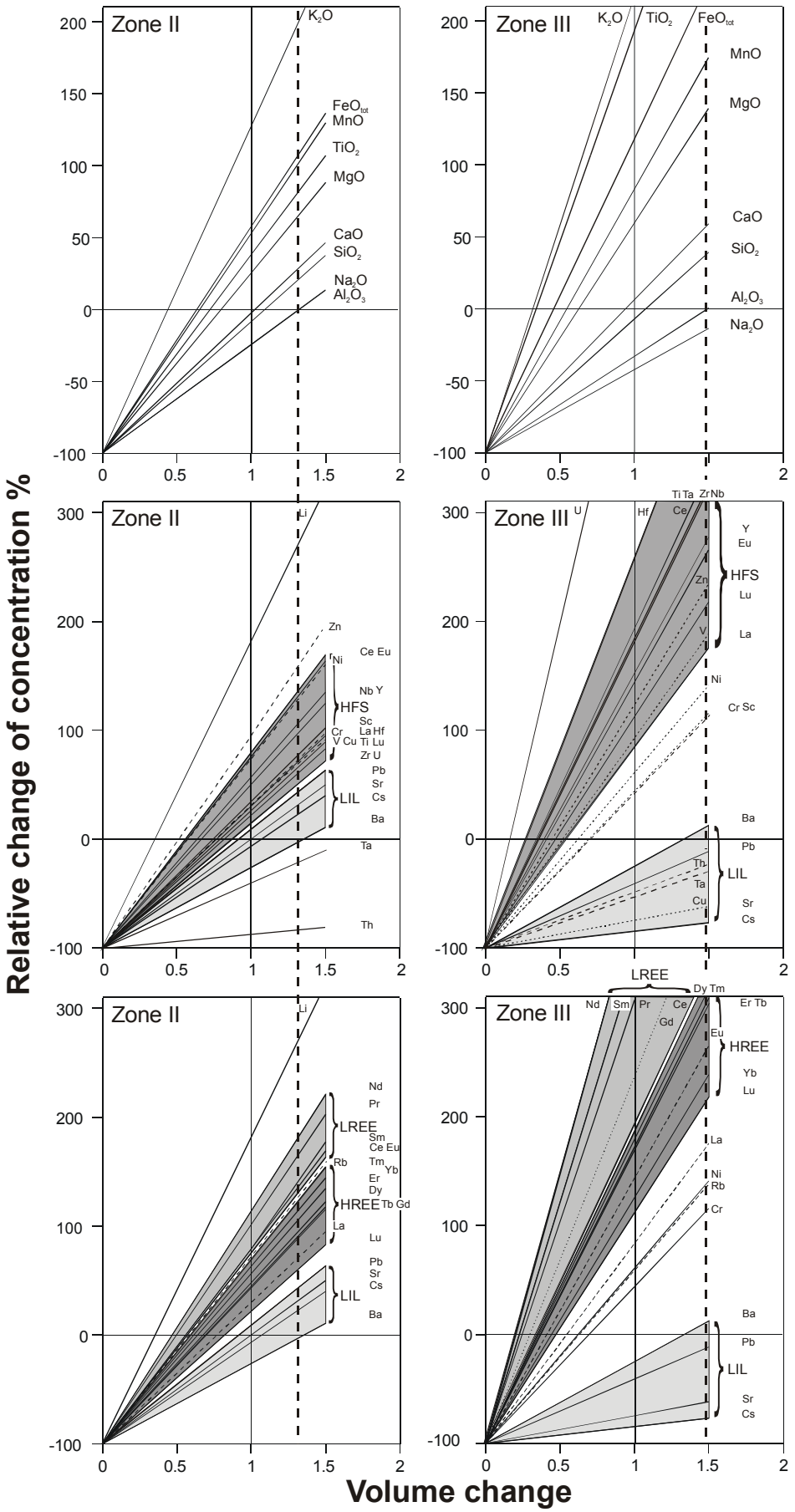

Fig. 2.23. Composition-volume diagrams for different stages of hydration in a metagabbro from Bolschoi Khed: Zone II weakly hydrated metagabbro; zone III near to the centre of hydration.

Table 2.5. Absolute changes of oxide (wt%) and element (ppm) concentrations across hydration zones from the Kolvitsa complex. Volume factors (v. f.) were determined from composition-volumes diagrams. (n.d: not determined)

locality	Kataransky Cape		Bolschoi Khed		Nikolkina Island				Leonard Cape				
Hydr. Z.	zoneII	zone III	zoneII	zone III	zoneII	zone III	zoneII	zone III	zone IV	zoneII	zone III	zoneII	zone III
Sample	1008-B2	1008-B1	0708-4	0708-5	0708-4	0708-5	0308-K-2	0308-K-4	0308-K-3	0808-5	0808-6	0808-2	0808-3
v. f.	**vf 0.92**	**vf 1.05**	**vf 1.32**	**vf 1.49**	**vf 1**	**vf 1**	**vf 1.1**	**vf 0.98**	**vf 1.0**	**vf 0.94**	**vf 1.04**	**vf 0.99**	**vf 1.1**
SiO_2	-3.2	3.9	10.7	19.5	-4.3	-3.6	9.6	2.6	-0.9	*-14.9*	*-11.0*	*-4.4*	*-3.3*
TiO_2	-0.1	0.2	0.2	1.0	0.1	0.6	0.4	-0.5	0.4	*0.5*	*1.4*	*0.2*	*1.4*
Al_2O_3	0.0	0.0	0.0	0.0	-4.5	-6.1	0.0	0.0	-0.1	*0.0*	*0.0*	*0.0*	*0.0*
FeO_{tot}	-0.5	3.6	6.7	14.0	3.6	7.4	1.3	-4.2	2.5	*4.3*	*12.4*	*1.9*	*12.1*
MnO	0.0	0.0	0.1	0.2	0.1	0.1	0.1	-0.1	0.0	*0.1*	*0.2*	*0.0*	*0.2*
MgO	-0.8	2.1	7.1	11.9	3.3	5.2	0.3	-0.5	0.7	*2.1*	*6.6*	*1.1*	*6.6*
CaO	-2.1	-0.8	3.3	6.7	-0.3	0.7	1.4	-1.4	1.0	*3.0*	*6.2*	*0.9*	*6.4*
Na_2O	0.1	0.3	0.0	-0.4	-0.6	-1.1	-0.5	0.2	-0.6	*-1.0*	*-2.1*	*-1.0*	*-3.1*
K_2O	0.2	0.5	0.3	0.6	0.2	0.3	0.5	1.2	1.3	*-0.2*	*0.3*	*0.1*	*0.4*
P_2O_5	0.0	0.0	0.0	0.1	0.0	0.0	0.0	-0.2	0.0	*0.1*	*0.3*	*0.1*	*0.3*
Li	-3.36	-3.33	13.15	9.02	8.81	4.50	-3.18	10.14	30.34	*n. d.*	*n. d.*	*n. d.*	*n. d.*
Sc	-15.92	-10.73	27.41	38.66	12.31	14.53	4.92	-27.46	2.89	*-4.10*	*4.98*	*5.08*	*28.47*
V	-123	-60	149	473	52	236	56	-245	16	*49*	*169*	*30*	*191*
Cr	-69	-27	280	438	119	168	-71	-72	-75	*21*	*77*	*13*	*68*
Ni	-26	-20	126	136	72	59	-46	-86	-84	*9*	*86*	*23*	*105*
Cu	22.19	-18.00	10.46	-9.95	4.08	-11.89	-205.69	-235.05	-468.92	*-10.15*	*-2.63*	*48.32*	*27.89*
Zn	-4.49	-3.48	84.22	115.73	52.06	61.88	-47.38	-82.18	-26.72	*33.75*	*143.59*	*28.38*	*151.88*
Rb	3.34	-0.80	1.81	1.63	1.03	0.63	7.07	50.02	37.94	*-21.57*	*-3.63*	*4.13*	*1.57*
Sr	-29.99	-144.64	103.43	-201.62	-0.21	-241.72	-134.16	-128.79	-276.97	*-42.97*	*-169.73*	*-34.84*	*-192.52*
Y	-3.59	-2.85	10.67	29.95	5.44	16.54	16.18	-17.70	23.19	*20.43*	*49.35*	*0.15*	*54.91*
Zr	-3.98	6.41	6.68	26.02	-1.25	8.95	146.60	20.81	188.34	156.20	542.24	-13.89	186.78
Nb	-0.04	0.66	0.86	2.64	0.46	1.51	4.00	-1.08	15.33	*11.21*	*13.23*	*11.08*	*26.78*
Cs	0.17	-0.09	0.03	-0.09	-0.01	-0.10	0.00	0.77	0.70	*n. d.*	*n. d.*	*n. d.*	*n. d.*
Ba	5.71	-36.63	-3.35	15.63	-35.49	-34.09	-103.72	125.47	237.27	*14.61*	*99.37*	*-17.39*	*25.80*
La	-0.34	-0.90	3.54	8.58	1.48	4.14	15.40	-5.97	18.21	*62.12*	*91.70*	*7.12*	*82.09*
Ce	-1.37	-1.85	15.10	37.11	8.76	21.31	36.03	-15.36	31.59	*35.06*	*175.60*	*-6.73*	*116.56*
Nd	-1.37	-1.14	11.77	41.18	7.35	25.55	15.50	-12.42	10.16	*22.01*	*77.58*	*14.18*	*31.62*
Sm	-0.35	-0.24	2.19	8.79	1.28	5.39	2.93	-3.07	2.06	*5.53*	*9.75*	*5.03*	*9.42*
Eu	-0.22	-0.38	1.06	2.12	0.61	1.16	-0.54	-1.75	-0.37	*n. d.*	*n. d.*	*n. d.*	*n. d.*
Pb	2.60	1.00	1.94	-0.54	0.39	-1.82	-0.28	3.58	2.76	*1.74*	*16.71*	*0.01*	*5.69*

2.4.5 Volume of fluids and estimates of fluid influx

The previously presented mass balance calculations provided estimates of chemical changes caused by fluid-rock interaction. The data show that hydration was associated with a loss of SiO_2 and a gain in MgO and FeO. These data can be used to assess the volume of the metasomatising fluids needed to account for the observed mass transfer. Assuming that the observed element changes are entirely due to fluid-rock interaction and that local equilibrium was attained, geochemical fluid-rock ratios and time-integrated fluid fluxes can be estimated (Dipple & Ferry, 1992) .

Volumetric fluid-rock ratios

Element solubility in an aqueous fluid depends on temperature, pressure, salinity and pH of the solvent and since element transfer is mineralogically controlled on host-rock mineralogy. The solubility of SiO_2 in water is relatively insensitive to pH and salinity (Anderson & Burnham, 1967; Xie & Walther, 1993). Consequently, it was assumed that the SiO_2 solubility in water depends only on temperature and pressure. With the equation of Fournier & Potter (1982) and specific volume data for water from Burnham *et al.* (1969) changes in silica concentration with pressure and temperature were calculated (Fig. 2.24). At the estimated pressure conditions of hydration (6 – 10 kbar), the silica concentration increases with increasing temperature, but shows no pressure dependence. The decrease of SiO_2 contents in the hydration zones at Leonard Cape and Bolschoi Island indicates that fluid flow occurred in the direction of increasing temperature (up-temperature fluid flow), dissolving silica from the infiltrated rock. In the direction of decreasing temperature (down-temperature fluid flow), on the other hand, quartz should be precipitated, as evidenced by the presence of quartz veins in many shear zones (e.g. Dipple & Ferry, 1992; Streit & Cox, 1998). The up-temperature fluid flow in the studied hydration zones can presumably be attributed to large-scale thrusting in the course of continental collision of the Belomorian foreland with the Central Kola terrane *c.* 1.9 Ga ago, causing inverted temperature gradients between the footwall and the hanging wall.

At the estimated *P-T* conditions of 6 kbar & 700 °C and 9 kbar & 700 °C for the hydration stage, silica solubility ranges from 0.42 to 0.55 mol/kgH_2O which is equivalent to 25.5 to 33.1 gSiO_2/kgH_2O or approximately 3 wt% SiO_2 (Fig. 2.24).

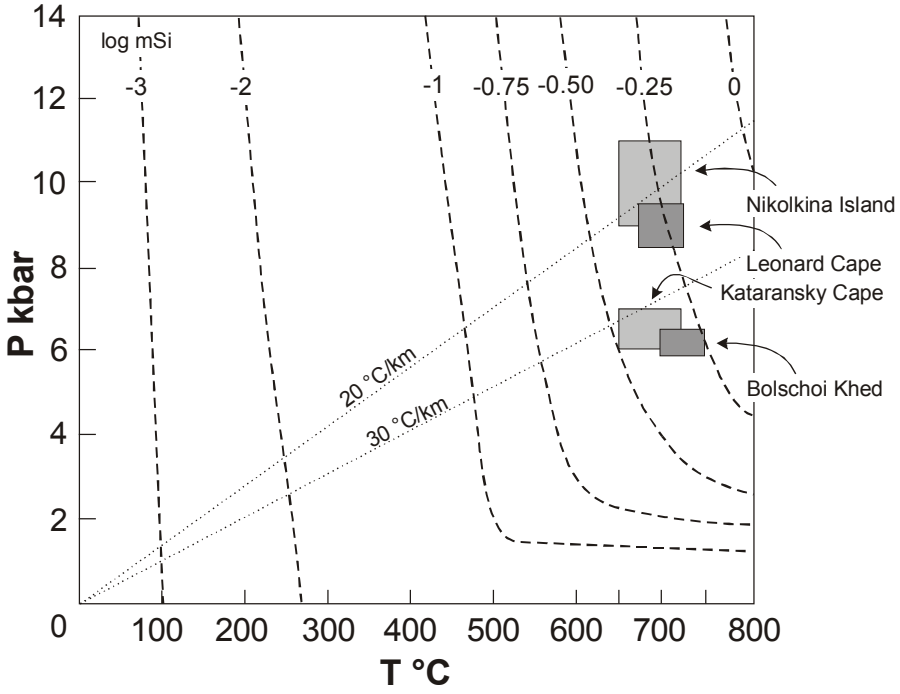

Fig. 2.24. P-T diagram shows *P-T* estimates for the amphibolite-facies stage. Changes in Si solubility (molal silica concentration) with pressure and temperature are indicated as isolines. The isolines were calculated after Fournier & Potter (1982) using specific volume data for water from Burnham *et al.* (1969).

As an example hydration zones at Leonard Cape will be considered, where depletion of SiO_2 occurred throughout the hydration zone and amounts to 11.3 - 15.3 g SiO_2 with reference to 100 g protolith. This quantity, based on a protolith density of about 2.9 g/cm^3, corresponds to a SiO_2 loss of 0.32 – 0.43 g/cm^3 protolith. At 9 kbar and 700 °C, 0.03 g SiO_2 are dissolved in 1 cm^3 water. This allows the calculation of minimum volumetric fluid-rock ratios needed to account for the observed SiO_2 loss, over a wide range of silica saturation levels from 0 to 90% (Tab. 2.6).

Table 2.6. Volumetric fluid-rock ratios for different hydration zones.

locality/sample	loss or gain SiO_2 g/100g$_{protolith}$	density protolith	change SiO_2 g/cm$^3{}_{protolith}$	calculated SiO_2 solubility in water g/cm$^3{}_{H2O}$	volumetric fluid-rock ratio	volumetric fluid-rock ratio
					0% silica satur.	90% silica satur.
Leonard Cape:						
example I:						
zone II (0808-5)	-15.3	2.9	0.43	0.0296	15	150
zone III (0808-6)	-11.3	2.9	0.32	0.0296	11	110
example II:						
zone II (0808-2)	-4.5	2.9	0.13	0.0296	4	40
zone III (0808-3)	-2	2.9	0.06	0.0296	2	20
Bolschoi Khed:						
zone II (0708-5)	-4.3	3.1	0.13	0.0223	6	60
zone III (0708-6)	-3.7	3.1	0.11	0.0223	5	50
Kataransky Cape:						
zone II (1008-B2)	-3.3	3	0.1	0.0202	5	50
zone III (1008-B1)	4	3	0.12	0.0202	6	60
Nikolkina Island:						
zone II (0308-K2)	9.7	3.1	0.3	0.0294	10	100
zone III (0308-K4)	1	3.1	0.08	0.0227	4	40
zone IV (0308-K3)	-1	3.1	0.03	0.0198	1	10

Notes: temperature and pressure dependent SiO_2 solubility in water was calculated from the equation given by Fournier & Potter (1982) with data of the specific volume of H_2O (Burnham *et al*., 1969).

In the case that no SiO_2 was dissolved in the fluid prior to infiltration, estimates of the volumetric fluid-rock ratio yield ratios of 15:1 for zone II and 11:1 for zone III. With the assumption that the fluids were almost saturated with SiO_2, the estimated volumetric fluid-rock ratios are 150:1 for zone II and 110:1 for zone III. Since, fluids are believed to have been generated by prograde dehydration reactions in the lower plate/footwall, it appears reasonable to assume that the released and uprising fluids were saturated with silica. A scenario of SiO_2 saturated fluids appears also more likely for fluids generated at mid-crustal level (see also Selverstone *et al*., 1991; Argue, 1994; Ring, 1999; Cartwright & Barnicoat, 2003). Volumetric fluid-rock ratios for hydration zones from Bolschoi Khed, Kataransky Cape, Leonard Cape (example II) and Nikolkina Island yielded fluid-rock ratios between 35:1 and 60:1. Due to the complementary element patterns between the marginal and central parts of individual hydration zones at Kataransky Cape and Nikolkina Island, estimates of fluid-rock ratios are problematic. Since element transfer in these cases obviously was not only controlled by the composition of the infiltrating fluid, but also by bilateral element transfer driven by concentration gradients between the centre and the marginal front of the fluid infiltration zone, assessment of applied SiO_2 is difficult. Ignoring the effects of lateral redistribution, the estimated fluid-rock ratios are in the magnitude (10^1:1) of the evaluated volumetric fluid-rock ratios for hydration zones from Leonard Cape (example II) and Bolschoi Khed (Tab. 2.6). High volumetric fluid-rock ratios in the order of 10^1:1 to 10^2:1 are in agreement with fluid-rock ratios (10^1:1 to 10^3:1) determined from shear zones characterised by significant element transfer (e.g. O'Hara, 1988; Selverstone *et al*., 1991; Yonkee *et al*., 2003).

Time integrated fluid fluxes

Assuming local fluid-rock equilibrium, the volumes of metasomatising fluids required to cause the observed silica depletion can be calculated (Dipple & Ferry, 1992). The time-integrated fluid flux (q) can be estimated by following equations:

$$q = \text{volumetric fluid-rock ratio} * z, \quad (3)$$

where z is the length of the fluid flow parallel to the flow direction

&

$$q = n_i/[(dX_i/dT)_P*(dT/dz) + (dX_i/dP)_T*(dP/dz)], \quad (4)$$

where n_i is the gain or loss of element i, (dX_i/dT) & (dX_i/dP) are the concentrations of element i in the fluid as function of temperature and pressure, and (dT/dz) & (dP/dz) are temperature and pressure gradients as function of depth. Equation (3) depends on the volumetric fluid-rock ratios and the length of the flow path and is based on the assumption that the initial composition of the infiltrating fluid does not change. Equation (4) accounts for changes of fluid composition along flow paths driven by a thermal and baric gradient. Assuming local fluid-rock equilibrium along the flow path, externally derived fluids evolve along temperature and pressure gradients.

Since $(dX_{Si}/dT)_P$ is relatively insensitive to fluid salinity (mainly Cl) and pH, changes in SiO_2 are used to estimate time-integrated fluid fluxes (Tab. 2.7). Based on the assumption that the temperature gradient is greater than the pressure gradient, the term $(dX_i/dP)_T*(dP/dz)$ can be neglected (Dipple & Ferry, 1992). At Leonard Cape (example I) hydration zones in the metadiorite were affected by a SiO_2 loss of *c.* 11 – 15 g/100g protolith. For an assumed protolith density of 2.9 gcm^{-3}, this corresponds to a change of silica in the range of *c.* 0.0054 – 0.0074 mol/cm^3 protolith. At 9 kbar and 700 °C, $(dX_{Si}/dT)_P$ is *c.* $2.3*10^{-5}$ (calculated with the equation given by Fournier & Potter, 1982 and specific volume data for H_2O from Burnham *et al.*, 1969). Assuming a geothermal gradient of 25 °C/km, estimated time integrated fluid fluxes range from $9.5*10^5$ to $2.3*10^6$ $[mol/cm^2]$. For a molar volume of H_2O of 20 cm^3 at the assumed *P-T* conditions (Burnham *et al.*, 1969), this corresponds to a volume fluid flux of $1.9*10^7$ – $2.6*10^7$ cm^3/cm^2 or $1.9*10^5$ - $2.6*10^5$ m^3/m^2. Time integrated fluid fluxes for hydration zones from Bolschoi Khed, Kataransky Cape, Leonard Cape (example II) and Nikolkina Island yielded c. $3*10^5$ mol/cm^2 or $5*10^6$ cm^3/cm^2 and are somewhat lower, but within the same order of magnitude. Fluid fluxes in direction of increasing temperature, required for mass losses of SiO_2, are in the order of 10^5 mol/cm^2 or 10^6 cm^3/cm^2. Compared to time integrated fluid fluxes described in the literature (10^3 – 10^7 m^3/m^2) (e.g. Selverstone et al, 1991; Dipple & Ferry, 1992; Streit & Cox, 1998; Yonkee et al, 2003; Cartwright & Barnicoat, 2003), the calculated/derived averaged fluid fluxes are in the lower range. But as mentioned by Dipple & Ferry (1992), fluid fluxes greater than 10^4 mol/cm^2 are expected to cause significant chemical changes in the infiltrated rock.

Calculations of element solubility with temperature were performed by Dipple & Ferry (1992) for a wide range of rock types. The results show that the solubilities of Si and K increase with increasing temperatures, whereas solubilities of Mg, Ca and Na decrease. The observed increase in Mg, Ca and Na and decreasing Si concentrations comply with the inferred up-temperature fluid flow.

Table 2.7. Time integrated fluid fluxes for different hydration zones.

locality/sample	ΔSiO_2 [$g/100g_{prot.}$]	density protolith	change Si [$mol/cm^3_{prot.}$]	dXSi/dT [mol/°C]	q [mol/cm^2]	q [mol/m^2]	q [cm^3/cm^2]	q [m^3/m^2]
Leonard Cape:								
example I:								
zone II (0808-5)	-15.3	2.9	0.0074	$2.3*10^{-5}$	$1.3*10^{6}$	$1.3*10^{10}$	$2.6*10^{7}$	$2.6*10^{5}$
zone III (0808-6)	-11.3	2.9	0.0054	$2.3*10^{-5}$	$9.5*10^{5}$	$9.5*10^{9}$	$1.9*10^{7}$	$1.9*10^{5}$
example II:								
zone II (0808-2)	-4.5	2.9	0.0022	$2.3*10^{-5}$	$3.7*10^{5}$	$3.7*10^{9}$	$7.5*10^{6}$	$7.5*10^{4}$
zone III (0808-3)	-2	2.9	0.001	$2.3*10^{-5}$	$1.5*10^{5}$	$1.5*10^{9}$	$3.1*10^{6}$	$3.1*10^{4}$
Bolschoi Khed:								
zone II (0708-5)	-4.3	3.1	0.0022	$2.8*10^{-5}$	$3.2*10^{5}$	$3.2*10^{9}$	$7.3*10^{6}$	$7.3*10^{4}$
zone III (0708-6)	-3.7	3.1	0.0019	$2.8*10^{-5}$	$2.7*10^{5}$	$2.7*10^{9}$	$6.2*10^{6}$	$6.2*10^{4}$
Kataransky Cape:								
zone II (1008-B2)	-3.3	3	0.0017	$2.8*10^{-5}$	$2.4*10^{5}$	$2.4*10^{9}$	$5.4*10^{6}$	$5.4*10^{4}$
zone III (1008-B1)	4	3	0.002	$2.8*10^{-5}$	$2.9*10^{5}$	$2.9*10^{9}$	$6.6*10^{6}$	$6.6*10^{4}$
Nikolkina Island:								
zone II (0308-K2)	9.7	3.1	0.005	$2.3*10^{-5}$	$8.7*10^{5}$	$8.7*10^{9}$	$1.7*10^{7}$	$1.7*10^{5}$
zone III (0308-K4)	1	3.1	0.0013	$2.3*10^{-5}$	$2.3*10^{5}$	$2.3*10^{9}$	$4.7*10^{6}$	$4.7*10^{4}$
zone IV (0308-K3)	-1	3.1	0.0005	$2.3*10^{-5}$	$8.6*10^{4}$	$8.6*10^{8}$	$1.7*10^{6}$	$1.7*10^{4}$

Notes: $dXSiO_2/dT$ was calculated from the equation given by Fournier & Potter (1982) with data of the specific volume of H_2O (Burnham *et al*., 1969). Q was calculated assuming a geothermal gradient of 25°C/km.

2.5 Stable isotope geochemistry

2.5.1 Analytical technique

For mineral separation, pre-concentrates of the 125 - 250 μm grain size fraction of crushed and sieved hand specimen were made by conventional magnetic separation. Pure mineral separates were obtained by hand-picking. 10-15 mg aliquots of powdered mineral separates or whole-rock powders were used for oxygen isotope analysis. The oxygen extraction line is made of glass and was manufactured in-house at the Mineralogical – Petrological Institute of the University Bonn. For the extraction of oxygen from silicates, purified fluorine (Asprey, 1976) was used. The oxygen was converted to CO_2 over a heated graphite spindle (Clayton & Mayeda, 1963).
Garnet behaved refractory during fluorination, and high fluorine overpressures (3 bar) at temperatures of 650 – 700 °C had to be applied. $^{18}O/^{16}O$ measurements were carried out using a SiraA-9 triple-collector mass spectrometer by VG-Isogas. All isotope analyses are presented in the usual δ-notation as per mil (‰) referred to Standard Mean Ocean Water (SMOW). The analytical reproducibility of the δ-values is 0.1 ‰. Commercial very clean CO_2, calibrated with carbonate and silicate standards, was used as reference gas.

2.5.2 Results

Oxygen isotope whole-rock compositions of 23 metagabbro and metanorite samples from the Kolvitsa and Por'ya Guba Complex are presented in Table 2.8 and Figure 2.27. The rocks are characterised by $\delta^{18}O$ values of 6.1 ‰ to 6.7 ‰. These values are slightly higher than the typical upper mantle values of 5.7 ‰ – 6.0 ‰ (Muehlenbachs, 1986).
The amphibolitised zones/domains show somewhat lower $\delta^{18}O$ values (4.7 to 5.6 ‰) compared to their granulite-facies equivalents (Fig. 2.25 – 2.27). The shifts to lighter isotopic compositions range from 0.55 ‰ (Bolschoi Khed) to 1.6 ‰ (Nikolkina Island).

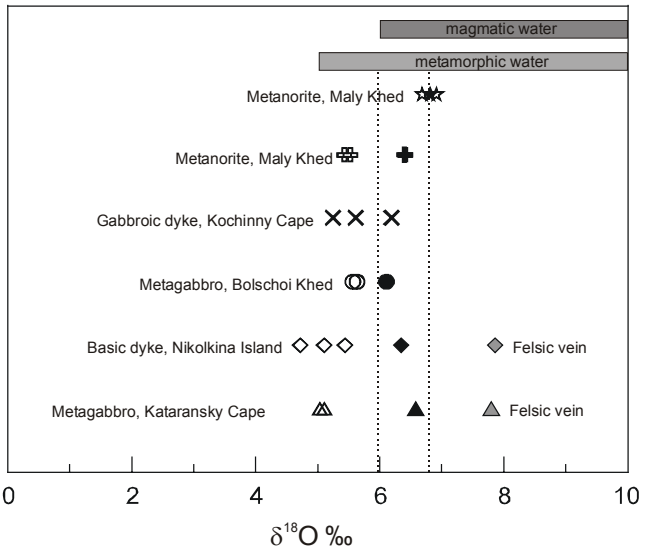

Fig. 2.25. Oxygen isotope composition of the whole rock silicate fraction from protoliths (filled symbols) and altered zones (open symbols). For comparison isotopic composition across hydration zones from Maly Khed (Por'ya Guba) and gabbroic dykes from Kochinny Cape (Kolvitsa) are shown. Grey bars indicate $\delta^{18}O$ values for magmatic (6-10 ‰) and metamorphic (5-25 ‰) aqueous fluids (Hoefs, 1997).

The amphibole felses within the central parts of the fluid infiltration zones show a complete mineralogical and textural re-equilibration at amphibolite-facies conditions. This suggests that the newly formed minerals, mainly amphibole, attained isotopic equilibrium with the infiltrating fluid.

The marginally lower $\delta^{18}O$ values of the amphibolitised domains compared to their protoliths, thus may indicate either equilibration with fluids of similar isotopic composition or, if the amounts of infiltrating fluids were low, isotopic buffering by the rocks.
The fractionation of oxygen isotopes between phases is a function of temperature and non-sensitive to pressure. For this reason, isotopic fractionations between mineral phases which are in isotopic equilibrium can be used for thermometry. The isotopic composition of the ambient fluid phase, on the other hand, can be assessed for a given equilibrium temperature via mineral-water fractionations.
In order to calculate temperatures and isotopic compositions of the fluid phase from the measured $\delta^{18}O$ values of minerals, fractionation factors of mineral-mineral and mineral-water equilibria had to be determined.
The increment method is a semi-empirical technique and allows to calculate oxygen-isotope fractionation factors between silicates of known chemical composition and structure (Schütze, 1980; Richter & Hoernes, 1988; Hoffbauer *et al.*, 1994). Thereby, the calculated ^{18}O index ($I^{18}O$) takes into account the bonding strength of each element in a mineral and thus this method is especially suitable for solid solutions (Hoffbauer *et al.*, 1994). Experimentally based temperature-dependent β-factors are linked to the calculated $I^{18}O$ indices and act as reference frame. A detailed description of the method is given by Richter & Hoernes (1988) and Hoffbauer *et al.* (1994).
For the calculation of the isotopic composition of the fluid phase, the calibration of the oxygen isotope fractionation between Qtz-H_2O (Richter & Hoernes, 1988) was used (Tab. 2.8 & Fig. 2.26 – 2.27). Temperatures from mineral pairs were determined using Qtz-Cc (Hoffbauer et al., 1994) and Qtz-H_2O (Richter & Hoernes, 1988) as reference-mineral-pairs and are compiled in Table 2.9. Temperature and pressure estimates obtained from classical thermobarometry and multi-equilibrium thermobarometry (TWEEQU 1.02, Berman, 1988 & 1991) yielded 650 – 700 °C and 6 – 10 kbar.

Kataransky Cape

$\delta^{18}O$ values of the fluid phase estimated from quartz-, plagioclase- and hornblende-water fractionations at 650 °C and 700 °C vary between 7 – 7.6 ‰ and 7.1 – 8 ‰, respectively (Fig. 2.26 & Tab. 2.8). Highest values of *c.* 7.6 ‰ at 650 °C and *c.* 7.9 ‰ at 700 °C based on quartz-water and plagioclase-water fractionations were obtained for the felsic vein. Mineral-water fractionation data for plagioclase and hornblende from the hydration zone III yielded only slightly lower $\delta^{18}O$ values (7 – 7.3 ‰) for the fluid phase. Oxygen isotope thermometry on quartz-plagioclase (felsic vein) and plagioclase-hornblende pairs (hydration zone III) yielded consistent estimates of 700 and 680 °C (Qtz-Cc) and 655 and 640 °C (Qtz-H_2O). These temperatures comply well with results from classical Hbl-Pl thermometry that gave 650 – 720 °C at a pressure of 6 – 6.5 kbar. The concordance of temperature estimates, together with the uniform $\delta^{18}O$ values for the infiltrating fluid suggests that isotopic equilibrium was achieved during hydration and dynamic re-crystallisation and remained preserved.

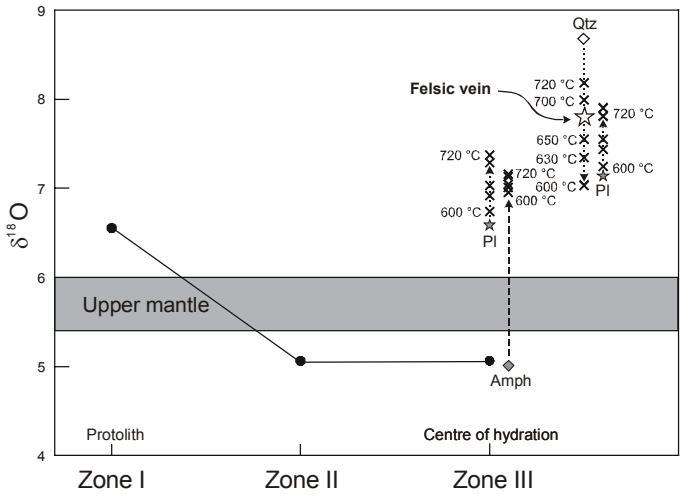

Fig. 2.26. Oxygen isotope composition across a shear zone at Kataransky Cape. Also shown are $\delta^{18}O$ data of minerals and the estimated isotopic composition of the coexisting hydrous fluid phase at different temperatures.

Oxygen isotope thermometry on Pl-Grt and Grt-Cpx pairs of the granulite-facies gabbroic protolith yielded too high (1077 °C) or too low temperatures (432 °C) suggesting isotopic disequilibrium. Discordant temperatures may result from diffusive exchange between minerals with different closure temperatures. Further, effects of incomplete fluorination of refractory phases and/or the presence of impurities/inclusions in the mineral separates on the thermometric data cannot be excluded. Garnet has in fact a high closure temperature (>900 °C) for oxygen diffusion (Valley *et al.*, 1986; Hoffbauer *et al.*, 1994) and usually behaves refractory during fluorination. Clinopyroxene is susceptible to alteration and is characterised by a higher oxygen diffusivity (Farquhar *et al.*, 1993; Hoefs, 1997). Furthermore, clinopyroxene includes minute plagioclase inclusions that probably were not completely eliminated during separation. The similar $\delta^{18}O$ values of plagioclase (6.83 ‰) and clinopyroxene (6.89 ‰) and the discordant temperature estimates indicate that their peak metamorphic isotopic compositions were not preserved.

Nikolkina Island

The isotopic composition of the fluid phase in equilibrium with quartz, plagioclase, garnet, titanite and hornblende from the hydration zones and the felsic vein shows a large spread in the $\delta^{18}O$ values, from 6.2 to 8.5 ‰ at 650 °C (Tab. 2.8 & Fig. 2.27). The high values of 8.2 – 8.5 ‰ at 650 °C and 8.5 – 8.9 ‰ at 700 °C are obtained from plagioclase-water and quartz-water fractionation data, while hornblende-water and titanite-water fractionation data at 650 °C and 700 °C give the lowest values of 6.2 – 6.8 ‰ and 6.3 – 6.8 ‰, respectively. Intermediate values of 7.5 ‰ are derived from garnet-water fractionation data.

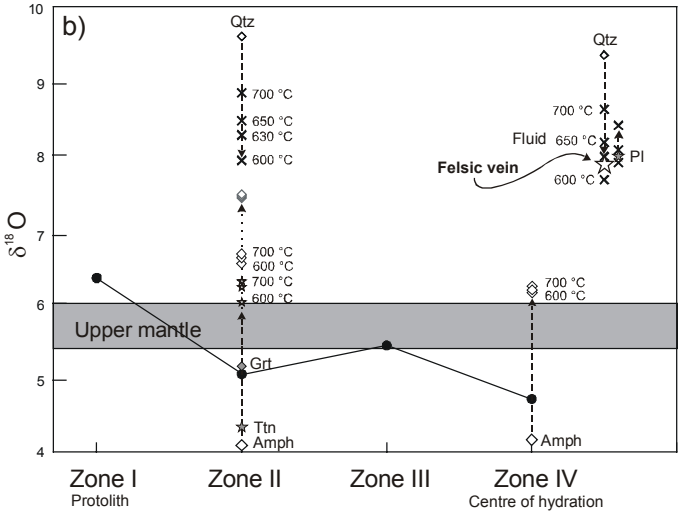

Fig. 2.27. Oxygen isotope composition across shear zones at Nikolkina Island. Also shown are $\delta^{18}O$ data of minerals and the estimated isotopic composition of the coexisting hydrous fluid phase at different temperatures.

The spread in $\delta^{18}O$ values for the coexisting fluid phase points to isotopic disequilibrium which may have resulted from small fluid-rock ratios typical for a rock-buffered system. In such case, newly formed and isotopically equilibrated minerals would occur beside relict minerals. The thoroughly annealed microtextures, results from multi-equilibrium modelling (TWEEQU) and temperatures up to 720 °C, however, argue against an incomplete isotopic re-equilibration during amphibolite-facies hydration. It appears more reasonable to assume that the wholesale isotopic equilibrium was disturbed during cooling. In minerals with low closure temperatures, the retrograde oxygen isotope exchange continues to lower temperatures. Thereby, diffusive oxygen isotope exchange between minerals with different closure temperatures is controlled by the modal amount of the refractory mineral phase (Hoefs, 1997). At the temperature conditions of hydration (650 – 700 °C), garnet and hornblende are regarded as less susceptible to diffusive oxygen isotope exchange than quartz and feldspar (Giletti, 1986; Valley *et al.*, 1986; Farquhar et al., 1996, Hoefs, 1997). Hydration zone II is characterised by the mineral assemblage Grt-Hbl-Qtz-Pl-Ttn. High fluid $\delta^{18}O$ values (up to 8.9 ‰) obtained from Qtz-H_2O fractionation presumably result from retrograde isotopic exchange between the fast-diffusing

quartz and the slow-diffusing garnet and hornblende, respectively. Alternatively, retrograde isotopic exchange between quartz and the fluid phase continued to lower temperatures at which isotopic exchange between garnet and hornblende and the fluid phase had ceased.
Oxygen isotope thermometry yielded discordant temperature estimates for both the upper-amphibolite to granulite facies stage and the amphibolite facies hydration stage (Tab. 2.9). The latter is characterised by reasonable isotopic temperature estimates of 665 °C (Qtz-Cc) and 627 °C (Qtz-H_2O) obtained from fractionation data of Qtz-Pl pairs in the felsic vein at the centre of the fluid infiltration zone. These results are consistent with temperature estimates of *c.* 650 – 720 °C from Hbl-Pl and Grt-Hbl thermometry and multi-equilibrium thermobarometry (TWEEQU 1.02, Berman, 1988 & 1991). Compared to the Qtz-Pl temperature data for the felsic vein, temperature estimates for Qtz-Grt (576 °C/553 °C) and especially Qtz-Hbl (503 °C/489 °C) and Qtz-Ttn (450 °C/441 °C) for the hydration zone II are too low. Discordant temperatures may be attributed to diffusive oxygen isotope exchange during cooling or oxygen isotope exchange with a circulating residual fluid.
Hornblende from the almost monomineralic hydration zone IV near the centre of fluid infiltration is characterised by a very low $\delta^{18}O$ value of *c.* 4.2 ‰. This low $\delta^{18}O$ value is presumably caused by the presence of minute inclusions of ore as well as late alteration products, such as secondary chlorite and prehnite, intergrown with hornblende. The resultant $\delta^{18}O$ values for the ambient fluid are therefore regarded as erroneous.
The $\delta^{18}O$ value of quartz from the felsic vein (9.35 ‰) corresponds to $\delta^{18}O$ values obtained for quartz from hydration zone II (9.6 ‰). This finding documents similar oxygen isotope exchange conditions during the hydration stage and the late vein-forming stage. Concordant temperature estimates and the uniform isotopic composition of the fluid indicate that quartz and plagioclase from the felsic vein together with garnet and hornblende from hydration zone II reflect attainment of isotopic equilibrium.

Bolschoi Khed

The $\delta^{18}O$ values of the fluid phase derived from plagioclase-water fractionation data of hydration zones I and II range from 8.6 to 8.9 ‰, whereas hornblende-water fractionation data yielded $\delta^{18}O$ values between 7.3 – 7.6 ‰ at temperatures between 650 - 700 °C (Tab. 2.8). Again $\delta^{18}O$ values for the infiltrating fluid based on plagioclase-water fractionation are conspicuously higher.
Temperature estimates obtained from plagioclase-hornblende pairs vary from 438 °C/418 °C (Qtz-Cc/Qtz-H_2O) for zone II to 472 °C/448 °C (Qtz-Cc/Qtz-H_2O) for zone III (Tab. 2.9). Results from mineralogical Hbl-Pl thermometry gave 700 – 750 °C at 6 kbar (cf. part I). The apparent isotopic temperatures are 200 – 300 °C too low and indicate isotopic disequilibrium. Hornblende is the major constituent of hydration zone II and of the almost monomineralic hydration zone III. Compared to plagioclase, hornblende is characterised by a low oxygen isotope diffusion. Oxygen isotope exchange between the grain boundaries of the abundant slow-diffusing hornblende and the fast-diffusing plagioclase has large effects on the isotopic composition of plagioclase and thus on apparent temperatures (Eiler *et al.*, 1992 & 1993; Hoefs, 1997). Estimates of the isotopic composition of the fluid phase obtained from hornblende-water fractionation (7.3 – 7.6 ‰) are therefore regarded as plausible and agree with the fluid $\delta^{18}O$ data from Nikolkina Island (7 - 8.5 ‰) and Kataransky Cape (7 – 8 ‰).

Table. 2. 8. Oxygen isotope data of minerals, the silicate whole rock fractions and the coexisting fluid phase.

		$\delta^{18}O$ index	$\delta^{18}O$ ‰	1000lnα min-H_2O	1000lnα min-H_2O	1000lnα min-H_2O	$\delta^{18}O$ ‰ fluid	$\delta^{18}O$ ‰ fluid	$\delta^{18}O$ ‰ fluid	$\delta^{18}O$ ‰ whole rock
	mineral-H_2O	mineral	mineral	630 °C	650 °C	700 °C	630 °C	650 °C	700 °C	silicate fraction
Kataransky Cape										
felsic vein	(An_{50}-H_2O)	0.819	7.15	-0.36	-0.47	-0.71	7.51	7.62	7.86	**7.80**
felsic vein	(An_{45}-H_2O)	0.825	7.15	-0.30	-0.41	-0.66	7.45	7.56	7.81	
felsic vein	(Qtz-H_2O)	1.00	8.68	1.33	1.13	0.70	7.35	7.55	7.98	
zone I										**6.65**
zone II										**5.04**
zone III	(An_{50}-H_2O)	0.819	6.59	-0.36	-0.47	-0.71	6.95	7.06	7.30	**5.02**
zone III	(Hbl-H_2O)	0.645	5.01	-1.98	-2.00	-2.06	6.99	7.01	7.07	
Nikolkina Island										
felsic vein	(An_{20}-H_2O)	0.855	7.99	-0.02	-0.15	-0.43	8.01	8.14	8.42	**7.85**
felsic vein	(An_{30}-H_2O)	0.841	7.99	-0.13	-0.25	-0.52	8.12	8.24	8.51	
felsic vein	(Qtz-H_2O)	1.00	9.35	1.33	1.13	0.70	8.02	8.22	8.65	
zone I										**6.35**
zone II	(Qtz-H_2O)	1.00	9.60	1.33	1.13	0.70	8.27	8.47	8.90	**5.04**
zone II	(Grt-H_2O)	0.612	5.16	-2.28	-2.29	-2.32	7.44	7.45	7.48	
zone II	(Ttn-H_2O)	0.667	4.34	-1.77	-1.81	-1.89	6.11	6.15	6.23	
zone II	(Hbl-H_2O)	0.647	4.76	-1.96	-1.99	-2.05	6.72	6.75	6.81	
zone III										**5.44**
zone IV	(Hbl-H_2O)	0.641	4.17	-2.01	-2.04	-2.09	6.18	6.21	6.26	**4.72**
Bolschoi Khed										
zone I										**6.10**
zone II	(An_{40}-H_2O)	0.831	8.23	-0.25	-0.36	-0.62	8.48	8.59	8.85	**5.56**
zone II	(Hbl-H_2O)	0.655	5.36	-1.88	-1.92	-14.98	7.24	7.28	7.34	
zone III	An_{50}-H_2O)	0.819	8.24	-0.36	-0.47	-0.71	8.60	8.71	8.95	**5.57**
zone III	(An_{40}-H_2O)	0.831	8.28	-0.25	-0.36	-0.62	8.53	8.64	8.90	
zone III	(Hbl-H_2O)	0.654	5.60	-1.89	-1.92	-1.99	7.49	7.52	7.59	
Kochinny Cape										
zone I										**6.19**
zone II										**5.61**
zone III										**5.25**
zone IV										**5.60**
Maly Khed										
zone I (34-12)										**6.81**
zone II (34-15)										**6.94**
zone III (34-16)										**6.77**
zone I (0208-11)										**6.40**
zone II (0208-12)										**6.37**
zone III (0208-13)										**5.35**

Notes: For the calculations of the isotopic index, the computer program OXY (Grimmeisen *et al*., 1993) was used. $\delta^{18}O$ values are given in ‰ relative to SMOW. Whole rock data from Kochinny Cape (Kolvitsa nappe) Maly Khed (Por'ya Guba nappe) are shown for comparison.

Table 2.9. Oxygen isotope data of minerals from protoliths and amphibolite zones. Isotopic temperatures were calculated from mineral-mineral fractionation according to the increment method (Schütze, 1980; Richter & Hoernes, 1988; Hoffbauer *et al.*, 1994). As reference, experimentally determined quartz-calcite (Chiba *et al*., 1989) and quartz-H_2O (Richter *et al*, 1985; Richter & Hoernes, 1988) fractionation were used to obtain temperature dependent β-factors.

		^{18}O-index	δ^{18}O ‰	Min-min	Δ ‰	T °C Ref. Qtz-Cc	T °C Ref. Qtz-H_2O
Kataransky Cape							
zone I	Pl An_{50}	0.819	6.83	Pl-Grt	0.95	1077	
	Grt	0.609	5.88	Grt-Cpx	1.52	432	
	Cpx	0.67	6.89				
zone III	Pl An_{50}	0.819	6.59	Pl-Hbl	1.58	680	640
	Hbl	0.645	5.01				
felsic vein	Pl An_{45}	0.825	8.68	Qtz-Pl	1.53	699	654
	Qtz	1	7.15				
Nikolkina Island							
zone I	Qtz	1	9.23	Qtz-Pl	1.64	581	
	Pl An_{20}	0.855	7.59	Qtz-Grt	4.71	559	
	Grt	0.605	4.52	Qtz-Cpx	3.93	546	
	Cpx	0.681	5.30	Qtz-Hbl	2.7	541	
	Hbl	0.638	4.89	Cpx-Grt	0.78	622	
				Hbl-Grt	0.37	587	
				Cpx-Hbl	0.41	652	
zone II	Qtz	1	9.60	Qtz-Grt	4.44	576	553
	Grt	0.612	5.16	Qtz-Hbl	4.84	503	489
	Hbl	0.647	4.76	Qtz-Ttn	5.26	450	441
	Ttn	0.667	4.34				
zone IV	Hbl	0.641	4.17				
felsic vein	Pl An_{20}	0.855	7.99	Qtz-Pl	1.63	665	627
	Qtz	1	9.35				
Bolschoi Khed							
zone I	Pl An_{45}	0.825	8.23	Pl-Grt	1.52	805	
	Grt	0.611	6.71	Pl-Cpx	2.97	387	
	Cpx	0.668	5.26	Pl-Opx	3.13	373	
	Opx	0.667	5.10				
zone II	Pl An_{40}	0.831	8.23	Pl-Hbl	2.87	438	418
	Hbl	0.655	5.36				
zone III	Pl	0.831	8.28	Pl-Hbl	2.63	472	448
	Hbl	0.654	5.60				

2.5.3 Interpretation

The similarity in oxygen isotope compositions of both the protoliths and their retrogressed amphibolite-facies equivalents is not a direct evidence for significant influx of externally derived fluids. The minimum amount of water necessary to hydrate the granulite-facies precursors can be estimated from the modal amount of newly formed hydrous mineral phases. The almost monomineralic amphibole felses in the centre of hydration domains contain 80 to 100 vol% hornblende. Assuming a water content of 2 wt% in hornblende, the estimated water/rock ratio is 0.016 and 0.02, respectively. In such case, changes in the isotopic composition of the hydrated rock are expected to be negligible, unless the infiltrating fluid had an 'exotic' isotopic composition (see also Fiorentini *et al.*, 1990; Hoernes & van Reenen, 1992). Evidently the small shifts in the isotopic composition preclude the involvement of an isotopically exotic fluid. The very low water/rock ratios derived above are only minimum values required to explain the appearance of newly formed hornblende. It is obvious that much higher fluid/rock ratios are required to explain the observed significant chemical changes. The conformity of isotopic compositions (7 to 8.5 ‰) of the infiltrating fluids at the different localities studied suggests that the infiltrating fluids were derived from a uniform reservoir. The geological setting suggests that the fluids were produced through biotite/hornblende-dehydration reactions in the footwall units, i.e. the Kandalaksha amphibolites and Belomorian tonalitic gneisses, in response to loading and heat-input from the up-thrust hangingwall units in the course of the formation of the Lapland-Kola collisional orogen. Palaeoproterozoic reworking of the Belomorian basement is documented by renewed partial melting and migmatization of gneisses (Bibikova *et al.*, 2001). The Kandalaksha amphibolites comprise mainly basic metavolcanic rocks with subordinate meta-graywackes and meta-conglomerates which could have been affected by devolatilisation and dehydration reactions. The *P-T* history of the volcanic rocks of the Kandalaksha complex is not well constrained and an early metamorphic overprint at *c.* 570 °C & 5 kbar could have been occurred prior to nappe thrusting, whereas metamorphic overprint at 600 – 650 °C and 8 – 10 kbar was a response of burial and crustal thickening (Bogdanova & Yefimov, 1993).

Fluid flow during regional metamorphism can be driven by mechanical or thermal gradients. Equilibrium fluid flow along temperature gradients can cause significant shifts in the oxygen isotope composition which provide information about the flow directions and thus the prevailing palaeo-temperature gradients (Dipple & Ferry, 1992; Cartwright & Buick, 1994).

The uniform oxygen isotope compositions (*c.* 5 ‰) of amphibolites developed in different protoliths at various localities at temperatures above 650 °C suggest that isotopic equilibrium was attained between the rock and the infiltrating fluid (conditions of a fluid-buffered system). The achievement of a local isotope exchange equilibrium is a basic requirement for the assessment of fluid flow along temperature gradients (Dipple & Ferry, 1992; Cartwright & Buick, 1994). Assuming a one-dimensional fluid flow, and that advective transport and resetting of the oxygen isotopes is solely caused by exchange with the fluid, the change in isotopic rock composition and the propagation of the infiltration front can be estimated by equation (5):

$$\delta^{18}O_{rock}\,(z, t_x) - \delta^{18}O_{rock}\,(z, t_0) = \delta^{18}O_{fluid}\,(z - B, t_0) - \delta^{18}O_{fluid}\,(z, t_0), \qquad (5)$$

where z is the distance, t is time and B is linked to the time-integrated molar fluid flux q_m (mol fluid per cm^2rock) via V_r (mol oxygen per cm^3 rock) to $B = q_m / V_r$ (Blattner & Lassey, 1989; Dipple & Ferry, 1992). As the oxygen isotope fractionation between rock (mineral) and water is temperature dependent, up-temperature fluid flow is in general linked to decreasing $\Delta^{18}O$ rock-H_2O and down-temperature fluid flow accompanied by increasing Δrock-H_2O fractionation. As a result of which the isotopic compositions of both the fluid and the rock change with the temperature gradient along the flow path.

Changes in bulk rock composition obtained from mass balance calculations have already indicated up-temperature fluid flow, whereby Si was significantly depleted during fluid infiltration. These results

correlate with the observed depletion of $\delta^{18}O_{rock}$ values in the hydration zones. Equation (5) can be used to predict shifts in the isotopic composition, resulting from temperature-up fluid flow. Dipple & Ferry (1992) modelled up-temperature fluid flow through a calcite or quartz-feldspar dominated rock and showed that lowest $\delta^{18}O$ values were achieved if time-integrated fluid flux was in the order of 10^5 mol H_2O/cm^2.

In the cases studied here, a plagioclase (An_{50})-dominated model rock with an initial $\delta^{18}O$ value of 6.3 ‰ was used to simulate up-temperature fluid flow through the anorthosite-gabbro association. The isotopic composition of the coexisting fluid in equilibrium with the model rock was calculated with the increment method (Richter & Hoernes, 1988) yielding $\delta^{18}O$ values of 6.2 – 6.35 ‰ at 560 – 580 °C and 7 - 7.2 ‰ at 700 – 750 °C. Assuming up-temperature fluid flow, the isotopic shift achieved during hydrous alteration at 700 - 750 °C can be obtained from equation (5) and give 0.7 – 1 ‰ thus leading to a final $\delta^{18}O_{rock}$ value of 5.3 – 5.6 ‰. Since the calcite-H_2O fractionation is similar to that of quartz and feldspar, a calcite model rock was assumed ($\delta^{18}O_{rock}$=6.3). The isotopic composition of the coexisting fluid is then 5.7 – 6.9 ‰ at 560 – 580 °C and ranges from 6.8 to 7 ‰ between 700 and 750 °C. The resulting final $\delta^{18}O_{rock}$ value varies from 5 – 5.4 ‰.

The model calculation agrees with the observed negative isotopic shifts of 1 to 1.5 ‰ and is consistent with up-temperature fluid flow. Since the term $B= q_m /V_r$ describes the propagation of the fluid front for a distance (z), z corresponds to B and thus $z = q_m /V_r$ or $q_m= z * V_r$. Minimum time-integrated fluid fluxes can then be estimated for a given geothermal gradient, e.g. 25 °C/km or 15 °C/km. The resulting time-integrated fluid fluxes (q_m) are $6.4 * 10^4$ mol/cm^2 ($1.5 * 10^4$ m^3/m^2) and $1 * 10^5$ mol/cm^2 ($2.3 * 10^4$ m^3/m^2), respectively. To explain the observed alteration patterns in terms of up-temperature fluid flow, large amounts of fluid and fluid flow distances of several kilometres are required. Although the time-integrated fluid fluxes can only be regarded as order-of-magnitude estimates, they provide an insight into the amounts of fluids required to account for the isotopic and chemical changes caused during fluid flow along temperature gradients.

For the above boundary conditions, up-temperature fluid flows would account for the observed alterations, but a change in the initial boundary conditions from 560 °C to 650 °C would result in smaller isotopic shifts. Isotopic alteration patterns may then be explained by an infiltrating fluid with a lower $\delta^{18}O$ value than the rock-fluid equilibrium value at 650 °C. Assuming that no temperature gradient existed during fluid infiltration, the observed isotopic changes may be caused by fluids with a lower $\delta^{18}O$ value. It becomes apparent that the isotopic patterns alone do not provide straightforward information about the fluid source and the fluid flow direction (Dipple & Ferry, 1992). The results from model calculations are only valid for the specified boundary conditions and have to be supported by additional mineralogical and chemical data. The plausibility of the model depends on a reasonable geological context.

In the case of the Lapland-Kola Orogen, the assumption of ascending up-temperature fluids complies well with an inverted metamorphic gradient. The heat was released from the overthrust hot granulite nappes. Inverse metamorphic gradients were already postulated and documented by geothermometric data for the Lapland-Granulite-Belt (Barbey & Raith, 1990) and are inferred by many authors also for the Kolvitsa-Umba Belt (Timmerman, 1996; Bibikova *et al.*, 2001; Daly *et al.*, 2001).

The simplified assumptions required for the modelling of thermally driven fluid flow may not be fulfilled in real fluid flow systems. In fact, fluid flow in natural systems may be more complex. The infiltrated rocks are more heterogeneous in composition and spatial differences in permeability may exist (fractures, shear zones, rock boundaries).

The overthrust nappe units comprise detached parts of large layered anorthosite-gabbro bodies and several generations of dykes. Also the path of ascending fluids is not known and fluid flow may be strongly channelled along zones of weakness (shear zones and rock boundaries). If fluid flow was strongly channelled and was characterised by high flow velocities, isotopic equilibration along the fluid path may not be achieved. Lateral dispersion, mainly diffusive, may occur normal to the channelled flow direction (e.g. Cartwright, 1994; Cartwright & Buick, 1996). Complementary element patterns observed across two of the studied amphibolite zones (Kataransky Cape & Nikolkina Island) are

evidence of diffusive element transfer between the centre and the outer front of fluid infiltration. However, thermal gradients are ubiquitous in many metamorphic regions (Dipple & Ferry, 1992). For this reason, the probability that fluid flow was connected with temperature gradients is high and tallies with the geological setting.

Temperature estimates for hydration at Kataransky Cape obtained from oxygen isotope thermometry on quartz-plagioclase (felsic veins) and plagioclase-hornblende pairs range from 670 to 700 °C and agree with results from cation exchange thermometry (650 – 750 °C). In contrast, discordant temperature data for the granulite-facies protoliths and for the amphibolite zones at Bolschoi Khed and Nikolkina Island point to an oxygen isotope disequilibrium between the mineral phases. Disequilibrium may be caused by decoupled diffusional oxygen exchange during cooling, isotopic zonation of minerals or a partly open system behaviour during particular evolutionary stages.

In the granulite-facies precursors and their hydration zones (Bolschoi Khed & Kataransky Cape), minerals (granulites: garnet, ortho- and clinopyroxene; amphibolitised zones: plagioclase) show pronounced chemical zonation patterns. These patterns clearly reflect chemical disequilibrium between the mineral core and the outer rim. Maybe this disequilibrium is also reflected by the oxygen isotope composition of the mineral. In contrast, hornblende in the hydration zones is chemically homogeneous and shows well developed equilibrium textures, indicating chemical and textural equilibrium.

The different oxygen isotope diffusivities in respective mineral phases cause different closure/blocking temperatures for intercrystalline oxygen isotope exchange and are supposed to be major factors controlling the attainment and preservation of isotopic oxygen equilibria. Compared to plagioclase, quartz and pyroxene, garnet and hornblende can be regarded as slow-diffusing minerals and their modal abundance has large effects on the isotopic composition of fast-diffusing minerals and thus on isotopic temperature estimates (Eiler *et al.*, 1992 & 1993; Hoefs, 1997). In addition pyroxene is susceptible to retrograde alteration. Secondary amphibole in granulite-facies protoliths and prehnite together with chlorite in the amphibole felses, indicate the presence of aqueous pore fluids which trigger retrograde oxygen isotope exchange. For these reasons temperature estimates for the granulite-facies and to some extent also for the amphibolite-facies stage, may be erroneous.

2.6 Age determination and isotopic data

2.6.1 U-Pb dating of titanite

Titanite is a common accessory mineral in manifold lithologies and has a wide stability range. As several phases can incorporate Ti and Ca, titanite behaves reactive in high temperature environments (Scott & St. Onge, 1995; Frost *et al.*, 2000) and, provided its paragenetic setting can be ascertained from textural and compositional criteria, U-Pb dating of this mineral offers a powerful tool to determine the timing of metamorphism and deformation in low to medium grade terranes (Scott & St. Onge, 1995; Resor *et al.,* 1996).
In this study, titanite is exclusively found in the amphibolitic domains of the hydration zones, documenting that its growth was linked to fluid infiltration and metasomatism. In strongly foliated amphibolite felses (e.g. Fig. 2.28, Medvezhy Island) titanite occurs as well-orientated crystals with rhombic to sphenoidal cross-sections, that grew during dynamic re-crystallisation and thus may date not only metasomatic alteration but also concomitant shearing.

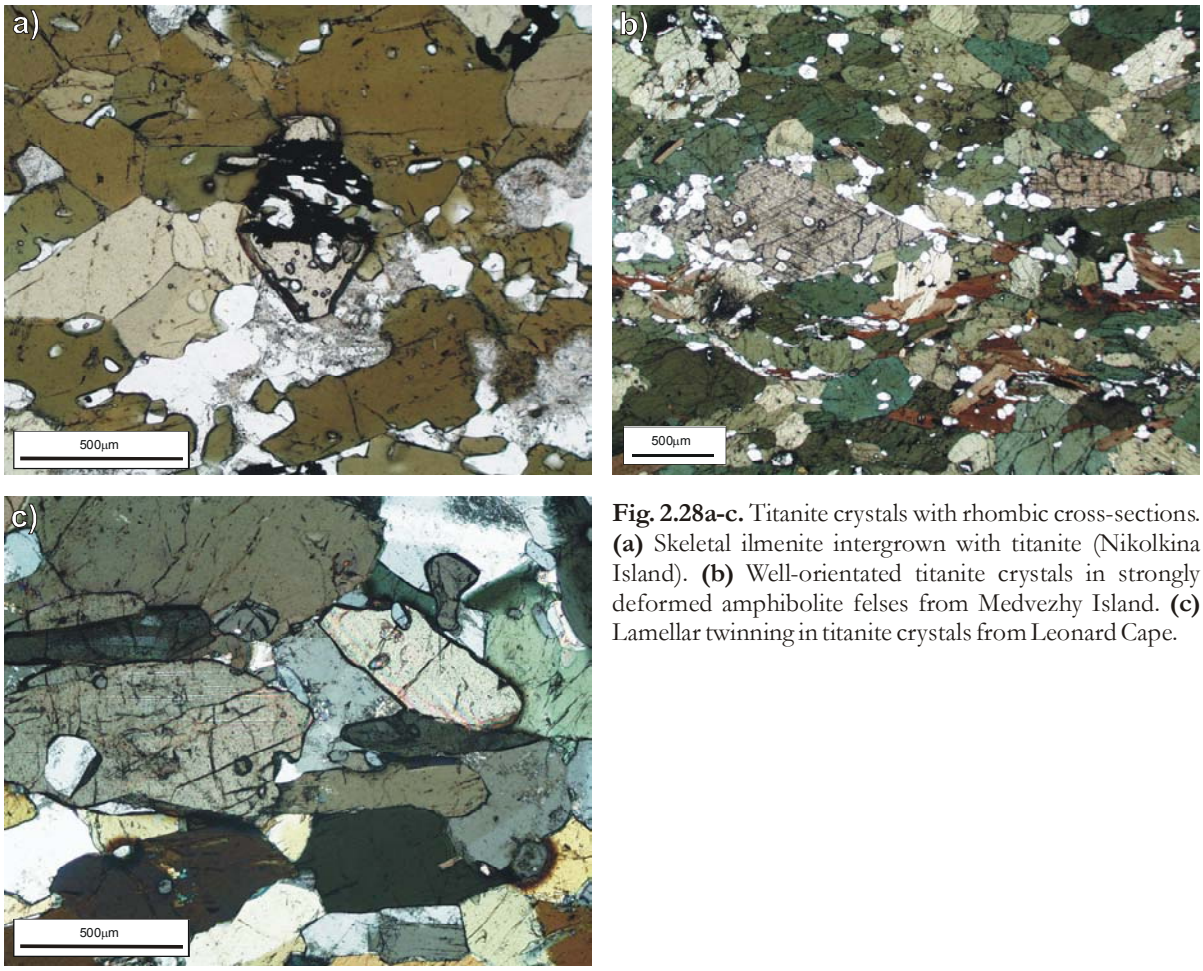

Fig. 2.28a-c. Titanite crystals with rhombic cross-sections. **(a)** Skeletal ilmenite intergrown with titanite (Nikolkina Island). **(b)** Well-orientated titanite crystals in strongly deformed amphibolite felses from Medvezhy Island. **(c)** Lamellar twinning in titanite crystals from Leonard Cape.

The closure temperature for diffusion of uranium and radiogenic lead is an important parameter, which describes the increasing influence of diffusive resetting compared to mineral growth (Frost *et al.*, 2000). Although new studies indicate that the U-Pb systematics of titanite are strongly influenced by recrystallisation or growth of new titanite (Verts *et al.*, 1996, Frost *et al.*, 2000), at high temperatures diffusive resetting may possibly occur. For a meaningful interpretation of geochronological data both, the closure behaviour of the U-Pb system as well as microtextures, must be considered. Previous estimates for the closure temperature of the U-Pb system in titanite range

from 500 to 630 °C for crystals of 500 – 1000 μm diameter (Gascoyne, 1986; Mezger *et al.*, 1991 & 1993). Experimental studies of Cherniak (1993) document closure temperatures of 640 and 670 °C for a diffusion radius of 500 μm and a cooling rate of 2 °C/Ma and 10 °C/Ma, respectively. Recent petrological studies point to higher closure temperatures in the range of 660 – 700 °C (Schärer *et al.*, 1994; Scott & St. Onge, 1995; Verts *et al.*, 1996; Essex *et al.*, 1997) and possibly even >700 °C (Pidgeon *et al.*, 1996; Zhang & Schärer, 1996). The inferred high closure temperatures suggest that U-Pb ages of titanite grown at amphibolite facies conditions presumably record crystallisation and are suitable to date metamorphism and deformation (Frost *et al.*, 2000).
Titanite crystals in the dated samples have a yellow to pale-brown colour and vary in size from 250 - 500 μm (Nikolkina Island & Leonard Cape) to 5 mm (Medvezhy Island). Occasional lamellar twinning is observed in titanite from Leonard Cape (Fig. 2.28: Leonard Cape). To avoid inclusions of and intergrowths with relict ilmenite (Fig. 2.28: Nikolkina Island), grain size fractions less than 250 μm were used for the geochronological study.

2.6.1.1 Analytical technique

Geochronological studies were performed at the Institute of Precambrian Geology and Geochronology (Russian Academy of Sciences, St. Petersburg) on a Finnigan MAT 261 8-collector mass-spectrometer in static mode.
Hand-picked titanite fractions were analysed following the method of Manhes *et al.* (1978) with some modification, namely U purification with UTHEVA resin (Horwitz *et al.*, 1992). All samples were spiked with a ^{235}U-^{208}Pb mixed tracer. Total blanks were 0.1 ng Pb and 0.005 ng U. Air-abrasion followed the technique of Krogh (1982). The PBDAT and ISOPLOT programs of Ludwig (1991, 1999) were used for calculating the uncertainties, correlations of U/Pb ratios, regression lines, concordia intercept ages and concordia ages. All errors are reported at the 2σ level. The decay constants of Steiger and Jäger (1977) were used for age calculation, and corrections for common Pb were made using the values of Stacey and Kramers (1975).

2.6.1.2 Results

Titanites of three amphibolitic samples from hydration zones at the localities Leonard Cape and Nikolkina Island (Kolvitsa Complex) and Medvezhy Island (Por'ya Guba Complex) were chosen for the U-Pb isotopic study. Grain-size fractions of < 250 μm were analysed and titanites were additionally subjected to air-abrasion.
The U concentrations range from 6 to 120 ppm (Tab. 2.10). Titanite from the retrogressed metabasite from Medvezhy Island is characterised by lowest U contents of 6 – 10 ppm, whereas titanite from the hydration zone of the basic dyke at Nikolkina Island shows higher U concentrations of *c.* 60 ppm. Titanite from the retrogressed metadiorite (Leonard Cape) has U concentrations up to 120 ppm and are thus about several magnitudes higher.
Three titanite fractions, one of them air-abraded, from the hydration zone of a metadiorite at Leonard Cape (sample: 0808-5) define a discordia line with an upper intercept at 1896.9 ±2.2 Ma (MSWD= 0.66) and a lower intercept at 378 ±230 Ma (Fig. 2.29a). Two near-concordant analyses yield a concordia age of 1896 ±4 Ma.
Two titanite fractions from the hydration zone of a basic dyke at Nikolkina Island (sample: 0308-K2) yield an identical $^{207}Pb/^{206}Pb$ age of 1896 Ma (±1 and 2 Ma, respectively) (Tab. 2.10). The two analyses are concordant within the 2 σ error and give a concordia age of 1898 ±4 Ma (Fig. 2.29b).
The three titanite fractions from Medvezhy Island (Por'ya Guba Complex) define a discordia line with intercepts at 1891.6 ±4.2 Ma and 435 ±110 Ma (MSWD= 1.2) (Fig. 2.29c). One air-abraded grain fraction (40%) overlaps the concordia and has a $^{207}Pb/^{206}Pb$ age of 1891 ±1 Ma (Tab. 2.10). Discordance expressed as deviation of the $^{207}Pb/^{206}Pb$ age from the $^{206}Pb/^{238}U$ age is 0.05 %. The resulting concordia age is 1891 ±4.8 Ma.

The lower intercept ages of titanites from Medvezhy Island (0508-10: 435 ±110 Ma) and Leonard Cape (0808-5: 378 ±230 Ma) are within error and point to a thermal or hydrothermal overprint in the Devonian.

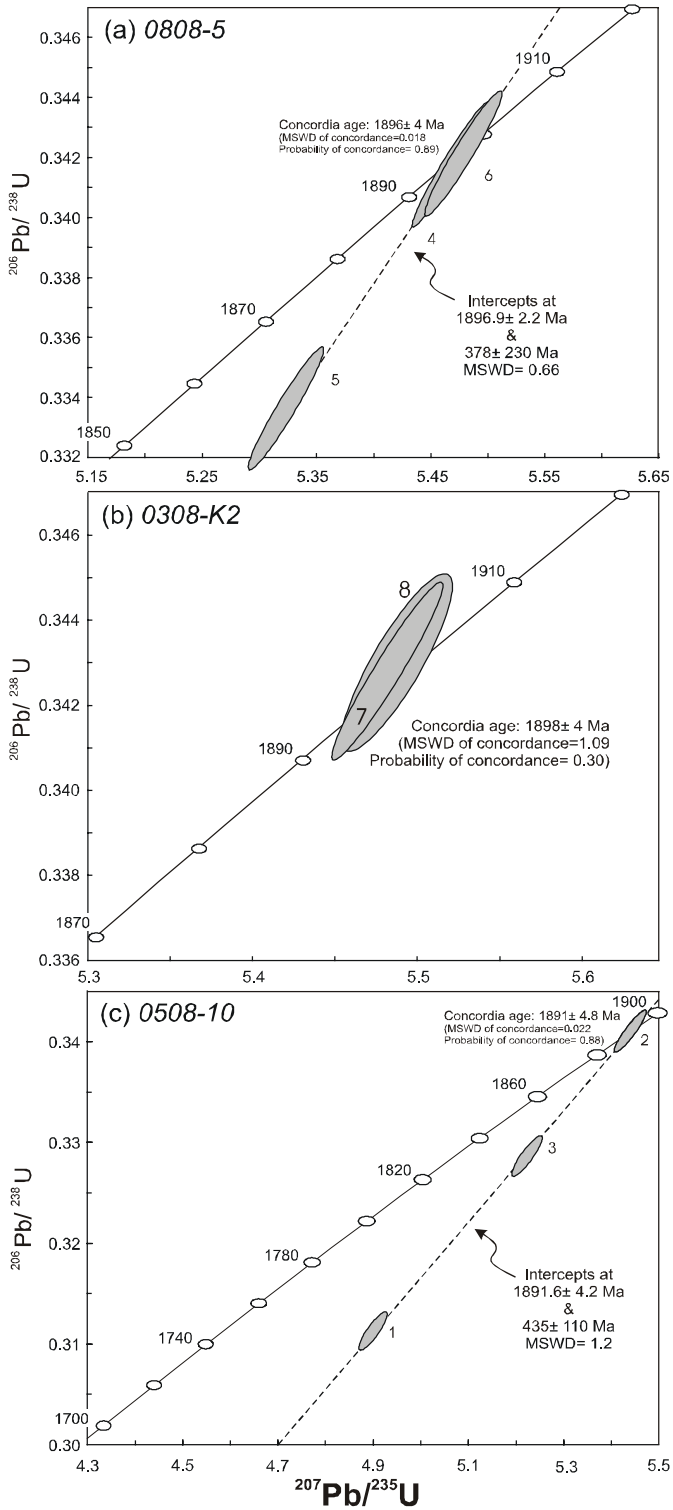

Fig. 2.29. U-Pb concordia diagrams for titanites from amphibolites of the Kolvitsa and Por'ya Guba Complex. Data-points are plotted as 2 σ error ellipses. **(a)** Titanites from sample 0808-5 (metadiorite, hydration zone II) of the Leonard outcrop define a discordia line. Two near-concordant analyses yielded $^{207}Pb/^{206}Pb$ ages of 1896 ± 1 Ma and 1898 ± 1 Ma. **(b)** U-Pb concordia diagram shows two concordant titanite analyses from sample 0308-K2 (metabasic dyke, hydration zone II, Nikolkina Island). The calculated $^{207}Pb/^{206}Pb$ age is 1898 ± 4 Ma. **(c)** Titanites from sample 0508-10 (amphibole fels, Medvezhy Island, Por'ya Guba Complex) define a discordia line with an upper intercept age of 1892 ± 4Ma . One analyses overlaps the concordia and has a $^{207}Pb/^{206}Pb$ age of 1891 ± 1 Ma.

Table 2.10. U-Pb isotope data for titanite < 250 μm from samples 0508-10 (amphibolite fels, Medvezhy Island, Por'ya Guba Complex), 0808-5 (metadiorite, Leonard Cape, Kolvitsa Complex) and 0308-K2 (basic dyke, Nikolkina Island, Kolvitsa Complex).

N	characteristic	Weight	Concentrations ppm		Isotopic ratios corrected for blank and common Pb[b]						Age, Ma			Disc.%[d]
		mg	Pb	U	$^{206}Pb/^{204}Pb$[a]	$^{207}Pb/^{206}Pb$	$^{208}Pb/^{206}Pb$	$^{207}Pb/^{235}U$	$^{206}Pb/^{238}U$	Rho[c]	$^{207}Pb/^{235}U$	$^{206}Pb/^{238}U$	$^{207}Pb/^{206}Pb$	
0508-10														
1		3.6	5.68	9.94	251	0.1142±1	0.7425±1	4.9001±98	0.3112±6	0.87	1802±4	1747±3	1867±1	-6.87
2	abr. 40%	4.93	3.83	6.04	241	0.1157±1	0.7585±1	5.4394±109	0.3410±7	0.92	1891±4	1892±4	1891±1	0.05
3	abr. 50%	2.02	4.9	7.55	169	0.1153±1	0.7651±1	5.2233±127	0.3286±7	0.89	1856±5	1831±4	1885±2	-2.95
0808-5														
4		2.66	41	104	1285	0.1160±1	0.1740±1	5.4676±109	0.3418±7	0.97	1896±4	1895±4	1896±1	-0.05
5		0.97	47.4	123	1059	0.1158±1	0.1632±1	5.3247±106	0.3336±7	0.96	1873±4	1856±4	1892±1	-1.94
6	abr. 50%	0.89	43.3	106	950	0.1161±1	0.1965±1	5.4786±110	0.3421±7	0.96	1897±4	1897±4	1898±1	-0.05
0308-K2														
7		2.18	30	66.7	757	0.1160±1	0.3215±1	5.4829±110	0.3428±7	0.96	1898±4	1900±4	1896±1	0.21
8	abr. 30%	0.41	26.2	58.1	486	0.1161±1	0.2863±1	5.4887±110	0.3430±7	0.86	1899±4	1901±4	1896±2	0.26

[a] measured ratio.

[b] uncertainties (95% confidence level) refer to last digits of corresponding ratios.

[c] correlation coefficients of $^{207}Pb/^{235}U$ versus $^{206}Pb/^{238}U$ ratios.

[d] Discordance expressed as deviation of the $^{207}Pb/^{206}Pb$ age from the $^{206}Pb/^{238}U$ age.

abr. 20%: amount of titanite removed during the air-abrasion.

2.6.1.3 Interpretation

Since titanite is exclusively bounded to the metasomatic hydration zones, growth of titanite can be attributed to hydration under amphibolite facies conditions. Orientated titanite crystals in dynamically recrystallised amphibolites are not only evidence for syn-metamorphic but also for syn-kinematic mineral growth.

U-Pb titanite data define near concordant or upper intercept ages ranging from 1891 to 1898 Ma. The lower intercept ages have larger errors and vary from 378 ±230 Ma to 435 ±110 Ma. Magmatic ages for carbonatitic to lamprophyric dykes from the Kandalaksha area document Devonian alkaline magmatism *c.* 370 – 380 Ma ago (U-Pb zircon ages: Claesson *et al.*, 2000 & K-Ar ages: Beard et al., 1996). Thus Devonian lower intercept ages point to thermal influence by alkaline magmatism.

Whether U-Pb titanite ages date the growth during hydration and deformation or date the cooling through the closure temperature, depends on the prevailing *P-T* conditions and the assumed closure temperature (T_C) for lead diffusion in titanite. Temperature estimates for the hydration stage were obtained from Hbl-Pl and Grt-Hbl thermometry and multi-equilibrium thermobarometry (TWEEQU *1.02*, Berman, 1988 & 1991) and yielded 650 – 730 °C. Since the high closure temperatures inferred in recent studies (650 – 700 °C: Cherniak, 1993; Schärer *et al.*, 1994; Scott & St. Onge, 1995; Essex *et al.*, 1997; > 700 °C: Pidgeon *et al.*, 1996; Zhang & Schärer, 1996) are in the same order as the metamorphic temperature estimates, the U-Pb ages should date the growth of titanite rather than the cooling through the closure temperature. However, if lower closure temperatures are assumed (500 – 630 °C; Gascoyne, 1986; Mezger *et al.*, 1991 & 1993), the U-Pb ages would date cooling.

Although recent work points to T_C in the range of upper amphibolite facies thermal conditions, recrystallisation and growth of new titanite becomes important and may outrank diffusive resetting during metamorphism (Verts *et al.*, 1996; Frost *et al.*, 2000). The Dodson-type model for closure temperatures, applying for volume diffusion only, account for cooling rates, diffusion radii and the activation energy for diffusion in the particular mineral (Dodson, 1973; McDougall & Harrison, 1988; Spear, 1993). The diffusion radius, on the other hand, may not be equivalent to the grain-size (Frost et al., 2000), and the likely effects of fluids, micro-cracks, strain (dislocations, deffects) and mineral composition are not considered in the Dodson-type models (Miller, 2001) and strongly influence non-diffusive mechanisms such as recrystallisation and mineral growth.

For example, strain is focused in shear zones and these may act as pathways for fluids. The attendance of reactive fluids may lower the crystallisation temperature as well as the closure temperature and may cause the growth or complete re-crystallisation of titanite (Pan *et al.*, 1993; Resor *et al.*, 1996; Verts *et al.*, 1996; Bibikova *et al.*, 2001). Due to the complex control of mobilisation of uranium or radiogenic lead, the concept of a single closure temperature for a specific mineral is possibly erroneous.

Obviously, a comprehensive understanding of the geological environment and the micro-textural and petrological relationships/characteristics is indispensable for a meaningful interpretation of U-Pb titanite data. In this study, the microtextural features and the similar morphology, colour, uranium and lead contents of titanite point to a single stage metamorphic growth and the U-Pb ages thus are likely to date the crystallisation of titanite.

2.6.2 ^{40}Ar-^{39}Ar mineral ages

2.6.2.1 Analytical technique

For ^{40}Ar-^{39}Ar dating, hornblende and biotite from hydration zones of the four studied localities were separated by conventional magnetic separation techniques. Pure aliquots of 80 – 100 mg were obtained by hand-picking from the 125 – 250 μm grain size fractions. The concentrates were irradiated at the Budapest nuclear research reactor in the Atomic Energy Research Institute (Hungary). After a cooling period of *c.* 3 months, ^{40}Ar/^{39}Ar step-heating analyses were performed at the Institute of Geology, University of Vienna. A detailed description of the analytical techniques is given by Frimmel & Frank (1998).
Aliquots of irradiated amphibole and biotite separates (25 – 70 mg) were filled in annealed cylindrical tantalum capsules and were incrementally step-heated, using a high vacuum resistance furnace. The Ar-extraction and purification line is mainly made of glass and were manufactured in-house at the Geological Institute (University of Vienna). The radio frequency (RF)-induction furnace is made of quartz glass and the hot portion of the extraction furnace is double-walled. Ar was released through step-wise heating in the temperature range from 800 – 1300 °C for the amphibole and 580 – 1250 °C for the biotite. Depending on the degassing behaviour, temperature increments varied from 5 to 50 °C. Temperatures were monitored with a calibrated pyrometer. The energy output of the radio frequency generator is controlled by the pyrometer reading. The stability of the pre-set diffusion temperature is within 1 °C. Because of the quick temperature rise, practically no overheating occurred.
The released gases were cleaned by a combination of cold traps, Ti-sponge- and a SAE-getters. Subsequent isotopic measurements were carried out with a VG-5400 gas mass spectrometer. Data were corrected for mass discrimination and radioactive decay from irradiation-induced Ar-isotopes derived from Ca, K, Cl and ^{37}Ar & ^{39}Ar, respectively. Correction factors used were: $(^{36}Ar/^{37}Ar)_{Ca}$= 0.00027, $(^{39}Ar/^{37}Ar)_{Ca}$= 0.00039, $(^{40}Ar/^{39}Ar)_{K}$= 0.0254. The K/Ca ratio is obtained from the ^{39}Ar/^{37}Ar ratio using the conversion factor of 0.247. This factor was determined from a plagioclase with uniform and well known composition. The *J*-value was obtained from internal laboratory standards, calibrated by international standards (muscovite Bern 4M, Burghele (1987); amphibole Mm 1Hb, Samson & Alexander (1987); Fish Canyon sanidine, Renne *et al.* (1994)).
Ages were calculated using the decay constant recommended by Steiger & Jäger (1977). Ages of individual steps do not include the uncertainty in the *J*-value and have analytical error only (1 σ level). Plateau ages are weighted mean values for at least three consecutive steps with similar apparent Ca/K ratios, representing ≥ 55 % of the released ^{39}Ar. *J*-value uncertainty (±0.4%) is included in the errors of the plateau and total gas ages.

2.6.2.2 Age spectra of hornblende

In this study, seven amphibole concentrates from hydration profiles at three contrasting localities were analysed. The ^{40}Ar/^{39}Ar data are given in Tables 2.11 – 2.14 and illustrated in Figures 2.30 – 2.33.

Leonard Cape

The studied hydration zone at Leonard Cape, close to the south-western margin of the Kolvitsa Complex, developed in metadiorite (0808-3, 0808-4, 0808-5 and 0808-6).
Samples 0808-4, 0808-5 and 0808-6 represent a sequence of samples ranging from weak to complete hydration (zone I – zone III). Total gas ages as well as plateau ages increase with the degree of hydration from 1907.7 ±10.1 Ma to 1929.1 ±11.0 Ma and from 1880.3 ±11.3 Ma to 1925.5 ±9.6 Ma respectively (Fig. 2.30a – c).

The age spectrum of the metadiorite (0808-4) from zone I, shows progressively decreasing apparent ages, indicating excess argon diffusing from grain boundaries towards the cores of the grains (Fig. 2.30a & Tab. 2.11). Hornblende from this sample yielded a total gas age of 1907.7 ±10.0 Ma. The plateau age of 1880.3 ±11.3 Ma is defined by 5 steps and an ^{39}Ar release of 32 % only. Due to massive degassing at 1020 °C with 63.9 % of the ^{39}Ar released, heating with smaller temperature increments should result in a better plateau age. Because of misleading young apparent ages (*c.* 1.6 Ga) between 840 and 920 °C (technical problems), steps 2 – 5 with a gas volume of 3.2 % were eliminated from the age spectrum. Uniform Ca/K ratios in conformity with results from EMP analysis indicate a single hornblende generation.

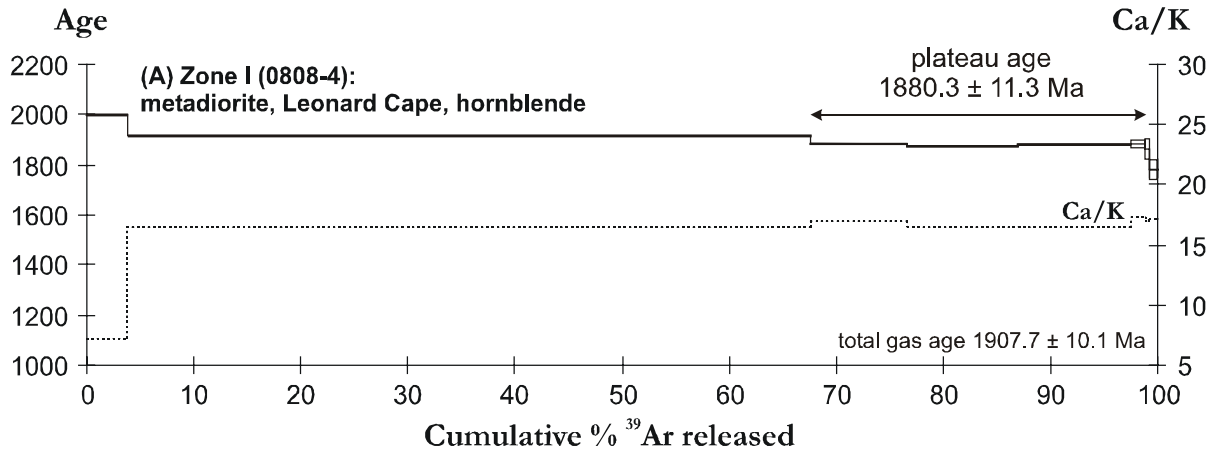

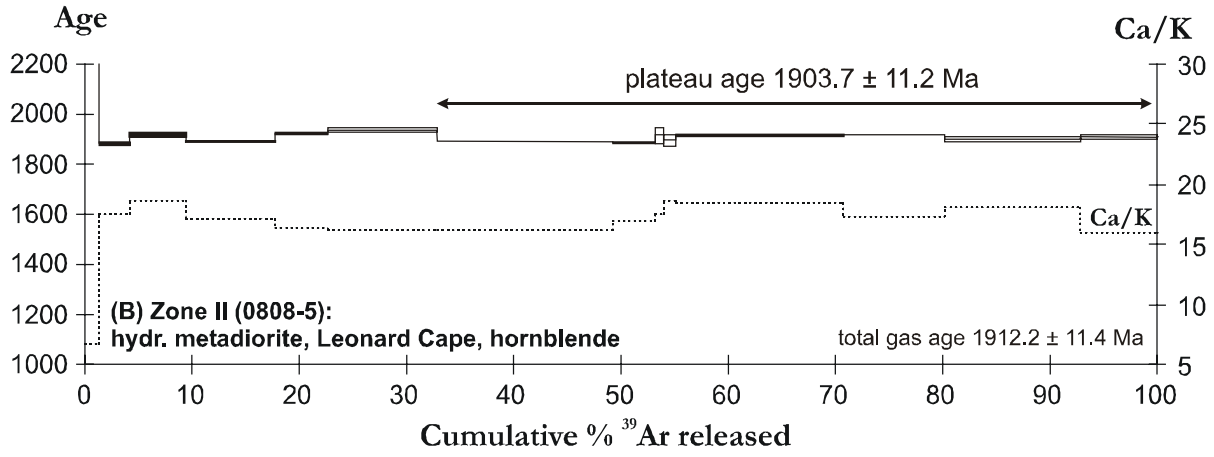

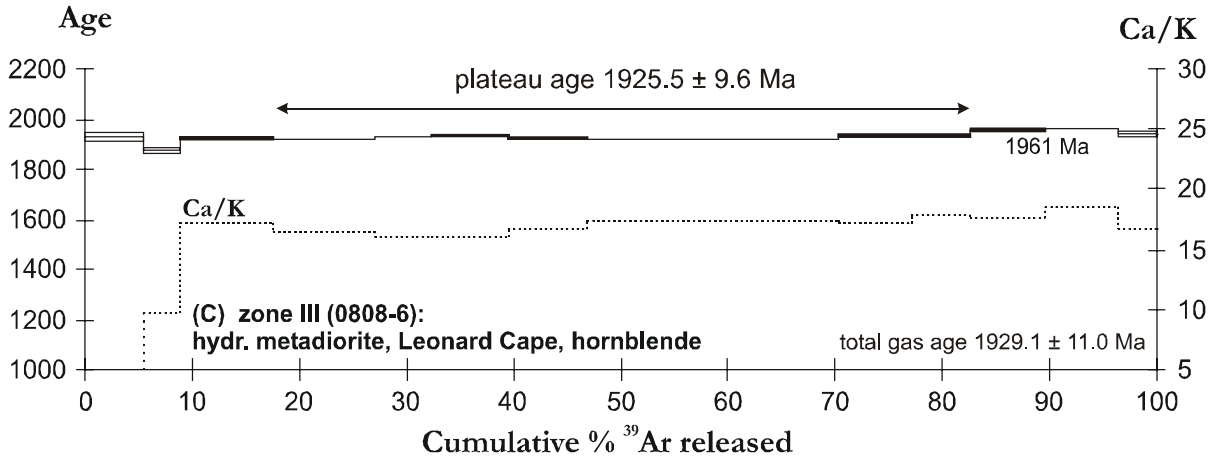

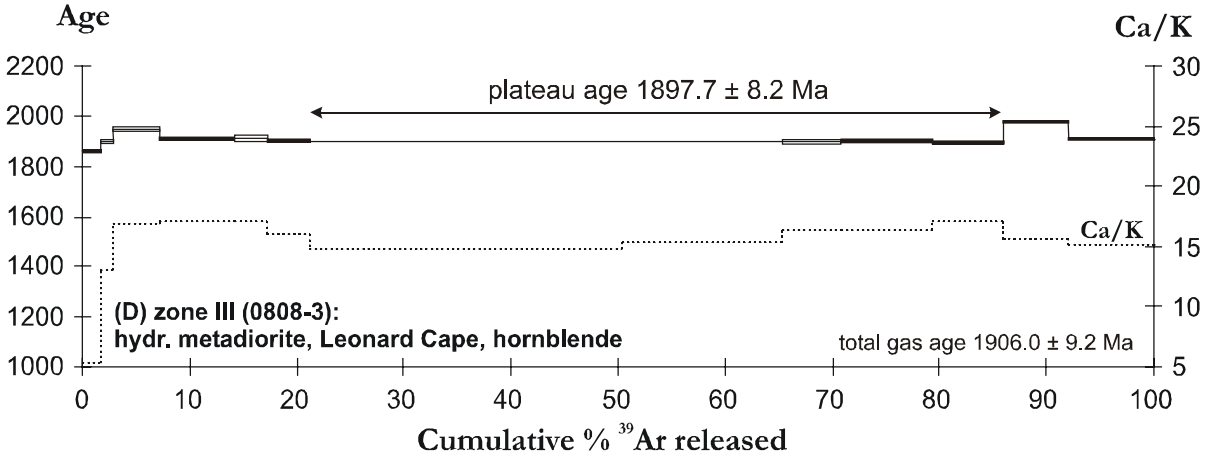

Fig.2.30a-d. $^{40}Ar/^{39}Ar$ age spectra and Ca/K spectra of hornblende from metadiorites affected by different degrees of fluid infiltration (Leonard Cape).

Hornblende from sample 0808-5 (zone II) yielded a total gas age of 1912.2 ±11.4 Ma (Fig. 2.30b & Tab. 2.11). Eight consecutive steps with 67 % of the ^{39}Ar released define a plateau age of 1903.7 ±11.2 Ma. The first apparent age step is discordant and points to excess argon bound to mineral rims or to the presence of a K-rich mineral phase (low Ca/K ratio). Ca/K ratios show little intra-sample variation and do not correlate with apparent step ages.

Sample 0808-6 (zone III) was strongest affected by fluid infiltration and is characterised by a total gas age of 1929.1 ±11.10 Ma (Fig. 2.30c & Tab. 2.11). The plateau age of 1925.5 ±9.6 Ma is defined by seven steps, including 65 % of the released ^{39}Ar. Low Ca/K ratios in the first two steps (1.8 & 9.8) are attributed to the presence of K-bearing mineral phases, such as biotite intergrown at the amphibole rims. 13.8 % of the ^{39}Ar released, degassed at higher temperatures (1120 – 1140 °C) and yielded higher apparent ages of *c.* 1960 Ma and may be attributed to older domains in the mineral cores. Contrary to zones I and II (0808-4 & 0808-5), the mineral rims do not contain excess argon.

Sample 0808-3 represents the completely hydrated central part (zone III) of a further hydration zone (zone III) developed in a metadiorite from the Leonard outcrop. The obtained total gas age is 1906.0 ±9.2 Ma (Fig. 2.30d & Tab. 2.12). The plateau age is defined by 6 consecutive steps with 69 % of the ^{39}Ar released and yielded 1897.7 ±8.2 Ma. The outer mineral rims do not contain excess argon and are characterised by low Ca/K ratio (5.3). At lower temperatures (800 – 955 °C) mineral rims show a slight argon gain, pointing to the presence of excess argon. 70 % of the age spectrum is characterised by a homogeneous age distribution and uniform Ca/K ratios (*c.* 16). ^{39}Ar released at high temperature (1140 °C) yielded an apparent age of 1975.1 ±5.3 Ma and may point to older core domains. No correlation exists between Ca/K ratios and apparent ages.

Table 2.11. $^{40}Ar/^{39}Ar$ data of hornblende in samples across a hydration zone at Leonard Cape (0808-4 to 0808-6).

zone I (0808-4): pristine metadiorite; weight: 39.9 mg										
J: 0.010675 ± 0.4										
Step	T[°C]	$^{39}Ar_K$ (%)	$^{40}Ar^*$ (mV)	$^{40}Ar^*$ (%)	$^{39}Ar_K/^{37}Ar_{Ca}$	Ca/K	^{36}Ca (%)	$^{40}Ar^*/^{39}Ar_K$	Age Ma	error (1σ)
1	800	3.7%	335.35	97.3%	0.554	7.3	2.66%	190.20	1999.0	6.5
6	1020	63.9%	5410.04	99.8%	0.246	16.4	57.02%	177.66	1917.6	3.0
7[a]	1060	9.2%	754.82	99.7%	0.239	16.9	37.00%	172.68	1884.1	3.9
8[a]	1100	10.3%	838.34	99.7%	0.247	16.4	43.26%	171.19	1874.0	4.0
9[a]	1150	10.5%	868.22	99.7%	0.247	16.4	43.32%	172.70	1884.2	4.7
10[a]	1200	1.3%	103.81	99.0%	0.233	17.4	16.54%	171.71	1877.5	16.6
11[a]	1250	0.4%	32.70	95.2%	0.237	17.1	3.82%	169.23	1860.6	36.8
12	1300	0.8%	60.06	95.5%	0.236	17.1	4.40%	158.40	1784.7	36.5
		100.0%	Total gas age:	1907.7 ± 10.1 Ma				32% [a]Plateau age:	1880.3 ± 11.3 Ma	

zone II (0808-5): hydrated metadiorite, transition zone (Leonard Cape); weight: 44.6 mg										
J: 0.010675 ± 0.4										
Step	T[°C]	$^{39}Ar_K$ (%)	$^{40}Ar^*$ (mV)	$^{40}Ar^*$ (%)	$^{39}Ar_K/^{37}Ar_{Ca}$	Ca/K	^{36}Ca (%)	$^{40}Ar^*/^{39}Ar_K$	Age Ma	error (1σ)
1	800	1.3%	215.94	97.9%	0.598	6.8	2.57%	241.36	2300.0	12.2
2	920	2.9%	353.57	99.0%	0.232	17.5	16.37%	172.23	1883.0	7.7
3	955	5.1%	637.94	99.7%	0.218	18.5	41.22%	177.42	1917.8	5.6
4	980	8.3%	1009.31	99.9%	0.237	17.1	66.41%	173.46	1891.3	1.9
5	995	5.0%	622.16	99.9%	0.246	16.4	64.28%	177.56	1918.7	5.1
6	1003	10.1%	1283.29	99.9%	0.251	16.1	65.77%	180.60	1938.9	9.0
7[a]	1010	16.5%	2008.25	100.0%	0.250	16.2	84.68%	173.62	1892.3	2.8
8[a]	1015	4.0%	478.89	99.9%	0.238	17.0	72.53%	172.54	1885.1	6.8
9[a]	1020	0.7%	86.02	99.6%	0.232	17.4	36.68%	176.93	1914.6	33.2
10[a]	1035	1.0%	126.19	99.6%	0.216	18.7	33.00%	174.23	1896.5	26.0
11[a]	1080	15.8%	1953.69	99.9%	0.220	18.4	61.15%	176.78	1913.6	3.5
12[a]	1105	9.4%	1170.45	99.8%	0.235	17.3	57.08%	177.31	1917.1	3.2
13[a]	1140	12.6%	1543.57	99.9%	0.225	18.0	72.82%	174.60	1898.9	7.4
14[a]	1300	7.1%	881.83	98.4%	0.252	16.1	9.90%	176.13	1909.3	10.5
		100.0%	Total gas age:	1912.2 ± 11.4 Ma				67% [a]Plateau age:	1903.7 ± 11.2 Ma	

zone III (0808-6): hydrated metadiorite, centre of hydration (Leonard Cape); weight: 67.6mg										
J: 0.010675 ± 0.4										
Step	T[°C]	$^{39}Ar_K$ (%)	$^{40}Ar^*$ (mV)	$^{40}Ar^*$ (%)	$^{39}Ar_K/^{37}Ar_{Ca}$	Ca/K	^{36}Ca (%)	$^{40}Ar^*/^{39}Ar_K$	Age Ma	error (1σ)
1	800	5.4%	864.73	98.9%	2.254	1.8	1.79%	178.57	1925.5	15.5
2	920	3.5%	542.84	99.3%	0.415	9.8	14.52%	171.56	1878.4	11.8
3	955	8.5%	1362.12	99.8%	0.235	17.2	45.57%	178.76	1926.7	4.1
4[a]	980	9.5%	1509.24	99.8%	0.247	16.4	56.08%	177.57	1918.8	4.8
5[a]	995	5.4%	859.96	99.9%	0.253	16.0	57.46%	179.05	1928.7	3.7
6[a]	1003	7.2%	1156.24	99.9%	0.251	16.1	67.01%	179.88	1934.1	6.8
7[a]	1008	7.3%	1155.14	100.0%	0.244	16.6	85.32%	178.37	1924.1	5.8
8[a]	1040	23.4%	3714.04	99.9%	0.233	17.4	79.63%	177.77	1920.1	1.2
9[a]	1070	6.9%	1102.21	99.8%	0.235	17.2	54.60%	179.89	1934.2	3.6
10[a]	1090	5.4%	869.56	99.8%	0.227	17.8	52.70%	180.34	1937.2	6.2
11	1120	7.1%	1164.23	99.8%	0.229	17.7	54.59%	183.58	1958.4	4.7
12	1140	6.7%	1100.78	99.9%	0.219	18.5	70.29%	183.98	1960.9	3.6
13	1300	3.7%	589.20	99.7%	0.244	16.6	40.92%	180.47	1938.0	8.1
		100.0%	Total gas age:	1929.1 ± 11.0 Ma				65% [a]Plateau age:	1925.5 ± 9.6 Ma	

$^{40}Ar^*$: radiogenic ^{40}Ar; $^{39}Ar_K$: formed from K; $^{37}Ar_{Ca}$: formed from Ca; errors of plateau ages & total gas ages include an uncertainty (0.4%) in the *J*-value, apparent step ages only account for the analytical errors; correcting factors:Daly/Hf: 150 ± 5.0; $(^{40}Ar/^{36}Ar)_{air}$: 299 ±1.0; $(^{36}Ar/^{37}Ar)_{Ca}$: 0.00027; $(^{39}Ar/^{37}Ar)_{Ca}$: 0.00039; $(^{40}Ar/^{39}Ar)_K$: 0.0254; K/Ca-conversion factor: 0.247.

Nikolkina Island

At the studied locality on Nikolkina Island, located opposite to the coast of Kochinny Cape (Kolvitsa Complex), fluid infiltration proceeding from a felsic vein caused hydration of a basic dyke. Sample 0308-K2 from the outer part of the infiltration zone (zone II) yielded a total gas age of 1963.6 ±10.1 Ma (Fig. 2.31a & Tab. 2.12). The first two discordant steps of the age spectrum are characterised by high apparent ages up to 3630 Ma, pointing to excess argon bound to the mineral rims and fractures. In the first third of the age spectrum, diffusion of excess argon from the grain boundaries towards the cores caused decreasing apparent ages. This argon is bound to less-retentive sites as documented by 36.2 % of the ^{39}Ar released at low temperatures (800 – 980 °C). At higher temperatures (1000 – 1300 °C) the plateau age is defined by eight consecutive steps with an ^{39}Ar release of 64 % and yielded 1922.9 ±11.1 Ma. The Ca/K ratio does not correlate with the apparent ages. Ca-rich impurities in the mineral rims caused elevated Ca/K ratios (16 – 22), while 93 % of the age spectrum is characterised by uniform Ca/K ratios (14).

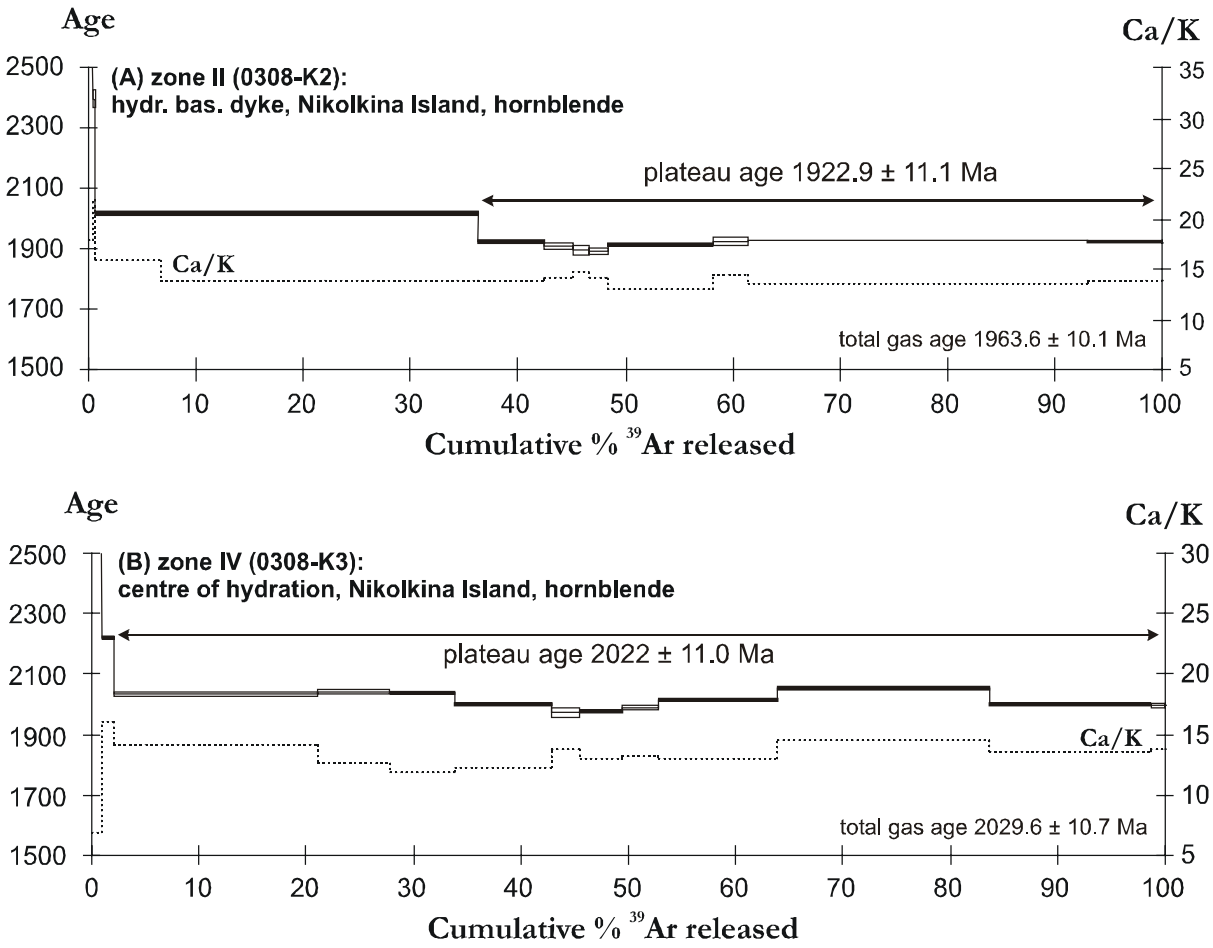

Fig. 2.31a-b. ^{40}Ar/^{39}Ar age spectra and Ca/K spectra of hornblende from hydration zones on Nikolkina Island.

The almost monomineralic amphibolite sample 0308-K3 from the centre of the infiltration zone (zone IV) yielded a total gas age of 2029.6 ±10.7 Ma (Fig. 2.31b & Tab. 2.12). At low temperatures (800 – 890 °C) two steps with high apparent ages (up to 2584 Ma) are caused by excess argon. A low Ca/K ratio points to contamination by a K-rich phase, possibly biotite. 98 % of the released ^{39}Ar defines a plateau age (11 steps) of 2022.4 ±10.7 Ma. Part of the degassed argon (18.9 %) was only weakly bound and released at low temperatures (step 3: 955 °C). The high plateau age points to excess argon that was homogeneously distributed in the mineral grains. Partial rejuvenation (steps 6 – 10) may have been caused by later argon loss.

Table 2.12. $^{40}Ar/^{39}Ar$ data of hornblende in hydration zones from Leonard Cape and Nikolkina Island.

zone III (0808-3): hydrated metadiorite (Leonard Cape); weight:54.7 mg *J*: 0.010675 ± 0.4

Step	T[ºC]	$^{39}Ar_K$ (%)	$^{40}Ar^*$ (mV)	$^{40}Ar^*$ (%)	$^{39}Ar_K/^{37}Ar_{Ca}$	Ca/K	^{36}Ca (%)	$^{40}Ar^*/^{39}Ar_K$	Age Ma	error (1σ)
1	800	1.7%	251.33	98.0%	0.765	5.3	2.95%	168.91	1860.3	3.1
2	890	1.2%	176.73	99.0%	0.312	13.0	12.44%	174.85	1900.7	9.3
3	955	4.4%	677.68	99.7%	0.241	16.8	39.79%	181.58	1945.3	9.3
4	975	6.9%	1047.40	99.9%	0.236	17.1	58.92%	176.54	1912.0	6.5
5	990	3.1%	467.64	99.9%	0.238	17.0	70.99%	176.28	1910.3	8.6
6[a]	1000	3.9%	585.38	99.9%	0.254	16.0	77.09%	175.53	1905.2	4.8
7[a]	1010	29.1%	4346.70	100.0%	0.273	14.8	86.24%	174.33	1897.2	1.7
8[a]	1025	15.0%	2236.31	99.9%	0.263	15.4	80.48%	174.28	1896.8	2.0
9[a]	1035	5.5%	822.78	99.9%	0.247	16.4	67.41%	174.48	1898.2	5.4
10[a]	1080	8.5%	1273.07	99.9%	0.247	16.4	73.72%	174.79	1900.2	4.1
11[a]	1100	6.6%	985.77	99.9%	0.236	17.1	69.53%	173.90	1894.2	4.3
12	1140	6.0%	957.59	100.0%	0.259	15.6	97.96%	186.16	1975.1	5.3
13	1300	8.0%	1205.14	99.8%	0.268	15.1	45.10%	175.96	1908.1	2.7
		100.0%	Total gas age:	1906.0 ± 9.2 Ma				69% [a]Plateau age:	1897.7 ± 8.2 Ma	

zone II (0308-K2): hydrated basic dyke, transition zone (Nikolkina Island); weight: 44.4 mg *J*: 0.010675 ± 0.4

Step	T[ºC]	$^{39}Ar_K$ (%)	$^{40}Ar^*$ (mV)	$^{40}Ar^*$ (%)	$^{39}Ar_K/^{37}Ar_{Ca}$	Ca/K	^{36}Ca (%)	$^{40}Ar^*/^{39}Ar_K$	Age Ma	error (1σ)
1	800	0.3%	149.74	96.6%	0.227	17.8	1.61%	606.43	3630.1	8.2
2	880	0.3%	61.99	93.4%	0.185	21.9	2.28%	263.23	2414.1	20.6
3	955	6.1%	897.80	99.5%	0.258	15.7	23.64%	193.14	2019.5	4.3
4	980	29.5%	4355.76	99.8%	0.295	13.7	39.45%	192.78	2017.3	1.8
5[a]	1000	6.2%	852.54	99.5%	0.293	13.8	23.72%	178.42	1924.5	5.2
6[a]	1005	2.6%	344.95	99.8%	0.286	14.2	46.78%	176.23	1909.9	10.7
7[a]	1010	1.7%	220.87	99.7%	0.277	14.6	38.44%	174.16	1896.0	14.2
8[a]	1015	1.7%	224.06	99.8%	0.285	14.2	46.98%	173.97	1894.7	12.0
9[a]	1035	9.9%	1335.70	99.9%	0.309	13.1	65.71%	176.75	1913.4	6.7
10[a]	1060	3.2%	433.45	99.8%	0.283	14.3	50.11%	178.18	1922.9	14.8
11[a]	1120	31.7%	4350.53	99.9%	0.298	13.6	74.24%	179.16	1929.4	3.0
12[a]	1300	6.9%	935.18	99.7%	0.295	13.7	33.07%	178.21	1923.0	6.2
		100.0%	Total gas age:	1963.6 ± 10.1 Ma				64% [a]Plateau age:	1922.9 ± 11.1 Ma	

zone IV (0308-K3): hydrated basic dyke, centre of hydration (Nikolkina Island); weight: 35 mg *J*: 0.010675 ± 0.4

Step	T[ºC]	$^{39}Ar_K$ (%)	$^{40}Ar^*$ (mV)	$^{40}Ar^*$ (%)	$^{39}Ar_K/^{37}Ar_{Ca}$	Ca/K	^{36}Ca (%)	$^{40}Ar^*/^{39}Ar_K$	Age Ma	error (1σ)
1	800	0.9%	171.44	98.6%	0.592	6.8	3.07%	298.40	2583.8	11.2
2	890	1.2%	179.94	99.0%	0.253	16.0	12.15%	227.58	2224.2	3.9
3[a]	955	18.9%	2451.11	99.8%	0.284	14.2	42.15%	195.35	2033.4	5.5
4[a]	975	6.8%	891.88	99.8%	0.319	12.7	47.84%	196.75	2042.2	5.8
5[a]	990	6.0%	786.77	99.9%	0.341	11.9	51.47%	196.45	2040.3	4.8
6[a]	1000	9.0%	1128.08	99.9%	0.328	12.3	60.78%	189.83	1998.6	3.7
7[a]	1005	2.7%	327.11	99.8%	0.295	13.7	46.22%	186.23	1975.5	14.1
8[a]	1015	3.9%	477.41	99.8%	0.309	13.1	39.91%	186.72	1978.7	5.0
9[a]	1035	3.4%	428.64	99.7%	0.307	13.2	34.45%	188.66	1991.2	8.0
10[a]	1070	11.0%	1407.24	99.8%	0.311	13.0	41.72%	192.36	2014.6	4.3
11[a]	1100	19.8%	2612.49	99.8%	0.280	14.5	49.58%	198.85	2055.1	2.5
12[a]	1130	14.9%	1876.87	99.9%	0.298	13.6	62.33%	189.69	1997.7	3.3
13[a]	1170	1.4%	176.27	99.6%	0.292	13.9	26.91%	189.35	1995.6	7.5
		100.0%	Total gas age:	2029.6 ± 10.7 Ma				98% [a]Plateau age:	2022.4 ± 10.7 Ma	

$^{40}Ar^*$: radiogenic ^{40}Ar; $^{39}Ar_K$: formed from K; $^{37}Ar_{Ca}$: formed from Ca; errors of plateau ages & total gas ages include an uncertainty (0.4%) in the *J*-value, apparent step ages only account for the analytical errors; correcting factors: see Table 2.11.

Bolschoi Khed

A monomineralic amphibolite fels (sample 0708-5) from Bolschoi Khed Island (south-eastern Kolvitsa Complex), represents a completely hydrated end-member of fluid infiltration, developed in a metagabbro. Hornblende from this sample is characterised by a total gas age of 2213.3 ±12.8 Ma (Fig. 2.32 & Tab. 2.13). The obtained age spectrum is discordant and shows a stepwise decrease of apparent ages at lower temperatures and a saddle-shaped pattern at higher temperatures. High apparent ages at lower temperatures (780 – 920 °C) are due to extreme amounts of excess argon. Since no secondary alteration of the hornblende was observed, this argon was presumably derived/released from micro-fractures before diffusion in the amphibole lattice started.

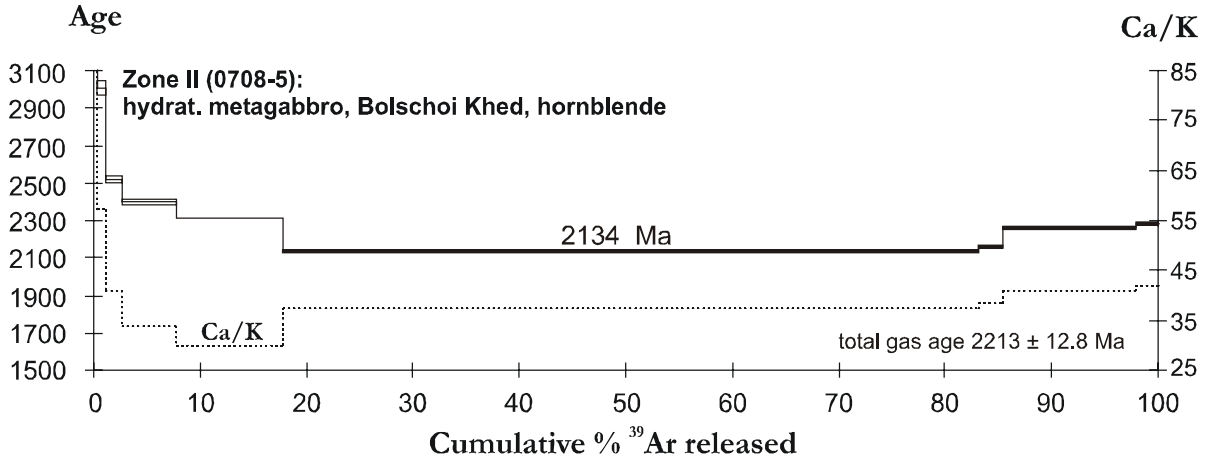

Fig. 2.32. $^{40}Ar/^{39}Ar$ age spectrum and Ca/K spectrum of a hornblende from a hydrated metagabbro at Bolschoi Khed.

The high Ca/K ratio is evidence for Ca-rich impurities degassing at lower temperatures. Hornblende from sample 0708-5 degassed over a narrow temperature range with 65.3 % of the ^{39}Ar released at 1030 °C (step 7). The apparent age of step 7 yielded 2133.5 ±4.2 Ma and defines the lowest apparent age of the saddle-shaped age spectrum. The high apparent ages pointing to an excess argon component that was homogeneously distributed in the mineral. Partial rejuvenation was presumably due to thermal loss of the excess argon after formation of the hornblende.

Table 2.13. $^{40}Ar/^{39}Ar$ data of a hornblende separate at Bolschoi Khed (zone II).

0708-5: hydrated metagabbro (Bolschoi Khed Island); weight: 22.3 mg										
Step	T[°C]	$^{39}Ar_K$ (%)	$^{40}Ar^*$ (mV)	$^{40}Ar^*$ (%)	$^{39}Ar_K/^{37}Ar_{Ca}$	Ca/K	^{36}Ca (%)	$^{40}Ar^*/^{39}Ar_K$	Age Ma	error (1σ)
1	780	0.2%	207.62	99.8%	0.019	214.5	26.00%	5232.23	7292.3	22.0
2	860	0.1%	27.49	97.0%	0.037	109.4	5.45%	1239.50	4792.6	37.1
3	920	0.8%	49.27	95.0%	0.071	57.1	5.13%	401.89	3006.5	36.3
4[a]	955	1.6%	72.28	99.1%	0.099	40.7	24.55%	283.94	2515.9	22.9
5[a]	990	5.1%	219.21	99.3%	0.120	33.8	28.23%	260.88	2402.2	15.1
6[a]	1005	10.0%	399.86	99.3%	0.136	29.8	24.91%	243.03	2309.0	3.9
7[a]	1030	65.3%	2264.70	99.7%	0.108	37.5	51.70%	211.82	2133.5	4.2
8[a]	1050	2.3%	80.25	97.7%	0.105	38.4	12.99%	215.87	2157.2	7.6
9[a]	1180	12.5%	478.79	99.3%	0.099	40.9	34.98%	234.07	2260.3	6.8
10[a]	1300	2.1%	80.72	95.8%	0.097	41.9	7.34%	238.29	2283.4	8.7
		100.0%	Total gas age:	2213.2 ± 12.8 Ma				99% [a]Plateau age:	2191.0 ± 12.4 Ma	

$^{40}Ar^*$: radiogenic ^{40}Ar; $^{39}Ar_K$: formed from K; $^{37}Ar_{Ca}$: formed from Ca; errors of plateau ages & total gas ages include an uncertainty (0.4%) in the *J*-value, apparent step ages only account for the analytical errors; correcting factors:Daly/Hf: 150 ± 5.0; $(^{40}Ar/^{36}Ar)_{air}$: 299 ±1.0; $(^{36}Ar/^{37}Ar)_{Ca}$: 0.00027; $(^{39}Ar/^{37}Ar)_{Ca}$: 0.00039; $(^{40}Ar/^{39}Ar)_K$: 0.0254; K/Ca-conversion factor: 0.247.

Medvezhy Island (Por'ya Guba Complex)

Sample 0508-10 is a biotite and titanite bearing amphibolite fels from Medvezhy Island, developed through fracture-controlled fluid infiltration in a metabasite. Biotite yielded a total gas age of 2091.7 ±14.2 Ma (Fig. 2.33 & Tab. 2.14).

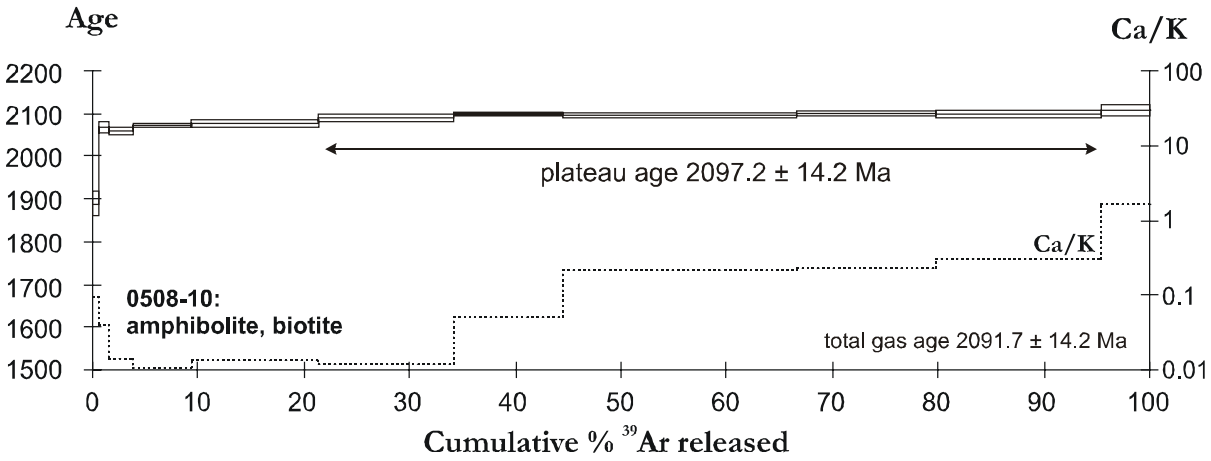

Fig. 2.33. $^{40}Ar/^{39}Ar$ age spectrum and Ca/K spectrum of biotite from an amphibolite fels of the central domain of a hydration zone (Medvezhy Island).

The plateau age is defined by 5 consecutive steps with 74 % of the ^{39}Ar released and yielded 2097.2 ±13.9 Ma. The apparent Ca/K ratios show variations, but no correlation between the apparent ages and the Ca/K ratios was observed, suggesting sample inhomogeneity. Impurities degassed at higher temperatures (920 – 1250 °C) are documented by elevated Ca/K ratios (0.2 – 1.7). Argon loss at low temperature (580 °C) is presumably due to weathering/alteration of the mineral rims. Again, the uniform high apparent ages may indicate a homogeneous distribution of excess argon in the mineral.

Table 2.14. $^{40}Ar/^{39}Ar$ data of a biotite in hydration zones from Medvezhy Island (Por'ya Guba complex).

0508-10; amphibolite fels (Medvezhy Island); weight: 4.0 mg J: 0.010675 ± 0.4										
Step	T[°C]	$^{39}Ar_K$ (%)	$^{40}Ar^*$ (mV)	$^{40}Ar^*$ (%)	$^{39}Ar_K/^{37}Ar_{Ca}$	Ca/K	^{36}Ca (%)	$^{40}Ar^*/^{39}Ar_K$	Age Ma	error (1σ)
1	580	0.5%	28.97	99.4%	42.590	0.1	0.18%	173.45	1889.4	27.5
4	630	0.9%	62.08	99.8%	103.346	0.0	0.26%	201.18	2067.5	14.5
5	700	2.3%	154.36	99.9%	286.054	0.0	0.26%	199.58	2057.7	8.5
6	740	5.5%	371.52	100.0%	379.448	0.0	0.29%	202.24	2073.9	3.9
7	780	12.1%	813.75	99.9%	302.483	0.0	0.29%	202.75	2077.1	8.9
8[a]	820	12.7%	861.62	100.0%	348.667	0.0	0.42%	204.97	2090.5	9.6
9[a]	860	10.3%	702.02	100.0%	78.515	0.1	3.09%	206.48	2099.6	4.2
10[a]	920	22.2%	1512.80	99.9%	19.003	0.2	4.11%	205.91	2096.2	8.3
11[a]	980	13.3%	909.90	99.9%	18.054	0.2	4.22%	206.80	2101.5	6.0
12[a]	1060	15.5%	1062.57	99.9%	13.348	0.3	4.17%	206.33	2098.7	8.8
13	1250	4.6%	317.75	99.8%	2.444	1.7	6.32%	207.78	2107.4	11.6
		100.0%	Total gas age:	2091.7 ± 14.2 Ma				74% [a]Plateau age:	2097.2 ± 13.9 Ma	

$^{40}Ar^*$: radiogenic ^{40}Ar; $^{39}Ar_K$: formed from K; $^{37}Ar_{Ca}$: formed from Ca; errors of plateau ages & total gas ages include an uncertainty (0.4%) in the J-value, apparent step ages only account for the analytical errors; correcting factors:Daly/Hf: 150 ± 5.0; $(^{40}Ar/^{36}Ar)_{air}$: 299 ±1.0; $(^{36}Ar/^{37}Ar)_{Ca}$: 0.00027; $(^{39}Ar/^{37}Ar)_{Ca}$: 0.00039; $(^{40}Ar/^{39}Ar)_K$: 0.0254; K/Ca-conversion factor: 0.247.

2.6.2.3 Interpretation

If all radiogenic ^{40}Ar remained trapped in the mineral and no contamination by excess argon occurred, $^{40}Ar/^{39}Ar$ ages may reflect either the time of cooling or the time of crystallisation/formation of the mineral. In the latter case, the peak metamorphic temperatures had to be lower than the closure temperature for argon diffusion/retention in the mineral. If metamorphic temperatures exceeding this closure temperature, the $^{40}Ar/^{39}Ar$ ages are interpreted to date the cooling below the temperature required for argon retention in the mineral.
Closure temperatures for hornblende and biotite range from 500 to 550 °C (Harrison, 1981; Harrison & Fitzgerald, 1986) and 300 to 320 °C, respectively (von Blankenburg *et al.*, 1989, Hames & Bowring, 1994). Since the temperature estimates of 630-750 °C for the hydration process in the Kolvitsa Belt exceed significantly the closure temperatures of both minerals, the $^{40}Ar/^{39}Ar$ ages have to be interpreted as the time of cooling below ~500 °C and ~300 °C. By the use of several geochronometers with different closure temperatures, information about the cooling rates can be obtained.
In general, undisturbed $^{40}Ar/^{39}Ar$ age spectra with well defined plateau ages, similar isochron ages and an initial atmospheric $^{40}Ar/^{36}Ar$ ratio, are believed to give geologically reasonable ages. Disturbed age spectra point to a partial loss of radiogenic ^{40}Ar or the presence of excess argon. In this case, microfractures, inclusions and exsolution lamellae with different argon retentivity can act as pathways for excess argon or radiogenic argon (FitzGerald, 1986, von Blanckenburg & Villa, 1988; Lee, 1995).
In this study, discordant age spectra with abnormally high apparent ages (up to 3630 Ma) at low degassing temperatures point to the incorporation of excess argon in the mineral rims. Systematic decrease of apparent ages towards higher temperatures during incremental heating may indicate that excess argon diffused into the grain interiors (samples: 0808-4, 0308-K2, 0708-5).
Total gas and plateau ages (1930 – 2213 Ma) obtained for amphiboles from central domains/parts of fluid infiltration zones are unreasonably high and may reflect the widespread presence of excess argon. The patterns indicate a homogenous incorporation of the excess argon in the lattice during mineral growth. Excess argon bound to the grain margins is less retentive, degassed at lower temperatures and presumably was trapped in microfractures or inclusions. Diffusion of excess argon into hornblende during cooling is documented by decreasing apparent ages during incremental heating experiments. Partial rejuvenation reflected by the saddle shaped age spectrum of sample 0708-5 (Bolschoi Khed), most likely was caused by rimward diffusion of the incorporated excess argon component.
The Ar-Ar ages obtained from biotite (sample 0508-10) show a concordant age spectrum with a total gas age of *c.* 2092 Ma. Due to the lower temperature for the retention of argon (*c.* 300 °C), biotite should record younger cooling ages than hornblende (Jäger, 1979; Dallmeyer & Rivers, 1982). The similarity of amphibole and biotite ages indicates that also biotite must contain a significant amount of excess argon. Concordant age spectra for hornblende and biotite both with well-defined apparent plateau ages, are described in the literature and have no geological meaning (Roddick *et al.*, 1980; von Blanckenburg & Villa, 1988; Maboko *et al.* 1991).
That these samples contain a significant amount of excess argon is supported by the lower U-Pb ages of titanites (1891 ±4.8 Ma, 1896 ±4 Ma & 1898 ±4 Ma) and U-Pb ages of metamorphic zircon from a nearby anorthosite (1905 ±26 Ma, Frisch *et al.*, 1995). Zircon has closure temperatures for lead diffusion above 900 °C and for titanite grains with radii of *c.* 300 μm, closure temperatures range from 650 to 700 °C at a cooling rate of around 2 °C/Ma (for references see Bibikova *et al.*, 2001). From the hierarchy of the closure temperatures, $^{40}Ar/^{39}Ar$ ages of hornblende and biotite should give the youngest ages. It is obvious that the high $^{40}Ar/^{39}Ar$ ages obtained for the samples 0308-K2 – 0308-K3 (Nikolkina Island), 0708-5 (Bolschoi Khed), 0808-6 (Leonard outcrop) and 0508-10 (Medvezhy Island) have no geological significance.
The amount of excess argon is most noticeable in amphibole from the centre of the infiltration zones. Together with the observed patterns of excess argon, this points to a correlation with the

extent of fluid influx. It follows that the infiltrating aqueous fluids responsible for the formation of amphibole and biotite were enriched in ^{40}Ar. Variations of the plateau ages also reflect the variable $^{40}Ar/^{36}Ar$ ratios of the infiltrating fluids.
The tectonic setting suggests that the fluids causing hydration in the hangingwall granulite facies metabasites of the Kolvitsa and Por'ya Guba Complex ascended along major/prominent shear zones or thrust boundaries from the footwall gneisses of the Belomorian Basement and the metavolcanic amphibolites of the Kandalaksha sequence during the Lapland-Kola orogeny *c.* 1.9 Ga ago. Excess argon presumably derived from K-rich minerals, such as biotite, amphibole or K-feldspar. Since these minerals have low closure temperatures or argon is only weakly bound to the mineral lattice, increasing temperatures caused a release of ^{40}Ar. Required metamorphic heat derived from the overthrusted hot granulite nappes during the Lapland-Kola orogeny.
Metamorphic reworking of the *c.* 2.7 Ga old tonalitic gneisses from the north-eastern marginal zone of the Belomorian Basement occurred 1.94 – 1.87 Ga ago, dated by U-Pb ages of titanite (Bibikova *et al.*, 2001). During Palaeoproterozoic reworking, temperatures exceeded 650 °C as indicated by the complete resetting of titanite and the widespread-occurrence of pegmatites (Bibikova *et al.*, 2001). In the Kandalaksha sequence well-annealed textures of strongly lineated amphibolites and intercalated biotite and amphibole-bearing meta-andesites are also evidence of thorough Palaeoproterozoic tectono-thermal reworking (Balagansky *et al.,* 2001). The fluids generated during this thermal event in the footwall acted as sinks for the ^{40}Ar released from K-rich minerals, such as biotite, amphibole or K-feldspar. In the fluid infiltration zones of the hangingwall metabasites, excess argon was trapped in hornblende and biotite because of the elevated partial pressure of this fluid species.
However, excess argon contents in hornblende of weakly hydrated samples (0808-3 & 0808-4) from the Leonard outcrop are insignificant. As a result, the $^{40}Ar/^{39}Ar$ plateau ages (1880.3 ±11.3 & 1897.7 ±8.2 Ma) are consistent with U-Pb ages of titanite from amphibolites (1896 ±4 Ma & 1898 ±4 Ma) and of zircon from a nearby anorthosite body (1905 ±26 Ma; Frisch *et al.*, 1995) and are interpreted to date cooling following amphibolite facies hydration.

2.6.3 Cooling history and P-T-t evolution

To obtain insights into the Palaeoproterozoic cooling and exhumation history of the Kolvitsa Complex, geochronological data from the literature (for a compilation see Balagansky *et al.*, 2001) and this study are combined with *P-T* estimates for distinct metamorphic stages. The age of high-grade metamorphic reworking of the layered gabbro-anorthosite complex is constrained by U-Pb data of metamorphic zircons from an anorthosite lens near Kataransky Cape (1905 ±26 Ma: Frisch *et al.*, 1995) and from dioritic dykes at Kochinny Cape (1919 ±18 Ma: Kaulina, 1996; Kaulina & Apanasevich, 1998). The near-concordant ages agree with zircon data from the Umba Granulite Terrane (1910 ±60 Ma; Tugiranov & Bibikova, 1980) and the granulitic mélange zone, where zircons from high-grade leucosomes post-date shearing yielded 1906 ±1 Ma (Kislitsyn *et al.*, 1998) and 1912 ±2 Ma (Kislitsyn *et al.*, 1999). Since the closure temperature for lead diffusion in zircon exceeds 900 °C (Cherniak & Watson, 2001), these data are considered as the age of high-grade metamorphism in the Kolvitsa Complex and thus may be linked to the *P-T* conditions estimated for the peak-metamorphic stage. Supporting the idea of an inverted metamorphic temperature gradient, *P-T* estimates for metagabbros near the shear zone, defining the south-eastern boundary of the Kolvitsa Complex, range from 12 to 13 kbar and 850 °C to 1000 °C, whereas temperatures are lower in the south-western part of the Kolvitsa Complex. In the coronitic dyke at Nikolkina Island temperatures did not exceed 800 °C.
High-grade metamorphism in the gabbro-anorthosite association of the Kolvitsa Complex presumably was caused by heat influx from the overthrust hot granulite nappes of the Por'ya Guba and Umba complexes. This would imply that high-grade metamorphism in the high-grade shear zones at the south-eastern boundary of the Kolvitsa Complex and the granulitic mélange zone preceded HT-metamorphism at Nikolkina Island and Kochinny Cape.

The timing of subsequent amphibolite facies hydration processes in the Kolvitsa and Por'ya Guba complexes is tightly constrained at 1896 – 1898 Ma by U-Pb titanite data (this study). As the estimated metamorphic temperatures of hydration (650 – 750 °C) do not exceed the closure temperature for lead diffusion in titanite, these ages are interpreted to date the crystallisation (growth) of this phase rather than cooling.
The rates of cooling from the peak-stage of granulite facies metamorphism (~1000-800 °C; *c.*1905 or 1912 Ma) to the stage of amphibolite facies hydration (650-750 °C; 1897 Ma) range from 14 - 6 °C/Ma at Nikolkina Island to 30 – 12 °C/Ma at Kataransky Cape and Bolschoi Khed. Suggesting that high-grade metamorphism close to the hot hangingwall units occurred earlier (*c.* 1912 ago), a cooling rate of 12 – 20 °C/Ma seems more likely for mylonitic gabbros from Kataransky Cape and Bolschoi Khed (Fig. 2.34). In contrast, retarded metamorphic reworking (*c.* 1905 Ma) at greater distance would indicate cooling rates of 9 – 14 °C/Ma for units exposed at Kochinny Cape and Nikolkina Island. In fact the vertical temperature distribution was presumably more complex and e.g. rocks from the south-eastern boundary of the Kolvitsa Complex, documenting a previous static granulite-facies stage as well as high-grade granulite-facies shearing, were presumably involved in different tectonic processes.

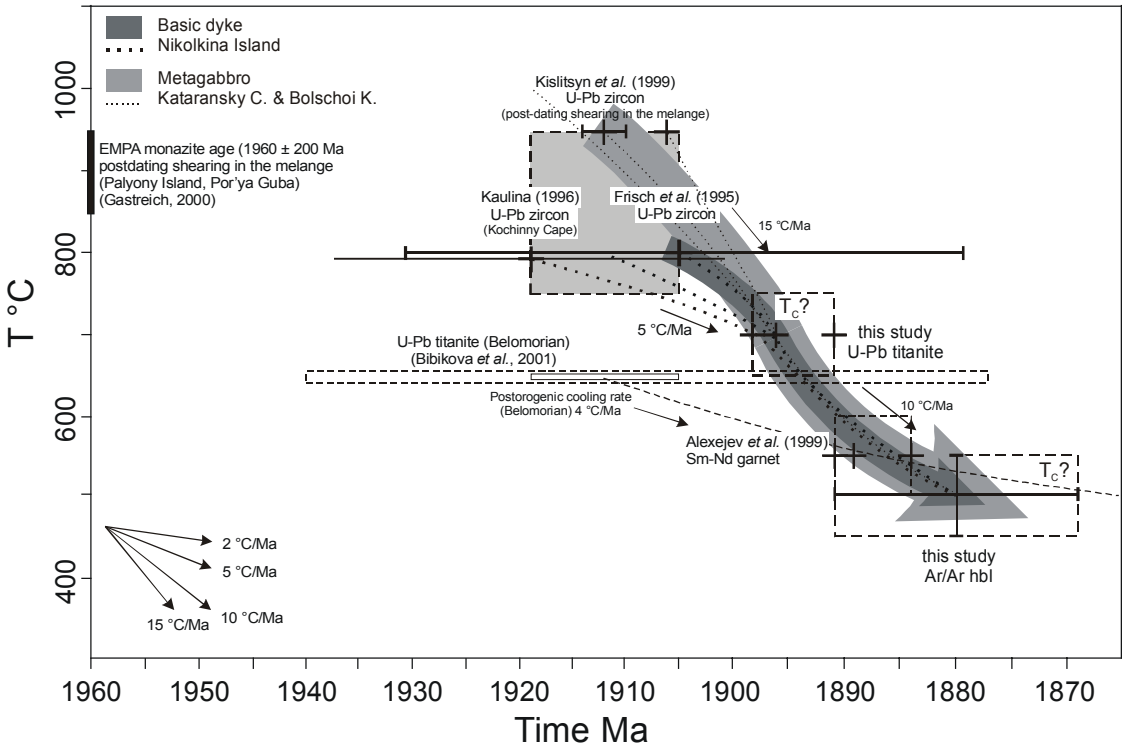

Fig. 2.33. Temperature-time plot showing thermochronometric data. Temperature estimates for high-grade metamorphism were obtained from thermobarometry. For U-Pb diffusion in titanite closure temperatures of 650 - 700 °C were adopted (Cherniak, 1993; Schärer *et al.*, 1994; Scott & St. Onge, 1995; Zang & Schärer, 1996; Frost *et al.*, 2000). For Sm-Nd systematics in garnet (Alexejev *et al.*, 1999) a closure temperature of 600 - 500 °C was assumed (Mezger *et al.*, 1992; Maboko & Nakamura, 1995; Wang *et al.*, 1998). Ar-Ar ages for hornblende document cooling through closure temperatures of 450- 500 °C (Harrison, 1981; Harrison & FitzGerald, 1986). For comparison U-Pb titanite ages and an assumed postorogenic cooling rate for the northeastern marginal zone of the Belomorian Belt are shown (Bibikova *et al.*, 2001).

The cooling history following the structurally controlled hydration processes is documented by ^{40}Ar-^{39}Ar hornblende ages and Sm-Nd garnet-whole rock ages (Alexejev *et al.,* 1999). Both are interpreted as cooling ages through the respective closure temperatures. Estimates of the closure temperature for the Ar retentivity in hornblende range from 450 to 500 °C (Harrison, 1981; Harrison & FitzGerald, 1986). Due to the presence of excess argon in several of the analysed samples, only the ^{40}Ar-^{39}Ar age of *c.* 1880 Ma obtained for sample (0808-4) is suitable for thermochronology and is considered as a credible cooling age. Sm-Nd garnet-whole rock isochrons yielded cooling ages of *c.*

1885 – 1890 Ma (Alexejev *et al.,* 1999), which are only slightly higher than the ^{40}Ar-^{39}Ar hornblende cooling age and slightly lower than the titanite U-Pb ages, confirming the assumptions of Balagansky *et al.* (2001) that Sm-Nd garnet ages record cooling below 600 °C. This indicates closure temperatures of the Sm-Nd system in garnet in the order of 500 to 600 °C, in agreement with studies of Mezger *et al.* (1992), Maboko & Nakamura (1995) and Wang *et al.* (1998). It follows that amphibolite facies metasomatic alteration was followed by cooling to c. ~450 at a rate of *c.* 10 °C/Ma (Fig. 2.34).

To assess the rate of exhumation, *P-T* estimates for distinct evolutionary stages were coupled with age data. Pressure estimates for the peak stage of upper amphibolite to granulite facies metamorphism (*c.* 1905 – 1912 Ma) gave *c.* 12 – 13 kbar, whereas the amphibolite facies stage of metasomatic alteration (*c.* 1896 – 1898 Ma) was characterised by pressures ranging from 6 - 7 kbar (Kataransky Cape & Bolschoi Khed) to 9 - 11 kbar (Nikolkina Island). The resulting exhumation rates are 0.7 – 1.5 mm/a for the basic dyke from Nikolkina Island and 1.2 up to 3 mm/a for metagabbros at Kataransky Cape and Bolschoi Khed (Fig. 2.35).

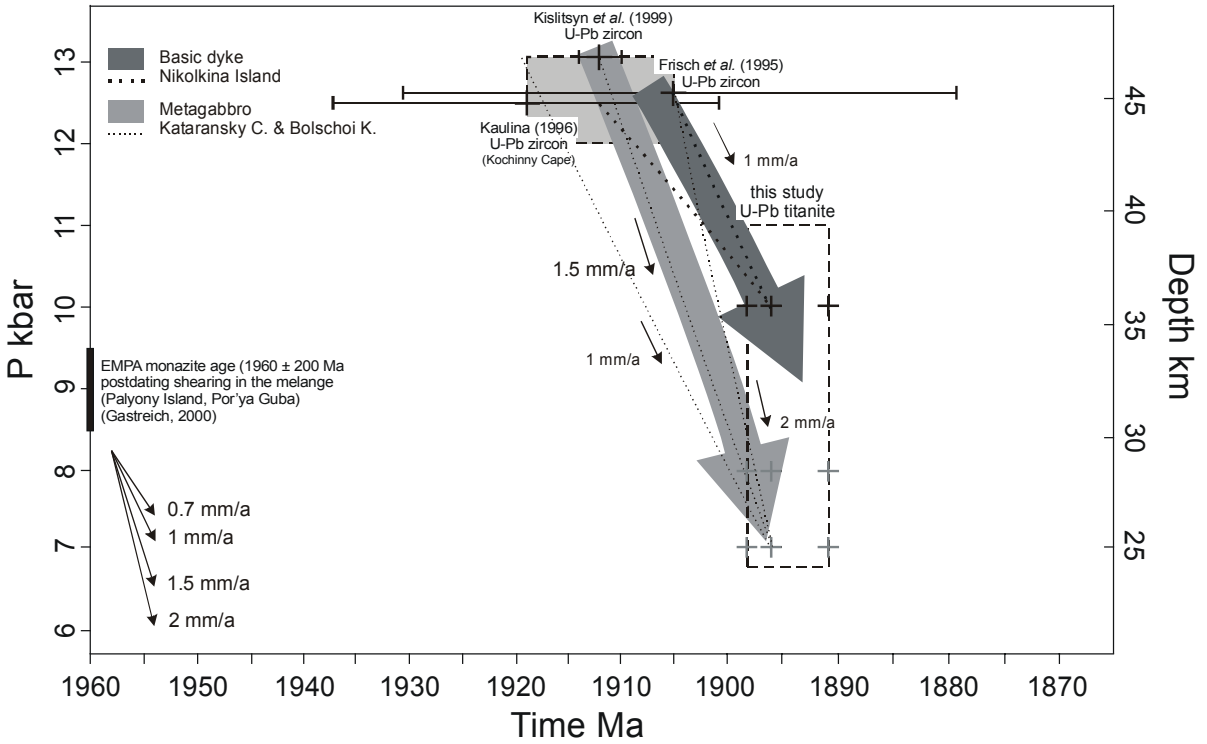

Fig. 2.32. T-t information is combined with quantitative *P-T* estimates (upper-amphibolite to granulite facies metamorphism & metasomatic alteration) to obtain exhumation rates. Because of high closure temperatures for U-Pb diffusion in zircon (> 900 °C) and titanite (650 - 700 °C or even > 700°C) the U-Pb ages are interpreted to date the crystallisation of these minerals.

Comparison of pressure estimates obtained from Grt-Hbl-Pl-Qtz and Al-in-hornblende barometry, indicate that results from Hbl barometry are about 1 – 2 kbar lower than estimates from Grt-Hbl-Pl-Qtz barometry. Because of the absence of garnet in hydration zones from Kataransky Cape and Bolschoi Khed, pressure estimates obtained from the Al content in hornblende (6 – 6.5 kbar) are treated with care and regarded as minimum estimates. Prevailing pressures reached presumably rather *c.* 8 kbar than only 6 – 6.5 kbar. Furthermore, no titanite occurs in samples from the hydration zones and age information of titanite-bearing samples from nearby locations (Nikolkina Island, Leonard Cape, Medvezhy Island) was used. Together with the assumption that the metamorphic peak condition near the shear zone was reached more likely *c.* 1912 Ma ago, exhumation rates in the range of 1 – 2 mm/a are believed to be more realistic.

The cooling and exhumation rates of 10 – 20 °C/Ma and 0.7 – 2 mm/a inferred for the Kolvitsa Complex point to fast exhumation following tectonic crustal thickening and burial in the Lapland-

Kola collisional orogen (Fig. 2.34 – 2.35). The cooling and uplift rates are in the range of what is known from younger orogenic belts (e.g. Alps and Himalayas) which suggests that plate tectonic processes were comparable to those operating today.

2.6.4 Sm-Nd systematics

2.6.4.1 Analytical technique

Isotopic studies were performed at the Institute of Precambrian Geology and Geochronology (Russian Academy of Sciences, St. Petersburg) on a Finnigan MAT 261 8-collector mass-spectrometer in static mode.

Rock powders for Sm-Nd studies were dissolved in a mixture of HF, HNO_3 and $HClO_4$. Before the decomposition all samples were totally spiked with a ^{149}Sm-^{150}Nd mixed solution. REE were separated using conventional cation-exchange techniques. Sm and Nd were separated by extraction chromatography on HDEHP-covered Teflon powder following the method of Richard (1976). Total blanks in the laboratory are 0.1-0.2 ng for Sm and 0.1-0.5 ng for Nd. Accuracy of the measurements of Sm and Nd contents is ±0.5%, $^{147}Sm/^{144}Nd$ - ±0.5%, $^{143}Nd/^{144}Nd$ - ±0.005% (2σ). $^{143}Nd/^{144}Nd$ ratios are relative to the value of 0.511860 for the La Jolla standard. During the period of work the weighted average of 9 La Jolla Nd-standard runs yielded 0.511852±8 (2σ) for $^{143}Nd/^{144}Nd$, using 0.7219 for $^{146}Nd/^{144}Nd$ to normalise.

The $\varepsilon_{Nd}(T)$ values were calculated using the present-day values for a chondritic uniform reservoir (CHUR) $^{143}Nd/^{144}Nd = 0.512638$ and $^{147}Sm/^{144}Nd = 0.1967$ (Jacobsen and Wasserburg, 1984). The model ages T_{DM} were calculated using a model (Goldstein and Jacobsen, 1988), according to which the Nd isotope composition of the depleted mantle has evolved linearly since 4.56 Ga ago and has the present-day value $\varepsilon_{Nd}(0)=+10$ ($^{143}Nd/^{144}Nd=0.513151$ and $^{147}Sm/^{144}Nd=0.2137$).

2.6.4.2 Results

Isotopic signatures of the magmatic protoliths

Constraints on the timing of magmatic events in the Kolvitsa Complex were obtained by U-Pb dating of igneous zircon (e.g. Frisch *et al.*, 1995; Mitrofanov *et al.*, 1995). The data indicate emplacement of layered anorthosite-gabbro complexes between 2450 ±7 Ma (Frisch *et al.*, 1995) and 2462 ±7 Ma (Mitrofanov *et al.*, 1995), closely followed by multiple intrusion of mafic dykes (2436 ±6 Ma for dioritic dykes in the Kochinny Cape area; Kaulina, 1996; see also Balagansky *et al.*, 2001).

Assuming a magmatic crystallisation age of 2.45 Ga, initial Nd isotope ratios and ε_{Nd} were calculated (Tab. 2.15 & Fig. 2.35). ε_{Nd} (2.45Ga) values of the metagabbro and basic dykes range from +0.6 to -0.1 and agree with published data (+0.3 to –0.6) for igneous rocks from the Kolvitsa Belt (Balagansky *et al.*, 1998b; in Balagansky *et al.*, 2001) and other coeval layered intrusions from the Kola and Karelia regions (-0.5 to –2) (Balashov *et al.*, 1993; Amelin & Semenov, 1996) (Fig. 2.35). An exception is the metagabbro from Bolschoi Khed with a positive ε_{Nd} (2.45Ga) value of 2.7.

Initial ε_{Nd} values and initial Sr isotope ratios may provide an indication of the mantle source and may be used as tracer for crustal contamination. Because during partial melting the parent nuclide Sm behaves more compatible than its daughter nuclide Nd, the Sm/Nd ratios in mantle-derived melts are lower than those of their reservoir e.g. CHUR or depleted mantle. As a result their $^{143}Nd/^{144}Nd$ ratios evolve distinctly (Rollinson, 1993). Positive ε_{Nd} values at the time of melt-generation indicate that the melts were derived from a depleted mantle source, whereas negative ε_{Nd} values point to a derivation from an enriched mantle source, provided crustal contamination can be excluded.

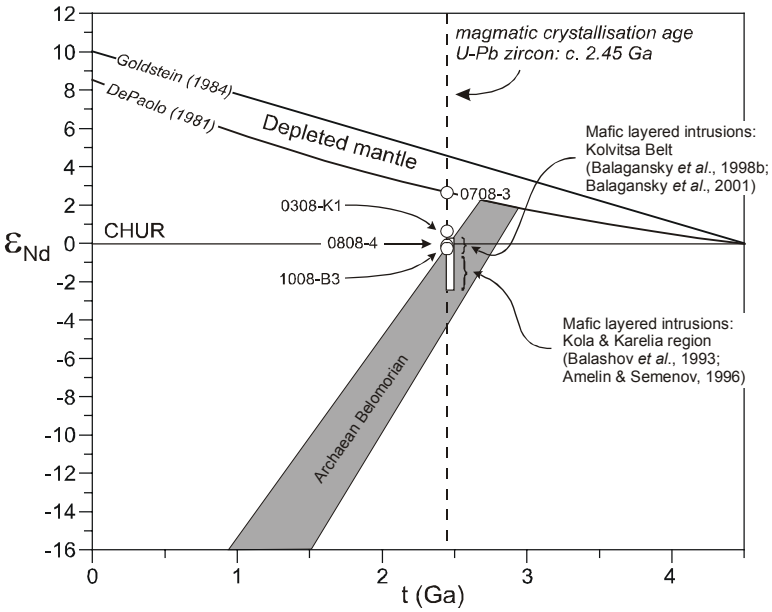

Fig. 2.35. Sm-Nd evolution diagram expressed as epsilon notation for basic rock types from the Kolvitsa Complex. Shown for comparison are data from mafic layered intrusions of the Kolvitsa Belt (Balagansky *et al.*, 1998; Balagansky *et al.*, 2001) and the Kola and Karelian regions (Balashov *et al.*, 1993; Amelin & Semenov, 1996) as well as Sm-Nd data from surrounding Archaean areas (Timmerman & Daly, 1995; Daly *et al.,* 2001). Depleted mantle evolution curves according to Goldstein (1984) and DePaolo (1981).

Igneous rocks from the Kolvitsa Complex show ε_{Nd} values between +0.6 and -0.1 which, if taken as primary signature, would suggest a mantle plume source with CHUR-type isotopic characteristics. Yet, crustal contamination of the melts or their derivation from an enriched mantle source would cause comparable isotopic Nd signatures. Amelin & Semenov (1996) and Balagansky *et al.* (1998b & 2001) presented Nd and Sr isotopic data for layered intrusions of the Kola and Karelian regions (ε_{Nd} –1 to –2 & $^{87}Sr/^{86}Sr_{in}$ 0.7010 – 0.7034) and the Kolvitsa Belt (ε_{Nd} +0.3 to –0.6 & $^{87}Sr/^{86}Sr_{in}$ 0.7011 - 0.7027), and argued for an enriched lithospheric mantle source or a mantle plume source followed by minor crustal contamination of the melts. Although the Sm/Nd systematics for the studied rocks apparently support such interpretation, the trace element data presented before, such as the depletion of Nb, Th and P, an enrichment in LILE suggest that crustal contamination possibly played a major role. The Sm-Nd evolution diagram in Fig. 2.35 shows that contamination of melts derived from depleted mantle or plume sources with Archaean crustal material (Timmerman & Daly, 1995) could indeed account for the observed isotopic signatures.

Influence of fluid infiltration on the isotopic signatures

The metasomatic alteration as dated by U-Pb titanite ages occurred at *c.* 1896 Ma. ε_{Nd} values at 1896 Ma for the igneous mafic protoliths and their respective hydration zones are illustrated in Fig. 2.36. Compared to their protoliths, rocks from the hydration zones show lower ε_{Nd} values.

Mass balance calculations already indicated that REE behaved mobile during fluid infiltration and were enriched in amphibolitised zones via an infiltrating fluid. As possible sources of the infiltrating fluids, the overthrust Archaean Belomorian basement gneisses and/or Kandalaksha metavolcanic sequence were considered earlier. The *c.* 2.7 – 2.75 Ga tonalitic gneisses (Bogdanova & Bibikova, 1993; Bibikova *et al.*, 1996; Balagansky *et al.*, 1998b) show low Sm/Nd ratios and ε_{Nd}(1896 Ma) values in the order of -6 to -11 (Timmerman & Daly, 1995). Fluids derived from them thus could have caused the observed negative isotopic shifts (Fig. 2.34).

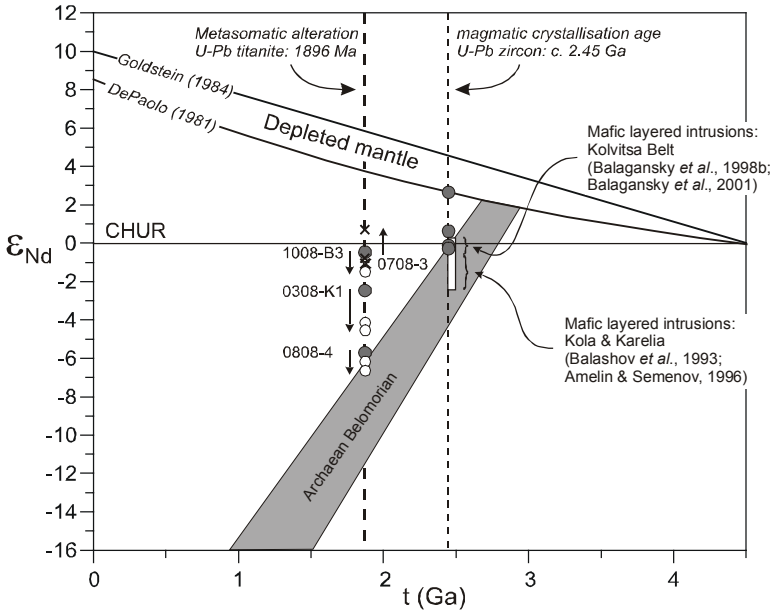

Fig. 2.36. Sm-Nd evolution diagram expressed as epsilon notation for basic rock types and respective metasomatic alteration zones from the Kolvitsa Complex. Sm-Nd data from surrounding Archaean areas are shown for comparison (Timmerman & Daly, 1995; Daly *et al.*, 2001). Depleted mantle evolution curves according to Goldstein (1984) and DePaolo (1981).

Table 2.15. Sm-Nd whole rock isotope data of mafic rock types and their hydrated equivalents from the Kolvitsa nappe unit.

Sample	rock type	Sm	Nd	$^{147}Sm/^{144}Nd$	$^{143}Nd/^{144}Nd$	Err	ε_{Nd}	ε_{Nd}	ε_{Nd}
		ppm	ppm				today	1.9 Ga	2.45 Ga
0708-3	metagabbro	1.27	5.27	0.1454	0.511947	8	-13.48	-0.97	2.70
0708-4	amphibolite	2.09	9.49	0.1332	0.511806	8	-16.23	-0.75	3.80
0708-5	amphibolite	1.39	4.51	0.1863	0.512547	9	-1.78	0.77	1.52
1008-B3	metagabbro	0.81	2.54	0.1918	0.512557	7	-1.58	-0.40	-0.05
1008-B1	amphibolite	4.50	19.07	0.1426	0.511891	4	-14.57	-1.37	2.50
0308-K1	basic dyke	3.25	12.74	0.1540	0.511980	7	-12.84	-2.43	0.63
0308-K2	amphibolite	6.00	26.79	0.1354	0.511646	6	-19.35	-4.43	-0.05
0308-K3	amphibolite	6.52	27.42	0.1438	0.511771	5	-16.91	-4.02	-0.23
0808-4	metadiorite	4.21	21.89	0.1163	0.511340	7	-25.32	-5.75	0.00
0808-5	amphibolite	7.71	38.60	0.1207	0.511378	7	-24.58	-6.07	-0.64
0808-6	amphibolite	12.47	69.37	0.1086	0.511201	4	-28.03	-6.57	-0.27

CHUR today: $^{143}Nd/^{144}Nd$ 0.512638 (Jacobsen and Wasserburg, 1984 & Goldstein, 1984), $^{147}Sm/^{144}Nd$ 0.1967 (Jacobsen and Wasserburg, 1984)

2.7 Conclusion

Influx of externally derived fluids occurred coeval with the tectonic exhumation of the nappe pile of the Kolvitsa Belt. Zones of weakness, such as large thrust and shear zones as well as lithological boundaries formed pathways for the ascending fluids. Infiltration of hydrous fluids caused dramatic changes in mineralogy and led to the replacement of the Grt-Cpx-Pl ±Opx, Qtz assemblage in the mafic host granulites by nearly monomineralic Hbl ±Pl, Ttn felses. Beside hydration and retrogression of the more or less dry host rocks, fluid infiltration was accompanied by mineralogically controlled element transfer and fluid-enhanced deformation. In hydration zones decreasing viscosity towards the centre of hydration caused strain gradients and localised strain into zones of amphibolitisation. Hydration and re-crystallisation under static conditions, on the other hand, led to increasing grain size and caused the loss of the granulite-facies foliation.
Metasomatic zones are characterised by a loss of SiO_2, whereas MgO, FeO, CaO and TiO_2 contents increase. Due to negligible volume changes, hydration can be regarded as an isovolumetric process. Element transfer is interpreted as resulting from up-temperature fluid flow of an externally derived, low $\delta^{18}O$ fluid (7 – 8.5 ‰) which was enriched in silica and ^{40}Ar. Volumetric fluid-rock ratios and minimum time-integrated fluid fluxes were estimated on the basis of Si solubility in water and range from 50:1 to 150:1 and from 10^6 to 10^7 cm^3/cm^2. High fluid-rock ratios and fluid fluxes are in agreement with those of shear zones characterised by significant element transfer (e.g. O'Hara, 1988; Selverstone *et al.*, 1991; Dipple & Ferry, 1992; Streit & Cox, 1998; Cartwright & Barnicoat, 2003; Yonkee *et al.*, 2003; Barnes *et al.*, 2004). Decrease in $\delta^{18}O$ values in zones of amphibolitisation agree also with up-temperature fluid flow. The conformity of the estimated $\delta^{18}O$ values of the infiltrating fluids at the locations studied points to a uniform fluid reservoir. As possible sources of the infiltrating fluids, the gneisses of the Belomorian basement or the metavolcanic rocks of the Kandalaksha sequence are suggested. Fluids were produced by dehydration reactions during Palaeoproterozoic reworking. In both cases the assumption of up-temperature fluid flow agrees with an inverted metamorphic gradient. Part of the heat budget required for dehydration of hydrous mineral phase (Amph, Bt) in the footwall units was then released from the overthrust hot granulite nappes.
Beside element transfer controlled by temperature gradients and the composition of the infiltrating fluid, complementary element patterns between the marginal and central parts of individual hydration zones document also bilateral element transfer. Lateral redistribution was caused by concentration gradients between the centre and the marginal front of fluid infiltration in narrow shear zones.
This study also provides further evidence for the mobility of HFS elements and REE during amphibolite-facies hydration processes. Accessory minerals, such as titanite and zircon acted as sinks and document for mineralogically controlled element transfer. Sm-Nd whole rock isotope data show negative isotopic shifts in zones of amphibolitisation and are further evidence for the mobility of REE via an infiltrating fluid. Fluids derived from the overthrust Archaean Belomorian basement gneisses would account for the lower Sm/Nd ratios in the zones of amphibolitisation.
The timing of amphibolitisation and deformation is constrained by U-Pb titanite data at *c.* 1891 - 1898 Ma. Zones of amphibolitisation were formed at temperatures between 650 and 750 °C and pressures up to 7 - 11 kbar. Uniform age spectra, similar *P-T* conditions and alteration styles in metasomatic zones are consistent with a single episode of fluid infiltration at mid-crustal levels. Estimated rates of cooling and exhumation from the peak-stage of granulite-facies metamorphism to the stage of amphibolite-facies hydration range from 10 to 20 °C and 1 to 2 mm/a, pointing to fast exhumation following tectonic crustal thickening and burial in the Lapland-Kola Orogen. Further cooling history was constrained by a $^{40}Ar/^{39}Ar$ hornblende age, documenting cooling to *c.* ~450 °C at a rate of *c.* 10 °C/Ma.

Although hydration processes in the Kolvitsa nappe were confined to small-scale shear and hydration zones, fluid infiltration phenomena are widespread in the mafic rock associations of the Kolvitsa Complex. The inferred large volumes of fluids are only minimum estimates and argue for significant fluid flow during the tectonic exhumation of the nappe pile. Major thrust zones separating the nappe units may act as important pathways for large volumes of ascending fluids.

References

Ague, J. J., 1994. Mass transfer during Barrovian metamorphism of pelites, south-central Connecticut. I: Evidence for changes in composition and volume. *American Journal of Science,* **294**, 989-1057.

Alexejev, N., Huhma, H., Belyatsky, B. & Balagansky, V. V., 1999. Sm-Nd Grt-WR ages on the Kolvitsa-Umba Zone and Pongoma area, Belomorian-Lapland Belt, Baltic Shield, Russia. *Abstracts of the SVEKALAPKO workshop,* 18. – 21. 11. 1999, Lammi, Finland, **1**.

Alirezaei, S. & Cameron, E. M., 2002. Mass balance during gabbro-amphibolite transition, Bamble Sector, Norway: implications for petrogenesis and tectonic setting of the gabbros. *Lithos*, **60**, 21-45.

Amelin, Yu. V. & Semenov, V. S., 1996. Nd and Sr isotopic geochemistry of mafic layered intrusions in the eastern Baltic Shield: implications of the evolution of Palaeoproterozoic continental mafic magmas. *Contributions to Mineralogy and Petrology*, **124**, 255-272.

Amelin, Yu. V., Heaman, L. V. & Semenov, V. S., 1996. U-Pb geochronology of layered mafic intrusions in the eastern Baltic Shield: implication of the timing and duration of Palaeoproterozoic continental rifting. *Precambrian Research*, **75**, 31-46.

Anderson, D. J., Lindsley, D. H. & Davidson, P. M., 1993. QUILF: a PASCAL program to assess equilibria among Fe-Mg-Mn-Ti oxides, pyroxenes, olivine and quartz. *Computers and Geosciences*, **9**, 1333-1350.

Anderson, G. M. & Burnham, C. W., 1967. Reactions of quartz and corundum with aqueous chloride and hydroxide solutions at high temperatures and pressures. *American Journal of Science,* **265**, 12-27.

Anderson, L. J. & Smith, D. R., 1995. The effects of temperature and fO_2 on the Al-in-hornblende barometer. *American Mineralogist*, **80**, 549-559.

Anovitz, L. M., 1991. Al-zoning in pyroxene and plagioclase: window on the late prograde to early retrograde P-T paths in granulite terranes. *American Mineralogist*, **76**, 1328-1343.

Asprey, L. B., 1976. The preparation of very pure fluorine gas. *Journal of fluorine Chemistry,* **7**, 359-361.

Balagansky, V. V., Timmerman, M. J. , Kozlova, N. Ye. & Kislitsyn, R. V., 2001. A 2.44 Ga syn-tectonic mafic dyke swarm in the Kolvitsa Belt, Kola Peninsula, Russia: implications for early Palaeoproterozoic tectonics in the north-eastern Fennoscandian Shield. *Precambrian Research*, **105**, 269-287.

Balagansky, V. V., Glaznev, V. N. & Osipenko, L. G., 1998a. Early Proterozoic evolution of the northeastern Baltic Shield: a terrane analysis. *Geotektonica (in Russian)*, **2**, 16-28.

Balagansky, V. V., Timmerman, M. J., Kislitsyn, R. V., Daly, J. S., Balashov, Yu. A., Gannibal, L. F., Sherstennikova, O. G. & Ryungen, G. I., 1998b. Isotopic age of rocks from the Kolvitsa Belt and the Umba block (the south-eastern extension of the Lapland Granulite Belt), Kola peninsula. *Proceedings of the Murmansk State Technical University*, **1 (3)**, 19-32. (in Russian).

Balagansky, V. V., Bogdanova, M. N. & Kozlova, N. Ye., 1986a. Structural and Metamorphic Evolution of the North-Western Belomorian Region. *Kola Branch of USSR Academy of Sciences*, Apatity, 100 p. (in Russian).

Balagansky, V. V., Timmerman, M. J. & Kislitsyn, R. V., 1994. 2.5-1.9 Ga magmatism, metamorphism and deformation in the southeastern branch of the Lapland granulite belt, Kola Peninsula, Russia. *Terra Nova*, **6**, p. 2.

Balashov, Yu. A., Bayanova, T. B. & Mitrofanov, F. P., 1993. Isotope data on the age and genesis of layered basic-ultrabasic intrusions in the Kola Peninsula and the northern Karelia. *Precambrian Research*, **64**, 197-205.

van Baalen, M. R., 1993. Titanium mobility in metamorphic systems. *Chemical Geology,* **110**, 233-249.

Barbey, P. & Raith, M., 1990. The granulite belt of Lapland. In: Granulites and Crustal Evolution (Ed. Vielzeuf, D., Vidal, Ph.), NATO ASI Series. Kluver, Dordrcht, pp. 111-132.

Barbey, P., Convert, J., Moreau, B., Capdevila, R. & Hameurt, J., 1984. Petrogenesis and evolution of an early Proterozoic collisional orogenic belt: the Granulite belt of Lapland and Belomorides (Fennoscandia). *Bulletin of the Geological Society of Finland,* **56**, 161-188.

Barnes, D., Selverstone, J. & Sharp, Z. D., 2004. Interactions between serpentinite devolatilisation, metasomatism and strike-slip strain localisation during deep-crustal shearing in the Eastern Alps. *Journal of metamorphic Geology*, **22**, 283-300.

Bogdanova, M. & Yefimov, M., 1993. Origin of parental anorthosite magmas, tectonic and metamorphic processes in the evolution of anorthosite (Kolvitsa anorthosite association). IGCP Project 290: Origin of anorthosites, guidebook of geological excursion, Geological Institute, RAS, KSC, Apatity.

Bégin, N. J. & Pattison, D. R. M., 1994. Metamorphic evolution of granulites in the Minto Block, northern Québec: extraction of peak P-T conditions taking account of late Fe-Mg exchange. *Journal of Metamorphic Geology*, **12**, 411-428.

Berman, R. G. & Aranovich, L. Y, 1996. Optimised standard state and mixing properties of minerals: I. Model calibration for olivine, orthopyroxene, cordierite, garnet and ilmenite in the system FeO-MgO-CaO-Al_2O_3-SiO_2-TiO_2. *Contributions to Mineralogy and Petrology*, **126**, 1-24.

Berman, R. G., Aranovich, L. Y. & Pattison, D. R. M., 1995. Reanalysis of the garnet-clinopyroxene Fe-Mg exchange thermometer. II. Thermodynamic analysis. *Contributions to Mineralogy and Petrology,* **119**, 30-42.

Berman, R. G., 1991. Thermobarometry using multiequilibrium calculations: a new technique with petrologic applications. *Canadian Mineralogist*, **29**, 833-855.

Berman, R. G., 1990. Mixing properties of Ca-Mg-Fe-Mn garnets. *American Mineralogist*, **75**, 833-855.

Berman, R. G., 1988. Internally-consistent thermodynamic data for stoichiometric minerals in the system Na_2O-K_2O-CaO-MgO-FeO-Fe_2O_3-Al_2O_3-SiO_2-TiO_2-H_2O-CO_2. *Journal of Petrology*, **29**, 445-522.

Bernard-Griffiths, J., Peucat, J. J., Postaire, B., Vidal, Ph., Convert, J. & Moreau, B., 1984. Isotopic data (U-Pb, Rb-Sr, Pb-Pb, and Sm-Nd) on mafic granulites from Finnish Lapland. *Precambrian Research*, **23**, 325-348.

Bhattacharya, A., Krishnakumar, K. R., Raith, M. & Sen, S. K., 1991. An improved set of a-X parameters for Fe-Mg-Ca garnets and refinements of the orthopyroxene-garnet thermometer and the orthopyroxene-garnet-plagioclase-quartz barometer. *Journal of Petrology*, **32**, 629-656.

Bibikova, E., Skiöld, T., Bogdanova, S., Gorbatschev, R. & Slabunov, A., 2001. Titanite-rutile thermochronometry across the boundary between the Archaean Craton in Karelia and the Belomorian Mobile Belt, eastern Baltic Shield. *Precambrian Research,* **105**, 315-330.

Bibikova, E. V., Skiold, T. & Bogdanova, S. V., 1996. Age and geodynamic aspects of the oldest rocks in the Precambrian Belomorian Belt of the Baltic (Fennoscandian) shield. In: Precambrian Crustal Evolution in the North Atlantic Region (Ed.: Brewer, T. S.), *Geological Society Special Publications,* **112**, 58-68.

Bibikova, E. V., Bogdanova, M. N. & Skiold, T., 1995a. New U-Pb isotope data for the Archaean in the North-West Belomorian area. *Doklady Akademii Nauk*, **344**, 794-797.

Bibikova, E. V., Slabunov, A. I., Kirnozova, T. I., Makarov, V. A. & Kevlich, V. I., 1995b. U-Pb zircon age of the Keret granite-greenstone system in the junction zone between the Karelian and the Belomorian structure of the Baltic shield. *Doklady Akademii Nauk,* **343**, 517-521.

Bibikova, E. V., Tugarinov, A. I., Gracheva, T. V & Konstantinova, M. V., 1973. The age of granulites of the Kola Peninsula. *Geochem. Int.,* **10**, 508-518.

von Blankenburg, F, Villa, I. M., Baur, H., Morteani, G. & Steiger, R. H., 1989. Time calibration of a P-T-path from the Western Tauern Window, Eastern Alps: the problem of closure temperatures. *Contributions to Mineralogy & Petrology*, **101**, 1-11.

von Blankenburg, F & Villa, I. M., 1988. Argon retentivity and argon excess in amphiboles from the garbenschists of the Western Tauern Window, Eastern Alps. *Contributions to Mineralogy & Petrology*, **100**, 1-11.

Blattner, P. & Lassey, K. R., 1989. Stable isotope exchange fronts, Damköhler numbers, and fluid to rock ratios. *Chemical Geology,* **78**, 381-392.

Bogdanova, M. N., Yefimov, M. M., Sorokhtin, N. O., Balashov, Yu. A., Gannibal, L. F. & Ryungenen, G. I., 1993. Evolution of polymetamorphism in the Granulite Belt of the Kola Peninsula(Kolvitsa zone) and U-Pb dating of diaphtoresis of an anorthosite association. *Doklady Alademii Nauk*, **331**, 332-334. (in Russian).

Bogdanova, S., V., Bibikova, E. V., 1993. The 'Saamian' of the Belomorian mobile belt: new geochronological constrains. *Precambrian Research*, **64**, 131-152.

Bohlen, S. R. & Liotta, J. J., 1986. A barometer for garnet amphibolites and garnet granulites. *Journal of Petrology*, **27**, 1025-1034.

Brey, G. P. & Köhler, T., 1990. Geothermobarometry in four-phase lherzolites. II. New thermobarometers, and practical assessment of existing thermobarometers. *Journal of Petrology*, **31**, 1353-1378.

Bridgwater, D., Scott, D. J., Balagansky, V. V., Timmerman, M. J., Marker, M., Bushim, N. L. & Daly, J. S., 2001. Age and provenance of early Precambrian metasedimentary rocks in the Lapland-Kola Belt, Russia: evidence from Pb and Nd isotopic data. *Terra Nova*, **13**, 32-37.

Bridgwater, D, Scott, D, Balagansky, V. V., Timmerman, M. J., Marker, M., Bushmin, S. A., Alexejev, N. L. & Daly, J. S., 1999. Provenance of early Precambrian metasediments in the Lapland-Kola belt as shown by $^{207}Pb/^{206}Pb$ dating of single grains of zircon and whole rock Sm-Nd isotope studies. *Doklady Akademii Nauk*, **366**, 664-668. (in Russian).

Bridgwater, D., Mengel, F., Fryer, B., Wagner, P. & Hansen, S. C., 1995. Proterozoic mafic dykes in the North Atlantic and Baltic cratons: field setting and chemistry of distinctive dyke swarms. In: *Early Precambrian Processes* (ed. Coward, M. P. & Ries, A. C.). *Geological Society Special Publication, London*, **5**, 193-210.

Bridgwater, D., Glebovitsky, V. A., Sedova, I., Miller, J., Alexejew, N., Bogdanova, M. N., Yefimov, M. M., Chekulaev, V. P., Arestova, N. A. & Lobach-Zhuchernko, S., 1994 Sub-horizontal stretching fabrics and high grade metamorphic assemblages in ca. 2.5 – 2.35 Ga syntectonic igneous suites from the Belomorian fold belt. Evidence of acid-basic igneous activity during extension in the deep crust. *Terra Abstracts*, **4**, 4.

Bridgwater, D., Marker, M. & Mengel, F., 1992. The eastern extension of the Early Proterozoic Torngat orogenic zone across the Atlantic. In: Lithoprobe, Eastern Canadian Shield Onshore-Offshore Transect (ECSOOT) (Ed. Wardle, R. J., Hall, J.), Report No. 27. Memorial University of Newfoundland, 76-91.

Bughele, A., 1987. Propagation of error and choice of standards in the ^{40}Ar-^{39}Ar technique. *Chemical Geology*, **66**, 17-19.

Burnham, C. W., Holloway, J. R. & Davis, N. F., 1969. Thermodynamic properties of water to 1000 °C and 10000 bars. *Geological Society of America, Special Paper,* **132**.

Butler, J. C., 1979. Trends in ternary petrological variation diagrams-fact or fantasy?. *American Mineralogist*, **64**, 115-1121.

Carswell, D. A. & O'Brian, P. J., 1993. Thermobarometry and geotectonic significance of high-pressure granulites: examples from the Moldanubian Zone of the Bohemian Massif in Lower Austria. *Journal of Petrology*, **34**, 427-459.

Cartwright, I. & Barnicoat, A. C., 2003. Geochemical and stable isotope resetting in shear zones from Täschalp: constrains on fluid flow during exhumation in the Western Alps. *Journal of Metamorphic Geology,* **21**, 143-161.

Cartwright, I. & Buick, I. S., 1996. Determining the direction of contact metamorphic fluid flow: an assessment of mineralogical and stable isotope criteria. *Journal of metamorphic Geology,* **14**, 289-305.

Cartwright, I., 1994. The two-dimensional pattern of metamorphic fluid flow at Mary Kathleen, Australia: fluid focusing, transverse dispersion, and implications for modelling fluid flow. *American Mineralogist,* **79**, 526-535.

Chacko, T., Lamb, M. & Farquhar, J., 1996. Ultra-high temperature metamorphism in the Kerala Khondalite Belt. In*: The Archaean and Proterozoic Terranes in Southern India within Gondwana* (ed. Santosh, M. & Yoshida, M.). Gondwana Research Group Memoir, **3**, 157-165.

Chakraborty, S. & Ganguly, J., 1991. Compositional zoning and cation diffusion in garnets. In: *Diffusion, Atomic Ordering, and Mass Transport* (ed. Ganguly, J.), *Advances in Physical Geochemistry*, **8**, pp. 120-175, Springer-Verlag.

Cherniak, D. J. & Watson, E. B., 2001, Pb diffusion in zircon: *Chemical Geology*, 172, 5-24.

Clayton, R. N. & Mayeda, T. K., 1963. The use of bromine pentafluoride in the extraction of oxygen from oxides and silicates for isotopic analysis. *Geochimica et Cosmochimica Acta*, **27**, 43-52.

Cole, D. R & Ohmoto, H., 1986. Kinetics of isotopic exchange at elevated temperatures and pressures. In: Stable Isotopes in High Temperature Geological Processes (Ed.: Valley *et al.*), *Reviews in Mineralogy,* **16**, 41-87.

Condie, K. C. & Sinha, A. K., 1996. Rare earth and other trace element mobility during mylonitisation: a comparison of the Brevard and Hope Valley shear zones in the Appalachian Mountains, USA. *Journal of Metamorphic Geology,* **14**, 213-226.

Dallmeyer, R. D & Rivers, T., 1983. Recognition of extraneous argon components through incremental-release $^{40}Ar/^{39}Ar$ analysis of biotite and hornblende across the Grenvillian metamorphic gradient in southwestern Labrador. *Geochimica et Cosmochimica Acta*, **47**, 413-428.

Daly, J. S., Balagansky, V. V., Timmerman, M. J., Whitehouse, M. J., de Jong, K., Guise, P., Bogdanova, S., Gorbatschev, R. & Bridgwater, D., 2001. Ion microprobe U-Pb zircon geochronology and isotopic evidence for a trans-crustal suture in the Lapland-Kola Orogen, northern Fennoscandian Shield. *Precambrian Research*, **105**, 289-314.

Daly, J. S., Timmerman, M. J., Balagansky, V. V., Bridgwater, D. & Marker, M., 1997. A telescoped passive margin to back-arc transition in the Lapland-Kola Orogen (LKO). Northern Fennoscandian Shield. *Su ppl. No. 1 Terra Nova*, **9**, 129.

DePoalo, D. J., 1981. Neodymium isotopes in the Colorado Frant range and crust-mantle evolution in the Proterozoic. *Nature***, 291**, 193-196.

Dipple, G. M. & Ferry, J. M., 1992. Metasomatism and fluid flow in ductile fault zones. *Contributions to Mineralogy & Petrology*, **112**, 149-164.

Dipple, G. M. & Ferry, J. M., 1992. Fluid flow and stable isotopic alteration in rocks at elevated temperatures with applications to metamorphism. *Geochimica et Cosmochimica Acta,* **56**, 3539-3550.

Dipple, G. M., Wintsch, R. P. & Andrews, M. S., 1990. Identification of the scales of differential element mobility in a ductile fault zone. *Journal of metamorphic Geology*, **8**, 645-661.

Dodson, M. H., 1973. Closure temperature in cooling geochronologic and petrologic systems. *Contributions to Mineralogy & Petrology*, **40**, 259-274.

Eckert, J. O. Jr., Newton, R. C. & Kleppa, O. J., 1991. The ΔH of reaction and recalibration of garnet-pyroxene-plagioclase-quartz geobarometers in the CMAS system by solution calorimetry. *American Mineralogist*, **76**, 148-160.

Eiler, J. M., Valley, J. W. & Baumgartner, L. P., 1993. A new look at stable isotope thermometry. *Geochimica et Cosmochimica Acta,* **57**, 2571-2583.

Eiler, J. M., Baumgartner, L. P. & Valley, J. W., 1992. Intercrystalline stable isotope diffusion: a fast grain boundary model. *Contributions to Mineralogy & Petrology,* **112**, 543-557.

Ellis, D. J. & Green, D. H., 1979. An experimental study of the effect of Ca upon garnet-clinopyroxene Fe-Mg exchange equilibria. *Contributions to Mineralogy and Petrology*, **71**, 13-22.

Engel, A. E. J. & Engel, C. G., 1962b. Hornblendes formed during progressive metamorphism of amphibolites, northwest Adirondack Mountains, *New York. Bulletin of the Geological Society of America*, **73**, 1499-1514.

Essex, , R. M., Gromet, L. P., Andréasson, P.-G. & Albrecht, L., 1997. Early Ordovician U-Pb metamorphic ages of the eclogite-bearing Seve Nappes, Northern Scandinavian Caledonides. *Journal of metamorphic Geology*, **15** 665-676.

Etheridge, M. A., Wall, V. J. & Vernon, R. H., 1983. The role of the fluid phase during metamorphism and deformation. *Journal of Metamorphic Geology*, **1**, 205-226.

Farquhar, J., Chacko, T. & Ellis, D. J., 1996. Preservation of oxygen isotopic composition in granulites from Northwestern Canada and Enderby Land, Antarctica: implications for high-temperature isotopic thermometry. *Contributions to Mineralogy & Petrology,* **125**, 213-224.

Farquhar, J., Chacko, T. and Frost, B. R., 1993. Strategies for high temperature oxygen isotope thermometry: a worked example from the Laramie Anorthosite Complex, Wyoming, USA. *Earth & Planetary Science Letters,* **117**, 407-422.

Fiorentini, E. Hoernes, S., Hoffbauer, R. & Vitanage, P. W., 1990. Nature and scale of exchange in granulitegrade rocks of Sri Lanka: A stable isotope study. In: Granulites and Continental Differentiation (Ed.: Vielzeuf, D.), Kluwer, Dordrecht, NATO-ASI Series, **113**, 311-338.

Fitzsimons , I. C. & Harley, S. L., 1994. The influence of retrograde cation exchange on granulite of P-T estimates and convergence technique for the recovery of peak metamorphic conditions. *Journal of Petrology*, **35**, 543-576.

Franz, G. & Spear, F. S., 1985. Aluminous titanite (sphene) from the Eclogite Zone, South-Central Tauern Window, Austria. *Chemical Geology*, **50**, 33-46.

Frimmel, H. E. & Frank, W., 1998. Neoproterozoic tectono-thermal evolution of the Gariep Belt and its basement, Namibia and South Africa. *Precambrian Research*, **90**, 1-28.

Frisch, T., Jackson, G. D., Glebovitsky, V. A., Yefimof, M. M., Bogdanova, M. N. & Parrish, R. R., 1995. U-Pb ages of zircon from the Kolvitsa gabbro-anorthosite complex, southern Kola Peninsula, Russia. *Petrology*, **3**, 219-225.

Frost, B. R. & Chacko, T., 1989. The granulite uncertainty principle: limitations on thermobarometry in granulites. *Journal of Geology*, **97**, 435-450.

Frost, b. R., Chamberlain, K. R.. & Schumacher, J. C., 2000. Sphene (titanite): phase relations and role as a geochronometer. *Chemical Geology*, **172**, 131-148.

Fuhrman, M. L. & Lindsley, D. H., 1988. Ternary-feldspar modelling and thermometry. *American Mineralogist*, **79**, 201-215.

Fournier, R. O. & Potter, R. W., 1982. An equation correlating the solubility of quartz in water from 25 °C to 900 °C at pressures to 10000 bars. *Geochimica et Cosmochimica Acta,* **46**, 1969-1974.

Ganguly, J., 1979. Garnet and clinopyroxene solid solutions, and geothermometry based on Fe-Mg distribution coefficient. *Geochimica et Cosmochimica Acta*, **43**, 1021-1029.

Gascoyne, M., 1986. Evidence for the stability of the potential nuclear waste host, sphene, over geological time, from uranium-lead ages and uranium-series measurements. *Applied Geochemistry*, **1**, 199-210.

Gastreich, M. 2000. Stoffliche Natur und metamorphe Entwicklung eines Orthopyroxen-Sillimanit-Gneis der Umba-Kolvitsa-Suturzone (Kola-Halbinsel). Unpublished diploma thesis, Rheinische Friedrich-Wilhelms University, Bonn, 67 p.

Giletti, B. J., 1986. Diffusion effect on oxygen isotope temperatures of slowly cooled igneous and metamorphic rocks. *Earth & Planetary Science Letters,* **77**, 218-228.

Glebovitsky, V. A., Marker, M., Alexejev, N., Bridgwater, D., Sedova, I., Salnikova, E. & Berezhnaya, N., 2001. Age, evolution and regional setting of the Palaeoproterozoic Umba igneous suite in the Kolvitsa-Umba zone, Kola Peninsula: constrains from new geological, geochemical and U-Pb zircon data. *Precambrian Research*, **105**, 247-267.

Glebovitsky, V. A., 1993. Tectonics and metamorphism of early Precambrian: the Eastern Baltic Shield. *Regionalnaya Geologia I Metallogeniya*, **1**, 7-27.

Goldstein S. L. & Jacobsen S. B., 1988. Nd and Sr isotopic systematics of rivers water suspended material: implications for crustal evolution. *Earth & Planetary Science Letters*, **87**, 249–265.

Goldstein, S. L., O'Nions, R. K. Hamilton, P. J., 1984. A Sm-Nd study of atmospharic dusts and particulates from major river systems. *Earth & Planetary Science Letters*, **70**, 221-236.

Graham, C. M. & Powell, R., 1984. A garnet-hornblende geothermometer: calibration, testing and application to the Pelona Schist, Southern California. *Journal of metamorphic Geology*, **2**, 13-31.

Grant, J. A., 1986. The isocon diagram-a simple solution to Gresen's equation for metasomatic alteration. *Economic Geology*, **81**, 1976-1982.

Green, D. H. & Ringwood, A. E., 1967. An experimental investigation of the gabbro to eclogite transformation and its petrological applications. *Geochimica et Cosmochimica Acta*, **16**, 84-114.

Gresens, R. L., 1967. Composition-volume relationships of metasomatism. *Chemical Geology,* **2**, 46-65.

Hames, W. E. and Bowring, S. A., 1994. An empirical evaluation of the argon diffusion geometry in muscovite. *Earth & Planetary Science Letters*, **124**, 161-167.

Harley, S. L., 1998a. Ultrahigh temperature granulite metamorphism (1050 °C, 12 kbar) and decompression in garnet (Mg70)-orthopyroxene-sillimanite gneisses from the Rauer Group, East Antarctica. *Journal of metamorphic Geology*, **16**, 541-562.

Harley, S. L., 1992. Proterozoic granulites. In: *Proterozoic Crustal Evolution, Developments in Precambrian Geology* (ed. Condie, K. C.), **10**, pp. 301-359. Elsevier, Amsterdam.

Harley, S. L., 1989. The origins of granulites: a metamorphic perspective. *Geological Magazine*, **126**, 215-247.

Harley, S. L., 1984a. An experimental study of the partitioning of Fe and Mg between garnet and orthopyroxene. *Contributions of Mineralogy and Petrology*, **86**, 359-373.

Harley, S. L., 1984b. The solubility of alumina in orthopyroxene coexisting with garnet in FeO-MgO-Al_2O_3-SiO_2. *Journal of Petrology*, **25**, 665-696.

Harley, S. L. & Green, D. H., 1982. Garnet-orthopyroxene barometry for granulites and peridotites. *Nature*, **300**, 697-701.

Hartel, T. H. D. & Pattison, D. R. M., 1996. Genesis of the Kapuskasing (Ontario) migmatitic mafic granulites by dehydration melting of amphibolite: the importance of quartz to reaction progress. *Journal of metamorphic Geology*, **14**, 591-611.

Harrison, T. M. & FitzGerald, J. D., 1986. Exsolution in hornblende and its consequence of the $^{40}Ar/^{39}Ar$ age spectra and closure temperature. *Geochimica et Cosmochimica Acta*, **50**, 247-253.

Harrison, T. M. & McDougall, I., 1981. Excess ^{40}Ar in metamorphic rocks from Broken Hill, New South Wales: implications for $^{40}Ar/^{39}Ar$ age spectra and thermal history of the region. *Earth & Planetary Science Letters*, **55**, 123-149.

Hjelt, S.-E., Daly, J. S., and SVEKALAPKO Colleagues., 1996. SVEKALAPKO: evolution of palaeoproterozoic and Archaean lithosphere. In: EUROPROBE 1996 – Lithosphere Dynamics: Origin and Evolution of Continents (ed. Gee, D. G., Zeyen, H. J.), EUROPROBE Secretariat, Uppsala Univ., Uppsala, Sweden, pp. 56-67.

Hoefs, J., 1997. *Stable Isotope Geochemistry*. pp. 201, Springer-Verlag Berlin Heidelberg.

Hoernes, S. & van Reenen, D. D., 1992. The oxygen-isotopic composition of granulites and retrogressed granulites from the Limpopo Belt as a monitor of fluid-rock interaction. *Precambrian Research,* **55**, 353-364.

Hoffbauer, R., Hoernes, S. & Fiorentini, E., 1994. Oxygen isotope thermometry based on a refined increment method and its application to granulite-grade rocks from Sri Lanka. *Precambrian Research,* **66**, 199-220.

Holland, T. & Blundy, J., 1994. Non-ideal interactions in calcic amphiboles and their bearing on amphibole-plagioclase thermometry. *Contributions to Mineralogy and Petrology*, **116**, 433-447.

Holland, T. J. B., 1983. The experimental determination of activities in disordered and short-range ordered jadeite clinopyroxenes. *Contributions to Mineralogy and Petrology*, **82**, 214-220.

Holland, T. J. B., 1980. The reaction albite = jadeite + quartz determined experimentally in the range of 600 – 1200 °C. *American Mineralogist*, **65**, 129-134.

Hollister, L. S., Grissom, G. C., Peters, E. K., Stowell, H. H. & Sisson, V. B., 1987. Confirmation of the empirical correlation of Al in hornblende with pressure of solidification of calc-alkaline plutons. *American Mineralogist*, **72**, 231-239.

Horwitz E. P., Dietz M. L., Chiarizia R. & Diamond H., 1992. Separation and preconcentration of uranium from acidic media by extraction chromatography. *Analytica Chimica Acta*, **266**, 25-37.

Huhma, H. & Meriläinen, K., 1991. Provenance of paragneisses from the Lapland Granulite Belt, abstract. In: Metamorphism, Deformation and Structure of the Crust (ed. Tuisku, P., Laajoki, K.), *les. Terrae. Ser. A*, **No. 5**, p. 26. University of Oulu.

Jacobsen S. B. & Wasserburg G. J. ,1984. Sm-Nd evolution of chondrites and a chondrites. *Earth & Planetary Science Letters*, **67**, 137–150.

Jäger, E., 1979. Introduction to geochronology. In : Lectures in Isotopic Geology, Ed., E. Jäger & J. C Hunziker, Springer-Verlag.

Johannes, W., 1980. Metastable melting in the granite system Qz-Or-Ab-An-H_2O. *Contributions to Mineralogy and Petrology*, **72**, 73-80.

Johannes, W., 1978. Melting of plagioclase in the system Ab-An-H_2O and Qz-Ab-An-H_2O at PH_2O= 5 kbar, an equilibrium problem. *Contributions to Mineralogy and Petrology*, **66**, 295-303.

Johnson, M. C. & Rutherford, M. J., 1989. Experimental calibration of the aluminium-in-hornblende geobarometer with application to Long Valley Caldera (California). *Geology*, **17**, 837-841.

Kaulina, T. V., 1999. U-Pb zircon ages for rocks of the Tanaelv Belt, Kola Peninsula, Russia. *J. Conf. Abstr. 4*, **1**, p. 134.

Kaulina, T. V., 1996. U-Pb dating of zircon from indicative geological objects in the Belomorian-Lapland belt (north-western Belomorian region). Ph. D. dissertation extended abstract. St. Petersburg, 18 pp.

Kaulina, T. V. & Apanasevich, E. A.,1998. The northwestern Belomorian region (Kola peninsula, Russia): U-Pb isotopic data. In: Abstracts of the SVEKALAPKO Workshop, 26-29. 11. 1998, Lammi, Finland, p. 30.

Kerrich, R., 1986. Fluid infiltration into fault zones: chemical, isotopic and mechanical effects. *Pure Applied Geophysics*, **124**, 225-268.

Kislitsyn, R. V., Balagansky, V. V., Mänttäri, I., Timmerman, M. J. & Daly, J. S., 1999a. Age of accretion and collision in the Palaeoproterozoic Lapland-Kola Belt and the Umba Granulite Terrane (UGT). In: Abstracts of the SVEKALAPKO Workshop, 18-21.11.1999, Lammi, Finland, p. 33.

Kislitsyn, R. V., Timmerman, M. J., Daly, J. S., Balagansky, V. V. & Mänttäri, I., 1999b. Isotope data (U-Pb and Sm-Nd) on the Umba granitoid complex, Kola Peninsula, Russia. In: Abstracts of the SVEKALAPKO Workshop, 18-21.11.1999, Lammi, Finland, p. 34.

Kislitsyn, R. V., Balagansky, V. V., Daly, J. S, Timmerman, M. J. & Apanasevich, E. A., 1998. U-Pb age of granulite metamorphism in the melange between the Kolvitsa volcano-plutonic belt and the Umba block of metasedimentary granulites. In: Abstracts of the SVEKALAPKO Workshop, 26-29. 11. 1998, Lammi, Finland, p. 31.

Kohn, M. J. & Spear, F. S., 1990. Two new geobarometers for garnet amphibolites, with applications to southeastern Vermont. *American Mineralogist*, **75**, 89-96.

Kozlova, N. Ye., Balagansky, V. V., Bogdanova, M. N., Rezhenova, S. A., 1991. A structural-petrological study of an orthopyroxene-sillimanite assemblage from the Lapland granulites. *Izvestiya Akademii Nauk, seriya geologicheskaya*, **4**, 66-76. (in Russian).

Krill, A. G., 1985. Svecokarelian thrusting with thermal inversion in the Karasjov-Levajok area of the northern Baltic Shield. *Norges Geologiske Undersógelse Bull*, **403**, 89-101.

Krogh Ravna, E., 2000. The garnet-clinopyroxene Fe^{2+}-Mg geothermometer: an updated calibration. *Journal of metamorphic Geology*, **18**, 211-219.

Krogh, E. J., 1988. The garnet-clinopyroxene Fe-Mg geothermometer: A reinterpretation of existing experimental data. *Contributions to Mineralogy and Petrology*, **99**, 44-48.

Krogh, T. E. , 1982. Improved accuracy of U-Pb zircon ages by creation of concordant systems using an air-abrasion technique. *Geochimica et Cosmochimica Acta*, **46**, 637-649.

Laird, J. & Albee, A. L., 1981a. High-pressure metamorphism in mafic schist from northern Vermont. *American Journal of Science*, **281**, 97-126.

Laird, J. & Albee, A. L., 1981b. Pressure, temperature, and time indicators in mafic schist: Their application to reconstructing the polymetamorphic history of Vermont. *American Journal of Science*, **281**, 127-175.

Lasaga, , A. C., 1983. Geospeedometry: an extension of geothermometry. In: *Kinetics and Equilibrium in Mineral Reactions* (ed. Saxena, S. K.) pp. 8-114. Advances in Physical Geochemistry, 3. Springer-Verlag, New York.

Leake, B. E., 1965. The relationship between tetrahedral aluminium and the maximum possible octahedral aluminium in natural calciferous and sub-calciferous amphiboles. *American Mineralogist*, **50**, 843-851.

Leake B. E. et al., 1998. Nomenclature of amphiboles. Report of the Subcommittee on Amphiboles of the International Mineralogical Association Commission on new minerals and mineral names. *European Journal of Mineralogy*. **9**, 623-651.

Leake, B. E., 1998. Widespread secondary Ca garnet and other C silicates in the Galaway Granite and its satellite plutons caused by fluid movements, western Ireland. *Mineralogical Magazine*, **62**, 381.386.

Lee, J. K. W., 1995. Multipath diffusion in geochronology. *Contributions to Mineralogy and Petrology*, **120**, 60-82.

Liou, J. G. , Kim H. S. & Maruyama, S., 1983. Prehnite-Epidote and their petrologic applications. *Journal of Petrology*, **1983**, 321-342.

Liou, J. G. , 1971. Synthesis and stability relations of prehnite, $Ca_2Al_2Si_3O_{10}(OH)_2$. *American Mineralogist*, **56**, 507-531.

Ludwig K. R., 1999. ISOPLOT/Ex.Version 2.06. A geochronological toolkit for Microsoft Excel. *Berkley Geochronology Center Special Publications*, **1a**, 49.

Ludwig K. R., 1991b. PbDat for MS-DOS, version 1.21. *U.S. Geol. Survey Open-File Rept.* 88-542. 35p.

Maboko, M. A. H. & Nakamura,E., 1995. Sm-Nd garnet ages from the Uluguru granulite complex of Eastern Tanzania: further evidence for post-metamorphic slow cooling in the Mozambique belt. *Precambrian Research*, **74**, 195-202.

Maboko, M. A. H., McDougall, I., Zeitler, P. K. & FitzGerald, J. D., 1991. Discordant ^{40}Ar-^{39}Ar ages from the Musgrave Ranges, central Australia: Implications for the significance of hornblende ^{40}Ar/^{39}Ar spectra. *Chemical Geology*, **86**, 139-160.

MacLean, W. H., 1988. Rare earth element mobility at constant inter-element ratios in the alteration zone of the Phelps Dodge massive sulphide deposit, Matagami, Quebec. *Mineralium Deposita*, **23**, 231-238.

Mäder, U. K., Percival, J. A. & Berman, R. G., 1994. Thermobarometry of garnet-clinopyroxene-hornblende granulites from the Kapuskasing structural zone. *Canadian Journal of Earth Science*, **31**, 1134-1145.

Manhés G., Minster J. F. & Allégre C. J. ,1978. Comparative uranium-thorium-lead and rubidium-strontium of Saint Severine amphoterite: consequences for Early solar system chronology. *Earth & Planetary Science Letters*, **39**, 14-24.

Marquer, D., 1994. Fluid advection in shear zones: evidence from geological and geochemical relationships in the Aiguilles Rouges Massif (Western Alps, Switzerland). *Schweizerische Mineralogische & Petrologische Mitteilungen,* **74**, 137-148.

Marquer, D. & Burkhard, M., 1992. Fluid circulation, progressive deformation and mass transfer processes in the upper crust: the example of basement-cover relationships in the External Crystalline Massifs, Switzerland. *Journal of Structural Geology,* **14**, 1047-1057.

Marquer, D., 1989. Transfert de matière et déformation des granitoïds. Aspects méthodologiques. *Schweizerisch Mineralogische & Petrologische Mitteilungen,* **69**, 13-33.

McCaig, A. M., Wickham, S. M. & Taylor, H. P., 1990. Deep fluid circulation in alpine shear zones, Pyrenees, France: field and oxygen isotope studies. *Contributions to Mineralogy and Petrology,* **106**, 41-60.

McCarthy, T. C. & Patino Douce, A. E., 1998. Empirical calibration of the silica-Ca-tschemak's-anorthite (SCAn) geobarometer. *Journal of metamorphic Geology*, **16**, 675-686.

McDougall, I. & Harrison, T. M., 1988. Geochronology and thermochronology by the ^{40}Ar/^{39}Ar method. Oxford, New York.

Mezger, K., Essene, E. J., van der Pluijm, B. A. & Halliday, A. N., 1993. U-Pb geochronology of the Grenville Orogen of Ontario and New York: constrains on ancient crustal tectonics. *Contributions to Mineralogy and Petrology*, **114**, 13-26.

Mezger, K., Essene, E. J. & Halliday, A. N., 1992. Closure temperature of the Sm-Nd system in metamorphic garnets. *Earth & Planetary Science Letters*, **113**, 397-409.

Mezger. K., Rawnseley, C. M., Bohlen, S. R. & Hanson, G. N., 1991. U-Pb garnet, sphene, monazite, and rutile ages: implications for the duration of the high-grade metamorphism and cooling histories, Adirondack Mts., New York. *Journal of Geology*, **99**, 415-428.

Miller, B. V., 2001. U-Pb closure temperatures and metamorphic cooling rates from coexisting rutile and titanite. *Geological Society of America-50th annual meeting*, **33**, 7.

Mitrofanov, F. P. (Editor-in-Chief), 1996. Geological Map of the Kola Region (North-Eastern Baltic Shield). Scale 1:500000. *Geological Institute, Kola Science Centre, Russian Academy of Science*, Apatity, 1996.

Mitrofanov, F. P., Balagansky, V. V., Balashov, Yu. A., Dokuchehaeva, V. S., Gannibal, L. F., Nerovich, L. I., Radachenko & M. K., Ryungenen, G. I., 1995b. U-Pb age of gabbro-anorthosite massifs in the Lapland Granulite Belt. *Norges Geologiske Undersögelse*, **7**, Special Publication, 179-183.

Morimoto, N. et al., 1988. Nomenclature of pyroxenes. Subcommittee on Pyroxenes, Commission on New Minerals and Mineral Names International Mineralogical Association. *Mineralogy and Petrology,* **39**, 55-76.

Muehlenbachs, K., 1986. Alteration of the oceanic crust and the ^{18}O history of seawater. In: Stable Isotopes in High Temperature Geological Processes (Ed. Valley *et al.*), *Reviews in Mineralogy,* **16**, 425-444.

Newton, R. C., 1983. Geobarometry of high-grade metamorphic rocks. *American Journal of Science*,, **283-A**, 1-28.

Newton, R. C. & Perkins, D., 1982. Thermodynamic calibration of geobarometers based on the assemblage garnet-plagioclase-orthopyroxene (clinopyroxene)-quartz. *American Mineralogist*, **67**, 203-222.

O'Hara, K., 1990. State of strain in mylonites from the western Blue Ridge province, southern Appalachians: the role of volume loss. *Journal of Structural Geology,* **12**, 419-430.

O'Hara, K., 1988. Fluid flow and volume loss during mylonitisation: an origin for phyllonite in an overthrust setting, North Carolina, USA. *Tectonophysics,* **156**, 21-36.

Oliver, N. H. S., 1996. Review and classification of structural controls on fluid flow during regional metamorphism. *Journal of Metamorphic Geology*, **14**, 477-492.

Pan, , Y., Fleet, M. E. & MacRae, N. D., 1993. Late alteration in titanite (Ca TiSiO5): redistribution and remobilization of rare earth elements and implications for U-Pb and Th-Pb geochronology and nuclear waste disposal. *Geochimica et Cosmochimica Acta*, **57**, 355-367.

Paria, P., Bhattacharya, A. & Sen, S. K., 1988. The reaction garnet + clinopyroxene + quartz = 2 orthopyroxene + anorthite: A potential geobarometer for granulites. *Contributions to Mineralogy and Petrology*, **99**, 126-133.

Park, R. G., 1994. Early Proterozoic tectonic overview of the northern British Isles and neighbouring terrains in Laurentia and Baltica. *Precambrian Research*, **68**, 65-79.

Pattison, D. R. M., Chacko, T., Farquhar, J. & McFarlane, C. R. M., 2003. Temperatures of granulite-facies metamorphism: Constrains from experimental phase equilibria and thermobarometry corrected for retrograde exchange. *Journal of Petrology*, **44**, 867-900.

Pattison, D. R. M., 2003. Petrogenetic significance of orthopyroxene-free garnet + clinopyroxene + plagioclase-bearing metabasites with respect to the amphibolite and granulite facies. *Journal of Metamorphic Geology*, **21**, 21-34.

Pattison, D. R. M. & Bégin, N. J.,1994. Zoning patterns in orthopyroxene and garnet in granulites: implications for geothermometry. *Journal of Metamorphic Geology*, **12**, 387-410.

Pattison, D. R. M., 1991. Infiltration-driven dehydration and anatexis in granulite facies metagabbro, Grenville Province, Ontario, Canada. *Journal of metamorphic Geology*, **9**, 315-332.

Perchuk, l. L., Aranovich, L. Y., Podleskii, K. K., Lavrent'eva, I. V., Gerasimov, V. Y. U., Fredk'in, V. V., Kitsul, V. I., Karsakov, L. P. & Berdnikov, N. V., 1985. Precambrian granulites of the Aldan Shield, eastern Siberia, USSR. *Journal of metamorphic Geology*, **3**, 265-310.

Perkins, D. III & Chipera, S. J., 1985 Garnet-orthopyroxene-plagioclase-quartz barometry: refinement and application to the English River subprovince and the Minnesota River valley. *Contributions to Mineralogy and Petrology*, **89**, 6-80.

Perkins, D. III &Newton, R. C., 1981. Charnockite geobarometers based on coexisting garnet-pyroxene-plagioclase-quartz. *Nature*, **292**, 144-146.

Pidgeon, , R. T., Bosch, D. & Bruguier, O., 1996. Inherited zircon and titanite U-Pb systems in an Acheaen syenite from southwestern Australia: implications for U-Pb stability of titanite. *Earth & Planetary Science Letters*, **141**, 187-198.

Piwinskii, A. J., 1969. Experimental studies of igneous rock series: Central Sierra Nevada Batholith, California. *Journal of Geology*, **76**, 548-570.

Potdevin, J. L. & Marquer, D., 1987. Méthodes de quantification des transferts de matière par les fluides dans les roches métamorphiques déformées. *Geodinamica Acta,* **1**, 3, 193-206.

Powell, R., 1985. Regression diagnostics and robust regression in geothermometer/geobarometer calibration: The garnet-clinopyroxene geothermometer revisited. *Journal of metamorphic Geology*, **3**, 231-243.

Powell, D. R. M. & Holland, T. J. B., 1988. An internally consistent dataset with uncertainties and correlations: 3. Applications to geobarometry, worked examples and computer program. *Journal of Metamorphic Geology***, 6**, 173-204.

Powneby, M. I., Wall, V. J & O'Neill, H. St.. C., 1987. Fe-Mn partitioning between garnet and ilmenite: experimental calibration and applications. *Contributions to Mineralogy and Petrology*, **97**, 116-126.

Powneby, M. I., Wall, V. J & O'Neill, H. St.. C., 1987 Erratum. Fe-Mn partitioning between garnet and ilmenite: experimental calibration and applications. *Contributions to Mineralogy and Petrology*, **97**, 539.

Powneby, M. I., Wall, V. J & O'Neill, H. St.. C., 1991. An experimental study of the effect of Ca upon garnet-ilmenite Fe-Mg exchange equilibria. *American Mineralogist*, **76**, 1580-1588.

Raase , P., 1974. Al and Ti contents of hornblende, indicators of pressure and temperature of regional metamorphism. *Contributions to Mineralogy and Petrology*, **45**, 231-236.

Renne, P. R., Deino, A. L., Walter, R. C., Turrin, B. D., Swisher, C. C., Becker, T. A., Curtis, G. H., Sharp, W. D. & Jaouni, A.-R., 1994. Intercalibration of astronomical and radioisotopic time. *Chemical Geology*, **66**, 27-34.

Resor, P. G., Chamberlain, K. R., Frost, C. D., Snoke, A. W. & Frost, B. R., 1996. Direct dating of deformation: U-Pb age of syndeformational sphene growth in the Proterozoic Laramie Peak shear zone. *Geology*, **24**, 623-626.

Richard P., Shimizu N. & Allégre C. J., 1976. $^{143}Nd/^{144}Nd$, a natural tracer: An application to oceanic basalts. *Earth & Planetary Science Letters*, **31**, 269-278.

Richter, R. & Hoernes, S., 1988. The application of the increment method in comparison with experimentally derived calculated O-isotope fractionations. *Chemie der Erde,* **48**, 1-18.

Ring, U., 1999. Volume loss, fluid flow, and coaxial versus noncoaxial deformation in retrograde, amphibolite facies shear zones, northern Malawi, east-central Africa. *GSA Bulletin,* **111**, 123-142.

Rivers, T. & Mengel, F. C., 1988. Contrasting assemblages and petrogenetic evolution of corona and noncorona gabbros in the Grenville Province of western Labrador. *Canadian Journal of Earth Sciences*, **25**, 1629-1648.

Robinson, P., 1982. The composition space of terrestrial pyroxenes – internal and external limits. *Reviews in Mineralogy*, **7**, *Mineralogical Society of America*, 419-494.

Roddick, J. C., Cliff, R. A. & Rex, D. C., 1980. The evolution of excess argon in alpine biotites $^{40}Ar/^{39}Ar$ analysis. *Earth & Planetary Science Letters*, **48**, 185-208.

Rollinson, H., 1993. Using geochemical data: evaluation, presentation, interpretation. John Wiley and Sons, New York. 352 p.

Samson , S. D. & Alexander, E. C., 1987. Calibration of the interlaboratory ^{40}Ar-^{39}Ar dating standard, MMhb-1. *Chemical Geology*, **66**, 27-34.

Schärer, U., Zhang, L.-S. & Tapponier, P., 1994. Duration of strike-slip movements in large shear zones: the Red River belt, China. *Earth & Planetary Science Letters*, **126**, 379-397.

Schmidt, M. W., 1992. Amphibole composition in tonalite as a function of pressure: an experimental calibration of the Al-in-hornblende barometer. *Contributions to Mineralogy and Petrology*, **110**, 304-310.

Schütze, H., 1980. Der Isotopenindex - eine Inkrementmethode zur näherungsweisen Berechnung von Isotopenaustauschgleichgewichten zwischen kristallinen Substanzen. *Chemie der Erde,* **39**, 321-271.

Scott, D. J. & St-Onge, M. R., 1995. Constrains on Pb closure temperature in titanite based on rocks from the Ungava Orogen, Canada; implications for U-Pb geochronology and P-T-t path determination. *Geology*, **23**, 1123-1126.

Selverstone, J., Morteani, G. & Staude, J. M., 1991. Fluid channelling during ductile shearing: transformation of granodiorite into aluminous schist in the Tauern Window, eastern Alps. *Journal of Metamorphic Geology,* **9**, 419-431.

Sorjonen-Ward, P., Claoué-Long, J. & Huhma, H., 1994. SHRIMP isotope studies of granulite zircons and their relevance to Early Proterozoic tectonics in Northern Fennoscandia. *Us Geol. Surv. Circ.,* **1107**, p. 299.

Spear, F. S., 1993. *Metamorphic Phase Equilibria and Pressure-Temperature-Time Paths*, pp. 511-545. Mineralogical Society of America Monograph. Washington.

Spear, F. S., 1981. An experimental study of hornblende stability and compositional variability in amphibolite. *American Journal of Science*, **281**, 697-734.

Stacey J. S. & Kramers I. D., 1975. Approximation of terrestrial lead isotope evolution by a two-stage model. *Earth & Planetary Science Letters*, **26**, 207-221.

Stähle, H. J., Raith, M., Hoernes, S. & Delfs, A., 1987. Element mobility during incipient granulite formation at Kabbaldurga, southern India. *Journal of Petrology*, **28**, 803 – 834.

Steiger R. H. & Jager E., 1977. Subcomission on geochronology: convention on the use of decay constants in geo- and cosmochronology. *Earth & Planetary Science Letters*, **36**, 359-362.

St-Onge, M. R. & Ijewliw, O. J., 1996. Mineral corona formation during high-P retrogression of granulitic rocks, Ungava Orogen, Canada. *Journal of Petrology*, **37**, 553-582.

Streit, J. E. & Cox, S. F., 1998. Fluid infiltration and volume change during mid-crustal mylonitisation of Proterozoic granite, King Island, Tasmania. *Journal of Metamorphic Geology,* **16**, 197-212.

Thomson, R. N., Morrison, M. A., Hendry, G. L. & Parry, S. J., 1984. An assessment of the relative roles of a crust and mantle in magma genesis: an elemental approach. *Phil. Trans. R. Soc. London,* **A310**, 549-590.

Timmerman, M. J., Balagansky, V. V., Daly, J. S. & Kislitsyn, R. V., 1997. HT-HP metamorphism during Palaeoproterozoic (C. 1.9 Ga) terrane accretion in the south-eastern Lapland-Kola Belt. In: *Abstracts of the SVEKALAPKO Workshop*, 27.-30. 11. 1997., Lammi, Finland, p. 71.

Timmerman, M. J., 1996. Crustal evolution of the Kola Region, Baltic Shield, Russia. *Unpublished Ph. D. Thesis.* National University of Ireland, Dublin, 233 p.

Timmerman, M. J. & Daly, J. S., 1995. Sm-Nd evidence for late Archaean crust formation in the Lapland-Kola Mobile Belt, Kola Peninsula, Russia and Norway. *Precambrian Research*, **72**, 97-107.

Timmerman, M. J. & Balagansky, V. V., 1994. Tectonic and thermal evolution of the Palaeoproterozoic Kolvitsa Belt, Kola Peninsula, Russia. *Terra Nova,* **6 (2)**, 19.

Tracy, R. J., 1982. Compositional zoning and inclusions in metamorphic minerals. In: *Characterisation of Metamorphism Trough Mineral Equilibria* (ed. Ferry, J. M.), *Mineralogical Society of America Reviews in Mineralogy*, **10**, 355-397.

Tugarinov, A. I. & Bibikova, E. V., 1980. Geochronology of the Baltic Shield on zircon age data. Nauka Publishing House, Moscow, 131 pp. (in Russian).

Tulloch, A. J., 1979. Secondary Ca-Al silicates as low-grade alteration products of granitoid biotite. *Contributions to Mineralogy and Petrology*, **69**, 105-117.

Valley, J. W., 1986. Stable isotope geochemistry of metamorphic rocks. In: Stable Isotopes in High Temperature Geological Processes (Ed.: Valley et al.), *Reviews in Mineralogy,* **16**, 445-489.

Verts, L. A., Chamberlain, K. R. & Frost, C. D., 1996. U-Pb sphene dating of metamorphism: the importance of sphene growth in the contact aureole of the Red Mountain Pluton, Laramie Mountains, Wyoming. *Contributions to Mineralogy and Petrology*, **125**, 186-199.

Wang, X. D., Söderlund, U., Lindh, A. & Johansson, L., 1998. U-Pb and Sm-Nd dating of high-pressure granulite- and upper amphibolite facies rocks from SW Sweden. *Precambrian Research*, **92**, 319-339.

Witt-Eikschen, G. & Seck, H. A., 1991. Solubility of Ca and Al in orthopyroxene from spinel peridotite: An improved version of an empirical geothermometer. *Contributions to Mineralogy and Petrology*, **106**, 431-439.

Willson, M., 1995. Igneous Petrogenesis-A global tectonic approach. Chapman & Hall, London.

Wolf, M. B. & Wyllie, P. J., 1994. Dehydration-melting of amphibole at 10 kbar: the effects of temperature and time. *Contribution to Mineralogy and Petrology*, **115**, 369-383.

Wyllie, P. J. & Wolf, M. B., 1993. Amphibolite dehydration-melting: sorting out the solidus. In: *Magmatic Processes and Plate Tectonics*, Special publication (ed. Prichard, H. M., Alabaster, T., Harris, N. B. W. & Neary, C. R.), **76**, pp. 405-416, Geological Society, London.

Xie, Z. & Walther, J. V., 1993. Quartz solubilities in NACl solutions with and Without wollastonite at elevated temperatures and pressures. *Geochimica et Cosmochimica Acta,* **57**, 1947-1955.

Yonkee, W. A., Parry, W. T. & Bruhn, R. L., 2003. Relations between progressive deformation and fluid-rock interaction during shear-zone growth in a basement-cored thrust sheet, Sevier orogenic belt, Utah. *American Journal of Science,* **303**, 1-59.

Zhang, L. S. & Schärer, U., 1996. Inherited Pb components in magmatic titanite and their consequence for the interpretation of U-Pb ages, *Earth & Planetary Science Letters*, **138**, 1-4.

Zhao, G. C., Wilde, S. A., Cawood, P. A. & Lu, L. Z., 2000. Petrology and P-T path of the Fuping mafic granulites: implications for tectonic evolution of the central zone of the North China craton. *Journal of metamorphic Geology*, **18**, 375-391.

EMP analyses of amphibole cores, rims, symplectites and inclusions from different rock types. Analyses were recalculated on an unhydrous basis of 23 oxygens. General amphibole formulae were recalculated with minpet.

	0708-3: metagabbro Bolschoi Khed											0708-4: hydr. Bolschoi		
wt.-%	*#61 sympl.*	*#74 core*	*#75*	*#76 rim*	*#84 rim*	*#95 core*	*#96 rim*	*#105 sympl.*	*#106 sympl.*	*#107 sympl.*	*#111 sympl.*	*#1 core*	*#2*	*#3 rim*
SiO_2	45.37	45.25	47.93	48.46	46.17	48.40	49.02	46.42	45.34	43.71	43.90	45.02	45.90	44.73
TiO_2	0.00	0.91	0.91	1.20	0.09	1.29	1.00	0.61	0.80	0.60	1.44	0.38	0.36	0.32
Al_2O_3	31.18	10.35	8.45	6.27	27.60	6.45	6.11	12.65	12.65	18.53	14.05	12.00	11.35	12.25
FeO	2.60	8.07	5.54	6.38	0.76	6.16	6.06	7.93	7.14	7.18	7.63	12.53	11.89	12.20
Cr_2O_3	0.00	0.00	0.00	0.00	0.00	0.00	0.00	0.00	0.00	0.00	0.00	0.00	0.00	0.00
MnO	0.08	0.03	0.10	0.07	0.01	0.04	0.13	0.04	0.04	0.11	0.10	0.21	0.26	0.24
MgO	2.32	12.72	12.50	13.96	2.33	14.20	14.22	16.92	16.46	12.88	15.14	14.34	14.39	14.16
CaO	14.95	19.84	22.57	20.71	18.26	20.29	21.36	12.03	12.28	12.72	12.13	11.33	11.38	11.36
Na_2O	1.62	1.17	0.75	0.71	1.25	0.69	0.69	0.93	1.05	1.21	1.34	1.36	1.33	1.30
K_2O	0.10	0.34	0.03	0.25	0.06	0.29	0.08	0.65	0.86	0.67	1.10	0.46	0.40	0.45
F	0.00	0.00	0.00	0.00	0.00	0.00	0.00	0.00	0.00	0.00	0.00	0.00	0.00	0.00
Cl	0.00	0.00	0.00	0.00	0.00	0.00	0.00	0.00	0.00	0.00	0.00	0.00	0.00	0.00
Total	98.22	98.68	98.78	98.01	96.53	97.81	98.67	98.18	96.62	97.61	96.83	97.63	97.26	97.01
CTotal	100.46	100.85	100.98	100.25	98.71	100.03	100.97	100.60	98.97	99.94	99.33	99.82	99.44	99.23
TSi	6.64	6.74	7.19	7.25	7.00	7.23	7.28	6.49	6.48	6.24	6.33	6.46	6.60	6.45
TAl	1.36	1.26	0.81	0.73	1.00	0.77	0.69	1.51	1.52	1.76	1.67	1.54	1.40	1.55
TFe^{3+}	0.00	0.00	0.00	0.02	0.00	0.00	0.03	0.00	0.00	0.00	0.00	0.00	0.00	0.00
TTi	0.00	0.00	0.00	0.00	0.00	0.00	0.00	0.00	0.00	0.00	0.00	0.00	0.00	0.00
CAl	4.01	0.55	0.68	0.38	3.93	0.37	0.38	0.57	0.61	1.35	0.72	0.49	0.53	0.53
CCr	0.00	0.00	0.00	0.00	0.00	0.00	0.00	0.00	0.00	0.00	0.00	0.00	0.00	0.00
CFe^{3+}	0.00	0.38	0.32	0.29	0.00	0.28	0.33	0.63	0.43	0.00	0.20	0.79	0.61	0.76
CTi	0.00	0.10	0.10	0.14	0.01	0.15	0.11	0.06	0.09	0.06	0.16	0.04	0.04	0.04
CMg	0.51	2.82	2.80	3.12	0.53	3.16	3.15	3.53	3.51	2.74	3.25	3.07	3.09	3.05
CFe^{2+}	0.32	0.62	0.38	0.49	0.10	0.48	0.40	0.21	0.38	0.84	0.67	0.61	0.72	0.61
CMn	0.01	0.00	0.01	0.01	0.00	0.01	0.02	0.00	0.00	0.01	0.01	0.01	0.02	0.02
CCa	0.16	0.52	0.71	0.58	0.43	0.55	0.62	0.00	0.00	0.00	0.00	0.00	0.00	0.00
BFe^{2+}	0.00	0.00	0.00	0.00	0.00	0.00	0.00	0.09	0.05	0.02	0.05	0.11	0.10	0.10
BMn	0.00	0.00	0.00	0.00	0.00	0.00	0.00	0.00	0.00	0.01	0.01	0.01	0.02	0.02
BCa	2.00	2.00	2.00	2.00	2.00	2.00	2.00	1.80	1.88	1.95	1.87	1.74	1.75	1.76
BNa	0.00	0.00	0.00	0.00	0.00	0.00	0.00	0.11	0.06	0.03	0.07	0.14	0.13	0.13
ACa	0.19	0.65	0.92	0.74	0.54	0.70	0.79	0.00	0.00	0.00	0.00	0.00	0.00	0.00
ANa	0.46	0.34	0.22	0.21	0.37	0.20	0.20	0.15	0.23	0.31	0.31	0.24	0.24	0.23
AK	0.02	0.07	0.01	0.05	0.01	0.06	0.02	0.12	0.16	0.12	0.20	0.08	0.07	0.08

	0708-4: hydr. Metagabbro Bolschoi Khed																
wt.-%	*#9 core*	*#10 rim*	*#11 core*	*#12*	*#13 rim*	#11	#12	#13	#14	#19	#20	#21	#22	#23	#24	#25	#26
SiO_2	45.25	42.52	45.30	44.80	44.84	46.20	46.50	45.77	46.59	46.61	46.32	46.00	46.60	44.89	45.62	45.87	45.97
TiO_2	0.40	0.45	0.41	0.40	0.40	0.32	0.32	0.30	0.32	0.28	0.39	0.37	0.35	0.36	0.38	0.38	0.39
Al_2O_3	12.17	13.50	11.80	12.25	12.43	11.92	11.91	12.33	11.24	11.72	11.90	11.81	11.37	12.77	11.84	11.93	11.63
FeO	12.27	13.18	11.86	12.04	12.71	11.52	11.35	11.47	11.74	12.15	11.95	12.26	12.19	12.81	12.49	12.41	12.70
Cr_2O_3	0.00	0.00	0.00	0.00	0.00	0.07	0.06	0.04	0.03	0.13	0.11	0.04	0.13	0.05	0.05	0.03	0.04
MnO	0.11	0.19	0.19	0.21	0.21	0.17	0.21	0.25	0.18	0.19	0.20	0.25	0.23	0.19	0.20	0.14	0.20
MgO	14.26	13.35	14.21	13.86	14.09	14.79	14.84	14.66	15.51	14.67	14.58	14.66	14.97	13.76	14.49	14.65	14.71
CaO	11.48	11.59	11.36	11.47	11.51	11.66	11.91	11.67	11.79	11.40	11.53	11.56	11.63	11.63	11.68	11.44	11.62
Na_2O	1.37	1.49	1.42	1.29	1.28	1.30	1.42	1.35	1.20	1.29	1.34	1.44	1.45	1.55	1.36	1.43	1.40
K_2O	0.43	0.51	0.45	0.43	0.42	0.43	0.39	0.44	0.31	0.32	0.41	0.45	0.40	0.37	0.43	0.46	0.45
F	0.00	0.00	0.00	0.00	0.00	0.10	0.00	0.00	0.09	0.00	0.15	0.07	0.02	0.10	0.04	0.09	0.00
Cl	0.00	0.00	0.00	0.00	0.00	0.06	0.07	0.07	0.07	0.08	0.07	0.08	0.06	0.07	0.08	0.07	0.09
Total	97.74	96.78	97.00	96.75	97.89	98.47	98.92	98.31	99.04	98.71	98.84	98.95	99.27	98.50	98.61	98.87	99.16
CTotal	99.94	98.90	99.14	98.94	100.27	100.59	101.08	100.44	101.14	100.94	100.98	101.05	101.50	100.58	100.73	100.96	101.30
TSi	6.48	6.20	6.54	6.49	6.42	6.56	6.57	6.51	6.55	6.59	6.56	6.52	6.57	6.42	6.49	6.50	6.50
TAl	1.52	1.81	1.46	1.51	1.58	1.44	1.43	1.50	1.45	1.41	1.44	1.48	1.43	1.58	1.51	1.50	1.50
TFe^{3+}	0.00	0.00	0.00	0.00	0.00	0.00	0.00	0.00	0.00	0.00	0.00	0.00	0.00	0.00	0.00	0.00	0.00
TTi	0.00	0.00	0.00	0.00	0.00	0.00	0.00	0.00	0.00	0.00	0.00	0.00	0.00	0.00	0.00	0.00	0.00
CAl	0.54	0.51	0.55	0.58	0.51	0.55	0.56	0.57	0.41	0.54	0.55	0.49	0.45	0.57	0.47	0.50	0.44
CCr	0.00	0.00	0.00	0.00	0.00	0.01	0.01	0.00	0.00	0.02	0.01	0.00	0.01	0.01	0.01	0.00	0.00
CFe^{3+}	0.69	0.88	0.59	0.63	0.80	0.63	0.54	0.64	0.82	0.68	0.62	0.69	0.68	0.66	0.73	0.72	0.76
CTi	0.04	0.05	0.05	0.04	0.04	0.03	0.03	0.03	0.03	0.03	0.04	0.04	0.04	0.04	0.04	0.04	0.04
CMg	3.05	2.90	3.06	2.99	3.01	3.13	3.13	3.11	3.25	3.09	3.08	3.10	3.15	2.93	3.07	3.10	3.10
CFe^{2+}	0.68	0.65	0.74	0.74	0.62	0.65	0.72	0.63	0.47	0.63	0.69	0.66	0.65	0.78	0.67	0.64	0.64
CMn	0.01	0.01	0.01	0.01	0.01	0.01	0.01	0.02	0.01	0.01	0.01	0.02	0.01	0.01	0.01	0.01	0.01
CCa	0.00	0.00	0.00	0.00	0.00	0.00	0.00	0.00	0.00	0.00	0.00	0.00	0.00	0.00	0.00	0.00	0.00
BFe^{2+}	0.11	0.08	0.10	0.09	0.10	0.10	0.08	0.09	0.09	0.12	0.11	0.10	0.10	0.09	0.09	0.12	0.10
BMn	0.01	0.01	0.01	0.01	0.01	0.01	0.01	0.02	0.01	0.01	0.01	0.02	0.01	0.01	0.01	0.01	0.01
BCa	1.76	1.81	1.76	1.78	1.77	1.77	1.80	1.78	1.78	1.73	1.75	1.76	1.76	1.78	1.78	1.74	1.76
BNa	0.13	0.10	0.13	0.12	0.13	0.12	0.10	0.12	0.12	0.15	0.13	0.13	0.13	0.12	0.12	0.14	0.13
ACa	0.00	0.00	0.00	0.00	0.00	0.00	0.00	0.00	0.00	0.00	0.00	0.00	0.00	0.00	0.00	0.00	0.00
ANa	0.25	0.32	0.27	0.25	0.23	0.24	0.29	0.25	0.21	0.21	0.24	0.27	0.27	0.31	0.26	0.25	0.26
AK	0.08	0.10	0.08	0.08	0.08	0.08	0.07	0.08	0.06	0.06	0.07	0.08	0.07	0.07	0.08	0.08	0.08

	0708-4			0708-5: hydrated metagabbro Bolschoi Khed									1008-B3: metagabbro	
wt.-%	#27	#28	#29	*#1 core*	*#2*	*#3*	*#4 rim*	*#7*	*#8 rim*	*#9*	*#10*	*#11*	*#23*	*#28 incl.*
SiO_2	46.15	45.70	46.33	45.95	45.18	45.82	45.77	45.70	45.57	44.85	45.09	45.01	46.57	43.33
TiO_2	0.39	0.36	0.36	0.81	0.81	0.73	0.79	0.81	0.86	0.96	0.91	0.94	1.10	2.17
Al_2O_3	11.72	11.60	11.57	10.77	11.00	10.51	10.63	10.74	11.65	11.59	11.49	11.79	11.48	14.28
FeO	12.31	12.41	12.38	13.51	13.37	13.59	13.18	13.36	13.50	13.89	13.50	13.92	9.53	9.04
Cr_2O_3	0.09	0.13	0.13	0.00	0.00	0.00	0.00	0.00	0.00	0.00	0.00	0.00	0.00	0.00
MnO	0.21	0.19	0.21	0.17	0.24	0.17	0.24	0.26	0.20	0.20	0.16	0.18	0.05	0.01
MgO	14.68	14.45	14.76	14.10	13.79	13.96	13.95	13.73	13.50	13.44	13.46	13.37	15.62	14.59
CaO	11.68	11.36	11.43	11.31	11.35	11.23	11.30	11.40	11.32	11.48	11.37	11.27	12.15	11.97
Na_2O	1.41	1.46	1.41	1.36	1.45	1.41	1.30	1.38	1.45	1.47	1.46	1.54	1.00	1.61
K_2O	0.43	0.40	0.44	0.42	0.44	0.43	0.47	0.48	0.44	0.53	0.49	0.52	0.90	1.25
F	0.06	0.13	0.03	0.00	0.00	0.00	0.00	0.00	0.00	0.00	0.00	0.00	0.00	0.00
Cl	0.07	0.06	0.07	0.00	0.00	0.00	0.00	0.00	0.00	0.00	0.00	0.00	0.00	0.00
Total	99.11	98.12	98.99	98.40	97.63	97.85	97.63	97.86	98.49	98.41	97.93	98.54	98.40	98.25
CTotal	101.27	100.27	101.21	100.58	99.90	100.02	99.79	100.09	100.67	100.63	100.10	100.70	100.56	100.35
TSi	6.53	6.53	6.55	6.58	6.53	6.60	6.61	6.60	6.53	6.46	6.51	6.47	6.60	6.22
TAl	1.47	1.47	1.45	1.42	1.47	1.40	1.40	1.40	1.47	1.54	1.49	1.53	1.40	1.78
TFe^{3+}	0.00	0.00	0.00	0.00	0.00	0.00	0.00	0.00	0.00	0.00	0.00	0.00	0.00	0.00
TTi	0.00	0.00	0.00	0.00	0.00	0.00	0.00	0.00	0.00	0.00	0.00	0.00	0.00	0.00
CAl	0.48	0.48	0.48	0.39	0.41	0.39	0.41	0.42	0.50	0.42	0.47	0.46	0.52	0.63
CCr	0.01	0.02	0.02	0.00	0.00	0.00	0.00	0.00	0.00	0.00	0.00	0.00	0.00	0.00
CFe^{3+}	0.68	0.69	0.71	0.69	0.65	0.66	0.63	0.58	0.57	0.65	0.58	0.62	0.37	0.22
CTi	0.04	0.04	0.04	0.09	0.09	0.08	0.09	0.09	0.09	0.10	0.10	0.10	0.12	0.23
CMg	3.10	3.08	3.11	3.01	2.97	3.00	3.00	2.96	2.89	2.89	2.90	2.86	3.30	3.12
CFe^{2+}	0.68	0.68	0.64	0.82	0.87	0.86	0.86	0.94	0.94	0.93	0.95	0.94	0.69	0.79
CMn	0.01	0.01	0.01	0.01	0.02	0.01	0.02	0.02	0.01	0.01	0.01	0.01	0.00	0.00
CCa	0.00	0.00	0.00	0.00	0.00	0.00	0.00	0.00	0.00	0.00	0.00	0.00	0.00	0.00
BFe^{2+}	0.10	0.11	0.11	0.11	0.10	0.11	0.10	0.10	0.11	0.10	0.10	0.11	0.07	0.07
BMn	0.01	0.01	0.01	0.01	0.02	0.01	0.02	0.02	0.01	0.01	0.01	0.01	0.00	0.00
BCa	1.77	1.74	1.73	1.73	1.76	1.73	1.75	1.76	1.74	1.77	1.76	1.74	1.85	1.84
BNa	0.12	0.14	0.14	0.14	0.13	0.14	0.13	0.13	0.14	0.12	0.13	0.14	0.08	0.09
ACa	0.00	0.00	0.00	0.00	0.00	0.00	0.00	0.00	0.00	0.00	0.00	0.00	0.00	0.00
ANa	0.26	0.27	0.24	0.24	0.28	0.25	0.23	0.26	0.27	0.29	0.28	0.29	0.19	0.36
AK	0.08	0.07	0.08	0.08	0.08	0.08	0.09	0.09	0.08	0.10	0.09	0.10	0.16	0.23

1008-B2: hydrated metagabbro Kataransky Cape

wt.-%	*#6 sympl.*	*#7 sympl.*	*#9 sympl.*	*#11 sympl.*	*#18 symp.*	*#22 rim*	*#23*	*#24 core*	*#25 core*	*#26 rim*	*#27 sympl.*	*#40 core*	*#41*	*#42 rim*
SiO_2	46.74	45.52	45.90	45.61	45.49	45.58	44.96	47.44	46.05	46.01	44.01	45.44	45.17	45.26
TiO_2	0.46	0.46	0.43	0.51	0.50	0.35	0.35	0.25	0.28	0.32	0.30	0.52	0.50	0.52
Al_2O_3	10.44	10.76	10.59	10.93	11.43	11.08	11.72	9.57	10.77	10.86	12.10	11.40	11.39	11.24
FeO	13.17	14.20	13.60	14.07	14.03	14.17	14.19	13.81	14.22	14.00	15.05	14.82	14.71	14.37
Cr_2O_3	0.00	0.00	0.00	0.00	0.00	0.00	0.00	0.00	0.00	0.00	0.00	0.00	0.00	0.00
MnO	0.25	0.23	0.23	0.28	0.25	0.23	0.24	0.28	0.27	0.31	0.29	0.20	0.26	0.26
MgO	12.91	12.71	12.75	12.34	12.14	12.47	12.03	13.57	12.77	12.46	11.94	11.88	12.05	12.18
CaO	12.09	12.08	12.15	12.02	12.10	12.08	12.09	12.02	11.95	11.91	11.91	11.85	11.84	11.83
Na_2O	1.11	1.16	1.14	1.22	1.23	1.17	1.27	1.08	1.17	1.07	1.28	1.33	1.32	1.31
K_2O	0.53	0.53	0.55	0.55	0.62	0.55	0.59	0.39	0.50	0.48	0.67	0.57	0.59	0.56
F	0.00	0.00	0.00	0.00	0.00	0.00	0.00	0.00	0.00	0.00	0.00	0.00	0.00	0.00
Cl	0.00	0.00	0.00	0.00	0.00	0.00	0.00	0.00	0.00	0.00	0.00	0.00	0.00	0.00
Total	97.70	97.65	97.34	97.53	97.79	97.68	97.44	98.41	97.98	97.42	97.55	98.01	97.83	97.53
CTotal	99.75	99.74	99.50	99.58	99.89	99.73	99.50	100.50	100.05	99.47	99.57	100.07	99.89	99.63
TSi	6.79	6.64	6.71	6.67	6.64	6.65	6.59	6.82	6.68	6.71	6.45	6.63	6.60	6.62
TAl	1.21	1.37	1.29	1.33	1.36	1.36	1.41	1.18	1.32	1.29	1.55	1.37	1.40	1.38
TFe^{3+}	0.00	0.00	0.00	0.00	0.00	0.00	0.00	0.00	0.00	0.00	0.00	0.00	0.00	0.00
TTi	0.00	0.00	0.00	0.00	0.00	0.00	0.00	0.00	0.00	0.00	0.00	0.00	0.00	0.00
CAl	0.58	0.48	0.53	0.55	0.61	0.55	0.61	0.44	0.52	0.58	0.54	0.59	0.56	0.56
CCr	0.00	0.00	0.00	0.00	0.00	0.00	0.00	0.00	0.00	0.00	0.00	0.00	0.00	0.00
CFe^{3+}	0.25	0.48	0.35	0.34	0.29	0.42	0.36	0.47	0.47	0.40	0.60	0.33	0.40	0.38
CTi	0.05	0.05	0.05	0.06	0.06	0.04	0.04	0.03	0.03	0.04	0.03	0.06	0.06	0.06
CMg	2.80	2.76	2.78	2.69	2.64	2.71	2.63	2.91	2.76	2.71	2.61	2.59	2.63	2.66
CFe^{2+}	1.32	1.21	1.28	1.34	1.39	1.27	1.35	1.14	1.20	1.26	1.21	1.42	1.34	1.33
CMn	0.02	0.01	0.01	0.02	0.02	0.01	0.02	0.02	0.02	0.02	0.02	0.01	0.02	0.02
CCa	0.00	0.00	0.00	0.00	0.00	0.00	0.00	0.00	0.00	0.00	0.00	0.00	0.00	0.00
BFe^{2+}	0.04	0.04	0.03	0.04	0.03	0.04	0.03	0.05	0.05	0.05	0.04	0.06	0.05	0.05
BMn	0.02	0.01	0.01	0.02	0.02	0.01	0.02	0.02	0.02	0.02	0.02	0.01	0.02	0.02
BCa	1.88	1.89	1.90	1.88	1.89	1.89	1.90	1.85	1.86	1.86	1.87	1.85	1.85	1.86
BNa	0.06	0.06	0.05	0.06	0.06	0.06	0.05	0.08	0.08	0.07	0.07	0.08	0.08	0.08
ACa	0.00	0.00	0.00	0.00	0.00	0.00	0.00	0.00	0.00	0.00	0.00	0.00	0.00	0.00
ANa	0.25	0.27	0.27	0.28	0.29	0.27	0.31	0.22	0.25	0.23	0.29	0.30	0.30	0.30
AK	0.10	0.10	0.10	0.10	0.12	0.10	0.11	0.07	0.09	0.09	0.13	0.11	0.11	0.11

	1008-B2			1008-B1: hydrated metagabbro Kataransky Cape											
wt.-%	*#48 sympl.*	*#49 sympl.*	*#50 sympl.*	*#10*	*#7 core*	*#8*	*#9 rim*	*#28 core*	*#29*	*#30 core*	*#40 vein*	*#41 vein*	#15	#16	#17
SiO_2	45.40	45.47	43.26	44.03	43.80	43.18	43.61	43.91	42.81	43.70	48.36	43.54	44.70	43.89	45.06
TiO_2	0.46	0.39	0.34	0.52	0.54	0.61	0.60	0.54	0.57	0.57	0.35	0.69	0.51	0.55	0.52
Al_2O_3	11.86	11.65	11.96	12.26	12.15	12.90	12.44	12.76	13.11	12.76	6.91	11.89	12.40	12.18	11.46
FeO	13.85	14.28	14.85	14.66	14.67	14.65	14.45	14.53	15.21	14.59	15.09	15.16	14.71	14.88	14.22
Cr_2O_3	0.00	0.00	0.00	0.00	0.00	0.00	0.00	0.00	0.00	0.00	0.00	0.00	0.04	0.13	0.05
MnO	0.26	0.25	0.25	0.24	0.25	0.22	0.20	0.25	0.26	0.24	0.25	0.24	0.20	0.24	0.28
MgO	11.89	12.05	12.09	11.25	11.00	10.77	11.11	11.06	10.67	11.04	12.04	10.54	11.81	11.88	12.36
CaO	11.90	11.91	12.02	11.77	11.82	11.74	11.83	11.99	11.78	11.85	12.01	11.83	12.00	11.71	11.95
Na_2O	1.28	1.21	1.35	1.44	1.39	1.46	1.43	1.26	1.44	1.30	0.66	0.91	1.19	1.19	1.25
K_2O	0.64	0.58	0.64	0.92	0.98	1.05	0.92	0.98	1.08	0.97	0.44	1.54	0.85	0.91	0.79
F	0.00	0.00	0.00	0.00	0.00	0.00	0.00	0.00	0.00	0.00	0.00	0.00	0.01	0.03	0.22
Cl	0.00	0.00	0.00	0.00	0.00	0.00	0.00	0.00	0.00	0.00	0.00	0.00	0.10	0.19	0.10
Total	97.54	97.79	96.76	97.09	96.60	96.58	96.59	97.28	96.93	97.02	96.11	96.34	98.48	97.65	98.21
CTotal	99.61	99.85	98.80	99.14	98.63	98.67	98.63	99.32	98.95	99.07	98.14	98.35	100.55	99.76	100.19
TSi	6.65	6.63	6.39	6.53	6.54	6.46	6.50	6.50	6.39	6.48	7.20	6.55	6.50	6.44	6.57
TAl	1.36	1.37	1.61	1.47	1.46	1.54	1.50	1.50	1.62	1.52	0.80	1.45	1.50	1.56	1.43
TFe^{3+}	0.00	0.00	0.00	0.00	0.00	0.00	0.00	0.00	0.00	0.00	0.00	0.00	0.00	0.00	0.00
TTi	0.00	0.00	0.00	0.00	0.00	0.00	0.00	0.00	0.00	0.00	0.00	0.00	0.00	0.00	0.00
CAl	0.69	0.63	0.48	0.67	0.68	0.73	0.69	0.72	0.69	0.71	0.42	0.66	0.63	0.54	0.54
CCr	0.00	0.00	0.00	0.00	0.00	0.00	0.00	0.00	0.00	0.00	0.00	0.00	0.01	0.02	0.01
CFe^{3+}	0.22	0.35	0.65	0.24	0.19	0.19	0.21	0.23	0.30	0.25	0.13	0.17	0.40	0.54	0.41
CTi	0.05	0.04	0.04	0.06	0.06	0.07	0.07	0.06	0.06	0.06	0.04	0.08	0.06	0.06	0.06
CMg	2.59	2.62	2.66	2.49	2.45	2.40	2.47	2.44	2.37	2.44	2.67	2.37	2.56	2.60	2.69
CFe^{2+}	1.43	1.34	1.16	1.53	1.61	1.60	1.56	1.54	1.56	1.52	1.73	1.71	1.34	1.23	1.28
CMn	0.02	0.02	0.02	0.02	0.02	0.01	0.01	0.02	0.02	0.02	0.02	0.02	0.01	0.02	0.02
CCa	0.00	0.00	0.00	0.00	0.00	0.00	0.00	0.00	0.00	0.00	0.00	0.00	0.00	0.00	0.00
BFe^{2+}	0.05	0.05	0.03	0.05	0.04	0.04	0.04	0.03	0.04	0.04	0.02	0.03	0.05	0.06	0.04
BMn	0.02	0.02	0.02	0.02	0.02	0.01	0.01	0.02	0.02	0.02	0.02	0.02	0.01	0.02	0.02
BCa	1.87	1.86	1.90	1.87	1.89	1.88	1.89	1.90	1.88	1.88	1.92	1.91	1.87	1.84	1.87
BNa	0.07	0.07	0.05	0.07	0.06	0.06	0.06	0.05	0.06	0.06	0.05	0.05	0.07	0.09	0.07
ACa	0.00	0.00	0.00	0.00	0.00	0.00	0.00	0.00	0.00	0.00	0.00	0.00	0.00	0.00	0.00
ANa	0.29	0.27	0.34	0.34	0.34	0.36	0.36	0.31	0.35	0.31	0.15	0.22	0.27	0.25	0.28
AK	0.12	0.11	0.12	0.17	0.19	0.20	0.18	0.19	0.21	0.18	0.08	0.30	0.16	0.17	0.15

	1008-B1: hydrated metagabbro Kataransky Cape												0308-K1: mafic dyke Nikolkina Island					
wt.-%	#18	#19	#20	#21	#22	#23	#24	#30	#31	#32	#33	#34	*#1core*	*#2 rim*	*#5 core*	*#6 core*	*#7 core*	*#14 core*
SiO_2	44.66	44.05	44.34	44.16	43.60	43.35	43.70	43.72	43.64	43.68	44.18	43.75	44.17	44.94	44.23	44.89	44.87	45.41
TiO_2	0.53	0.61	0.53	0.55	0.58	0.58	0.58	0.58	0.52	0.55	0.51	0.60	1.72	1.46	1.77	1.17	0.90	0.97
Al_2O_3	11.86	12.61	12.15	12.33	12.33	12.33	12.42	12.08	11.99	12.05	11.78	12.57	12.13	11.47	11.62	11.50	11.40	10.87
FeO	14.92	15.22	15.10	15.34	15.42	15.04	15.62	14.32	14.51	14.36	14.44	14.25	14.48	13.76	14.04	14.38	14.21	14.25
Cr_2O_3	0.09	0.06	0.04	0.06	0.08	0.04	0.04	0.07	0.01	0.00	0.07	0.06	0.00	0.00	0.00	0.00	0.00	0.00
MnO	0.17	0.25	0.27	0.26	0.27	0.29	0.22	0.22	0.24	0.20	0.22	0.24	0.03	0.05	0.08	0.01	0.00	0.01
MgO	12.04	11.77	11.80	11.81	11.75	11.74	11.88	11.80	11.70	11.61	11.79	11.74	12.11	12.40	12.18	12.53	12.84	12.88
CaO	11.80	11.87	11.68	11.66	11.75	11.78	11.80	11.95	12.03	11.92	11.90	11.88	11.41	11.68	11.58	11.30	11.57	11.66
Na_2O	1.29	1.42	1.42	1.43	1.39	1.43	1.40	1.30	1.24	1.31	1.30	1.38	2.03	1.84	1.94	1.88	1.75	1.75
K_2O	0.83	0.96	0.82	0.90	0.91	0.88	0.94	0.91	0.92	0.91	0.93	0.81	0.85	0.82	0.85	0.84	0.78	0.71
F	0.06	0.05	0.06	0.06	0.02	0.00	0.12	0.01	0.07	0.00	0.00	0.00	0.00	0.00	0.00	0.00	0.00	0.00
Cl	0.09	0.14	0.10	0.09	0.13	0.11	0.11	0.11	0.11	0.13	0.10	0.13	0.00	0.00	0.00	0.00	0.00	0.00
Total	98.25	98.95	98.27	98.59	98.15	97.53	98.79	97.00	96.97	96.72	97.15	97.35	98.93	98.42	98.29	98.50	98.32	98.51
CTotal	100.35	101.01	100.31	100.66	100.23	99.57	100.80	99.06	98.94	98.70	99.22	99.41	101.02	100.49	100.42	100.56	100.40	100.58
TSi	6.51	6.41	6.48	6.43	6.39	6.39	6.37	6.47	6.47	6.49	6.53	6.44	6.44	6.56	6.49	6.54	6.53	6.60
TAl	1.49	1.60	1.52	1.57	1.61	1.61	1.63	1.53	1.53	1.51	1.47	1.56	1.57	1.44	1.51	1.46	1.47	1.40
TFe^{3+}	0.00	0.00	0.00	0.00	0.00	0.00	0.00	0.00	0.00	0.00	0.00	0.00	0.00	0.00	0.00	0.00	0.00	0.00
TTi	0.00	0.00	0.00	0.00	0.00	0.00	0.00	0.00	0.00	0.00	0.00	0.00	0.00	0.00	0.00	0.00	0.00	0.00
CAl	0.55	0.56	0.57	0.55	0.51	0.53	0.50	0.57	0.57	0.60	0.58	0.62	0.52	0.54	0.49	0.51	0.48	0.46
CCr	0.01	0.01	0.01	0.01	0.01	0.01	0.01	0.01	0.00	0.00	0.01	0.01	0.00	0.00	0.00	0.00	0.00	0.00
CFe^{3+}	0.46	0.47	0.46	0.51	0.57	0.53	0.61	0.39	0.41	0.34	0.35	0.38	0.27	0.19	0.20	0.32	0.37	0.30
CTi	0.06	0.07	0.06	0.06	0.06	0.06	0.06	0.07	0.06	0.06	0.06	0.07	0.19	0.16	0.20	0.13	0.10	0.11
CMg	2.62	2.55	2.57	2.57	2.57	2.58	2.58	2.60	2.59	2.57	2.60	2.58	2.63	2.70	2.66	2.72	2.79	2.79
CFe^{2+}	1.29	1.32	1.32	1.29	1.27	1.28	1.24	1.35	1.36	1.41	1.40	1.33	1.40	1.42	1.44	1.32	1.27	1.34
CMn	0.01	0.02	0.02	0.02	0.02	0.02	0.01	0.01	0.02	0.01	0.01	0.02	0.00	0.00	0.01	0.00	0.00	0.00
CCa	0.00	0.00	0.00	0.00	0.00	0.00	0.00	0.00	0.00	0.00	0.00	0.00	0.00	0.00	0.00	0.00	0.00	0.00
BFe^{2+}	0.06	0.06	0.06	0.07	0.06	0.05	0.06	0.04	0.03	0.04	0.04	0.04	0.10	0.08	0.08	0.11	0.09	0.09
BMn	0.01	0.02	0.02	0.02	0.02	0.02	0.01	0.01	0.02	0.01	0.01	0.02	0.00	0.00	0.01	0.00	0.00	0.00
BCa	1.84	1.85	1.83	1.82	1.84	1.86	1.84	1.89	1.91	1.90	1.88	1.87	1.78	1.83	1.82	1.76	1.80	1.82
BNa	0.08	0.08	0.09	0.10	0.08	0.08	0.08	0.06	0.05	0.05	0.06	0.07	0.12	0.09	0.10	0.13	0.11	0.10
ACa	0.00	0.00	0.00	0.00	0.00	0.00	0.00	0.00	0.00	0.00	0.00	0.00	0.00	0.00	0.00	0.00	0.00	0.00
ANa	0.28	0.32	0.31	0.31	0.31	0.33	0.31	0.32	0.31	0.32	0.31	0.33	0.46	0.43	0.46	0.41	0.39	0.40
AK	0.15	0.18	0.15	0.17	0.17	0.17	0.18	0.17	0.17	0.17	0.18	0.15	0.16	0.15	0.16	0.16	0.15	0.13

	0308-K1: mafic dyke Nikolkina Island										0308-K2: hydrated mafic dyke Nikolkina Island						
wt.-%	*#18 core*	*#45*	*#74 core*	*#75 core*	*#90 core*	*#91 rim*	*#92 rim*	*#95*	*#96*	*#113*	*#15 rim*	*#16 core*	*#17 rim*	*#18*	*#19 core*	*#26*	*#27*
SiO_2	45.94	42.88	45.73	44.43	43.39	42.46	43.32	44.87	47.54	45.27	40.81	41.63	41.16	41.28	41.45	42.82	40.92
TiO_2	1.45	1.77	0.97	1.29	1.92	1.94	2.69	1.62	1.16	1.46	1.88	2.06	1.82	2.11	2.03	1.60	2.07
Al_2O_3	9.79	12.15	10.20	11.53	12.29	12.92	12.12	10.82	8.02	9.75	12.74	12.57	12.76	12.90	12.69	12.11	13.07
FeO	13.74	14.89	14.04	14.71	13.83	13.68	13.62	14.33	13.75	14.22	17.07	17.60	17.53	17.76	16.84	16.68	17.17
Cr_2O_3	0.00	0.00	0.00	0.00	0.00	0.00	0.00	0.00	0.00	0.00	0.00	0.00	0.00	0.00	0.00	0.00	0.00
MnO	0.04	0.07	0.04	0.04	0.05	0.05	0.07	0.04	0.00	0.06	0.11	0.07	0.07	0.08	0.07	0.15	0.06
MgO	13.03	10.99	13.16	11.95	11.80	11.49	12.06	12.34	13.63	12.11	9.40	9.30	9.39	9.49	9.33	9.97	9.19
CaO	11.64	11.62	11.70	11.57	11.39	11.50	11.84	11.38	11.66	11.58	11.21	11.46	11.58	11.59	11.40	11.58	11.74
Na_2O	1.74	1.91	1.62	1.86	1.93	2.03	1.95	1.83	1.45	1.62	1.87	1.86	1.79	1.89	1.87	1.67	1.88
K_2O	0.69	1.07	0.75	0.86	0.92	1.03	0.89	0.84	0.57	0.81	1.21	1.23	1.29	1.32	1.30	1.00	1.27
F	0.00	0.00	0.00	0.00	0.00	0.00	0.00	0.00	0.00	0.00	0.00	0.00	0.00	0.00	0.00	0.00	0.00
Cl	0.00	0.00	0.00	0.00	0.00	0.00	0.00	0.00	0.00	0.00	0.00	0.00	0.00	0.00	0.00	0.00	0.00
Total	98.06	97.35	98.21	98.24	97.52	97.10	98.56	98.07	97.78	96.88	96.30	97.78	97.39	98.42	96.98	97.58	97.37
CTotal	100.13	99.43	100.28	100.33	99.55	99.28	100.79	100.15	99.85	98.96	98.33	99.77	99.42	100.43	98.96	99.61	99.35
TSi	6.72	6.41	6.66	6.52	6.42	6.33	6.36	6.59	6.94	6.74	6.23	6.28	6.23	6.19	6.30	6.41	6.21
TAl	1.29	1.59	1.34	1.48	1.58	1.67	1.64	1.41	1.06	1.26	1.77	1.72	1.77	1.81	1.70	1.59	1.79
TFe^{3+}	0.00	0.00	0.00	0.00	0.00	0.00	0.00	0.00	0.00	0.00	0.00	0.00	0.00	0.00	0.00	0.00	0.00
TTi	0.00	0.00	0.00	0.00	0.00	0.00	0.00	0.00	0.00	0.00	0.00	0.00	0.00	0.00	0.00	0.00	0.00
CAl	0.40	0.55	0.41	0.52	0.56	0.60	0.45	0.46	0.31	0.45	0.53	0.51	0.50	0.47	0.57	0.55	0.54
CCr	0.00	0.00	0.00	0.00	0.00	0.00	0.00	0.00	0.00	0.00	0.00	0.00	0.00	0.00	0.00	0.00	0.00
CFe^{3+}	0.21	0.13	0.32	0.24	0.20	0.15	0.13	0.25	0.23	0.14	0.23	0.18	0.21	0.22	0.13	0.19	0.11
CTi	0.16	0.20	0.11	0.14	0.21	0.22	0.30	0.18	0.13	0.16	0.22	0.23	0.21	0.24	0.23	0.18	0.24
CMg	2.84	2.45	2.86	2.62	2.60	2.55	2.64	2.70	2.96	2.69	2.14	2.09	2.12	2.12	2.11	2.23	2.08
CFe^{2+}	1.39	1.67	1.32	1.49	1.42	1.48	1.48	1.42	1.37	1.56	1.88	1.98	1.96	1.95	1.95	1.84	2.03
CMn	0.00	0.00	0.00	0.00	0.00	0.00	0.00	0.00	0.00	0.00	0.01	0.00	0.00	0.01	0.00	0.01	0.00
CCa	0.00	0.00	0.00	0.00	0.00	0.00	0.00	0.00	0.00	0.00	0.00	0.00	0.00	0.00	0.00	0.00	0.00
BFe^{2+}	0.08	0.06	0.08	0.08	0.09	0.07	0.06	0.10	0.08	0.07	0.07	0.06	0.05	0.06	0.06	0.06	0.04
BMn	0.00	0.00	0.00	0.00	0.00	0.00	0.00	0.00	0.00	0.00	0.01	0.00	0.01	0.01	0.01	0.01	0.00
BCa	1.82	1.86	1.83	1.82	1.81	1.84	1.86	1.79	1.82	1.85	1.84	1.85	1.88	1.86	1.86	1.86	1.91
BNa	0.09	0.07	0.09	0.10	0.10	0.09	0.07	0.11	0.09	0.08	0.09	0.08	0.07	0.07	0.08	0.08	0.05
ACa	0.00	0.00	0.00	0.00	0.00	0.00	0.00	0.00	0.00	0.00	0.00	0.00	0.00	0.00	0.00	0.00	0.00
ANa	0.40	0.48	0.36	0.43	0.45	0.50	0.48	0.41	0.32	0.39	0.47	0.47	0.46	0.48	0.48	0.41	0.50
AK	0.13	0.20	0.14	0.16	0.17	0.20	0.17	0.16	0.11	0.15	0.24	0.24	0.25	0.25	0.25	0.19	0.25

0308-K2: hydrated mafic dyke Nikolkina Island

wt.-%	*#28*	*#29*	#13	#16	#17	#18	#20	#21	#22	#23	#24	#25	#34	#37	#38	#39	#40	#41	#42
SiO_2	41.77	41.68	41.14	41.51	42.28	42.07	40.36	40.98	41.06	41.50	41.29	41.73	42.06	41.24	40.91	42.09	42.32	43.19	41.83
TiO_2	1.81	2.04	1.62	1.82	1.51	1.58	1.89	1.77	2.02	2.04	2.01	2.08	1.59	1.91	1.68	1.82	1.99	1.83	1.79
Al_2O_3	12.74	12.76	12.68	12.73	12.35	12.79	14.25	13.44	13.27	12.90	12.94	13.10	12.79	13.00	12.82	13.25	13.39	13.10	13.36
FeO	17.22	17.23	17.92	17.20	17.44	17.29	17.63	17.00	17.32	16.74	17.28	17.52	16.77	16.96	17.73	16.42	15.17	14.70	16.82
Cr_2O_3	0.00	0.00	0.05	0.04	0.02	0.02	0.02	0.00	0.01	0.07	0.03	0.00	0.01	0.00	0.03	0.04	0.04	0.00	0.02
MnO	0.15	0.13	0.11	0.12	0.11	0.11	0.11	0.07	0.09	0.11	0.17	0.11	0.02	0.04	0.13	0.10	0.06	0.05	0.10
MgO	9.26	9.38	9.48	9.34	9.02	9.27	8.53	9.22	9.02	9.27	9.18	9.27	9.11	9.12	9.17	9.87	10.87	11.26	9.58
CaO	11.53	11.56	11.49	11.48	11.68	11.43	11.51	11.44	11.38	11.40	11.30	11.47	11.33	11.33	11.41	11.36	11.63	11.49	11.53
Na_2O	1.78	1.88	1.76	1.77	1.45	1.67	1.61	1.64	1.75	1.71	1.75	1.75	1.60	1.75	1.74	1.77	1.84	1.72	1.81
K_2O	1.19	1.32	1.25	1.29	1.15	1.17	1.30	1.26	1.39	1.33	1.33	1.27	1.18	1.32	1.14	1.22	1.18	1.07	1.30
F	0.00	0.00	0.16	0.01	0.08	0.02	0.02	0.05	0.03	0.05	0.01	0.02	0.08	0.00	0.01	0.00	0.00	0.04	0.00
Cl	0.00	0.00	0.05	0.05	0.05	0.05	0.06	0.02	0.07	0.07	0.05	0.06	0.05	0.05	0.06	0.05	0.06	0.04	0.04
Total	97.45	97.98	97.66	97.32	97.12	97.45	97.27	96.89	97.40	97.12	97.31	98.38	96.58	96.72	96.80	97.95	98.51	98.49	98.16
CTotal	99.50	99.98	99.61	99.33	99.07	99.44	99.25	98.84	99.36	99.13	99.31	100.36	98.52	98.68	98.78	99.99	100.57	100.51	100.18
TSi	6.31	6.28	6.21	6.28	6.41	6.34	6.12	6.21	6.22	6.29	6.25	6.25	6.40	6.28	6.22	6.29	6.25	6.34	6.26
TAl	1.69	1.72	1.79	1.72	1.59	1.66	1.88	1.79	1.78	1.71	1.75	1.75	1.60	1.72	1.78	1.72	1.75	1.66	1.74
TFe^{3+}	0.00	0.00	0.00	0.00	0.00	0.00	0.00	0.00	0.00	0.00	0.00	0.00	0.00	0.00	0.00	0.00	0.00	0.00	0.00
TTi	0.00	0.00	0.00	0.00	0.00	0.00	0.00	0.00	0.00	0.00	0.00	0.00	0.00	0.00	0.00	0.00	0.00	0.00	0.00
CAl	0.58	0.54	0.47	0.55	0.61	0.61	0.67	0.62	0.59	0.60	0.56	0.56	0.69	0.62	0.52	0.62	0.58	0.61	0.61
CCr	0.00	0.00	0.01	0.01	0.00	0.00	0.00	0.00	0.00	0.01	0.00	0.00	0.00	0.00	0.00	0.01	0.01	0.00	0.00
CFe^{3+}	0.16	0.14	0.34	0.18	0.13	0.19	0.20	0.21	0.17	0.14	0.20	0.20	0.13	0.15	0.29	0.22	0.21	0.24	0.18
CTi	0.21	0.23	0.18	0.21	0.17	0.18	0.22	0.20	0.23	0.23	0.23	0.23	0.18	0.22	0.19	0.20	0.22	0.20	0.20
CMg	2.09	2.11	2.13	2.11	2.04	2.08	1.93	2.08	2.04	2.10	2.07	2.07	2.07	2.07	2.08	2.20	2.39	2.47	2.14
CFe^{2+}	1.97	1.97	1.86	1.95	2.04	1.92	1.98	1.88	1.96	1.92	1.92	1.93	1.93	1.94	1.91	1.76	1.60	1.48	1.86
CMn	0.01	0.01	0.01	0.01	0.01	0.01	0.01	0.00	0.01	0.01	0.01	0.01	0.00	0.00	0.01	0.01	0.00	0.00	0.01
CCa	0.00	0.00	0.00	0.00	0.00	0.00	0.00	0.00	0.00	0.00	0.00	0.00	0.00	0.00	0.00	0.00	0.00	0.00	0.00
BFe^{2+}	0.05	0.06	0.06	0.06	0.04	0.07	0.05	0.06	0.07	0.06	0.07	0.07	0.07	0.07	0.06	0.08	0.07	0.09	0.06
BMn	0.01	0.01	0.01	0.01	0.01	0.01	0.01	0.01	0.01	0.01	0.01	0.01	0.00	0.00	0.01	0.01	0.00	0.00	0.01
BCa	1.87	1.87	1.86	1.86	1.90	1.85	1.87	1.86	1.85	1.85	1.83	1.84	1.85	1.85	1.86	1.82	1.84	1.81	1.85
BNa	0.07	0.07	0.08	0.07	0.06	0.08	0.07	0.08	0.08	0.08	0.09	0.09	0.08	0.08	0.08	0.10	0.09	0.10	0.08
ACa	0.00	0.00	0.00	0.00	0.00	0.00	0.00	0.00	0.00	0.00	0.00	0.00	0.00	0.00	0.00	0.00	0.00	0.00	0.00
ANa	0.45	0.48	0.44	0.45	0.37	0.41	0.40	0.41	0.43	0.42	0.43	0.42	0.39	0.44	0.44	0.42	0.44	0.39	0.44
AK	0.23	0.25	0.24	0.25	0.22	0.23	0.25	0.24	0.27	0.26	0.26	0.24	0.23	0.26	0.22	0.23	0.22	0.20	0.25

	0308-K3: hydrated mafic dyke Nikolkina Island								0808-5: hydrated metadiorite Leonard Cape									
wt.-%	*#1 core*	*#3*	*#2 rim*	*#7*	*#14*	*#15*	*#16*	*#33*	*#4*	*#5*	*#26 core*	*#27*	*#28 rim*	*#46 core*	*#47*	*#48*	*#49*	*#50 rim*
SiO_2	40.42	40.12	40.05	40.16	51.70	45.30	40.07	40.52	42.82	40.85	41.36	41.16	41.34	41.35	41.32	41.36	41.32	41.63
TiO_2	1.59	1.46	0.98	1.42	0.03	0.11	1.31	1.10	1.01	1.24	1.41	1.34	1.12	1.36	1.33	1.33	1.35	1.25
Al_2O_3	13.76	13.78	14.19	14.02	2.07	8.34	13.58	13.78	12.03	14.60	14.10	14.24	14.21	13.84	13.96	14.00	13.97	14.22
FeO	19.22	19.69	21.44	19.79	18.71	20.74	19.59	20.60	20.31	18.65	18.06	18.22	18.40	18.51	18.62	18.41	18.50	18.39
Cr_2O_3	0.00	0.00	0.00	0.00	0.00	0.00	0.00	0.00	0.00	0.00	0.00	0.00	0.00	0.00	0.00	0.00	0.00	0.00
MnO	0.28	0.31	0.31	0.21	0.25	0.23	0.24	0.24	0.27	0.36	0.33	0.37	0.35	0.30	0.34	0.33	0.31	0.33
MgO	7.32	7.30	5.95	7.47	11.50	8.05	7.15	6.90	7.82	8.01	8.36	8.42	8.21	8.63	8.42	8.57	8.45	8.38
CaO	11.56	11.51	11.40	11.48	12.47	12.09	11.50	11.72	10.02	11.39	11.25	11.32	11.39	11.11	11.42	11.23	11.17	11.28
Na_2O	1.45	1.51	1.42	1.53	0.19	0.73	1.44	1.36	2.14	1.59	1.69	1.67	1.66	1.66	1.68	1.68	1.57	1.64
K_2O	1.63	1.55	1.02	1.43	0.07	0.40	1.50	1.02	0.96	1.07	1.04	1.03	0.87	1.02	1.07	1.08	1.01	0.96
F	0.00	0.00	0.00	0.00	0.00	0.00	0.00	0.00	0.00	0.00	0.00	0.00	0.00	0.00	0.00	0.00	0.00	0.00
Cl	0.00	0.00	0.00	0.00	0.00	0.00	0.00	0.00	0.00	0.00	0.00	0.00	0.00	0.00	0.00	0.00	0.00	0.00
Total	97.23	97.23	96.76	97.51	96.99	95.99	96.38	97.24	97.38	97.76	97.60	97.77	97.55	97.78	98.16	97.99	97.65	98.08
CTotal	99.19	99.30	98.73	99.49	99.00	97.97	98.35	99.27	99.39	99.77	99.61	99.82	99.59	99.82	100.16	100.02	99.69	100.08
TSi	6.20	6.16	6.18	6.13	7.71	6.95	6.20	6.19	6.51	6.15	6.23	6.19	6.23	6.21	6.20	6.20	6.21	6.23
TAl	1.80	1.84	1.82	1.87	0.29	1.05	1.80	1.81	1.49	1.85	1.77	1.81	1.78	1.79	1.80	1.80	1.79	1.77
TFe^{3+}	0.00	0.00	0.00	0.00	0.00	0.00	0.00	0.00	0.00	0.00	0.00	0.00	0.00	0.00	0.00	0.00	0.00	0.00
TTi	0.00	0.00	0.00	0.00	0.00	0.00	0.00	0.00	0.00	0.00	0.00	0.00	0.00	0.00	0.00	0.00	0.00	0.00
CAl	0.69	0.65	0.76	0.64	0.08	0.46	0.68	0.67	0.67	0.74	0.73	0.71	0.74	0.65	0.67	0.68	0.68	0.74
CCr	0.00	0.00	0.00	0.00	0.00	0.00	0.00	0.00	0.00	0.00	0.00	0.00	0.00	0.00	0.00	0.00	0.00	0.00
CFe^{3+}	0.13	0.23	0.32	0.31	0.14	0.28	0.19	0.36	0.38	0.33	0.26	0.31	0.30	0.38	0.32	0.34	0.36	0.31
CTi	0.18	0.17	0.11	0.16	0.00	0.01	0.15	0.13	0.12	0.14	0.16	0.15	0.13	0.15	0.15	0.15	0.15	0.14
CMg	1.67	1.67	1.37	1.70	2.56	1.84	1.65	1.57	1.77	1.80	1.88	1.89	1.84	1.93	1.88	1.92	1.89	1.87
CFe^{2+}	2.31	2.27	2.41	2.18	2.19	2.38	2.32	2.25	2.05	1.97	1.95	1.92	1.97	1.86	1.96	1.90	1.89	1.93
CMn	0.02	0.02	0.02	0.01	0.03	0.02	0.02	0.02	0.02	0.02	0.02	0.02	0.02	0.02	0.02	0.02	0.02	0.02
CCa	0.00	0.00	0.00	0.00	0.00	0.00	0.00	0.00	0.00	0.00	0.00	0.00	0.00	0.00	0.00	0.00	0.00	0.00
BFe^{2+}	0.03	0.03	0.03	0.04	0.00	0.00	0.03	0.02	0.16	0.05	0.07	0.06	0.05	0.08	0.06	0.07	0.07	0.07
BMn	0.02	0.02	0.02	0.01	0.00	0.01	0.02	0.02	0.02	0.02	0.02	0.02	0.02	0.02	0.02	0.02	0.02	0.02
BCa	1.90	1.89	1.89	1.88	1.99	1.99	1.91	1.92	1.63	1.84	1.82	1.82	1.84	1.79	1.84	1.80	1.80	1.81
BNa	0.05	0.06	0.06	0.07	0.00	0.01	0.05	0.04	0.19	0.09	0.10	0.09	0.09	0.11	0.09	0.10	0.11	0.10
ACa	0.00	0.00	0.00	0.00	0.00	0.00	0.00	0.00	0.00	0.00	0.00	0.00	0.00	0.00	0.00	0.00	0.00	0.00
ANa	0.38	0.39	0.36	0.39	0.05	0.21	0.38	0.36	0.44	0.38	0.40	0.39	0.40	0.37	0.40	0.38	0.35	0.37
AK	0.32	0.30	0.20	0.28	0.01	0.08	0.30	0.20	0.19	0.21	0.20	0.20	0.17	0.20	0.21	0.21	0.19	0.18

	0808-5			0808-6: hydrated metadiorite Leonard Cape										0908-1: dyke Water S.		
wt.-%	*#52 core*	*#53 rim*	*#54 core*	*#6 core*	*#7 rim*	*#8 incl.*	*#19 vein*	*#28*	*#37 core*	*#38*	*#39 rim*	*#40 core*	*#41 rim*	#6	#7	#8
SiO_2	41.50	41.55	41.11	41.76	41.07	41.58	40.37	41.46	41.37	40.21	40.44	40.87	40.98	44.57	44.49	47.53
TiO_2	1.23	1.00	1.31	1.40	1.27	1.22	1.55	1.13	1.42	1.39	1.20	1.42	1.41	0.17	0.23	0.11
Al_2O_3	14.24	14.99	14.08	13.89	13.96	13.99	13.96	14.50	14.01	14.10	14.16	14.23	14.40	15.09	15.45	11.87
FeO	18.54	18.26	18.33	17.87	17.95	18.33	18.32	17.46	17.31	18.14	17.94	17.73	17.37	11.34	11.78	11.93
Cr_2O_3	0.00	0.00	0.00	0.00	0.00	0.00	0.00	0.00	0.00	0.00	0.00	0.00	0.00	0.00	0.00	0.00
MnO	0.36	0.34	0.32	0.27	0.18	0.21	0.21	0.23	0.21	0.33	0.26	0.25	0.18	0.07	0.00	0.09
MgO	8.31	7.90	8.27	8.94	8.95	8.97	8.91	9.01	9.02	9.00	8.79	8.95	8.86	13.06	13.24	15.01
CaO	11.26	11.49	11.21	11.49	11.29	11.28	11.17	11.38	11.39	11.51	11.36	11.41	11.38	11.21	11.19	10.65
Na_2O	1.71	1.47	1.65	1.84	1.81	1.80	1.83	1.75	1.86	1.88	1.84	1.85	1.62	1.39	1.36	1.02
K_2O	1.12	0.97	1.10	0.81	1.02	1.00	1.12	0.99	1.00	1.06	1.00	1.02	1.04	0.38	0.56	0.21
F	0.00	0.00	0.00	0.00	0.00	0.00	0.00	0.00	0.00	0.00	0.00	0.00	0.00	0.00	0.00	0.00
Cl	0.00	0.00	0.00	0.00	0.00	0.00	0.00	0.00	0.00	0.00	0.00	0.00	0.00	0.00	0.00	0.00
Total	98.27	97.97	97.38	98.27	97.50	98.38	97.44	97.91	97.59	97.62	96.99	97.73	97.24	97.28	98.30	98.42
CTotal	100.30	100.03	99.41	100.31	99.51	100.42	99.44	99.95	99.61	99.62	98.97	99.75	99.30	99.38	100.42	100.57
TSi	6.22	6.22	6.21	6.23	6.18	6.20	6.09	6.19	6.22	6.06	6.12	6.14	6.17	6.40	6.32	6.67
TAl	1.78	1.78	1.79	1.77	1.82	1.80	1.91	1.81	1.78	1.94	1.88	1.86	1.83	1.60	1.68	1.33
TFe^{3+}	0.00	0.00	0.00	0.00	0.00	0.00	0.00	0.00	0.00	0.00	0.00	0.00	0.00	0.00	0.00	0.00
TTi	0.00	0.00	0.00	0.00	0.00	0.00	0.00	0.00	0.00	0.00	0.00	0.00	0.00	0.00	0.00	0.00
CAl	0.73	0.87	0.72	0.67	0.65	0.65	0.57	0.74	0.70	0.56	0.65	0.65	0.72	0.95	0.91	0.63
CCr	0.00	0.00	0.00	0.00	0.00	0.00	0.00	0.00	0.00	0.00	0.00	0.00	0.00	0.00	0.00	0.00
CFe^{3+}	0.29	0.25	0.29	0.28	0.35	0.38	0.44	0.31	0.24	0.47	0.39	0.33	0.30	0.46	0.56	0.76
CTi	0.14	0.11	0.15	0.16	0.14	0.14	0.18	0.13	0.16	0.16	0.14	0.16	0.16	0.02	0.03	0.01
CMg	1.86	1.76	1.86	1.99	2.01	1.99	2.00	2.01	2.02	2.02	1.98	2.00	1.99	2.79	2.81	3.14
CFe^{2+}	1.96	1.99	1.96	1.89	1.84	1.83	1.79	1.80	1.87	1.78	1.83	1.84	1.83	0.78	0.71	0.46
CMn	0.02	0.02	0.02	0.02	0.01	0.01	0.01	0.01	0.01	0.02	0.02	0.02	0.01	0.00	0.00	0.01
CCa	0.00	0.00	0.00	0.00	0.00	0.00	0.00	0.00	0.00	0.00	0.00	0.00	0.00	0.00	0.00	0.00
BFe^{2+}	0.07	0.05	0.07	0.06	0.07	0.08	0.08	0.07	0.06	0.05	0.06	0.06	0.07	0.13	0.14	0.18
BMn	0.02	0.02	0.02	0.02	0.01	0.01	0.01	0.02	0.01	0.02	0.02	0.02	0.01	0.00	0.00	0.01
BCa	1.81	1.84	1.82	1.84	1.82	1.80	1.81	1.82	1.83	1.86	1.84	1.84	1.84	1.72	1.70	1.60
BNa	0.10	0.08	0.10	0.09	0.10	0.11	0.10	0.10	0.09	0.08	0.08	0.09	0.09	0.15	0.16	0.14
ACa	0.00	0.00	0.00	0.00	0.00	0.00	0.00	0.00	0.00	0.00	0.00	0.00	0.00	0.00	0.00	0.00
ANa	0.39	0.34	0.39	0.45	0.43	0.41	0.43	0.41	0.45	0.47	0.46	0.45	0.39	0.24	0.22	0.14
AK	0.21	0.19	0.21	0.15	0.20	0.19	0.22	0.19	0.19	0.20	0.19	0.20	0.20	0.07	0.10	0.04

	0908-1: ophitic dyke Water Sign								35-5: meta-anorthosite Beloozerskaya Guba										
wt.-%	#9	#27	#28	#29	#30	#36	#37	#46	#1	#2	#18	#19	#20	#32	#38	#40	#43	#44	#48
SiO_2	46.33	54.72	54.86	48.12	48.10	55.52	47.17	43.82	45.23	44.41	43.09	43.14	42.97	45.56	41.55	42.39	41.35	43.79	44.73
TiO_2	0.13	0.01	0.01	0.25	0.26	0.04	0.29	0.65	1.12	1.10	0.40	0.60	0.58	1.15	0.34	0.36	0.24	0.24	0.47
Al_2O_3	13.56	1.46	0.84	10.91	10.12	0.93	10.82	15.06	13.93	14.47	16.73	16.66	16.07	14.12	18.43	17.16	18.19	16.38	14.66
FeO	11.88	19.82	20.16	10.96	10.75	20.71	11.16	12.82	4.23	4.12	7.58	7.32	7.05	3.97	7.61	7.36	7.14	6.49	6.77
Cr_2O_3	0.00	0.00	0.02	0.02	0.00	0.00	0.03	0.03	0.03	0.00	0.04	0.03	0.00	0.00	0.05	0.00	0.03	0.05	0.04
MnO	0.06	0.19	0.25	0.09	0.02	0.21	0.05	0.15	0.01	0.04	0.04	0.07	0.07	0.01	0.00	0.08	0.06	0.07	0.05
MgO	14.33	21.18	21.76	15.10	15.71	21.64	15.41	12.44	17.58	17.20	15.57	15.26	15.34	17.32	14.64	14.97	14.77	15.69	16.00
CaO	11.22	1.15	0.71	11.25	11.48	0.78	11.15	11.10	10.48	11.67	12.16	12.44	12.28	10.83	12.02	12.10	12.17	12.30	12.16
Na_2O	1.19	0.07	0.03	0.97	0.89	0.03	0.94	1.42	3.05	3.21	2.02	2.00	1.84	3.32	2.06	1.99	2.01	1.85	1.75
K_2O	0.24	0.00	0.00	0.16	0.20	0.01	0.22	0.34	1.10	0.76	0.98	1.11	1.02	0.76	1.55	1.41	1.50	1.18	1.11
F	0.00	0.00	0.00	0.00	0.00	0.00	0.00	0.00	0.00	0.00	0.00	0.00	0.00	0.00	0.00	0.00	0.00	0.00	0.00
Cl	0.00	0.00	0.00	0.00	0.00	0.00	0.00	0.00	0.00	0.00	0.00	0.00	0.00	0.00	0.00	0.00	0.00	0.00	0.00
Total	98.94	98.60	98.62	97.81	97.53	99.87	97.21	97.80	96.73	96.98	98.57	98.60	97.22	97.04	98.20	97.82	97.43	97.99	97.70
CTotal	101.08	100.78	100.82	99.96	99.65	102.08	99.35	99.92	98.88	99.09	100.74	100.75	99.32	99.16	100.36	99.92	99.55	100.16	99.85
TSi	6.50	7.27	7.26	6.80	6.81	7.28	6.70	6.29	6.47	6.36	6.08	6.11	6.15	6.50	5.92	6.06	5.93	6.21	6.36
TAl	1.50	0.23	0.13	1.20	1.19	0.14	1.30	1.71	1.54	1.64	1.92	1.89	1.85	1.50	2.08	1.94	2.07	1.80	1.64
TFe^{3+}	0.00	0.50	0.61	0.00	0.00	0.58	0.00	0.00	0.00	0.00	0.00	0.00	0.00	0.00	0.00	0.00	0.00	0.00	0.00
TTi	0.00	0.00	0.00	0.00	0.00	0.00	0.00	0.00	0.00	0.00	0.00	0.00	0.00	0.00	0.00	0.00	0.00	0.00	0.00
CAl	0.74	0.00	0.00	0.62	0.50	0.00	0.51	0.84	0.81	0.81	0.86	0.89	0.86	0.88	1.02	0.95	1.01	0.94	0.81
CCr	0.00	0.00	0.00	0.00	0.00	0.00	0.00	0.00	0.00	0.00	0.00	0.00	0.00	0.00	0.01	0.00	0.00	0.01	0.00
CFe^{3+}	0.70	0.65	0.60	0.54	0.63	0.62	0.74	0.57	0.25	0.06	0.42	0.24	0.28	0.12	0.31	0.26	0.31	0.22	0.22
CTi	0.01	0.00	0.00	0.03	0.03	0.00	0.03	0.07	0.12	0.12	0.04	0.06	0.06	0.12	0.04	0.04	0.03	0.03	0.05
CMg	3.00	4.19	4.29	3.18	3.32	4.23	3.26	2.66	3.75	3.67	3.27	3.22	3.28	3.69	3.11	3.19	3.16	3.31	3.39
CFe^{2+}	0.55	0.15	0.09	0.62	0.53	0.13	0.44	0.84	0.07	0.34	0.40	0.58	0.51	0.19	0.52	0.56	0.49	0.49	0.52
CMn	0.00	0.01	0.01	0.01	0.00	0.01	0.00	0.01	0.00	0.00	0.00	0.00	0.00	0.00	0.00	0.01	0.00	0.00	0.00
CCa	0.00	0.00	0.00	0.00	0.00	0.00	0.00	0.00	0.00	0.00	0.00	0.00	0.00	0.00	0.00	0.00	0.00	0.00	0.00
BFe^{2+}	0.14	0.90	0.93	0.13	0.12	0.93	0.14	0.13	0.19	0.10	0.07	0.05	0.05	0.16	0.08	0.06	0.06	0.06	0.07
BMn	0.00	0.01	0.02	0.01	0.00	0.01	0.00	0.01	0.00	0.00	0.00	0.00	0.00	0.00	0.00	0.01	0.00	0.00	0.00
BCa	1.69	0.16	0.10	1.70	1.74	0.11	1.70	1.71	1.61	1.79	1.84	1.89	1.88	1.66	1.84	1.85	1.87	1.87	1.85
BNa	0.16	0.01	0.00	0.13	0.12	0.00	0.13	0.16	0.21	0.11	0.09	0.06	0.06	0.18	0.09	0.08	0.07	0.07	0.08
ACa	0.00	0.00	0.00	0.00	0.00	0.00	0.00	0.00	0.00	0.00	0.00	0.00	0.00	0.00	0.00	0.00	0.00	0.00	0.00
ANa	0.16	0.01	0.00	0.13	0.12	0.00	0.13	0.24	0.64	0.78	0.47	0.49	0.45	0.74	0.48	0.47	0.49	0.44	0.40
AK	0.04	0.00	0.00	0.03	0.04	0.00	0.04	0.06	0.20	0.14	0.18	0.20	0.19	0.14	0.28	0.26	0.28	0.21	0.20

	35-5: meta-anorthosite Beloozerskaya Guba			
wt.-%	#82	#88	#101	#102
SiO_2	41.12	41.61	42.68	42.49
TiO_2	1.50	1.94	0.52	0.75
Al_2O_3	16.26	15.94	16.05	16.12
FeO	9.08	8.49	8.22	8.45
Cr_2O_3	0.00	0.06	0.05	0.01
MnO	0.05	0.03	0.09	0.09
MgO	13.89	13.74	15.13	14.50
CaO	11.90	12.02	12.03	12.18
Na_2O	2.03	1.88	1.91	1.87
K_2O	1.26	1.28	1.40	1.41
F	0.00	0.00	0.00	0.00
Cl	0.00	0.00	0.00	0.00
Total	97.09	96.93	98.03	97.86
CTotal	99.15	99.05	100.18	99.96
TSi	5.99	6.07	6.10	6.11
TAl	2.01	1.93	1.90	1.89
TFe^{3+}	0.00	0.00	0.00	0.00
TTi	0.00	0.00	0.00	0.00
CAl	0.78	0.81	0.80	0.84
CCr	0.00	0.01	0.01	0.00
CFe^{3+}	0.25	0.12	0.37	0.24
CTi	0.16	0.21	0.06	0.08
CMg	3.02	2.99	3.22	3.11
CFe^{2+}	0.79	0.86	0.54	0.73
CMn	0.00	0.00	0.01	0.01
CCa	0.00	0.00	0.00	0.00
BFe^{2+}	0.06	0.06	0.07	0.05
BMn	0.00	0.00	0.01	0.01
BCa	1.86	1.88	1.84	1.88
BNa	0.08	0.07	0.09	0.07
ACa	0.00	0.00	0.00	0.00
ANa	0.50	0.47	0.45	0.46
AK	0.23	0.24	0.26	0.26

EMP analyses of clinopyroxene cores, rims, inclusions and coronal clinopyroxene from different rock types. Analyses were recalculated on the basis of 6 oxygens.

	0708-3: metagabbro Bolschoi Khed															
wt.-%	#35 core	#36 core	#57 sympl.	#58 sympl.	#77 rim	#78	#79	#80 core	#81 core	#82	#83 rim	#85 core	#86 rim	#112 core	#113 rim	#114 rim
SiO_2	49.19	54.81	49.66	49.93	49.07	47.94	48.36	48.64	46.92	48.14	47.42	48.04	51.68	48.52	51.34	52.92
TiO_2	0.93	0.01	1.20	0.90	1.09	1.15	1.09	0.76	0.95	0.87	1.19	0.90	0.60	0.63	0.72	0.02
Al_2O_3	6.60	28.11	5.74	4.94	6.71	7.17	8.78	8.19	11.41	9.16	9.34	10.12	2.99	5.02	4.91	2.21
Cr_2O_3	0.11	0.03	0.16	0.23	0.25	0.08	0.15	0.14	0.13	0.09	0.13	0.13	0.17	7.61	1.63	0.93
Fe_2O_3	3.16	0.00	2.18	1.97	2.04	4.60	1.94	3.41	2.30	3.53	3.86	2.17	1.77	0.03	0.08	0.09
FeO	3.21	0.19	3.90	3.84	4.08	2.19	4.61	2.76	5.03	3.38	4.45	5.11	3.71	0.00	3.52	17.54
MnO	0.06	0.04	0.12	0.15	0.10	0.08	0.08	0.06	0.08	0.06	0.08	0.07	0.10	0.11	0.14	0.31
MgO	13.33	0.01	14.15	13.93	13.78	13.33	12.58	12.82	12.65	13.15	13.54	13.21	15.00	15.62	14.99	25.21
CaO	22.70	10.61	21.43	22.35	21.63	22.73	21.84	22.83	18.73	21.05	18.36	18.85	23.26	21.56	22.78	0.36
Na_2O	0.74	5.97	0.70	0.63	0.61	0.62	0.77	0.82	0.93	0.85	0.95	1.00	0.42	0.80	0.50	0.00
K_2O	0.04	0.16	0.17	0.04	0.13	0.10	0.04	0.04	0.33	0.19	0.39	0.24	0.02	0.40	0.05	0.01
Σ	100.06	99.94	99.43	98.92	99.49	100.00	100.24	100.48	99.45	100.48	99.71	99.83	99.71	100.31	100.65	99.61
Si	1.81	1.86	1.84	1.86	1.82	1.77	1.78	1.78	1.73	1.76	1.75	1.77	1.91	1.79	1.87	1.94
Al^{IV}	0.19	0.14	0.16	0.14	0.18	0.23	0.22	0.22	0.27	0.24	0.25	0.23	0.09	0.21	0.13	0.06
Al^{VI}	0.10	0.98	0.09	0.08	0.11	0.08	0.16	0.14	0.23	0.16	0.16	0.20	0.04	0.00	0.08	0.03
Ti	0.03	0.00	0.03	0.03	0.03	0.03	0.03	0.02	0.03	0.02	0.03	0.03	0.02	0.02	0.02	0.00
Fe^{3+}	0.09	0.00	0.06	0.06	0.06	0.13	0.05	0.09	0.06	0.10	0.11	0.06	0.05	0.21	0.05	0.03
Cr	0.00	0.00	0.01	0.01	0.01	0.00	0.00	0.00	0.00	0.00	0.00	0.00	0.01	0.00	0.00	0.00
Mg	0.73	0.00	0.78	0.77	0.76	0.73	0.69	0.70	0.70	0.72	0.75	0.72	0.83	0.86	0.81	1.38
Fe^{2+}	0.10	0.01	0.12	0.12	0.13	0.07	0.14	0.09	0.16	0.10	0.14	0.16	0.11	0.00	0.11	0.54
Mn^{2+}	0.00	0.00	0.00	0.01	0.00	0.00	0.00	0.00	0.00	0.00	0.00	0.00	0.00	0.00	0.00	0.01
Ca	0.90	0.39	0.85	0.89	0.86	0.90	0.86	0.90	0.74	0.83	0.73	0.74	0.92	0.85	0.89	0.01
Na	0.05	0.39	0.05	0.05	0.04	0.05	0.06	0.06	0.07	0.06	0.07	0.07	0.03	0.06	0.04	0.00
K	0.00	0.01	0.01	0.00	0.01	0.01	0.00	0.00	0.02	0.01	0.02	0.01	0.00	0.02	0.00	0.00
Wo	51.88	98.48	48.53	49.96	49.18	52.89	50.86	53.32	46.53	50.14	45.15	45.73	49.47	49.80	49.12	0.74
En	42.40	0.13	44.57	43.33	43.58	43.14	40.76	41.65	43.71	43.57	46.31	44.60	44.37	50.20	44.96	71.39
Fs	5.73	1.39	6.90	6.71	7.24	3.98	8.38	5.03	9.76	6.29	8.55	9.68	6.15	0.00	5.92	27.87
XMg	0.88	0.09	0.87	0.87	0.86	0.92	0.83	0.89	0.82	0.87	0.84	0.82	0.88	1.00	0.88	0.72

	0708-3: metagabbro Bolschoi Khed								1008-B3: metagabbro Kataransky Cape									
wt.-%	#117 rim	#17 core	#18	#19	#20	#21	#22	#23 rim	#15	#16	#34 core	#35	#36 rim	#46 core	#47	#49	#48 rim	#51 core
SiO_2	49.45	47.55	48.63	46.81	47.30	47.91	48.99	50.28	50.72	52.12	51.89	52.04	53.12	51.36	51.39	51.74	51.94	50.04
TiO_2	0.95	1.27	1.01	1.05	1.02	1.00	0.93	0.89	0.37	0.39	0.40	0.37	0.17	0.45	0.48	0.42	0.37	0.51
Al_2O_3	7.66	9.49	8.23	9.50	9.95	8.57	8.23	5.13	3.01	3.14	3.24	3.24	2.13	3.61	3.75	3.45	3.19	6.27
Cr_2O_3	0.92	3.06	2.55	4.82	4.96	4.97	2.96	3.05	0.04	0.04	0.00	0.02	0.10	0.05	0.11	0.07	0.03	0.08
Fe_2O_3	0.10	0.19	0.13	0.13	0.19	0.15	0.19	0.17	3.79	1.59	2.22	2.79	2.14	1.68	1.30	1.62	1.74	1.81
FeO	4.72	5.20	4.74	3.76	3.58	2.80	4.82	4.02	3.65	5.46	5.37	4.91	4.33	5.46	5.77	5.48	5.50	5.93
MnO	0.07	0.11	0.05	0.08	0.09	0.14	0.04	0.07	0.09	0.09	0.10	0.13	0.08	0.08	0.11	0.08	0.09	0.08
MgO	14.57	13.21	13.20	13.14	12.86	13.06	13.86	14.46	14.66	14.18	14.49	14.44	15.28	14.19	13.89	14.21	14.37	13.59
CaO	19.83	18.46	20.94	19.20	19.56	21.21	19.47	21.72	22.34	22.64	22.34	22.48	23.19	22.24	22.28	22.65	22.49	20.82
Na_2O	0.70	0.95	0.74	0.87	1.07	0.88	0.87	0.57	0.54	0.60	0.53	0.64	0.49	0.54	0.58	0.50	0.51	0.70
K_2O	0.19	0.36	0.16	0.34	0.29	0.25	0.29	0.19	0.00	0.03	0.01	0.01	0.01	0.00	0.00	0.00	0.01	0.05
Σ	99.15	99.84	100.38	99.69	100.88	100.93	100.65	100.56	99.23	100.27	100.59	101.07	101.03	99.67	99.66	100.23	100.25	99.87
Si	1.82	1.76	1.79	1.73	1.73	1.75	1.79	1.85	1.89	1.92	1.91	1.90	1.94	1.90	1.91	1.91	1.92	1.85
Al^{IV}	0.18	0.24	0.21	0.27	0.27	0.25	0.21	0.16	0.11	0.08	0.09	0.10	0.06	0.10	0.09	0.09	0.09	0.15
Al^{VI}	0.16	0.17	0.14	0.15	0.16	0.12	0.15	0.07	0.02	0.06	0.05	0.04	0.03	0.06	0.07	0.06	0.05	0.12
Ti	0.03	0.04	0.03	0.03	0.03	0.03	0.03	0.03	0.01	0.01	0.01	0.01	0.01	0.01	0.01	0.01	0.01	0.01
Fe^{3+}	0.03	0.09	0.07	0.13	0.14	0.14	0.08	0.08	0.11	0.04	0.06	0.08	0.06	0.05	0.04	0.05	0.05	0.05
Cr	0.00	0.01	0.00	0.00	0.01	0.00	0.01	0.01	0.00	0.00	0.00	0.00	0.00	0.00	0.00	0.00	0.00	0.00
Mg	0.80	0.73	0.72	0.73	0.70	0.71	0.76	0.79	0.81	0.78	0.79	0.79	0.83	0.78	0.77	0.78	0.79	0.75
Fe^{2+}	0.15	0.16	0.15	0.12	0.11	0.09	0.15	0.12	0.11	0.17	0.17	0.15	0.13	0.17	0.18	0.17	0.17	0.18
Mn^{2+}	0.00	0.00	0.00	0.00	0.00	0.00	0.00	0.00	0.00	0.00	0.00	0.00	0.00	0.00	0.00	0.00	0.00	0.00
Ca	0.78	0.73	0.82	0.76	0.77	0.83	0.76	0.85	0.89	0.89	0.88	0.88	0.91	0.88	0.89	0.90	0.89	0.82
Na	0.05	0.07	0.05	0.06	0.08	0.06	0.06	0.04	0.04	0.04	0.04	0.05	0.03	0.04	0.04	0.04	0.04	0.05
K	0.01	0.02	0.01	0.02	0.01	0.01	0.01	0.01	0.00	0.00	0.00	0.00	0.00	0.00	0.00	0.00	0.00	0.00
Wo	45.30	45.14	48.69	47.51	48.60	51.04	45.79	48.28	49.02	48.56	47.85	48.44	48.49	48.10	48.32	48.50	48.08	46.95
En	46.29	44.94	42.70	45.23	44.45	43.71	45.36	44.74	44.73	42.30	43.17	43.30	44.44	42.69	41.91	42.34	42.74	42.62
Fs	8.41	9.92	8.61	7.26	6.95	5.25	8.85	6.98	6.26	9.14	8.98	8.26	7.07	9.22	9.77	9.17	9.18	10.43
XMg	0.85	0.82	0.83	0.86	0.87	0.89	0.84	0.87	0.88	0.82	0.83	0.84	0.86	0.82	0.81	0.82	0.82	0.80

	1008-B3: metagabbro Kataransky Cape							**P-20: noritic dyke Water Sign**										
wt.-%	#52	#53	#54	#55 rim	#58	#59	#64	#1 core	#2 rim	#4 rim	#5 rim	#9 core	#10 rim	#11	#13 core	#14 core	#15 rim	#26 core
SiO_2	50.38	50.93	51.03	50.71	52.61	51.89	51.52	49.26	49.38	50.01	51.52	52.26	52.29	52.79	52.24	52.18	52.30	51.51
TiO_2	0.59	0.65	0.63	0.47	0.34	0.49	0.35	0.68	0.50	0.50	0.53	0.34	0.31	0.08	0.32	0.32	0.40	0.48
Al_2O_3	5.61	4.73	4.69	3.53	2.59	3.53	3.17	6.78	4.11	5.36	4.49	3.68	2.90	2.31	3.73	3.80	3.53	4.30
Cr_2O_3	0.04	0.05	0.05	0.07	0.07	0.06	0.08	2.60	4.36	1.41	0.65	0.92	1.64	0.00	0.68	0.65	0.34	1.54
Fe_2O_3	2.00	1.92	1.31	3.07	1.20	1.52	2.48	0.10	0.25	0.12	0.04	0.09	0.01	0.00	0.03	0.07	0.03	0.03
FeO	5.63	4.94	5.67	3.85	5.18	5.69	5.11	4.33	2.63	5.65	6.10	5.83	5.08	21.06	6.73	6.31	6.11	5.15
MnO	0.05	0.10	0.05	0.04	0.11	0.12	0.12	0.10	0.07	0.10	0.07	0.09	0.15	0.23	0.08	0.08	0.14	0.14
MgO	13.59	13.79	13.96	14.15	14.59	13.96	14.32	12.97	13.80	12.88	13.74	14.41	14.38	23.05	13.93	13.84	13.87	13.88
CaO	21.37	22.87	22.23	23.18	23.27	22.69	22.57	22.49	23.44	22.35	22.63	22.45	23.36	0.41	22.51	22.62	23.12	23.01
Na_2O	0.66	0.52	0.48	0.48	0.45	0.59	0.49	0.64	0.45	0.58	0.52	0.51	0.44	0.00	0.48	0.56	0.49	0.53
K_2O	0.14	0.05	0.09	0.00	0.00	0.00	0.00	0.06	0.03	0.08	0.00	0.02	0.00	0.00	0.01	0.01	0.01	0.01
Σ	100.06	100.54	100.19	99.56	100.41	100.53	100.21	100.01	99.01	99.04	100.31	100.59	100.56	99.93	100.74	100.45	100.35	100.59
Si	1.86	1.87	1.88	1.88	1.93	1.91	1.90	1.82	1.85	1.87	1.90	1.92	1.92	1.95	1.92	1.92	1.93	1.89
Al^{IV}	0.14	0.13	0.12	0.12	0.07	0.09	0.10	0.18	0.15	0.13	0.10	0.08	0.08	0.05	0.08	0.08	0.08	0.11
Al^{VI}	0.10	0.08	0.09	0.04	0.05	0.06	0.04	0.12	0.03	0.11	0.09	0.08	0.05	0.05	0.08	0.08	0.08	0.08
Ti	0.02	0.02	0.02	0.01	0.01	0.01	0.01	0.02	0.01	0.01	0.02	0.01	0.01	0.00	0.01	0.01	0.01	0.01
Fe^{3+}	0.06	0.05	0.04	0.09	0.03	0.04	0.07	0.07	0.12	0.04	0.02	0.03	0.05	0.00	0.02	0.02	0.01	0.04
Cr	0.00	0.00	0.00	0.00	0.00	0.00	0.00	0.00	0.01	0.00	0.00	0.00	0.00	0.00	0.00	0.00	0.00	0.00
Mg	0.75	0.76	0.77	0.78	0.80	0.77	0.79	0.72	0.77	0.72	0.75	0.79	0.79	1.27	0.76	0.76	0.76	0.76
Fe^{2+}	0.17	0.15	0.18	0.12	0.16	0.18	0.16	0.13	0.08	0.18	0.19	0.18	0.16	0.65	0.21	0.19	0.19	0.16
Mn^{2+}	0.00	0.00	0.00	0.00	0.00	0.00	0.00	0.00	0.00	0.00	0.00	0.00	0.01	0.01	0.00	0.00	0.00	0.00
Ca	0.85	0.90	0.88	0.92	0.92	0.89	0.89	0.89	0.94	0.90	0.89	0.88	0.92	0.02	0.89	0.89	0.91	0.91
Na	0.05	0.04	0.03	0.04	0.03	0.04	0.04	0.05	0.03	0.04	0.04	0.04	0.03	0.00	0.03	0.04	0.04	0.04
K	0.01	0.00	0.00	0.00	0.00	0.00	0.00	0.00	0.00	0.00	0.00	0.00	0.00	0.00	0.00	0.00	0.00	0.00
Wo	47.85	49.82	48.24	50.54	48.87	48.75	48.55	51.21	52.44	50.02	48.65	47.72	49.35	0.84	47.75	48.34	49.00	49.66
En	42.32	41.78	42.15	42.91	42.64	41.71	42.87	41.10	42.96	40.11	41.11	42.61	42.27	65.56	41.11	41.14	40.89	41.68
Fs	9.83	8.40	9.61	6.55	8.49	9.54	8.58	7.69	4.60	9.87	10.24	9.67	8.38	33.60	11.15	10.52	10.10	8.67
XMg	0.81	0.83	0.81	0.87	0.83	0.81	0.83	0.84	0.90	0.80	0.80	0.82	0.83	0.66	0.79	0.80	0.80	0.83

P-20: noritic dyke Water Sign

wt.-%	#12 cor.	#13 cor.	#14 cor.	#30	#31 cor.	#32 cor.	#33 cor.	#38 core	#39	#40	#41	#42	#43	#44	#45	#47 rim	#48 cor.	#49 cor.
SiO_2	51.83	51.66	51.64	52.37	50.80	51.49	52.58	51.00	51.30	50.86	50.60	50.89	50.88	50.76	51.13	51.32	51.90	52.08
TiO_2	0.39	0.40	0.40	0.19	0.37	0.25	0.24	0.52	0.48	0.47	0.51	0.49	0.46	0.56	0.51	0.40	0.40	0.36
Al_2O_3	3.44	3.86	3.40	2.01	4.50	2.52	2.22	4.98	5.01	4.82	4.79	4.85	4.88	4.70	4.43	3.29	3.62	3.37
Cr_2O_3	0.00	0.03	0.00	0.05	0.02	0.01	0.00	0.00	0.00	0.07	0.02	0.10	0.03	0.00	0.01	0.00	0.00	0.04
Fe_2O_3	1.78	1.37	2.40	3.08	2.35	2.95	2.67	1.95	1.77	1.54	2.25	2.26	2.24	2.49	2.20	2.64	1.52	1.72
FeO	5.21	5.63	5.28	3.27	5.42	3.51	3.91	5.83	5.98	5.96	5.65	5.97	5.89	5.29	5.62	4.61	6.16	5.85
MnO	0.08	0.09	0.17	0.11	0.10	0.10	0.10	0.12	0.07	0.13	0.08	0.06	0.03	0.16	0.14	0.08	0.11	0.11
MgO	14.28	14.02	14.37	15.07	14.07	14.83	15.12	12.99	13.18	13.15	13.27	13.46	13.26	13.42	13.74	13.82	14.07	14.19
CaO	22.73	22.25	21.97	23.73	21.45	22.89	23.23	21.65	21.61	21.75	21.93	21.35	21.81	22.24	22.11	23.21	22.05	22.21
Na_2O	0.53	0.62	0.62	0.45	0.64	0.52	0.51	0.99	0.98	0.83	0.75	0.84	0.81	0.72	0.64	0.57	0.61	0.63
K_2O	0.00	0.00	0.01	0.02	0.00	0.01	0.00	0.00	0.00	0.00	0.01	0.00	0.00	0.00	0.02	0.02	0.01	0.00
Σ	100.27	99.94	100.25	100.35	99.75	99.07	100.58	100.03	100.37	99.58	99.85	100.26	100.28	100.34	100.55	99.97	100.45	100.54
Si	1.91	1.91	1.90	1.92	1.88	1.92	1.93	1.89	1.89	1.89	1.88	1.88	1.88	1.87	1.88	1.90	1.91	1.92
Al^{IV}	0.09	0.09	0.10	0.08	0.12	0.09	0.07	0.11	0.11	0.11	0.12	0.12	0.12	0.13	0.12	0.10	0.09	0.09
Al^{VI}	0.06	0.08	0.05	0.01	0.08	0.03	0.02	0.10	0.11	0.10	0.09	0.09	0.09	0.08	0.08	0.05	0.07	0.06
Ti	0.01	0.01	0.01	0.01	0.01	0.01	0.01	0.01	0.01	0.01	0.01	0.01	0.01	0.02	0.01	0.01	0.01	0.01
Fe^{3+}	0.05	0.04	0.07	0.09	0.07	0.08	0.07	0.05	0.05	0.04	0.06	0.06	0.06	0.07	0.06	0.07	0.04	0.05
Cr																		
Mg	0.78	0.77	0.79	0.83	0.78	0.82	0.83	0.72	0.72	0.73	0.73	0.74	0.73	0.74	0.75	0.76	0.77	0.78
Fe^{2+}	0.16	0.17	0.16	0.10	0.17	0.11	0.12	0.18	0.18	0.19	0.18	0.18	0.18	0.16	0.17	0.14	0.19	0.18
Mn^{2+}	0.00	0.00	0.01	0.00	0.00	0.00	0.00	0.00	0.00	0.00	0.00	0.00	0.00	0.01	0.00	0.00	0.00	0.00
Ca	0.90	0.88	0.87	0.93	0.85	0.91	0.91	0.86	0.85	0.87	0.87	0.84	0.86	0.88	0.87	0.92	0.87	0.88
Na	0.04	0.05	0.04	0.03	0.05	0.04	0.04	0.07	0.07	0.06	0.05	0.06	0.06	0.05	0.05	0.04	0.04	0.05
K	0.00	0.00	0.00	0.00	0.00	0.00	0.00	0.00	0.00	0.00	0.00	0.00	0.00	0.00	0.00	0.00	0.00	0.00
Wo	48.70	48.21	47.68	50.23	47.40	49.47	49.09	48.89	48.44	48.66	48.96	47.72	48.62	49.38	48.48	50.42	47.50	47.74
En	42.59	42.27	43.38	44.38	43.25	44.60	44.46	40.82	41.09	40.94	41.20	41.87	41.13	41.45	41.91	41.77	42.15	42.44
Fs	8.71	9.51	8.94	5.40	9.35	5.92	6.45	10.28	10.46	10.41	9.84	10.42	10.25	9.17	9.61	7.81	10.36	9.81
XMg	0.83	0.82	0.83	0.89	0.82	0.88	0.87	0.80	0.80	0.80	0.81	0.80	0.80	0.82	0.81	0.84	0.80	0.81

P-20: noritic dyke Water Sign

wt.-%	#61 incl.	#63 incl.	#64 incl.	#65 incl.	#66 incl.	#67 incl.	#68 incl.	#79 cor.	#80 cor.	#94 core	#95 rim	#96 core	#100 core	#101 rim	#102 rim	#105 cor.
SiO_2	51.41	49.39	50.14	51.02	51.23	51.77	51.34	52.40	52.24	50.99	51.20	51.18	50.52	51.19	50.97	51.21
TiO_2	0.46	0.52	0.69	0.46	0.57	0.54	0.47	0.24	0.29	0.50	0.55	0.53	0.56	0.45	0.46	0.39
Al_2O_3	5.07	5.10	5.29	4.93	5.18	5.08	4.63	2.11	3.01	5.07	4.59	4.94	5.21	3.51	3.95	3.42
Cr_2O_3	0.09	0.02	0.07	0.07	0.07	0.05	0.04	0.11	0.17	0.05	0.03	0.03	0.03	0.00	0.01	0.04
Fe_2O_3	3.24	5.86	4.57	4.19	2.51	2.24	3.84	1.96	1.25	1.89	2.59	1.49	2.19	2.41	2.71	2.31
FeO	3.87	3.27	3.03	2.56	4.15	4.24	2.04	4.50	5.56	6.26	4.99	5.75	5.48	4.87	4.13	5.12
MnO	0.08	0.05	0.13	0.04	0.07	0.12	0.14	0.08	0.07	0.20	0.15	0.14	0.08	0.13	0.12	0.09
MgO	13.53	13.08	13.84	13.58	13.21	13.37	14.11	14.87	14.32	13.04	13.61	13.30	13.02	13.43	13.94	13.83
CaO	21.04	20.37	20.22	21.53	20.93	21.08	22.18	23.21	22.72	20.57	21.77	21.47	21.90	23.36	22.93	22.54
Na_2O	1.47	1.45	1.46	1.52	1.55	1.55	1.30	0.44	0.53	1.15	0.95	0.98	0.87	0.59	0.62	0.61
K_2O	0.02	0.02	0.02	0.00	0.00	0.00	0.02	0.00	0.01	0.01	0.00	0.00	0.02	0.00	0.00	0.00
Σ	100.28	99.13	99.45	99.90	99.47	100.05	100.10	99.93	100.16	99.71	100.44	99.81	99.89	99.95	99.85	99.57
Si	1.88	1.84	1.85	1.88	1.89	1.90	1.88	1.93	1.93	1.89	1.88	1.89	1.87	1.90	1.89	1.90
Al^{IV}	0.12	0.16	0.15	0.12	0.11	0.10	0.12	0.07	0.07	0.11	0.12	0.11	0.13	0.10	0.11	0.10
Al^{VI}	0.10	0.07	0.08	0.09	0.12	0.12	0.08	0.03	0.06	0.11	0.08	0.11	0.10	0.05	0.06	0.05
Ti	0.01	0.02	0.02	0.01	0.02	0.02	0.01	0.01	0.01	0.01	0.02	0.02	0.02	0.01	0.01	0.01
Fe^{3+}	0.09	0.17	0.13	0.12	0.07	0.06	0.11	0.06	0.04	0.05	0.07	0.04	0.06	0.07	0.08	0.07
Cr																
Mg	0.74	0.73	0.76	0.74	0.73	0.73	0.77	0.82	0.79	0.72	0.75	0.73	0.72	0.74	0.77	0.77
Fe^{2+}	0.12	0.10	0.09	0.08	0.13	0.13	0.06	0.14	0.17	0.19	0.15	0.18	0.17	0.15	0.13	0.16
Mn^{2+}	0.00	0.00	0.00	0.00	0.00	0.00	0.00	0.00	0.00	0.01	0.01	0.00	0.00	0.00	0.00	0.00
Ca	0.83	0.82	0.80	0.85	0.83	0.83	0.87	0.92	0.90	0.82	0.86	0.85	0.87	0.93	0.91	0.90
Na	0.10	0.11	0.11	0.11	0.11	0.11	0.09	0.03	0.04	0.08	0.07	0.07	0.06	0.04	0.05	0.04
K	0.00	0.00	0.00	0.00	0.00	0.00	0.00	0.00	0.00	0.00	0.00	0.00	0.00	0.00	0.00	0.00
Wo	49.05	49.54	48.33	50.76	49.19	49.04	51.10	48.95	48.37	47.18	48.81	48.29	49.45	50.94	50.35	49.24
En	43.90	44.26	46.01	44.53	43.19	43.26	45.23	43.64	42.40	41.62	42.45	41.61	40.90	40.76	42.57	42.03
Fs	7.05	6.20	5.66	4.71	7.62	7.70	3.67	7.41	9.23	11.21	8.74	10.10	9.65	8.30	7.08	8.74
XMg	0.86	0.88	0.89	0.90	0.85	0.85	0.93	0.86	0.82	0.79	0.83	0.81	0.81	0.83	0.86	0.83

	P-20: noritic dyke Water Sign					**35-5: meta-anorthosite Beloozerskaya Guba**											
wt.-%	#107 cor.	#108 cor.	#125 rim	#126 rim	#127 cor.	#34	#35	#49	#50	#51	#52	#53	#54	#55	#58	#59	#67
SiO_2	51.33	51.48	51.17	51.80	51.11	50.12	52.14	49.23	51.40	49.92	49.07	49.37	49.49	49.47	47.31	49.56	50.75
TiO_2	0.49	0.55	0.45	0.42	0.43	1.12	0.54	1.06	0.76	0.93	1.08	1.06	1.02	1.04	1.13	0.96	0.50
Al_2O_3	3.58	3.83	3.65	3.12	3.92	5.87	4.64	8.98	6.43	7.99	8.66	8.63	9.07	8.47	11.29	8.06	8.51
Cr_2O_3	0.00	0.02	0.00	0.00	0.00	0.05	0.07	0.11	0.06	0.07	0.08	0.05	0.11	0.12	0.20	0.21	0.00
Fe_2O_3	2.56	1.97	1.94	1.90	2.39	2.45	1.51	2.37	0.68	1.87	2.16	1.99	2.04	2.39	2.12	2.43	1.74
FeO	5.61	5.18	5.80	5.98	5.40	2.54	2.97	2.08	3.37	2.40	2.22	2.49	2.23	2.00	3.37	2.61	2.66
MnO	0.02	0.07	0.17	0.13	0.12	0.14	0.07	0.07	0.14	0.13	0.12	0.06	0.12	0.13	0.05	0.02	0.03
MgO	13.66	13.61	13.20	13.37	13.45	14.35	14.81	13.79	14.33	13.58	13.61	13.42	13.61	13.37	12.72	13.35	13.00
CaO	22.13	23.08	22.94	23.30	22.70	23.11	23.22	21.88	22.90	22.97	22.09	22.75	22.26	23.12	19.87	22.72	21.04
Na_2O	0.75	0.64	0.58	0.54	0.63	0.66	0.78	1.07	0.79	0.94	1.02	0.93	1.06	0.96	1.24	0.98	1.79
K_2O	0.01	0.01	0.00	0.01	0.00	0.01	0.01	0.03	0.02	0.00	0.01	0.02	0.02	0.00	0.10	0.01	0.00
Σ	100.13	100.43	99.89	100.56	100.15	100.42	100.75	100.69	100.88	100.79	100.12	100.76	101.03	101.10	99.38	100.91	100.03
Si	1.90	1.90	1.90	1.91	1.89	1.83	1.89	1.78	1.86	1.81	1.79	1.79	1.79	1.79	1.74	1.80	1.84
Al^{IV}	0.10	0.10	0.10	0.09	0.11	0.17	0.11	0.22	0.14	0.19	0.21	0.21	0.21	0.21	0.26	0.20	0.16
Al^{VI}	0.06	0.06	0.06	0.05	0.06	0.09	0.09	0.17	0.14	0.15	0.16	0.16	0.17	0.15	0.23	0.15	0.21
Ti	0.01	0.02	0.01	0.01	0.01	0.03	0.02	0.03	0.02	0.03	0.03	0.03	0.03	0.03	0.03	0.03	0.01
Fe^{3+}	0.07	0.06	0.05	0.05	0.07	0.07	0.04	0.07	0.02	0.05	0.06	0.05	0.06	0.07	0.06	0.07	0.05
Cr						0.00	0.00	0.00	0.00	0.00	0.00	0.00	0.00	0.00	0.01	0.01	0.00
Mg	0.75	0.75	0.73	0.74	0.74	0.78	0.80	0.75	0.77	0.73	0.74	0.73	0.73	0.72	0.70	0.72	0.70
Fe^{2+}	0.17	0.16	0.18	0.19	0.17	0.08	0.09	0.06	0.10	0.07	0.07	0.08	0.07	0.06	0.10	0.08	0.08
Mn^{2+}	0.00	0.00	0.01	0.00	0.00	0.00	0.00	0.00	0.00	0.00	0.00	0.00	0.00	0.00	0.00	0.00	0.00
Ca	0.88	0.91	0.91	0.92	0.90	0.91	0.90	0.85	0.89	0.89	0.86	0.89	0.86	0.90	0.78	0.88	0.82
Na	0.05	0.05	0.04	0.04	0.05	0.05	0.06	0.08	0.06	0.07	0.07	0.07	0.07	0.07	0.09	0.07	0.13
K	0.00	0.00	0.00	0.00	0.00	0.00	0.00	0.00	0.00	0.00	0.00	0.00	0.00	0.00	0.01	0.00	0.00
Wo	48.62	50.12	50.06	50.04	49.75	51.30	50.33	51.25	50.38	52.53	51.67	52.47	51.85	53.41	49.43	52.43	51.06
En	41.77	41.11	40.06	39.94	41.00	44.30	44.65	44.94	43.84	43.20	44.27	43.05	44.10	42.98	44.03	42.86	43.90
Fs	9.62	8.78	9.88	10.02	9.25	4.40	5.02	3.81	5.78	4.28	4.06	4.48	4.06	3.61	6.54	4.71	5.04
XMg	0.81	0.82	0.80	0.80	0.82	0.91	0.90	0.92	0.88	0.91	0.92	0.91	0.92	0.92	0.87	0.90	0.90

35-5: meta-anorthosite Beloozerskaya

wt.-%	#70	#89	#94	#95	#96	#104
SiO_2	51.30	50.32	46.54	47.01	47.48	47.56
TiO_2	0.48	0.55	1.06	1.07	1.32	1.10
Al_2O_3	8.86	8.35	10.98	11.55	11.18	11.06
Cr_2O_3	0.02	0.00	0.18	0.14	0.09	0.09
Fe_2O_3	1.23	2.52	3.32	2.91	1.47	2.23
FeO	2.86	1.81	1.79	2.38	3.41	2.40
MnO	0.05	0.04	0.02	0.07	0.04	0.01
MgO	13.11	13.05	12.12	12.56	12.09	12.71
CaO	21.08	21.43	22.19	20.70	22.07	21.69
Na_2O	1.83	1.75	0.99	1.12	0.97	1.04
K_2O	0.01	0.00	0.05	0.20	0.05	0.06
Σ	100.84	99.83	99.24	99.71	100.18	99.96
Si	1.85	1.83	1.72	1.72	1.74	1.74
Al^{IV}	0.15	0.17	0.28	0.28	0.26	0.26
Al^{VI}	0.22	0.19	0.20	0.22	0.22	0.21
Ti	0.01	0.02	0.03	0.03	0.04	0.03
Fe^{3+}	0.03	0.07	0.09	0.08	0.04	0.06
Cr	0.00	0.00	0.01	0.00	0.00	0.00
Mg	0.70	0.71	0.67	0.69	0.66	0.69
Fe^{2+}	0.09	0.06	0.06	0.07	0.10	0.07
Mn^{2+}	0.00	0.00	0.00	0.00	0.00	0.00
Ca	0.81	0.84	0.88	0.81	0.87	0.85
Na	0.13	0.12	0.07	0.08	0.07	0.07
K	0.00	0.00	0.00	0.01	0.00	0.00
Wo	50.73	52.28	54.85	51.72	53.11	52.59
En	43.90	44.28	41.70	43.64	40.49	42.87
Fs	5.37	3.44	3.45	4.64	6.41	4.54
XMg	0.89	0.93	0.92	0.90	0.86	0.90

EMP analyses of garnet cores, rims and coronal garnet from different rock types. Analyses were recalculated on the basis of 12 oxygens.

	0708-3: metagabbro Bolschoi Khed																		
wt.-%	#1 rim	#2	#3	#4	#5	#6 core	#7	#8	#9	#10	#11	#12	#13 rim	#14 core	#15	#16	#17	#18	#19 rim	#22
SiO_2	39.13	39.46	39.89	39.80	40.00	40.27	40.42	38.46	40.65	40.28	39.18	39.67	39.39	38.94	39.31	39.39	38.63	37.80	37.64	39.58
TiO_2	0.05	0.06	0.08	0.08	0.07	0.11	0.11	0.06	0.10	0.03	0.06	0.08	0.04	0.07	0.06	0.04	0.05	0.02	0.02	0.03
Al_2O_3	22.73	22.62	22.87	23.02	23.08	23.15	22.91	22.94	22.85	23.02	23.05	22.99	22.54	23.12	22.91	22.85	22.98	22.62	22.61	22.71
Cr_2O_3	0.00	0.09	0.08	0.07	0.10	0.11	0.00	0.08	0.06	0.09	0.05	0.00	0.07	0.15	0.09	0.07	0.06	0.08	0.05	0.08
Fe_2O_3	1.42	1.23	1.32	1.72	1.68	1.09	0.72	4.11	0.26	2.51	2.70	2.40	1.79	3.24	2.49	1.81	3.52	3.68	4.06	2.08
FeO	18.03	16.95	15.89	15.10	14.61	14.52	15.02	12.78	15.74	14.39	14.05	15.59	16.87	13.33	14.43	15.69	15.32	16.75	17.37	15.89
MnO	0.69	0.55	0.46	0.33	0.37	0.38	0.36	0.36	0.36	0.48	0.41	0.43	0.53	0.28	0.41	0.41	0.53	0.71	0.92	0.44
MgO	10.82	11.55	12.58	13.05	13.31	13.58	13.35	13.34	13.22	13.61	13.03	12.74	12.21	13.68	12.95	12.38	12.19	11.22	11.07	12.44
CaO	6.88	7.14	7.02	7.00	7.16	7.13	7.22	7.12	7.05	7.06	7.19	6.85	6.21	6.74	7.13	6.99	6.76	6.06	5.46	6.91
Σ	99.77	99.65	100.20	100.18	100.38	100.36	100.11	99.25	100.27	101.50	99.71	100.75	99.65	99.54	99.76	99.63	100.04	98.94	99.21	100.15
Si	2.95	2.96	2.96	2.94	2.95	2.96	2.98	2.87	2.99	2.94	2.91	2.93	2.95	2.89	2.92	2.94	2.89	2.88	2.87	2.94
Al^{IV}	0.05	0.04	0.04	0.06	0.06	0.04	0.02	0.13	0.01	0.06	0.09	0.07	0.05	0.11	0.08	0.06	0.12	0.12	0.13	0.06
Al^{VI}	1.97	1.96	1.96	1.95	1.95	1.96	1.97	1.89	1.98	1.92	1.93	1.93	1.94	1.91	1.93	1.95	1.91	1.91	1.90	1.93
Cr	0.00	0.01	0.01	0.00	0.01	0.01	0.00	0.01	0.00	0.01	0.00	0.00	0.00	0.01	0.01	0.00	0.00	0.01	0.00	0.01
Fe^{3+}	0.08	0.07	0.07	0.10	0.09	0.06	0.04	0.23	0.01	0.14	0.15	0.13	0.10	0.18	0.14	0.10	0.20	0.21	0.23	0.12
Ti	0.00	0.00	0.01	0.00	0.00	0.01	0.01	0.00	0.01	0.00	0.00	0.00	0.00	0.00	0.00	0.00	0.00	0.00	0.00	0.00
Fe^{2+}	1.14	1.06	0.99	0.93	0.90	0.89	0.93	0.80	0.97	0.88	0.87	0.96	1.06	0.83	0.90	0.98	0.96	1.07	1.11	0.99
Mg	1.22	1.29	1.39	1.44	1.46	1.49	1.47	1.48	1.45	1.48	1.44	1.40	1.36	1.51	1.44	1.38	1.36	1.27	1.26	1.38
Mn^{2+}	0.04	0.04	0.03	0.02	0.02	0.02	0.02	0.02	0.02	0.03	0.03	0.03	0.03	0.02	0.03	0.03	0.03	0.05	0.06	0.03
Ca	0.56	0.57	0.56	0.56	0.57	0.56	0.57	0.57	0.56	0.55	0.57	0.54	0.50	0.54	0.57	0.56	0.54	0.49	0.45	0.55

0708-3: metagabbro Bolschoi Khed

wt.-%	#37 rim	#38	#39	#40	#41 core	#42	#43	#44 rim	#63 rim	#64	#65	#66	#67 core	#68	#69 rim	#97	#1	#2	#3
SiO_2	39.14	39.37	39.61	40.16	39.81	40.48	39.80	40.28	39.32	40.17	40.21	40.28	40.03	40.19	39.62	38.25	38.94	39.74	39.79
TiO_2	0.05	0.09	0.09	0.05	0.10	0.10	0.07	0.11	0.09	0.09	0.12	0.12	0.09	0.17	0.07	0.10	0.00	0.07	0.03
Al_2O_3	22.19	22.53	22.82	22.65	22.82	23.10	22.69	22.71	22.67	22.96	22.81	22.97	22.81	22.76	22.39	22.23	22.70	22.21	22.77
Cr_2O_3	0.05	0.11	0.02	0.09	0.07	0.08	0.09	0.07	0.00	0.00	0.08	0.06	0.19	0.19	0.12	0.02	0.10	0.06	0.08
Fe_2O_3	0.83	1.09	2.07	1.30	2.79	1.11	1.36	1.07	0.51	0.00	1.00	0.18	0.39	0.69	0.00	2.39	2.59	1.12	1.26
FeO	20.43	18.36	16.86	15.11	13.55	15.32	17.80	15.94	20.40	18.31	16.37	16.09	15.50	16.10	19.69	20.73	20.38	20.19	19.31
MnO	0.93	0.55	0.44	0.45	0.37	0.34	0.56	0.43	0.96	0.54	0.43	0.38	0.28	0.34	0.89	1.08	1.01	0.89	0.69
MgO	10.10	11.02	11.96	13.36	13.91	13.50	11.96	13.00	9.96	11.38	12.50	12.89	12.87	12.74	10.47	8.59	9.75	10.05	10.74
CaO	5.83	6.72	6.89	6.78	7.01	6.85	6.22	6.81	6.23	6.80	7.11	6.88	7.19	7.07	6.29	6.78	6.08	6.69	6.60
Σ	99.56	99.83	100.75	99.94	100.42	100.87	100.56	100.40	100.12	100.25	100.64	99.85	99.36	100.25	99.54	100.17	101.55	101.04	101.27
Si	2.98	2.96	2.94	2.97	2.93	2.97	2.96	2.97	2.97	2.99	2.97	2.98	2.98	2.97	3.00	2.92	2.92	2.98	2.96
Al^{IV}	0.02	0.04	0.06	0.03	0.07	0.04	0.04	0.03	0.03	0.01	0.03	0.02	0.02	0.03	0.00	0.08	0.08	0.02	0.04
Al^{VI}	1.97	1.96	1.93	1.95	1.90	1.96	1.95	1.95	1.99	2.01	1.96	1.99	1.98	1.96	1.99	1.93	1.93	1.94	1.96
Cr	0.00	0.01	0.00	0.01	0.00	0.01	0.01	0.00	0.00	0.00	0.01	0.00	0.01	0.01	0.01	0.00	0.01	0.00	0.00
Fe^{3+}	0.05	0.06	0.12	0.07	0.15	0.06	0.08	0.06	0.03	0.00	0.06	0.01	0.02	0.04	0.00	0.14	0.15	0.06	0.07
Ti	0.00	0.01	0.01	0.00	0.01	0.01	0.00	0.01	0.01	0.01	0.01	0.01	0.01	0.01	0.00	0.01	0.00	0.00	0.00
Fe^{2+}	1.30	1.16	1.05	0.94	0.83	0.94	1.11	0.99	1.29	1.14	1.01	1.00	0.97	1.00	1.25	1.33	1.28	1.27	1.20
Mg	1.15	1.24	1.32	1.47	1.52	1.47	1.33	1.43	1.12	1.26	1.38	1.42	1.43	1.41	1.18	0.98	1.09	1.12	1.19
Mn^{2+}	0.06	0.04	0.03	0.03	0.02	0.02	0.04	0.03	0.06	0.03	0.03	0.02	0.02	0.02	0.06	0.07	0.06	0.06	0.04
Ca	0.48	0.54	0.55	0.54	0.55	0.54	0.50	0.54	0.50	0.54	0.56	0.55	0.57	0.56	0.51	0.56	0.49	0.54	0.53

	0708-3: metagabbro Bolschoi Khed											1008-B3: metagabbro Kataransky Cape							
wt.-%	#5	#8	#9	#10	#11 core	#12	#17	#24	#26	#27	#28 rim	#1 rim	#2	#3	#4	#5	#6	#7 core	#8
SiO_2	40.24	39.86	39.69	39.50	39.74	39.70	39.57	39.05	39.16	38.72	39.13	39.08	39.49	39.18	39.69	39.77	39.92	39.45	39.42
TiO_2	0.08	0.05	0.07	0.06	0.13	0.09	0.07	0.05	0.07	0.02	0.09	0.05	0.06	0.02	0.08	0.07	0.05	0.08	0.04
Al_2O_3	22.83	22.96	23.25	23.26	22.96	23.14	22.82	22.35	22.21	22.31	22.36	22.18	22.32	22.48	22.53	22.60	22.55	22.46	22.50
Cr_2O_3	0.04	0.06	0.01	0.03	0.13	0.04	0.03	0.08	0.04	0.04	0.06	0.00	0.00	0.00	0.00	0.00	0.00	0.02	0.00
Fe_2O_3	1.94	2.78	3.81	4.06	3.00	4.06	3.46	1.60	1.12	2.69	1.42	1.10	1.15	2.12	1.19	1.42	1.27	1.84	1.80
FeO	16.89	14.27	12.96	12.45	12.73	12.41	14.97	19.65	18.39	18.51	19.71	23.96	21.98	20.58	20.32	19.64	19.79	19.19	19.29
MnO	0.52	0.33	0.35	0.36	0.37	0.36	0.47	0.96	0.67	0.74	0.91	0.69	0.67	0.56	0.50	0.47	0.45	0.43	0.50
MgO	12.33	13.40	13.90	14.03	14.19	14.40	12.83	10.13	10.99	10.65	10.25	8.11	9.33	10.04	10.24	10.71	10.78	10.93	10.86
CaO	6.86	7.20	7.36	7.39	7.22	7.12	7.08	6.28	6.43	6.30	6.23	5.98	6.24	6.11	6.59	6.58	6.49	6.34	6.27
Σ	101.73	100.90	101.41	101.14	100.46	101.31	101.31	100.15	99.08	99.98	100.15	101.15	101.24	101.09	101.14	101.26	101.31	100.73	100.69
Si	2.95	2.93	2.89	2.88	2.91	2.89	2.91	2.95	2.97	2.93	2.96	2.97	2.97	2.94	2.97	2.96	2.97	2.95	2.95
Al^{IV}	0.05	0.07	0.11	0.12	0.09	0.11	0.09	0.05	0.03	0.07	0.04	0.03	0.03	0.06	0.03	0.04	0.03	0.05	0.05
Al^{VI}	1.93	1.91	1.89	1.89	1.90	1.88	1.89	1.95	1.96	1.92	1.95	1.96	1.95	1.93	1.96	1.95	1.95	1.93	1.94
Cr	0.00	0.00	0.00	0.00	0.01	0.00	0.00	0.01	0.00	0.00	0.00	0.00	0.00	0.00	0.00	0.00	0.00	0.00	0.00
Fe^{3+}	0.11	0.15	0.21	0.22	0.17	0.22	0.19	0.09	0.06	0.15	0.08	0.06	0.07	0.12	0.07	0.08	0.07	0.10	0.10
Ti	0.00	0.00	0.00	0.00	0.01	0.01	0.00	0.00	0.00	0.00	0.01	0.00	0.00	0.00	0.00	0.00	0.00	0.00	0.00
Fe^{2+}	1.04	0.88	0.79	0.76	0.78	0.76	0.92	1.24	1.17	1.17	1.25	1.52	1.38	1.29	1.27	1.22	1.23	1.20	1.21
Mg	1.35	1.47	1.51	1.53	1.55	1.56	1.41	1.14	1.24	1.20	1.15	0.92	1.05	1.12	1.14	1.19	1.20	1.22	1.21
Mn^{2+}	0.03	0.02	0.02	0.02	0.02	0.02	0.03	0.06	0.04	0.05	0.06	0.05	0.04	0.04	0.03	0.03	0.03	0.03	0.03
Ca	0.54	0.57	0.58	0.58	0.57	0.56	0.56	0.51	0.52	0.51	0.50	0.49	0.50	0.49	0.53	0.53	0.52	0.51	0.50

1008-B3: metagabbro Kataransky Cape

wt.-%	#9	#10	#11	#12	#13 rim	#29 coe	#30	#31	#33	#32 rim	#44 core	#45 rim	#18 core	#19	#20	#21	#22 rim	#27 core
SiO_2	39.65	39.32	39.63	39.13	39.50	39.45	39.11	38.94	39.03	38.75	39.18	39.45	39.88	39.96	39.92	39.65	39.38	39.65
TiO_2	0.05	0.04	0.05	0.02	0.03	0.07	0.05	0.05	0.07	0.07	0.04	0.03	0.01	0.07	0.07	0.08	0.04	0.03
Al_2O_3	22.52	22.46	22.51	22.18	22.27	22.40	22.17	22.27	22.23	22.11	22.17	22.26	21.66	22.18	21.56	21.93	21.75	21.65
Cr_2O_3	0.01	0.00	0.00	0.00	0.01	0.04	0.00	0.00	0.00	0.00	0.00	0.06	0.04	0.00	0.01	0.00	0.04	0.03
Fe_2O_3	1.94	1.74	1.32	2.19	0.31	1.06	1.18	2.07	1.75	1.77	1.66	0.94	0.32	0.42	0.00	0.13	0.20	0.21
FeO	19.46	19.62	20.61	20.63	23.34	21.47	21.03	20.90	21.14	22.38	21.98	23.01	20.02	18.75	18.81	19.66	23.18	21.48
MnO	0.54	0.56	0.55	0.64	0.74	0.53	0.54	0.56	0.58	0.70	0.68	0.70	0.53	0.46	0.45	0.50	0.71	0.57
MgO	10.84	10.66	10.28	9.98	8.54	9.21	9.00	9.10	8.65	8.03	9.17	8.74	9.54	9.43	9.10	8.50	8.54	9.63
CaO	6.35	6.14	6.20	6.05	6.20	6.88	7.17	6.96	7.49	7.03	6.16	6.16	7.92	9.23	9.41	9.49	6.25	6.42
Σ	101.37	100.56	101.15	100.82	100.94	101.11	100.25	100.86	100.93	100.83	101.03	101.37	99.92	100.50	99.33	99.95	100.09	99.65
Si	2.95	2.95	2.97	2.95	2.99	2.97	2.97	2.95	2.96	2.95	2.96	2.98	3.02	3.00	3.04	3.01	3.01	3.02
Al^{IV}	0.05	0.05	0.03	0.05	0.01	0.03	0.03	0.05	0.05	0.05	0.04	0.02	0.00	0.00	0.00	0.00	0.00	0.00
Al^{VI}	1.93	1.94	1.95	1.92	1.98	1.96	1.96	1.93	1.94	1.94	1.94	1.96	1.94	1.96	1.93	1.96	1.96	1.94
Cr	0.00	0.00	0.00	0.00	0.00	0.00	0.00	0.00	0.00	0.00	0.00	0.00	0.00	0.00	0.00	0.00	0.00	0.00
Fe^{3+}	0.11	0.10	0.07	0.12	0.02	0.06	0.07	0.12	0.10	0.10	0.10	0.05	0.02	0.02	0.00	0.01	0.01	0.01
Ti	0.00	0.00	0.00	0.00	0.00	0.00	0.00	0.00	0.00	0.00	0.00	0.00	0.00	0.00	0.00	0.01	0.00	0.00
Fe^{2+}	1.21	1.23	1.29	1.30	1.48	1.35	1.34	1.32	1.34	1.43	1.39	1.45	1.27	1.18	1.20	1.25	1.48	1.37
Mg	1.20	1.19	1.15	1.12	0.97	1.03	1.02	1.03	0.98	0.91	1.03	0.98	1.08	1.06	1.03	0.96	0.97	1.09
Mn^{2+}	0.03	0.04	0.04	0.04	0.05	0.03	0.04	0.04	0.04	0.05	0.04	0.05	0.03	0.03	0.03	0.03	0.05	0.04
Ca	0.51	0.50	0.50	0.49	0.50	0.56	0.58	0.56	0.61	0.57	0.50	0.50	0.64	0.74	0.77	0.77	0.51	0.52

	1008-B3	**0808-5: metadiorite**				**0308-K1: mafic dyke Nikolkina Island**												
wt.-%	#28 rim	#12	#15	#22	#23	#8	#9	#10	#11	#12	#13	#21 core	#22	#23 rim	#48	#49 rim	#51	#52
SiO_2	39.19	36.47	37.82	37.61	37.59	38.04	38.45	38.58	38.72	38.53	38.62	38.51	38.96	38.42	38.11	38.59	38.05	37.94
TiO_2	0.02	0.05	0.04	0.05	0.06	0.06	0.04	0.06	0.03	0.04	0.03	0.06	0.08	0.08	0.08	0.01	0.06	0.13
Al_2O_3	21.37	21.16	21.28	21.58	21.37	21.74	22.02	21.78	22.08	21.78	21.94	21.73	21.88	21.72	20.67	20.94	21.18	21.18
Cr_2O_3	0.03	0.00	0.02	0.03	0.00	0.04	0.03	0.00	0.05	0.00	0.03	0.06	0.00	0.00	0.00	0.04	0.07	0.02
Fe_2O_3	0.22	3.35	1.20	0.81	0.86	1.35	2.45	1.66	1.00	1.62	1.53	1.87	1.06	1.91	2.44	0.48	2.88	2.18
FeO	23.08	23.08	24.88	25.24	24.34	27.23	25.96	25.95	25.08	26.49	26.48	20.29	20.94	23.31	21.26	24.58	21.03	21.48
MnO	0.72	3.96	4.12	3.75	4.59	0.55	0.42	0.42	0.40	0.42	0.51	0.83	0.70	0.69	0.62	0.49	0.53	0.55
MgO	8.34	2.38	2.27	2.46	2.11	5.62	6.50	6.06	5.86	6.07	6.17	4.29	4.42	4.57	5.20	5.23	6.03	6.05
CaO	6.41	9.62	9.49	9.05	9.57	6.04	6.28	7.04	8.11	6.53	6.41	13.52	13.37	10.81	11.31	9.18	10.34	9.88
Σ	99.37	100.08	101.12	100.57	100.49	100.66	102.15	101.54	101.34	101.48	101.73	101.16	101.41	101.53	99.69	99.55	100.15	99.42
Si	3.02	2.90	2.98	2.97	2.98	2.96	2.94	2.96	2.97	2.96	2.96	2.96	2.98	2.96	2.97	3.02	2.95	2.96
Al^{IV}	0.00	0.10	0.03	0.03	0.03	0.04	0.06	0.04	0.03	0.04	0.04	0.04	0.02	0.05	0.03	0.00	0.06	0.04
Al^{VI}	1.94	1.89	1.95	1.98	1.97	1.95	1.92	1.93	1.97	1.94	1.94	1.92	1.95	1.92	1.87	1.93	1.88	1.90
Cr	0.00	0.00	0.00	0.00	0.00	0.00	0.00	0.00	0.00	0.00	0.00	0.00	0.00	0.00	0.00	0.00	0.00	0.00
Fe^{3+}	0.01	0.20	0.07	0.05	0.05	0.08	0.14	0.10	0.06	0.09	0.09	0.11	0.06	0.11	0.14	0.03	0.17	0.13
Ti	0.00	0.00	0.00	0.00	0.00	0.00	0.00	0.00	0.00	0.00	0.00	0.00	0.01	0.01	0.01	0.00	0.00	0.01
Fe^{2+}	1.49	1.54	1.64	1.67	1.61	1.77	1.66	1.67	1.61	1.70	1.70	1.30	1.34	1.50	1.39	1.61	1.36	1.40
Mg	0.96	0.28	0.27	0.29	0.25	0.65	0.74	0.69	0.67	0.70	0.71	0.49	0.50	0.52	0.60	0.61	0.70	0.70
Mn^{2+}	0.05	0.27	0.28	0.25	0.31	0.04	0.03	0.03	0.03	0.03	0.03	0.05	0.05	0.05	0.04	0.03	0.04	0.04
Ca	0.53	0.82	0.80	0.77	0.81	0.50	0.51	0.58	0.67	0.54	0.53	1.11	1.10	0.89	0.95	0.77	0.86	0.83

0308-K1: mafic dyke Nikolkina Island

wt.-%	#53	#54 core	#55	#56 rim	#78 core	#79 rim	#84	#85 core	#86 rim	#94	#126	#127	#5 cor.	#6 cor.	#7 cor.	#15 cor.	#16 cor.	#19
SiO_2	37.81	37.94	37.39	37.77	38.17	38.09	38.22	37.73	38.08	37.87	37.84	38.20	38.81	37.67	37.06	38.23	38.35	38.25
TiO_2	0.02	0.04	0.06	0.09	0.05	0.04	0.06	0.06	0.06	0.14	0.01	0.02	0.05	0.06	0.06	0.09	0.14	0.05
Al_2O_3	21.03	20.92	20.62	20.87	21.51	21.57	21.77	21.93	21.52	20.87	21.53	21.54	21.69	21.56	21.57	21.40	21.25	21.29
Cr_2O_3	0.00	0.00	0.00	0.00	0.01	0.00	0.03	0.04	0.00	0.16	0.04	0.00	0.02	0.01	0.02	0.05	0.01	0.00
Fe_2O_3	2.15	1.65	2.64	2.04	1.12	1.65	1.32	2.41	0.95	2.11	2.43	1.50	1.10	1.46	2.48	1.87	1.55	1.11
FeO	24.02	24.55	24.67	24.41	25.75	25.82	25.66	23.62	25.83	26.67	25.81	27.43	26.00	27.27	25.34	26.96	25.19	27.07
MnO	0.55	0.76	0.69	0.61	0.59	0.52	0.49	0.52	0.52	0.66	0.49	0.51	0.54	0.70	0.67	0.62	0.57	0.66
MgO	5.52	5.31	5.00	5.31	5.85	5.63	5.86	5.67	5.55	4.04	5.73	5.35	5.24	4.33	4.96	4.34	4.99	4.53
CaO	8.44	8.29	8.19	8.39	6.96	7.18	7.15	8.52	7.29	8.49	6.82	6.42	8.25	7.33	7.43	8.19	8.84	7.77
Σ	99.55	99.47	99.24	99.49	100.01	100.51	100.56	100.49	99.79	101.01	100.70	100.96	101.71	100.39	99.58	101.74	100.87	100.74
Si	2.96	2.98	2.96	2.97	2.98	2.96	2.96	2.92	2.98	2.96	2.94	2.97	2.98	2.96	2.92	2.96	2.98	2.99
Al^{IV}	0.04	0.02	0.04	0.03	0.02	0.04	0.04	0.08	0.02	0.04	0.06	0.03	0.02	0.04	0.08	0.04	0.03	0.02
Al^{VI}	1.91	1.92	1.88	1.90	1.95	1.94	1.95	1.93	1.96	1.89	1.91	1.94	1.95	1.95	1.92	1.92	1.92	1.94
Cr	0.00	0.00	0.00	0.00	0.00	0.00	0.00	0.00	0.00	0.01	0.00	0.00	0.00	0.00	0.00	0.00	0.00	0.00
Fe^{3+}	0.13	0.10	0.16	0.12	0.07	0.10	0.08	0.14	0.06	0.12	0.14	0.09	0.06	0.09	0.15	0.11	0.09	0.07
Ti	0.00	0.00	0.00	0.01	0.00	0.00	0.00	0.00	0.00	0.01	0.00	0.00	0.00	0.00	0.00	0.01	0.01	0.00
Fe^{2+}	1.58	1.61	1.63	1.60	1.68	1.68	1.66	1.53	1.69	1.74	1.68	1.78	1.67	1.79	1.67	1.75	1.63	1.77
Mg	0.64	0.62	0.59	0.62	0.68	0.65	0.68	0.65	0.65	0.47	0.66	0.62	0.60	0.51	0.58	0.50	0.58	0.53
Mn^{2+}	0.04	0.05	0.05	0.04	0.04	0.03	0.03	0.03	0.04	0.04	0.03	0.03	0.04	0.05	0.05	0.04	0.04	0.04
Ca	0.71	0.70	0.69	0.71	0.58	0.60	0.59	0.71	0.61	0.71	0.57	0.54	0.68	0.62	0.63	0.68	0.74	0.65

	0308-K1: mafic dyke Nikolkina Island										0308-K2: hydrated dyke Nikolkina Island								
wt.-%	#20	#23 cor	#24 cor	#28 core	#29	#30	#31	#32	#33	#34	#20 rim	#21	#22	#23 core	#1 core	#2	#3	#4	#5
SiO_2	38.23	37.38	36.92	37.68	38.53	37.91	37.54	37.64	37.70	36.83	37.70	37.75	38.00	37.62	37.61	38.13	38.01	38.21	38.08
TiO_2	0.07	0.05	0.03	0.07	0.06	0.06	0.03	0.04	0.06	0.04	0.15	0.24	0.27	0.35	0.35	0.33	0.32	0.10	0.11
Al_2O_3	21.52	21.74	21.82	22.12	21.82	21.87	22.02	22.13	21.95	21.90	21.12	21.16	21.21	20.81	20.28	20.98	21.05	21.42	21.28
Cr_2O_3	0.05	0.00	0.07	0.02	0.00	0.01	0.00	0.00	0.00	0.02	0.03	0.00	0.00	0.04	0.02	0.00	0.01	0.00	0.00
Fe_2O_3	0.89	2.20	3.12	2.21	0.00	1.65	1.87	2.34	2.26	2.86	1.65	1.86	1.91	2.10	1.28	1.03	0.85	1.28	1.46
FeO	25.64	23.72	24.10	22.82	23.93	23.43	24.25	24.26	24.34	23.68	23.82	23.88	24.26	23.78	23.84	24.20	24.42	24.60	24.46
MnO	0.53	0.59	0.61	0.52	0.46	0.44	0.48	0.43	0.53	0.56	0.62	0.71	0.74	0.78	0.83	0.83	0.85	0.82	0.87
MgO	4.66	4.72	5.18	5.77	5.70	5.69	6.19	6.21	6.14	6.08	3.60	3.29	3.25	3.09	2.89	2.99	3.08	3.20	3.42
CaO	8.82	9.38	7.98	8.96	8.99	8.87	7.15	7.24	7.27	7.02	11.20	11.63	11.62	11.89	12.05	12.11	11.68	11.43	11.08
Σ	100.41	99.79	99.82	100.17	99.48	99.93	99.53	100.29	100.24	98.99	99.87	100.51	101.25	100.46	99.16	100.60	100.29	101.06	100.76
Si	2.98	2.93	2.90	2.92	3.00	2.95	2.93	2.92	2.93	2.90	2.96	2.96	2.96	2.95	2.99	2.98	2.98	2.97	2.97
Al^{IV}	0.02	0.07	0.10	0.08	0.00	0.05	0.07	0.08	0.07	0.10	0.04	0.05	0.04	0.05	0.01	0.02	0.02	0.03	0.03
Al^{VI}	1.96	1.94	1.91	1.94	2.00	1.95	1.96	1.94	1.94	1.93	1.92	1.91	1.90	1.88	1.89	1.92	1.93	1.94	1.93
Cr	0.00	0.00	0.00	0.00	0.00	0.00	0.00	0.00	0.00	0.00	0.00	0.00	0.00	0.00	0.00	0.00	0.00	0.00	0.00
Fe^{3+}	0.05	0.13	0.18	0.13	0.00	0.10	0.11	0.14	0.13	0.17	0.10	0.11	0.11	0.12	0.08	0.06	0.05	0.08	0.09
Ti	0.00	0.00	0.00	0.00	0.00	0.00	0.00	0.00	0.00	0.00	0.01	0.01	0.02	0.02	0.02	0.02	0.02	0.01	0.01
Fe^{2+}	1.67	1.55	1.58	1.48	1.56	1.52	1.58	1.57	1.58	1.56	1.57	1.56	1.58	1.56	1.59	1.58	1.60	1.60	1.60
Mg	0.54	0.55	0.61	0.67	0.66	0.66	0.72	0.72	0.71	0.71	0.42	0.38	0.38	0.36	0.34	0.35	0.36	0.37	0.40
Mn^{2+}	0.04	0.04	0.04	0.03	0.03	0.03	0.03	0.03	0.04	0.04	0.04	0.05	0.05	0.05	0.06	0.06	0.06	0.05	0.06
Ca	0.74	0.79	0.67	0.75	0.75	0.74	0.60	0.60	0.60	0.59	0.94	0.98	0.97	1.00	1.03	1.02	0.98	0.95	0.93

	0308-K2: hydrated dyke Nikolkina Island									0908-1: ophitic dyke Kataransky Cape								
wt.-%	#6	#7	#8	#9 rim	#19 rim	#32 core	#33 rim	#43 incl.	#44 incl.	#1	#4	#5	#11	#12	#13	#14	#33	#38
SiO_2	38.21	37.95	38.30	38.05	37.88	37.89	37.66	38.09	38.27	38.76	38.49	38.75	38.74	38.76	38.21	38.18	39.89	38.31
TiO_2	0.12	0.21	0.26	0.10	0.07	0.30	0.09	0.27	0.12	0.00	0.00	0.04	0.02	0.05	0.01	0.00	0.03	0.03
Al_2O_3	21.27	21.02	21.14	21.15	21.25	20.88	21.04	21.16	21.63	21.87	21.89	21.85	21.98	21.91	22.02	21.88	22.08	22.04
Cr_2O_3	0.00	0.00	0.00	0.00	0.01	0.00	0.00	0.01	0.00	0.02	0.00	0.00	0.00	0.00	0.01	0.00	0.00	0.01
Fe_2O_3	0.96	1.06	1.30	1.17	0.95	0.67	0.35	0.31	0.67	0.00	0.03	0.00	0.00	0.00	0.50	0.40	1.27	0.99
FeO	24.57	24.09	24.38	25.10	26.13	23.43	26.50	24.63	24.51	25.93	25.87	26.82	24.88	26.05	25.27	25.82	22.79	25.70
MnO	0.82	0.79	0.77	0.87	1.16	0.97	1.47	0.86	1.08	0.78	0.76	0.89	0.88	1.08	0.90	0.99	0.42	0.86
MgO	3.45	3.62	3.70	3.48	3.56	3.76	2.90	3.78	3.28	6.91	6.52	6.61	6.93	6.19	6.46	6.57	13.11	7.19
CaO	11.12	11.10	11.13	10.46	9.15	11.28	9.34	10.58	11.25	4.85	6.05	4.97	5.76	5.71	6.25	5.56	0.89	5.04
Σ	100.52	99.85	100.99	100.40	100.16	99.19	99.35	99.68	100.81	99.13	99.63	99.94	99.17	99.75	99.62	99.40	100.49	100.16
Si	2.99	2.98	2.98	2.98	2.98	2.99	3.00	3.00	2.98	3.02	3.00	3.01	3.01	3.01	2.97	2.98	2.99	2.96
Al^{IV}	0.02	0.02	0.02	0.02	0.02	0.01	0.00	0.01	0.02	0.00	0.01	0.00	0.00	0.00	0.03	0.02	0.01	0.04
Al^{VI}	1.94	1.93	1.92	1.94	1.95	1.93	1.97	1.96	1.97	2.01	2.00	2.00	2.01	2.01	1.99	2.00	1.94	1.97
Cr	0.00	0.00	0.00	0.00	0.00	0.00	0.00	0.00	0.00	0.00	0.00	0.00	0.00	0.00	0.00	0.00	0.00	0.00
Fe^{3+}	0.06	0.06	0.08	0.07	0.06	0.04	0.02	0.02	0.04	0.00	0.00	0.00	0.00	0.00	0.03	0.02	0.07	0.06
Ti	0.01	0.01	0.02	0.01	0.00	0.02	0.01	0.02	0.01	0.00	0.00	0.00	0.00	0.00	0.00	0.00	0.00	0.00
Fe^{2+}	1.61	1.58	1.59	1.65	1.72	1.55	1.76	1.62	1.60	1.69	1.68	1.74	1.62	1.69	1.65	1.69	1.43	1.66
Mg	0.40	0.42	0.43	0.41	0.42	0.44	0.34	0.44	0.38	0.80	0.76	0.77	0.80	0.72	0.75	0.76	1.46	0.83
Mn^{2+}	0.05	0.05	0.05	0.06	0.08	0.07	0.10	0.06	0.07	0.05	0.05	0.06	0.06	0.07	0.06	0.07	0.03	0.06
Ca	0.93	0.94	0.93	0.88	0.77	0.95	0.80	0.89	0.94	0.40	0.51	0.41	0.48	0.48	0.52	0.47	0.07	0.42

P-20: noritic dyke Water Sign

wt.-%	#22 cor.	#24 cor.	#25 cor.	#35 cor.	#36 cor.	#53 cor.	#54 cor.	#85 cor.	#86 cor.	#87 cor.	#88 cor.	#103 incl.	#104 incl.	#110 cor.	#130 cor.
SiO_2	39.30	39.27	39.51	38.90	38.77	38.92	38.57	39.10	39.60	39.10	39.21	38.50	38.33	39.50	38.40
TiO_2	0.02	0.03	0.01	0.02	0.01	0.03	0.02	0.03	0.00	0.03	0.03	0.03	0.03	0.05	0.02
Al_2O_3	21.53	22.48	22.45	22.51	22.15	21.54	21.93	22.09	22.40	22.30	22.49	21.95	21.78	22.16	22.16
Cr_2O_3	0.00	0.00	0.01	0.00	0.02	0.00	0.05	0.04	0.00	0.11	0.00	0.00	0.01	0.00	0.02
Fe_2O_3	2.19	2.67	2.37	2.72	3.47	2.03	1.98	2.28	2.48	2.22	1.78	2.26	1.78	1.87	2.65
FeO	22.03	19.85	20.41	21.11	19.73	23.85	23.62	20.75	20.22	19.86	19.76	22.86	22.73	20.99	22.67
MnO	0.66	0.58	0.59	0.69	0.65	1.05	0.80	0.65	0.55	0.45	0.58	0.84	0.78	0.53	0.95
MgO	9.40	10.82	10.60	9.54	10.07	7.67	7.91	9.93	10.74	10.60	10.64	8.05	7.92	9.21	7.76
CaO	5.91	5.66	5.74	6.02	6.27	6.22	5.93	5.98	5.81	5.90	5.94	6.25	6.42	7.28	6.62
Σ	101.04	101.38	101.70	101.53	101.13	101.33	100.82	100.85	101.80	100.57	100.43	100.74	99.78	101.59	101.23
Si	2.98	2.93	2.95	2.93	2.92	2.97	2.95	2.95	2.95	2.94	2.95	2.94	2.96	2.97	2.93
Al^{IV}	0.02	0.07	0.05	0.08	0.08	0.03	0.05	0.05	0.05	0.06	0.05	0.06	0.04	0.04	0.07
Al^{VI}	1.90	1.91	1.92	1.92	1.88	1.91	1.93	1.92	1.91	1.92	1.95	1.92	1.94	1.92	1.92
Cr	0.00	0.00	0.00	0.00	0.00	0.00	0.00	0.00	0.00	0.01	0.00	0.00	0.00	0.00	0.00
Fe^{3+}	0.13	0.15	0.13	0.15	0.20	0.12	0.11	0.13	0.14	0.13	0.10	0.13	0.10	0.11	0.15
Ti	0.00	0.00	0.00	0.00	0.00	0.00	0.00	0.00	0.00	0.00	0.00	0.00	0.00	0.00	0.00
Fe^{2+}	1.40	1.24	1.27	1.33	1.24	1.52	1.51	1.31	1.26	1.25	1.24	1.46	1.47	1.32	1.45
Mg	1.06	1.21	1.18	1.07	1.13	0.87	0.90	1.12	1.19	1.19	1.19	0.92	0.91	1.03	0.88
Mn^{2+}	0.04	0.04	0.04	0.04	0.04	0.07	0.05	0.04	0.04	0.03	0.04	0.05	0.05	0.03	0.06
Ca	0.48	0.45	0.46	0.49	0.51	0.51	0.49	0.48	0.46	0.48	0.48	0.51	0.53	0.59	0.54

35-5: meta-anorthosite Beloozerskaya Guba

wt.-%	#3	#6	#8	#9	#10	#16	#22	#31	#83	#93	#100	#105	#106	#107
SiO_2	40.41	40.52	41.21	40.89	40.37	39.33	39.66	41.10	40.14	40.07	40.89	40.76	39.58	39.79
TiO_2	0.05	0.04	0.06	0.11	0.08	0.09	0.13	0.06	0.09	0.05	0.09	0.08	0.11	0.09
Al_2O_3	23.26	23.24	23.37	22.98	22.78	22.41	22.67	23.15	22.66	23.26	23.35	23.57	22.97	22.83
Cr_2O_3	0.09	0.04	0.00	0.02	0.04	0.00	0.01	0.01	0.02	0.08	0.00	0.00	0.03	0.00
Fe_2O_3	3.28	2.99	1.44	2.02	2.51	2.62	2.03	1.54	0.95	2.89	1.90	2.85	2.46	2.11
FeO	12.57	12.18	13.19	13.15	13.21	17.00	17.34	13.54	17.56	12.70	11.19	10.76	17.02	16.67
MnO	0.26	0.31	0.21	0.33	0.28	0.63	0.81	0.27	0.44	0.41	0.17	0.31	0.47	0.50
MgO	15.65	15.86	15.87	15.60	15.39	12.28	12.23	15.62	11.72	15.06	14.24	16.14	11.69	11.92
CaO	5.97	6.03	5.97	6.01	5.80	5.92	5.92	5.89	7.18	6.25	9.55	7.01	7.09	7.20
Σ	101.52	101.21	101.31	101.10	100.46	100.28	100.80	101.18	100.76	100.76	101.39	101.49	101.43	101.10
Si	2.92	2.93	2.97	2.96	2.95	2.94	2.94	2.97	2.98	2.92	2.95	2.92	2.93	2.94
Al^{IV}	0.08	0.07	0.03	0.04	0.05	0.06	0.06	0.03	0.02	0.08	0.05	0.08	0.08	0.06
Al^{VI}	1.90	1.90	1.95	1.92	1.91	1.91	1.93	1.94	1.96	1.91	1.94	1.91	1.92	1.93
Cr	0.01	0.00	0.00	0.00	0.00	0.00	0.00	0.00	0.00	0.00	0.00	0.00	0.00	0.00
Fe^{3+}	0.18	0.16	0.08	0.11	0.14	0.15	0.11	0.08	0.05	0.16	0.10	0.15	0.14	0.12
Ti	0.00	0.00	0.00	0.01	0.01	0.01	0.01	0.00	0.01	0.00	0.01	0.01	0.01	0.01
Fe^{2+}	0.76	0.74	0.79	0.80	0.81	1.06	1.08	0.82	1.09	0.77	0.68	0.65	1.05	1.03
Mg	1.68	1.71	1.70	1.68	1.67	1.37	1.35	1.68	1.30	1.63	1.53	1.72	1.29	1.31
Mn^{2+}	0.02	0.02	0.01	0.02	0.02	0.04	0.05	0.02	0.03	0.03	0.01	0.02	0.03	0.03
Ca	0.46	0.47	0.46	0.47	0.45	0.47	0.47	0.46	0.57	0.49	0.74	0.54	0.56	0.57

EMP analyses of orthopyroxene cores, rims, symplectites and coronas from different rock types. Analyses were recalculated on the basis of 6 oxygens.

	0708-3: metagabbro Bolschoi Khed											
wt.-%	#25 sympl.	#26 sympl.	#27 sympl.	#28 sympl.	#29 sympl.	#31 sympl.	#45 sympl.	#46 sympl.	#47 sympl.	#54 sympl.	#93 core	#94 core
SiO_2	52.27	52.64	53.49	53.29	53.54	53.30	53.86	53.60	52.88	52.49	52.40	52.05
TiO_2	0.01	0.05	0.02	0.05	0.10	0.07	0.06	0.07	0.07	0.05	0.05	0.11
Al_2O_3	3.33	2.88	2.69	2.36	2.00	2.31	1.63	1.59	2.58	3.72	2.27	2.57
Fe_2O_3	1.56	2.45	0.03	0.69	0.46	1.29	1.50	1.66	1.16	1.25	1.85	3.04
Cr_2O_3	0.25	0.26	0.25	0.09	0.03	0.11	0.05	0.06	0.30	0.28	0.09	0.08
FeO	14.95	14.19	16.74	15.45	16.49	15.77	14.94	15.43	14.42	13.86	17.08	16.21
MnO	0.20	0.21	0.25	0.16	0.19	0.23	0.24	0.30	0.11	0.18	0.31	0.31
MgO	26.27	26.94	26.15	26.74	26.34	26.66	27.28	26.82	27.14	27.12	25.11	25.34
CaO	0.32	0.32	0.26	0.36	0.33	0.19	0.35	0.35	0.25	0.27	0.35	0.41
Na_2O	0.02	0.02	0.01	0.00	0.01	0.00	0.02	0.02	0.00	0.01	0.01	0.01
K_2O	0.01	0.02	0.00	0.00	0.00	0.01	0.03	0.02	0.02	0.01	0.01	0.02
Σ	99.19	99.98	99.89	99.20	99.50	99.95	99.95	99.94	98.94	99.25	99.54	100.15
Si	1.90	1.90	1.94	1.94	1.95	1.93	1.94	1.94	1.92	1.90	1.92	1.90
Al^{IV}	0.10	0.10	0.06	0.06	0.05	0.07	0.06	0.06	0.08	0.10	0.08	0.10
Al^{VI}	0.05	0.02	0.05	0.04	0.03	0.03	0.01	0.01	0.03	0.06	0.02	0.01
Ti	0.00	0.00	0.00	0.00	0.00	0.00	0.00	0.00	0.00	0.00	0.00	0.00
Fe^{3+}	0.04	0.07	0.00	0.02	0.01	0.04	0.04	0.05	0.03	0.03	0.05	0.08
Cr	0.01	0.01	0.01	0.00	0.00	0.00	0.00	0.00	0.01	0.01	0.00	0.00
Mg	1.43	1.45	1.41	1.45	1.43	1.44	1.47	1.45	1.47	1.46	1.37	1.38
Fe^{2+}	0.46	0.43	0.51	0.47	0.50	0.48	0.45	0.47	0.44	0.42	0.52	0.50
Mn^{2+}	0.01	0.01	0.01	0.01	0.01	0.01	0.01	0.01	0.00	0.01	0.01	0.01
Ca	0.01	0.01	0.01	0.01	0.01	0.01	0.01	0.01	0.01	0.01	0.01	0.02
Na	0.00	0.00	0.00	0.00	0.00	0.00	0.00	0.00	0.00	0.00	0.00	0.00
K	0.00	0.00	0.00	0.00	0.00	0.00	0.00	0.00	0.00	0.00	0.00	0.00
Wo	0.65	0.66	0.53	0.74	0.67	0.39	0.70	0.70	0.52	0.55	0.72	0.84
En	75.31	76.68	73.18	74.97	73.51	74.79	75.97	75.07	76.63	77.30	71.86	72.97
Fs	24.04	22.66	26.29	24.30	25.83	24.82	23.34	24.22	22.85	22.15	27.42	26.19
XMg	0.76	0.77	0.74	0.76	0.74	0.75	0.77	0.76	0.77	0.78	0.72	0.74

0708-3: metagabbro Bolschoi Khed

wt.-%	#98 sympl.	#101 core	#102	#103	#104 rim	#70 core	#71	#73	#72 rim	#37 core	#38 core	#39 core	#40 core	#41 core	#42 rim	#43 rim
SiO_2	53.10	52.23	52.71	53.45	52.71	51.98	52.45	50.47	52.50	50.32	50.32	51.32	50.93	50.28	53.61	53.62
TiO_2	0.02	0.11	0.12	0.10	0.11	0.23	0.09	0.69	0.08	0.12	0.41	0.14	0.13	0.15	0.04	0.08
Al_2O_3	4.93	5.86	4.62	3.54	4.03	5.59	5.45	6.70	2.93	7.49	8.38	6.79	6.72	6.94	2.34	2.50
Fe_2O_3	0.00	1.54	1.60	1.51	1.22	3.76	1.61	2.44	1.68	1.57	2.23	1.27	1.69	2.30	1.00	0.86
Cr_2O_3	0.02	0.04	0.00	0.01	0.15	0.09	0.08	0.10	0.08	0.10	0.12	0.08	0.12	0.16	0.09	0.07
FeO	16.59	11.64	11.29	12.34	13.15	8.97	11.44	8.43	14.14	15.93	13.93	15.55	16.39	15.39	17.07	17.53
MnO	0.28	0.08	0.07	0.13	0.17	0.15	0.10	0.05	0.19	0.30	0.21	0.31	0.25	0.25	0.38	0.35
MgO	22.85	28.31	28.13	28.72	27.78	27.42	28.52	23.66	27.04	24.50	23.39	24.78	24.61	24.59	26.02	25.67
CaO	1.24	0.25	1.21	0.25	0.19	3.21	0.29	6.83	0.23	0.25	2.48	0.92	0.33	0.47	0.21	0.39
Na_2O	0.33	0.01	0.01	0.00	0.00	0.05	0.01	0.34	0.00	0.01	0.31	0.06	0.02	0.03	0.00	0.00
K_2O	0.01	0.01	0.01	0.00	0.01	0.00	0.00	0.00	0.01	0.01	0.03	0.01	0.00	0.01	0.01	0.01
Σ	99.34	100.08	99.77	100.06	99.54	101.45	100.04	99.71	98.88	100.60	101.81	101.23	101.18	100.57	100.77	101.09
Si	1.93	1.85	1.88	1.90	1.89	1.83	1.86	1.82	1.91	1.82	1.79	1.84	1.83	1.82	1.94	1.93
Al^{IV}	0.07	0.15	0.12	0.10	0.11	0.17	0.14	0.18	0.09	0.19	0.21	0.16	0.17	0.18	0.07	0.07
Al^{VI}	0.15	0.10	0.07	0.05	0.06	0.06	0.09	0.10	0.04	0.13	0.15	0.12	0.12	0.11	0.03	0.04
Ti	0.00	0.00	0.00	0.00	0.00	0.01	0.00	0.02	0.00	0.00	0.01	0.00	0.00	0.00	0.00	0.00
Fe^{3+}	0.00	0.04	0.04	0.04	0.03	0.10	0.04	0.07	0.05	0.04	0.06	0.03	0.05	0.06	0.03	0.02
Cr	0.00	0.00	0.00	0.00	0.00	0.00	0.00	0.00	0.00	0.00	0.00	0.00	0.00	0.00	0.00	0.00
Mg	1.24	1.50	1.49	1.52	1.49	1.44	1.51	1.27	1.47	1.32	1.24	1.32	1.32	1.32	1.40	1.38
Fe^{2+}	0.51	0.35	0.34	0.37	0.40	0.26	0.34	0.25	0.43	0.48	0.42	0.47	0.49	0.47	0.52	0.53
Mn^{2+}	0.01	0.00	0.00	0.00	0.01	0.01	0.00	0.00	0.01	0.01	0.01	0.01	0.01	0.01	0.01	0.01
Ca	0.05	0.01	0.05	0.01	0.01	0.12	0.01	0.26	0.01	0.01	0.10	0.04	0.01	0.02	0.01	0.02
Na	0.02	0.00	0.00	0.00	0.00	0.00	0.00	0.02	0.00	0.00	0.02	0.00	0.00	0.00	0.00	0.00
K	0.00	0.00	0.00	0.00	0.00	0.00	0.00	0.00	0.00	0.00	0.00	0.00	0.00	0.00	0.00	0.00
Wo	2.70	0.52	2.45	0.50	0.39	6.64	0.59	14.74	0.46	0.53	5.41	1.94	0.69	1.00	0.42	0.79
En	69.13	80.83	79.61	80.16	78.70	78.87	81.14	71.06	76.96	72.88	70.90	72.52	72.30	73.27	72.79	71.73
Fs	28.16	18.65	17.94	19.33	20.91	14.48	18.27	14.20	22.58	26.59	23.69	25.54	27.01	25.73	26.79	27.48
XMg	0.71	0.81	0.82	0.81	0.79	0.85	0.82	0.83	0.77	0.73	0.75	0.74	0.73	0.74	0.73	0.72

	1008-B3: metagabbro Kataransky Cape												**P-20: dyke Water Sign**		
wt.-%	#17 sympl.	#18 symp.	#21 sympl.	#24 sympl.	#25 sympl.	#34 core	#35	#36 rim	#39 core	#40 core	#11	#29	#1 core	#2 core	#3
SiO_2	52.40	52.02	52.13	52.33	51.99	51.89	52.04	53.12	52.67	52.33	52.79	53.41	52.82	53.00	52.27
TiO_2	0.08	0.08	0.06	0.04	0.04	0.40	0.37	0.17	0.07	0.03	0.08	0.07	0.12	0.09	0.10
Al_2O_3	2.10	2.08	1.78	2.17	2.27	3.24	3.24	2.13	1.36	2.19	2.31	2.04	2.77	2.61	2.71
Fe_2O_3	0.02	0.01	0.00	0.00	0.08	0.00	0.02	0.10	0.02	0.06	0.00	0.00	3.03	1.87	3.29
Cr_2O_3	2.55	2.50	2.64	1.80	2.45	2.22	2.79	2.14	1.22	1.57	0.00	0.01	0.00	0.01	0.00
FeO	19.24	19.46	18.83	19.25	18.98	5.37	4.91	4.33	19.94	18.68	21.06	20.64	16.64	17.00	16.65
MnO	0.19	0.19	0.22	0.16	0.19	0.10	0.13	0.08	0.23	0.11	0.23	0.25	0.23	0.24	0.23
MgO	23.90	23.63	24.00	23.97	23.82	14.49	14.44	15.28	23.75	24.30	23.05	23.64	24.84	24.82	25.25
CaO	0.41	0.36	0.36	0.34	0.36	22.34	22.48	23.19	0.39	0.33	0.41	0.34	1.45	1.31	0.50
Na_2O	0.04	0.00	0.02	0.01	0.02	0.53	0.64	0.49	0.01	0.01	0.00	0.01	0.05	0.06	0.01
K_2O	0.00	0.01	0.00	0.00	0.00	0.01	0.01	0.01	0.00	0.01	0.00	0.02	0.00	0.01	0.00
Σ	100.93	100.34	100.05	100.08	100.19	100.59	101.07	101.03	99.67	99.61	99.93	100.44	101.96	101.03	101.02
Si	1.92	1.92	1.92	1.93	1.92	1.91	1.90	1.94	1.95	1.93	1.95	1.96	1.90	1.92	1.90
Al^{IV}	0.08	0.08	0.08	0.07	0.08	0.09	0.10	0.06	0.05	0.07	0.05	0.04	0.10	0.08	0.11
Al^{VI}	0.01	0.01	0.00	0.02	0.01	0.05	0.04	0.03	0.01	0.03	0.05	0.05	0.02	0.03	0.01
Ti	0.00	0.00	0.00	0.00	0.00	0.01	0.01	0.01	0.00	0.00	0.00	0.00	0.00	0.00	0.00
Fe^{3+}	0.07	0.07	0.07	0.05	0.07	0.06	0.08	0.06	0.03	0.04	0.00	0.00	0.08	0.05	0.09
Cr	0.00	0.00	0.00	0.00	0.00	0.00	0.00	0.00	0.00	0.00	0.00	0.00	0.00	0.00	0.00
Mg	1.30	1.30	1.32	1.32	1.31	0.79	0.79	0.83	1.31	1.34	1.27	1.29	1.33	1.34	1.37
Fe^{2+}	0.59	0.60	0.58	0.59	0.59	0.17	0.15	0.13	0.62	0.58	0.65	0.63	0.50	0.52	0.51
Mn^{2+}	0.01	0.01	0.01	0.01	0.01	0.00	0.00	0.00	0.01	0.00	0.01	0.01	0.01	0.01	0.01
Ca	0.02	0.01	0.01	0.01	0.01	0.88	0.88	0.91	0.02	0.01	0.02	0.01	0.06	0.05	0.02
Na	0.00	0.00	0.00	0.00	0.00	0.04	0.05	0.03	0.00	0.00	0.00	0.00	0.00	0.00	0.00
K	0.00	0.00	0.00	0.00	0.00	0.00	0.00	0.00	0.00	0.00	0.00	0.00	0.00	0.00	0.00
Wo	0.85	0.75	0.74	0.70	0.75	47.85	48.44	48.49	0.81	0.67	0.84	0.70	2.96	2.67	1.02
En	68.30	67.88	68.92	68.47	68.59	43.17	43.30	44.44	67.42	69.39	65.56	66.65	70.53	70.31	72.25
Fs	30.85	31.36	30.33	30.84	30.67	8.98	8.26	7.07	31.77	29.94	33.60	32.65	26.51	27.02	26.73
XMg	0.69	0.68	0.69	0.69	0.69	0.83	0.84	0.86	0.68	0.70	0.66	0.67	0.73	0.72	0.73

P-20: noritic dyke Water Sign

wt.-%	#4	#6	#7	#8	#9	#10 rim	#15 cor.	#29 rim	#69 core	#70	#71	#72	#73	#74	#75	#76	#77	#78 rim
SiO_2	52.25	52.50	52.71	52.72	53.19	52.68	52.81	51.26	52.03	52.29	52.07	52.24	52.37	52.23	52.29	53.36	52.01	52.36
TiO_2	0.08	0.05	0.07	0.08	0.06	0.05	0.05	0.06	0.07	0.05	0.06	0.06	0.09	0.06	0.08	0.05	0.15	0.07
Al_2O_3	2.66	2.78	2.58	2.44	2.06	2.16	1.48	2.14	2.77	2.95	2.86	2.86	2.57	2.78	2.71	2.73	2.64	2.44
Fe_2O_3	2.95	3.05	2.75	2.16	1.46	2.27	1.53	3.63	2.58	3.00	3.30	2.46	2.33	2.20	2.76	0.33	2.91	2.04
Cr_2O_3	0.00	0.02	0.04	0.05	0.00	0.03	0.02	0.00	0.11	0.03	0.07	0.06	0.03	0.02	0.00	0.06	0.07	0.08
FeO	16.70	17.29	17.77	16.30	18.63	19.02	20.29	17.64	16.52	16.22	15.64	16.29	16.88	16.67	16.16	17.47	16.99	18.83
MnO	0.24	0.22	0.20	0.11	0.26	0.18	0.20	0.25	0.25	0.25	0.31	0.20	0.18	0.18	0.32	0.22	0.24	0.24
MgO	25.26	25.05	24.95	23.48	24.45	24.10	23.70	23.96	25.21	25.54	25.65	25.53	25.29	25.33	25.52	25.55	24.95	24.16
CaO	0.43	0.46	0.45	3.46	0.86	0.67	0.34	0.57	0.42	0.36	0.41	0.37	0.38	0.37	0.42	0.32	0.47	0.39
Na_2O	0.01	0.02	0.01	0.09	0.01	0.00	0.00	0.00	0.01	0.02	0.03	0.00	0.01	0.01	0.02	0.04	0.00	0.00
K_2O	0.00	0.00	0.00	0.00	0.01	0.00	0.00	0.00	0.00	0.01	0.00	0.01	0.00	0.00	0.00	0.01	0.00	0.01
Σ	100.57	101.43	101.53	100.91	101.00	101.15	100.41	99.52	99.98	100.72	100.39	100.08	100.14	99.85	100.27	100.13	100.42	100.64
Si	1.90	1.90	1.91	1.92	1.94	1.92	1.95	1.90	1.90	1.90	1.89	1.90	1.91	1.91	1.90	1.94	1.90	1.92
Al^{IV}	0.10	0.10	0.09	0.08	0.07	0.08	0.06	0.09	0.10	0.11	0.11	0.10	0.09	0.09	0.10	0.06	0.10	0.08
Al^{VI}	0.02	0.02	0.02	0.02	0.02	0.01	0.01	0.09	0.02	0.02	0.01	0.03	0.02	0.03	0.02	0.05	0.01	0.02
Ti	0.00	0.00	0.00	0.00	0.00	0.00	0.00	0.00	0.00	0.00	0.00	0.00	0.00	0.00	0.00	0.00	0.00	0.00
Fe^{3+}	0.08	0.08	0.08	0.06	0.04	0.06	0.04	0.10	0.07	0.08	0.09	0.07	0.06	0.06	0.08	0.01	0.08	0.06
Cr	0.00	0.00	0.00	0.00	0.00	0.00	0.00	0.00	0.00	0.00	0.00	0.00	0.00	0.00	0.00	0.00	0.00	0.00
Mg	1.37	1.35	1.34	1.27	1.33	1.31	1.30	1.33	1.37	1.38	1.39	1.39	1.38	1.38	1.38	1.38	1.36	1.32
Fe^{2+}	0.51	0.52	0.54	0.50	0.57	0.58	0.63	0.55	0.51	0.49	0.48	0.50	0.52	0.51	0.49	0.53	0.52	0.58
Mn^{2+}	0.01	0.01	0.01	0.00	0.01	0.01	0.01	0.01	0.01	0.01	0.01	0.01	0.01	0.01	0.01	0.01	0.01	0.01
Ca	0.02	0.02	0.02	0.14	0.03	0.03	0.01	0.02	0.02	0.01	0.02	0.01	0.02	0.01	0.02	0.01	0.02	0.02
Na	0.00	0.00	0.00	0.01	0.00	0.00	0.00	0.00	0.00	0.00	0.00	0.00	0.00	0.00	0.00	0.00	0.00	0.00
K	0.00	0.00	0.00	0.00	0.00	0.00	0.00	0.00	0.00	0.00	0.00	0.00	0.00	0.00	0.00	0.00	0.00	0.00
Wo	0.89	0.93	0.93	7.08	1.75	1.36	0.69	1.20	0.86	0.73	0.85	0.76	0.79	0.76	0.87	0.65	0.98	0.80
En	72.30	71.42	70.78	66.87	68.83	68.38	67.08	69.93	72.49	73.19	73.88	73.07	72.19	72.47	73.15	71.81	71.65	69.02
Fs	26.81	27.65	28.29	26.04	29.42	30.27	32.23	28.88	26.65	26.08	25.27	26.17	27.03	26.77	25.99	27.54	27.37	30.18
XMg	0.73	0.72	0.71	0.72	0.70	0.69	0.68	0.71	0.73	0.74	0.75	0.74	0.73	0.73	0.74	0.72	0.72	0.70

P-20: noritic dyke Water Sign

wt.-%	#97 lam.	#98 lam.	#99 lam.	#121 lam.	#122 lam.	#123 lam.
SiO_2	51.30	51.73	51.83	51.40	51.50	50.99
TiO_2	0.08	0.08	0.12	0.07	0.05	0.06
Al_2O_3	3.23	3.18	3.17	2.30	2.02	2.93
Fe_2O_3	0.58	1.22	1.16	2.02	2.78	3.37
Cr_2O_3	0.00	0.00	0.04	0.00	0.04	0.08
FeO	21.08	20.91	20.20	21.45	20.19	19.03
MnO	0.24	0.42	0.33	0.35	0.39	0.38
MgO	22.18	22.49	23.08	22.06	22.77	23.03
CaO	0.42	0.37	0.31	0.30	0.32	0.41
Na_2O	0.00	0.00	0.00	0.00	0.00	0.00
K_2O	0.00	0.01	0.00	0.00	0.01	0.01
Σ	99.13	100.40	100.25	99.96	100.05	100.30
Si	1.92	1.91	1.91	1.92	1.92	1.89
Al^{IV}	0.08	0.09	0.09	0.08	0.09	0.11
Al^{VI}	0.06	0.05	0.05	0.02	0.00	0.02
Ti	0.00	0.00	0.00	0.00	0.00	0.00
Fe^{3+}	0.02	0.03	0.03	0.06	0.08	0.09
Cr	0.00	0.00	0.00	0.00	0.00	0.00
Mg	1.24	1.24	1.27	1.23	1.26	1.27
Fe^{2+}	0.66	0.65	0.62	0.67	0.63	0.59
Mn^{2+}	0.01	0.01	0.01	0.01	0.01	0.01
Ca	0.02	0.02	0.01	0.01	0.01	0.02
Na	0.00	0.00	0.00	0.00	0.00	0.00
K	0.00	0.00	0.00	0.00	0.00	0.00
Wo	0.89	0.77	0.65	0.63	0.67	0.87
En	64.64	65.22	66.64	64.29	66.33	67.74
Fs	34.47	34.01	32.72	35.07	33.00	31.40
XMg	0.65	0.66	0.67	0.65	0.67	0.68

EMP analyses of plagioclase cores, rims, symplectites, inclusions and coronas from different rock types. Analyses were recalculated on the basis of 8 oxygens.

	0708-3: metagabbro Bolschoi Khed											
wt.-%	#23 sympl.	#24 sympl.	#32 sympl.	#33 sympl.	#48 sympl.	#49 sympl.	#50 sympl.	#52 sympl.	#53 sympl.	#55 core	#56 core	#59 sympl.
SiO_2	46.33	47.35	54.41	47.38	50.81	54.69	55.38	54.47	48.05	54.41	55.31	46.26
TiO_2	0.00	0.01	0.03	0.00	0.00	0.01	0.00	0.03	0.00	0.02	0.02	0.02
Al_2O_3	34.03	33.70	28.75	33.59	30.33	28.97	28.07	29.55	33.05	28.70	28.57	34.38
Fe_2O_3	0.27	0.20	0.25	0.18	0.24	0.30	0.28	0.20	0.33	0.13	0.03	0.24
MgO	0.00	0.01	0.01	0.00	0.02	0.00	0.00	0.02	0.01	0.03	0.01	0.00
CaO	17.68	16.75	11.09	16.91	13.43	10.96	9.95	11.17	15.87	10.45	9.97	17.43
Na_2O	1.83	2.29	5.68	2.15	4.03	5.66	6.27	5.68	2.82	6.07	6.17	1.85
K_2O	0.05	0.09	0.07	0.03	0.10	0.20	0.11	0.17	0.06	0.14	0.25	0.03
Σ	100.20	100.41	100.29	100.25	98.96	100.80	100.06	101.28	100.20	99.95	100.33	100.22
Si	2.13	2.17	2.45	2.17	2.34	2.45	2.50	2.43	2.20	2.46	2.49	2.13
Al^{IV}	1.85	1.82	1.53	1.81	1.64	1.53	1.49	1.56	1.78	1.53	1.51	1.86
Fe^{3+}	0.01	0.01	0.01	0.01	0.01	0.01	0.01	0.01	0.01	0.01	0.00	0.01
Mg	0.00	0.00	0.00	0.00	0.00	0.00	0.00	0.00	0.00	0.00	0.00	0.00
Na	0.16	0.20	0.50	0.19	0.36	0.49	0.55	0.49	0.25	0.53	0.54	0.17
Ca	0.87	0.82	0.54	0.83	0.66	0.53	0.48	0.54	0.78	0.51	0.48	0.86
K	0.00	0.01	0.00	0.00	0.01	0.01	0.01	0.01	0.00	0.01	0.02	0.00
Ab	15.73	19.72	47.91	18.68	34.99	47.75	52.99	47.48	24.24	50.84	52.06	16.06
An	84.00	79.75	51.69	81.16	64.43	51.12	46.42	51.59	75.44	48.39	46.52	83.75
Or	0.27	0.53	0.39	0.17	0.58	1.12	0.59	0.93	0.33	0.77	1.42	0.20

0708-3: metagabbro Bolschoi Khed

wt.-%	#60 sympl.	#87 incl.	#88 incl.	#89 core	#90 core	#91 core	#92 core	#99 sympl.	#100 sympl.	#110 sympl.	#115 rim	#116 core	#118 sympl.
SiO_2	47.86	54.15	54.40	56.05	56.20	54.06	53.48	46.96	47.58	45.02	55.21	56.66	46.98
TiO_2	0.01	0.03	0.01	0.02	0.00	0.01	0.00	0.00	0.02	0.02	0.02	0.00	0.00
Al_2O_3	33.21	29.17	28.76	28.13	27.78	28.54	29.45	33.41	33.00	35.59	28.90	28.20	34.00
Fe_2O_3	0.14	0.21	0.13	0.06	0.12	0.63	0.51	0.24	0.39	0.55	0.14	0.08	0.18
MgO	0.01	0.00	0.01	0.00	0.00	0.01	0.01	0.01	0.00	0.16	0.01	0.00	0.01
CaO	16.23	11.31	11.17	9.91	9.56	10.97	11.85	16.35	15.80	18.40	10.29	9.50	16.82
Na_2O	2.58	5.27	5.34	6.09	6.18	5.26	4.92	2.49	2.67	1.04	5.64	6.09	2.03
K_2O	0.05	0.17	0.17	0.20	0.29	0.24	0.17	0.06	0.07	0.02	0.20	0.28	0.05
Σ	100.08	100.31	99.99	100.46	100.14	99.73	100.40	99.52	99.52	100.80	100.42	100.83	100.07
Si	2.19	2.44	2.46	2.51	2.53	2.45	2.41	2.17	2.19	2.06	2.48	2.53	2.16
Al^{IV}	1.79	1.55	1.53	1.49	1.47	1.53	1.57	1.82	1.79	1.92	1.53	1.48	1.84
Fe^{3+}	0.01	0.01	0.00	0.00	0.00	0.02	0.02	0.01	0.01	0.02	0.01	0.00	0.01
Mg	0.00	0.00	0.00	0.00	0.00	0.00	0.00	0.00	0.00	0.01	0.00	0.00	0.00
Na	0.23	0.55	0.54	0.48	0.46	0.53	0.57	0.81	0.78	0.90	0.49	0.45	0.83
Ca	0.80	0.46	0.47	0.53	0.54	0.46	0.43	0.22	0.24	0.09	0.49	0.53	0.18
K	0.00	0.01	0.01	0.01	0.02	0.01	0.01	0.00	0.00	0.00	0.01	0.02	0.00
Ab	22.27	45.32	45.95	52.06	53.01	45.83	42.48	21.51	23.30	9.25	49.22	52.86	17.88
An	77.45	53.75	53.11	46.80	45.35	52.79	56.55	78.16	76.29	90.62	49.62	45.54	81.82
Or	0.28	0.94	0.94	1.15	1.64	1.38	0.98	0.34	0.41	0.14	1.17	1.60	0.30

0708-3: metagabbro Bolschoi Khed

wt.-%	#119 sympl.	#120 sympl.	#121 sympl.	#122 sympl.	#123	#124 core	#127	#1 rim	#2	#3	#4	#5	#6	#7	#9
SiO_2	45.54	45.31	46.19	46.10	49.39	55.75	53.86	53.44	54.63	55.01	55.47	55.88	56.00	56.40	55.88
TiO_2	0.00	0.00	0.00	0.00	0.02	0.00	0.00	0.03	0.02	0.01	0.00	0.03	0.00	0.00	0.00
Al_2O_3	34.87	34.57	34.70	33.95	31.86	28.19	29.06	30.12	29.10	29.19	28.93	28.58	28.35	28.12	28.16
Fe_2O_3	0.46	0.24	0.34	0.24	0.20	0.14	0.80	0.10	0.07	0.08	0.06	0.01	0.10	0.12	0.07
MgO	0.20	0.08	0.01	0.01	0.00	0.01	0.00	0.01	0.01	0.02	0.00	0.00	0.01	0.01	0.01
CaO	17.53	17.30	17.27	16.55	14.27	9.51	10.57	12.38	11.28	11.26	11.00	10.68	10.37	10.39	10.17
Na_2O	1.39	1.58	1.76	2.19	3.51	6.13	5.87	4.70	5.36	5.26	5.44	5.44	5.77	5.81	5.86
K_2O	0.03	0.02	0.03	0.04	0.09	0.21	0.08	0.07	0.13	0.16	0.17	0.18	0.18	0.18	0.16
Σ	100.02	99.11	100.30	99.09	99.34	99.95	100.26	100.86	100.59	100.99	101.07	100.80	100.79	101.03	100.32
Si	2.10	2.11	2.12	2.14	2.27	2.51	2.43	2.40	2.45	2.46	2.48	2.50	2.50	2.51	2.51
Al^{IV}	1.89	1.89	1.88	1.86	1.73	1.50	1.55	1.59	1.54	1.54	1.52	1.50	1.49	1.48	1.49
Fe^{3+}	0.02	0.01	0.01	0.01	0.01	0.01	0.03	0.00	0.00	0.00	0.00	0.00	0.00	0.00	0.00
Mg	0.01	0.01	0.00	0.00	0.00	0.00	0.00	0.00	0.00	0.00	0.00	0.00	0.00	0.00	0.00
Na	0.87	0.86	0.85	0.82	0.70	0.46	0.51	0.41	0.47	0.46	0.47	0.47	0.50	0.50	0.51
Ca	0.12	0.14	0.16	0.20	0.31	0.54	0.51	0.60	0.54	0.54	0.53	0.51	0.50	0.50	0.49
K	0.00	0.00	0.00	0.00	0.01	0.01	0.01	0.00	0.01	0.01	0.01	0.01	0.01	0.01	0.01
Ab	12.50	14.13	15.54	19.26	30.67	53.20	49.89	40.57	45.88	45.38	46.78	47.47	49.67	49.81	50.56
An	87.31	85.74	84.27	80.52	68.81	45.58	49.64	59.01	53.36	53.72	52.28	51.50	49.31	49.20	48.52
Or	0.19	0.14	0.19	0.22	0.52	1.22	0.47	0.42	0.76	0.90	0.94	1.03	1.01	0.99	0.93

	0708-3: metagabbro Bolschoi Khed												1008-B3: metagabbro Kataransky Cape			
wt.-%	#10	#11	#12 rim	#13 rim	#14 core	#15 core	#16 rim	#25 incl.	#29 core	#30 rim	#44	#45	#14 sympl.	#19 sympl.	#22 sympl.	#26 sympl.
SiO_2	56.19	57.00	56.26	56.45	55.90	56.66	56.51	52.95	55.82	57.51	48.92	49.57	54.49	54.11	55.77	55.02
TiO_2	0.01	0.00	0.00	0.02	0.02	0.00	0.02	0.02	0.00	0.03	0.01	0.01	0.00	0.00	0.01	0.00
Al_2O_3	28.07	27.77	28.29	27.26	28.46	27.74	27.83	29.60	28.44	27.93	32.96	32.48	27.25	29.02	28.89	28.62
Fe_2O_3	0.08	0.03	0.04	0.05	0.03	0.04	0.05	0.21	0.07	0.05	0.13	0.09	0.34	0.15	0.10	0.22
MgO	0.01	0.00	0.00	0.00	0.00	0.00	0.00	0.01	0.00	0.03	0.01	0.00	0.00	0.00	0.00	0.00
CaO	10.17	10.23	10.25	9.55	10.46	10.02	10.10	12.40	10.80	9.89	16.37	15.93	10.97	11.01	10.38	10.73
Na_2O	5.89	6.00	5.99	5.71	5.87	6.07	6.10	4.98	5.73	6.29	2.58	2.92	5.62	5.53	5.96	5.84
K_2O	0.18	0.17	0.14	0.20	0.19	0.25	0.20	0.18	0.24	0.21	0.07	0.05	0.12	0.24	0.27	0.20
Σ	100.60	101.21	100.97	99.26	100.94	100.79	100.81	100.34	101.10	101.95	101.05	101.06	98.79	100.06	101.38	100.62
Si	2.51	2.53	2.51	2.55	2.50	2.53	2.52	2.40	2.49	2.54	2.22	2.25	2.49	2.45	2.48	2.47
Al^{IV}	1.48	1.45	1.49	1.45	1.50	1.46	1.46	1.58	1.50	1.45	1.76	1.73	1.47	1.55	1.52	1.52
Fe^{3+}	0.00	0.00	0.00	0.00	0.00	0.00	0.00	0.01	0.00	0.00	0.01	0.00	0.01	0.01	0.00	0.01
Mg	0.00	0.00	0.00	0.00	0.00	0.00	0.00	0.00	0.00	0.00	0.00	0.00	0.00	0.00	0.00	0.00
Na	0.51	0.52	0.52	0.50	0.51	0.53	0.53	0.44	0.50	0.54	0.23	0.26	0.50	0.48	0.51	0.51
Ca	0.49	0.49	0.49	0.46	0.50	0.48	0.48	0.60	0.52	0.47	0.80	0.77	0.54	0.53	0.50	0.52
K	0.01	0.01	0.01	0.01	0.01	0.01	0.01	0.01	0.01	0.01	0.00	0.00	0.01	0.01	0.02	0.01
Ab	50.68	51.02	50.97	51.34	49.84	51.54	51.62	41.66	48.34	52.89	22.08	24.85	47.78	46.97	50.19	49.08
An	48.31	48.05	48.23	47.45	49.10	47.04	47.24	57.37	50.34	45.95	77.54	74.86	51.57	51.70	48.32	49.82
Or	1.01	0.94	0.80	1.20	1.06	1.41	1.14	0.97	1.32	1.16	0.39	0.30	0.66	1.33	1.48	1.10

1008-B3: metagabbro Kataransky Cape

wt.-%	#27 sympl.	#37	#38	#41 rim	#42	#43 core	#60 core	#61	#63	#62 rim	#6 rim	#7 rim	#8 core	#12 rim	#16 core	#17 rim	#23 rim
SiO_2	55.72	54.92	54.66	55.32	55.14	55.72	54.91	55.26	55.71	52.72	54.74	55.78	54.78	53.28	56.03	55.40	56.27
TiO_2	0.00	0.02	0.01	0.01	0.02	0.00	0.03	0.04	0.00	0.01	0.00	0.01	0.00	0.01	0.01	0.00	0.02
Al_2O_3	28.32	28.64	28.39	28.47	27.94	27.56	27.51	27.93	28.52	29.50	29.05	28.67	29.15	30.02	28.25	28.67	28.21
Fe_2O_3	0.17	0.13	0.23	0.14	0.10	0.08	0.02	0.06	0.09	0.19	0.12	0.10	0.08	0.25	0.05	0.16	0.13
MgO	0.00	0.00	0.01	0.00	0.02	0.00	0.00	0.01	0.01	0.01	0.01	0.00	0.01	0.00	0.00	0.00	0.00
CaO	10.37	10.53	10.56	10.45	10.17	10.20	10.46	10.62	10.56	12.29	11.12	10.50	11.20	12.42	10.44	11.01	10.24
Na_2O	5.89	5.85	5.88	5.94	6.03	6.14	5.92	5.85	5.77	4.79	5.16	5.66	5.30	4.50	5.66	5.35	5.73
K_2O	0.23	0.25	0.25	0.27	0.28	0.29	0.25	0.25	0.28	0.20	0.26	0.22	0.19	0.23	0.30	0.20	0.32
Σ	100.71	100.33	100.00	100.62	99.70	99.99	99.11	100.03	100.93	99.70	100.47	100.95	100.70	100.71	100.74	100.79	100.92
Si	2.50	2.47	2.47	2.48	2.50	2.51	2.50	2.49	2.49	2.40	2.46	2.49	2.46	2.40	2.51	2.48	2.51
Al^{IV}	1.49	1.52	1.51	1.51	1.49	1.47	1.48	1.49	1.50	1.58	1.54	1.51	1.54	1.59	1.49	1.51	1.48
Fe^{3+}	0.01	0.00	0.01	0.01	0.00	0.00	0.00	0.00	0.00	0.01	0.00	0.00	0.00	0.01	0.00	0.01	0.00
Mg	0.00	0.00	0.00	0.00	0.00	0.00	0.00	0.00	0.00	0.00	0.00	0.00	0.00	0.00	0.00	0.00	0.00
Na	0.51	0.51	0.52	0.52	0.53	0.54	0.52	0.51	0.50	0.42	0.45	0.49	0.46	0.39	0.49	0.46	0.50
Ca	0.50	0.51	0.51	0.50	0.49	0.49	0.51	0.51	0.51	0.60	0.54	0.50	0.54	0.60	0.50	0.53	0.49
K	0.01	0.01	0.01	0.02	0.02	0.02	0.02	0.01	0.02	0.01	0.02	0.01	0.01	0.01	0.02	0.01	0.02
Ab	50.06	49.44	49.53	49.91	50.95	51.33	49.89	49.21	48.95	40.88	44.99	48.75	45.66	39.10	48.68	46.24	49.37
An	48.67	49.19	49.11	48.58	47.51	47.09	48.70	49.42	49.51	58.01	53.55	49.98	53.28	59.60	49.63	52.61	48.82
Or	1.27	1.38	1.36	1.51	1.54	1.58	1.41	1.37	1.54	1.12	1.47	1.27	1.06	1.30	1.69	1.14	1.81

	1008-B3			**P-20: metanorite Water Sign**												
wt.-%	#24 core	#25 rim	#33 sympl.	#19	#20 cor.	#21 cor.	#27 rim	#28 core	#34 cor.	#37 rim	#51 cor.	#52 cor.	#55 rim	#56 core	#60 core	#83 cor.
SiO_2	55.94	51.93	55.56	58.86	58.53	56.04	56.03	56.32	56.18	55.04	57.43	57.30	57.33	56.43	57.08	57.03
TiO_2	0.00	0.04	0.00	0.00	0.01	0.00	0.03	0.01	0.01	0.00	0.01	0.01	0.02	0.00	0.01	0.00
Al_2O_3	28.09	31.25	28.67	25.17	24.93	26.33	27.18	27.49	27.35	27.64	26.39	26.10	25.75	26.61	26.30	25.69
Fe_2O_3	0.08	0.08	0.19	0.10	0.18	0.73	0.18	0.11	0.16	0.16	0.20	0.22	0.14	0.08	0.04	0.20
MgO	0.01	0.00	0.01	0.00	0.00	0.34	0.02	0.03	0.01	0.01	0.00	0.00	0.00	0.01	0.01	0.01
CaO	10.34	13.68	10.81	7.77	7.92	8.74	9.38	9.77	9.27	10.05	8.84	8.71	8.39	9.10	9.26	8.69
Na_2O	5.61	3.91	5.44	7.27	6.90	6.52	6.29	6.09	6.46	5.90	6.56	6.54	6.91	6.44	6.28	6.76
K_2O	0.28	0.13	0.21	0.12	0.23	0.08	0.19	0.24	0.21	0.12	0.26	0.30	0.21	0.29	0.24	0.08
Σ	100.34	101.03	100.90	99.30	98.70	98.77	99.29	100.05	99.65	98.91	99.70	99.18	98.75	98.96	99.21	98.45
Si	2.51	2.34	2.48	2.65	2.65	2.55	2.54	2.53	2.54	2.51	2.59	2.59	2.60	2.56	2.58	2.60
Al^{IV}	1.49	1.66	1.51	1.34	1.33	1.41	1.45	1.46	1.46	1.48	1.40	1.39	1.38	1.42	1.40	1.38
Fe^{3+}	0.00	0.00	0.01	0.00	0.01	0.03	0.01	0.00	0.01	0.01	0.01	0.01	0.01	0.00	0.00	0.01
Mg	0.00	0.00	0.00	0.00	0.00	0.02	0.00	0.00	0.00	0.00	0.00	0.00	0.00	0.00	0.00	0.00
Na	0.49	0.34	0.47	0.63	0.61	0.58	0.55	0.53	0.57	0.52	0.57	0.57	0.61	0.57	0.55	0.60
Ca	0.50	0.66	0.52	0.38	0.38	0.43	0.46	0.47	0.45	0.49	0.43	0.42	0.41	0.44	0.45	0.42
K	0.02	0.01	0.01	0.01	0.01	0.01	0.01	0.01	0.01	0.01	0.02	0.02	0.01	0.02	0.01	0.00
Ab	48.76	33.86	47.07	62.44	60.41	57.17	54.22	52.29	55.15	51.19	56.46	56.61	59.15	55.24	54.34	58.23
An	49.65	65.40	51.73	36.87	38.29	42.34	44.72	46.34	43.70	48.15	42.07	41.70	39.68	43.13	44.30	41.34
Or	1.59	0.74	1.20	0.69	1.30	0.49	1.06	1.36	1.15	0.66	1.47	1.69	1.17	1.63	1.37	0.43

	P-20: me	P-20: metanorite Water Sign															
wt.-%	#84 cor.	#89 rim	#90 core	#91 rim	#92 cor.	#93 cor.	#106	#109 cor.	#111 rim	#112	#113	#114	#115	#116	#117	#118	#119 core
SiO_2	55.12	53.99	53.36	52.80	57.80	57.16	57.33	56.34	54.23	54.21	53.86	54.54	53.43	53.71	53.34	53.64	52.78
TiO_2	0.00	0.03	0.00	0.00	0.00	0.00	0.00	0.01	0.00	0.00	0.00	0.00	0.01	0.01	0.04	0.00	0.02
Al_2O_3	27.38	29.29	29.91	30.33	26.74	27.23	26.51	27.23	28.72	28.68	28.58	28.10	29.06	28.97	29.20	29.13	29.00
Fe_2O_3	0.23	0.25	0.02	0.09	0.21	0.25	0.19	0.10	0.12	0.05	0.08	0.00	0.06	0.00	0.16	0.10	0.12
MgO	0.00	0.01	0.00	0.00	0.00	0.00	0.01	0.01	0.00	0.00	0.00	0.00	0.01	0.00	0.02	0.01	0.00
CaO	9.23	11.32	12.06	12.51	8.63	9.05	8.80	9.45	10.98	11.35	11.05	11.17	11.49	11.34	11.44	11.41	11.36
Na_2O	6.40	5.37	4.89	4.58	6.89	6.80	6.76	6.40	5.64	5.30	5.36	5.17	5.18	5.26	5.15	5.16	5.34
K_2O	0.05	0.04	0.03	0.03	0.10	0.03	0.19	0.17	0.02	0.06	0.09	0.20	0.23	0.28	0.25	0.27	0.12
Σ	98.42	100.30	100.27	100.33	100.36	100.53	99.79	99.72	99.72	99.64	99.03	99.19	99.46	99.58	99.60	99.73	98.74
Si	2.52	2.43	2.41	2.38	2.58	2.55	2.58	2.54	2.46	2.46	2.46	2.48	2.43	2.44	2.43	2.43	2.42
Al^{IV}	1.48	1.56	1.59	1.61	1.41	1.43	1.41	1.45	1.53	1.53	1.54	1.51	1.56	1.55	1.57	1.56	1.57
Fe^{3+}	0.01	0.01	0.00	0.00	0.01	0.01	0.01	0.00	0.00	0.00	0.00	0.00	0.00	0.00	0.01	0.00	0.00
Mg	0.00	0.00	0.00	0.00	0.00	0.00	0.00	0.00	0.00	0.00	0.00	0.00	0.00	0.00	0.00	0.00	0.00
Na	0.57	0.47	0.43	0.40	0.60	0.59	0.59	0.56	0.50	0.47	0.47	0.46	0.46	0.46	0.45	0.45	0.48
Ca	0.45	0.55	0.58	0.61	0.41	0.43	0.42	0.46	0.53	0.55	0.54	0.54	0.56	0.55	0.56	0.56	0.56
K	0.00	0.00	0.00	0.00	0.01	0.00	0.01	0.01	0.00	0.00	0.01	0.01	0.01	0.02	0.01	0.02	0.01
Ab	55.50	46.10	42.27	39.75	58.78	57.54	57.53	54.53	48.10	45.65	46.51	45.04	44.34	44.89	44.26	44.32	45.65
An	44.20	53.67	57.57	60.08	40.68	42.30	41.43	44.51	51.76	54.02	52.96	53.80	54.38	53.53	54.34	54.13	53.65
Or	0.30	0.24	0.16	0.17	0.53	0.16	1.04	0.96	0.14	0.33	0.54	1.16	1.29	1.58	1.40	1.55	0.70

35-5: meta-anorthosite Beloozerskaya Guba

wt.-%	#120 core	#17	#21	#27	#28	#29	#41	#42	#45	#47	#57	#60	#61	#62	#63	#64	#65
SiO_2	53.13	55.80	46.76	51.85	46.61	49.92	45.06	46.44	49.39	48.35	56.43	54.58	49.90	49.49	50.12	48.53	50.00
TiO_2	0.05	0.02	0.01	0.00	0.03	0.00	0.03	0.00	0.01	0.00	0.00	0.02	0.00	0.00	0.04	0.00	0.02
Al_2O_3	29.31	28.42	33.85	29.54	34.13	31.16	34.56	34.09	32.13	32.83	27.90	28.64	32.06	32.44	32.06	32.25	31.71
Fe_2O_3	0.16	0.05	0.23	0.21	0.19	0.21	0.20	0.00	0.12	0.21	0.02	0.05	0.06	0.07	0.10	0.02	0.07
MgO	0.01	0.00	0.12	0.00	0.00	0.00	0.02	0.01	0.00	0.00	0.00	0.00	0.00	0.00	0.00	0.02	0.01
CaO	11.74	10.39	16.91	11.38	16.82	13.62	17.81	16.98	14.99	15.29	9.54	10.80	14.68	14.88	14.87	15.41	14.36
Na_2O	4.99	5.79	1.91	5.27	1.96	4.01	1.36	1.80	3.16	2.78	6.10	5.58	3.10	3.03	3.08	2.93	3.31
K_2O	0.16	0.05	0.04	0.05	0.02	0.05	0.03	0.02	0.06	0.04	0.19	0.20	0.08	0.07	0.09	0.09	0.11
Σ	99.54	100.51	99.83	98.31	99.78	98.98	99.07	99.34	99.89	99.52	100.18	99.87	99.88	99.98	100.36	99.24	99.59
Si	2.42	2.50	2.15	2.39	2.15	2.30	2.10	2.15	2.26	2.22	2.53	2.47	2.28	2.26	2.28	2.24	2.29
Al^{IV}	1.57	1.50	1.84	1.61	1.85	1.69	1.90	1.86	1.73	1.78	1.47	1.53	1.72	1.75	1.72	1.75	1.71
Fe^{3+}	0.01	0.00	0.01	0.01	0.01	0.01	0.01	0.00	0.00	0.01	0.00	0.00	0.00	0.00	0.00	0.00	0.00
Mg	0.00	0.00	0.01	0.00	0.00	0.00	0.00	0.00	0.00	0.00	0.00	0.00	0.00	0.00	0.00	0.00	0.00
Na	0.44	0.50	0.17	0.47	0.18	0.36	0.12	0.16	0.28	0.25	0.53	0.49	0.27	0.27	0.27	0.26	0.29
Ca	0.57	0.50	0.83	0.56	0.83	0.67	0.89	0.84	0.74	0.75	0.46	0.52	0.72	0.73	0.72	0.76	0.70
K	0.01	0.00	0.00	0.00	0.00	0.00	0.00	0.00	0.00	0.00	0.01	0.01	0.00	0.00	0.01	0.01	0.01
Ab	43.09	50.08	16.90	45.49	17.42	34.66	12.14	16.07	27.53	24.72	53.08	47.77	27.52	26.79	27.13	25.45	29.22
An	56.00	49.64	82.89	54.22	82.44	65.08	87.66	83.82	72.11	75.05	45.85	51.12	72.04	72.81	72.37	74.05	70.16
Or	0.91	0.29	0.21	0.29	0.14	0.26	0.20	0.10	0.36	0.23	1.07	1.12	0.44	0.40	0.50	0.50	0.62

	35-5: meta-anorthosite Beloozerskaya Guba														**0908-1: oph. dyke Kataransky**			
wt.-%	#66	#71	#72	#81	#85	#86	#87	#90	#91	#92	#97	#98	#99	#103	#10	#15	#16	#17
SiO_2	48.72	50.56	57.05	46.36	47.02	46.37	45.55	58.09	56.42	55.02	54.16	49.84	50.15	50.65	54.79	55.14	55.04	53.16
TiO_2	0.01	0.03	0.01	0.00	0.02	0.03	0.03	0.00	0.02	0.02	0.00	0.02	0.02	0.00	0.02	0.00	0.00	0.00
Al_2O_3	32.74	30.94	27.62	33.94	34.01	34.69	34.76	26.62	27.38	28.50	29.48	32.14	31.94	31.86	29.22	28.90	28.52	29.11
Fe_2O_3	0.00	0.01	0.09	0.48	0.00	0.19	0.18	0.00	0.04	0.26	0.00	0.09	0.17	0.00	0.26	0.05	0.02	0.07
MgO	0.01	0.02	0.00	0.18	0.01	0.00	0.00	0.02	0.02	0.00	0.01	0.00	0.02	0.01	0.01	0.00	0.00	0.00
CaO	15.74	13.88	9.54	17.39	17.38	17.70	18.03	8.12	9.28	10.85	11.63	15.07	14.61	14.55	11.04	10.66	10.29	11.19
Na_2O	2.76	3.75	6.16	1.64	1.64	1.54	1.39	7.08	6.25	5.70	5.04	3.08	3.24	3.43	5.61	5.87	6.10	5.38
K_2O	0.07	0.14	0.27	0.02	0.01	0.01	0.00	0.23	0.19	0.18	0.16	0.18	0.19	0.07	0.01	0.03	0.03	0.06
Σ	100.05	99.32	100.75	100.02	100.10	100.53	99.95	100.17	99.60	100.53	100.49	100.43	100.34	100.58	100.96	100.65	100.01	98.98
Si	2.23	2.32	2.54	2.13	2.16	2.12	2.10	2.60	2.54	2.47	2.44	2.27	2.28	2.29	2.45	2.47	2.48	2.43
Al^{IV}	1.77	1.67	1.45	1.84	1.84	1.87	1.89	1.40	1.46	1.51	1.56	1.72	1.71	1.70	1.54	1.53	1.52	1.57
Fe^{3+}	0.00	0.00	0.00	0.02	0.00	0.01	0.01	0.00	0.00	0.01	0.00	0.00	0.01	0.00	0.01	0.00	0.00	0.00
Mg	0.00	0.00	0.00	0.01	0.00	0.00	0.00	0.00	0.00	0.00	0.00	0.00	0.00	0.00	0.00	0.00	0.00	0.00
Na	0.25	0.33	0.53	0.15	0.15	0.14	0.12	0.61	0.55	0.50	0.44	0.27	0.29	0.30	0.49	0.51	0.53	0.48
Ca	0.77	0.68	0.46	0.86	0.85	0.87	0.89	0.39	0.45	0.52	0.56	0.74	0.71	0.71	0.53	0.51	0.50	0.55
K	0.00	0.01	0.02	0.00	0.00	0.00	0.00	0.01	0.01	0.01	0.01	0.01	0.01	0.00	0.00	0.00	0.00	0.00
Ab	24.00	32.57	53.07	14.56	14.56	13.60	12.23	60.40	54.37	48.23	43.56	26.72	28.33	29.80	47.87	49.81	51.69	46.36
An	75.59	66.62	45.38	85.31	85.37	86.37	87.76	38.29	44.56	50.76	55.52	72.24	70.57	69.79	52.08	50.02	48.15	53.31
Or	0.41	0.81	1.55	0.14	0.07	0.04	0.01	1.31	1.07	1.01	0.92	1.04	1.10	0.41	0.05	0.17	0.17	0.33

	0908-1: ophitic dyke Kataransky Cape															0808-4: metadiorite		
wt.-%	#18	#19	#20	#21	#22	#23	#24	#25	#39	#40	#41	#42	#43	#44	#45	#13	#14	#15
SiO_2	52.73	53.59	53.76	53.46	53.05	51.55	55.59	55.40	53.44	53.76	53.42	53.78	53.18	53.22	53.39	60.43	60.00	60.69
TiO_2	0.00	0.00	0.00	0.01	0.00	0.00	0.02	0.01	0.00	0.00	0.01	0.00	0.00	0.03	0.01	0.00	0.02	0.01
Al_2O_3	29.86	29.42	29.23	29.58	30.07	30.44	28.82	28.52	30.18	29.80	29.87	29.93	30.04	30.19	29.93	25.18	25.09	25.09
Fe_2O_3	0.06	0.03	0.00	0.01	0.06	0.02	0.01	0.00	0.07	0.02	0.02	0.00	0.00	0.08	0.03	0.09	0.05	0.07
MgO	0.00	0.00	0.02	0.00	0.01	0.00	0.00	0.00	0.02	0.00	0.01	0.00	0.00	0.01	0.00	0.00	0.00	0.00
CaO	11.78	11.45	11.13	11.69	12.07	12.61	10.35	10.19	11.97	11.68	11.73	11.86	12.14	12.02	11.97	6.02	5.96	6.02
Na_2O	4.94	5.40	5.47	5.17	4.89	4.55	6.13	6.10	4.98	5.15	5.06	5.11	4.91	4.83	4.93	8.51	8.60	8.62
K_2O	0.05	0.04	0.04	0.05	0.04	0.03	0.04	0.04	0.05	0.06	0.07	0.04	0.06	0.07	0.07	0.15	0.16	0.16
Σ	99.43	99.93	99.66	99.97	100.18	99.20	100.97	100.26	100.70	100.47	100.19	100.73	100.34	100.45	100.34	100.38	99.89	100.66
Si	2.40	2.43	2.44	2.42	2.40	2.36	2.48	2.49	2.40	2.42	2.41	2.42	2.40	2.40	2.41	2.68	2.68	2.69
Al^{IV}	1.60	1.57	1.56	1.58	1.60	1.64	1.52	1.51	1.60	1.58	1.59	1.58	1.60	1.60	1.59	1.32	1.32	1.31
Fe^{3+}	0.00	0.00	0.00	0.00	0.00	0.00	0.00	0.00	0.00	0.00	0.00	0.00	0.00	0.00	0.00	0.00	0.00	0.00
Mg	0.00	0.00	0.00	0.00	0.00	0.00	0.00	0.00	0.00	0.00	0.00	0.00	0.00	0.00	0.00	0.00	0.00	0.00
Na	0.44	0.47	0.48	0.45	0.43	0.40	0.53	0.53	0.43	0.45	0.44	0.45	0.43	0.42	0.43	0.73	0.74	0.74
Ca	0.58	0.56	0.54	0.57	0.58	0.62	0.50	0.49	0.58	0.56	0.57	0.57	0.59	0.58	0.58	0.29	0.29	0.29
K	0.00	0.00	0.00	0.00	0.00	0.00	0.00	0.00	0.00	0.00	0.00	0.00	0.00	0.00	0.00	0.01	0.01	0.01
Ab	43.04	45.94	46.96	44.32	42.22	39.43	51.63	51.88	42.85	44.21	43.65	43.75	42.12	41.93	42.51	71.32	71.66	71.52
An	56.69	53.83	52.83	55.39	57.55	60.38	48.17	47.90	56.90	55.45	55.95	56.06	57.55	57.66	57.09	27.87	27.47	27.61
Or	0.27	0.23	0.21	0.29	0.23	0.19	0.21	0.23	0.26	0.35	0.40	0.20	0.33	0.42	0.41	0.81	0.87	0.87

0808-4: metadiorite Leonard Cape

wt.-%	#16	#17	#37	#38	#39	#41	#42	#43	#44	#45	#53
SiO_2	59.48	65.47	59.42	59.79	62.80	64.87	65.22	66.81	58.42	64.58	60.35
TiO_2	0.02	0.00	0.01	0.00	0.00	0.01	0.00	0.00	0.00	0.01	0.02
Al_2O_3	25.14	21.83	25.65	25.73	20.56	23.16	22.17	21.10	25.30	21.49	24.97
Fe_2O_3	0.10	0.05	0.17	0.06	0.07	0.24	0.02	0.01	0.05	0.01	0.11
MgO	0.00	0.00	0.00	0.01	0.02	0.13	0.00	0.02	0.00	0.00	0.00
CaO	6.17	1.30	6.77	6.74	0.35	1.13	0.54	0.15	6.68	1.28	5.93
Na_2O	8.43	11.56	8.14	8.08	4.33	8.99	11.92	11.99	8.25	11.54	8.61
K_2O	0.15	0.04	0.11	0.18	10.21	1.46	0.16	0.08	0.08	0.05	0.14
Σ	99.50	100.26	100.27	100.59	98.35	99.98	100.04	100.15	98.79	98.96	100.15
Si	2.67	2.87	2.65	2.65	2.90	2.85	2.87	2.92	2.64	2.87	2.69
Al^{IV}	1.33	1.13	1.35	1.35	1.12	1.20	1.15	1.09	1.35	1.13	1.31
Fe^{3+}	0.00	0.00	0.01	0.00	0.00	0.01	0.00	0.00	0.00	0.00	0.00
Mg	0.00	0.00	0.00	0.00	0.00	0.01	0.00	0.00	0.00	0.00	0.00
Na	0.73	0.98	0.70	0.70	0.39	0.77	1.02	1.02	0.72	1.00	0.74
Ca	0.30	0.06	0.32	0.32	0.02	0.05	0.03	0.01	0.32	0.06	0.28
K	0.01	0.00	0.01	0.01	0.60	0.08	0.01	0.00	0.01	0.00	0.01
Ab	70.60	93.92	68.11	67.77	38.50	85.00	96.70	98.90	68.77	93.99	71.85
An	28.55	5.85	31.29	31.26	1.74	5.89	2.43	0.69	30.78	5.75	27.36
Or	0.85	0.23	0.60	0.97	59.75	9.11	0.87	0.41	0.45	0.27	0.79

EMP analyses of plagioclase cores, rims, symplectites, inclusions and coronas from different hydrated rock types. Analyses were recalculated on the basis of 8 oxygens.

	0708-4: hydrated metagabbro Bolschoi Khed																
wt.-%	#6 core	#7 rim	#8 core	#14 core	#15 alt.	#16 alt.	#17 alt.	#19 alt.	#22 alt.	#25 alt.	#26 core	#27 core	#1	#2	#3	#4	#5
SiO_2	54.19	55.57	55.34	55.07	64.20	64.05	61.90	66.52	64.07	57.50	55.07	55.77	55.50	55.39	55.11	55.04	54.90
TiO^2	0.02	0.00	0.04	0.02	0.00	0.00	0.01	0.00	0.02	0.00	0.00	0.00	0.00	0.03	0.00	0.00	0.01
Al_2O_3	28.85	28.39	27.80	28.57	22.62	23.11	25.67	21.93	24.38	29.52	28.62	28.30	28.44	28.28	28.23	28.29	28.53
Fe_2O_3	0.16	0.03	0.09	0.11	0.00	0.13	0.03	0.01	0.23	0.27	0.15	0.08	0.04	0.02	0.06	0.03	0.06
MgO	0.02	0.02	0.00	0.02	0.02	0.05	0.05	0.01	0.03	0.59	0.02	0.00	0.00	0.00	0.00	0.00	0.00
CaO	10.41	10.08	9.78	10.31	2.55	2.12	1.79	0.92	1.23	0.94	10.40	10.22	10.00	10.05	10.08	10.33	10.15
Na_2O	5.87	6.10	6.07	5.87	10.22	9.88	7.86	11.20	8.59	5.90	5.55	5.79	5.90	5.86	5.71	5.82	5.95
K_2O	0.03	0.03	0.07	0.03	0.01	0.10	1.82	0.09	1.46	5.63	0.03	0.04	0.05	0.08	0.07	0.03	0.07
Σ	99.54	100.22	99.18	100.01	99.63	99.44	99.13	100.69	100.01	100.36	99.84	100.21	99.94	99.71	99.26	99.57	99.65
Si	2.46	2.50	2.51	2.48	2.84	2.83	2.75	2.90	2.81	2.57	2.48	2.50	2.50	2.50	2.50	2.49	2.48
Al^{IV}	1.54	1.50	1.49	1.52	1.18	1.20	1.35	1.13	1.26	1.56	1.52	1.50	1.51	1.50	1.51	1.51	1.52
Fe^{3+}	0.01	0.00	0.00	0.00	0.00	0.00	0.00	0.00	0.01	0.01	0.01	0.00	0.00	0.00	0.00	0.00	0.00
Mg	0.00	0.00	0.00	0.00	0.00	0.00	0.00	0.00	0.00	0.04	0.00	0.00	0.00	0.00	0.00	0.00	0.00
Na	0.52	0.53	0.53	0.51	0.88	0.85	0.68	0.95	0.73	0.51	0.49	0.50	0.52	0.51	0.50	0.51	0.52
Ca	0.51	0.49	0.48	0.50	0.12	0.10	0.09	0.04	0.06	0.05	0.50	0.49	0.48	0.49	0.49	0.50	0.49
K	0.00	0.00	0.00	0.00	0.00	0.01	0.10	0.01	0.08	0.32	0.00	0.00	0.00	0.01	0.00	0.00	0.00
Ab	50.41	52.18	52.71	50.67	87.82	88.85	78.24	95.17	83.99	58.28	49.04	50.49	51.48	51.08	50.41	50.40	51.27
An	49.43	47.67	46.90	49.14	12.12	10.54	9.87	4.33	6.63	5.13	50.77	49.28	48.22	48.45	49.20	49.41	48.36
Or	0.16	0.16	0.39	0.19	0.06	0.62	11.90	0.50	9.38	36.58	0.20	0.22	0.30	0.47	0.39	0.20	0.37

	0708-4: hydrated metagabbro Bolschoi Khed												1008-B2: hydrated metagabbro Kataransky Cape				
wt.-%	#6	#7	#8	#9	#15	#16	#17	#18	#30	#31	#32	#33	#1 core	#2	#5	#4	#3 rim
SiO_2	54.78	54.97	55.38	54.17	55.67	56.10	56.64	55.39	55.84	54.47	55.17	55.98	56.13	54.98	50.55	54.82	48.11
TiO^2	0.00	0.00	0.00	0.00	0.00	0.03	0.00	0.00	0.00	0.01	0.01	0.01	0.00	0.01	0.00	0.00	0.02
Al_2O_3	28.27	28.39	28.55	28.79	28.69	28.74	27.66	27.85	27.76	27.94	28.07	28.05	27.34	27.90	30.26	28.42	32.72
Fe_2O_3	0.12	0.09	0.30	0.09	0.00	0.03	0.04	0.07	0.03	0.13	0.11	0.15	0.05	0.06	0.08	0.07	0.17
MgO	0.01	0.00	0.00	0.01	0.00	0.00	0.01	0.00	0.00	0.00	0.00	0.01	0.00	0.02	0.02	0.01	0.01
CaO	9.91	10.05	10.10	10.16	10.46	10.45	9.60	10.67	10.27	11.01	10.91	10.30	9.83	10.53	14.03	11.03	16.20
Na_2O	6.24	6.09	5.96	5.89	5.98	6.03	6.36	5.72	5.97	5.50	5.48	5.84	6.37	5.94	3.96	5.71	2.58
K_2O	0.08	0.06	0.03	0.03	0.03	0.04	0.02	0.06	0.05	0.01	0.03	0.02	0.14	0.13	0.05	0.09	0.05
Σ	99.40	99.65	100.33	99.14	100.84	101.43	100.33	99.76	99.93	99.08	99.77	100.36	99.87	99.56	98.96	100.16	99.86
Si	2.48	2.49	2.49	2.46	2.49	2.49	2.54	2.50	2.52	2.48	2.49	2.51	2.53	2.49	2.33	2.47	2.21
Al^{IV}	1.51	1.51	1.51	1.54	1.51	1.50	1.46	1.48	1.47	1.50	1.49	1.48	1.45	1.49	1.64	1.51	1.77
Fe^{3+}	0.00	0.00	0.01	0.00	0.00	0.00	0.00	0.00	0.00	0.01	0.00	0.01	0.00	0.00	0.00	0.00	0.01
Mg	0.00	0.00	0.00	0.00	0.00	0.00	0.00	0.00	0.00	0.00	0.00	0.00	0.00	0.00	0.00	0.00	0.00
Na	0.55	0.53	0.52	0.52	0.52	0.52	0.55	0.50	0.52	0.49	0.48	0.51	0.56	0.52	0.35	0.50	0.23
Ca	0.48	0.49	0.49	0.50	0.50	0.50	0.46	0.52	0.50	0.54	0.53	0.50	0.48	0.51	0.69	0.53	0.80
K	0.00	0.00	0.00	0.00	0.00	0.00	0.00	0.00	0.00	0.00	0.00	0.00	0.01	0.01	0.00	0.01	0.00
Ab	53.05	52.13	51.55	51.11	50.74	50.94	54.46	49.06	51.13	47.43	47.53	50.55	53.55	50.16	33.73	48.15	22.32
An	46.52	47.56	48.25	48.70	49.08	48.81	45.40	50.60	48.60	52.49	52.28	49.32	45.69	49.12	65.98	51.37	77.41
Or	0.43	0.31	0.20	0.19	0.18	0.25	0.14	0.34	0.28	0.08	0.18	0.14	0.75	0.72	0.30	0.49	0.27

1008-B2: hydrated metagabbro Kataransky Cape

wt.-%	#8 sympl.	#13 sympl.	#14 sympl.	#15 sympl.	#16 sympl.	#17 sympl.	#20 rim	#21 core	#29 sympl.	#30 core	#31	#32	#33	#34 rim	#35
SiO_2	50.35	51.38	48.86	52.47	48.74	48.97	51.04	52.24	47.46	55.90	55.46	55.39	54.18	52.58	55.84
TiO^2	0.01	0.00	0.00	0.01	0.02	0.00	0.03	0.02	0.00	0.00	0.02	0.02	0.02	0.00	0.00
Al_2O_3	31.40	31.45	33.15	30.70	33.27	33.26	31.41	30.76	32.52	27.92	28.21	28.54	28.29	30.01	28.57
Fe_2O_3	0.16	0.21	0.21	0.17	0.19	0.23	0.16	0.09	0.24	0.07	0.08	0.07	0.04	0.08	0.05
MgO	0.01	0.01	0.00	0.01	0.00	0.01	0.00	0.01	0.00	0.00	0.00	0.01	0.01	0.01	0.00
CaO	14.61	13.76	15.87	12.85	15.90	15.95	13.69	12.90	15.97	10.33	10.38	10.51	10.87	12.13	10.47
Na_2O	3.59	4.04	2.72	4.45	2.74	2.86	4.00	4.60	2.55	6.09	5.88	5.87	5.59	4.89	5.96
K_2O	0.06	0.06	0.04	0.06	0.02	0.03	0.06	0.07	0.03	0.15	0.15	0.15	0.11	0.09	0.15
Σ	100.18	100.92	100.85	100.72	100.89	101.31	100.39	100.68	98.77	100.45	100.19	100.55	99.12	99.80	101.04
Si	2.29	2.32	2.22	2.36	2.21	2.22	2.31	2.36	2.20	2.51	2.50	2.48	2.47	2.39	2.49
Al^{IV}	1.69	1.67	1.77	1.63	1.78	1.77	1.68	1.64	1.78	1.48	1.50	1.51	1.52	1.61	1.50
Fe^{3+}	0.01	0.01	0.01	0.01	0.01	0.01	0.01	0.00	0.01	0.00	0.00	0.00	0.00	0.00	0.00
Mg	0.00	0.00	0.00	0.00	0.00	0.00	0.00	0.00	0.00	0.00	0.00	0.00	0.00	0.00	0.00
Na	0.32	0.35	0.24	0.39	0.24	0.25	0.35	0.40	0.23	0.53	0.51	0.51	0.49	0.43	0.52
Ca	0.71	0.67	0.77	0.62	0.77	0.77	0.67	0.62	0.79	0.50	0.50	0.51	0.53	0.59	0.50
K	0.00	0.00	0.00	0.00	0.00	0.00	0.00	0.00	0.00	0.01	0.01	0.01	0.01	0.01	0.01
Ab	30.66	34.60	23.61	38.36	23.75	24.49	34.44	39.05	22.41	51.19	50.21	49.85	47.88	41.94	50.30
An	69.01	65.07	76.17	61.27	76.13	75.37	65.21	60.56	77.45	48.00	48.95	49.31	51.48	57.56	48.87
Or	0.33	0.33	0.23	0.36	0.12	0.15	0.35	0.39	0.15	0.81	0.84	0.84	0.63	0.50	0.82

	1008-B2: hydrated metagabbro Kataransky Cape								**1008-B1: hydrated metagabbro Kataransky Cape**							
wt.-%	#36 core	#37	#38	#39 rim	#47	#51 sympl.	#52 sympl.	#53 sympl.	#1 core	#2	#3	#4	#5	#6 rim	#11	#12 alt.
SiO_2	55.55	55.81	55.52	54.40	55.96	45.32	47.37	46.14	54.54	55.80	57.11	57.17	57.02	57.03	56.66	58.84
TiO^2	0.01	0.00	0.00	0.00	0.00	0.02	0.00	0.00	0.01	0.00	0.00	0.01	0.00	0.03	0.00	0.00
Al_2O_3	28.38	28.43	28.36	28.59	28.69	33.63	33.41	34.23	29.20	28.17	27.45	27.50	27.45	27.04	27.42	25.84
Fe_2O_3	0.04	0.02	0.10	0.10	0.06	0.22	0.19	0.19	0.06	0.08	0.04	0.05	0.08	0.15	0.13	0.05
MgO	0.00	0.01	0.00	0.01	0.01	0.01	0.00	0.01	0.00	0.00	0.00	0.00	0.00	0.00	0.01	0.01
CaO	10.34	10.48	10.31	11.12	10.28	17.10	16.18	16.77	11.35	10.19	9.23	9.29	8.97	9.19	9.53	7.31
Na_2O	5.85	5.94	5.87	5.47	5.88	1.82	2.29	1.95	5.36	5.97	6.58	6.56	6.59	6.60	6.57	7.11
K_2O	0.12	0.11	0.13	0.10	0.10	0.04	0.04	0.06	0.15	0.19	0.22	0.15	0.29	0.08	0.11	0.18
Σ	100.29	100.80	100.28	99.79	100.96	98.16	99.47	99.35	100.68	100.42	100.63	100.73	100.41	100.11	100.43	99.36
Si	2.49	2.50	2.49	2.46	2.49	2.13	2.18	2.14	2.45	2.50	2.55	2.55	2.55	2.56	2.54	2.64
Al^{IV}	1.50	1.50	1.50	1.53	1.51	1.86	1.81	1.87	1.55	1.49	1.44	1.45	1.45	1.43	1.45	1.37
Fe^{3+}	0.00	0.00	0.00	0.00	0.00	0.01	0.01	0.01	0.00	0.00	0.00	0.00	0.00	0.01	0.00	0.00
Mg	0.00	0.00	0.00	0.00	0.00	0.00	0.00	0.00	0.00	0.00	0.00	0.00	0.00	0.00	0.00	0.00
Na	0.51	0.52	0.51	0.48	0.51	0.17	0.21	0.18	0.47	0.52	0.57	0.57	0.57	0.57	0.57	0.62
Ca	0.50	0.50	0.50	0.54	0.49	0.86	0.80	0.83	0.55	0.49	0.44	0.44	0.43	0.44	0.46	0.35
K	0.01	0.01	0.01	0.01	0.01	0.00	0.00	0.00	0.01	0.01	0.01	0.01	0.02	0.00	0.01	0.01
Ab	50.22	50.31	50.39	46.83	50.56	16.09	20.34	17.33	45.69	50.91	55.65	55.59	56.12	56.26	55.20	63.05
An	49.07	49.09	48.90	52.62	48.87	83.70	79.43	82.30	53.47	48.01	43.13	43.55	42.23	43.30	44.22	35.87
Or	0.71	0.59	0.71	0.55	0.58	0.22	0.23	0.37	0.85	1.08	1.22	0.86	1.65	0.44	0.58	1.08

1008-B1: hydrated metagabbro Kataransky Cape

wt.-%	#16 alt.	#17 alt.	#18 core	#19	#20	#21	#22	#23 rim	#26 incl.	#27 incl.	#32 vein	#33 vein	#36 vein	#37 vein	#50 vein	#51 vein	#56 vein
SiO_2	56.32	57.10	55.15	54.85	55.91	55.80	55.66	55.90	57.09	56.74	58.48	55.29	66.00	60.58	57.05	57.25	57.60
TiO^2	0.00	0.01	0.01	0.02	0.01	0.01	0.00	0.00	0.00	0.00	0.00	0.00	0.00	0.00	0.00	0.00	0.00
Al_2O_3	27.75	26.47	28.58	28.28	27.74	27.73	27.25	27.41	27.64	27.73	26.92	26.41	23.02	25.27	27.54	27.56	27.34
Fe_2O_3	0.05	0.07	0.13	0.06	0.06	0.05	0.05	0.13	0.12	0.14	0.05	0.07	0.00	0.00	0.07	0.04	0.00
MgO	0.00	0.00	0.00	0.00	0.01	0.00	0.01	0.00	0.00	0.00	0.01	0.00	0.02	0.01	0.00	0.00	0.00
CaO	9.94	8.96	10.64	10.54	9.91	9.92	9.51	9.42	9.23	9.44	8.33	11.53	2.33	5.74	9.09	9.11	8.08
Na_2O	6.13	6.73	5.67	5.67	6.11	6.20	6.20	6.49	6.64	6.40	7.16	6.19	9.95	8.15	6.81	6.63	7.20
K_2O	0.17	0.16	0.17	0.17	0.17	0.19	0.19	0.08	0.14	0.12	0.05	0.03	0.14	0.09	0.09	0.11	0.05
Σ	100.36	99.51	100.35	99.59	99.92	99.90	98.89	99.44	100.86	100.58	100.99	99.52	101.46	99.85	100.66	100.70	100.28
Si	2.53	2.58	2.48	2.48	2.52	2.52	2.53	2.53	2.54	2.54	2.59	2.52	2.86	2.69	2.55	2.55	2.57
Al^{IV}	1.47	1.41	1.51	1.51	1.47	1.47	1.46	1.46	1.45	1.46	1.41	1.42	1.17	1.32	1.45	1.45	1.44
Fe^{3+}	0.00	0.00	0.00	0.00	0.00	0.00	0.00	0.00	0.00	0.01	0.00	0.00	0.00	0.00	0.00	0.00	0.00
Mg	0.00	0.00	0.00	0.00	0.00	0.00	0.00	0.00	0.00	0.00	0.00	0.00	0.00	0.00	0.00	0.00	0.00
Na	0.53	0.59	0.49	0.50	0.53	0.54	0.55	0.57	0.57	0.55	0.62	0.55	0.83	0.70	0.59	0.57	0.62
Ca	0.48	0.43	0.51	0.51	0.48	0.48	0.46	0.46	0.44	0.45	0.40	0.56	0.11	0.27	0.43	0.44	0.39
K	0.01	0.01	0.01	0.01	0.01	0.01	0.01	0.01	0.01	0.01	0.00	0.00	0.01	0.01	0.01	0.01	0.00
Ab	52.24	57.09	48.65	48.85	52.25	52.51	53.52	55.26	56.12	54.71	60.72	49.22	87.85	71.63	57.28	56.53	61.56
An	46.82	41.99	50.41	50.17	46.80	46.43	45.40	44.29	43.07	44.60	39.02	50.63	11.35	27.86	42.22	42.88	38.16
Or	0.93	0.92	0.95	0.98	0.95	1.05	1.09	0.45	0.80	0.69	0.26	0.15	0.80	0.51	0.50	0.59	0.28

1008-B1: hydrated metagabbro Kataransky Cape

wt.-%	#57 vein	#59 vein	#60 vein	#63 vein	#65 vein	#66 vein	#4	#5	#7	#9	#10	#11	#12	#13	#14	#26	#27
SiO_2	55.80	56.04	57.07	56.65	57.10	56.04	54.75	54.01	53.74	55.45	55.46	55.50	55.90	56.87	57.55	55.90	56.49
TiO^2	0.00	0.02	0.01	0.01	0.01	0.00	0.03	0.00	0.00	0.00	0.01	0.00	0.00	0.00	0.00	0.00	0.01
Al_2O_3	27.30	27.94	27.69	27.50	27.25	26.86	28.99	28.90	28.77	28.79	28.73	28.33	28.18	27.69	27.13	28.11	28.30
Fe_2O_3	0.01	0.04	0.05	0.07	0.00	0.02	0.06	0.08	0.06	0.03	0.08	0.05	0.05	0.12	0.18	0.07	0.00
MgO	0.00	0.01	0.00	0.00	0.01	0.00	0.00	0.00	0.00	0.00	0.00	0.01	0.00	0.00	0.02	0.00	0.00
CaO	9.07	9.69	9.11	9.51	8.97	9.47	10.66	10.56	10.74	10.77	10.57	10.13	10.02	9.38	8.81	9.81	9.83
Na_2O	6.80	6.50	6.80	6.57	6.91	6.64	5.67	5.56	5.67	5.70	5.64	5.85	5.92	6.46	6.86	6.00	6.05
K_2O	0.08	0.06	0.06	0.08	0.06	0.07	0.16	0.16	0.15	0.14	0.15	0.14	0.13	0.08	0.05	0.17	0.16
Σ	99.07	100.29	100.78	100.39	100.31	99.11	100.34	99.29	99.13	100.89	100.64	100.03	100.21	100.60	100.59	100.06	100.85
Si	2.53	2.52	2.54	2.54	2.56	2.54	2.46	2.46	2.45	2.48	2.48	2.50	2.51	2.54	2.57	2.51	2.52
Al^{IV}	1.46	1.48	1.45	1.45	1.44	1.44	1.54	1.55	1.55	1.52	1.52	1.50	1.49	1.46	1.43	1.49	1.49
Fe^{3+}	0.00	0.00	0.00	0.00	0.00	0.00	0.00	0.00	0.00	0.00	0.00	0.00	0.00	0.00	0.01	0.00	0.00
Mg	0.00	0.00	0.00	0.00	0.00	0.00	0.00	0.00	0.00	0.00	0.00	0.00	0.00	0.00	0.00	0.00	0.00
Na	0.60	0.57	0.59	0.57	0.60	0.58	0.49	0.49	0.50	0.49	0.49	0.51	0.52	0.56	0.59	0.52	0.52
Ca	0.44	0.47	0.44	0.46	0.43	0.46	0.51	0.51	0.52	0.52	0.51	0.49	0.48	0.45	0.42	0.47	0.47
K	0.01	0.00	0.00	0.00	0.00	0.00	0.01	0.01	0.01	0.01	0.01	0.01	0.01	0.00	0.00	0.01	0.01
Ab	57.28	54.66	57.27	55.33	58.02	55.71	48.60	48.35	48.47	48.52	48.71	50.69	51.28	55.22	58.33	52.01	52.23
An	42.25	45.02	42.41	44.24	41.63	43.93	50.49	50.72	50.71	50.68	50.42	48.49	47.97	44.35	41.42	47.01	46.84
Or	0.47	0.33	0.32	0.44	0.35	0.36	0.91	0.92	0.83	0.80	0.87	0.82	0.76	0.43	0.25	0.98	0.93

	0308-K2: hydrated dyke Nikolkina Island												**0308-K3: vein Nikolkina I.**		
wt.-%	#2	#3	#7	#31	#32	#10	#27	#28	#29	#30	#35	#36	#29 vein	#30 vein	#31 vein
SiO_2	60.05	61.37	60.99	60.48	65.53	61.30	65.63	60.64	61.73	61.13	62.13	60.59	60.22	64.11	63.63
TiO^2	0.76	0.12	0.02	0.00	0.01	0.02	0.01	0.00	0.01	0.00	0.01	0.02	0.00	0.00	0.01
Al_2O_3	24.86	25.19	25.20	24.49	23.74	24.85	23.25	25.21	24.73	24.78	24.11	24.44	25.39	21.89	22.97
Fe_2O_3	0.91	0.19	0.05	0.16	0.11	0.28	0.19	0.17	0.08	0.10	0.13	0.22	0.03	0.03	0.00
MgO	0.00	0.01	0.01	0.02	0.01	0.00	0.06	0.00	0.00	0.00	0.00	0.00	0.00	0.00	0.00
CaO	6.04	5.99	6.23	6.00	1.32	6.20	1.42	6.11	5.73	5.66	5.07	6.16	6.99	3.33	3.98
Na_2O	8.72	8.70	8.68	8.58	9.89	8.29	9.85	8.37	8.63	8.47	8.71	8.36	8.35	10.13	10.07
K_2O	0.03	0.06	0.09	0.06	0.91	0.05	0.77	0.08	0.08	0.11	0.16	0.10	0.06	0.07	0.06
Σ	101.38	101.63	101.27	99.79	101.52	100.99	101.16	100.60	100.98	100.25	100.32	99.89	101.03	99.57	100.73
Si	2.65	2.69	2.68	2.70	2.84	2.70	2.85	2.68	2.72	2.71	2.75	2.70	2.66	2.84	2.80
Al^{IV}	1.29	1.30	1.31	1.29	1.21	1.29	1.19	1.32	1.28	1.29	1.26	1.28	1.32	1.14	1.19
Fe^{3+}	0.03	0.01	0.00	0.01	0.00	0.01	0.01	0.01	0.00	0.00	0.00	0.01	0.00	0.00	0.00
Mg	0.00	0.00	0.00	0.00	0.00	0.00	0.00	0.00	0.00	0.00	0.00	0.00	0.00	0.00	0.00
Na	0.75	0.74	0.74	0.74	0.83	0.71	0.83	0.72	0.74	0.73	0.75	0.72	0.72	0.87	0.86
Ca	0.29	0.28	0.29	0.29	0.06	0.29	0.07	0.29	0.27	0.27	0.24	0.29	0.33	0.16	0.19
K	0.00	0.00	0.01	0.00	0.05	0.00	0.04	0.01	0.01	0.01	0.01	0.01	0.00	0.00	0.00
						5.00	4.99	5.02	5.01	5.01	5.00	5.02	5.04	5.02	5.04
Ab	72.17	72.17	71.22	71.83	88.20	70.54	88.42	70.94	72.83	72.59	75.00	70.64	68.18	84.29	81.79
An	27.63	27.44	28.30	27.78	6.48	29.19	7.03	28.59	26.70	26.81	24.10	28.80	31.53	15.31	17.88
Or	0.19	0.39	0.48	0.39	5.31	0.26	4.56	0.47	0.47	0.59	0.90	0.57	0.30	0.40	0.33

	0808-5: hydrated metadiorite Leonars Cape																**0808-6**	
wt.-%	#8 core	#9	#10	#11 rim	#17	#18 alt.	#19	#24	#42	#43	#45	#55	#56	#57 alt.	#58 alt.	#59 alt.	#13	#14 alt.
SiO_2	58.76	58.67	58.23	57.59	59.18	63.08	60.45	59.71	59.98	60.42	60.29	59.97	60.46	67.74	63.06	66.51	59.34	67.25
TiO^2	0.00	0.03	0.00	0.00	0.00	0.00	0.00	0.01	0.00	0.00	0.02	0.01	0.01	0.02	0.01	0.03	0.04	0.02
Al_2O_3	25.82	25.43	25.94	26.10	26.15	24.60	25.69	26.41	25.36	26.19	25.89	25.71	25.71	22.53	25.41	23.64	25.31	21.16
Fe_2O_3	0.08	0.01	0.13	0.24	0.04	0.12	0.15	0.18	0.05	0.07	0.06	0.03	0.06	0.01	0.19	0.07	0.22	0.08
MgO	0.00	0.01	0.00	0.00	0.00	0.05	0.01	0.00	0.01	0.00	0.00	0.00	0.02	0.00	0.08	0.00	0.01	0.00
CaO	6.55	6.49	6.72	7.02	7.68	1.23	6.64	7.32	6.68	6.71	6.82	6.87	6.80	1.17	0.94	1.16	6.78	0.25
Na_2O	8.37	8.31	8.24	8.04	7.57	8.65	8.26	7.99	8.31	8.00	8.20	8.03	8.33	10.43	7.72	10.14	8.44	12.21
K_2O	0.10	0.06	0.09	0.06	0.08	1.79	0.07	0.07	0.09	0.09	0.10	0.10	0.10	0.23	2.63	0.62	0.05	0.06
Σ	99.68	99.02	99.35	99.06	100.71	99.53	101.28	101.69	100.50	101.49	101.38	100.73	101.49	102.12	100.03	102.17	100.17	101.04
Si	2.63	2.65	2.62	2.60	2.63	2.79	2.66	2.63	2.66	2.65	2.65	2.66	2.66	2.90	2.78	2.85	2.65	2.92
Al^{IV}	1.36	1.35	1.38	1.39	1.37	1.28	1.33	1.37	1.33	1.36	1.34	1.34	1.33	1.14	1.32	1.20	1.33	1.08
Fe^{3+}	0.00	0.00	0.00	0.01	0.00	0.00	0.01	0.01	0.00	0.00	0.00	0.00	0.00	0.00	0.01	0.00	0.01	0.00
Mg	0.00	0.00	0.00	0.00	0.00	0.00	0.00	0.00	0.00	0.00	0.00	0.00	0.00	0.00	0.01	0.00	0.00	0.00
Na	0.73	0.73	0.72	0.70	0.65	0.74	0.71	0.68	0.72	0.68	0.70	0.69	0.71	0.87	0.66	0.84	0.73	1.03
Ca	0.32	0.31	0.32	0.34	0.37	0.06	0.31	0.35	0.32	0.32	0.32	0.33	0.32	0.05	0.04	0.05	0.32	0.01
K	0.01	0.00	0.01	0.00	0.01	0.10	0.00	0.00	0.01	0.01	0.01	0.01	0.01	0.01	0.15	0.03	0.00	0.00
	5.05	5.04	5.05	5.05	5.02	4.99	5.02	5.03	5.03	5.01	5.03	5.02	5.03	4.97	4.96	4.98	5.05	5.05
Ab	69.43	69.66	68.59	67.23	63.80	82.34	68.97	66.14	68.89	68.01	68.15	67.51	68.53	92.90	77.43	90.60	69.07	98.58
An	30.04	30.04	30.92	32.45	35.76	6.48	30.63	33.50	30.63	31.49	31.32	31.91	30.91	5.78	5.22	5.74	30.66	1.12
Or	0.53	0.30	0.50	0.31	0.45	11.18	0.40	0.36	0.49	0.50	0.53	0.58	0.57	1.32	17.34	3.67	0.28	0.31

0808-6: hydrated metadiorite Leonars Cape

wt.-%	#15 alt.	#16 alt.	#17 alt.	#18 alt.	#22 kfsp	#23 kfsp	#27 kfsp	#29	#30	#31 alt.	#34 alt.	#35
SiO_2	64.79	59.14	66.88	63.91	63.56	63.57	63.07	60.13	62.08	61.61	58.53	60.25
TiO^2	0.00	0.04	0.02	0.00	0.01	0.00	0.15	0.00	0.00	0.07	0.03	0.00
Al_2O_3	22.56	24.32	21.12	22.63	19.35	18.55	19.05	25.80	26.11	24.96	28.27	25.78
Fe_2O_3	0.27	0.13	0.11	0.11	0.28	0.22	0.09	0.06	0.14	1.48	0.25	0.10
MgO	0.06	0.00	0.00	0.02	0.01	0.00	0.00	0.00	0.04	0.33	0.08	0.00
CaO	0.55	5.69	0.31	1.87	0.00	0.02	0.08	6.59	4.15	2.37	3.54	6.70
Na_2O	10.61	9.07	12.50	11.06	0.15	0.20	0.21	8.52	8.76	7.94	6.58	8.51
K_2O	1.04	0.04	0.08	0.20	16.46	16.59	16.48	0.04	0.44	2.50	2.63	0.06
Σ	99.88	98.44	101.03	99.81	99.82	99.15	99.13	101.13	101.70	101.26	99.91	101.40
Si	2.86	2.68	2.91	2.83	2.95	2.97	2.95	2.65	2.70	2.72	2.61	2.65
Al^{IV}	1.17	1.30	1.08	1.18	1.06	1.02	1.05	1.34	1.34	1.30	1.49	1.34
Fe^{3+}	0.01	0.00	0.00	0.00	0.01	0.01	0.00	0.00	0.01	0.05	0.01	0.00
Mg	0.00	0.00	0.00	0.00	0.00	0.00	0.00	0.00	0.00	0.02	0.01	0.00
Na	0.91	0.80	1.06	0.95	0.01	0.02	0.02	0.73	0.74	0.68	0.57	0.73
Ca	0.03	0.28	0.02	0.09	0.00	0.00	0.00	0.31	0.19	0.11	0.17	0.32
K	0.06	0.00	0.01	0.01	0.98	0.99	0.98	0.00	0.02	0.14	0.15	0.00
	5.04	5.07	5.07	5.06	5.01	5.01	5.02	5.04	5.01	5.02	5.00	5.04
Ab	91.47	74.07	98.21	90.49	1.39	1.78	1.87	69.92	77.26	72.85	64.10	69.45
An	2.64	25.69	1.36	8.46	0.02	0.11	0.38	29.88	20.21	12.04	19.05	30.21
Or	5.89	0.24	0.44	1.05	98.59	98.11	97.75	0.20	2.53	15.12	16.85	0.35